# Simulation and Data Analysis for LISA (Instrumental Modeling, Time-Delay Interferometry, Noise-Reduction Performance Study, and Discrimination of Transient Gravitational Signals)

Jean-Baptiste Bayle

École Doctorale 560 :
Sciences de la Terre et de l'Environnement et Physique de l'Univers

Thèse de doctorat

de l'Université de Paris préparée à l'Université Paris Diderot
au laboratoire Astroparticules et Cosmologie

# Simulation and Data Analysis for LISA

## Instrumental Modeling, Time-Delay Interferometry, Noise-Reduction Performance Study, and Discrimination of Transient Gravitational Signals

*présentée par*

**Jean-Baptiste Bayle**

*Sous la direction de*
**Antoine Petiteau**

Soutenue publiquement le 21 octobre 2019 devant le jury composé de :

| | |
|---|---|
| Président | **Sylvain Chaty** (CEA, APC, France) |
| Rapporteur | **Gerhard Heinzel** (Albert Einstein Institute, Allemagne) |
| Rapporteur | **Michele Vallisneri** (Jet Propulsion Laboratory, NASA, États-Unis) |
| Directeur de thèse | **Antoine Petiteau** (Université Paris Diderot, APC, France) |
| Examinatrice | **Frédérique Marion** (Université Savoie Mont-Blanc, LAPP, France) |
| Examinatrice | **Isabelle Petitbon** (CNES, France) |
| Examinateur | **Gilles Theureau** (Observatoire de Paris, LPC2E, France) |

To Pierre Binétruy.

# Abstract

The Laser Interferometer Space Antenna is a European Space Agency mission that aims to measure gravitational waves in the millihertz range. Three spacecraft are placed in a quasi-equilateral triangular formation whose barycenter trails the Earth on its heliocentric orbit. Laser beams are exchanged to monitor pico-metric variations between the test masses due to gravitational waves. Because various instrumental noise sources couple to the measurements, several data processing techniques are used to reduce them before we can extract gravitational-wave signals.

We propose a realistic instrumental model to study these noise-reduction algorithms. We investigate how the main noise sources appear in the measurements and work out their residuals in almost noise-free combinations. To validate these results, we develop a flexible numerical simulation tool that aims to generate realistic measurements: LISANode propagates noise time series between the spacecraft and in the optical benches, all the way down to the phasemeters and the on-board computers. It also computes the response to gravitational waves. LISANode is capable of executing the main noise-reduction algorithms, including the computation of Time-Delay Interferometry laser noise-free combinations, as well as clock-calibrated combinations.

As we account for instrumental and numerical imperfections, noises do not exactly vanish in the final combinations. In particular, we study the performance hit of the constellation flexing and the on-board data processing on the laser-noise reduction. We model the *flexing-filtering* coupling and propose a technique to mitigate this effect. Moreover, we derive exact clock-noise calibration expressions. Simulations are used to validate these results and confirm that the dominant sources of noise can be reduced to the required levels.

We also investigate machine-learning techniques to discriminate between instrumental glitches and transient gravitational signals. Analytic studies show that both appear differently in noise-free combinations and experiments suggest that some neural networks are capable of distinguishing between them.

**Associated Keywords** *gravitational wave, gravitational astronomy, LISA, LISA Pathfinder, time-delay interferometry, TDI, simulation, calibration, noise reduction.*

# Résumé

Laser Interferometer Space Antenna est une mission de l'Agence Spatiale Européenne visant à mesurer les ondes gravitationnelles dans le domaine millimétrique. Trois satellites en formation triangulaire autour du Soleil s'échangent des faisceaux lasers. Les variations de distances entre masses d'épreuve, dues aux ondes gravitationnelles, sont mesurées au picomètre près. Plusieurs algorithmes de réduction des bruits instrumentaux qui contaminent les mesures sont utilisés avant l'extraction des signaux gravitationnels.

Afin d'évaluer la performance de ces algorithmes, nous étudions la manière dont les bruits instrumentaux apparaissent dans les mesures, ainsi que leurs résidus après calibration. Un outil de simulation numérique flexible, destiné à générer les mesures de manière réaliste, permet de valider ces résultats. En effet, LISANode propage les séries temporelles de bruit entre les satellites et sur les bancs optiques, jusqu'aux phasemètres et aux ordinateurs embarqués. Il calcule aussi la réponse aux ondes gravitationnelles. Par ailleurs, LISANode permet de générer les combinaisons Time-Delay Interferometry exemptes de bruit laser, ainsi que la calibration pour les bruits d'horloge.

Malheureusement, ces bruits ne disparaissent pas totalement si l'on tient compte des imperfections instrumentales et numériques. Nous étudions en particulier l'impact de la déformation de la constellation, ainsi que du traitement des données en vol. Nous modélisons le couplage *déformation-filtrage* et proposons une technique permettant de réduire cet effet. En outre, nous proposons une méthode de calibration exacte des bruits d'horloge. Les simulations permettent de valider ces résultats, et confirment la possibilité de réduire les bruits dominants aux niveaux requis.

Nous considérons aussi les techniques d'apprentissage automatique pour discriminer les artéfacts instrumentaux et les signaux gravitationnels courts. Une étude analytique montre un couplage différemment dans les mesures, et les premières expériences suggèrent que certains réseaux de neurones peuvent distinguer ces deux types de signaux.

**Mot-clef associés** *onde gravitationnelle, astronomie gravitationnelle, LISA, LISA Pathfinder, interférométrie retardée, TDI, simulation, calibration, réduction de bruit.*

*– La gravité est-elle essentielle ?*
*– Oui, la gravité est nécessaire sinon le punch s'envole*
*et l'on est obligé de courir après avec le bol.*
Le cœur a ses raisons

# Contents

# List of Figures

# Acronyms

**ADC** Analog-to-Digital Converter. 87, 103, 159, 162, 200, 205, 214

**APC** AstroParticule et Cosmologie Laboratory. 131

**ASD** Amplitude Spectral Density. 76, 94

**DFACS** Drag-Free Attitude Control System. 85, 202

**DPLL** Digital Phase-Locked Loop. 103, 105

**EM** Electromagnetic. 93, 94, 97, 104

**EMRI** Extreme Mass-Ratio Inspiral. 32, 33, 197

**EOM** Electro-Optic Modulator. 166, 167

**ESA** European Space Agency. 22, 23, 27, 38, 72, 107, 230

**FIR** Finite Impulse Response. 95, 146, 148, 177

**GRS** Gravitational Reference System. 89

**IIR** Infinite Impulse Response. 147

**LCM** Least Common Multiple. 216

**LDC** LISA Data Challenge. 76, 123, 198

**LISA** Laser Interferometer Space Antenna. 1, 21–24, 26–30, 32–34, 36–41, 59, 62, 64, 65, 67, 74, 75, 77–80, 83, 84, 86, 99, 103, 111, 115, 124, 126, 131, 132, 136, 147–149, 151, 154, 156, 159, 166, 175, 177, 182, 183, 189–191, 195, 197–199, 217, 247, 259, 269, 274, 279, 281, 283, 304, 307

**LOT** LISA-On-Table. 131

**LTPDA** LISA Technology Package Data Analysis. 82

**MOSA** Movable Optical Sub-Assembly. 65, 88, 89, 132, 248, 250–257, 263, 264, 294–297, 300, 301, 304, 305, 307, 308, 317–319

**OMS** Optical Metrology System. 85, 86, 89, 99, 101, 102, 106

**PSD** Power Spectral Density. 75, 82–84, 86–88, 111, 119, 122, 162, 164, 177, 207, 208

**RMS** Root Mean Square. 87

**SSB** Solar-System Barycenter. 73, 78, 79, 81, 289–292

**TCB** Barycentric Coordinate Time. 199–201, 203–218

**TDI** Time-Delay Interferometry. 40, 64, 83, 103, 111–113, 115–118, 120, 123–126, 128, 131, 132, 134–136, 138, 144, 145, 148–151, 154, 156, 159, 160, 163–165, 170, 175, 177, 182–184, 189, 195, 197, 198, 268, 293, 294, 300, 304, 307, 311, 321, 322

**TDIR** Time-Delay Interferometry Ranging. 128

**UFLIS** University of Florida LISA Simulator. 131

**USO** Ultra-Stable Oscillator. 87–89, 103, 107, 159–161, 176, 200, 217, 218

# Chapter 1

# Introduction

In this introductory chapter, I briefly describe how gravitational waves naturally arise in the framework of the General Theory of Relativity when one considers small perturbations of the metric in an almost flat spacetime. I then explore their main properties, and their effect on matter using the canonical example of a ring of particles. In the second part, I present the past and ongoing efforts to observe gravitational waves and the various associated techniques. I describe in particular detection using light interferometry used for the current ground-based detectors LIGO and Virgo, as well as future detectors such as the space-based Laser Interferometer Space Antenna (LISA) mission. For this last experiment, I give a brief historical overview of the mission, as well as of the launch and success of the technological demonstrator LISA Pathfinder. In the last section, I present the various astrophysical and cosmological sources of gravitational waves that we expect to observe with LISA. For each of these sources, I attempt to sketch the underlying current models, the characteristics of the associated gravitational radiations, as well as the main measurements that LISA will be able to perform. This gives me a good opportunity to build the science case of the LISA mission, by outlining the scientific objectives associated with each of these sources.

## 1.1 Gravitational Waves

### 1.1.1 Rise and Fall of Newton's Law of Universal Gravitation

For more than two centuries, Isaac Newton's Law of Universal Gravitation has set a solid theoretical basis for mechanics. A great number of natural phenomena, that were thought

unrelated, could be explained and predicted with great precision within a unified framework. The theory uses a few key concepts that are now the core of classical mechanics, such as inertia, acceleration, and forces. The motion of a cannonball, that of the Moon around the Earth, and the positions of the planets in our sky are some examples of what could be computed using Newton's theory of gravitation.

During the $19^{\text{th}}$ century, several theoretical and observational concerns had been raised regarding Newton's Law of Universal Gravitation. Newton himself was uncomfortable with the concept of instantaneous action at a distance, without any identified mediator. In 1693, he wrote [Ein93]: "It is inconceivable that inanimate brute matter should, without the mediation of something else which is not material, operate upon and affect other matter without mutual contact... That one body may act upon another at a distance through a vacuum without the mediation of anything else, by and through which their action and force may be conveyed from one another, is to me so great an absurdity that, I believe, no man who has in philosophic matters a competent faculty of thinking could ever fall into it." Besides, accumulated years of astronomical observations showed that the orbit of Mercury has a non-vanishing precession, *i.e.* that its perihelion advances slightly after each rotation around the Sun. Newtonian mechanics, accounting for the influence of other planets in the Solar System as well as the oblateness of the Sun, cannot explain this mismatch of about $43''$ (arc-second) per century.

In physics, it is a well-established procedure that two main families of hypothesis are proposed when observations are incompatible with the mainly accepted theory. On the one hand, ontological proposals attempt to resolve the theoretical discrepancy by assuming the existence of a new entity, which is yet to be observed. Among those proposals, the presence of an undetected planet whose mass supposedly perturbs Mercury's orbit; after numerous attempts to observe such a planet, this idea, like many others, was discarded. On the other hand, legislative solutions suggest to revise or replace the mainstream theory to make it compatible with the new observations. Among such proposed new theories, the General Theory of Relativity provided a definitive explanation.

### 1.1.2 Einstein's General Theory of Relativity

Albert Einstein proposed in 1915 [Ein15] a new interpretation of gravity, compatible with his Special Theory of Relativity. In this framework, spacetime is no longer flat and described by a Minkowski metric, but instead curved by its mass and energy content. The curvature of spacetime drives in turn the trajectory of free-falling bodies. The latter follow geodesics, or lines of shortest distance, which are no longer straight lines on a curved spacetime. One

interprets these curved trajectories as the effect of the gravitational force. Paraphrasing a famous John Wheeler's quote, this is often summarized as follows: matter tells spacetime how to curve, and spacetime tells matter how to move.

Einstein's field equations relate the curvature of spacetime, expressed through the metric tensor $g_{\mu\nu}$, with the stress-energy tensor $T_{\mu\nu}$,

$$R_{\mu\nu} - \frac{1}{2} R g_{\mu\nu} = T_{\mu\nu} \,, \tag{1.1}$$

where $R_{\mu\nu}$ is the Ricci tensor computed from Christoffel's symbols, themselves functions of the metric; $R = R^{\mu}_{\mu}$ is the scalar curvature obtained by total contraction of the Ricci tensor. Behind a rather simple appearance, this set of six independent scalar equations[1] is complicated. Indeed, the Ricci tensor and scalar curvature depend on the metric tensor in a nonlinear manner. Therefore Einstein's field equations are a set of nonlinear, partial differential equations whose complete solutions are not known without making approximations.

As expected, the General Theory of Relativity reduces to Newton's Law of Universal Gravitation in the regime of weak gravitational fields and slow motions. This is a valid approximation for most of the planets in our Solar System, which does not hold for the planets orbiting close to the Sun. Einstein carried out the full relativistic computation of Mercury's orbit [Ein06] and found an extra perihelion precession compatible with observations made by astronomers [Le 59]. This deviation from Newton's theory of about $43''$ is explained by the contribution of gravity on the geometry of spacetime, or self-force.

Although this result crowned the General Theory of Relativity as the accepted successor of Newton's Law of Gravitation, the development of this new theory was guided by theoretical considerations, and in particular the Equivalence Principle. The Equivalence Principle states that no local experiment could distinguish between an accelerated frame of reference and an inertial frame of reference inside a gravitational field. This foundation finds its origin in a famous thought experiment, proposed by Albert Einstein and presented in fig. 1.1: the equations of motion for an observer in a cabin at rest on the surface of the Earth, or an observer on a cabin far from any mass, uniformly accelerated, take the same form. Einstein, therefore, postulated that both these situations are identical, and free-falling bodies are only subjected to inertial motion, by contrast with Newton's view of gravity as an external force.

[1] Indeed, Einstein's field equations relate symmetric $4\times4$ tensors, which contain 10 components. Bianchi's identity reduces the number of independent equations to 6.

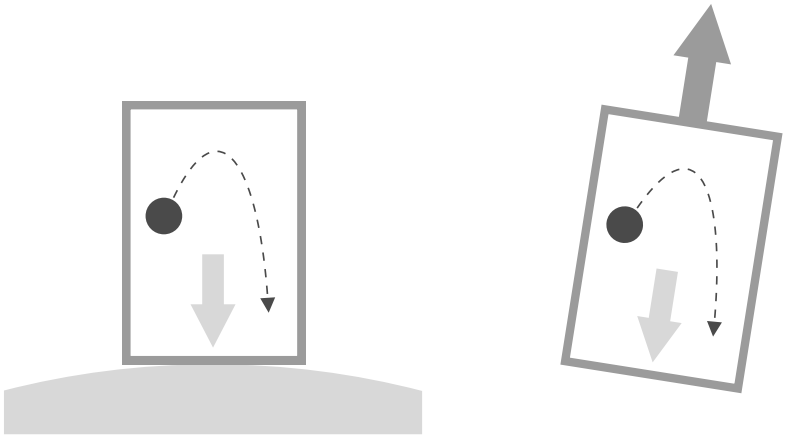

Figure 1.1: Schematics of the famous thought experiment proposed by Einstein, to illustrate the Equivalence Principle. On the left-hand side, an experiment is performed in a cabin immersed in the Earth gravitational field. On the right-hand side, the same experiment is performed in a uniformly accelerated cabin, far from any mass. The results of both experiments are identical.

### 1.1.3 Weak-Field Regime

Solving Einstein's field equations (eq. (1.1)) is a notoriously non-trivial task without dedicated approximations. A small number of exact solutions exist and are used in a range of astrophysical and cosmological problems. The Schwarzschild metric, for example, describes a spacetime containing only a static, spherical distribution of mass and is commonly used in astrophysics. Cosmologists extensively use the Friedmann–Lemaître–Robertson–Walker metric to describe a homogenous isotropic and expanding Universe.

Another approach to solving Einstein's equations is to study perturbative solutions in the regime of weak gravitational fields. We will show that the free-space solutions for a nearly flat Minkowski spacetime take the form of a wave equation propagating at the speed of light. These propagating waves are called gravitational waves and were predicted by Einstein already in 1916. It was not clear at that time whether they were physical, or artifacts of calculus; the debate has been resolved in the 1950s when the properties of gravitational waves have been fully understood.

Let us consider a flat Minkowski spacetime, whose associated metric tensor under the

timelike sign convention is given by

$$\eta_{\mu\nu} = \begin{pmatrix} 1 & & & \\ & -1 & & \\ & & -1 & \\ & & & -1 \end{pmatrix} . \tag{1.2}$$

We consider a first-order perturbation $h_{\mu\nu}$ with respect to this flat metric, and assume that $|h_{\mu\nu}| \ll 1$ for all $\mu$ and $\nu$ in the following discussion. We can find a coordinate system in which the total metric tensor can be simply expressed as the sum of the flat metric and the perturbation

$$g_{\mu\nu} \approx \eta_{\mu\nu} + h_{\mu\nu} \, . \tag{1.3}$$

Linearizing eq. (1.1) using the first-order metric defined in eq. (1.3), we obtain the evolution equation for the metric perturbation

$$\eta^{\alpha\beta} h_{\mu\nu,\alpha\beta} - \frac{\eta^{\alpha\beta}\eta_{\mu\nu} h_{,\alpha\beta}}{2} = \frac{16\pi G}{2} T_{\mu\nu} \, , \tag{1.4}$$

where one recognizes the universal gravitational constant $G$. Opting for the Lorentz gauge condition, and considering transverse and traceless perturbations, we define the reduced metric perturbation

$$\bar{h}_{\mu\nu} = h_{\mu\nu} - \frac{1}{2} h^{\alpha}_{\alpha} \eta_{\mu\nu} \, . \tag{1.5}$$

Inserting this reduced variable in eq. (1.4) yields wave solutions of the metric perturbation, propagating at the speed of light $c$,

$$\eta^{\mu\nu} \partial_\mu \partial_\nu \bar{h}_{\mu\nu} = \frac{16\pi G}{c^4} T_{\mu\nu} \, . \tag{1.6}$$

We call *gravitational waves* these propagating solutions in free space.

### 1.1.4 Properties of Gravitational Waves

In this section, we explore the properties of solutions to eq. (1.6). In general, Fourier analysis shows that every solution can be expressed as a superposition of monochromatic plane waves, propagating at $c$. Let us consider one unique plane wave,

$$\bar{h}_{\mu\nu} = A_{\mu\nu} \exp(i k_\alpha x^\alpha) \, , \tag{1.7}$$

where $A_{\mu\nu}$ is the (complex) wave amplitude, and $k_\alpha$ the wave vector.

$A_{\mu\nu}$ is a symmetric $4 \times 4$ tensor, and is therefore described by 10 independent components. It follows from the Lorentz gauge condition that $A_{\mu\alpha}k^{\alpha} = 0$, leaving 6 independent components for $A_{\mu\nu}$. This number can be further reduced using the remaining 4 degrees of freedom in our gauge choice. Opting for the traceless and transverse gauge yields the equality $h_{\mu\nu} = \bar{h}_{\mu\nu}$, and only 2 independent components remain.

In this gauge, the wave is transverse and non-vanishing components of the wave amplitude are perpendicular to its propagation direction. If we consider a gravitational wave propagating along the $z$-direction, we are left with 4 non-vanishing components $A_{xx}, A_{xy}, A_{yx}$ and $A_{yy}$. By symmetry of the wave amplitude, and because its trace must cancel, we have two conditions

$$A_{xy} = A_{yx} \quad \text{and} \quad A_{xx} = -A_{yy}\,. \tag{1.8}$$

These two independent components are assimilated to two polarization states of the gravitational wave, denoted $h_+$ and $h_\times$ for reasons that will become obvious in section 1.1.6.

A standard polarization basis is formed by

$$\left\{\mathbf{e}^{+} = \hat{\mathbf{e}}_x \otimes \hat{\mathbf{e}}_x - \hat{\mathbf{e}}_y \otimes \hat{\mathbf{e}}_y, \mathbf{e}^{\times} = \hat{\mathbf{e}}_x \otimes \hat{\mathbf{e}}_y + \hat{\mathbf{e}}_y \otimes \hat{\mathbf{e}}_x\right\}, \tag{1.9}$$

so that we can write the metric perturbation

$$h_{\mu\nu} = h_+ \mathbf{e}^{+}_{\mu\nu} + h_\times \mathbf{e}^{\times}_{\mu\nu}\,, \tag{1.10}$$

or in a matrix form

$$\bar{h}_{\mu\nu} = \begin{pmatrix} 0 & 0 & 0 & 0 \\ 0 & h_+ & h_\times & 0 \\ 0 & h_\times & -h_+ & 0 \\ 0 & 0 & 0 & 0 \end{pmatrix}. \tag{1.11}$$

Like electromagnetic waves, it can be shown that gravitational waves carry away energy, linear momentum, and angular momentum. As we will see in the next sections, this has important consequences for astrophysical gravitational wave sources.

However, unlike its electromagnetic counterparts, gravitational waves are hardly affected by matter. Electromagnetic waves can suffer lensing, scattering, or absorption, while gravitational waves follow their geodesics essentially unaffected. As we will see in section 1.3, their interaction with matter is indeed very weak because of their very small amplitude. The back-effect of the matter on gravitational waves is of the same order of smallness. This property makes gravitational waves highly prized messengers, carrying information from sources located in very distant regions of the Universe. We can detect them at a

great distance and from the first seconds after the Big Bang, through dust clouds or galaxy centers.

Gravitational waves exhibit a shift of wavelength and frequency due to the relative velocity of the source and the observer. In particular, they are redshifted due to cosmic expansion. It is important to keep in mind this phenomenon when characterizing distant astrophysical sources with the received gravitational signals.

### 1.1.5 Effect of Gravitational Waves

Let us define a frame of reference, in which we consider a free particle at rest. We describe its four-velocity $U^\alpha$ according to the transverse and traceless gauge. The particle is free-falling, and therefore satisfy the geodesic equation

$$\frac{\mathrm{d}U^\alpha}{\mathrm{d}\tau} + \Gamma^\alpha_{\mu\nu} U^\mu U^\nu = 0\,, \tag{1.12}$$

where $\tau$ is the proper time.

The particle is initially at rest, *i.e.* $U^\alpha = \delta^\alpha_t$, and we can write the initial acceleration of the particle as

$$\left.\frac{\mathrm{d}U^\alpha}{\mathrm{d}\tau}\right|_0 = -\Gamma^\alpha_{tt} = -\frac{1}{2}\eta^{\alpha\beta}\left(\frac{\partial h_{\beta t}}{\partial t} + \frac{\partial h_{t\beta}}{\partial t} - \frac{\partial h_{tt}}{\partial \beta}\right). \tag{1.13}$$

From eq. (1.11), we find that all components of the gravitational wave that appear in the previous equation vanish, and therefore

$$\left.\frac{\mathrm{d}U^\alpha}{\mathrm{d}\tau}\right|_0 = 0\,. \tag{1.14}$$

Hence the coordinates of a free particle initially at rest will never change when they are expressed in the transverse and traceless gauge. As a gravitational wave passes, our coordinate system adapts itself to the ripples in spacetime, so that the particle remains attached to the same position.

This does not provide any geometrical information about spacetime, and we will instead study the proper distance of two nearby particles initially at rest. One is at the origin of the coordinate system, and the other has the spatial coordinates $x = \epsilon$, $y = z = 0$. The proper distance between the particles is given by

$$\Delta l = \int \sqrt{|g_{\mu\nu}\,\mathrm{d}x^\mu\,\mathrm{d}x^\nu|} = \int_0^\epsilon \sqrt{|g_{xx}|}\,\mathrm{d}x^x\,. \tag{1.15}$$

If $\epsilon$ is very small with respect to the characteristic length of evolution of the metric, we can approximate

$$\Delta l \approx \sqrt{|g_{xx}(x=0)|}\epsilon \tag{1.16}$$

Using eq. (1.3), we have $g_{xx}(x=0) \approx \eta_{\mu\nu} + h_{xx}(x=0)$. Expanding the square root to first order in $h_{xx}$ yields

$$\Delta l \approx \epsilon\left(1 + \frac{1}{2}h_{xx}(x=0)\right). \tag{1.17}$$

In general, $h_{xx}(x=0)$ is not constant so that the proper distance between our free-falling particles varies with time as a gravitational wave passes. This is why the effect of gravitational waves is often compared to that of a tidal force. Gravitational-wave detectors essentially attempt to measure this change in the proper distance between two test bodies.

### 1.1.6 Ring of Particles and Polarization States

The effect of gravitational waves is often illustrated by the deformation of a ring of test particles. Let us generalize the previous result, by defining the four-vector $\xi^\mu$ which connects two free particles. It can be shown that in the weak-field regime, and assuming that the proper time is approximately the time coordinate,

$$\frac{\partial^2 \xi^\alpha}{\partial t^2} = R^\alpha_{\mu\nu\beta} U^\mu U^\nu \xi^\beta \,, \tag{1.18}$$

where $U^\mu$ is the four-velocity of the particles.

We suppose that the first particle is initially at rest at the origin, and the other on a circle of radius $\epsilon$ centered on the first particle, with an angle $\theta$ defined in fig. 1.2. We initially have $U^\mu = (1,0,0,0)^T$ and $\xi^\alpha = (\epsilon\cos\theta, \epsilon\sin\theta, 0, 0)^T$. eq. (1.18) reduces to

$$\frac{\partial^2 \xi^\alpha}{\partial t^2} = \epsilon\cos\theta R^\alpha_{ttx} + \epsilon\sin\theta R^\alpha_{tty} \,. \tag{1.19}$$

Working in the transverse and traceless gauge, we can use the non-vanishing components of the metric perturbation to compute the Riemann tensor. Finally, the separation vector for the two particles obey the differential equations

$$\frac{\partial^2 \xi^x}{\partial t^2} = \frac{1}{2}\epsilon\cos\theta\frac{\partial^2 h_{xx}}{\partial t^2} + \frac{1}{2}\epsilon\sin\theta\frac{\partial^2 h_{xy}}{\partial t^2} \,, \tag{1.20}$$

$$\frac{\partial^2 \xi^y}{\partial t^2} = \frac{1}{2}\epsilon\cos\theta\frac{\partial^2 h_{xy}}{\partial t^2} - \frac{1}{2}\epsilon\sin\theta\frac{\partial^2 h_{xx}}{\partial t^2} \,. \tag{1.21}$$

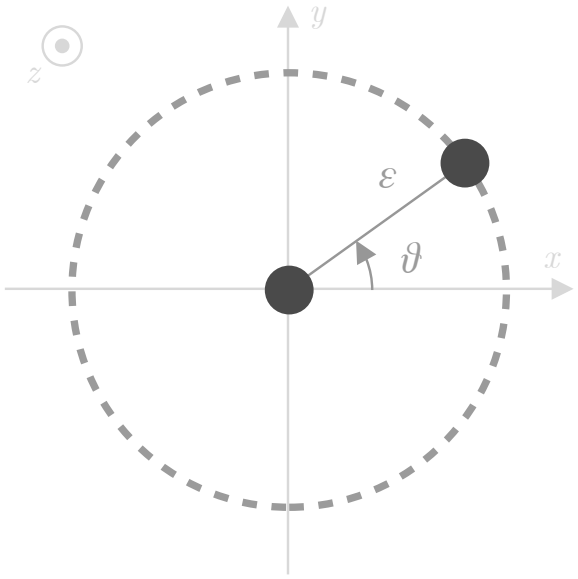


Figure 1.2: The separation vector $\xi^\alpha$ connects a particle initially at rest at the origin, and a second particle on a circle of radius $\epsilon$ and centered at the origin.

In the transverse and traceless gauge, we can write for a plane wave propagating along the $z$-direction,

$$h_{xx}(t) = h_+ \cos[\omega(t-z)]\,, \tag{1.22}$$

and

$$h_{xy}(t) = h_\times \cos[\omega(t-z)]\,. \tag{1.23}$$

Inserting these expressions in eqs. (1.20) and (1.21), we can identify the solution, which reads

$$\xi^x = \epsilon\cos\theta + \frac{1}{2}\epsilon\cos\theta h_+\cos(\omega t) + \frac{1}{2}\epsilon\sin\theta h_\times\cos(\omega t)\,, \tag{1.24}$$

$$\xi^y = \epsilon\sin\theta + \frac{1}{2}\epsilon\cos\theta h_\times\cos(\omega t) - \frac{1}{2}\epsilon\sin\theta h_+\cos(\omega t)\,. \tag{1.25}$$

The parameter $\theta$ is a free-running variable so that we can study the effect of the passage of a gravitational wave, propagating along the $z$-axis, on a ring of test particles. If the wave has $h_+ \neq 0$ and $h_\times = 0$, we have

$$\xi^x(t) = \epsilon\cos\theta\left[1 + \frac{1}{2}h_+\cos(\omega t)\right] \quad \text{and} \quad \xi^y(t) = \epsilon\sin\theta\left[1 - \frac{1}{2}h_+\cos(\omega t)\right], \tag{1.26}$$

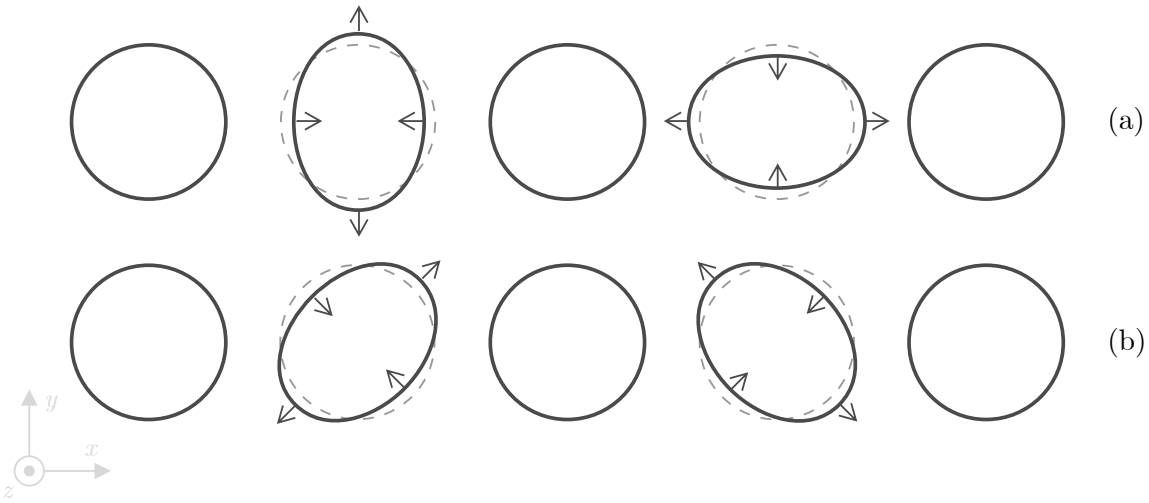


Figure 1.3: Effect of a gravitational wave propagating along the $z$-axis, on a ring of free particles. ($a$) show the effect of the "plus" polarization state, and ($b$) the effect of the "cross" polarization state.

We understand that the ring has its proper distances increased along the $x - axis$ and reduced along the perpendicular $y - axis$ for a half-period, and conversely for the second half-period. This is illustrated in fig. 1.3. This study justifies the naming of this "plus" polarization state, and the notation $h_+$ for the related wave amplitude components.

Now if we consider a wave such that $h_+ \neq 0$ and $h_\times = 0$, the separation vector reads

$$\xi^x(t) = \epsilon \cos\theta + \frac{1}{2}\epsilon \sin\theta h_\times \cos(\omega t)\,, \tag{1.27}$$

and

$$\xi^y(t) = \epsilon \sin\theta + \frac{1}{2}\epsilon \cos\theta h_\times \cos(\omega t)\,. \tag{1.28}$$

The relationship between this solution and the "plus" polarization state becomes clear if we define a new set of axes $(x', y')$, rotated by $-\pi/4$ with respect to the original coordinate axes. We then have

$$x' = \frac{1}{\sqrt{2}}(x - y) \quad \text{and} \quad y' = \frac{1}{\sqrt{2}}(x + y)\,. \tag{1.29}$$

Using these expressions, one finds that in this new coordinate system, the separation vector has the same form as in eq. (1.26), up to a rotation of $\pi/4$,

$$\xi'^x(t) = \epsilon \cos\Big(\theta + \frac{\pi}{4}\Big)\left[1 + \frac{1}{2}h_\times \cos(\omega t)\right], \tag{1.30}$$

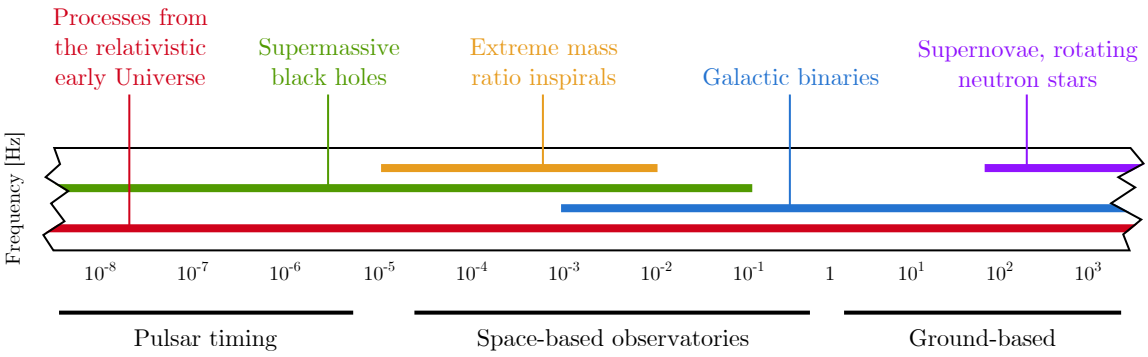


Figure 1.4: Gravitational spectrum, with the frequency bands associated with the main sources of gravitational waves, and the main three detection techniques.

and

$$\xi'^{y}(t) = \epsilon \sin\left(\theta + \frac{\pi}{4}\right)\left[1 - \frac{1}{2}h_{\times}\cos(\omega t)\right]. \tag{1.31}$$

This justifies why this polarization state is therefore called the "cross" polarization, and associated wave amplitude components are denoted $h_{\times}$.

## 1.2 Detection of Gravitational Waves

### 1.2.1 Gravitational-Wave Astronomy

The first astronomical observations were originally conducted with naked eyes, using the visible light. During the second half of the $16^{\text{th}}$ century, Galileo Galilei notably used telescopes to enhance the quality of these observations, and today we have access to high-precision telescopes. However, visible light only represents a small fraction of the entire electromagnetic spectrum, and not all objects in the Universe shine significantly in that band. This became clear when the first observations using radio wavelengths, in the first half of the $20^{\text{th}}$ century, led to the discoveries of pulsars and quasars. The opening of the microwave-band astronomy revealed the Cosmic Microwave Background, an imprint of the Big Bang. Similarly, the development of gamma-ray, X-ray, ultraviolet and infrared astronomy led to new astrophysical and cosmological insights. But the gravitational spectrum (fig. 1.4) remains untouched.

Today, the hope is that observations of gravitational waves could provide a further means

of making new astrophysical observations. This is known as the "gravitational-wave astronomy".

Gravitational waves possess two unique properties. On the one hand, gravitational waves pass through matter essentially unimpeded, as explained in section 1.1.5. Although light from distant objects can be blocked, *e.g.* by dust clouds, gravitational waves can carry information on astrophysical objects across large distances.

On the other hand, a lot of astrophysical phenomena emit gravitational waves. In particular, the most violent processes are expected to be significant gravitational radiation sources. They grant us access to regions that are not directly accessible with electromagnetic observations. For example, the electromagnetic radiation coming from the collapsing core of a supernova is scattered a great number of times before it can escape the dense medium surrounding the explosion. In the process, it loses information about the phenomenon. On the contrary, gravitational waves travel directly from the core of the supernova to the Earth. Let us take another example: an accretion disc is needed around binary systems of black holes, so we can observe a signal in the electromagnetic spectrum. The detection is therefore indirect, while the emission of gravitational waves does not require matter around the binary system, as we will see in section 1.3.

### 1.2.2 Early Days of Gravitational-Wave Detection

The technical challenges in building and running a gravitational-wave detector are enormous since the expected gravitational wave amplitudes are so small. The properties of gravitational waves were well understood in the 1950s, but long technological developments were needed before the first measurement could be made. This was achieved in 2016 by the LIGO-Virgo Collaboration with the announcement of the first direct detection of gravitational waves emitted by the merger of a binary system of black holes [AAA$^+$16a].

The first design for a gravitational-wave detector is attributed to Joseph Weber in 1961. He used resonant bars, solid masses vibrating at a resonance frequency when a gravitational wave interacts. In the early 1970s, Weber published several papers announcing the first detections of gravitational radiations. Follow-up investigations proved him wrong and showed that Weber's signal was, most likely, noise. Weber worked on improving his equipment until his death, but the sensitivity could never be brought to the required level. As of today, no firm detection could be claimed using this kind of detector. If we take reasonable orders of magnitude for our detector, a strong resonant gravitational wave of amplitude $10^{-20}$ will excite the bar with an energy of $10^{-20}\,\mathrm{J}$. This corresponds to a vibration am-

plitude of around $10^{-15}$ m, which is about the diameter of an atomic nucleus. Besides, the sensitivity of such detectors is limited to a very narrow frequency band, around the bar resonance. Only a small fraction of an astrophysical signal sweeping different frequencies can be measured, as what is expected for binary mergers, *c.f.* section 1.3.2.

The first indirect evidence for the existence of gravitational waves was provided by Russell Alan Hulse and Joseph Horton Taylor. In 1974, Hulse and Taylor detected pulsed radio signals using the Arecibo antenna. They could identify it as a pulsar, *i.e.* a highly magnetized, rapidly rotating neutron star. PSR B1913+16 rotates on its axis 17 times per second so that its pulse period is 59 ms. However, they observed a systematic variation in the radio pulses' times of arrival, as some of them arrived a little sooner than expected, and some later. They concluded that the pulsar was in a binary system, rotating with a companion neutron star around their common center of mass. By studying the variations in the pulses' times of arrival, they could estimate the orbital diameter of the binary system. They showed that the orbital distance decays at a rate that matches the predictions of the General Theory of Relativity: gravitational waves carry energy away from the binary system, whose orbital distance decreases. The discovery of this system and their analysis earned them the Physics Nobel Prize is 1993.

### 1.2.3 Measuring Distances with Light

As of today, the only demonstrated technique to measure the tiny variations in the proper distance between two free-falling bodies is light interferometry. It is the detection principle upon which all modern gravitational wave detectors are based. Given its central role in the Theory of Relativity, light is used as a probe of the spacetime curvature. A pulse of electromagnetic radiations is sent on a geodesic and we measure its time of arrival. We show here that this time of arrival is affected by the passage of gravitational waves. The derivation of this time of arrival, as well as the presentation of the various detection techniques, are mostly taken from [Sch12, Hen07].

Let us consider two free-falling bodies, not necessarily close to each other. We assume without loss of generality that they are placed on the $x$-axis, with respective coordinates $(0,0,0)$ and $(L,0,0)$. We consider a gravitational wave propagating in the $z$-direction, with a pure "plus" polarization. In the transverse and traceless gauge, the metric reads

$$\mathrm{d}s^2 = c\,\mathrm{d}t^2 - (1-h_+)\,\mathrm{d}x^2 - (1+h_+)\,\mathrm{d}y^2 - \mathrm{d}z^2 \ . \tag{1.32}$$

A photon emitted by the first body, and received by the second one, travels on a null

geodesic $\mathrm{d}t^2 = 0$, so that the times of emission $t_0$ and arrival $t_1$ are given by

$$\int_{t_0}^{t_1} c\,\mathrm{d}t = c(t_1 - t_0) = \int_0^L \sqrt{1 - h_+(t(x))}\,\mathrm{d}x\,. \tag{1.33}$$

Using the fact that the metric perturbation $h_+$ is small, we can expand the previous equation to first order around 1. We now have

$$t_1 \approx t_0 + \frac{L}{c} - \frac{1}{2c}\int_0^L h_+(t(x))\,\mathrm{d}x\,, \tag{1.34}$$

and we must express the argument of $h_+$ as an explicit function of $x$. On a flat spacetime, $t(x) = t_0 + x/c$. Any correction due to the effect of the gravitational wave will be of second order in $h_+$, so that if we restrict ourselves to first-order expressions,

$$t_1 \approx t_0 + \frac{L}{c} - \frac{1}{2c}\int_0^L h_+\Big(t_0 + \frac{x}{c}\Big)\,\mathrm{d}x\,. \tag{1.35}$$

To gain physical understanding, let us assume that the gravitational wavelength is large compared to $L$. This means that $h_+(t_0 + x/c) \approx h_+(t_0)$ and eq. (1.35) now reads

$$t_1 \approx t_0 + \frac{L}{c}\left[1 - \frac{h_+(t_0)}{2}\right], \tag{1.36}$$

so that the time of arrival is proportional to the proper distance between the two bodies, as measured in the transverse and traceless gauge. We already obtained this result in eq. (1.17), for two particles very close to each other.

More generally, we can differentiate the photon time of arrival $t_1$ with respect to its time of emission $t_0$. Using eq. (1.36), we find that

$$\frac{\mathrm{d}t_1}{\mathrm{d}t_0} = 1 - \frac{1}{2}\left[h_+\left(t_0 + \frac{L}{c}\right) - h_+(t_0)\right]. \tag{1.37}$$

It is remarkable to note that the rate of change of the time of arrival only depends on the wave amplitude at the emission and reception times. The wave amplitude during the photon's propagation plays no role.

Let us imagine now that the first body emits a continuous electromagnetic wave at a given frequency $\nu_0$. We can apply the previous reasoning to each "crest" of the wave, so that the frequency of the received wave $\nu_1$ is such that $\nu_1/\nu_0 = \mathrm{d}t_1/\mathrm{d}t_0$. Using this result in eq. (1.37) yields

$$\frac{\nu_1 - \nu_0}{\nu_0} = -\frac{h_+(t_0 + L/c) - h_+(t_0)}{2}\,. \tag{1.38}$$

Measuring the change of frequency, or equivalently measuring the phase of the returning wave, provides a direct measurement of the amplitude of the gravitational wave.

In general, the vector connecting our two free-falling bodies is not in the plane orthogonal to the direction of wave propagation. If we parametrize the former with an inclination angle $\iota$ and the polarization angle $\psi$[2], it can be showed that previous equations hold, with an effective wave amplitude of

$$h_+^{\text{eff}} = h_+ \sin^2 \iota \cos 2\psi \,. \tag{1.39}$$

For a wave with in a pure "plus" polarization state, the effect is strongest when $\iota = \pi/2$ and $\psi = 0$, *i.e.* the case studied above. On the contrary, the detector is blind to the effect of a gravitational wave with $\iota = 0$ or $\psi = \pi/4$.

These results can be generalized to a gravitational wave with a pure "cross" polarization, and then to a combination of both polarization states.

### 1.2.4 Light Interferometry

Let us now plug some numbers in eq. (1.38). The expected gravitational wave amplitude is of the order of $10^{-20}$. The precision required on the measurement of the photon's time of arrival, or equivalently, the change of frequency, if of the same order. Today, the best clocks do not provide stability at tens of zeptoseconds and another technique should be used.

An interferometer provides a way to measure very small variations in phase or frequency. In the Michelson setup, the light from a very stable laser source is split into two beams, which travel in perpendicular directions. At the end of both arms, the light is reflected onto a mirror, and travels back to recombine on a photodiode. This is illustrated in fig. 1.5 for a gravitational wave with a pure "plus" polarization.

Since the phases of the two beams are correlated, they interfere constructively or destructively depending on the optical path difference between the two arms of the interferometer. Let us suppose that an electromagnetic wave is emitted with a frequency $\nu_0$ so that its electric component reads

$$\mathbf{E}(t) = \mathbf{A} e^{j2\pi\nu_0 t} \,. \tag{1.40}$$

A beam splitter divides it into two beams of equal amplitudes propagating in perpendicular directions. The beam propagating along the $x$-axis bounces off the first mirror, and reaches back the beam splitter. Using eq. (1.38), and setting the phase reference to zero at the

[2]Refer to section 3.2.6 for details about the source parametrization.

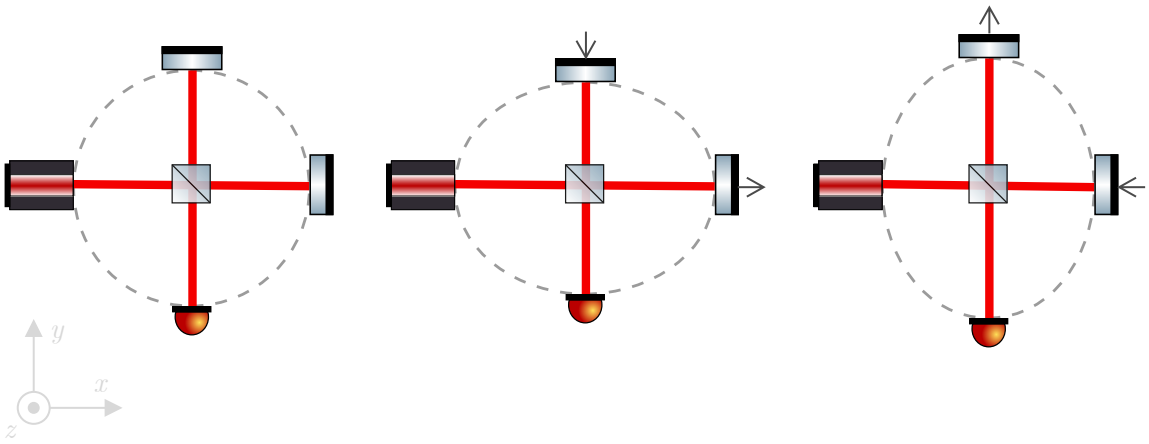


Figure 1.5: Schematics of a Michelson interferometer when a gravitational wave with a pure "plus" polarization propagates along the $z$-axis.

beam splitter, the contribution of this beam to the total electric field reads

$$\mathbf{E}_1 = \frac{j}{2}\mathbf{A}e^{j4\pi L\nu_1} = \frac{j}{2}\mathbf{A}e^{j4\pi L\nu_0\left(1-\frac{1}{2}[h_+(t_0+2L)-h_+(t_0)]\right)}\,, \tag{1.41}$$

and similarly for the beam propagating along the $y$-axis, we have

$$\mathbf{E}_2 = \frac{j}{2}\mathbf{A}e^{j4\pi L\nu_0\left(1+\frac{1}{2}[h_+(t_0+2L)-h_+(t_0)]\right)}\,. \tag{1.42}$$

The power at the photodiode is the squared sum of these two contributions, and reads

$$P = |\mathbf{E}_1+\mathbf{E}_2|^2 = \frac{|\mathbf{A}|^2}{2}\Big[1+\cos\left(4\pi L\nu_0[h_+(t_0)-h_+(t_0+2L)]\right)\Big]\,. \tag{1.43}$$

When a gravitational wave in a pure "plus" polarization state passes through our equal-arm Michelson interferometer, the power at the photodiode is modulated by the difference of the wave amplitude at splitter time and recombinaison time, scaled by the interferometer armlength.

Let us estimate the orders of magnitude entering this last formula, and assume that the interferometer armlengths are of the order of the kilometer, *i.e.* $L \approx 10^3\,\mathrm{m}$, and that the laser frequency is at the tens of terahertz, $\nu_0 \approx 10^{14}\,\mathrm{Hz}$. For an wave amplitude of $h_+ \approx 10^{-20}$, the contrast is given by

$$\kappa = \frac{P-P_0}{P_0} \approx \cos(4\pi L\nu_0 h_+) \approx 99.992\,\%\,, \tag{1.44}$$

which can be measured. Of course, this contrast is proportional to the armlength, and increasing it is a straightforward way to enhance the detector sensitivity.

### 1.2.5 Ground-Based Observatories

The LIGO and Virgo interferometers are gravitational-wave observatories based on the technique presented in section 1.2.4. As of today, they are the only instruments that succeeded in the direct detection of gravitational signals.

The Hanford and Livingston LIGO Observatories are Michelson light interferometers with 4 km-long armlengths, located in the United States. Semi-transparent mirrors are used in both arms to create Fabry-Perrot cavities so that the effective optical path lengths are larger than the "physical" armlengths, represented in fig. 1.6. The interferometer is calibrated on the dark fringe. Thus the power is zero at the photodetector. When a gravitational wave passes, the power does not vanish and its value is a direct measurement of the wave amplitude.

The Virgo Observatory is a gravitational-wave detector run by a French-Italian collaboration, located in Cascina, Italy. Its design is very similar to that of the LIGO detectors, although the physical armlengths are three-kilometer long. An aerial photograph of the facilities is presented in fig. 1.7.

On the 11 February 2016, the LIGO-Virgo Collaboration announced the first direct detection of gravitational waves [AAA$^+$16a], opening the era of gravitational-wave astronomy (*c.f.* section 1.2.1). The signal GW150914 was detected in full coincidence in both LIGO observatories on the 14 September 2015, with a slight delay corresponding to the time of flight between the two detectors. The signal was shown to be fully compatible with the signal expected from the merger of two black holes, with masses of 35 and 30 solar masses, in a binary system at a luminosity distance of around 440 Mpc from us. For their work leading to this discovery, Barry Barish, Kip Thorne and Rainer Weiss were awarded the 2017 Nobel Prize in Physics.

Shortly after the first detection, the Virgo instrument joined LIGO in the search for gravitational events. GW150914 was followed by many other events [AAA$^+$16b, AAA$^+$17b, AAA$^+$17a]. On the 17 August 2017, a signal compatible with a neutron star binary merger was detected for the first time by the LIGO interferometers [AAA$^+$17c]. For this event, electromagnetic counterparts were measured in multiple parts of the spectrum, ranging from gamma-rays, X-rays, visible light, down to radio wavelengths. No high-energy neutrinos burst could be associated with GW170817. Nevertheless, this event opened the promising

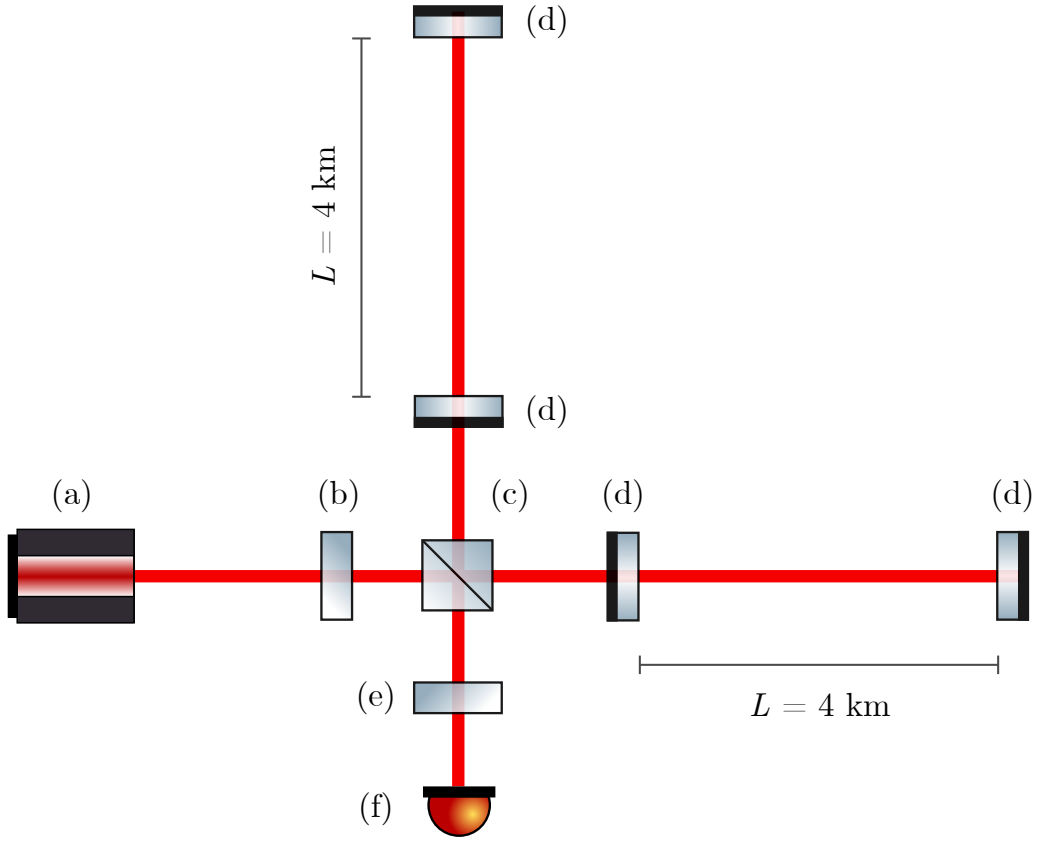


Figure 1.6: Schematics of a gravitational-wave detector using interferometry. A laser source (a) sends an electromagnetic wave, which goes through a power recycling mirror (b). The beam splitter (c) splits the signals into two beams traveling along perpendicular arms, 4 km (resp. 3 km) long in the case of the LIGO (resp. Virgo) observatories. Free-falling mirrors (d) create resonating cavities, which increase the effective optical path length. The beams are recombined and go through a signal recycling mirror (e) before it reaches the photodiode (f).

Figure 1.7: Aerial view of the Virgo Observatory facilities in Cascina, Italy. Credits: the Virgo collaboration.

era of multi-messenger astronomy, as gravitational-wave observations complement observations made in the electromagnetic spectrum.

In the coming years, the Japanese Kamioka Gravitational Wave Detector (KAGRA) and the Indian Initiative in Gravitational-wave Observations (INDIGO) detector will join the network of running gravitational-wave observatories. By simultaneous detection of the same event on these multiple detectors, a precise location in the sky can be pinpointed for the source of the detected waves. This will help follow-ups in other spectra, fostering the development of multi-messenger astronomy. Third-generation observatories, such as the European Einstein Telescope, are under study and expected to be the successors of LIGO and Virgo detectors. They are designed to circumvent some fundamental limitations of the current detectors but are not expected before the 2030s.

### 1.2.6 Shortcomings of Ground-Based Interferometry

The sensitivity of light interferometer gravitational-wave detectors is limited by the various noises entering the measurements [MHA+16]. We review here the main sources of noise in the running ground-based detectors and show a schematics of the LIGO noise budget in fig. 1.8.

Below 10 Hz, the so-called gravity gradient noise couples in the measurements. The variations of the gravitational field, due to the motion of ocean waves, clouds, tectonic plates, etc., induce a motion of the detector test mirrors. The associated signals mimic a stochastic

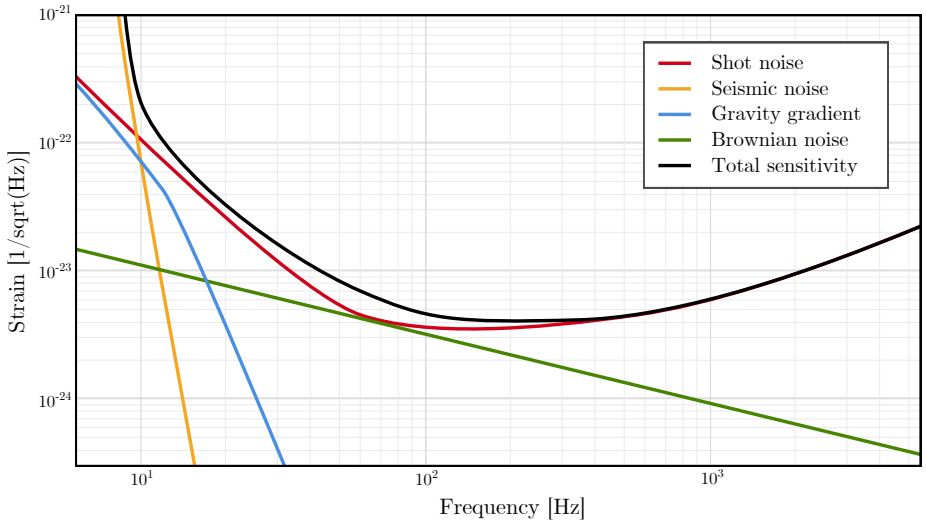


Figure 1.8: Schematics of the LIGO Observatory noise budget.

background of gravitational waves and therefore constitute a noise [HT98].

At frequencies above $10^3$ Hz, the sensitivity is limited by the shot noise, which is the quantum uncertainty when counting the photons reaching the surface of the photodetector. This fluctuation of the incident power can be misinterpreted as the passage of the gravitational wave. Increasing the laser power reduces this noise, but increases the thermo-mechanical coupling between the laser beams and the test mirrors. This is, therefore, a fundamental quantum limit for interferometer detectors, although "light squeezing" techniques are being developed to overcome it [AAA+13].

One of the main challenges for ground-based observatories is to isolate the free-falling mirrors from any other spurious forces. Indeed, such forces create signals in the photodetectors which can mimic gravitational signals, or create a loud background in which the real gravitational signals are lost. Staged suspensions and pendulums are used to isolate the mirrors and decouple their motions from ground vibrations. Unfortunately, these mechanical systems are low-pass filters and ground vibrations remain the limiting factor at frequencies below 10 Hz.

Because gravity cannot be shielded, it is natural to imagine a detector operating in space, not subjected to seismic vibrations, and far from important gravity gradients. Because the armlengths are not limited in space as they are on Earth (by the Earth curvature or the cost of tunneling for example), they are chosen of the order of millions of kilometers, shifting the frequency band of such space observatories to below $10^{-4}$ Hz and up to 0.1 Hz.

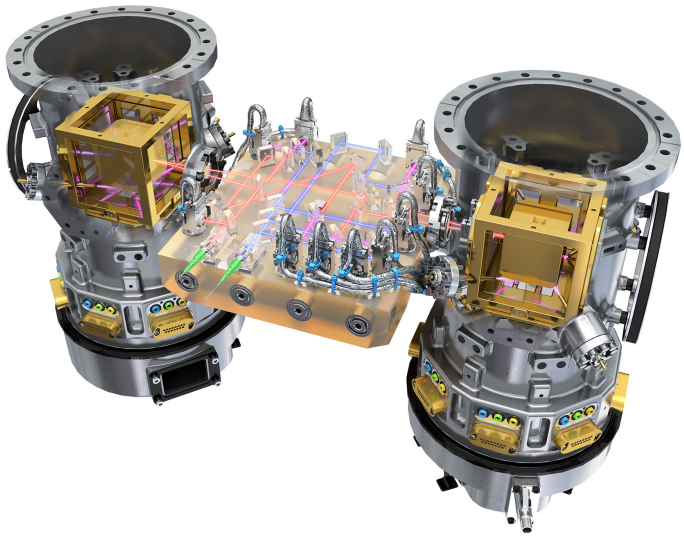

Figure 1.9: Illustration of the LISA Pathfinder Technology Package core assembly. The two free-falling gold-platinum test masses are enclosed in vacuum containers. The optical bench interferometer monitors the differential acceleration between the two test masses. Credits: ESA.

Therefore the observations of space-based detectors are very complementary to those of ground-based interferometers. In particular, we will see in section 1.3 that both types of observatories will not access the same astrophysical sources. The rest of this thesis focuses on such a space-borne observatory.

### 1.2.7 LISA Pathfinder

The first design studies for a space-borne observatory dates back to the 1980s. Already in these early days a technological demonstrator was foreseen to validate the critical subsystems for such a mission. The proof-of-concept mission LISA Pathfinder was proposed in the early 2000s. Its objective was to prove that two test masses can fly in free fall, untouched yet shielded by the hosting spacecraft. The so-called drag-free system ensures that the spacecraft follows the test masses, such that they remain at the center of their housings. Laser interferometry was used to measure deviations from geodesic motion, with an accuracy of around $30\,\mathrm{fm\,Hz^{-1/2}}$ at high frequencies. LISA Pathfinder's interferometer was based on LISA's local interferometer, with arms reduced from millions of kilometers to 38 cm, see fig. 1.9.

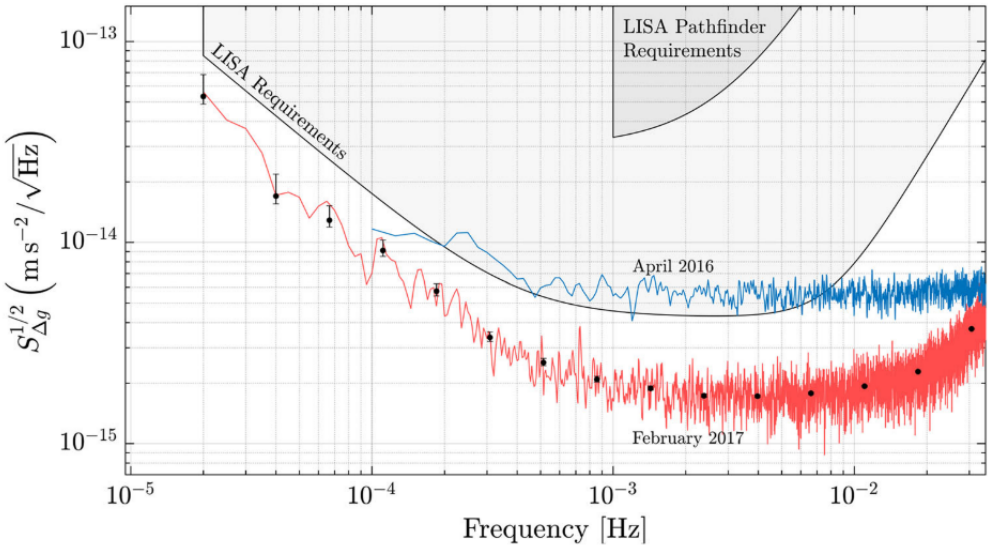


Figure 1.10: Amplitude spectral density of the spurious differential acceleration between the two test masses. First results published in [AAA+16c] are in blue, while the final results from [AAB+18] are colored in red. They are both far below the LISA Pathfinder requirements at all frequencies, and the final results are even below LISA requirements. Taken from [AAB+18].

After significant technical delays, LISA Pathfinder was launched on 3 December 2015 onboard a Vega rocket and placed in a Lissajous orbit around the Lagrange point $L_1$. After two months of scientific investigation, the first results showed that the technology developed for space-based gravitational-wave detection exceeded the expectations [AAA+16c]. After 576 days of mission, LISA Pathfinder was decommissioned on 30 June 2017 and finally passivated on 17 July 2017. The excellent final results [AAB+18] published in 2018, and presented in fig. 1.10, confirmed the feasibility for a drag-free control system of a spacecraft hosting two test masses, space interferometric measurements at the desired precision and frequency band, as well as the reliability of the necessary components.

### 1.2.8 LISA, Space-Borne Observatory

Laser Interferometer Space Antenna (LISA) was proposed as a mission to European Space Agency (ESA) in the early 1990s, and in the next decade, its design was refined to three spacecraft in a 5 km-long triangular configuration, as NASA joined the project. In the

2000s LISA was proposed as a joint ESA-NASA candidate for the L1 slot in ESA's Cosmic Vision 2015-2025 program. NASA announced in early 2011 its decision to withdraw from the project, due to budget costs. ESA chose to push forward a descoped version of LISA.

Due to the LISA Pathfinder shifting schedule, the L1 slot was finally attributed to the JUICE mission and the LISA mission was postponed. In 2013, ESA selected the theme called "the Gravitational Universe" for the L3 slot. Following the first detection by the LIGO-Virgo Collaboration (*c.f.* section 1.2.5), NASA announced its interest in joining back the mission as a junior partner. Following the ESA call for mission and based on the excellent results of LISA Pathfinder, a proposal for a 2.5 million kilometer-arm LISA was submitted on January 2017 [DASpAh$^+$17]. The mission was selected for the L3 slot, and successfully underwent analysis and identification (phase 0). As of today, feasibility studies (phase A) are conducted and coordinated by ESA, the industry, NASA, and the LISA Consortium, to formulate a mission design and architecture compatible with the scientific objectives. My work is part of this effort.

I will now sketch the baseline mission characteristics, as they are currently foreseen [DASpAh$^+$17]. Although this design is subject to changes, the main choices and ideas will most probably still apply during the future mission phases.

LISA is a European Space Agency scientific space mission, which aims to measure gravitational waves in the millihertz range [DASpAh$^+$17, LL18]. LISA will consist of three spacecraft flying in a nearly-equilateral triangle formation, which will orbit the Sun at a distance of 1 au (astronomical unit). As presented in fig. 1.11, the constellation's center of mass will trail the Earth by about 20°, and all spacecraft will exchange laser beams along arms of $2.5 \times 10^6$ km. Essentially based on the light interferometry technique described in section 1.2.4, the exchanged laser beams are bounced on free-falling test masses inside each spacecraft, before they are made to interfere. However, we will see in chapter 3 that LISA uses heterodyne interferometry and the *split-interferometry* configuration. The test masses are protected from external spurious forces, such that they fly on geodesics and play the role of inertial references.

We will see in chapter 4 that the measurement along each arm can be combined in various ways to synthesize Michelson interferometers, which are sensitive to the two polarizations of incoming gravitational waves. Moreover, as the constellation orbits the Sun, its antenna pattern sweeps the sky and allows for a wide field of view, as well as a good localization of the source.

Conversely, several complications arise from the very principles of the LISA mission. It is impossible to anchor the spacecraft in space, and therefore the armlengths will vary

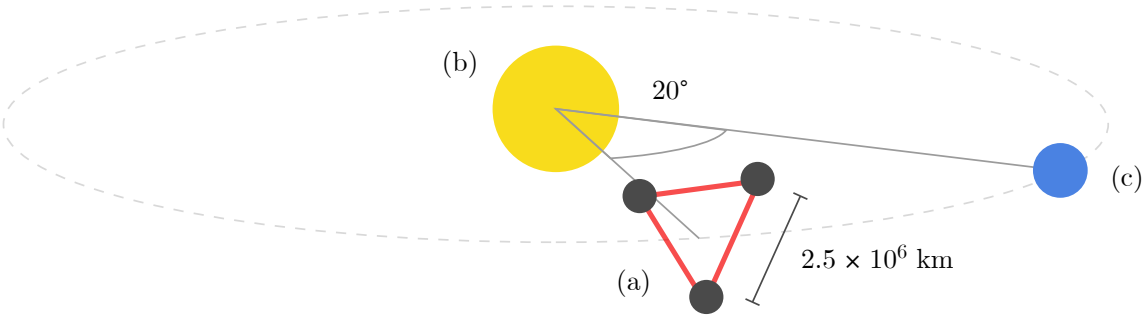


Figure 1.11: Schematics of the LISA constellation (a), orbiting the Sun (b) and trailing the Earth (c) by about 20°. The armlengths are $2.5 \times 10^6$ km.

with time over a year. These long-term variations are at the root of multiple technical challenges. For example, the angle at which the outgoing beams are emitted on each spacecraft must be adjusted in real-time. Moreover, the relative motion of the spacecraft induces a Doppler shift in the transmitted laser signals, which sets requirements on the phasemeter and the choice of laser frequencies. Finally, we will see that unequal and time-varying-arm interferometry demands sophisticated data processing to synthesize usual Michelson measurements.

This thesis focuses on modeling and simulating the LISA instrument, as well as studying the key factors affecting its sensitivity.

### 1.2.9 Pulsar Timing

A third technique to detect gravitational waves with frequencies below $10^{-6}$ Hz uses radio bursts emitted by rapidly-rotating, highly-magnetized neutron stars, which are called pulsars. For some millisecond pulsars, the regularity of the pulses is higher than what it is possible to achieve with atomic clocks. Therefore, by monitoring the deviations from the expected times of arrival for multiple pulsars, astrophysicists hope to detect specific patterns of correlations, which would be the sign of the effect of a gravitational wave.

Three main pulsar timing array projects are currently working on this technique, gathered in the International Pulsar Timing Array project. As of today, no gravitational wave has been detected but constraints on the amplitude of such waves have been set [HAA+10]. It is expected that the accumulation of high-precision data, the improvement of the detector

sensitivity, the use of more pulsars, the understanding of the noise and calibration, as well as the development of new computational methods and resources will allow for the detection of very low-amplitude gravitational waves in the next decade.

## 1.3 Gravitational Wave Sources and Science Goals

### 1.3.1 Quadrupole Formula

To understand how a system can produce gravitational wave, we build an analogy with electromagnetic radiations. Let us define the electric dipole moment $\delta$ of an ensemble of charges $q_i$, with positions $\mathbf{x}_i$ for $1 \leq i \leq n$, by

$$\delta = \sum_{i=1}^{n} q_i \mathbf{x}_i \,. \tag{1.45}$$

The dominant effect for accelerating charges is due to the change in their dipole, as it can be shown that the total radiated power is

$$L_{\text{electric dipole}} \propto \frac{\mathrm{d}^2\delta}{\mathrm{d}t^2} = \sum_{i=1}^{n} q_i \frac{\mathrm{d}^2\mathbf{x}_i}{\mathrm{d}t^2} \,. \tag{1.46}$$

The gravitational analog of the electric dipole moment is the mass dipole moment, defined as

$$\delta = \sum_{i=1}^{n} m_i \mathbf{x}_i \,, \tag{1.47}$$

where $m_i$ are the rest masses of the particles. The first derivative of this mass dipole moment, in fact the total linear momentum $\mathbf{p}$, as

$$\frac{\mathrm{d}\delta}{\mathrm{d}t} = \sum_{i=1}^{n} m_i \frac{\mathrm{d}\mathbf{x}_i}{\mathrm{d}t} = \mathbf{p} \,. \tag{1.48}$$

Since this quantity is conserved, the associated radiated power is

$$L_{\text{mass dipole}} \propto \frac{\mathrm{d}^2\delta}{\mathrm{d}t^2} = \frac{\mathrm{d}\mathbf{p}}{\mathrm{d}t} = 0 \,, \tag{1.49}$$

and we deduce that there is no dipolar gravitational radiations.

The next-order electromagnetic effects are due to a change in the magnetic dipole and the electric quadrupole moment. The magnetic dipole moment $\mu$ is defined, for the same ensemble of particles, by

$$\mu = \sum_{i=1}^{n} \mathbf{x}_i \times q_i \frac{\mathrm{d}\mathbf{x}_i}{\mathrm{d}t} = \sum_{i=1}^{n} \mathbf{x}_i \times (q_i \mathbf{v}_i)\,, \tag{1.50}$$

and the associated magnetic dipole radiation has a power

$$L_{\text{magnetic dipole}} \propto \frac{\mathrm{d}^2\mu}{\mathrm{d}t^2}\,. \tag{1.51}$$

Following our gravitational analogy, we express the equivalent of the magnetic dipole moment for a distribution of masses,

$$\mu = \sum_{i=1}^{n} \mathbf{x}_i \times (m_i \mathbf{v}_i) = \mathbf{J}\,, \tag{1.52}$$

and we see that it is the total angular momentum of our system. Since it is a conserved quantity, the associated radiation vanishes.

In conclusion, there can be no dipolar emission of gravitational waves because of the conservation of linear and angular momenta. Therefore a system cannot emit gravitational radiation if it is spherically symmetric, and the dominant form of gravitational emission is quadrupolar.

The mass quadrupole moment $I_{ij}$ is the tensor defined by

$$I_{ij} = \sum_{l}^{n} m_l (x_{il} x_{jl} - \frac{1}{3} \|\mathbf{x}_l\|^2 \delta_{ij})\,. \tag{1.53}$$

It can be shown [Sch12] that in the slow-motion approximation, the metric perturbation tensor $h_{\mu\nu}$ at a distance $r$ of the source is given by the so-called quadrupole formula

$$h_{\mu\nu} = \frac{2G}{rc^4} \frac{\mathrm{d}^2 I_{\mu\nu}}{\mathrm{d}t^2}\,. \tag{1.54}$$

Therefore a system with a time-varying quadrupolar moment emits gravitational waves, whose amplitude goes like the inverse of the distance to the system. For a binary system of two spherical stars with the same mass $M$, in a circular orbit of radius $R$ and orbital frequency $f$, in the plane $(Oxy)$ such that at $t = 0$ both objects are aligned along the $x$-axis, we find from eq. (1.53) and eq. (1.54) that

$$h_+ = \frac{32\pi^2 G M R^2 f^2}{rc^4} \cos(4\pi f t) \quad \text{and} \quad h_\times = -\frac{32\pi^2 G M R^2 f^2}{rc^4} \sin(4\pi f t)\,. \tag{1.55}$$

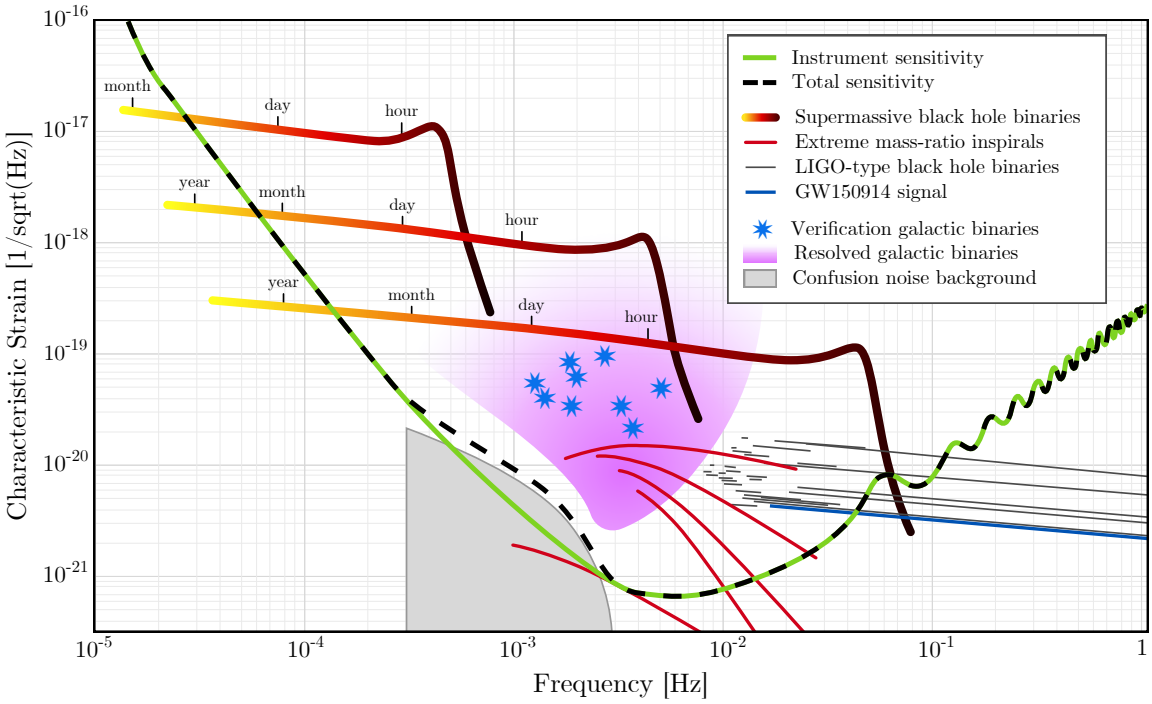


Figure 1.12: Main sources expected to be detected by LISA, superimposed with the sensitivity of the instrument. The time to coalescence is indicated for supermassive black hole binary signals. Taken from [DASpAh$^+$17].

In the following sections, we review the main astrophysical and cosmological sources that we expect to see in the LISA band. For each of them, we briefly sketch the main models which are used to describe the source, and then give the main characteristic of the associated gravitational wave signals, as will be detected by LISA. In particular, we list the parameters of interests that will be inferred from the gravitational signals. We use this opportunity to give the associated scientific objectives that physicists hope to solve with the detection of such sources.

Most of the materials in this section are extracted from the LISA mission proposal [DASpAh$^+$17], the LISA science requirement document [LL18], and the lecture notes on binary black hole astrophysics from M. Celoria, R. Oliveri, A. SESAna, and M. Mapelli [COSM18].

### 1.3.2 Compact Galactic Binaries

The gravitational signals of millions of compact binary systems from our Galaxy are expected to be detected by LISA [NYZ01]. They mainly consist of white dwarves, neutron stars, stellar-mass black holes, or combinations thereof, orbiting around each other in quasi-circular orbits. These objects have masses less than a million of Solar masses[3], and a small mass ratio. Because they are in their early inspiral phase, the energy lost by gravitational radiation is not important enough to have a noticeable impact on the orbital radius. Therefore we expect that these systems will emit continuous, quasi-monochromatic gravitational-wave signals. They are often modeled with a constant frequency $f_0 = 2/P_{\text{orbital}}$, which is twice the inverse of the orbital period (see section 1.3.1). In the non-relativistic case, the Kepler laws yield a gravitational signal frequency

$$f_0 = \sqrt{\frac{GM_{\text{total}}}{\pi^2 R^3}}\,, \tag{1.56}$$

where $M_{\text{total}}$ is the total mass of the system, and $R$ the separation between the two bodies. We sometimes add a non-vanishing first derivative of the frequency to the model.

The amplitude of such a binary system can be numerically approximated [Pet08] to

$$h \approx 6 \times 10^{-21} \left(\frac{1\,\text{kpc}}{d}\right) \left(\frac{M_{\text{total}}}{M_\odot}\right)^{5/3} \left(\frac{f_0}{1\,\text{Hz}}\right)^{2/3} q\,, \tag{1.57}$$

where $d$ is the source luminosity distance, $M_{\text{total}} = M_1 + M_2$ the total mass of the binary, and $q = M_1 M_2 / M_{\text{total}}$ the mass ratio between 0 and 1/4 for equal masses. For LISA, we can see that such binary systems can be detected up to a few kiloparsecs, which limit the detection to the galactic region.

The heaviest galactic systems, such as neutron star or black hole binaries, will appear with frequencies above 1 mHz. Since most of the estimated mass distribution functions for compact objects drop for larger masses, the number of such systems per frequency bin is low (around 1, with an integration time of 1 yr according to [NYZ01]). Consequently, we expect to perform individual analyses to extract their signals and provide good estimates of their parameters. Below 1 mHz, a large population of about $3 \times 10^7$ white dwarf binaries will produce a superimposition of gravitational signals. We expect they will form a stochastic confusion background of non-resolvable sources, apart from a few systems with high signal-to-noise ratios. An iterative procedure to extract loud galactic binaries from this confusion background is foreseen but remains to be demonstrated with realistic data.

[3] A good order of magnitude to keep in mind is that $1\,\text{M}_\odot \approx 2 \times 10^{30}\,\text{kg}$.

We expect to measure the orbital periods of about 25 000 resolved systems with great accuracy, by integrating their signals over long periods. Similarly, we will measure the chirp masses and orientations of the most massive, highest-frequency and closest compact galactic binaries. Besides, the orbital motion of LISA will provide an estimate of their sky localizations with a $1\,\mathrm{deg}^2$ precision. These measurements allow to work out distribution functions and help discriminate between the formation and evolution scenarios of our Galaxy.

As of today, we know from X-ray observations more than 15 neutron star binaries in our Galaxy, whose parameters have been measured. We are confident that LISA will be able to detect their gravitational-wave signals. Since they will serve to check the quality of the instrument as soon as it will be turned on, we call those sources "verification binaries", and many more will be discovered in the coming years, thanks to surveys such as Gaia or LSST.

Joint observations in the electromagnetic spectrum will also help understand the physical processes at play in compact binary systems, and in particular, the tidal forces exerted which we expect to play a role in energy dissipation necessary to bring the bodies close enough so that they merge.

### 1.3.3 LIGO-Type Black Hole Binaries

We don't expect any compact galactic binary to merge in the LISA frequency band. However, the recent detections of merging stellar-mass black hole binaries by ground-based interferometers (*c.f.* section 1.2.5) opened new possibilities for gravitation-wave multi-band astronomy. Joint observations of gravitational waves at millihertz frequencies and second or third-generation ground-based detectors around tens of Hertz could maximize the science returns [Ses16, SBK$^+$19].

Indeed, during their early inspiral phase, binary systems of objects of a few tens of solar masses will emit gravitational waves in the LISA band years before they are detectable by the ground-based detectors. During this time, it will be possible to estimate their parameters, some of which cannot be measured around the merger. In particular, their eccentricities, sky locations and times to coalescence will be estimated to good precision. With this information, we can make sure that ground-based gravitational-wave observatories are up and running, and tuned for these specific events. In the perspective of multi-messenger astronomy, this allows pointing electromagnetic telescopes in the correct direction. Astrophysicists hope to disentangle between different formation channels. To do so, the measurements of the system eccentricities obtained in the early inspiral phase will be combined with the spins obtained at the merger [BRL$^+$16].

### 1.3.4 Supermassive Black Hole Binaries

Supermassive black holes, with masses of millions or billions of solar masses, are expected to be found at the center of most galaxies. Accretion of gas around such objects is the process that we think is responsible for powering quasars and other types of active galactic nuclei. The latter is detected at cosmological distances in many parts of the electromagnetic spectrum.

In the case of the Milky Way, the detection of bright infrared and X-ray flares [SOG$^+$02], as well as the observation of a number of stars orbiting very close to the Galactic center [SOG$^+$02, GET$^+$09], points towards the existence of a supermassive black hole of about 4 million solar masses, dubbed Sagittarius A*. More recently, the GRAVITY Collaboration measured the gravitational redshift of the S2 star near its periapsis and found that it is compatible with the theoretical predictions for Sagittarius A* [GAA$^+$18]. In April 2019, the Event Horizon Telescope project released for the first image of a supermassive black hole. M87* lies at the center of the M87 galaxy more than 16 pc away from our Galaxy, and has a mass of six billion solar masses [AAA$^+$19].

We have observational evidence and theoretical hints that such objects can form binary systems, *i.e.* when two galaxies hosting supermassive black holes merge. Supermassive black hole binaries emit high signal-to-noise ratio transient gravitational signals, lasting from years to days in the LISA frequency band. We expect that LISA will detect a few supermassive black hole binary mergers per year [KBS$^+$16], up to very large redshifts, that is almost anywhere in the Universe. This is illustrated in fig. 1.12.

It is generally accepted that supermassive black holes descend from seeds at large redshifts, as no known physical process can form black holes of millions of solar masses. While the observation of supermassive black holes at a redshift larger than 7 favors an early formation and rapid growth, the precise origin and evolution of supermassive black holes in cosmological timescales lack convincing models.

Three main formation scenarios have been proposed [Vol10, KBS$^+$16]. In the first picture, metal-free molecular clouds collapse without fragmentation, to give birth to Population III stars of thousands of solar masses. These metal-free stars leave remnant black holes of similar masses at the end of their lives, and these light seeds grow through the accretion of the surrounding halo and successive mergers. This scenario is now questioned, as Population III stars may not be as massive as previously thought, and therefore might not settle in the center of protogalaxies. The second scenario gathers various models, in which the most massive protogalaxies accrete gas from the cosmic web at a very high rate. The direct

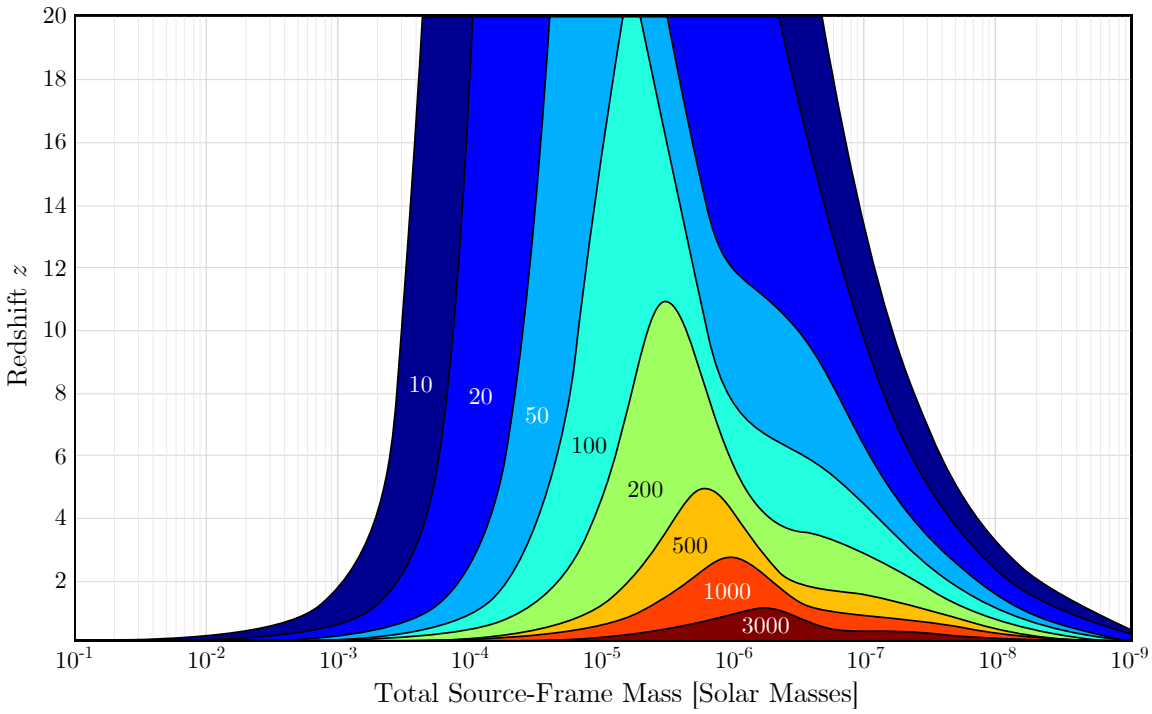


Figure 1.13: Contours of constant signal-to-noise ratios in LISA, for supermassive black hole binaries with a mass ratio of 0.2. We plot these contours as a function of the total mass in the source frame, and the redshift. Reproduced from [LL18].

collapse of these gas clouds leads to the formation of heavy black hole seeds, with masses of tens of thousands of solar masses. Lastly, it is proposed in the third scenario that compact clusters of massive stars are a common occurrence at large redshifts. Such clusters can be subject to rapid segregation of the most massive stars towards its center before a significant mass loss, leading to runaway mergers. This leaves a single star at the center of the cluster, which ends its life as a black hole of hundreds to thousands of solar masses.

Combining a precise measurement of the luminosity distance with an accurate localization for high signal-to-noise ratio signals, we can identify the galaxy cluster hosting the supermassive black hole binary system. Therefore, we have access to the redshift, and thus an estimate of the Hubble constant $H_0$ as well as other cosmological parameters. Finally, the motion of the two supermassive black holes provides a check of the General Theory of Relativity in the strong-field regime.

We expect LISA to detect supermassive black hole binaries up to redshifts larger than 10, yielding information about today's supermassive black hole seeds and their merger history. The measure of the parameters of such systems, and in particular redshifted masses and spins, will help discriminate between different formation channels.

### 1.3.5 Extreme Mass-Ratio Inspirals

As described in section 1.3.4, we expect that the nucleus of most galaxies is composed of a few-parsec-large cluster of millions of stars orbiting a central supermassive black hole. A star cannot form a binary system with an inspiral phase, as it is torn apart as soon as it passes near the central body. However, other compact objects are expected to form such systems. We call Extreme Mass-Ratio Inspiral (EMRI) the long-lasting plunging of a stellar-mass black hole into the supermassive central object. The mass ratio of such binary objects is around $10^4$ or higher, hence perturbation theory must be used to study their dynamics. We expect that the light object describe $10^5$ to $10^6$ highly relativistic orbits before coalescence, with very large periapsis precessions [ASGF$^+$07].

EMRIs are expected to emit in the LISA frequency band continuous year-long gravitational-wave signals, composed of multiple harmonics that encode the orbit of the light compact object. These harmonics will typically be buried into the instrumental and confusion noise (*c.f.* fig. 1.12), and a dedicated analysis technique must be used to extract EMRI gravitational signals. The formation and evolution processes of galaxy nuclei are not well constrained, and the merger rate has very large uncertainties. Pessimistic scenarios expect that one EMRI will merge in the LISA band per year [ASGF$^+$07], while optimistic estimates

predict a few million per year [BGS+17].

With the detection of EMRI gravitational signals, we can follow closely motion of the light body, and therefore deduce the mass and angular momentum of the central body. These measurements help set constraints on the formation and evolution of supermassive black holes and galaxies, as described in section 1.3.4. In addition, they allow for an accurate mapping of spacetime in the vicinity of the supermassive black hole. This is a unique opportunity to perform tests of the General Theory of Relativity in the strong-field regime.

### 1.3.6 Extreme Mass-Ratio Bursts

In the previous section, we described the continuous gravitational signals associated with extreme mass-ratio systems in their inspiral phases. Such systems initially evolve from more eccentric orbits, resulting from the scattering of a compact object in the galactic core on the central supermassive black hole [BG13]. Such a process does not appear in LISA as a continuous signal, but as a burst of gravitational radiations when the compact object passes near its periapsis. We call such a transient signal an extreme mass-ratio burst (EMRB). It is important to note that all EMRBs are not expected to evolve to become EMRIs, as the compact object can plunge directly into the central body, or be scattered away. The detection rate in LISA for such events is currently estimated at one per year [BG13].

### 1.3.7 Processes from the Relativistic Early Universe

Various processes from the early Universe epoch may lead to gravitational wave sources. One property of great interest is that these gravitational radiations propagate freely in the early Universe, immediately after they are produced. Thus they carry valuable information about the state of the Universe at epochs inaccessible through other means.

Gravitational-wave sources from the early Universe typically lead to stochastic backgrounds of gravitational waves today. In that case, $h_{ij}$ is a random variable, and one must perform statistical analyses to characterize the sources and extract cosmological and theoretical information. Stochastic gravitational wave backgrounds are usually characterized by their power spectral density evaluated at the present time $S_h(f)$. We often use the energy density per logarithmic frequency interval $\mathrm{d}\rho_{\mathrm{GW}}/\mathrm{d}\log f$, defined such that the total energy is

$$\rho_{\mathrm{GW}} = \int \frac{\mathrm{d}f}{f}\left(\frac{\mathrm{d}\rho_{\mathrm{GW}}}{\mathrm{d}\log f}\right). \tag{1.58}$$

We review here the main mechanisms that LISA could detect [CF18, Buo03].

### Amplification of Vacuum Fluctuation during Inflation

The inflationary period is an early phase of accelerated expansion, introduced to solve the shortcomings of the hot Big Bang model, namely the horizon and flatness problems. Besides, it provides an elegant explanation for the large-scale structures that we can observe today. During inflation, the quantum fluctuations of any light field are stretched to reach super-Hubble scales, *i.e.* beyond the causal radius. When the modes re-enter the Hubble radius during the post-inflationary period, this leads to a classical, though the stochastic, scale-invariant background of gravitational waves.

This is an irreducible gravitational wave emission that is expected for any inflationary model, including the most widely accepted single-field slow-roll model. However, these gravitational waves leave an imprint of the cosmic microwave background B-modes. Current constrained, associated with the slow-roll model, show that the amplitudes of such stochastic gravitational-wave background are too small to be detected by LISA.

Some other models predict stochastic backgrounds with higher amplitudes other spectral shapes. This is, for instance, the case if additional fields intervene during the inflationary period, leading to strong particle creation. Spectator fields can also produce gravitational waves if they have time-dependent subliminal propagation velocities during inflation. Another possibility is that new symmetries give a non-vanishing mass to the graviton. Lastly, modified theories of gravity at play during inflation could produce a much louder stochastic background of gravitational waves.

### Reheating

After the inflationary period, the particle number density has been diluted away by the exponential stretching of space. To explain the current state of the Universe, we assume that it undergoes a period of particle creation, called the reheating stage. Particle creation is modeled by coupling the inflaton to the matter fields of the standard model. If we imagine non-perturbative coupling mechanisms, this process does not only reheat the Universe but can also create a large number of gravitational waves in the form of a stochastic background.

### First-Order Phase Transitions

During the adiabatic expansion of the Universe, its temperature has decreased, and it might have undergone several phase transitions, some of them predicted by the standard model of particle physics. Several processes related to first-order phase transitions can

create gravitational-wave backgrounds, which carry precious information about the physics of these phase transitions.

Indeed, a phase transition describes the spontaneous breaking of some symmetry. A new energy-favorable vacuum state, called the true vacuum, appears with an energy lower than that of the previous state, called the false vacuum. The transition to the true vacuum is not instantaneous in the Universe but triggered by the nucleation of bubbles of true vacuum. These bubbles grow in size because of the pressure on the domain walls enclosing the bubbles, and the latent heat is released to the medium. This energy can heat the surrounding primordial plasma, but it also accelerates the domain walls up to the speed of light. If we safely assume that the field driving the phase transition is coupled to the matter fields, then a part of the latent heat is converted to the bulk motion of the plasma.

Because spherical bubbles yield to spherical plasma motions, they do not produce any gravitational waves. But as the bubble grow to fill up the entire Universe, they collide and lose their spherical symmetry, and so do the domain walls and the plasma bulk motion. Since can be a source of a stochastic gravitational-wave background. The characteristics of this stochastic background depend on the temperature at the time of the transition. This drives the size of bubbles and their collision dynamics, as well as the latent heat, *i.e.* the energy density released during the phase transition and partially converted to gravitational waves. As a result, the amplitude density of the gravitational background.

### Cosmic Defects

We defined in the previous section a phase transition as a spontaneous breaking of symmetry, yielding the conversion of an unstable state to a more energy-favorable state. During such transitions, topological defects of various dimensions can arise, such as strings, monopoles or textures. We call these defects cosmic defects.

Cosmic strings are a well-motivated case of cosmic defects for particle physics, and they may produce gravitational waves through several mechanisms. Indeed, they are one-dimensional objects characterized by their linear energy density, which form loops of all sizes up to super-Hubble scales. This is illustrated in fig. 1.14. Because there is no observational evidence of the existence of cosmic strings today, they must have decayed in the past if they exist at all. The main decay channel is the emission of gravitational waves. Indeed, super-Hubble strings can intersect to produce small loops, oscillate at relativistic frequencies, radiate gravitationally, shrink and eventually evaporates. This phenomenon creates a stationary stochastic gravitational-wave background.

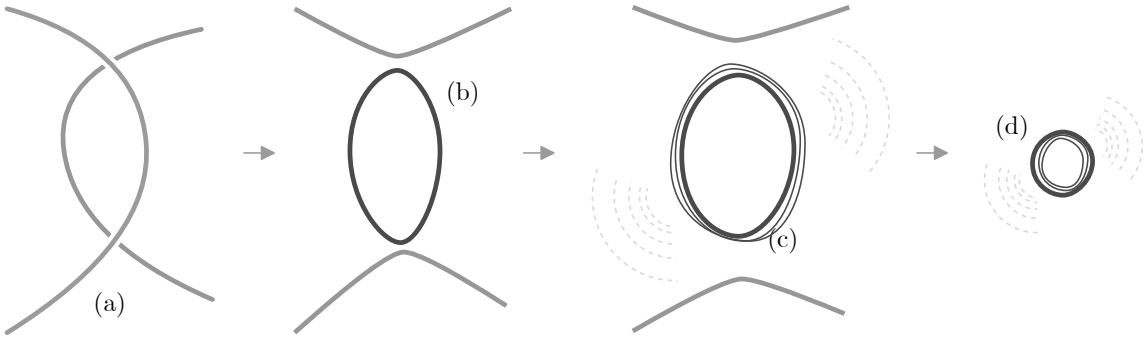


Figure 1.14: Schematics of two cosmic strings intersecting (a), and forming a loop (b). This loop decays by radiating away gravitational waves (c), until its disappearance (d).

In addition, strong bursts of gravitational waves are expected to be generated by cusps and kinks. These events are produced by loop shape discontinuities, which propagate along the string at the speed of light. The amplitude of such signals depends on the tension and the string size; in some models, cusps and kinks can be detected by LISA.

# Chapter 2

# LISANode

Designing, developing, and building a community of users and contributors around a flexible and realistic simulator for LISA is one important part of my work. It matches one of the main objectives of the LISA Simulation Working Group and fulfills the needs expressed by multiple groups inside the LISA Consortium, expressed in section 2.1.1. In this chapter, I first outline these needs in the form of draft requirements and use them to justify the main software design choices. The simulator software architecture and the main algorithms driving its execution are then described.

The project is accessible for full members of the LISA Consortium at `https://gitlab.in2p3.fr/j2b.bayle/LISANode`. A Wiki accompanies the codebase, and provides the user with a *Getting Started* manual, as well as detailed descriptions of the software. It is still a living project, with multiple contributors, and the current state of the project might differ from what is described in this chapter.

## 2.1 General Background

### 2.1.1 Need for a Simulator

LISA is a complex instrument, where measurements couple at many points with noise sources, some of which present non-linear behavior. Therefore the raw measurement signals correlate in complicated ways, which is hard to capture with simple analytical models. Plus, numerous calibration and data processing algorithms are required to produce science data, which can be used to answer astrophysical, cosmological and theoretical questions. These

processing steps add other levels of complexity and correlation in the data channels.

According to ESA's nomenclature, LISA is currently in an early phase of its development. The LISA Consortium aims to explore various instrumental configurations to identify and select the best alternatives. Design studies are therefore conducted to assess the instrumental and science performance, and build a realistic noise budget. The role of the LISA Simulation Working Group is to provide performance and physical models for critical subsystems. Flexible simulation software is undeniably a key asset for this task.

Because it implements the most recent physical models, such a tool can generate realistic data, close to what we expect to receive from the instrument when it flies. Having such data allows to check the data processing algorithms foreseen for the mission, assess their performance, and develop new ones if required. Realistic data is also necessary to study noise propagation and correlations, in particular in non-linear subsystems such as controllers. Lastly, it can be used to test the first analysis pipelines actively developed by the LISA Data Processing Group. Also, it can be integrated into the LISA Data Challenge dataset to evaluate the resilience of data analysis algorithms to several instrumental and calibration defects.

As we see, several ongoing activities of the LISA Consortium call for the immediate development of a flexible and realistic mission simulator. The latter must be able to generate measurement data, as well as execute a list of calibration algorithms. Since the exact specifications for an end-to-end mission simulator remain to be defined, and its development is not foreseen in the immediate future, the simulator that is being developed cannot be identified as the mission end-to-end simulation software. However, it can serve as a prototype: it enables us to gather the first requirements, to test a software architecture, and to build a community of scientists and developers.

### 2.1.2 Previous Simulators

LISANode is not the first nor the only simulator for LISA, for it draws its inspiration from other software that has been developed over the last fifteen years. I sketch here the features and limitations of the main simulation software which were used, along with the main findings that they enabled.

*SyntheticLISA* is a Python-based simulator developed by M. Vallisneri [Val05b]. It works in the time domain and uses an idealized and today out-of-date instrumental configuration to study the performance noise reduction algorithms for a constellation with time-varying armlengths, *c.f.* chapter 4.

*LISASimulator* was developed by N. Cornish to quickly generate LISA measurement data [RCP04]. The simulator works exclusively in the frequency domain and is based on transfer functions for a simple instrumental model of LISA.

At the time this Ph.D. work started, LISACode was the main simulation tool used by the LISA Simulation Working Group. LISACode takes advantage of the efficiency of C++, as well as the flexibility that such an object-oriented language offers. Indeed, a small number of classes represent high-level models of the main subsystems, gravitational waveforms, and instrumental noises. These classes are then connected to generate the response of the instrument to gravitational waves. This structure and the use of human-readable configuration files enable us to study a certain number of setups in a limited pre-defined configuration space. Besides, LISACode enables an easy generation of scientific products, such as sensitivity curves, signal-to-noise ratios, or parameter estimations.

However, LISACode does not exhibit a clear separation between the telemetry data, and the pre-processed calibrated time series. Moreover, the simulation scheme is hard-coded, and changes beyond simple adjustments of values are difficult. Indeed, an ominous object controls the simulation, configures and connects the different modules, and imposes the sampling rate. Although the project is now integrated with a collaborative development toolchain, such as Gitlab and Jenkins, contributing to the project remains hard and the learning curve is steep.

### 2.1.3 Simulation Requirements

LISANode must be designed with the following principles in mind: it must first exhibit high flexibility and modularity, as the mission specifications evolve quickly. This includes the possibility to fine-tune the simulation parameters and general structure, to study the different instrument setups, as well as the use of multiple timescales and sampling rates. This also enables us to refine models for subsystems without changing the general structure of the simulation, or interface LISANode with other tools dedicated, for example, to generating orbits or gravitational waveforms.

The simulator must also demonstrate good performance since one wants to generate a few years of data in a significantly shorter amount of time. The simulation timespan, including its duration and the start and end dates, must be adjustable. The entire execution of the simulation should be monitored, and intermediary products should be made available to perform sanity checks and re-run only parts of the simulation.

Lastly, LISANode should be as user-friendly as possible, as a large community of users,

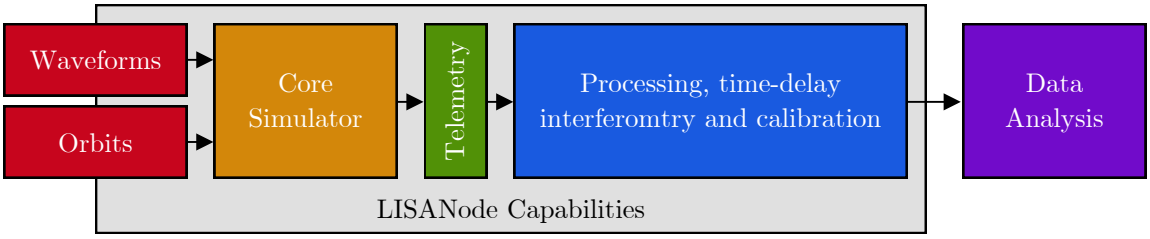


Figure 2.1: LISANode framework capabilities.

ranging from software engineers, instrumentalists, to astrophysicists, will eventually use it. LISANode must be portable to most platforms, and in particular, deployed on clusters to perform large simulations. The definition of its structure and the main algorithms must be language-agnostic, although its implementation will, of course, be based on a given set of languages, namely C++ and Python as explained below. The aim is to build a community of contributors and users around the simulator, and therefore contribution should be made easy with the use of collaborative development tools such as Gitlab, Wikis, or Continuous Integration, and an adopted contribution workflow. A clear documentation and user manual should be made available, and the code itself must be self-documented with references to the underlying models or numbers.

We present in fig. 2.1 the simulation chain, from the generation of the constellation orbits and the waveforms, the core instrumental simulation, the processing algorithms including Time-Delay Interferometry (TDI) and calibrations, down to data analysis which delivers the science products. LISANode must provide a unified framework that allows for the instrumental simulation and delivers telemetry data (L0 data), as well as the data processing algorithms (L1 data). It must be able to either generate simple orbits and waveforms for quick standalone analysis or read data generated with external software. There must be a very clear separation between the simulation of the instrument, and the on-ground processing, so that no information other than telemetry is communicated between the two. This strict restriction allows for realistic demonstrations of the performance of these processing algorithms.

The LISA End-to-End Performance Requirements Document [LIS19b] gathers the requirements for an end-to-end simulator. This document has been prepared using the experience gained from the development of LISANode, and conversely, the development of LISANode was largely inspired by this document. Its software architecture, described in the next section, fulfills most of the functional requirements, and in particular:

- The simulation time can be adjusted from hours to years.
- The simulation must not prevent implementing non-linear effects.
- Multiple and arbitrary sampling frequencies can be used.
- Simulation products must adopt an open data format.
- The simulator can be built using open-source software, and support multiple platforms (Windows, macOS, and Linux).
- Series of unit tests must be developed along with the simulator.

## 2.2 Software Architecture

In this section, I describe and justify the main architectural choices made to fulfill the requirements described in section 2.1.3. The main ideas and associated algorithms that drive the simulation are sketched, independently of the instrumental model developed for LISA.

This section is written in the hope that it can provide a smooth entry point to anyone who wishes to understand the simulator in depths to contribute to the project. Of course, the end-user who simply wishes to run simulations does not need to master the inner workings of LISANode. We refer these users to the next sections describing the instrumental model implemented in LISANode.

### 2.2.1 Overview

LISANode is a flexible and general framework that can be used to build simulations. It works exclusively in the time domain and can handle discrete time series with different sampling rates. In the following section, we call a time-dependent data stream a signal. Each simulation is represented in LISANode by a simulation graph, which describes the various nodes, used to generate or transform signals, and how these signals flow from and to the nodes. Users can compose their custom simulation graphs by assembling existing nodes, or simply run existing predefined simulation graphs.

Formally, a graph is defined as an ensemble of interconnected nodes. Each node represents a physical model and computes several output signals using a number of input signals, and some model parameters. As described in detail in section 2.2.2, the interface of a node is

indeed constituted by zero or more parameters, which can only be set before the simulation starts, as well as zero or more inputs and outputs, which can be connected to other nodes.

On the one hand, a node can represent a very simple model, such as the addition of two signals. In this case, we say that the node is atomic. It is defined as a C++ subclass of Node and placed in its header file. LISANode offers a library of atomic nodes, ranging from mathematical operations, logical gates, samplers, random number generators, deterministic signal generators, to input/output operations, digital filters, and delay operators. We give a list of these atomic nodes, their interface, and the underlying models in appendix B.

On the other hand, a node can itself be an entire graph, *i.e.* an ensemble of nodes encapsulated into one single opaque object. In that case, it is defined as a Python subclass of Graph, among other graphs in a Python script. Similarly to any other nodes, its interface is defined by several parameters, inputs, and outputs, and it can be connected to other nodes. This nested architecture is a powerful feature that allows us to create various levels of abstraction for complex operation, or to divide one instrument into different subsystems. It is also used to refine a model without changing the structure of the simulation, by simply replacing an atomic node with a much more complex graph.

When a node is used inside a simulation graph, it is given a name that uniquely identifies the node. Most of the time, the node type is used, but if multiple instances of the same type are used, these names must be different. One can access the parameters, inputs, and outputs of a node using a dot-chaining pattern, such as my_node.myparam, or my_other_node.awesome_output.

LISANode can make sense of a simulation graph, unwrap the compound nodes so that only atomic nodes remain, check the graph consistency, schedule the execution of each atomic node, compile an executable and run it. This is illustrated in fig. 2.2. Using a single command line, each of these steps is executed to produce the simulation products. In the following subsection, we describe the architecture of a node, the graph analysis algorithms performed by LISANode, and provide a brief description of the main commands provided by LISANode.

### 2.2.2 Graphs and Nodes

As pictured in fig. 2.3, each type of node has a unique and descriptive name, such as Addition, TravelTimes, or FractionalDelay. In addition, it defines an interface composed of:

- A set of *parameters*, which are used to adjust the model which supports the node.

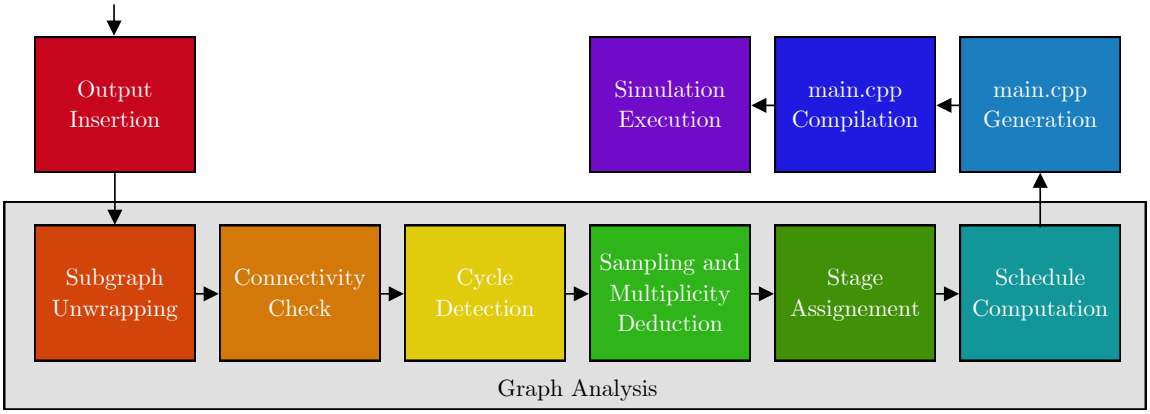


Figure 2.2: LISANode workflow. Each box represents an algorithm executed, to go from a Python class (the simulation graph), all the way down to the execution of a software (the simulation), and the generation of the simulation products.

The node parameters can be set before the simulation starts, but are kept constant when the simulation is executed. They are in particular used to configure the node or pre-compute values for efficiency.

- A set of *inputs* signals, used to feed the model. The node is responsible to store the previous input samples it needs to evaluate the model. An input can be set to a constant value or connected to another node's output. In the last case, we call *parents* the upstream connected nodes, and *children* the downstream nodes.
- A set of *output* signals, calculated from the model which supports the node. New samples for each output are computed when the node is executed.

### 2.2.3 Atomic Nodes

For atomic nodes, this interface is declared in the associated C++ class, as parameters, inputs, and outputs are member variables. Many atomic nodes use generic types <T>, *i.e.* their implementations are type-agnostic. They can, therefore, be used for a large variety of signals, and the type must be given when instances of the node are created, such as MyNode<double> or MyNode<int>. Failing to do so will result in an error during compilation.

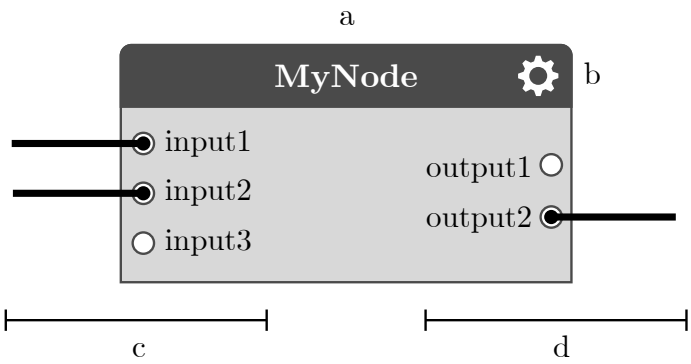


Figure 2.3: The anatomy of a fictitious node of type MyNode (a). A node defines a set of parameters, represented by the gear icon (b), and a number of named inputs (c) and outputs (b), which can be connected or not to other nodes.

All atomic nodes define a few common parameters, used to schedule the execution of the simulation. Among others, the sampling frequency defines the rate at which the node is fired, the time origin defines the timestamp associated with the first generated output samples, and the upsampling and downsampling factors are used when the sampling frequencies of the node's parents and children are not identical.

If needed, an atomic node stores previous samples of its input signals with a circular buffer. This is an efficient memory structure, and its size $N$ is defined when the node is configured. We use the standard BOOST library implementation boost:circular_buffer<T> for efficiency and quality. A new value is pushed into the buffer with push_front(), and previous values are accessed with subscript notation my_input[k], with $0 \leq k < N$, so that the most recent sample is for $k = 0$.

Only two methods must be implemented by an atomic node:

- prepare() is called after all parameters have been set on the node and before the simulation starts. This is where the node should configure its state, pre-compute values to optimize its execution or throw errors if invalid parameters have been used.
- fire (time) is called during the simulation, when the node should compute one new sample for every output signal. This is where the model that supports the node is implemented. This method is called a large number of times during the simulation, and a particular effort must be made to reduce the complexity of this method.

As an example, we give below the example of the WhiteNoise node, which generates stochastic white noise samples given an amplitude spectral density. The various parameters, inputs, and outputs are described in more detail in appendix B.

```
using namespace std;
using namespace boost;

/**
 Generate a Gaussian white noise.

 This node generates a noise realization for a given amplitude
 spectral density and sampling frequency.
 */
class WhiteNoise: public Node {

public:

    // MARK: Parameters

    /** On-off switch for the noise */
    bool enabled = true;

    /** Amplitude spectral density, in /sqrt(Hz) */
    double asd = 1.0;

    /**
     Seed used to initialize the sequence of random numbers.

     If the seed is set to its default value 0, a random seed
     is drawn instead. Set it to another value allows for
     reproducible results.
     */
    unsigned int seed = 0;

    // MARK: Outputs

    /** Generated noise */
    double result;

    void prepare() {

        // Draw a random seed, if needed
        prepared_seed = seed;
        if (seed == 0) { prepared_seed = seed_generator(); }

        // Set up random generator and pre-compute factors
```

```
        generator = mt19937(prepared_seed);
        double standard_deviation = asd * sqrt(sampling_frequency / 2.0);
        distribution = normal_distribution<double>(0.0, standard_deviation);

        result = 0.0;
    }

    void fire(double time) {
        if (enabled) {
            result = distribution(generator);
        }
    }

protected:

    mt19937 generator;
    unsigned int prepared_seed;
    random_device seed_generator;
    normal_distribution<double> distribution;

};
```

### 2.2.4 Graphs and Compound Nodes

As briefly mentioned in section 2.2.1, an entire simulation graph can also be viewed as a single node and therefore used to compose another graph. In this case, the content of the embedded graph is opaque for the embedding graph, following the encapsulation principle. Only its declared interface, that is the set of parameters, inputs, and outputs, is accessible, as pictured in fig. 2.4.

The interface of a compound node is declared in its Python class. This is done by publishing existing parameters, inputs, and outputs of inner nodes, using the respective methods publish_param(), publish1_input(), and publish_output(). Note that the published name does not have to match the corresponding inner node's.

When a graph is run as a simulation, the published parameters, inputs, and outputs are interpreted differently. Indeed, parameters and inputs become available as command-line options, so that the user can quickly change their values without compiling the simulation again. Outputs become the product of the simulation and are written to files for further processing.

As an example, we reproduce here the Python class associated with the graph illustrated

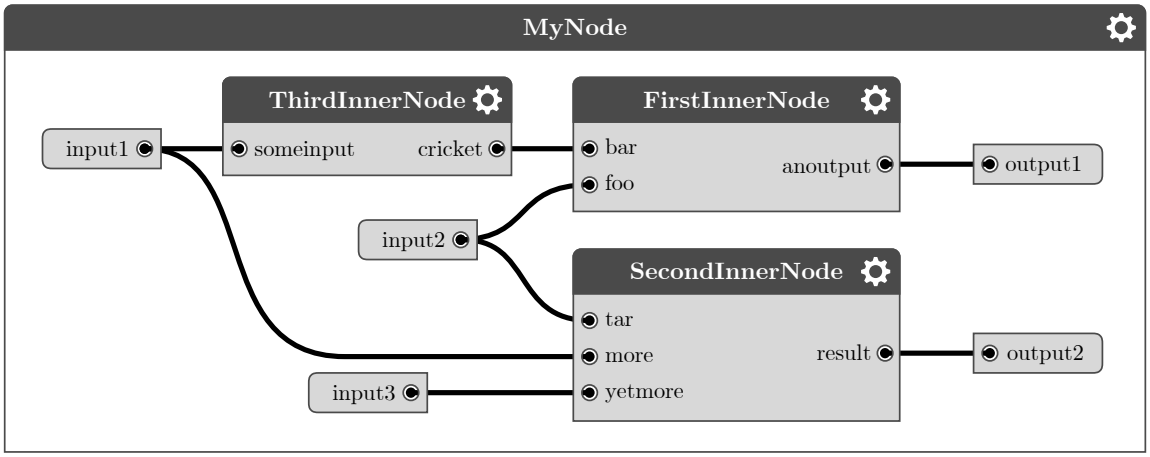


Figure 2.4: Exploded view of a graph which would correspond to the node pictured in fig. 2.3. Published inputs and outputs are connected to embedded nodes' input and outputs, and these node are interconnected. Note that published parameters follow the same pattern, but are not pictured here.

in fig. 2.5. This graph has one published input signal, which is first rescaled by a Gain node, whose gain parameter is also published so that it can be adjusted using a command-line option. Then a white noise is generated, whose amplitude spectral density is also published, and therefore adjustable. This noise is added to the rescaled input signal using the Addition node, and the result is published as sum. We also publish the white noise alone, as noise.

```
from lisanode import Graph


class MyGraph(Graph):
    def __init__(self):
        super().__init__("MyGraph")

        self.add("WhiteNoise", name="noise")
        self.add("Gain<double>", name="gain")
        self.add("Addition<double>", name="sum")

        self.connect("noise.result", "sum.a")
        self.connect("gain.result", "sum.b")

        self.nodes["noise"].fs = 1.0
```

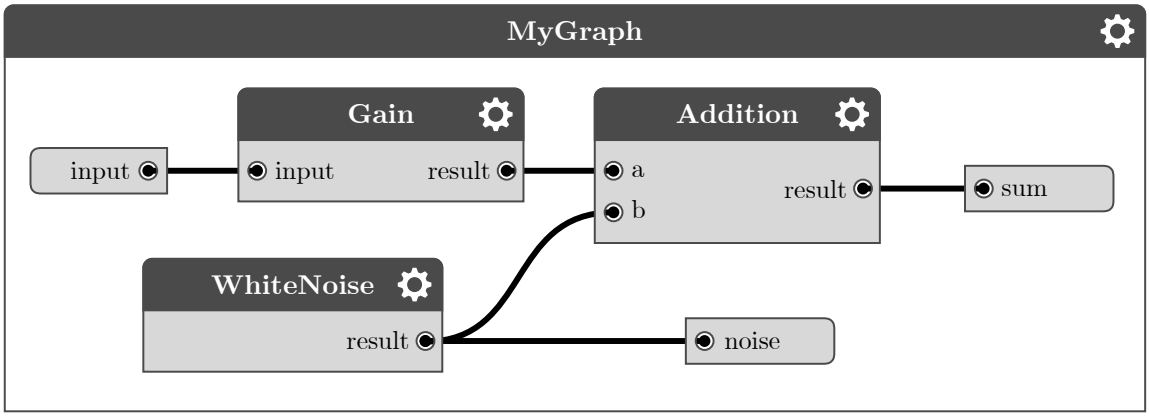


Figure 2.5: An example of a graph, which rescales an input signal, and adds a white noise to it.

```
        self.nodes["noise"].params = {'seed': 0}

        self.publish_param("noise.asd", "asd")
        self.publish_input("gain.input", "input")

        self.publish_output("sum.result", "sum")
        self.publish_output("noise.result", "noise")
```

## 2.3 Graph Analysis

We describe here the various steps illustrated in fig. 2.2, along with the associated algorithms. They are all implemented in the Python classes Graph and Node, and prevent from attempting to compile an inconsistent or ill-defined graph. The user can run the graph analysis algorithm from the terminal, using lisanode analyze GRAPH, where GRAPH is a path to the Python script, and the name of the graph, in the form of path/to/python/script.py:GraphName. Alternatively, if the graph is defined in a Python module, this can be the module path, and the name of the graph, in the form of lisanode.lisa.instrument:Phasemeter.

### 2.3.1 Output Insertion

LISANode inserts and connects WriteText nodes to each published output so that they are written to individual text files when the simulation is executed. Note that the name of the file matches the name of the published output. Because published outputs can be selectively disabled with the corresponding command-line option −{}−**enable** or −{}−disable, we only consider enabled published outputs here.

### 2.3.2 Subgraph Unwrapping

This algorithm flattens the graph, by recursively unwrapping all compound nodes until only atomic nodes remain. The steps are as follows:

1. The algorithm first transfers the internal nodes of each compound node to the embedding graph. The interconnections between these internal nodes are preserved, and the unwrapped compound nodes are removed from the graph.

2. Graph's published parameters, inputs, and outputs that point to compounds nodes are replaced so that they refer to the internal nodes of these compounds nodes.

3. Published parameters, inputs, and outputs of each compound nodes are rerouted to their internal nodes. In other words, parameters defined at the compound node level are set to the corresponding internal nodes. Similarly, parents and children of compound nodes are reconnected to the corresponding internal nodes.

### 2.3.3 Connectivity Check

We check here that the graph is connected, *i.e.* that there is a path between every pair of nodes, *i.e.* there is no unreachable or isolated node. In our case, an isolated node is a node that has no parent nor child, and which is not the only node in the graph. We also check that the graph defines at least one published output.

### 2.3.4 Cycle Detection

We require here that the graph is acyclic, *i.e.* that it does not contain direct connections forming a path, starting and ending at the same node. Indeed, such a cycle would indicate

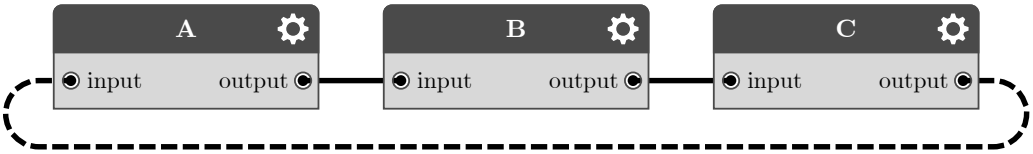


Figure 2.6: Example of cycle broken down using an indirect connection from **C** to **A**. Although **A** depends on **C**, the latter will use the former's previous output sample.

an acausal simulation structure, because the production of one signal sample would depend on that very same sample.

The simulation of feedback loops, for instance in controllers, is possible if one breaks the cycle. This is done by replacing usual, or direct, connections with indirect connections that allow for delays. No cycle is present in fig. 2.6: if **A** has a dependency in **C**, the connection is indirect so that there is an implicit delay. **A** will use **C**'s previous output samples.

### 2.3.5 Sampling and Multiplicity Deduction

Indeed, the user does not have to provide a sampling frequency for all nodes, but the information must be sufficient to deduce a sampling frequency for all nodes. This algorithm checks that the sampling frequencies defined on the nodes are consistent with each other, and fill the missing sampling frequencies.

In most cases, a node's sampling frequency $f_s$ must match that of its parents and children. In general, this sampling frequency changes when a node holds non-unity downsampling $d$ or upsampling $1/d$ ratios. The following rule, illustrated in fig. 2.7, is used to check the sampling consistency of the graph and deduce the missing sampling frequencies

$$\forall A \in \text{nodes}, \quad \forall B \in \text{parents}(A), \quad f_s^B = d^A f_s^A \,. \tag{2.1}$$

A graph must define at least one explicit sampling frequency, from which LISANode is able to deduce that of all other connected nodes, upstream and downstream.

From this equation, we can show that all sampling frequencies in one graph are linked by simple ratios,

$$\forall A, B \in \text{nodes}, \quad \exists p, q \in \mathbb{N}^*, \quad p f_s^A = q f_s^B \,. \tag{2.2}$$

The simulation sampling period, or atomic sampling period, is the smallest period that divides all node sampling periods. More formally, it is the greatest common divisor of all sampling periods. Therefore the simulation sampling frequency is defined as the least

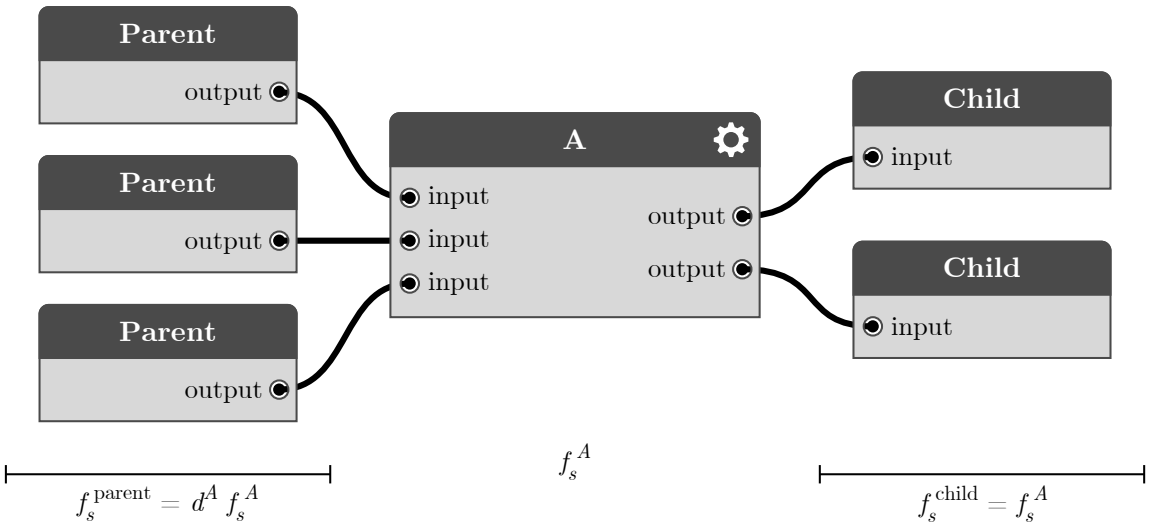


Figure 2.7: Relationship between a node's sampling frequency and that of its parents and children. It must be verified for all nodes of the graph. It is used to check that the sampling frequencies specified by the user are consistent with each other, and deduce missing sampling frequencies.

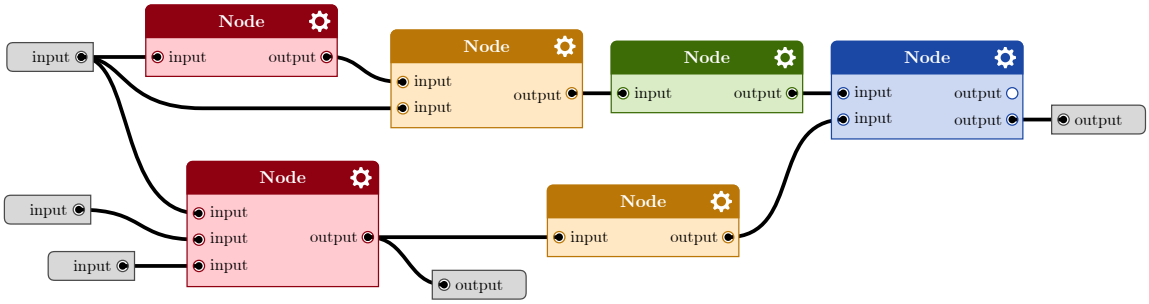


Figure 2.8: Simple simulation graph whose nodes have been assigned their stages. The stages 0, 1, 2, and 3 correspond respectively to nodes in red, orange, green, and blue.

common multiple of all node sampling frequencies,

$$f_s^{\text{simu}} = \text{lcm}(f_s^A, \quad \forall A \in \text{nodes}) \,. \tag{2.3}$$

Each node $A$ must be fired every $n^A$ atomic sampling periods, such that

$$f_s^{\text{simu}} = n^A f_s^A \,, \tag{2.4}$$

and we call $n^A$ the multiplicity of $A$. Using this formula, the algorithm assigns to each node its multiplicity, used to compute the schedule.

### 2.3.6 Stage Assignment

At this point, we are certain that the graph does not contain any cycle (see section 2.3.4), and that it is only made of atomic nodes because it has been unwrapped (see section 2.3.2). Here we partition these atomic nodes into different stages so that the following rule holds: for any node $A$ of stage $N$, all its direct parents are of stages strictly less than $N$, and all its children are of stages strictly greater than $N$. Formally,

$$\forall A \in \text{nodes}, \quad \forall B \in \text{parents}(A), \quad \text{stage}(B) < \text{stage}(A) \,. \tag{2.5}$$

This is illustrated by an example in fig. 2.8.

We use the Khan algorithm to build the stages, which is quick and always converges for acyclic graphs. A set $S$ of nodes that have not yet been processed is created, and we iterate over the nodes of $S$ until the set is empty, *i.e.* until all nodes have been assigned a stage. If

the node has no direct parents, we assign it to stage 0. If the node has at least one parent in $S$, it is skipped and left in $S$ for later processing. Finally, if the intersection of the node's direct parents and $S$ is empty, this means that all its direct parents have been processed and assigned a stage. We can, therefore, assign the maximum of the parent stages, augmented by 1, as the node's stage.

### 2.3.7 Simulation Scheduling

Now that we have ordered the nodes of our graphs in terms of dependencies, we can build a valid schedule, *i.e.* a procedure for the execution of the nodes, such that we produce the expected signals at the end of the chain.

It is very simple to understand in the case of graphs with only one sampling frequency: we run, possibly in parallel, all nodes in the first stage since they don't depend on any other nodes. Then, we run the nodes in the successive stages, once again possible in parallel. eq. (2.5) ensures that the input samples the nodes require from their direct parents are produced before they are used. A schedule is, therefore, a list of sets of nodes that can be executed in parallel. In this simple case, each set corresponds to exactly one stage.

In general, the schedule is composed of the content of $N$ super-sets, where $N$ is the schedule size given by

$$N = \mathrm{lcm}(n^A, \quad A \in \mathrm{nodes})\,. \tag{2.6}$$

To build the schedule, we append $N$ simple schedules, in which we keep only nodes whose multiplicity is a divisor of the super-set index. All other nodes are not executed.

As an example, let us consider the three-node simulation graph pictured in fig. 2.9. The user has specified a non-unity downsampling ratio of 2 for node $B$, as well as an upsampling ratio of 3 for node $C$, and the sampling frequency for node $A$, $f_s^A = 1\,\mathrm{Hz}$. From these information, the sampling deduction described in section 2.3.5) fills the missing sampling frequencies $f_s^B = 0.5\,\mathrm{Hz}$, and $f_s^C = 1.5\,\mathrm{Hz}$. Following the algorithm described in section 2.3.6, we distinguish three stages so that the simple schedule associated to this graph is

$$\{[A], [B], [C]\}\,. \tag{2.7}$$

Using eq. (2.3), we compute the simulation sampling frequency $f_s^{\mathrm{simu}} = \mathrm{lcm}(1, 0.5, 1.5) = 3\,\mathrm{Hz}$. The nodes therefore have the following multiplicities: $n^A = 3$, $n^B = 6$, and $n^C = 2$.

The schedule size is $N = \mathrm{lcm}(3, 6, 2) = 6$. The first super-set has index 0, and is exactly the simple schedule $\{[A], [B], [C]\}$. The second super-set is empty. The third keeps node

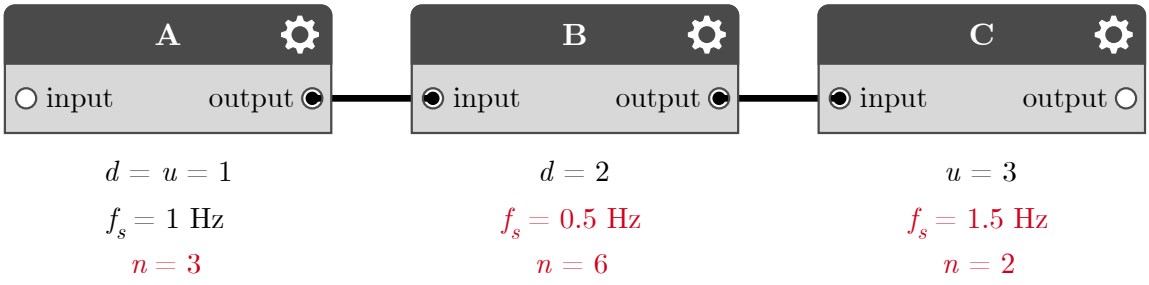


Figure 2.9: Simple simulation graph with multiple sampling frequencies. We give in black the downsampling or upsampling ratios and the sampling frequencies specified by the user, and in red the sampling frequencies and multiplicities deduced by LISANode.

$C$, and becomes $\{[C]\}$. The fourth is $\{[A]\}$, the fifth is $\{[C]\}$, and the sixth and last is once more empty.

Therefore the complete schedule reads:

$$\{[A], [B], [C], [C], [A], [C]\}\,. \tag{2.8}$$

## 2.4 Code Generation and Compilation

At the end of the graph analysis steps, described in section 2.3, the schedule is ready and LISANode can generate a valid main.cpp file. LISANode then uses the local C++ compiler to build this file into an executable and runs it.

The user can analyze, build, and run a graph using the single command lisanode run GRAPH in their terminal. Note that lisanode viz GRAPH can be used to obtain a graphical representation of the graph.

### 2.4.1 Structure of main.cpp

The generated main.cpp document contains the following elements:

1. A list of header files are imported, in which the classes associated with the atomic nodes used in the graph are defined.

2. The declaration of the various nodes of the graph, as well as the output nodes automatically inserted before the graph was analyzed, see section 2.3.1.

3. The declaration and configuration of the command-line argument parser. We include here the published parameters and inputs of the graph. If $-\{\}-$**help** is given, we print the help message and return.

4. The assignment of the parameters of each node. In particular, we assign the deduced sampling frequencies, upsampling and downsampling ratios, and all other node-specific parameters set at the graph level. If some parameters are published, we check whether they are given some values as command-line options. If this is the case, we assign these new values to the corresponding node's parameters.

5. We call prepare() on each node.

6. If some inputs are published, we check whether they are given some values as command-line options. It this is the case, we assign these new values to the corresponding node's parameters.

7. The main simulation loop, containing all the sets of the schedule. For each set, we execute all the nodes in this set by calling fire (), passing the current time. This time is computed from the loop iteration index, the set index, and the associated periods. We then push the generated output samples to the child nodes using the push_front() method.

As an example, we consider the graph illustrated in fig. 2.5, and described in section 2.2.2. We reproduce here the associated main.cpp, generated with LISANode.

```
#include "cxxopts.hpp"
#include "Gain.hpp"
#include "Addition.hpp"
#include "WhiteNoise.hpp"
#include "WriteText.hpp"

int main(int argc, char** argv) {

    // MARK: Node definitions

    WhiteNoise _noise;
    Gain<double> _gain;
    Addition<double> _sum;
    WriteText<double> _output_for_sum;
    WriteText<double>::type> _output_for_noise;
```

```
// MARK: Argument parsing

cxxopts::Options parser = cxxopts::Options("MyGraph");
parser.add_options()
("h,help", "show this help message and exit")
("d,duration", "simulation duration in seconds", cxxopts::value<double>())
("asd", "set asd on noise", cxxopts::value<double>())
("input", "input signal on gain", cxxopts::value<double>())
;

auto args = parser.parse(argc, argv);
if (args.count("help")) {
    std::cout << parser.help() << std::endl;
    exit(0);
}

// MARK: Parameter assignement

_noise.sampling_frequency = 1.0;
_noise.downsampling = 1;
_noise.upsampling = 1;
_noise.name = "noise";
_noise.seed = 0;

_gain.sampling_frequency = 1.0;
_gain.downsampling = 1;
_gain.upsampling = 1;
_gain.name = "gain";

_sum.sampling_frequency = 1.0;
_sum.downsampling = 1;
_sum.upsampling = 1;
_sum.name = "sum";

_output_for_sum.sampling_frequency = 1.0;
_output_for_sum.downsampling = 1;
_output_for_sum.upsampling = 1;
_output_for_sum.name = "output_for_sum";
_output_for_sum.path = "./sum.txt";

_output_for_noise.sampling_frequency = 1.0;
_output_for_noise.downsampling = 1;
_output_for_noise.upsampling = 1;
_output_for_noise.name = "output_for_noise";
_output_for_noise.path = "./noise.txt";
```

```
if (args.count("asd")) {
    _noise.asd = args["asd"].as<double>();
}

// MARK: Node preparation

_noise.prepare();
_gain.prepare();
_sum.prepare();
_output_for_sum.prepare();
_output_for_noise.prepare();

// MARK: Input assignement

if (args.count("input")) {
    _gain.input.assign(1, args["input"].as<double>());
}

// MARK: Simulation loop

double duration = 10.0;
if (args.count("duration")) { duration = args["duration"].as<double>(); }
int nloop = ceil(duration * 1.0);
progress_display show_progress(nloop);

for (int iloop = 0; iloop < nloop; iloop += 1) {
    show_progress += 1;

    // Set 1

    _noise.fire(1.0 * iloop + 0 * 1.0);
    _gain.fire(1.0 * iloop + 0 * 1.0);

    _sum.a.push_front(_noise.result);
    _output_for_noise.input.push_front(_noise.result);
    _sum.b.push_front(_gain.result);

    // Set 2

    _sum.fire(1.0 * iloop + 0 * 1.0);
    _output_for_noise.fire(1.0 * iloop + 0 * 1.0);

    _output_for_sum.input.push_front(_sum.result);

    // Set 3
```

```
        _output_for_sum.fire(1.0 * iloop + 0 * 1.0);
    }
}
```

### 2.4.2 Build and Run

Once the main.cpp is generated, LISANode issues a command in the terminal to build it using the locally-installed GCC, or clang on macOS, compiler. The product of the compilation is an executable named after the simulation graph and linked against all atomic nodes of the LISANode library, described in appendix B.

# Chapter 3

# Instrumental Model

In this chapter, I present the instrumental model implemented in the LISANode simulator. I first give a general overview of the mission and the instrument, with a description of the top-level simulation graphs used to simulate each spacecraft, their orbits, the propagation of optical signals between them, and the response function of the instrument to gravitational waves. In the second part, I present the various interferometric measurements performed onboard the spacecraft, as well as the various noise sources which enter those measurements. Lastly, I present how these measurements are processed by the phasemeters and the onboard computers before they are telemetered down to Earth.

We present here the main ideas behind the instrumental models. These models correspond to the current mission baseline, but might change since the mission is still in mid-phase A. The complete documentation of all simulations graphs and nodes dedicated to the simulation of LISA can be found in appendix C. Besides, the code itself is extensively documented, and we invite the interested reader to look it up if the answers are not presented in this thesis.

## 3.1 The LISA Mission

If not otherwise specified, the following paragraphs are mainly taken from the LISA Mission Proposal [DASpAh+17] and the LISA Payload Definition Document [LIS18a].

The LISA mission has been accepted for a duration of 4 years, with a possible mission extension of 10 years. Illustrated in fig. 1.11 are the three spacecraft, flying in a nearly-

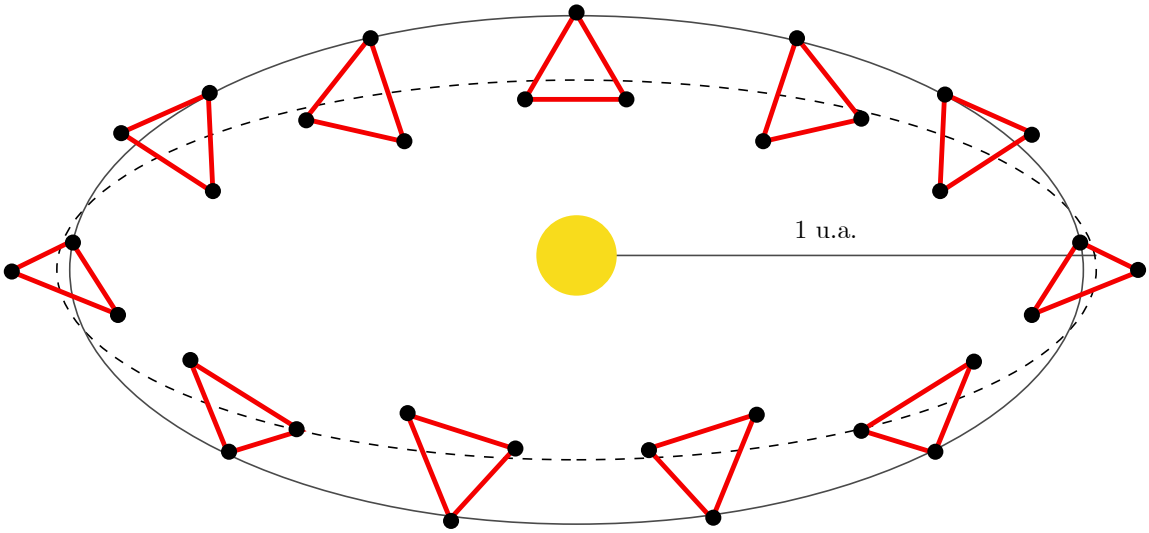


Figure 3.1: Cartwheel motion of the LISA constellation in a plane inclined with respect to the ecliptic plane, while its barycenter follows its heliocentric orbit.

equilateral triangular configuration. The constellation plane is inclined by around 60° with respect to the ecliptic plane, and its barycenter trails the Earth on its orbit around the Sun by about 50 million kilometers. During its yearly revolution, the constellation has cartwheel motion. This is illustrated on fig. 3.1. The distances between the spacecraft have an average value of 2.5 million kilometers and fluctuate along the year by plus or minus 1 % [NKDV06]. As a result, the spacecraft relative velocities are nonvanishing, and the laser beams exchanged by the spacecraft are submitted to Doppler effect. The mission will use a dedicated Ariane 6.4 launcher, and the transfer time will last more than a year.

Each spacecraft is equipped with two optical benches, two laser sources, and two inertial test masses. Each inertial test mass is a cube of solid gold-platinum alloy, measuring 4.6 cm on a side and weighing almost 2 kg. Once the spacecraft have been inserted in their correct orbits, the test masses are released inside their housings. Capacitive sensors and interferometric systems monitor the positions and orientations of the test masses with respect to the spacecraft. Micro-thrusters are used to steer the spacecraft so that it follows the test masses along their translational degrees of freedom, and in particular along the arms. Electrostatic actuators are used to apply the required forces and torques along the remaining degrees of freedom. As a result, the test masses are kept in free fall along the line of sight during the whole mission. Laser interferometry provides a precise measurement of

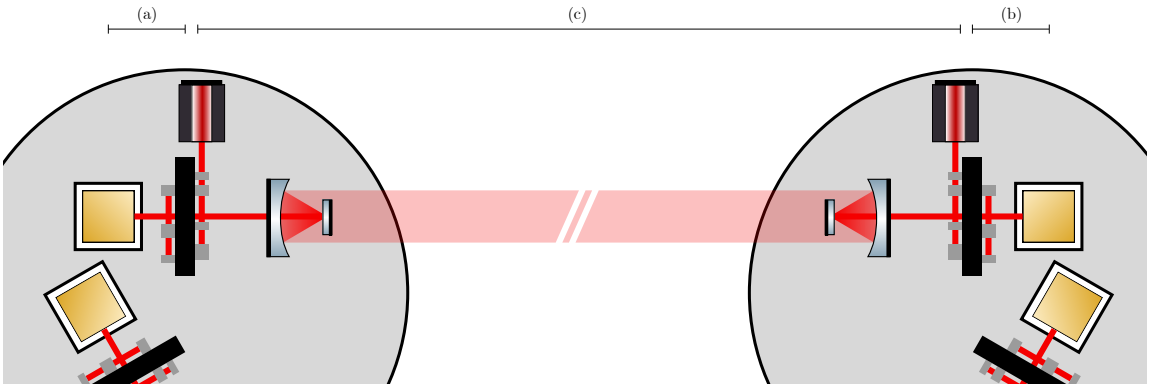


Figure 3.2: The test-mass-to-test-mass distance is reconstructed from the two test-mass-to-spacecraft (a), (b), and one long-baseline (c) measurements.

the test mass acceleration with respect to the optical bench, inside the spacecraft. These measurements are performed by the so-called *test-mass interferometer*.

Laser beams are exchanged between all three spacecraft. Telescope assemblies are dedicated to sending and collecting the light. The resulting long-baseline or *science interferometric measurements* are used to monitor the changes in the distances between the optical benches. Lastly, the *reference interferometers* measure the differences in the frequencies of the two local laser sources. All in all, six interferometric measurements are performed onboard each spacecraft in this *split interferometry* configuration (fig. 3.2). The optical frequencies of each laser source are slightly offset, and therefore these heterodyne measurements contain a beatnote. Offline processing of these beatnotes allows reconstructing the test-mass-to-test-mass distances.

For this purpose, a phasemeter tracks the beatnote frequencies and converts the optical signals to phase measurements. These phase measurements are then processed by the onboard computers. Communication windows are scheduled once a day: all data is collected by a single master spacecraft before it is telemetered down to Earth. The eighteen phase signals are then combined to monitor the differential optical pathlength variations between pairs of test masses, separated by millions of kilometers, *c.f.* chapter 4.

The effect of a gravitational wave is a tidal deformation of the constellation (*c.f.* section 1.1.5), which appears as a modulation in time of the optical pathlength between two test masses. These changes are small (a few pm to a few nm, *c.f.* section 1.2.1) with respect to the variations due to the spacecraft orbital motions (around 10 000 km), but can be dis-

tinguished because they occupy non-overlapping frequency ranges. Indeed, the former is at millihertz frequencies, whereas the latter have periods of many months.

Because of the beam divergence, the collected light at the distant spacecraft is only a fraction of the sent power. The laser sources onboard the spacecraft emit a few watts, thus the received signal does not exceed a few hundreds of picowatt [LIS18b]. A mere reflection is impossible, as the power received by the original spacecraft would not be sufficient to perform interferometric measurements at the required precision. Instead, the distant laser source has its phase locked on the incoming signal, with a given frequency offset. We use this laser source to send a fresh beam back to the original spacecraft. Not all lasers can be locked with each other, and several laser locking configurations are possible. However, it is not clear at the moment, what the best choice would be [Hei18].

The phasemeter can track beatnote frequencies between 5 MHz and 25 MHz. Unfortunately, the long-baseline beatnote frequencies vary due to the Doppler effect of the spacecraft orbital motion. These variations are so large that no set of laser frequency offset can ensure that all beatnote frequencies remain in the phasemeter range throughout the mission. Therefore, these frequency offsets must be changed with time, according to what is called a frequency plan. This frequency plan must be established so that several constraints are verified, mainly that all beatnotes must be within the phasemeter range. Additional constraints exist, due to potential cross-coupling when test-mass or reference beatnote frequencies cross science beatnote frequencies. A genetic algorithm was proposed in [Bar15], but exact solutions can be found using the geometrical approach described in [Hei18].

The LISA sensitivity is mainly limited by spurious forces and noise in the measurement of the optical pathlength. On the one hand, non-inertial forces are exerted on the test masses, making them deviate from their geodesic motion. The resulting stray acceleration can mimic the effect of a gravitational wave, and degrade the measurements. This is why the test masses are placed inside their housing, shielded from a number of these external forces. The spacecraft is still subjected to these spurious forces, but micro-thrusters constantly steer it so that it follows the test masses in a drag-free fashion. On the other hand, various instrumental noise sources couple into the measurements. Some can be expressed as optical pathlength variations, *e.g.* due to thermal deformation of the optical benches, or the non-reciprocal phase shift in the optical fiber, between two adjacent optical benches. Other noise sources are tied to the measurement processes themselves, such as the stray light on the optical benches, the photodiode shot noise, or the errors in the sampling processes due to imperfect onboard clocks. The various noise sources are discussed further in the next sections, and a high-level decomposition of the sensitivity is presented in fig. 3.3.

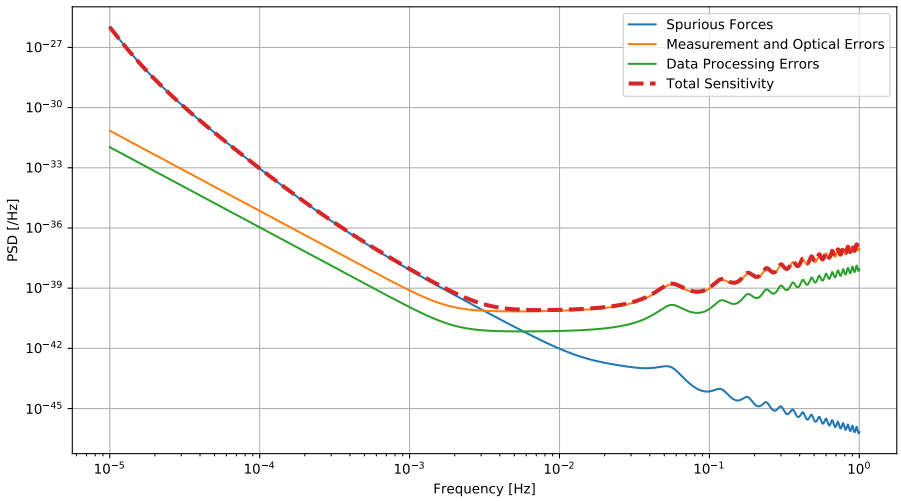


Figure 3.3: LISA noise budget, used to compute the sensitivity of the instrument. It is the sum of the effect of spurious forces applied on the test masses, the measurement and optical errors, and the effect of imperfect data processing algorithms.

Laser noise is the dominant noise source in the LISA measurement, as it appears many orders of magnitude above the expected gravitational wave signals. Offline techniques have been proposed to remove this noise, combining interferometric measurements at different times to synthesize virtual photon paths that suppress laser noise [TA99, TEA02, AET02]. Similarly, clock noise can be calibrated for with dedicated algorithms [OHD12, TH18]. These data processing procedures are not perfect and introduce additional errors in the final products of the mission. Their implementation in the simulator, as well as the study of their performance, are the objects of the following chapters.

## 3.2 Simulation of the Constellation

### 3.2.1 Project Architecture

One top-level simulation graph constitutes the usual entry point for the simulation. The LISA graph simulated the physics of gravitational waves, along with the response of the instrument, the propagation of the laser beams between the spacecraft and on each optical bench, and delivers the measurements as we expected we will receive them from telemetry. The on-ground data processing, described in chapter 4, is performed by another independent

top-level TDI graph to deliver L1 data.

To maintain a clean codebase, and allow for easy collaboration between multiple developers, the instrument is divided into mostly independent subsystems, themselves divided into smaller components matching as closely as possible the hardware subsystems. Similarly, data processing is executed as a succession of smaller steps. This is easily expressed in the LISANode framework, with the help of nested graphs, *c.f.* chapter 2.

Therefore, most of the code designed to simulate LISA specifically is organized in several Python files, located under `lisanode/lisa/`. These files define a series of graphs, which are then connected to build the entire LISA simulation. We describe here the files that are used, along with the graphs they contain:

- `config.py` contains the high-level options for the simulation, which cannot be set with command-line arguments because they change the structure of the graph.
- `instrument.py` defines the graphs for the main instrument systems and subsystems, including the optical bench, interferometer, phasemeter, on-board computer, spacecraft, laser links, and most importantly, the high-level graph for LISA.
- `propag.py` defines the graphs used to propagate the signals between the spacecraft, *i.e.* account for the finite propagation speed of light and the contribution of gravitational signals with the help of the instrument response. They are used for the laser links in `instrument.py`.
- `noises.py` defines the various instrumental noises that couple into the interferometric measurements, used in `instrument.py`.
- `intervar.py` contains the TDI intermediary variables, used to build the main channels in `tdi.py`, see chapter 4. The intermediary variables are used to remove some of the instrumental noises, such as the optical bench displacement noise, and half of the laser noise.
- `tdivar.py` defines the TDI algorithms and the graphs used to compute the main channels, such as Michelson $X$, $Y$, and $Z$ channels, quasi-orthogonal $A$, $E$, and $T$ variables, or Sagnac $\alpha$, $\beta$, $\gamma$, and $\xi$ variables, *c.f.* chapter 4. They are used in "tdi.py".
- `tdi.py` contains the high-level graphs used to compute the TDI algorithms, such as TDI, TDIFromText, and LISAWithTDI. *C.f.* chapter 4.
- `clockcal.py` defines graphs used to correct for clock noise, which are used in `tdi.py`.

- `ranging.py` defines nodes to model the absolute ranging estimation.
- In addition, `naming.py` defines functions to help maintaining consistent naming throughout the code.

Some atomic nodes requirement for the simulation of LISA are defined in `lisanode/toolbox/nodes/lisa/`. We mainly have

- The nodes used to compute the instrumental response of one LISA arm to a gravitational signal, such as LinkResponse.
- The nodes used to compute the spacecraft positions and velocities, and deduce the light travel times along each link, such as KeplerianOrbits, ArbitraryOrbits and TravelTime.
- The nodes used to compute the gravitational waveforms for various sources, such as GalacticBinary or read them from files.

### 3.2.2 Constellation Model

We consistently use the indexing conventions illustrated in fig. 3.4 to develop and implement our instrumental models. They match the conventions used in [Ott15, OHD12, Pet08, PAH$^+$08, BLPH19]. The spacecraft are indexed clockwise from 1 to 3; nevertheless, these indices run from 0 to 2 to be consistent with Python and C++ standards. The Movable Optical Sub-Assemblys (MOSAs), laser sources, optical benches, and test masses are indexed according to the associated spacecraft. MOSAs pointing clockwise have their indices primed, and the same rule applies for any system hosted by the MOSA, such as optical benches, telescopes, laser sources, or test masses.

We call an arm the path between two MOSAs and label them with the index of the opposite spacecraft. They are three arms in the LISA constellation. The six LISA links are the oriented paths between all pairs of MOSAs. They are indexed according to the associated arm, with primed numbers for links pointing clockwise. The length of a link is called *armlength* and is denoted $L_i$, where $i = 1, 1', 2, 2', 3, 3'$.

The LISA graph is the entry point for the instrumental simulation, as it represents the entire LISA constellation. It generates the interferometric measurements, as we expect to receive them from the instrument through telemetry, as well as the ranging estimates. A detailed documentation can be found in appendix C, while the interferometric measurements are described in section 3.4.

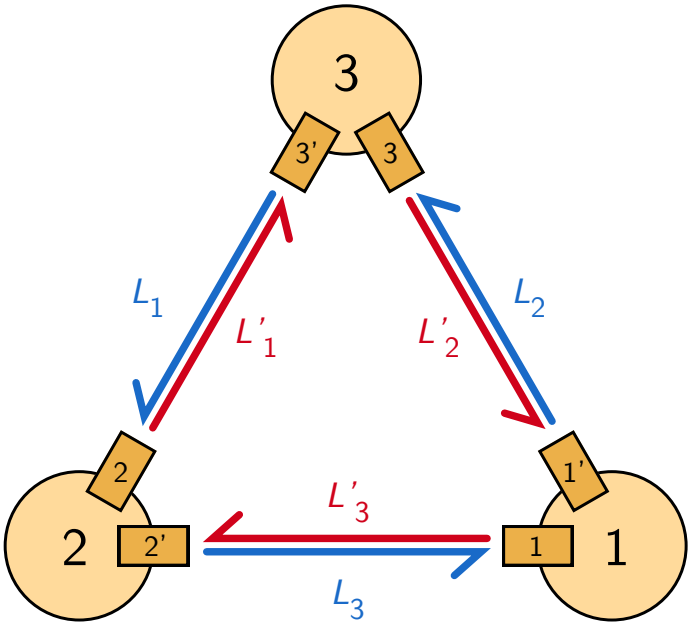


Figure 3.4: Conventions for labeling spacecraft, MOSAs, lasers, optical benches and arm-lengths. Primed indices are used for arms pointing clockwise, and for MOSAs and optical benches receiving light clockwise.

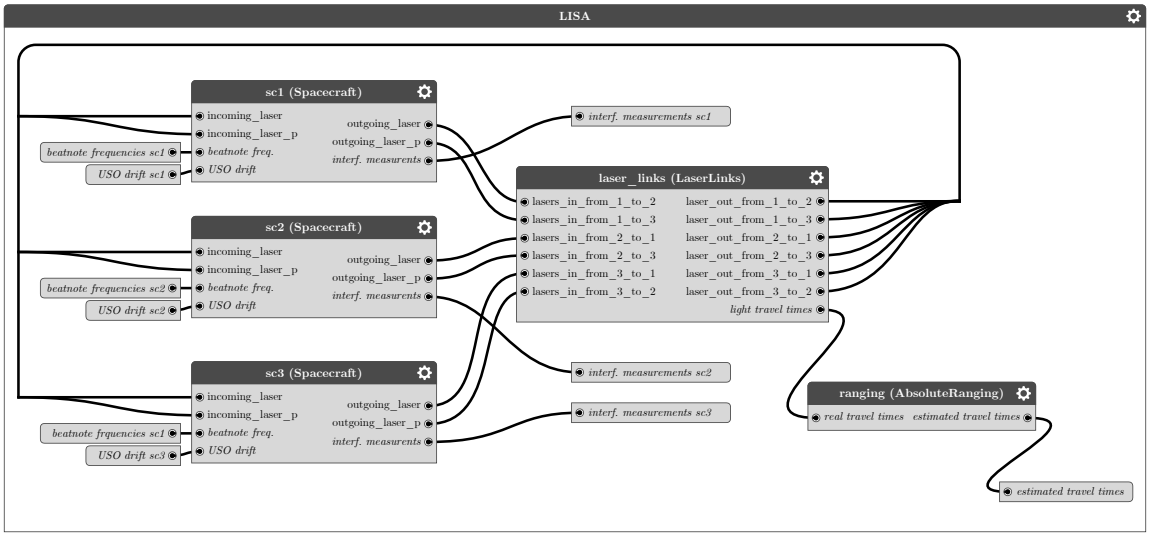


Figure 3.5: Schematics of the top-level LISA graph. It is used to simulate three spacecraft, which exchange laser beams and delivers the interferometric measurements, as well as an estimate of the light travel times along each link.

The LISA graph composed of three independent Spacecraft, which exchange laser beams with each other and deliver the interferometric measurements. The beams are propagated between the spacecraft by a LaserLinks node, which is also responsible for computing the orbit of each spacecraft, as well as the contributions of the different gravitational wave sources on each optical link. Lastly, AbsoluteRanging models the estimation of the light travel time between the spacecraft, which is telemetered to Earth alongside the interferometric measurements. This structure is represented in fig. 3.5.

LaserLinks has three main objectives. First, it computes the orbits or reads them from files, delivering the spacecraft positions and velocities, *c.f.* section 3.2.3. Secondly, it computes the light travel times and propagates the laser beams along each link, *c.f.* section 3.2.4. Lastly, this is where the gravitational wave response is computed, and their contributions are added to the propagating laser beams, as described in section 3.2.6. The structure of LaserLinks is represented in fig. 3.6.

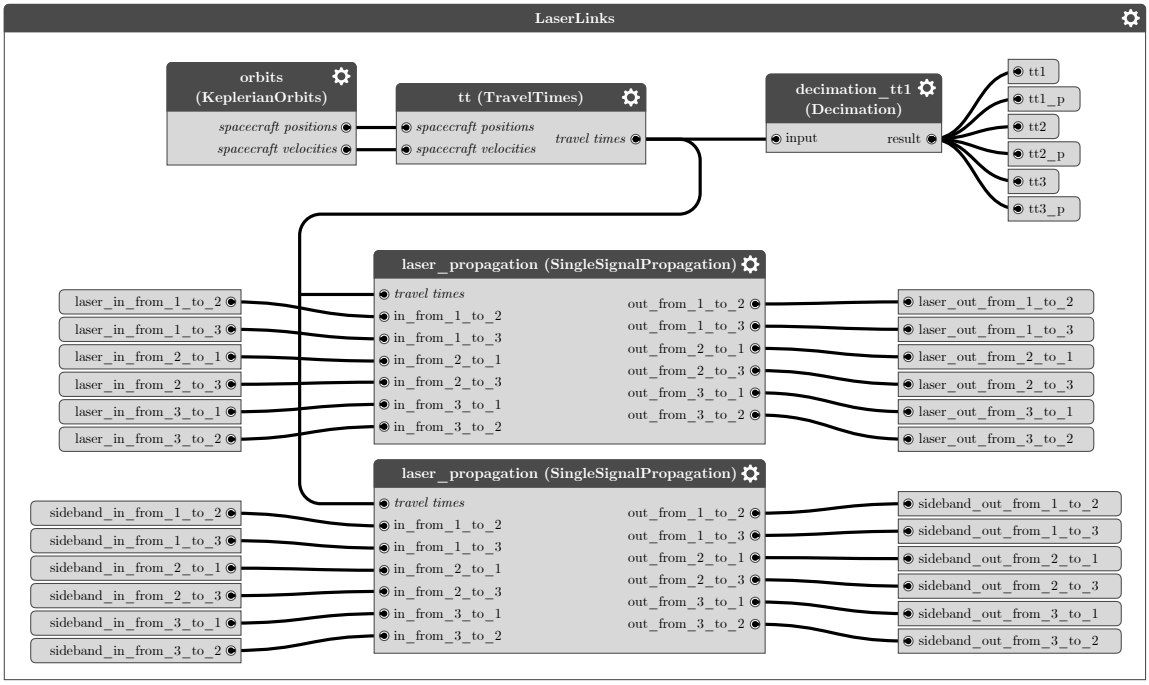


Figure 3.6: Schematics of the LaserLinks graph. It is used to compute orbits, travel times, and propagate the signals between the spacecraft. The nodes used to compute the instrument response to gravitational waves are not here represented.

### 3.2.3 Orbit Simulation

The three LISA spacecraft will be placed in heliocentric orbits, to minimize the relative spacecraft velocities (and thus the associated Doppler shifts) while remaining close enough to the Earth for a good data transmission quality. Analytic studies [DNKV05, NKDV06] of the two-body problem in the Keplerian framework have been conducted. They have shown that the previous conditions are fulfilled for a nearly-equilateral triangular constellation, trailing the Earth by about 20 deg in a heliocentric orbit. This is illustrated in fig. 3.1. The plane of the constellation has an angle of about 60 deg with the plane of the ecliptic[1], and the three spacecraft have a cartwheel motion around the constellation barycenter within this plane.

#### Keplerian Orbits

In the following paragraphs, we present the results obtained by Nayak, Rajesh, Koshti, Dhurandhar, and Vinet in [NKDV06]. We follow the conventions and notations from [CRVP05].

It had been showed previously that a triangular constellation, whose plane is tilted by $\pi/3$ with respect to the plane of the ecliptic, satisfies the aforementioned conditions [DNKV05]. In the article, the orbits are expanded to second order of $\alpha = l/(2R) \approx 1/60$, where $R \approx 1\,\mathrm{au}$ is the distance between the constellation barycenter and the Sun, and $l \approx 2.5 \times 10^6\,\mathrm{km}$ is the mean distance between the spacecraft. The authors show that there is a rather large residual variation of the armlengths, as well as important relative spacecraft velocities. This orbital motion is called constellation *flexing*, and at the origin of Doppler shifts in the received laser frequencies. As a conclusion, a set of optimized orbits are proposed, leading to armlength changes of 10 000 km, and a peak variation of the spacecraft relative velocity of about $5\,\mathrm{m\,s^{-1}}$.

We used these results to implement the KeplerianOrbits node, documented in appendix C. The node is used in LaserLinks if the configuration options ORBIT_TYPE is set to keplerian in `config.py`.

The tilt angle between the constellation and ecliptic planes is set to

$$\nu = \frac{\pi}{3} + \delta\alpha\,. \tag{3.1}$$

Here, $\delta$ is a small perturbation to the tilt angle, in units of the characteristic ratio $\alpha$[2]. This

[1] The plane of the ecliptic is the plane that supports the Earth orbit around the Sun.

[2] The reader will be careful not to mix the total tilt perturbation $\delta\alpha$, denoted $\delta$ in [NKDV06], with the

is the parameter used during the optimization procedure. The optimized set of orbits was found for $\delta = 5/8$, which is the default value set on the node.

The orbit of the first spacecraft is an ellipse with an inclination angle $\mu$ and eccentricity $e$. Geometrical considerations yield the exact relationship between $\alpha$ both these parameters,

$$e = \sqrt{1 + \frac{4\alpha\cos\nu}{\sqrt{3}} + \frac{4\alpha^2}{3}} - 1, \quad \tan\mu = \frac{\alpha\sin\nu}{\sin(\pi/3) + \alpha\cos\nu}\,. \tag{3.2}$$

To second order in $\alpha$, these equations become

$$e \approx \frac{\alpha}{\sqrt{3}} + \left(\frac{1}{2} - \delta\right)\alpha^2, \quad \mu \approx \alpha - \frac{\delta - 1}{\sqrt{3}}\alpha^2\,. \tag{3.3}$$

The eccentric anomaly $\Psi_k$ for the $k$-th spacecraft, where $k = 1, 2, 3$, is implicitly given by

$$\Psi_k - e\sin\Psi_k = \Omega t - (k-1)\frac{2\pi}{3} + \phi_0 = \phi_k(t)\,, \tag{3.4}$$

where $t$ is the time, $\phi_0$ is the initial constellation rotation, and $\Omega = 2\pi/1\,\mathrm{yr}$ is the average angular velocity. This equation can be solved iteratively to second order in $\alpha$. We then have

$$\Psi_k(t) \approx \phi_k + \frac{\sin\phi_k}{\sqrt{3}}\alpha + \frac{3 - 6\delta + 2\cos\phi_k}{6}\sin\phi_k\alpha^2\,. \tag{3.5}$$

Using the shorthand notation $\theta_k = (k-1)2\pi/3$, we can now write the positions of the $k$-th spacecraft

$$x_k(t) = R\Big[(\cos\Psi_k - e)\cos\mu\cos\sigma_k - \sqrt{1-e^2}\sin\Psi_k\sin\sigma_k\Big]\,, \tag{3.6}$$

$$y_k(t) = R\Big[(\cos\Psi_k - e)\cos\mu\sin\sigma_k + \sqrt{1-e^2}\sin\Psi_k\cos\sigma_k\Big]\,, \tag{3.7}$$

$$z_k(t) = -R(\cos\Psi_k - e)\sin\mu\,. \tag{3.8}$$

Taking the time derivative of eq. (3.4), we find that the derivative of the eccentric anomaly for the $k$-th spacecraft can be written as

$$\frac{\mathrm{d}\Psi_k}{\mathrm{d}t}(t) = \frac{\Omega}{1 - e\cos\Psi_k(t)}\,. \tag{3.9}$$

tilt perturbation in units of the characteristic ratio, here denoted $\delta$, but defined as $\delta/\alpha$ in [NKDV06]. These parameters have no name in [CRVP05], where the authors only define the total tilt angle $\nu$.

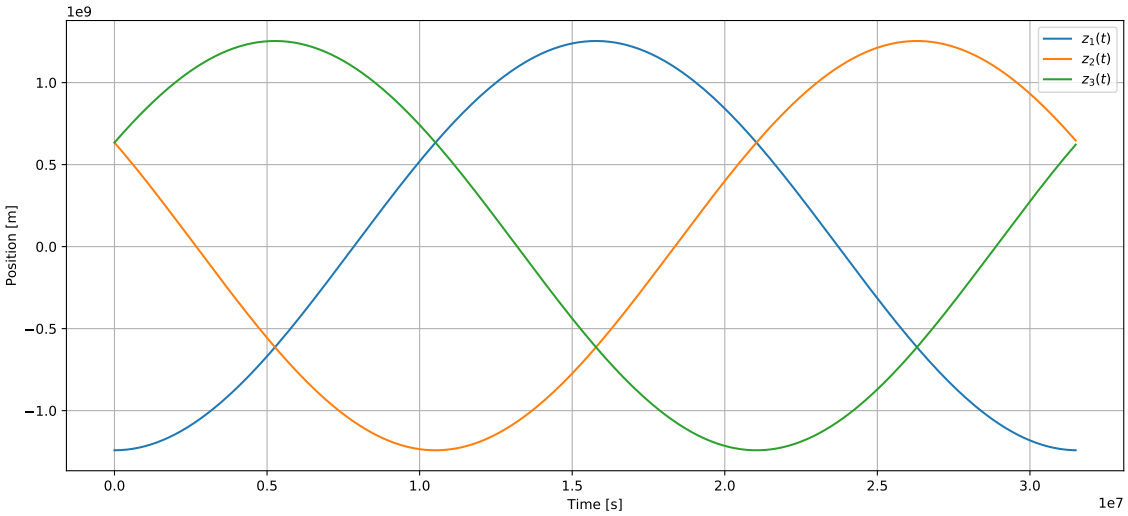


Figure 3.7: Spacecraft positions along the $z$-axis, using Keplerian orbits.

Using this result, and taking the time derivatives of the spacecraft position equations, one finds that the spacecraft velocity reads

$$v_{x_k}(t) = R\frac{\mathrm{d}\Psi_k}{\mathrm{d}t}\left[-\sin\Psi_k\cos\mu\cos\sigma_k - \sqrt{1-e^2}\cos\Psi_k\sin\sigma_k\right], \tag{3.10}$$

$$v_{y_k}(t) = R\frac{\mathrm{d}\Psi_k}{\mathrm{d}t}\left[-\sin\Psi_k\cos\mu\sin\sigma_k + \sqrt{1-e^2}\cos\Psi_k\cos\sigma_k\right], \tag{3.11}$$

$$v_{z_k}(t) = R\frac{\mathrm{d}\Psi_k}{\mathrm{d}t}\sin\Psi_k\sin\mu\,. \tag{3.12}$$

The positions along the $z$-axis of the three spacecraft, computed according to the Keplerian orbits, are plotted in fig. 3.7. We can see that the spacecraft are phase-shifted by a third of a year, and oscillate around the plane of the ecliptic.

### Arbitrary Orbits

To study the effects of the constellation deformation, it is also possible to use ad-hoc orbits, deduced from the armlength time series, given as inputs. In particular, the LISA graph can be configured to have linearly-varying armlengths by setting the ORBIT_TYPE parameter to linear_armlengths in `config.py`.

Arbitrary orbits are computed by the node ArbitraryOrbits, which replaces KeplerianOrbits in

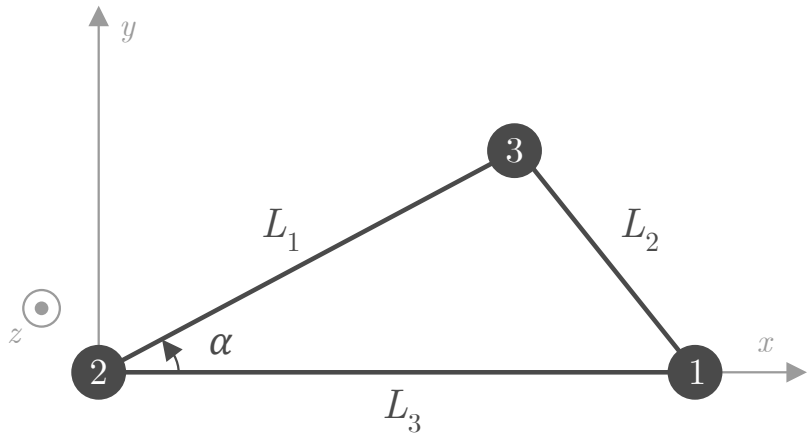


Figure 3.8: Schematics of the constellation, when using arbitrary orbits.

the LaserLinks graph. The armlengths $L_1(t)$, $L_2(t)$, and $L_3(t)$ are given as inputs, and we use the configuration given in fig. 3.8.

Assuming that the armlengths verify the triangular inequalities, the angle $\alpha$ between arms 1 and 3, illustrated in fig. 3.8, is first computed with

$$\cos\alpha(t) = \frac{L_1(t)^2 + L_3(t)^2 - L_2(t)^2}{2L_1(t)L_3(t)}\,. \tag{3.13}$$

Then the spacecraft positions are given by

$$x_1(t) = L_3(t)\,, \qquad y_1(t) = 0\,, \qquad z_1(t) = 0\,, \tag{3.14}$$

$$x_2(t) = 0\,, \qquad y_2(t) = 0\,, \qquad z_2(t) = 0\,, \tag{3.15}$$

$$x_3(t) = L_1(t)\cos\alpha(t)\,, \qquad y_3(t) = L_1(t)\sin\alpha(t)\,, \qquad z_3(t) = 0\,. \tag{3.16}$$

The spacecraft velocities are estimated using a first-order difference equation.

### Orbits from File

The real orbits will be computed using ESA's dedicated tools, to account for the gravitational effects of other bodies, such as the Earth, the Moon, Jupiter, etc. Moreover, real orbits are also chosen to optimize other mission parameters, such as the fuel required for the spacecraft to be installed on their orbits.

LISANode can be interfaced with such dedicated tools, and read orbit data files instead of using a simple model to compute the spacecraft positions and velocities. If ORBIT_TYPE

is set to from_file in `config.py`, the graph LaserLinks uses ReadText nodes to read and parse an orbit data files.

### 3.2.4 Light Travel Times

Accurate knowledge of the light times of flight along the six links is necessary to implement a realistic model of the instrument. Indeed, these times of flight are used to simulate the propagation of the laser beams between the spacecraft. On the other hand, these propagation delays are used in the data processing algorithms described in chapter 4. The delay time series must be computed with a precision high enough to match the requirements of the data processing algorithms, around the nanosecond. This is why we use the full relativistic treatment proposed by B. Chauvineau, T. Regimbau, J. Y. Vinet, and S. Pireaux in [CRVP05]. The model presented below, and implemented in the node TravelTimes, are taken from their work.

The light travel time $\tau_{AB}$ between spacecraft $A$ and $B$ is deduced by matching the geodesic equations of both spacecraft, with the null geodesic of a photon emitted by $A$ and received by $B$. The spacecraft positions and velocities are immediately given by the orbits, as the spacecraft must follow the free-falling test masses that they host to measure gravitational waves. As we saw in the previous section, and even for a set of optimized orbits, there is an irreducible constellation flexing. In other words, the light travel times along each link vary with time.

The atomic node TravelTimes takes as inputs the position and velocities of each spacecraft and computes the six light travel times. Due to the orbital motion of the spacecraft, these travel times are different for photons traveling in opposite directions. Therefore, one must be careful to specify the link, and not only the arm, along which the light travel time is devised. Please note that a complete description of the TravelTime node's interface can be found in appendix C.

The model uses an expansion of the null geodesic equation from $A$ to $B$, and the motion of spacecraft $B$, in powers of the parameter

$$\epsilon = \frac{GM_\odot}{rc^2} = \frac{R_{\mathrm{Schw}}}{2r}\,, \tag{3.17}$$

where $M_\odot$ is the mass of the Sun, $c$ is the speed of light, $R_{\mathrm{Schw}}$ the Sun Schwarzschild radius, and $r$ the distance of the considered spacecraft from the Sun.

One of the main conclusions of [CRVP05] is that one only needs to expand the light travel times to the first order in $\epsilon$ to reach the required precision. Then, the light travel time $\tau_{AB}$

can be computed as a sum of the various orders,

$$\tau_{AB} = t_B - t_A \approx \tau_{AB}^{(0)} + \tau_{AB}^{(1/2)} + \tau_{AB}^{(1)} \,. \tag{3.18}$$

Note that the time of flight of the photon is computed as a function of its arrival time $t_B$, and not its time of emission $t_A$. As a consequence, all values will be implicitly evaluated at arrival time $t_B$, and in particular we define in the Solar-System Barycenter (SSB)

- The respective positions $\mathbf{r}_A$ and $\mathbf{r}_B$, of spacecraft $A$ and $B$.
- Their respective velocities $\mathbf{v}_A$ and $\mathbf{v}_B$.
- The separation vector $\mathbf{r}_{AB} = \mathbf{r}_B - \mathbf{r}_A$.
- The link unit vector $\hat{\mathbf{n}} = \mathbf{r}_{AB}/\|\mathbf{r}_{AB}\|$, always taken at order zero in $\epsilon$ in the following.

Order zero corresponds to a flat spacetime, and a fixed constellation with spacecraft at rest. We trivially find

$$\tau_{AB}^{(0)} = \frac{\|\mathbf{r}_{AB}\|}{c} \,. \tag{3.19}$$

The next order accounts for the classical spacecraft motion, and aberration corrections,

$$\tau_{AB}^{(1/2)} = \tau_{AB}^{(0)} \times \frac{\mathbf{v}_B \cdot \hat{\mathbf{n}}}{c} \,. \tag{3.20}$$

It is interesting to note that this term is changed under a permutation of spacecraft. This means that the 1/2-order contribution is different for photons traveling in opposite directions along the same arm. This is the well-know Sagnac effect, named after the French physicist Georges Sagnac, and it is due to the rotational motion of the constellation illustrated in fig. 3.1. We find that

$$\tau_{AB}^{(1/2)} - \tau_{BA}^{(1/2)} = \tau_{AB}^{(0)} \times \hat{\mathbf{n}} \cdot \frac{\mathbf{v}_A + \mathbf{v}_B}{c} \neq 0 \,. \tag{3.21}$$

The last term $\tau_{AB}^{(1)}$ includes relativistic corrections. In particular, the Shapiro time-delay effect. We have

$$\begin{aligned}\tau_{AB}^{(1)} = \frac{\tau_{AB}^{(0)}}{2c^2}\Big[\|\mathbf{v}_B\|^2 + (\mathbf{v}_B \cdot \hat{\mathbf{n}})^2\Big] - \frac{c(\tau_{AB}^{(0)})^2 R_{\text{Schw}} \times \mathbf{r}_B \cdot \hat{\mathbf{n}}}{4\|\mathbf{r}_b\|^3} \\ + (1+\gamma)\frac{R_{\text{Schw}}}{2c^2} \ln\left(\frac{\mathbf{r}_A \cdot \hat{\mathbf{n}} + \|\mathbf{r}_{AB}\| + \sqrt{\|\mathbf{r}_A\|^2 - (\mathbf{r}_A \cdot \hat{\mathbf{n}})^2 + (\mathbf{r}_A \cdot \hat{\mathbf{n}} + \|\mathbf{r}_{AB}\|)^2}}{\hat{\mathbf{n}} \cdot \mathbf{r}_A + \|\mathbf{r}_A\|}\right) .\end{aligned} \tag{3.22}$$

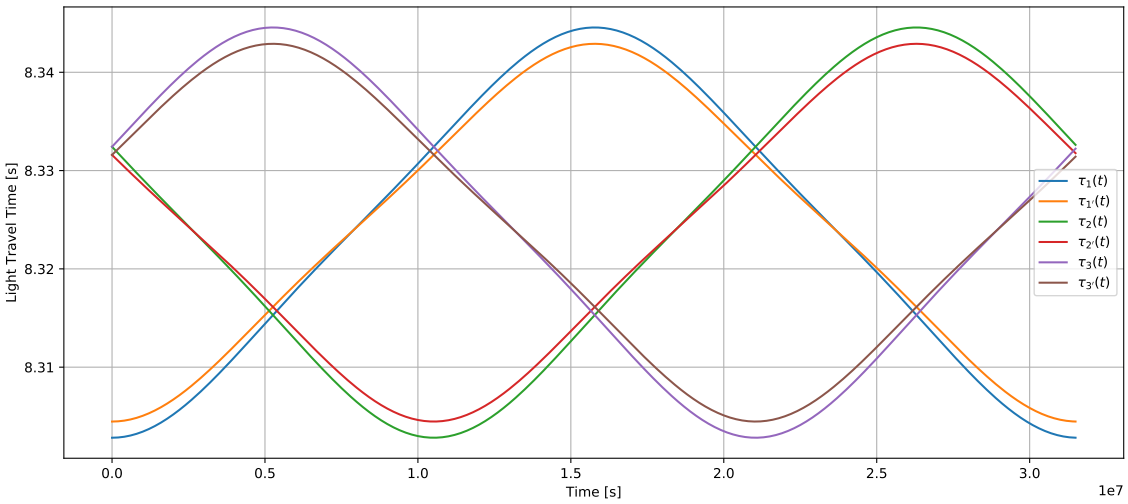


Figure 3.9: Light travel times along each LISA link. The yearly variation is due to the constellation *flexing*, while the difference between the time of flight in opposite directions is due to the Sagnac effect.

We represent in fig. 3.9 the light travel times along each LISA link, using the Keplerian orbits, as described in section 3.2.3.

### 3.2.5 Absolute Ranging

The computation of realistic light travel times along each LISA link is necessary to simulate the propagation of signals between the spacecraft, as described in the previous section. However, in reality, one does not have access to these *god-given* information. The inter-spacecraft distance, or absolute ranging, is estimated by modulating the exchanged laser beams with a pseudo-random code. The local and distant codes are then correlated to deduce the light time of flight between the spacecraft.

Because the clocks onboard each spacecraft are not actively synchronized, they can drift with respect to each other. Consequently, offline processing using Kalman-like filters must be applied, to correct for the clock drifts and provide correct light times of flight [Wan17]. This technique combines knowledge of the constellation orbits, the clock jitter Power Spectral Densitys (PSDs), and the pseudo-random codes to continuously calculate the optimal ranging estimates and clock jitters, in the least-square error sense. Simulations have shown

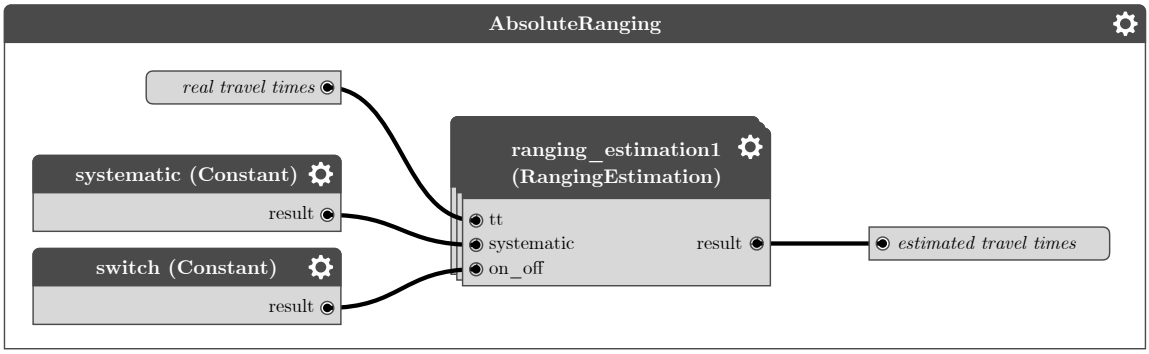


Figure 3.10: Schematic of the AbsoluteRanging graph. In reality, six instances of RangingEstimation are used, one for each link.

that it is possible to determine absolute ranging at the nanosecond precision [WHD14].

In our simulation, we model the imperfections of these algorithms by adding an error $r_i$ in the ranging estimates along the six links $i$. This error contains a systematic bias $r_{\text{systematic}}$[3], identical for all links, and an uncorrelated stochastic error $r_{\text{error},i}$,

$$r_i = r_{\text{systematic}} + r_{\text{error},i} \,. \tag{3.23}$$

The stochastic error is a Gaussian white noise with a pessimistic Amplitude Spectral Density (ASD) of $3 \times 10^{-9}\,\text{s}$, while we assume a vanishing systematic bias.

The node AbsoluteRanging, presented in fig. 3.10, contains an instance of RangingEstimate for each link. The latter makes use of RangingError nodes to generate the ranging error time series, and add them to the god-given light travel times computed from the orbits. This is illustrated in fig. 3.11. Please refer to appendix C for a complete documentation of these graphs.

### 3.2.6 Gravitational-Wave Response

In this section, I present the model used to compute the instrument response to gravitational waves. We follow the conventions proposed by the LISA Data Challenge (LDC) Manual [LIS19a].

[3]Such a systematic bias in the ranging estimates can be corrected for using Time-Delay Interferometry Ranging (TDIR) methods. More details are given in chapter 4.

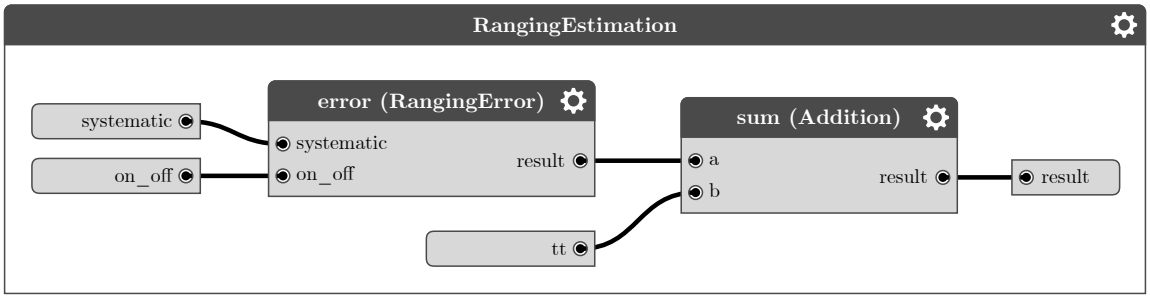


Figure 3.11: Schematic of the RangingEstimation graph.

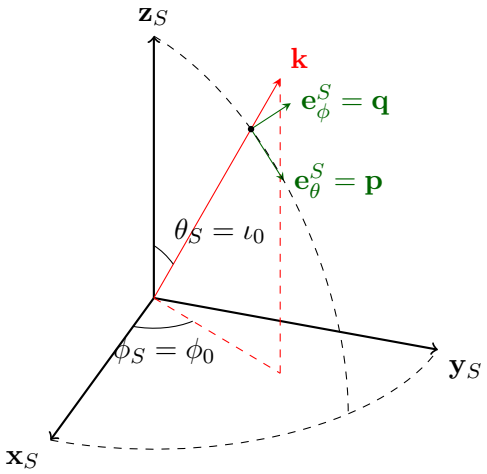


Figure 3.12: Source reference frame. Taken from [LIS19a].

### Source Reference Frame

We describe the dynamics of the gravitational-wave source in the so-called *source frame*, defined by its Cartesian basis $(\mathbf{x}_S, \mathbf{y}_S, \mathbf{z}_S)$. We also define the associated spherical basis vector $(\mathbf{e}_r^S, \mathbf{e}_\theta^S, \mathbf{e}_\phi^S)$ as presented fig. 3.12.

The unit vector $\mathbf{k}$ points towards LISA, *i.e.* it matches the gravitational wave *propagation direction*. Its coordinates are given in the source spherical coordinated $(\theta_S, \phi_S)$, so that

$$\mathbf{k} = \mathbf{e}_r^S \,. \tag{3.24}$$

We call *inclination* the angle $\iota_0 = \theta_S$ and *observer phase* the angle $\varphi = \phi_S$.

We introduce the *polarization basis* $(\mathbf{p}, \mathbf{q})$[4],

$$\mathbf{p} = \mathbf{e}_\theta^S = \frac{\partial \mathbf{e}_r^S}{\partial \theta_S}\,, \quad \text{and} \quad \mathbf{q} = \mathbf{e}_\phi^S = \frac{1}{\sin\theta_S}\frac{\partial \mathbf{e}_r^S}{\partial \phi_S}\,. \tag{3.25}$$

Together with the propagation direction vector $\mathbf{k}$, they form the *wave frame* $(\mathbf{p}, \mathbf{q}, \mathbf{k})$, such that $\mathbf{p} = \mathbf{q} \times \mathbf{k}$. The gravitational waveforms are almost always expressed in the transverse-traceless gauge, *c.f.* section 1.1.4. We define the *polarization tensors* as

$$\mathbf{e}^+ = (\mathbf{p} \otimes \mathbf{p} - \mathbf{q} \otimes \mathbf{q}) \quad \text{and} \quad \mathbf{e}^\times = (\mathbf{p} \otimes \mathbf{q} + \mathbf{q} \otimes \mathbf{p})\,, \tag{3.26}$$

so that we have

$$\mathbf{h} = h_+ \mathbf{e}^+ + h_\times \mathbf{e}^\times\,. \tag{3.27}$$

### Detector Reference Frame

LISA is described in the SSB frame $(\mathbf{x}, \mathbf{y}, \mathbf{z})$, aligned with the plane of the ecliptic. We introduce the spherical coordinates $(\theta, \phi)$, based on the orthonormal basis vectors $(\mathbf{e}_r, \mathbf{e}_\theta, \mathbf{e}_\phi)$. This is illustrated in fig. 3.13.

The source localization is parametrized by the *ecliptic latitude* $\beta = \pi/2 - \theta$ and the *ecliptic longitude* $\lambda = \phi$. In the SSB, the propagation vector is now

$$\mathbf{k} = -\mathbf{e}_r = (-\cos\beta\cos\lambda, -\cos\beta\sin\lambda, -\sin\beta)\,. \tag{3.28}$$

We can similarly express $\mathbf{e}_\theta$ and $\mathbf{e}_\phi$ in the SSB Cartesian coordinates.

We define the *reference polarization* vectors

$$\mathbf{u} = -\mathbf{e}_\phi \quad \text{and} \quad \mathbf{v} = -\mathbf{e}_\theta\,, \tag{3.29}$$

so that $(\mathbf{u}, \mathbf{v}, \mathbf{k})$ is a direct orthonormal basis. The relationship between the polarization basis and the reference polarization vectors is given by a rotation around the line of sight $k$ by an angle $\psi$. We call this angle the *polarization angle*, and we have

$$\mathbf{p} = \cos(\psi)\mathbf{u} + \sin(\psi)\mathbf{v} \quad \text{and} \quad \mathbf{q} = -\sin(\psi)\mathbf{u} + \cos(\psi)\mathbf{v}\,. \tag{3.30}$$

Similarly to the source polarization tensors, let us define the *reference polarization tensors*

$$\epsilon^+ = (\mathbf{u} \otimes \mathbf{u} - \mathbf{v} \otimes \mathbf{v}) \quad \text{and} \quad \epsilon^\times = (\mathbf{u} \otimes \mathbf{v} + \mathbf{v} \otimes \mathbf{u})\,. \tag{3.31}$$

[4]The projection of those vectors on the Cartesian basis can be found in [LIS19a].

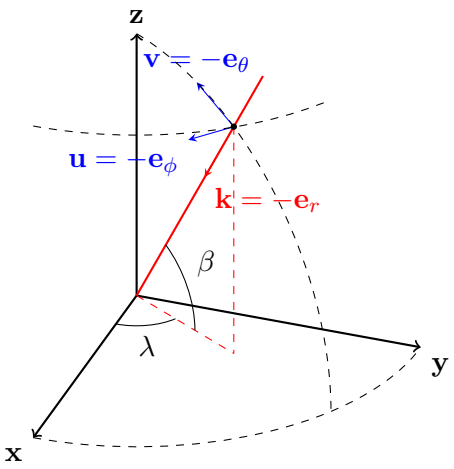


Figure 3.13: SSB frame. Taken from [LIS19a].

We can re-express the gravitational-wave strain from eq. (3.27) using the relation between $(\mathbf{u}, \mathbf{v})$ and $(\mathbf{p}, \mathbf{q})$,

$$h^{\mathrm{SSB}} = h_+^{\mathrm{SSB}} \epsilon^+ + h_\times^{\mathrm{SSB}} \mathbf{e}^\times \,, \tag{3.32}$$

if we define

$$h_+^{\mathrm{SSB}} = h_+ \cos 2\psi - h_\times \sin 2\psi \,, \tag{3.33}$$

$$h_\times^{\mathrm{SSB}} = h_+ \sin 2\psi + h_\times \cos 2\psi \,. \tag{3.34}$$

### Response Function

Let us express the deformation $H(t)$ induced on one LISA link. This can be computed by projecting the gravitational-wave strain on the link unit vector $\hat{\mathbf{n}}$, all expressed in the SSB. One gets

$$H(t) = h_+^{\mathrm{SSB}} \xi_+(\mathbf{u}, \mathbf{v}, \mathbf{n}) + h_\times^{\mathrm{SSB}} \xi_\times(\mathbf{u}, \mathbf{v}, \mathbf{n}) \,, \tag{3.35}$$

if the *antenna pattern functions* are defined such that

$$\xi_+(\mathbf{u}, \mathbf{v}, \mathbf{n}) = (\mathbf{u} \cdot \hat{\mathbf{n}})^2 - (\mathbf{v} \cdot \hat{\mathbf{n}})^2 \,, \tag{3.36}$$

$$\xi_\times(\mathbf{u}, \mathbf{v}, \mathbf{n}) = 2(\mathbf{u} \cdot \hat{\mathbf{n}})(\mathbf{v} \cdot \hat{\mathbf{n}}) \,. \tag{3.37}$$

Using eqs. (3.33) and (3.34), we can now write the link deformation as a function of the

gravitational-wave strain in the source frame,

$$\begin{aligned} H(t) = (h_+ \cos 2\psi - h_\times \sin 2\psi)\xi_+(\mathbf{u},\mathbf{v},\mathbf{n}) \\ + (h_+ \sin 2\psi + h_\times \cos 2\psi)\xi_\times(\mathbf{u},\mathbf{v},\mathbf{n})\,. \end{aligned} \tag{3.38}$$

Now we use a reasoning similar that exposed in section 1.2.3, but relax the assumption stating that the gravitational wavelength is far larger than a LISA armlength. Using the link deformation $H(\mathbf{x},t)$, eq. (1.35) reads

$$t_1 \approx t_0 + \frac{L}{c} - \frac{1}{2c}\int_0^L H(\mathbf{x}(x),t(x))\,\mathrm{d}x\,. \tag{3.39}$$

We now account for the wave propagation, using the first-order approximation $t(x) = t_0 + x/c$. Also, let us parametrize $\mathbf{x}(x) = \mathbf{x}_0(t_0) + x\hat{\mathbf{n}}$, where $\mathbf{x}_0(t_0)$ is the emitter position at emission time. One obtains

$$H(\mathbf{x}(x),t(x)) = H\left(t(x) - \frac{\mathbf{k}\cdot\mathbf{x}(x)}{c}\right) = H\left(t_0 - \frac{\mathbf{k}\cdot\mathbf{x}_0(t_0)}{c} + \frac{1-\mathbf{k}\cdot\hat{\mathbf{n}}}{c}x\right). \tag{3.40}$$

Combining eqs. (3.39) and (3.40) yields

$$t_1 \approx t_0 + \frac{L}{c} - \frac{1}{2c}\int_0^L H\left(t_0 - \frac{\mathbf{k}\cdot\mathbf{x}_0(t_0)}{c} + \frac{1-\mathbf{k}\cdot\hat{\mathbf{n}}}{c}x\right)\mathrm{d}x\,, \tag{3.41}$$

which can be differentiated to give the fractional frequency deviation[5] $y_{\mathrm{GW}}$ of a photon traveling along the LISA link,

$$y_{\mathrm{GW}}(t_0) \approx \frac{1}{2(\mathbf{k}\cdot\hat{\mathbf{n}})}\left[H\left(t_0 - \frac{\mathbf{k}\cdot\mathbf{x}_0(t_0)}{c}\right) - H\left(t_0 - \frac{\mathbf{k}\cdot\mathbf{x}_1}{c} + \frac{L}{c}\right)\right]. \tag{3.42}$$

Here, we have introduced the receiver position at reception time $\mathbf{x}_1(t_1) = \mathbf{x}_0(t_0) + L\hat{\mathbf{n}}$.

The instrument response is here given as a function of the emission time, whereas in our model, we need it at reception time. Using $t_1 = t_0 + L/c$, we find

$$y_{\mathrm{GW}}(t_1) \approx \frac{1}{2(\mathbf{k}\cdot\hat{\mathbf{n}})}\left[H\left(t_1 - \frac{L}{c} - \frac{\mathbf{k}\cdot\mathbf{x}_0(t_0)}{c}\right) - H\left(t_1 - \frac{\mathbf{k}\cdot\mathbf{x}_1(t_1)}{c}\right)\right]. \tag{3.43}$$

The expression of $H(t)$ is given by eq. (3.38).

[5] The fractional frequency deviation is defined in section 3.4.2.

### Implementation

We implement eqs. (3.38) and (3.43) in LISANode. Spacecraft motion is very slow with respect to the light time of flight along a LISA link, *i.e.* about 8 s. Therefore, we make the following assumption:

**Assumption 1** *In our model, we assume that the emitter spacecraft position is the same at emission or reception time, i.e.* $\mathbf{x}_0(t_0) \approx \mathbf{x}_0(t_1)$.

As a consequence, $\mathbf{x}_0$ and $\mathbf{x}_1$ are computed at reception time $t_1$. Equation (3.43) reads, with explicit time dependence,

$$y_{\mathrm{GW}}(t_1) \approx \frac{1}{2(\mathbf{k}\cdot\hat{\mathbf{n}}(t_1))}\left[H\left(t_1 - \frac{L(t_1)}{c} - \frac{\mathbf{k}\cdot\mathbf{x}_0(t_1)}{c}\right) - H\left(t_1 - \frac{\mathbf{k}\cdot\mathbf{x}_1(t_1)}{c}\right)\right]. \quad (3.44)$$

Inside the LaserLinks graph, GravitationalContributions adds gravitational-wave contributions for all links after the beams have been propagated by the SingleSignalPropagation nodes, *c.f.* section 3.2.4.

GravitationalContributions takes as parameters the intrinsic properties of a compact binary system: the gravitation-wave amplitude, its frequency $f_0$ and derivative $\mathrm{d}f_0/\mathrm{d}t$, and the source sky localization $\lambda, \beta$. It also takes as parameter the extrinsic parameters: the observer phase $\varphi$, the inclination angle $\iota_0$, and the polarization angle $\psi$.

For each link, an instance of SingleLinkGravitationalContribution is used. This graph is represented in fig. 3.14 and contains several nodes: GalacticBinary generates the gravitational waveform $h_+(t)$ and $h_\times(t)$ in the source frame, while SolarSystemBarycenterFrame converts the gravitational strains to the SSB according to eqs. (3.33) and (3.34) (the source inclination and polarization are given as parameters). Then, LinkResponse computes the light fractional frequency deviation due to the gravitational wave along one link, following eq. (3.43) (the sky localization of the source is given as parameter). Finally, Addition inserts the previously-computed effect in the propagating beam.

Complete documentation of these graphs and nodes can be found in C.

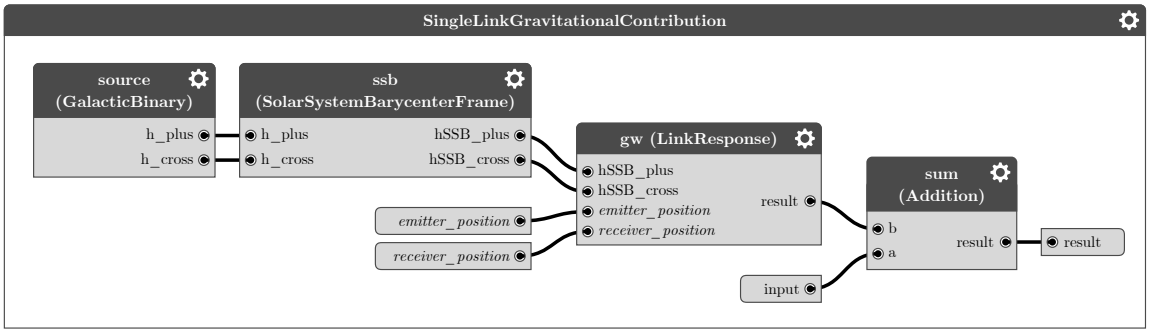


Figure 3.14: Schematic of the SingleLinkGravitationalContribution graph.

## 3.3 Simulation of Instrumental Noises

### 3.3.1 Noise Nodes

As for all measuring instruments, several noise sources must be accounted for to simulate realistic data. In this section, we give details about how the various noise sources are generated in LISANode, and the model chosen for each of them. Their couplings in the various interferometric measurements are given in section 3.4.

In our simulation, each noise time series is generated by a specific noise node defined in `lisanode/lisa/noise.py`. To allow an easy comparison with the legacy simulator LISACode, we implement the following procedure, also used in LISACode,

1. We first generate a white noise $x_n$, *i.e.* a stochastic signal with a constant PSD over a given frequency range. This is realized by drawing random samples from a zero-mean normal distribution, whose standard deviation $\sigma_x$ is a function of the sampling frequency $f_s$ and the PSD $S_x$,
$$\sigma_x^2 = \frac{S_x f_s}{2}\,, \tag{3.45}$$
The LISANode library provides the WhiteNoise node, documented in appendix B.

2. For colored noises, we filter the samples $x_n$ so that the resulting signal $y_n$ possesses the desired spectral shape. The LISANode library provides a number of digital filter nodes: Filter, EllipticFilter , PinkFilter, KaiserFilter, documented in appendix B.

3. An on/off switch, in the form of a on_off parameter on WhiteNoise, is used to enable or disable the noise generation. This is useful to study the individual impacts of

instrumental artifacts, and most of these switches are available at the top-level graphs, see appendix C.

This first implementation must be completed in a near future with other noise generation techniques. As an example, Franklin noise generator [Fra65] is extensively used in LISA Technology Package Data Analysis (LTPDA) and has the advantage of not requiring any warm-up time.

### 3.3.2 Laser Noise

The current mission baseline is to use standard Nd:YAG laser sources, with a wavelength of 1064 nm and an optical frequency of 282 THz. Such a choice exhibits some advantages. To begin with, we know how to build such lasers at the required power, and with frequency stability. Nd:YAG lasers are indeed a well-managed, reliable, and already space-qualified technology[6]. Also, the interaction with the space environment is negligible at this frequency as there are no bright sources in the sky. Beyond the visible spectrum, and below thermal radiations, this limits the risk of stray light in the photodetectors.

The current mission baseline is to use one pre-stabilized master laser source and lock the five other lasers on the master. Laser locking configurations are discussed in more details in section 3.5.4.

**Assumption 2** *In our instrumental model, we neglect laser locking. As a consequence, we assume that all six lasers are free-running. However, we account for the different beatnote frequencies, c.f. section 3.5.4.*

Although such free-running laser sources are very stable, one must account for the intrinsic frequency jitter. Indeed, this laser frequency noise is carried by the beam, down to the photodiode, where it couples into the measurements. We therefore attach independent laser noises $p_i(t)$ and $p_{1'}(t)$ to both laser sources onboard spacecraft $i$.

**Assumption 3** *We model the laser frequency noise by a white noise with a PSD of* $S_p = 10^{-26}\,\mathrm{Hz}^{-1}$ *in fractional frequency deviation (c.f. section 3.4.2). This is the state-of-the-art performance for a space-qualified laser source [TFD+11], and corresponds to an absolute frequency stability of*

$$\sqrt{S_p} = 28.8\,\mathrm{Hz}\,\mathrm{Hz}^{-1/2}\,. \tag{3.46}$$

[6] For instance, such laser sources were successfully flown onboard LISA Pathfinder.

Laser noise will most certainly be more complex than white noise, and this model is destined to evolve as the requirements become more precise. Meanwhile, it is a good enough approximation for our studies. Implementation details are given in appendix C.

If $10^{-13}\,\mathrm{Hz}^{-1/2}$ is a small value, let us keep in mind that we expect gravitational signals with amplitudes of the order of $10^{-21}$. Laser noise is, therefore, the dominant noise in LISA, many orders of magnitude above our signals of interest. To solve this issue and reduce laser noise, we use data processing techniques, and in particular, TDI, presented in chapter 4 and studied in chapter 5.

### 3.3.3 Test-Mass Acceleration Noise

LISA Pathfinder results [AAB+18] showed that, in reality, the six LISA test masses are not perfectly free-falling. External spurious forces push them out of their geodesics, which results in non-inertial residual accelerations. Among such forces, we can cite [LIS18b]:

- Masses onboard each spacecraft are placed to balance the gravity field in the vicinity of the test masses. Residual local gravity gradients result in inertial forces that can mimic tidal accelerations from gravitational waves.
- Although the test-mass housings are continuously vented to space, a few molecules are present around the test masses. Its thermal agitation exerts a Brownian force, and therefore, a noise on the test masses.
- Cosmic charged particles are deposited in the test masses, which suffer spurious electrostatic forces. Note that a discharging system based on the photoelectric effect is regularly employed to reduce this noise.
- The electrostatic forces used to constrain various test masses' degrees of freedom suffer imperfections and cross-couplings. This gives rise to actuation noise.

The test-mass acceleration noise PSD $S_\delta$ is expressed in acceleration units in the Error Budget and Performance Model Document [LIS18b]. It reads

$$S_\delta(f) = \left(2.4\times10^{-15}\right)^2\left[1+\left(\frac{0.4\times10^{-3}\,\mathrm{Hz}}{f}\right)^2\right]\left[1+\left(\frac{f}{8\times10^{-3}\,\mathrm{Hz}}\right)^4\right]\mathrm{m}^2\,\mathrm{s}^{-4}\,\mathrm{Hz}^{-1}\,, \tag{3.47}$$

and is the sum four independent noises obeying simple power laws.

**Assumption 4** *In our model, we neglect components in $f^2$ and $f^4$. Indeed, they contribute significantly only at high frequencies, where they are below other instrumental noise sources, such as optical-bench displacement noise. The test-mass acceleration then reads*

$$S_\delta(f) \approx \left(2.4 \times 10^{-15}\,\mathrm{m\,s^{-2}\,Hz^{-1/2}}\right)^2 \left[1 + \left(\frac{0.4 \times 10^{-3}\,\mathrm{Hz}}{f}\right)^2\right]. \tag{3.48}$$

In LISANode, we express the noise as an equivalent optical path change. As illustrated in fig. 3.16, the laser beam bounces on the test mass and travels twice the distance. As a result, we add a factor 2 in amplitude. Besides, the noise must be converted to fractional frequency deviations by adding an extra $1/(2\pi c)$ factor, *c.f.* section 3.4.2.

The implementation details are given in appendix C.

### 3.3.4 Optical Bench Acceleration Noise

In our model, we consider that the optical benches are solidly attached to the spacecraft structure. At any moment, the Drag-Free Attitude Control System (DFACS) steers the spacecraft to follow the test masses on their geodesic motions. The actuation[7] and the controller are not perfect, and much like the test masses, optical benches experience erratic spurious accelerations with respect to a local inertial frame.

We will see in chapter 4 that on-ground data processing reduces this optical-bench acceleration noise to a negligible level. Consequently, we decide not to implement this noise in our model for now.

**Assumption 5** *In our model, we disregard optical bench acceleration noise, as we assume it will completely be removed by on-ground data processing.*

However, this is something that one might want to integrate soon in the simulations. In particular, a study of the noise-reduction performance is expected. This is why we keep the optical-bench displacement noise terms in our equations throughout this chapter. Special care will be taken as where this noise appears if we consider the action of the DFACS.

[7] Indeed, the thrusters and the capacitive actuators have imperfections.

### 3.3.5 OMS Displacement Noise

We gather, under the umbrella term *Optical Metrology System (OMS) displacement noise*, all other instrumental artifacts that change the effective optical path of the laser beams. The OMS displacement noise gathers different contributions in the science, sideband, test-mass, and reference interferometers (described in section 3.4). We base our model on the official LISA Performance Model [LIS18b], so that

$$S_{N_s^{\mathrm{OMS}}}(f) = \left(6.35 \times 10^{-12}\,\mathrm{m\,Hz^{-1/2}}\right)^2, \tag{3.49}$$

$$S_{N_{\mathrm{sb}}^{\mathrm{OMS}}}(f) = \left(1.51 \times 10^{-11}\,\mathrm{m\,Hz^{-1/2}}\right)^2, \tag{3.50}$$

$$S_{N_\epsilon^{\mathrm{OMS}}}(f) = \left(1.42 \times 10^{-12}\,\mathrm{m\,Hz^{-1/2}}\right)^2, \tag{3.51}$$

$$S_{N_{\bar{\tau}}^{\mathrm{OMS}}}(f) = \left(3.32 \times 10^{-12}\,\mathrm{m\,Hz^{-1/2}}\right)^2. \tag{3.52}$$

Because in our model, all signals are expressed as fractional frequency deviations (*c.f.* section 3.4.2), the PSDs given above as displacements pick up extra factors $2\pi f/c$. This is implemented in the OMSDisplacementNoise node, extensively documented in appendix C.

The main effect in the science and sideband interferometers is shot noise, or photon counting noise. Because of the quantum nature of light, the precision when counting the photons reaching the photodiode is intrinsically limited. In particular, its PSD $S_N$ is constant and inversely proportional to the power of both interfering beams and the power fraction used for the interference $\epsilon$,

$$S_N \propto \frac{1}{\epsilon P_1 P_2}\,. \tag{3.53}$$

Note that the level of this shot noise depends on the armlength as the power of the distant beam is inversely proportional to the squared distance it travels, $P_{\mathrm{distant}} = P_{\mathrm{local}}/(4\pi L^2)$.

Shot-noise levels used in our model correspond to the *Long-Arm Noise* allocation in the Performance Model [LIS18b]. For the sideband interferometer, we rescale the science-interferometer value by 0.85/0.15 to account for the smaller power in the sideband. The contributions of the OMS displacement noise in the test-mass and reference interferometer respectively match the *Test-Mass IFO Noise* and *Reference IFO Noise* allocations of the Performance Model [LIS18b].

We gather in the UnallocatedNoise node other noise sources, which all are white noise when expressed in displacement. As an example, the unallocated noise in the science and sideband interferometers contains thermo-mechanical coupling: when temperature changes, the

mechanical structures of the optical bench, its components, and the telescope undergo thermoelastic distortion. As a result, the optical path changes as well. The unallocated noise in the test-mass interferometer gathers all couplings related to the motion of the spacecraft with respect to the test mass. One must keep in mind, though, that the current performance model does not capture correlations that might exist between noises.

We give here the PSDs for the unallocated noise in the various interferometers, expressed as displacements:

$$S_{N_s^{\mathrm{unalloc}}}(f) = \left(5 \times 10^{-12}\,\mathrm{m\,Hz^{-1/2}}\right)^2, \tag{3.54}$$

$$S_{N_{\mathrm{sb}}^{\mathrm{unalloc}}}(f) = S_{N_s^{\mathrm{unalloc}}}(f)\,, \tag{3.55}$$

$$S_{N_\epsilon^{\mathrm{unalloc}}}(f) = \left(4.24 \times 10^{-12}\,\mathrm{m\,Hz^{-1/2}}\right)^2, \tag{3.56}$$

$$S_{N_\tau^{\mathrm{unalloc}}}(f) = \left(2 \times 10^{-12}\,\mathrm{m\,Hz^{-1/2}}\right)^2. \tag{3.57}$$

Again, these PSDs are implemented as fractional frequency deviations in UnallocatedNoise by adding the conversion factor $2\pi f/c$. Please refer to appendix C for more information.

As the name suggests, the model for this noise needs to be refined. In particular, one might want to follow the nomenclature proposed in the Performance Model and use different noises for each effect.

### 3.3.6 Clock Noise

In the current mission design, an Ultra-Stable Oscillator (USO) serves as the frequency reference for all events onboard one spacecraft. Although such oscillators exhibit very good stability, one must account for their residual timing jitter. The latter is often characterized using Allan deviation, related to the timing jitter Root Mean Square (RMS). Because they are not actively synchronized, the three USOs can also drift independently with respect to each other. At long time scales, the Allan deviation is thus dominated by a linear drift of the oscillator frequency. The state-of-the-art specifications of the space-qualified USOs used for the GRAIL mission [WGR10] yield a linear frequency drift of $5 \times 10^{-26}\,\mathrm{s^{-1}}$. Over a 10 yr mission, we estimate that the maximum time deviation is around 25 s.

Consequently, clock error couples to various elements in the measurement chain:

- The USO signal is used to trigger the Analog-to-Digital Converters (ADCs), which are used to sample the analog electric signals of the photodiodes. These samples are

then fed to the phasemeter. If the samples are not recorded at the correct times, the phasemeter misinterpret the data and this yields an error in the phase measurements. This issue is discussed in section 3.5.1.

- The USO signals are used to timestamp the phase measurements. The latter is used in off-line processing algorithms (*c.f.* chapter 4), which assume that data is regularly and consistently sampled. Therefore, clock error degrades the performance of data processing.

- As discussed in section 3.2.5, we estimate absolute ranging by exchanging pseudo-random code between spacecraft. The comparison of the transmitted code with the local time reference then yields a preliminary ranging estimate. These preliminary estimates are then decoupled from the clock drifts by using Kalman-like filters.

For the needs of our model, we express the USO noise as a fractional frequency deviation series $q_i(t)$, normalized by the nominal laser frequency $\nu_0 = 282\,\mathrm{THz}$ (*c.f.* section 3.3.2). It is modeled ad-hoc as the sum of a deterministic frequency drift with time $f_{\mathrm{drift},i}$, and a stochastic flicker noise $n_i(t)$:

$$q_i(t) = f_{\mathrm{drift},i} \times t + n_i(t)\,, \tag{3.58}$$

The flicker noise PSD reads [WGR10]

$$S_q(f) = \left(6.7 \times 10^{-27}\,\mathrm{Hz}^{-1/2}\right)^2 f^{-1}\,. \tag{3.59}$$

**Assumption 6** *In our model, we assume that the clock frequency drifts are deterministic. Indeed, they are given as parameters at the beginning of the simulation.*

This model is implemented in the ClockNoise node, documented in appendix C.

### 3.3.7 Backlink Noise

The two local beams in a spacecraft must be delivered to the adjacent optical bench, to form the test-mass and reference signals, *c.f.* section 3.4.7. Because the MOSAs can rotate relative to each other, the optical backlink must be flexible. Two techniques are considered: free-beams or optical fibers. In the latter case, the two optical benches are connected by an optical fiber, in which the beams are exchanged. Today, this is the mission baseline.

This solution has an important drawback: the beams undergo non-reciprocal phase changes when they circulate in the backlink. This translates as different optical path lengths for beams circulating from the primed to the unprimed optical benches, and vice-versa. The current allocation for this backlink noise [LIS18b] is

$$S_\mu = \left(3 \times 10^{-12}\,\mathrm{m\,Hz^{-1/2}}\right)^2 \left[1 + \left(\frac{2 \times 10^{-3}\,\mathrm{Hz}}{f}\right)^4\right]. \tag{3.60}$$

**Assumption 7** *In our model, we disregard this noise.*

In the near future, one might want to add and study the effect of this noise in the model.

## 3.4 Simulation of Optical Signals

### 3.4.1 Spacecraft and Optical Bench

As described in section 3.1, each spacecraft contains one USO, a phasemeter, an onboard computer, two laser sources, and two MOSA units. Each of these MOSA units contains an optical bench, where the interferometric measurement is performed, a telescope, used to collect and send light from and to distant optical benches, and a Gravitational Reference System (GRS), containing the test mass. This instrumental configuration is illustrated in figs. 3.15 and 3.16.

In our instrumental model, we follow this configuration but decided to move the laser sources inside the OpticalBenches. As a result, the Spacecraft node contains

- Two instances of the MOSA graph, which makes use of the incoming and local laser beams to form the beatnote signals. These signals then fed to the phasemeter. The same MOSA nodes also produces the outgoing laser beams, which are transmitted to the distant optical benches.
- A ClockNoise node generating the clock timing jitter, used to model the coupling of the clock noise in the phasemeter, *c.f.* section 3.5.1).
- A Phasemeter node, used to add the measurement errors, such as the aforementioned clock noise. The phasemeter sends all the beatnote signals, including their errors, to the onboard computer.

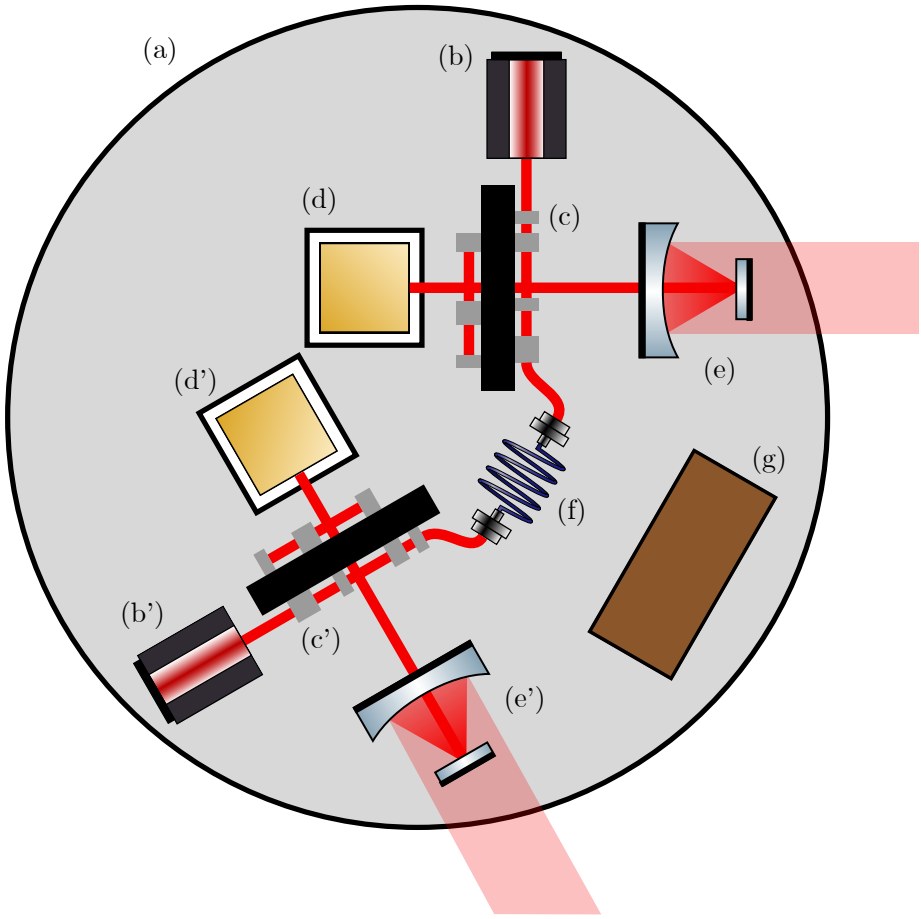


Figure 3.15: Illustration of one spacecraft (a). Two MOSA units gather each one laser source (b) and (b'), an optical bench (c) and (c'), a test mass (d) and (d'), a telescope that collects and sends light from and to the distant optical benches (e) and (e'), and a phasemeter and an onboard computer (g). An optical fiber (f) connects the two MOSAs.

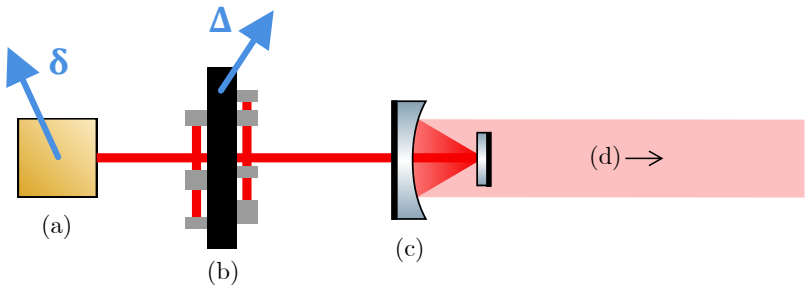


Figure 3.16: Current baseline for the optical configuration of a MOSA, used in the instrumental model. The test mass (a) is displaced by $\delta$ with respect to a local inertial frame. It is localized behind the optical bench (b), whose displacement is denoted $\mathbf{\Delta}$, and the telescope (c). The sensitive axis is aligned with these three components, and goes on towards the distant spacecraft (d).

- An OnboardComputer node, used to filter and downsample the measurement signals before they are sent to Earth, see section 3.5.5.

A schematics of the node is given in fig. 3.17.

Each MOSA node only contains a single instance of OpticalBench, illustrated in fig. 3.18. The latter forms four interferometric signals, which are the four beatnotes of the OMS described in section 3.4.6, section 3.5.2, and section 3.4.7. This is implemented using four instances of SingleSignalOMS, and a number of noise sources. In the following sections, we describe these noise sources, and how they couple into the measurements.

### 3.4.2 Laser Beam Model

Let us consider a laser beam; the information it carries is encoded in the complex amplitude of the associated Electromagnetic (EM) field. Taken at a given point in space, this amplitude is a function of time which reads

$$E(t) = E_0(t)e^{j\Phi(t)} = E_0(t)e^{j(2\pi\nu_0 t+\phi(t))}\,. \tag{3.61}$$

Here, $j$ is the unit imaginary number, $E_0(t)$ is the possibly time-varying field real amplitude, $\Phi(t)$ the instantaneous total phase in radian, $\nu_0$ the laser nominal frequency in Hertz, and $\phi(t)$ the instantaneous phase deviation from the nominal phase $\omega_0 t$, expressed in radian. The information content of the beam is encoded precisely in this last term.

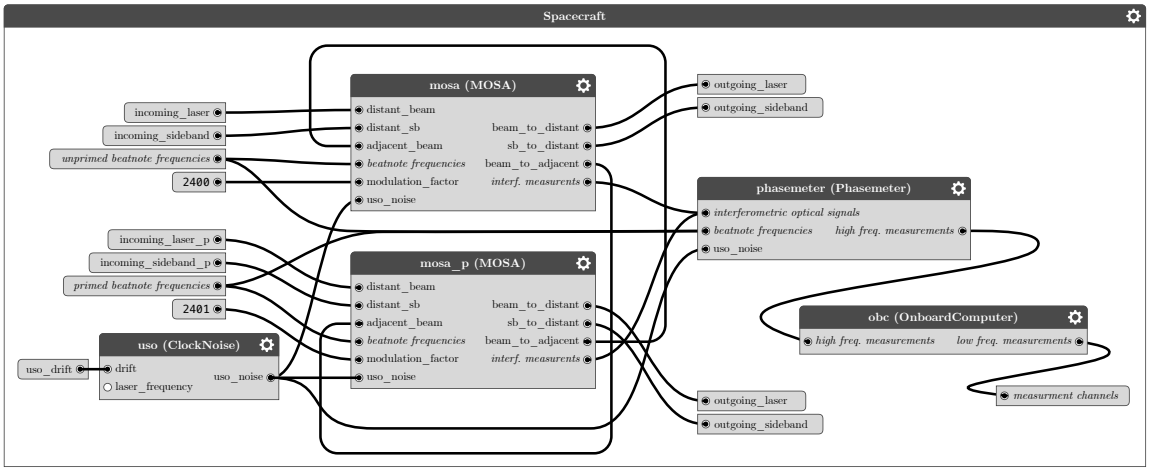


Figure 3.17: Schematics of the Spacecraft graph.

Alternatively, one can also use the instantaneous frequency,

$$\nu(t) = \frac{1}{2\pi}\frac{\mathrm{d}\Phi}{\mathrm{d}t} = \nu_0 + \frac{1}{2\pi}\frac{\mathrm{d}\phi}{\mathrm{d}t}\,, \tag{3.62}$$

to write the EM field as

$$E(t) = E_0(t)\exp\left(j2\pi\int_{t_0}^{t}\nu(\tau)\,\mathrm{d}\tau\right). \tag{3.63}$$

Let us define the timing jitter $x(t)$ in seconds, and the dimensionless fractional frequency deviation[8] $y(t)$, by

$$x(t) = \frac{\phi(t)}{2\pi\nu_o} \quad \text{and} \quad y(t) = \frac{\nu(t)-\nu_0}{\nu_0} = \frac{\mathrm{d}x}{\mathrm{d}t}\,, \tag{3.64}$$

so that

$$\Phi(t) = 2\pi\nu_0(t + x(t)) \quad \text{and} \quad \nu(t) = \nu_0(1 + y(t))\,. \tag{3.65}$$

**Assumption 8** *In our instrumental model, a laser beam and the information it carries is represented by its fractional frequency deviation time series $y(t)$.*

A back-of-the-envelop estimate of the dynamic range associated with such fractional frequency deviation time series shows that it is possible to implement them with the double-precision floating-point format. Indeed, the typical gravitational wave strain is around

[8] In the literature, $y(t)$ is also called relative frequency deviation, fractional frequency shift, relative frequency shift, or Doppler variable.

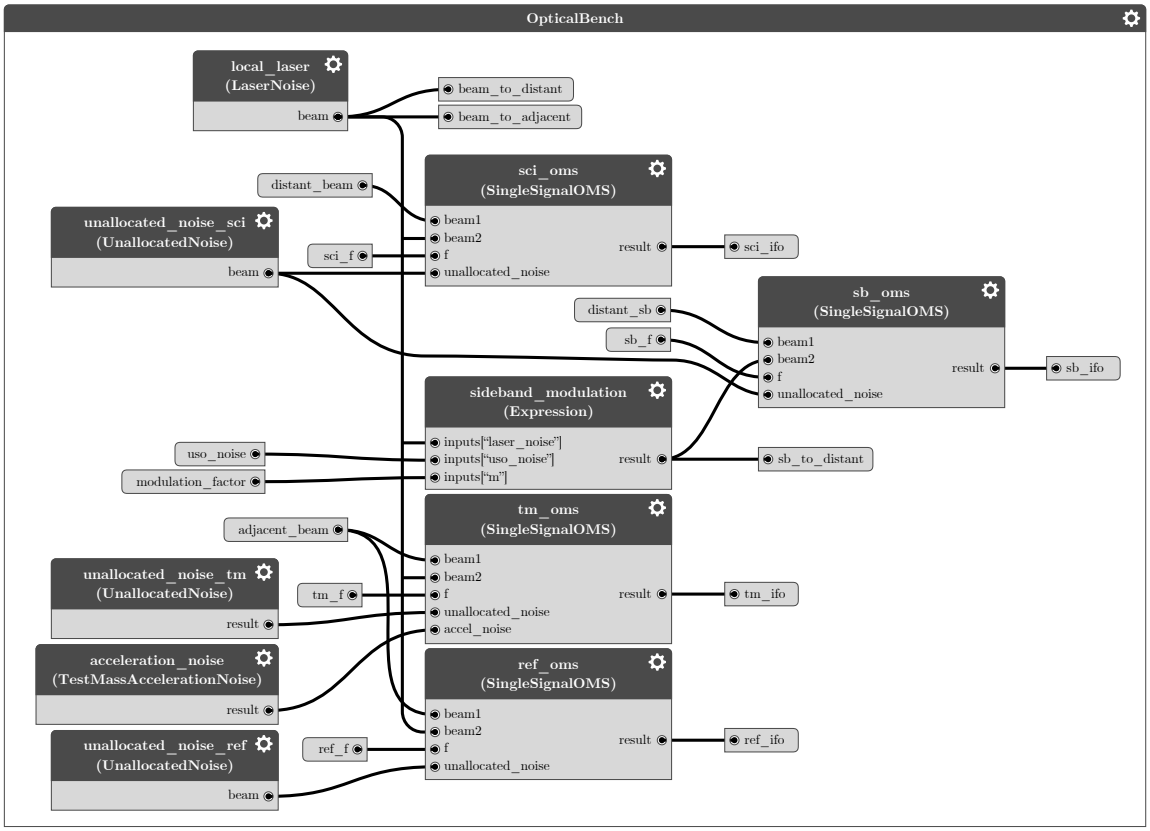


Figure 3.18: Schematics of the OpticalBench graph.

$10^{-20}$, `c.f.` section 1.3. The equivalent fractional frequency deviation is of the same order of magnitude, as discussed in section 1.1.5. The simulator should be able to track sub-dominant instrumental noises, many orders of magnitude below. As a result, the required resolution is around $10^{-26}$. Conversely, laser noise is the dominant noise source, with an ASD of $10^{-13}$ (section 3.4.6). Therefore, we require a precision of about $10^{-8}$, well within that of the double-precision floating-point format, $\epsilon_{\text{double}} = 2^{-53} - 1 \approx 10^{-16}$.

We will see in the next sections that the carrier frequencies, around 282 THz, and the all effects affecting this value (Doppler shifts or frequency offsets) are not simulated. *C.f.* sections 3.4.3, 3.4.5 and 3.5.4.

### 3.4.3 Beam Propagation

Let us here express the fractional frequency deviation $y_B(t)$ of a laser beam when it is collected by a distant spacecraft $B$, as a function of the same beam's fractional frequency deviation $y_A(t)$ at the time it is sent from the local spacecraft $A$. The emitted beam's EM field reads

$$E_A(t) = E_0(t) e^{j[2\pi\nu_A t + \phi_A(t)]} \,. \tag{3.66}$$

We assume a perfect pointing, a light travel time $\tau_{AB}$ between both spacecraft, and that the received power is a fraction $\rho$ of the sent power. Then the received beam's field reads

$$E_B(t) = \rho E_A(t - \tau_{AB}) \,. \tag{3.67}$$

Combining both expressions, we find that

$$E_B(t) = \rho E_0(t - \tau_{AB})\, e^{j[2\pi\nu_A t + \phi_A(t-\tau_{AB}) - 2\pi\nu_A\tau_{AB}]} \,. \tag{3.68}$$

The nominal laser frequencies are equal[9], and $\nu_A = \nu_B$. The instantaneous phase deviation of the propagated beam $\phi_B(t) = \phi_A(t-\tau_{AB}) - 2\pi\tau_{AB}$ is that of the outgoing beam, delayed by the light travel time along the arm. An additional term accounts for the additional phase due to the light travel time.

Applying the definition of the fractional frequency deviation from eq. (3.64), we find that[10]

$$y_A(t) = \frac{1}{2\pi\nu_A}\frac{\mathrm{d}\phi_A}{\mathrm{d}t} \quad \text{and} \quad y_B(t) = \frac{1}{2\pi\nu_B}\frac{\mathrm{d}\phi_B}{\mathrm{d}t} \,. \tag{3.69}$$

[9] Again, we neglect here the frequency offsets given by the frequency plan, as well as the Doppler shifts.
[10] In the following, and unless otherwise specified, all the derivatives are taken at time $t$.

Substituting the expressions of $\nu_B$ and $\phi_B(t)$, and keeping in mind that $\tau_{AB}(t)$ depends on time, we have

$$y_B(t) = \frac{1}{2\pi\nu_A}\frac{\mathrm{d}\phi_A}{\mathrm{d}t}(t-\tau_{AB}) - \left(1+\frac{1}{2\pi\nu_A}\frac{\mathrm{d}\phi_A}{\mathrm{d}t}(t-\tau_{AB})\right)\frac{\mathrm{d}\tau_{AB}}{\mathrm{d}t}\,. \tag{3.70}$$

The first term matches exactly the fractional frequency deviation $y_A(t)$, delayed by the light travel time along the considered arm. The second term, due to the light travel time variations, is the famous Doppler effect described in section 3.1. It is important to keep in mind that Doppler effect does not introduce new terms when beams are expressed as instantaneous phases or phase deviations, but is contained in the time-varying delay that we apply. Conversely, additional terms appear when beams are expressed as frequencies or fractional frequency deviations.

We limit the computation to order 1/2 and adopt the notations of section 3.2.4. We have

$$y_B(t) = y_A(t-\tau_{AB}) - \frac{1+y_A(t-\tau_{AB})}{c}\frac{\mathrm{d}\|\mathbf{r}_{AB}\|}{\mathrm{d}t}\,. \tag{3.71}$$

The spacecraft velocities are very small with respect to the speed of light, and so is the Doppler factor $|\mathrm{d}\|\mathbf{r}_{AB}\|/\mathrm{d}t|/c \approx 3\times10^{-9}\,\mathrm{m\,s^{-1}} \ll 1$. Since $y_A(t) \ll 1$, we neglect this term when it is in front of the Doppler factor. Expressing $\mathrm{d}\|\mathbf{r}_{AB}\|/\mathrm{d}t$ as a function of the spacecraft velocities $\mathbf{v}_A$ and $\mathbf{b}_B$, as well as the link unit vector $\hat{\mathbf{n}}_{AB}$, the previous equations can be written as

$$y_B(t) = y_A(t-\tau_{AB}) - \hat{\mathbf{n}}\cdot\frac{\mathbf{v}_B-\mathbf{v}_A}{c}\,. \tag{3.72}$$

**Assumption 9** *In our instrumental model, we neglect the Doppler factor that affects the fractional frequency deviation of a propagated beam and take*

$$y_B(t) \approx y_A(t-\tau_{AB})\,. \tag{3.73}$$

This justifies the model presented in section 3.2.4. In reality, these Doppler shifts must be accounted for, in particular for the GHz sidebands, *c.f.* section 3.5.2.

### 3.4.4 Delay Operators

In this thesis, we denote the delay operators related with the propagation of signals along the link $i$ as $\mathbf{D}_i$. Combining eqs. (3.18) and (3.73) and denoting $AB$ the link connecting

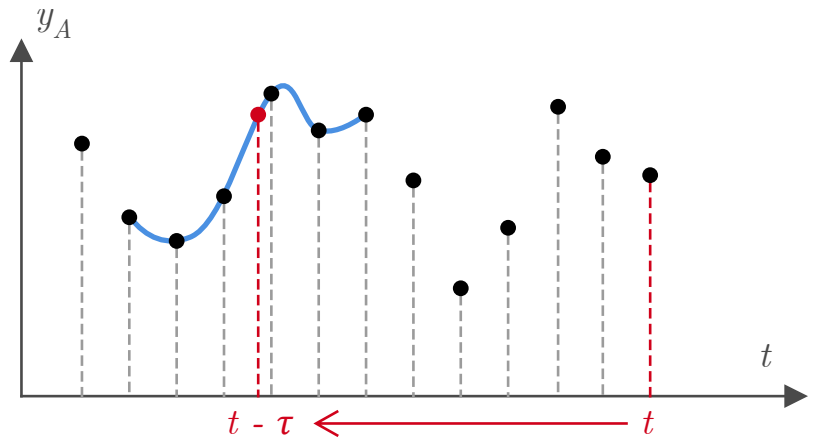


Figure 3.19: Lagrange interpolation scheme. The signal $y_A(t)$ must be delayed by $\tau$. Past samples around the interpolation time $t - \tau$ are used to build the Lagrange polynomials (in light blue). They are then evaluated at the interpolation time, yielding the interpolated sample, in red.

spacecraft $A$ to spacecraft $B$,

$$y_B(t) \approx \mathbf{D}_{AB}\, y_A(t) = y_A(t - \tau_{AB})\,. \tag{3.74}$$

Because the light time of flight $\tau_{AB}$ does not match an integer number of samples, we use fractional delay filters. In signal processing, a few filter designs, mostly Finite Impulse Response (FIR) filters, are used depending on the problem's requirements.

We choose to use Lagrange interpolating polynomials in our model. The idea, shown in fig. 3.19, is the following:

1. At all times, we store in memory past samples of the propagating signal. We use the circular buffers used to implement inputs on each node, *c.f.* section 2.2.2.

2. At each timestep, we select the input samples symmetrically around the interpolation time. The number of samples depends on the interpolation order, as discussed below.

3. We compute the Lagrange polynomials and evaluate them at the desired interpolation time. This yields our interpolated sample.

Because the light times of flight are time-varying, we cannot pre-compute the Lagrange polynomial coefficient as they change for each timestep. This time-varying fraction delay

operators are implemented by the VariableFractionalDelay atomic node. Details of implementation are described in great details in appendix C.

Lagrange interpolation exhibits the interesting property of being maximally flat at low frequencies. This means that at 0 Hz, the gain is unity, and the shift in phase is vanishing. This property holds as well for the $n$ first derivative in frequency, if $n$ is the interpolation order. However, in the vicinity of half the sampling frequency, or Nyquist frequency, the gain drops, and the phase shift becomes larger.

We nevertheless choose this method, because it remains flexible. One can choose a high interpolation order to improve the precision at high frequency, see [Hal18]. Of course, a higher interpolation order increases the computation time as well, so that the chosen value is the result of a tradeoff. In our instrumental model, we use interpolation orders of 31, *i.e.* 32 samples around the interpolation time. This value provides sufficient precision for the needs of the simulation while enabling reasonable computation times.

### 3.4.5 Interferometric Measurements

Let's derive the expression of the interferometric beatnote between two beams, as a function of the respective nominal frequencies $\nu_1$ and $\nu_2$ and relative frequency deviations $\phi_1(t)$ and $\phi_2(t)$.

The first and second beam's EM fields read

$$E_1(t) = E_{1,0}(t)e^{j(2\pi\nu_1 t+\phi_1(t))} \quad \text{and} \quad E_2(t) = E_{2,0}(t)e^{j(2\pi\nu_2 t+\phi_2(t))}\,. \tag{3.75}$$

The power measured at the photodiode is

$$P(t) \propto \left|E_1(t)e^{j\pi/2} + E_2(t)\right|^2, \tag{3.76}$$

where the extra phase of $\pi$ is picked up when the first beam is reflected on the beam splitter. Substituting in this equation the expressions of the two beams yields

$$P(t) = |E_1|^2 + |E_2|^2 + 2\,\mathrm{Im}(E_1{}^* E_2) \tag{3.77}$$

$$= \left(|E_1|^2 + |E_2|^2\right)\left(1 - \frac{2E_{1,0}E_{2,0}}{|E_1|^2 + |E_2|^2}\sin[2\pi(\nu_1-\nu_2)t + \phi_1(t) - \phi_2(t)]\right). \tag{3.78}$$

We have here denoted the complex conjugate of a signal with an asterisk.

We can write this last equation as

$$P(t) \propto 1 + \kappa\sin[2\pi\nu_{12}t + \phi_{12}(t)]\,, \tag{3.79}$$

where we have defined the nominal heterodyne beatnote frequency $\nu_{12} = \nu_1 - \nu_2$, the beatnote phase deviation $\phi_{12}(t) = \phi_1(t) - \phi_2(t)$, and the contrast $\kappa = -2E_{1,0}E_{2,0}/(|E_1|^2 + |E_2|^2)$.

The phasemeter always outputs the instantaneous beatnote frequency as a positive value. If the beatnote sign, or beatnote polarity, is denoted by

$$\theta_{12} = \mathrm{sign}(\nu_1 - \nu_2) = \pm 1\,, \tag{3.80}$$

then the phasemeter really sees

$$P(t) \propto 1 + \kappa \cos[2\pi\theta_{12}\nu_{12}t + \theta_{12}\phi_{12}(t)]\,, \tag{3.81}$$

where $\theta_{12}\nu_{12} = |\nu_{12}|$ is always positive, and is called the measured nominal heterodyne beatnote frequency.

By definition, $\nu_1 = \nu_2 + \nu_{12} = \nu_2(1 + \nu_{12}/\nu_2)$. The nominal laser frequencies $\nu_1$ and $\nu_2$ are of the order of the terahertz, while the nominal beatnote frequency always remains below 25 MHz and thus is far smaller. Therefore $\nu_{12}/\nu_2 \ll 1$.

**Assumption 10** *In our model, we consider that the nominal laser frequencies of both interfering beams are equal, i.e.* $\nu_1 \approx \nu_2 = \nu_0$. *However we consider non-vanishing nominal heterodyne beatnote frequencies* $\nu_{12}$ *when necessary, e.g. for the coupling of clock noise in the phasemeter, c.f. section 3.5.2. The nominal beatnote frequencies are given as inputs for each interferometer, see appendix C.*

In other words, we neglect the Doppler shifts and the frequency offsets given by the frequency plan, *c.f.* section 3.5.4. The underlying assumption here is that this frequency planning does not significantly modify the results we present in chapters 5 to 7. One will need to implement in LISANode the various laser frequencies and account for the Doppler shifts and frequency planning in order to validate this hypothesis. This is the object of an important study that must be conducted in a near future.

**Assumption 11** *In our model, the interferometric measurements* $y_{12}(t)$ *are expressed as dimensionless frequency deviations normalized by the nominal laser frequencies. Since the latter is assumed to be equal to* $\nu_0$, *we have*

$$y_{12}(t) \approx \frac{\theta_{12}}{2\pi\nu_0}\frac{\mathrm{d}\phi_{12}}{\mathrm{d}t} \approx \theta_{12}[y_1(t) - y_2(t)]\,. \tag{3.82}$$

The interferometric signal is therefore deduced from the two laser beams using a simple difference, and a factor accounting for the beatnote polarity. This justifies the implementation of the Interferometer node, described in appendix C.

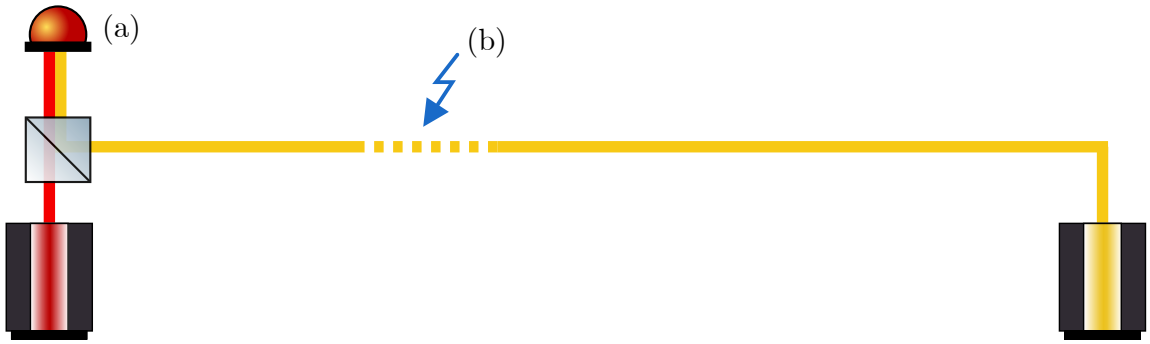


Figure 3.20: Optical schematics of the science interferometer. The local beam interferes on the photodiode (a) with the distant beam. This distant beam collects the gravitational wave contribution (b) during its propagation along the link.

### 3.4.6 Science Signals

In the following sections, we study the four interferometric measurements performed on each optical bench: the science, sideband, test-mass, and reference signals. In particular, we give the contribution of the various instrumental noises to each of these signals. We give the expressions for the optical bench 1 and $1'$; the remaining expressions can be deduced by a circular permutation of the indices $1 \to 2 \to 3 \to 1$.

The science signals $s_1(t)$ and $s_{1'}(t)$ correspond to the beatnotes between the distant and the local beams. The distant beam has traveled along one link of the constellation before it reaches the photodiode. An optical schematics of the science interferometer is presented in fig. 3.20.

Accounting for the relevant noise sources, discussed in section 3.3, and using eq. (3.82), we can express the science signal $s_1$ as the sum of:

- The gravitational wave contribution $H_1$, projected on the LISA arm and expressed as fractional frequency deviations. We use the instrumental response derived in section 3.2.6.
- The local laser $p_1$ and distant laser $\mathbf{D}_{2'}p_{2'}$ noise. The latter is taken with the delay corresponding to the propagation of the noise along the LISA link, as discussed in section 3.4.3.
- All OMS displacement noise sources, including shot noise, thermo-mechanical noise,

electronic noise, etc. are subsumed in $N_1^s$.

- The fractional frequency deviation due to the distant and local optical-bench displacement. Let us write them $\mathbf{D}_3\phi_{\Delta_{2'}} - \phi_{\Delta_1}$ when they are expressed as an optical path change, in meters. If we denote the optical-bench displacement vectors as $\mathbf{\Delta}_{2'}$ and $\mathbf{\Delta}_1$ (see fig. 3.16), and the link unit vectors as $\hat{\mathbf{n}}_3$ and $\hat{\mathbf{n}}_{3'}$,

$$\mathbf{D}_3\phi_{\Delta_{2'}} - \phi_{\Delta_1} = -\frac{2\pi\nu_0}{c}[\mathbf{D}_3\hat{\mathbf{n}}_3 \cdot \mathbf{D}_3\mathbf{\Delta}_{2'} + \hat{\mathbf{n}}_{3'} \cdot \mathbf{\Delta}_1]\,. \tag{3.83}$$

  We use eq. (3.64) to convert the previous expression to a fractional frequency deviation, and get

$$\frac{1}{2\pi\nu_0}\frac{\mathrm{d}(\mathbf{D}_3\phi_{\Delta_{2'}} - \phi_{\Delta_1})}{\mathrm{d}t} = -\frac{1}{c}\left[\mathbf{D}_3\hat{\mathbf{n}}_3 \cdot \mathbf{D}_3\frac{\mathrm{d}\mathbf{\Delta}_{2'}}{\mathrm{d}t} + \hat{\mathbf{n}}_{3'} \cdot \frac{\mathrm{d}\mathbf{\Delta}_1}{\mathrm{d}t}\right]. \tag{3.84}$$

  In the following, we assume that the link direction does not change as light propagates along an arm (about 8 s). Therefore, $\mathbf{D}_3\hat{\mathbf{n}}_3 \approx \hat{\mathbf{n}}_3$. If we denote the optical bench velocities $\mathbf{v}_{\Delta_{2'}} = \mathrm{d}\mathbf{\Delta}_{2'}/\mathrm{d}t$ and $\mathbf{v}_{\Delta_1} = \mathrm{d}\mathbf{\Delta}_1/\mathrm{d}t$, the noise now reads $-(\hat{\mathbf{n}}_3 \cdot \mathbf{D}_3\mathbf{v}_{\Delta_{2'}}/c + \hat{\mathbf{n}}_{3'} \cdot \mathbf{v}_{\Delta_1}/c)$.

The previous discussion relies on another assumption:

**Assumption 12** *In our model, we neglect the light propagation time for signals remaining inside one spacecraft.*

As discussed in section 3.4.5, we must also account for the beatnote polarity. Let us denote them $\theta_1^s$ and $\theta_{1'}^s$, such that

$$\theta_1^s = \mathrm{sign}(\nu_{2'} - \nu_1) \quad \text{and} \quad \theta_{1'}^s = \mathrm{sign}(\nu_3 - \nu_{1'})\,. \tag{3.85}$$

The science signals finally read

$$s_1 = \theta_1^s\left[H_1 + \mathbf{D}_3 p_{2'} - p_1 - \left(\hat{\mathbf{n}}_3 \cdot \mathbf{D}_3\frac{\mathbf{v}_{\Delta_{2'}}}{c} + \hat{\mathbf{n}}_{3'} \cdot \frac{\mathbf{v}_{\Delta_1}}{c}\right)\right] + N_1^s\,, \tag{3.86}$$

$$s_{1'} = \theta_{1'}^s\left[H_{1'} + \mathbf{D}_{2'} p_3 - p_{1'} - \left(\hat{\mathbf{n}}_{2'} \cdot \mathbf{D}_{2'}\frac{\mathbf{v}_{\Delta_3}}{c} + \hat{\mathbf{n}}_2 \cdot \frac{\mathbf{v}_{\Delta_{1'}}}{c}\right)\right] + N_{1'}^s\,. \tag{3.87}$$

### 3.4.7 Test-Mass and Reference Signals

Similarly, the test-mass signals $\epsilon_1(t)$ and $\epsilon_{1'}(t)$ are formed by the beatnotes between the adjacent and local beams, after the former has bounced on the local test mass. Figure 3.21 is a schematic of this interferometer.

We express the test-mass signal $\epsilon_1$ as the sum of:

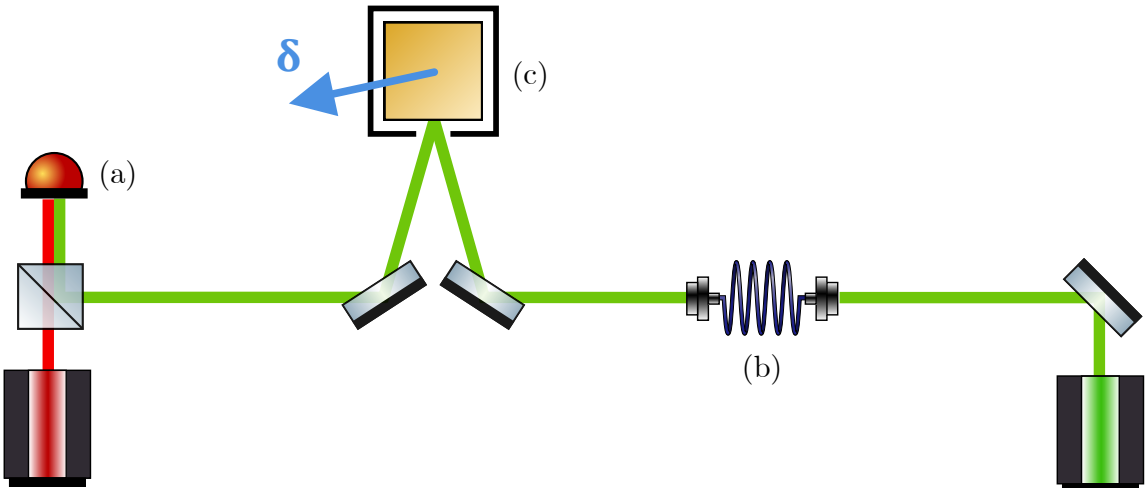


Figure 3.21: Optical schematics of the test-mass interferometer. The local beam interferes on the photodiode (a) with the adjacent beam. This adjacent beam collects noise from the backlink, or optical fiber (b), and the test-mass displacement noise $\delta$ when it is bounced onto the test mass (c).

- The local laser $p_1$ and adjacent laser $p_{1'}$ noise.
- The extra optical path length $\phi_{\delta_1}$ due to the test-mass and optical bench displacements. The factor 2 accounts for the return trip of light after it has bounced on the test mass. If $\delta_1$ is the test-mass displacement vector, and $\mathbf{\Delta}_1$ that of the optical bench, as illustrated in fig. 3.16[11],

$$\phi_{\delta_1} = 2\frac{2\pi\nu_0}{c}\hat{\mathbf{n}}_{3'} \cdot (\mathbf{\Delta}_1 - \delta_1)\,. \tag{3.88}$$

  We use eq. (3.64) to convert the previous expression to a fractional frequency deviation, and get

$$\frac{1}{2\pi\nu_0}\frac{\mathrm{d}\phi_{\delta_1}}{\mathrm{d}t} = 2\hat{\mathbf{n}}_{3'} \cdot \left(\frac{\mathbf{v}_{\Delta_1}}{c} - \frac{\mathbf{v}_{\delta_1}}{c}\right). \tag{3.89}$$

  In the previous expression, we denote the test-mass (respectively the optical bench) velocity $\mathbf{v}_{\delta_1} = \frac{\mathrm{d}\delta_1}{\mathrm{d}t}$ (resp. $\mathbf{v}_{\Delta_1} = \frac{\mathrm{d}\mathbf{\Delta}_1}{\mathrm{d}t}$).
- The backlink noise $\mu_{1'}$, expressed as a fractional frequency deviation, *c.f.* section 3.3.7.

[11] In [Ott15], the signs are flipped. It is now believed that this is an error given the current optical design from fig. 3.16.

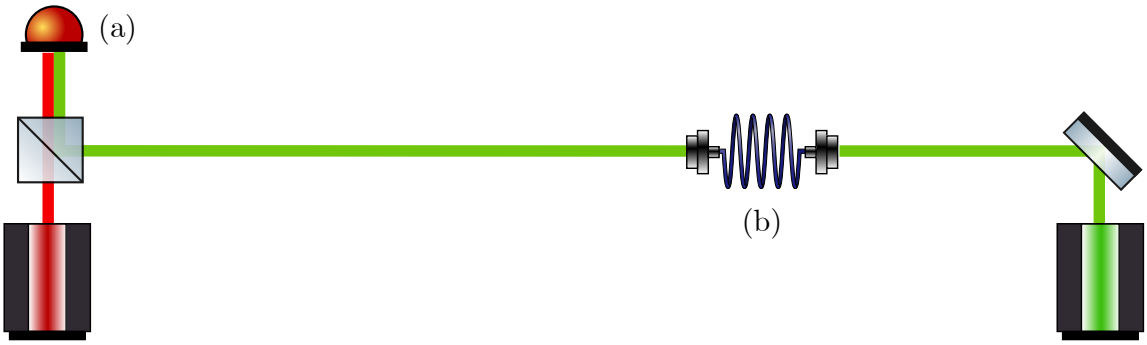


Figure 3.22: Optical schematics of the reference interferometer. The local beam interferes on the photodiode (a) with the adjacent beam. This adjacent beam collects noise from the backlink, or optical fiber (b).

- All OMS displacement noise sources, as discussed in section 3.3.5, subsumed in $N_1^\epsilon$.

Accounting for the beatnote polarity, which we denote

$$\theta_1^\tau = \text{sign}(\nu_{1'} - \nu_1) \quad \text{and} \quad \theta_{1'}^\tau = \text{sign}(\nu_1 - \nu_{1'}) = -\theta_1^\tau \,, \tag{3.90}$$

the test-mass signals read

$$\epsilon_1 = \theta_1^\tau \left[ p_{1'} - p_1 + 2\hat{\mathbf{n}}_{3'} \cdot \left( \frac{\mathbf{v}_{\Delta_1}}{c} - \frac{\mathbf{v}_{\delta_1}}{c} \right) + \mu_{1'} \right] + N_1^\epsilon \,, \tag{3.91}$$

$$\epsilon_{1'} = \theta_{1'}^\tau \left[ p_1 - p_{1'} + 2\hat{\mathbf{n}}_2 \cdot \left( \frac{\mathbf{v}_{\Delta_{1'}}}{c} - \frac{\mathbf{v}_{\delta_{1'}}}{c} \right) + \mu_1 \right] + N_{1'}^\epsilon \,. \tag{3.92}$$

The reference signals are formed by the beatnote between the adjacent and local beams, without any bouncing on the test mass. Figure 3.21 is a schematic of this interferometer.

We express the reference signal $\tau_1$ as the sum of:

- The local laser $p_1$ and adjacent laser $p_{1'}$ noise.
- The backlink noise $\mu_{1'}$, expressed as a fractional frequency deviation, *c.f.* section 3.3.7.
- All OMS displacement noise sources, as discussed in section 3.3.5, subsumed in $N_1^\tau$.

The nominal beatnotes are identical to those of the test-mass signals. As a result, so are

the beatnote polarities, and the reference signals onboard the first spacecraft read

$$\tau_1 = \theta_1^\tau[p_{1'} - p_1 + \mu_{1'}] + N_1^\tau \,, \tag{3.93}$$

$$\tau_{1'} = \theta_{1'}^\tau[p_1 - p_{1'} + \mu_1] + N_{1'}^\tau \,. \tag{3.94}$$

## 3.5 On-Board Data Processing

### 3.5.1 Clock Noise in the Phasemeter

As discussed in sections 3.1 and 3.3.6, the onboard USO provides the time reference used to trigger the ADC, which, in turn, sample the photodiode signal. The latter is used by the phasemeter's Digital Phase-Locked Loop (DPLL) to determine the beatnote phase deviations.

Unfortunately, the ADC does not record the samples at the times it is triggered by the clock and introduces additional noise. This noise already violates the LISA requirements [Bar15] and it is intrinsically local. Hence, it cannot be removed with off-line data processing similar to TDI, discussed in chapter 4. Instead, ADC jitter noise is reduced online by the so-called *pilot-tone* correction. A known reference signal, or pilot tone, is generated by the USO and sampled by the ADC. Any distortion on the sampled pilot tone, due to the ADC timing jitter, can be identified by comparing it with the reference signal. The inverse transformation is then applied to the sampled photodiode signal. We obtain a sampled signal free of the ADC timing jitter. Because the pilot tone is generated from the USO signal, clock noise entering the latter also affects the photodiode signal.

**Assumption 13** *In our model, we assume that pilot-tone correction removes completely the ADC timing jitter. As a result, the sampled photodiode signals are only affected by the USO noise, as it remains present in the pilot tone.*

In this thesis, the signed science interferometer beatnote frequencies[12] are defined as

$$a_1 = \nu_{2'} - \nu_1 \quad \text{and} \quad a_{1'} = \nu_3 - \nu_{1'} \,. \tag{3.96}$$

[12] As discussed in assumption 9, we neglect Doppler effect so that the distant laser beam has not its frequency shifted. Accounting for Doppler effect,

$$a_1 = \left(1 - \frac{\mathrm{d}\tau_3}{\mathrm{d}t}\right)\nu_{2'} - \nu_1 \quad \text{and} \quad a_{1'} = \left(1 - \frac{\mathrm{d}\tau_{2'}}{\mathrm{d}t}\right)\nu_3 - \nu_{1'} \,. \tag{3.95}$$

The signed test-mass and reference interferometer beatnote frequencies are equal and defined as

$$b_1 = \nu_{1'} - \nu_1 \quad \text{and} \quad b_{1'} = -b_1 = \nu_1 - \nu_{1'} \,. \tag{3.97}$$

This residual clock noise appears in the interferometric measurements, given in eqs. (3.86), (3.87) and (3.91) to (3.94), as the USO noise[13] $q_i(t)$ scaled by the relevant beatnote frequency (as measured, *i.e.* as a positive frequency). In the science signal $s_1(t)$, the extra term reads $-|a_1|q_1(t) = -\theta_1^s a_1 q_1(t)$. In the test-mass and reference signals $\epsilon_1(t)$ and $\tau_1(t)$, it reads $-\theta_1^\tau b_1 q_1(t)$. The signs are flipped relative to the expressions that once can find in [Ott15]. This is due to an error that is corrected in this thesis.

We obtain the following expressions:

$$s_1 = \theta_1^s \Big[ H_1 + \mathbf{D}_3 p_{2'} - p_1 - \Big( \hat{\mathbf{n}}_3 \cdot \mathbf{D}_3 \frac{\mathbf{v}_{\Delta_{2'}}}{c} + \hat{\mathbf{n}}_{3'} \cdot \frac{\mathbf{v}_{\Delta_1}}{c} \Big) - a_1 q_1 \Big] + N_1^s \,, \tag{3.98}$$

$$s_{1'} = \theta_{1'}^s \Big[ H_{1'} + \mathbf{D}_{2'} p_3 - p_{1'} - \Big( \hat{\mathbf{n}}_{2'} \cdot \mathbf{D}_{2'} \frac{\mathbf{v}_{\Delta_3}}{c} + \hat{\mathbf{n}}_2 \cdot \frac{\mathbf{v}_{\Delta_{1'}}}{c} \Big) - a_{1'} q_1 \Big] + N_{1'}^s \,, \tag{3.99}$$

$$\epsilon_1 = \theta_1^\tau \Big[ p_{1'} - p_1 + 2\hat{\mathbf{n}}_{3'} \cdot \Big( \frac{\mathbf{v}_{\Delta_1}}{c} - \frac{\mathbf{v}_{\delta_1}}{c} \Big) + \mu_{1'} - b_1 q_1 \Big] + N_1^\epsilon \,, \tag{3.100}$$

$$\epsilon_{1'} = \theta_{1'}^\tau \Big[ p_1 - p_{1'} + 2\hat{\mathbf{n}}_2 \cdot \Big( \frac{\mathbf{v}_{\Delta_{1'}}}{c} - \frac{\mathbf{v}_{\delta_{1'}}}{c} \Big) + \mu_1 - b_{1'} q_1 \Big] + N_{1'}^\epsilon \,, \tag{3.101}$$

$$\tau_1 = \theta_1^\tau [p_{1'} - p_1 + \mu_{1'} - b_1 q_1] + N_1^\tau \,, \tag{3.102}$$

$$\tau_{1'} = \theta_{1'}^\tau [p_1 - p_{1'} + \mu_1 - b_{1'} q_1] + N_{1'}^\tau \,. \tag{3.103}$$

### 3.5.2 Sideband Modulation

We have seen in the previous section that clock noise enters into the measurements as additional terms. To correct for this noise, one must transfer clock information from one spacecraft to another with a technique called *clock tone transfer*.

The local clock noise, *e.g.* $q_1(t)$, is first amplified with a large integer, say $m_1 \approx 32$. Then, it is imprinted on the local beam as phase modulation, creating two sidebands as shown in fig. 3.23. Indeed, if the modulation index $k_m$[14] is small enough, the EM field of the modulated local beam reads

$$E_{1,\mathrm{mod}}(t) = E_1(t)(1 + k_m \cos[2\pi\nu_{m_1} t + m_1 q_1(t)]) \,, \tag{3.104}$$

[13] As presented in section 3.3.6, clock noise $q_i(t)$ is expressed as fractional frequency deviations normalized by the laser frequency $\nu_0 = 282\,\mathrm{THz}$.

[14] The modulation index is foreseen to be around $k_m = 0.15$, such that 15 % of the beam power is used for the sideband signal.

where $\nu_{m_1}$ is the modulation frequency, and $E_1(t)$ the EM field associated with the unmodulated local beam. Using eq. (3.61) and expanding, the previous expression can be written as

$$\begin{aligned} E_{1,\mathrm{mod}}(t) = E_{1,0}(t)e^{j(2\pi\nu_1 t+\phi_1(t))} + \frac{k_m}{2}e^{j(2\pi[\nu_1+\nu_{m_1}]t+[\phi_1(t)+m_1 q_1(t)])} \\ + \frac{k_m}{2}e^{j(2\pi[\nu_1-\nu_{m_1}]t+[\phi_1(t)-m_1 q_1(t)])}\,. \end{aligned} \tag{3.105}$$

In reality, the upper and lower modulation frequencies are a bit different, and we denote them as $\nu^+_{m_1} \approx 2.4\,\mathrm{GHz}$ and $\nu^-_{m_1} \approx 2.401\,\mathrm{GHz}$[15]. Therefore, we have

$$\begin{aligned} E_{1,\mathrm{mod}}(t) = E_{1,0}(t)e^{j(2\pi\nu_1 t+\phi_1(t))} + \frac{k_m}{2}e^{j(2\pi[\nu_1+\nu^+_{m_1}]t+[\phi_1(t)+m_1 q_1(t)])} \\ + \frac{k_m}{2}e^{j(2\pi[\nu_1-\nu^-_{m_1}]t+[\phi_1(t)-m_1 q_1(t)])}\,. \end{aligned} \tag{3.106}$$

This beam is sent to the distant spacecraft.

Similarly, the local beam is modulated on optical bench 2' and sent to spacecraft 1. As discussed in section 3.4.3, the previous expression is received with a delay $\mathbf{D}_3$,

$$\begin{aligned} E_{2',\mathrm{mod}}(t) = E_{2',0}(t)e^{j(2\pi\nu_{2'} t+\mathbf{D}_3\phi_{2'}(t))} + \frac{k_m}{2}e^{j\left(2\pi[\nu_{2'}+\nu^+_{m_{2'}}]t+\mathbf{D}_3[\phi_{2'}(t)+m_{2'}q_2(t)]\right)} \\ + \frac{k_m}{2}e^{j\left(2\pi[\nu_{2'}-\nu^-_{m_{2'}}]t+\mathbf{D}_3[\phi_{2'}(t)-m_{2'}q_2(t)]\right)}\,. \end{aligned} \tag{3.107}$$

Both modulated beams then interfere on optical bench 1. Following section 3.4.5, we find that the photodiode signals contains several terms: a time-independent part, numerous terms with frequencies outside of the phasemeter range, and three beatnotes presented in fig. 3.23:

- The carrier-carrier beatnote $a_1 = \nu_{2'} - \nu_1$.
- The upper sideband-upper sideband beatnote $c_1 = (\nu_{2'} + \nu^+_{m_{2'}}) - (\nu_1 + \nu^+_{m_1}) = a_1 + (\nu^+_{m_{2'}} - \nu^+_{m_1})$.
- The lower sideband-lower sideband beatnote $(\nu_{2'} - \nu^-_{m_{2'}}) - (\nu_1 - \nu^-_{m_1}) = a_1 - (\nu^-_{m_{2'}} - \nu^-_{m_1})$, a bit different from the upper sideband-upper sideband beatnote frequency $c_1$.

These three beatnotes are tracked by dedicated DPLL in the phasemeter. Consequently, they are part of the interferometric signals that one must simulate.

[15] These values are proposed in [Hei18]. For a certain set of laser locking configuration (*c.f.* section 3.5.4), these values can be used in all spacecraft and kept constant in time.

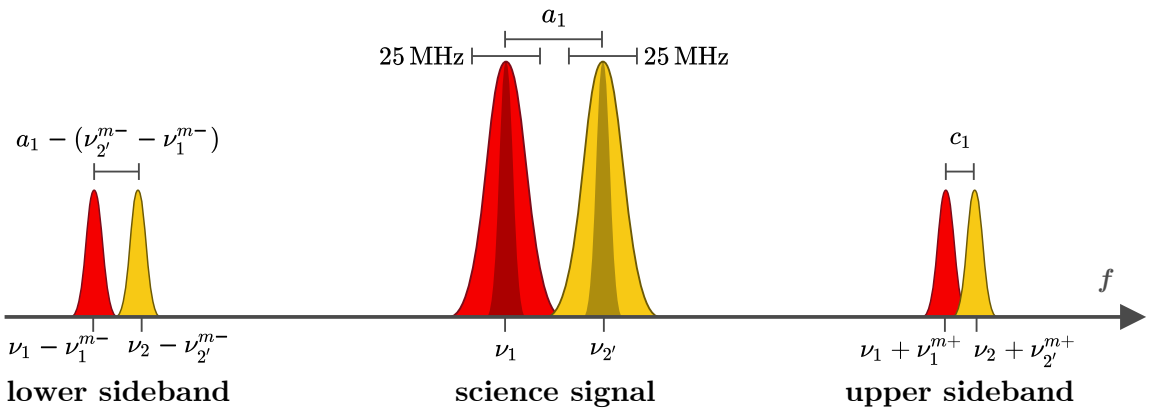


Figure 3.23: Frequency spectrum of the science interferometer. Three beatnote frequencies are within the phasemeter, and followed by dedicated DPLL. In dark red and dark yellow, are represented the gravitational wave contributions to lasers' frequency spectra.

**Assumption 14** *As the lower and upper sidebands carry the same information, we only consider the upper sideband in our model.*

We call *sideband signal* the beatnote formed by the interference of the local and distant upper sidebands.

Following section 3.4.2, the sideband signals are expressed as fractional frequency deviations. They read

$$\begin{aligned} s_1^{\mathrm{sb}} = \theta_1^s \Big[ & H_1 + \mathbf{D}_3 p_{2'} - p_1 + \mathbf{D}_3 m_{2'} q_2 - m_1 q_1 - \left( \hat{\mathbf{n}}_3 \cdot \mathbf{D}_3 \frac{\mathbf{v}_{\Delta_{2'}}}{c} + \hat{\mathbf{n}}_{3'} \cdot \frac{\mathbf{v}_{\Delta_1}}{c} \right) \\ & - c_1 q_1 \Big] + N_1^{\mathrm{sb}} \,, \end{aligned} \tag{3.108}$$

$$\begin{aligned} s_{1'}^{\mathrm{sb}} = \theta_{1'}^s \Big[ & H_{1'} + \mathbf{D}_{2'} p_3 - p_{1'} + \mathbf{D}_{2'} m_3 q_3 - m_{1'} q_1 - \left( \hat{\mathbf{n}}_{2'} \cdot \mathbf{D}_{2'} \frac{\mathbf{v}_{\Delta_3}}{c} + \hat{\mathbf{n}}_2 \cdot \frac{\mathbf{v}_{\Delta_{1'}}}{c} \right) \\ & - c_{1'} q_1 \Big] + N_{1'}^{\mathrm{sb}} \,, \end{aligned} \tag{3.109}$$

Note that in general $c_i \neq a_i$, due to the small difference in the modulation frequencies. Moreover, the sidebands have lower power than the main carrier signal. As a result, the science and sideband signals have different optical bench and OMS displacement noise. However, these differences are small with respect to the noise level.

**Assumption 15** *In our model, science and related sideband signals share the same optical bench and OMS displacement noise.*

### 3.5.3 Timestamping Errors

As mentioned in section 3.3.6, the clocks onboard each spacecraft are not actively synchronized. As a result, they drift relative to each other over time. Since measurement signals from all spacecraft are combined as part of data processing, any timestamping error degrades the performance of the instrument. In section 3.5.1, we studied the local effect of one USO's timing jitter on the interferometric measurements. In this section, we focus on the effect of clock drifting.

Simulating three drifting clocks is not a trivial task. In particular, one must make sure that the simulation structure remains flexible enough to allow control loops onboard each spacecraft, as well as the propagation of the beams between the spacecraft.

As the current LISANode's structure does not allow to simulate such effects, I have worked in collaboration with O. Hartwig (AEI Hannover, Germany) to study potential solutions. In particular, we have narrowed down the issues associated with the simulation of differential clock noise and proposed two main solutions. Appendix A summaries this work.

**Assumption 16** *In our model, we disregard timestamping errors in the interferometric measurements. A simple model of the ranging estimate errors after they have been calibrated is described and implemented in section 3.2.5.*

### 3.5.4 Beatnote Frequency Management

The phasemeter is capable of tracking beatnote frequencies between 5 MHz to 25 MHz. Each laser source is assigned a different optical frequency so that all the heterodyne signals fall inside the phasemeter range.

Unfortunately, these optical frequencies are submitted to changing Doppler shifts as the constellation flexes. Using eq. (3.72), Doppler shifts $\Delta\nu_i$ can be expressed as

$$\frac{\Delta\nu_1}{\nu_0} = \frac{\mathrm{d}\tau_3}{\mathrm{d}t} \quad \text{and} \quad \frac{\Delta\nu_{1'}}{\nu_0} = \frac{\mathrm{d}\tau_{2'}}{\mathrm{d}t}\,. \tag{3.110}$$

Using the analytic Keplerian orbits introduced section 3.2.3, and $\nu_0 = 282\,\mathrm{THz}$, one find Doppler shifts at the megahertz level, *c.f.* fig. 3.24. Using more realistic orbits from by ESA, one can show [Hei18] that the received laser frequencies can vary by $\pm 8\,\mathrm{Mhz}$. As a result, the beatnote vary with time and extend beyond the authorized frequency range.

A laser locking scheme and a frequency plan are needed to keep the beatnote in-band throughout the mission. A master laser is locked to a stable frequency using a resonant

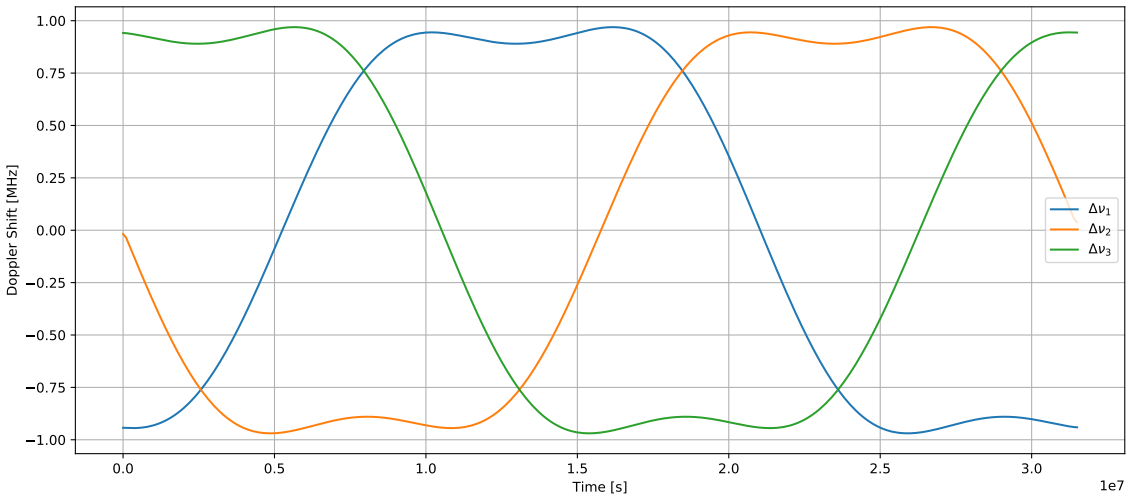


Figure 3.24: Doppler shifts computed with analytic Keplerian orbits presented in section 3.2.3.

cavity, while the remaining slave lasers are locked on each other. The phase-locking is performed by adding an adaptable frequency offset $\delta\nu$ to the received beam frequency. Many different locking configurations are possible; they have been extensively studied in [Hei18] but none stands out with clear advantages. An example of such a laser locking scheme is given in fig. 3.25.

If five beatnotes are locked, *i.e.* directly determined by the frequency offsets, four are *non-locking*. Frequency planning aims to switch regularly the frequency offsets such that all beatnotes remain in-band at all times. A situation where frequency offsets vary continuously with time is also possible and proposed in [Hei18].

As stated in assumption 2, we do not simulate the locking of the lasers, as we assume that they are all free-running. Consequently, we do not fully incorporate frequency planning in our instrumental model. However, we account for the various beatnote frequencies when computing the clock-noise coupling in the phasemeter, *c.f.* section 3.5.1.

### 3.5.5 Antialiasing Filters

Phase measurements are delivered at high frequency (30 Hz) by the onboard phasemeter. The available passband for telemetry does not allow to downlink such an amount of data.

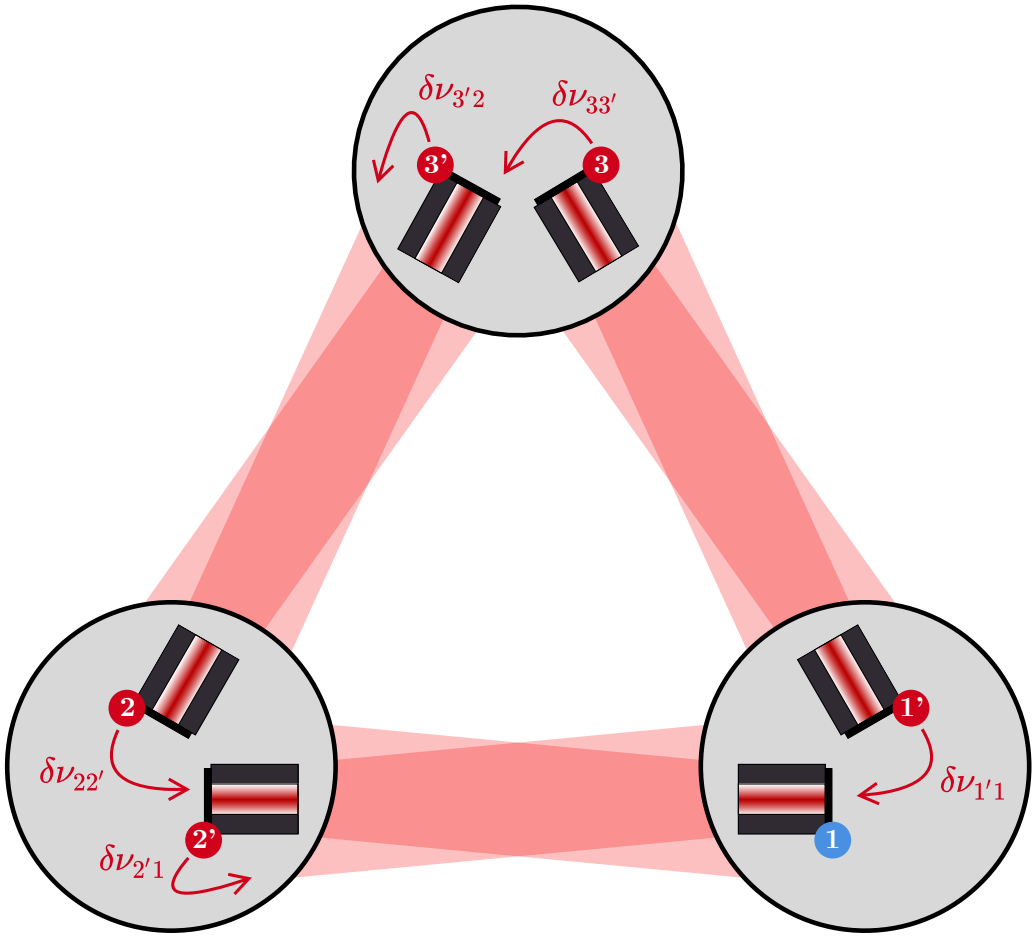


Figure 3.25: Example of laser locking scheme. Laser 1 is the master, while others are phase-locked on each other, with frequency offsets $\delta\nu_i$.

It must, therefore, be decimated by the on-board computers. To prevent power-folding onto the useful frequency band, the on-board computers apply antialiasing filters before carrying out a decimation. In this document, we assume that all filters are identical and can be represented by the filter operator $\mathcal{F}$. The precise filter design characteristic is given in chapter 5.

Filters are applied at the end of the measurement chain. As a result, filter operators apply to whole signal expressions. Taking signals derived in eqs. (3.86), (3.87) and (3.91) to (3.94), one obtain

$$s_1 = \mathcal{F}\Big\{\theta_1^s\Big[H_1 + \mathbf{D}_3 p_{2'} - p_1 - \Big(\hat{\mathbf{n}}_3 \cdot \mathbf{D}_3 \frac{\mathbf{v}_{\Delta_{2'}}}{c} + \hat{\mathbf{n}}_{3'} \cdot \frac{\mathbf{v}_{\Delta_1}}{c}\Big) - a_1 q_1\Big] + N_1^s\Big\} \tag{3.111}$$

$$s_{1'} = \mathcal{F}\Big\{\theta_{1'}^s\Big[H_{1'} + \mathbf{D}_{2'} p_3 - p_{1'} - \Big(\hat{\mathbf{n}}_{2'} \cdot \mathbf{D}_{2'} \frac{\mathbf{v}_{\Delta_3}}{c} + \hat{\mathbf{n}}_2 \cdot \frac{\mathbf{v}_{\Delta_{1'}}}{c}\Big) - a_{1'} q_1\Big] + N_{1'}^s\Big\} \tag{3.112}$$

$$\epsilon_1 = \mathcal{F}\Big\{\theta_1^\tau\Big[p_{1'} - p_1 + 2\hat{\mathbf{n}}_{3'} \cdot \Big(\frac{\mathbf{v}_{\Delta_1}}{c} - \frac{\mathbf{v}_{\delta_1}}{c}\Big) + \mu_{1'} - b_1 q_1\Big] + N_1^\epsilon\Big\} \tag{3.113}$$

$$\epsilon_{1'} = \mathcal{F}\Big\{\theta_{1'}^\tau\Big[p_1 - p_{1'} + 2\hat{\mathbf{n}}_2 \cdot \Big(\frac{\mathbf{v}_{\Delta_{1'}}}{c} - \frac{\mathbf{v}_{\delta_{1'}}}{c}\Big) + \mu_1 - b_{1'} q_1\Big] + N_{1'}^\epsilon\Big\} \tag{3.114}$$

$$\tau_1 = \mathcal{F}\{\theta_1^\tau[p_{1'} - p_1 + \mu_{1'} - b_1 q_1] + N_1^\tau\} \tag{3.115}$$

$$\tau_{1'} = \mathcal{F}\{\theta_{1'}^\tau[p_1 - p_{1'} + \mu_1 - b_{1'} q_1] + N_{1'}^\tau\} \tag{3.116}$$

Similarly, the sideband measurements are also filtered and read

$$\begin{aligned} s_1^{\mathrm{sb}} = \mathcal{F}\Big\{\theta_1^s\Big[&H_1 + \mathbf{D}_3 p_{2'} - p_1 + \mathbf{D}_3 m_{2'} q_2 - m_1 q_1 - \Big(\hat{\mathbf{n}}_3 \cdot \mathbf{D}_3 \frac{\mathbf{v}_{\Delta_{2'}}}{c} + \hat{\mathbf{n}}_{3'} \cdot \frac{\mathbf{v}_{\Delta_1}}{c}\Big) \\ &- c_1 q_1\Big] + N_1^{\mathrm{sb}}\Big\}, \end{aligned} \tag{3.117}$$

$$\begin{aligned} s_{1'}^{\mathrm{sb}} = \mathcal{F}\Big\{\theta_{1'}^s\Big[&H_{1'} + \mathbf{D}_{2'} p_3 - p_{1'} + \mathbf{D}_{2'} m_3 q_3 - m_{1'} q_1 - \Big(\hat{\mathbf{n}}_{2'} \cdot \mathbf{D}_{2'} \frac{\mathbf{v}_{\Delta_3}}{c} + \hat{\mathbf{n}}_2 \cdot \frac{\mathbf{v}_{\Delta_{1'}}}{c}\Big)] \\ &- c_{1'} q_1\Big] + N_{1'}^{\mathrm{sb}}\Big\}, \end{aligned} \tag{3.118}$$

# Chapter 4

# Time-Delay Interferometry

As discussed in the previous chapter, various noise sources enter the interferometric measurements of LISA. In particular, laser noise is expected at many orders of magnitude above the gravitational signals of interest. A method to reduce this noise, alongside others, must be devised before science studies.

In this chapter, I present the main data processing algorithms foreseen for LISA. In particular, I propose an intuitive, geometrical approach of laser noise-reducing TDI based on [Val05a]. Then, I give an updated formulation of these algorithms before I study the propagation of the main noise sources. Finally, I discuss the implementation of these algorithms in LISANode.

## 4.1 An Intuitive Approach

### 4.1.1 Problem Statement

As discussed in section 3.1, LISA will be able to detect gravitational waves by performing micro-radian interferometric measurements. Among the instrumental noise sources entering these interferometric signals, described in section 3.3, laser noise is dominant. In fact, it will be 8 orders of magnitude above the expected gravitational-wave signals[1]. The relative PSDs of laser and secondary noises are shown in fig. 4.1.

[1] Indeed, our model assumes a constant PSD of $30\,\mathrm{Hz}\,\mathrm{Hz}^{-1/2}$, or $10^{-13}\,\mathrm{Hz}^{-1/2}$, to be compared with the typical gravitational-wave amplitude of $10^{-21}$.

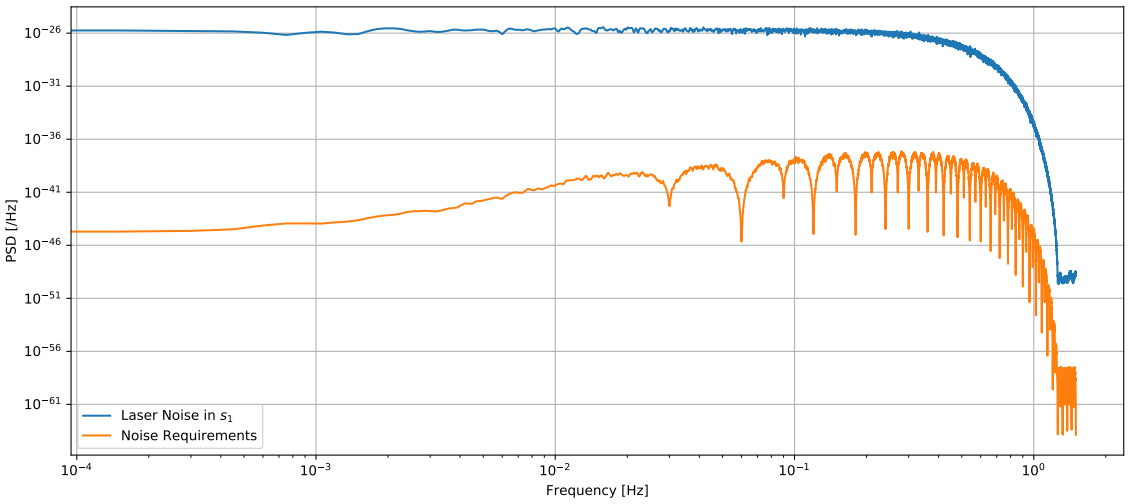


Figure 4.1: Laser noise level in $s_1$ signal, expressed as fractional frequency deviations. Here, the noise requirements match the level of all secondary noises.

Progress in laser technologies allowing to bridge the gap before launch is nor expected neither realistic. Therefore, a numerical method to reduce laser noise below the requirements is essential for the mission. TDI is such a method first proposed in [TA99, VN02, TEA02, AET02]. It is an offline technique that combines the interferometric signals so that laser noise is strongly suppressed under the assumption that the constellation does not flex. The method was later extended to account for time-varying armlengths in [STEA03, CH03, TEA04], giving birth to the so-called *second-generation* combinations. An algebraic study of TDI can be found in [AET02], while a nice geometrical interpretation was proposed in [Val05a]. We follow this last point of view in this chapter.

The existence of a laser noise-reducing algorithm does not guarantee the viability of the mission. Because the scientific analyses are performed on the TDI combinations, one must also study the method's response to gravitational waves. Similarly, understanding how instrumental noise couples in the TDI variables is essential to build a noise budget. These studies are presented at the end of this chapter.

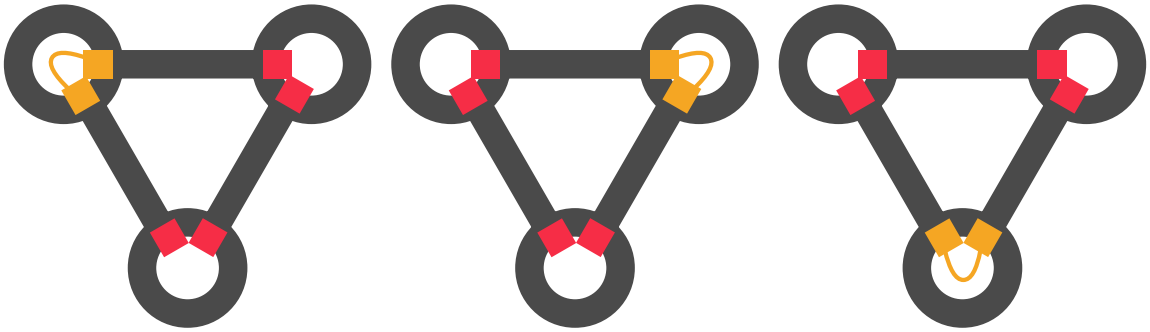

Figure 4.2: Lasers hosted in the same spacecraft appear as pairs in the reference signals.

### 4.1.2 Combining One-Way Measurements

TDI is based on the fact that the same laser noise appears in different interferometric measurements. This is obvious when looking at eqs. (3.86), (3.87) and (3.91) to (3.94). In particular, both lasers hosted by the same spacecraft appear in the reference signals (fig. 4.2). One can use these signals to reduce the number of free-running lasers to three, *c.f.* section 4.2.2. Consequently, in the following paragraphs, I assume that each spacecraft hosts a single laser source, shared by both optical benches.

Science signals have a different structure, as they contain laser noises from difference spacecraft. They represent the six *one-way interferometric measurements*, between one local and one remote clock noise. Note that the latter is delayed by the corresponding armlength. These one-way measurements are illustrated in fig. 4.3 and given by

$$s_1 = \mathbf{D}_3 p_2 - p_1, \quad s_{1'} = \mathbf{D}_{2'} p_3 - p_1\,, \tag{4.1}$$

$$s_2 = \mathbf{D}_1 p_3 - p_2, \quad s_{2'} = \mathbf{D}_{3'} p_1 - p_2\,, \tag{4.2}$$

$$s_3 = \mathbf{D}_2 p_1 - p_3, \quad s_{3'} = \mathbf{D}_{1'} p_2 - p_3\,. \tag{4.3}$$

From these building blocks, we can apply the reasoning outlined in [Val05a] to synthesize arbitrary virtual interferences of the form

$$\mathbf{D}_{i_n i_{n-1} \ldots i_1} p_A - p_B\,, \tag{4.4}$$

where the link indices $i_1, i_2, \ldots i_n$ correspond to a valid path connecting spacecraft $A$ to $B$. Formally, this means that

- The spacecraft pointed to by the link $i_k$ should be the starting point of link $i_{k+1}$.

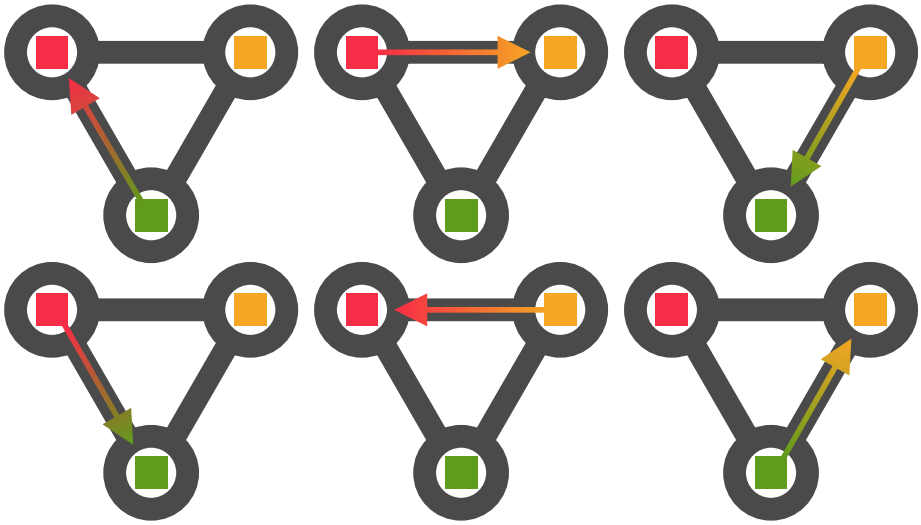

Figure 4.3: On-way measurements of laser noise in the science signals.

- The first link $i_1$ should start from spacecraft $A$.
- The last link $i_n$ should point to spacecraft $B$.

As an example, $s_3 + \mathbf{D}_2 s_1 = (\mathbf{D}_2 p_1 - p_3) + \mathbf{D}_2(\mathbf{D}_3 p_2 - p_1) = \mathbf{D}_{23} p_2 - p_3$ is the interference between photons carrying local laser noise $p_3$, and laser noise $p_2$ after it traveled along links 3 and 2. This is represented on the left panel of fig. 4.4.

### 4.1.3 Synthesizing Virtual Interference

Therefore, if the path described in eq. (4.4) is a round-trip, a single laser noise term appears. A simple example is the two-way measurement illustrated in the middle panel of fig. 4.4,

$$s_1 + \mathbf{D}_3 s_{2'} = \mathbf{D}_3 p_2 - p_1 + \mathbf{D}_3(\mathbf{D}_{3'} p_1 - p_2) = \mathbf{D}_{33'} p_1 - p_1 \,. \tag{4.5}$$

The formal condition, using the notations of eq. (4.4), is that $A = B$.

It is possible to combine such expressions to form virtual interferences between photons that have both traveled arbitrary paths. The only requirement is that the emitter and receiver spacecraft are identical for both expressions and that the signs agree. An example

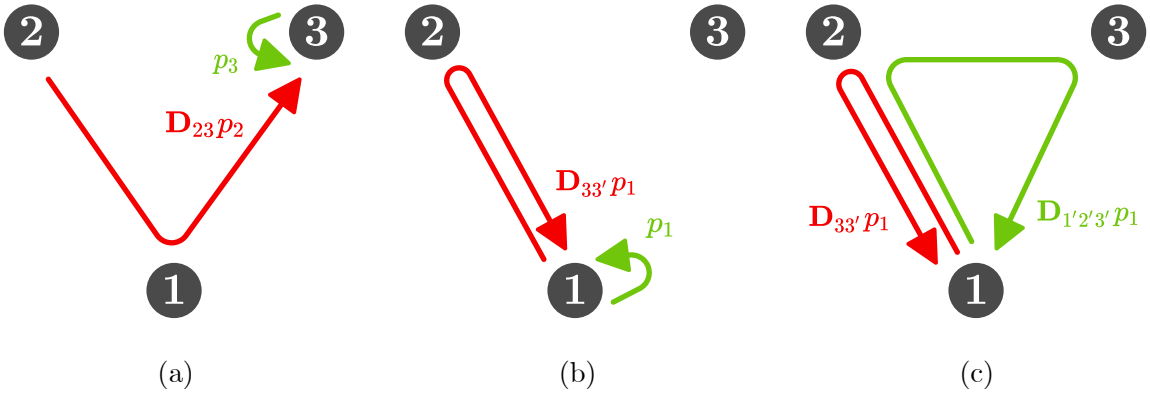


(a) (b) (c)

Figure 4.4: Examples of virtual interferences. For (a), $s_3 + \mathbf{D}_2 s_1 = \mathbf{D}_{23}p_2 - p_3$. For (b), $s_1 + \mathbf{D}_3 s_{2'} = \mathbf{D}_{33'}p_1 - p_1$. For (c), $(s_1 + \mathbf{D}_2 s_1) - (s_{1'} + \mathbf{D}_{2'} s_{3'} + \mathbf{D}_{1'2'} s_{2'}) = (\mathbf{D}_{33'} - \mathbf{D}_{1'2'3'})p_1$.

is given on the right of fig. 4.4:

$$(s_1 + \mathbf{D}_3 s_{2'}) - (s_{1'} + \mathbf{D}_{2'} s_{3'} + \mathbf{D}_{1'2'} s_{2'}) = (\mathbf{D}_{33'}p_1 - p_1) - (\mathbf{D}_{1'2'3'}p_1 - p_1) \tag{4.6}$$

$$= (\mathbf{D}_{33'} - \mathbf{D}_{1'2'3'})p_1 \,, \tag{4.7}$$

The idea behind TDI is now to find pairs of photon round-trip paths with equal delays. In that case, the delay operators cancel out, and so does laser noise. As stated above, both path must start and end at the same spacecraft.

Under the assumption that all armlengths are equal and constant, it is sufficient to check that the numbers of links involved in both photon paths are identical. An example is given by the left panel of fig. 4.5. To account for different armlengths, the photons must travel along the same links, but not necessarily in the same order. Two examples of such combinations are given in the central and right panels of fig. 4.5. It can be shown that these combinations do not cancel gravitational-wave signals.

### 4.1.4 Second-Generation Combinations

However, we saw in section 3.2.4 that the travel times of a photon along a LISA link is time-dependent. As a result, two photons traveling along the same links but in different orders do not have the same times of flight. Formally, delay operators do not commute. Indeed, if $x(t)$ is a time-dependent signal, we have from eq. (5.3),

$$\mathbf{D}_{ij}x(t) = \mathbf{D}_i x(t - \tau_j[t]) = x(t - \tau_i[t] - \tau_j[t - \tau_i(t)]) \,, \tag{4.8}$$

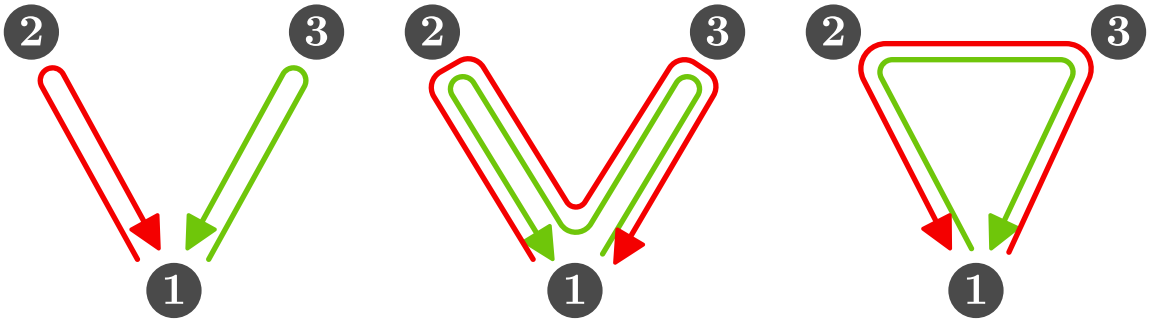


(a) (b) (c)

Figure 4.5: Examples of laser noise-calling virtual interferences. Panel (a) cancel laser noise under the assumption that armlengths are equal and constant. The first-generation Michelson $X_1$ and Sagnac $\alpha_1$ are represented, respectively, in panels (b) and (c).

and

$$\mathbf{D}_{ji}x(t) = \mathbf{D}_j x(t - \tau_i[t]) = x(t - \tau_j[t] - \tau_i[t - \tau_j(t)])\,, \tag{4.9}$$

so that, in general,

$$\mathbf{D}_{ij} \neq \mathbf{D}_{ji}\,. \tag{4.10}$$

Consequently, the previous combinations do not suppress laser noise.

As an example, the Michelson variable $X_1$ (defined in section 4.2.4) has a non-vanishing laser-noise residual that can be expressed as a function of a delay operator commutator,

$$X_1 = (\mathbf{D}_{2'233'} - \mathbf{D}_{33'2'2})p_1 = [\mathbf{D}_{2'2}, \mathbf{D}_{33'}]p_1\,. \tag{4.11}$$

New combinations, based on the former ones, were proposed in [STEA03, CH03, TEA04] to overcome this problem. They are the so-called *second-generation* TDI. It is important to note that second-generation combinations do not cancel exactly laser noise, but suppress it up to first order in the travel time derivatives $\mathrm{d}\tau_i/\mathrm{d}t$.

Multiple second-generation combinations can be used to suppress laser noise down to the required level. A systematic study can be found in [Val05a]. In section 4.2, we give the expressions for the main TDI combinations.

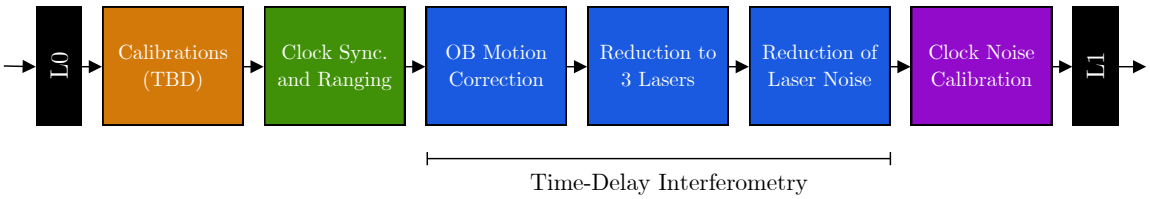


Figure 4.6: LISA calibration chain, from level-0 to level-1 data.

### 4.1.5 Calibration Chain

Before the main TDI combinations are formed, *intermediary variables* are computed to remove some instrumental noises. In particular, optical-bench displacement noise is measured by both test-mass and reference interferometers, *c.f.* section 3.4.7. This allows us to construct $\xi_i$ variables where this noise does not appear, while gravitational signals are kept untouched. Similarly, it is possible to combine the reference signals such as to isolate the noise of primed laser sources. One can then subtract these expressions to reduce the number of free-running lasers to three. These are the $\eta_i$ variables.

Only then, the main TDI combinations presented in the previous sections can be formed. Because precise absolute ranging estimates are necessary, clocks must be synchronized before and measurements must be aligned on a common sampling grid. Refer to section 3.2.5 for more details on absolute ranging. Once laser noise is suppressed to the required level, one has still to calibrate the results for clock noise. Sections 3.5.1 and 3.5.2 describe how clock noise enters the measurements and how clock tone is used to build sideband signals. Here, these sidebands are used to build calibrated clock noise-free variables, denoted with a $c$ exponent for *clock-calibrated*. We present in detail the clock-calibration algorithms and their limiting noises in chapter 6.

Schematics of the rather complex calibration chain, going from level-0 to level-1 data, is presented in fig. 4.6. Dedicated algorithms are then used to extract gravitational signals in the level-1 data and estimate the parameters of the sources. Lastly, these analyses are used to build the final product of the mission, or level-3 data: a gravitational-wave source catalog.

## 4.2 Current Formulation

In this section, we present the current expressions for the on-ground calibration algorithms. Intermediary variables first remove the optical-bench displacement noise and reduce the number of free-running lasers to three. Then, we form the main TDI combinations to reduce laser noise. Finally, we correct these TDI variables for clock noise by using clock-calibrating expressions.

These expressions make use of offline delay operators. The delays themselves match the constellation armlengths, *i.e.* the ranging estimates described in section 3.2.5. Fractional delays are implemented using similar techniques to those discussed in section 3.4.3, such as Lagrange polynomials. This is a sensitive operation, as we only have access to low-frequency, filtered, and telemetered samples of the interferometric measurements. We track the effect of this noise source by denoting differently the offline delay operators $\mathcal{D}_i \neq \mathbf{D}_i$. We introduce the nested delay notation,

$$\mathcal{D}_{i_1,i_2\ldots i_n} \equiv \mathcal{D}_{i_1}\mathcal{D}_{i_2}\ldots\mathcal{D}_{i_n}\,. \tag{4.12}$$

In the following, we present the equations for the first spacecraft. The remaining expressions are deduced by a circular permutation of the indices.

### 4.2.1 Removal of Optical-Bench Displacement Noise

The first step is to remove the optical-bench displacement noise, discussed in section 3.3.4. Because it is measured independently by test-mass and reference interferometers, we can isolate it and subtract it from the science signals,

$$\xi_1 = s_1 + \theta_1^s\theta_1^\tau\frac{\epsilon_1-\tau_1}{2} + \theta_1^s\theta_{2'}^\tau\frac{\mathcal{D}_3(\epsilon_{2'}-\tau_{2'})}{2}\,, \tag{4.13}$$

$$\xi_{1'} = s_{1'} + \theta_{1'}^s\theta_{1'}^\tau\frac{\epsilon_{1'}-\tau_{1'}}{2} + \theta_{1'}^s\theta_3^\tau\frac{\mathcal{D}_{2'}(\epsilon_3-\tau_3)}{2}\,. \tag{4.14}$$

If we disregard filters and assume that we have perfect knowledge of the absolute ranging, *i.e.* if $\mathbf{D}_i \approx \mathcal{D}_i$, then $\xi_1$ and $\xi_{1'}$ are free of optical-bench displacement noise. Otherwise, we are left with non-vanishing residuals reading

$$\xi_1^\Delta = \theta_1^s(\mathcal{F}\mathbf{D}_3 - \mathcal{D}_3\mathcal{F})(\hat{\mathbf{n}}_3\cdot\mathbf{v}_{\Delta_{2'}})\,, \tag{4.15}$$

$$\xi_{1'}^\Delta = \theta_{1'}^s(\mathcal{D}_{2'}\mathcal{F} - \mathcal{F}\mathbf{D}_{2'})(\hat{\mathbf{n}}_{2'}\cdot\mathbf{v}_{\Delta_3})\,. \tag{4.16}$$

If we neglect the ranging errors, the residuals can be expressed as the commutator of a delay and filter operators,

$$\xi_1^{\Delta} \approx \theta_1^s[\mathcal{F}, \mathcal{D}_3](\hat{\mathbf{n}}_3 \cdot \mathbf{v}_{\Delta_{2'}}) \,, \tag{4.17}$$

$$\xi_{1'}^{\Delta} \approx -\theta_{1'}^s[\mathcal{F}, \mathcal{D}_{2'}](\hat{\mathbf{n}}_{2'} \cdot \mathbf{v}_{\Delta_3}) \,. \tag{4.18}$$

In chapter 5, we describe this effect as the *flexing-filtering* coupling. If $S_{\Delta_i}(\omega)$ is the PSD of the $i$-th optical-bench displacement noise and we make use of all notations introduced in section 5.4.4, the PSD of the residual noise in $\xi_i$ reads

$$S_{\xi_1^{\Delta}}(\omega) \approx \omega^2 K_{\mathcal{F}}(\omega) \dot{L}_3^2 S_{\Delta_{2'}}(\omega) \,, \tag{4.19}$$

$$S_{\xi_{1'}^{\Delta}}(\omega) \approx \omega^2 K_{\mathcal{F}}(\omega) \dot{L}_{2'}^2 S_{\Delta_3}(\omega) \,. \tag{4.20}$$

### 4.2.2 Reduction to Three Lasers

The second intermediary variables are defined by

$$\eta_1 = \theta_1^s \xi_1 + \frac{\theta_{2'}^{\tau} \mathcal{D}_3(\tau_{2'} + \tau_2)}{2} \,, \tag{4.21}$$

$$\eta_{1'} = \theta_{1'}^s \xi_{1'} + \frac{\theta_1^{\tau}(\tau_{1'} + \tau_1)}{2} \,. \tag{4.22}$$

If we assume perfect ranging and neglect the filters once again, $\eta_1$ and $\eta_{1'}$ are free of *primed* laser noises. Indeed, they read

$$\eta_1 \approx \mathcal{D}_3 p_2 - p_1 \,, \tag{4.23}$$

$$\eta_{1'} \approx \mathbf{D}_{2'} p_3 - p_1 \,. \tag{4.24}$$

If we account for ranging imperfections and filtering, we are left with the non-vanishing primed laser-noise residuals

$$\eta_1^p = (\mathcal{F}\mathbf{D}_3 - \mathcal{D}_3\mathcal{F}) p_{2'} + \mathcal{D}_3 \mathcal{F} p_2 - \mathcal{F} p_1 \,, \tag{4.25}$$

$$\eta_{1'}^p = \mathcal{F}\mathbf{D}_{2'} p_3 - \mathcal{F} p_1 \,. \tag{4.26}$$

The dominant effect is the flexing-filtering coupling in $\eta_1$, preventing the exact cancellation of $p_{2'}$. Using section 5.4.4 and the associated notations, the residual's PSD can be estimated to

$$S_{\eta_1^{p_{2'}}}(\omega) \approx \omega^2 K_{\mathcal{F}}(\omega) \dot{L}_3^2 S_p(\omega) \,. \tag{4.27}$$

### 4.2.3 Reduction of Clock Noise

As discussed in section 3.5.1, clock noise couples into the interferometric measurements. Intermediary variables that aim to remove this noise were proposed in [OHD12]. Unfortunately, the algorithm, based on the assumption that $q_1$ can be disregarded, was shown to be incorrect in [TH18]. New approximate clock-calibration algorithms were proposed in the same article. They are no longer intermediary variables but are applied after the final TDI combinations are formed. They are given in chapter 6.

Unfortunately, they do not remove exactly laser noise if one accounts for the constellation flexing and filtering. In chapter 6, we propose an algorithm to devise exact clock noise-calibrating expressions for most of TDI combinations. In particular, we give the results for the Michelson and Sagnac combinations (*c.f.* next section). Then, we study the limiting factors to propose a realistic noise budget regarding clock noise.

### 4.2.4 Laser Noise Reduction

Several combinations reduce the laser noise contributions in the interferometric signals, as discussed in section 4.1.4. We present in this section the main ones.

#### First-Generation Michelson Combinations

First-generation Michelson variables $X_1, Y_1, Z_1$ synthesize equal-arm interferometers. It represents the interference of two photons that circulate in opposite directions along both arms each, back to the emitting optical bench. This is illustrated by the left panel of fig. 4.5.

All TDI combinations are defined up to a sign, which varies in the literature. We follow here the conventions adopted by [Ott15][2]. The factored and expanded expressions for the first-generation Michelson variable read

$$X_1 = (\eta_{1'} + \mathcal{D}_{2'}\eta_3) + \mathcal{D}_{2'2}(\eta_1 + \mathcal{D}_3\eta_{2'}) - [(\eta_1 + \mathcal{D}_3\eta_{2'}) + \mathcal{D}_{33'}(\eta_{1'} + \mathcal{D}_{2'}\eta_3)]\,, \tag{4.28}$$

$$X_1 = \eta_{1'} + \mathcal{D}_{2'}\eta_3 + \mathcal{D}_{2'2}\eta_1 - \mathcal{D}_{2'23}\eta_{2'} - \eta_1 - \mathcal{D}_3\eta_{2'} - \mathcal{D}_{33'}\eta_{1'} - \mathcal{D}_{33'2'}\eta_3\,. \tag{4.29}$$

Substituting in eq. (4.29) the expressions of the intermediary variables given in eqs. (4.25) and (4.26) yields laser-noise residuals in the Michelson variables. They can be expressed as

[2]The signs are flipped with respect to [PAH+08, Pet08].

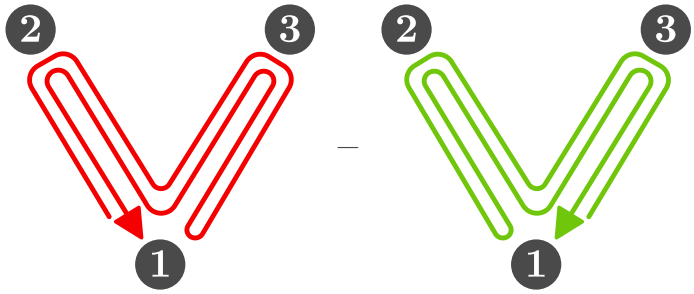


Figure 4.7: Second-generation Michelson variable $X_2$.

functions of the laser noises and filters,

$$\begin{aligned} X_1 = {} & (\mathcal{D}_{2'2}\mathcal{D}_3\mathcal{F}\mathbf{D}_{3'} - \mathcal{D}_3\mathcal{D}_{3'}\mathcal{D}_{2'2}\mathcal{F})p_1 \\ & + \mathcal{D}_3(\mathcal{D}_{3'}\mathcal{F} - \mathcal{F}\mathbf{D}_{3'})p_1 + (\mathcal{D}_{2'} - \mathcal{D}_{33'2'})(\mathcal{F}\mathbf{D}_2 - \mathcal{D}_2\mathcal{F})p_{1'} \\ & + (1 - \mathcal{D}_{2'2})(\mathcal{D}_3\mathcal{F} - \mathcal{F}\mathbf{D}_3)p_{2'} + (1 - \mathcal{D}_{33'})(\mathcal{D}_{2'}\mathcal{F} - \mathcal{F}\mathbf{D}_{2'})p_3 \,. \end{aligned} \tag{4.30}$$

If we neglect ranging errors, the underlying structure of these residuals is best revealed when expressed with commutators,

$$\begin{aligned} X_1 \approx {} & ([\mathcal{D}_{2'2}, \mathcal{D}_3]\mathcal{F}\mathcal{D}_{3'} + \mathcal{D}_{32'2}[\mathcal{F}, \mathcal{D}_{3'}] + \mathcal{D}_3[\mathcal{D}_{2'2}, \mathcal{D}_{3'}]\mathcal{F})p_1 \\ & + \mathcal{D}_3[\mathcal{D}_{3'}, \mathcal{F}]p_1 + (\mathcal{D}_{2'} - \mathcal{D}_{33'2'})[\mathcal{F}, \mathcal{D}_2]p_{1'} \\ & + (1 - \mathcal{D}_{2'2})[\mathcal{D}_3, \mathcal{F}]p_{2'} + (1 - \mathcal{D}_{33'})[\mathcal{D}_{2'}, \mathcal{F}]p_3 \,. \end{aligned} \tag{4.31}$$

We can distinguish two main contributions to these residuals. On one hand, the constellation flexing is responsible for the time variation of light travel times and appears as delay-delay commutators. On the other hand, filters couples to the flexing and yield the delay-filter commutators. This effect, dubbed *flexing-filtering coupling*, is presented and discussed in more details in chapter 5.

If we now neglect the filters and only account for the flexing of the constellation,

$$X_1 \approx ([\mathcal{D}_{2'2}, \mathcal{D}_3]\mathcal{D}_{3'} + \mathcal{D}_3[\mathcal{D}_{2'2}, \mathcal{D}_{3'}])p_1 \,. \tag{4.32}$$

Only by assuming that the armlengths are constant, we obtain $X_1 = 0$.

### Second-Generation Michelson Combinations

We have seen that $X_1$ cancels the laser noise only if we consider constant armlengths. If we expand the light travel times and account for a first time-derivative $\dot{\tau}_i$, we can devise

second-generation expressions $X_2$, $Y_2$, and $Z_2$ that cancel laser noise to first order in $\dot{\tau}_i$. In $X_2$, two photons sense each link twice as they circulate back and forth, as illustrated in fig. 4.7. The combination is given by

$$\begin{aligned} X_2 = {} & (\mathcal{D}_{2'233'} - 1)([\eta_1 + \mathcal{D}_3\eta_{2'}] + \mathcal{D}_{33'}[\eta_{1'} + \mathcal{D}_{2'}\eta_3]) \\ & - (\mathcal{D}_{33'2'2} - 1)([\eta_{1'} + \mathcal{D}_{2'}\eta_3] + \mathcal{D}_{2'2}[\eta_1 + \mathcal{D}_3\eta_{2'}])\,, \end{aligned} \tag{4.33}$$

$$\begin{aligned} X_2 = {} & \eta_{1'} + \mathcal{D}_{2'}\eta_3 + \mathcal{D}_{2'2}\eta_1 - \mathcal{D}_{2'23}\eta_{2'} + \mathcal{D}_{2'233'}\eta_1 \\ & + \mathcal{D}_{2'233'3}\eta_{2'} + \mathcal{D}_{2'233'33'}\eta_{1'} + \mathcal{D}_{2'233'33'2'}\eta_3 \\ & - \eta_1 - \mathcal{D}_3\eta_{2'} - \mathcal{D}_{33'}\eta_{1'} - \mathcal{D}_{33'2'}\eta_3 - \mathcal{D}_{33'2'2}\eta_{1'} \\ & - \mathcal{D}_{33'2'22'}\eta_3 - \mathcal{D}_{33'2'22'2}\eta_1 - \mathcal{D}_{33'2'22'23}\eta_{2'}\,. \end{aligned} \tag{4.34}$$

The laser-noise residuals in $X_2$ read

$$\begin{aligned} X_2 = {} & (\mathcal{D}_{2'2}\mathcal{D}_{33'}\mathcal{D}_3\mathcal{D}_{3'}\mathcal{D}_{2'2}\mathcal{F} - \mathcal{D}_{33'}\mathcal{D}_{2'2}\mathcal{D}_{2'2}\mathcal{D}_3\mathcal{F}\mathbf{D}_{3'})\mathcal{F}p_1 \\ & + (1 - \mathcal{D}_{2'2} - \mathcal{D}_{2'233'})\mathcal{D}_3(\mathcal{D}_{3'}\mathcal{F} - \mathcal{F}\mathbf{D}_{3'})p_1 \\ & + (1 - \mathcal{D}_{33'} - \mathcal{D}_{33'2'2} + \mathcal{D}_{2'233'33'})\mathcal{D}_{2'}(\mathcal{F}\mathbf{D}_2 - \mathcal{D}_2\mathcal{F})p_{1'} \\ & + (1 - \mathcal{D}_{33'} - \mathcal{D}_{2'233'} + \mathcal{D}_{33'2'22'2})(\mathcal{D}_3\mathcal{F} - \mathcal{F}\mathbf{D}_3)p_{2'} \\ & + (1 - \mathcal{D}_{33'} - \mathcal{D}_{33'2'2} + \mathcal{D}_{2'233'33'})(\mathcal{F}\mathbf{D}_{2'} - \mathcal{D}_{2'}\mathcal{F})p_3\,, \end{aligned} \tag{4.35}$$

and assuming perfect ranging, they reduce to

$$\begin{aligned} X_2 \approx {} & ([\mathcal{D}_{2'2}, \mathcal{D}_{33'}]\mathcal{D}_{33'2'2}\mathcal{F} + \mathcal{D}_{33'2'2}[\mathcal{D}_{33'}, \mathcal{D}_{2'2}]\mathcal{F} + \mathcal{D}_{33'2'22'23}[\mathcal{D}_{3'}, \mathcal{F}])\mathcal{F}p_1 \\ & + (1 - \mathcal{D}_{2'2} - \mathcal{D}_{2'233'})\mathcal{D}_3[\mathcal{D}_{3'}, \mathcal{F}]p_1 \\ & + (1 - \mathcal{D}_{33'} - \mathcal{D}_{33'2'2} + \mathcal{D}_{2'233'33'})\mathcal{D}_{2'}[\mathcal{F}, \mathcal{D}_2]p_{1'} \\ & + (1 - \mathcal{D}_{33'} - \mathcal{D}_{2'233'} + \mathcal{D}_{33'2'22'2})[\mathcal{D}_3, \mathcal{F}]p_{2'} \\ & + (1 - \mathcal{D}_{33'} - \mathcal{D}_{33'2'2} + \mathcal{D}_{2'233'33'})[\mathcal{F}, \mathcal{D}_{2'}]p_3\,. \end{aligned} \tag{4.36}$$

Disregarding filters and only accounting for the constellation flexing, we have

$$X_2 \approx ([\mathcal{D}_{2'2}, \mathcal{D}_{33'}]\mathcal{D}_{33'2'2} - \mathcal{D}_{33'2'2}[\mathcal{D}_{2'2}, \mathcal{D}_{33'}])p_1 = [[\mathcal{D}_{2'2}, \mathcal{D}_{33'}], \mathcal{D}_{33'2'2}]p_1\,. \tag{4.37}$$

As opposed to eq. (4.32), the residuals are here expressed as the commutator of a commutator. Therefore, we can understand that this is a next-to-leading order effect and that laser noise is better suppressed than in $X_1$. This is discussed in more details in chapter 5, where we estimate the PSD of such delay-delay commutators.

### Quasi-Orthogonal Combination

By construction, instrumental noises enter the Michelson variables correlated. This makes the source parameter estimation a hard task, as most of the existing algorithms work best with decoupled noise sources. Therefore, optimal combinations built from the Michelson variables to minimize the instrumental noise cross-correlation [ATL02]. They were named after TDI inventors Armstrong ($A_i$,), Estabrook $E_i$, and Tinto $T_i$. One can show that they synthesize signals from a perpendicular-arm interferometer.

The following equations[3] are valid for any generation $n$:

$$A_n = \frac{1}{\sqrt{2}}(Z_n - X_n), \quad E_n = \frac{1}{\sqrt{6}}(X_n - 2Y_n + Z_n), \quad T_n = \frac{1}{\sqrt{3}}(X_n + Y_n + Z_n) \tag{4.38}$$

### Sagnac Combinations

The three Sagnac variables $\alpha_i$, $\beta_i$, and $\gamma_i$ were proposed in [TEA02]. They synthesize the interference of photons circulating clockwise and counterclockwise the constellation, as shown in the right panel of fig. 4.5.

First-generation $\alpha_1$ reads

$$\alpha_1 = \eta_1 + \mathcal{D}_3\eta_2 + \mathcal{D}_{31}\eta_3 - [\eta_{1'} + \mathcal{D}_{2'1'}\eta_{2'} + \mathcal{D}_{2'}\eta_{3'}]\,, \tag{4.39}$$

while second-generation $\alpha_2$ is given by

$$\begin{aligned}\alpha_2 = (1 - \mathcal{D}_{2'1'3'})\eta_1 + (1 - \mathcal{D}_{2'1'3'})\mathcal{D}_3\eta_2 + (1 - \mathcal{D}_{2'1'3'})\mathcal{D}_{31}\eta_3 \\ - [(1 - \mathcal{D}_{312})\eta_{1'} + (1 - \mathcal{D}_{312})\mathcal{D}_{2'1'}\eta_{2'} + (1 - \mathcal{D}_{312})\mathcal{D}_{2'}\eta_{3'}]\,.\end{aligned} \tag{4.40}$$

In the latter, both virtual photons go twice around the constellation, *c.f.* fig. 4.8.

### Fully Symmetric Combination

The first-generation fully symmetric combination $\zeta_1$ senses the constellation rotation, and combine all interferometric signals with exactly one delay. The combination is given by [Ott15]

$$\zeta_1 = \mathcal{D}_{1'}\eta_{1'} + \mathcal{D}_{2'}\eta_{2'} + \mathcal{D}_{3'}\eta_{3'} - [\mathcal{D}_1\eta_1 + \mathcal{D}_2\eta_2 + \mathcal{D}_3\eta_3]\,. \tag{4.41}$$

[3] Here, we follow the equations from the original paper [ATL02] and those of the LDC manual [LIS19a].

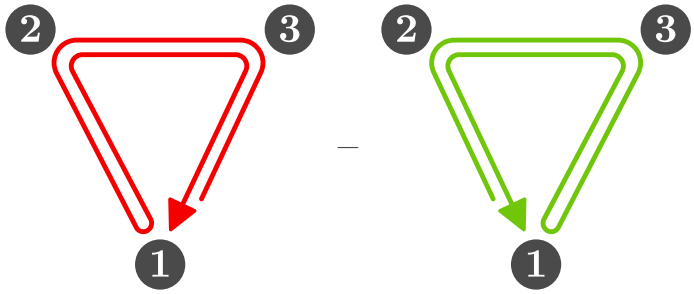


Figure 4.8: Second-generation Sagnac variable $\alpha_2$.

Its second-generation counterpart $\zeta_2$ reads

$$\begin{aligned}\zeta_2 = &(\mathcal{D}_{1'1} - \mathcal{D}_{321})\eta_1 + (\mathcal{D}_{12} - \mathcal{D}_{3'2'2})\eta_2 + (\mathcal{D}_{1'3'} - \mathcal{D}_{323'})\eta_3 \\ &- [(\mathcal{D}_{11'} - \mathcal{D}_{3'2'1'})\eta_{1'} + (\mathcal{D}_{12} - \mathcal{D}_{3'2'2})\eta_{2'} + (\mathcal{D}_{1'3'} - \mathcal{D}_{323'})\eta_{3'}] \,.\end{aligned} \tag{4.42}$$

**Beacon, Monitor, and Relay Combinations**

The beacon ($P_i$, $Q_i$, and $R_i$), monitor ($E_i$, $F_i$, and $G_i$), and relay ($U_i$, $V_i$, and $W_i$) combinations can be used in the case of the failure of a link. Their first-generation expressions read

$$P_1 = (\mathcal{D}_{12} - \mathcal{D}_{2'})\eta_2 + (\mathcal{D}_{2'} - \mathcal{D}_{1'12'})\eta_{2'} + (\mathcal{D}_{1'13} - \mathcal{D}_3)\eta_3 + (\mathcal{D}_3 - \mathcal{D}_{2'1'})\eta_{3'} \,, \tag{4.43}$$

$$E_1 = -(1 - \mathcal{D}_{11'})\eta_1 + (1 - \mathcal{D}_{1'1})\eta_{1'} - (\mathcal{D}_{3'} - \mathcal{D}_{21})\eta_2 + (\mathcal{D}_2 - \mathcal{D}_{3'1'})\eta_{3'} \,, \tag{4.44}$$

$$U_1 = \mathcal{D}_{11'3'}\eta_{1'} + \mathcal{D}_{11'}\eta_{2'} + \mathcal{D}_1\eta_{3'} + \eta_2 - (\mathcal{D}_{3'2'1'}\eta_2 + \mathcal{D}_{3'2'}\eta_{3'} + \mathcal{D}_{3'}\eta_{1'} + \eta_{2'}) \,. \tag{4.45}$$

## 4.3 Time-Delay Interferometry Simulation

In this section, we discuss the implementation of the LISA calibration chain presented in section 4.1.5 in LISANode. We then give some results and discuss the level of the residual noise in the main TDI combinations.

### 4.3.1 Implementation

The top-level graph TDI is the main entry point to simulate the LISA on-ground data processing. It implements the TDI algorithms, including the computation of intermediary

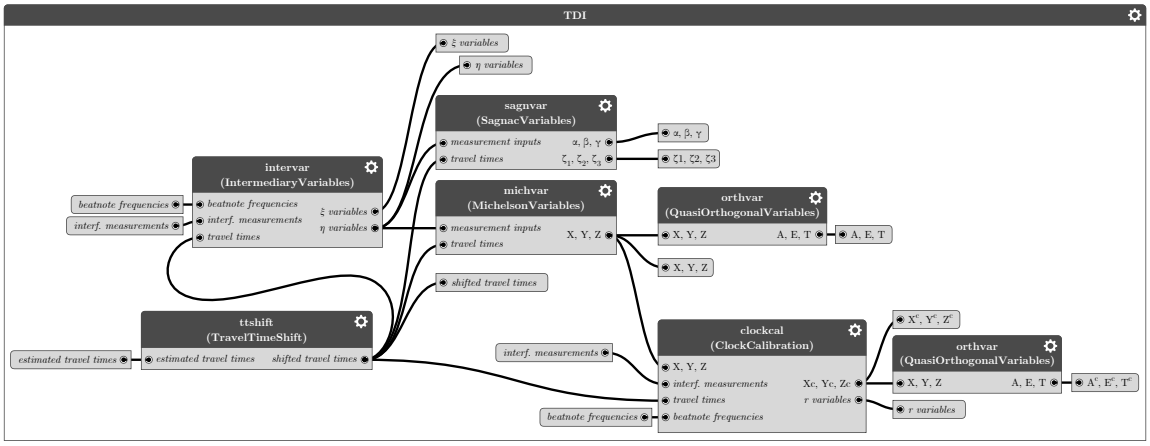


Figure 4.9: Schematics of the top-level TDI graph.

variables and laser noise-suppressing combinations, as well as the clock noise calibration. The content of the graph is represented in fig. 4.9.

As discussed in section 3.5.3, clocks must be synchronized before intermediary variables can be computed. As we disregard timestamping errors in the measurements (assumption 16), only ranging signals are affected in our model by clock noise. Kalman-like filters are expected to reduce these errors to an acceptable level and provide reliable ranging estimates. In our model, we implement the residual clock errors in the ranging estimates *after* clocks have been synchronized as a systematic bias and a stochastic error. The model is available in AbsoluteRanging and discussed in section 3.2.5.

Ranging estimates are then time-shifted by the antialiasing filter group delay. This ensures that the flexing-filtering coupling, described in chapter 5, is highly suppressed. Only then, TDI performance fulfills the requirements.

Next, these time-shifted ranging estimates are used to compute the intermediary variables $\xi_i$ and $\eta_i$ as formulated in sections 4.2.1 and 4.2.2. This is implemented by the IntermediaryVariables graph. Then, the requested laser noise-suppressing combinations are formed. Currently, first and second-generation Michelson ($X_i$, $Y_i$, and $Z_i$), Sagnac ($\alpha_i$, $\beta_i$, $\gamma_i$, and the fully symmetric $\zeta_i$), and quasi-orthogonal ($A_i$, $E_i$, and $T_i$) combinations are implemented. The user chooses the desired combinations using the corresponding simulation configuration options described in appendix C.6.

Lastly, clock calibration algorithms from chapter 6 are executed. They make use of the beat-

note frequencies and the sideband signals and can apply to Michelson or quasi-orthogonal combinations. Appendix C.6 describes available options.

### 4.3.2 Nested Delay Operators

We call *nested delays* the chaining of multiple delay operators, as described in eq. (4.12). Because the light travel time along one LISA link varies with time, delay operators have an effect on each other. Indeed, if $x(t)$ is a signal,

$$\mathcal{D}_{ij}x(t) = \mathcal{D}_i x(t - \tau_j(t)) = x(t - \tau_j(t - \tau_i) - \tau_i)\,. \tag{4.46}$$

More generally, define the signal $x(t)$ delayed $n$ times,

$$y_n(t) = \mathcal{D}_{i_1,i_2,\ldots i_n}x(t)\,. \tag{4.47}$$

By a simple recursive proof, we can show that $y_n$ can be written as

$$y_n(t) = x\left(t - \sum_{k=1}^{n} z_k(t)\right), \tag{4.48}$$

with

$$z_1 = \tau_{i_1} \quad \text{and} \quad z_n(t) = \tau_{i_n}\left(t - \sum_{k=1}^{n-1} z_k(t)\right). \tag{4.49}$$

Here, the original signal $x(t)$ is delayed only once. As a result, errors due to the imperfect delay operators, implemented as Lagrange polynomials (*c.f.* section 3.4.3), are limited. Light travel times are themselves time-shifted repeatedly, in a recursive manner. We use this formulation in the NestedDelays graph, documented in appendix C.

### 4.3.3 Simulation Results and Limitations

In figs. 4.10 and 4.11, one can compare the instrumental noise in the $s_1$ interferometric measurement and the residual noise in some first and second-generation TDI combinations. These simulations use a simple instrumental setup, where antialiasing filters have been disabled and interferometric signals are not downsampled. As a result, all measurements are taken at a frequency of 3 Hz. The light travel times are computed from the set of Keplerian orbits presented in section 3.2.3. Clock noise and ranging errors are disregarded in these simulations, so we can highlight the TDI reduction of laser and optical-bench displacement noise.

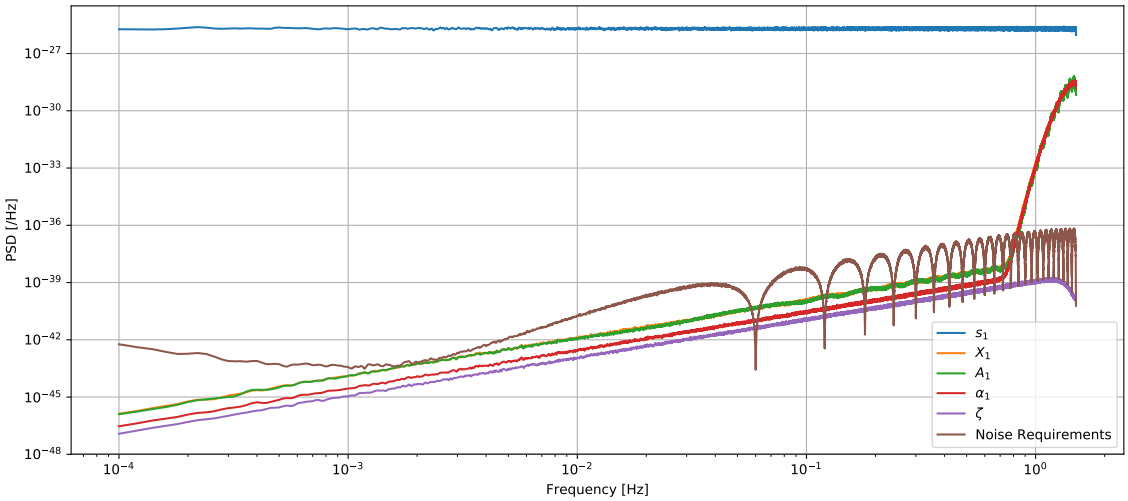


Figure 4.10: Instrumental noise in the $s_1$ interferometric signal, compared with the residual noise in the first-generation TDI $X_1$, $A_1$, $\alpha_1$, and $\zeta_1$ combinations.

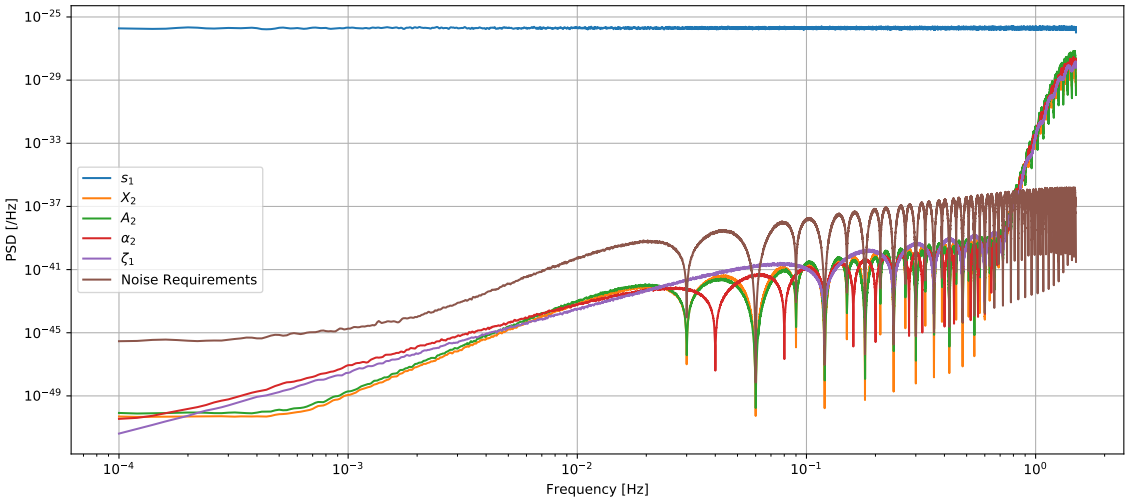


Figure 4.11: Instrumental noise in the $s_1$ interferometric signal, compared with the residual noise in the second-generation TDI $X_2$, $A_2$, $\alpha_2$, and $\zeta_2$ combinations.

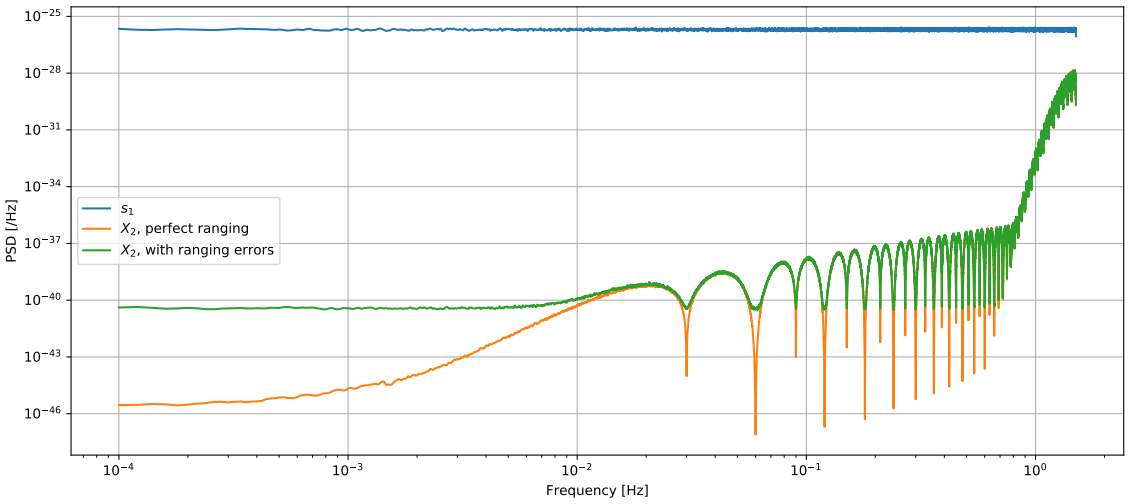


Figure 4.12: Instrumental noise in the $s_1$ interferometric signal, compared with the residual noise in the second-generation TDI $X_2$, $A_2$, $\alpha_2$, and $\zeta_2$ combinations.

As expected, both generations reduce the loudest instrumental noise (laser and optical-bench displacement noises) to below the LISA requirements, *i.e.* a level that allows for the detection of gravitational-wave signals. In figs. 4.10 and 4.11, this level is represented by that of the secondary noises, which are not suppressed but only modulated by TDI.

However, these results do not account for a number of effects which degrade the noise-reduction performance. Indeed, in a more realistic setup, the residual noise in the TDI combinations is notably higher than one would naively expect. First, the ranging estimates used to delay the interferometric measurements appearing in the TDI combinations are imperfect. As discussed in section 3.2.5, those estimates contain an error. Therefore, they do not match the real propagation times and the residual level increases. Figure 4.12 shows the effect of such ranging errors in second-generation Michelson $X_2$ combination.

Time-Delay Interferometry Ranging (TDIR) was proposed in [TVA05] to mitigate the effect of a constant bias in the ranging signals. It is a minimization algorithm that works together with the absolute ranging to minimize the residual noise in TDI combinations over long time periods. However, this technique has not been experimentally confirmed.

Also, the fractional delay operators cannot be exact as we only use a finite number of samples (*i.e.* a finite interpolation order in the case of Lagrange polynomials, *c.f.* section 3.4.3). As a result, numerical errors are introduced each time a delayed interferometric measurement

appears in the TDI combination. Results are even worse when delay operators are nested, as these numerical errors tend to accumulate. Noise-reduction performance is thus directly connected to the quality of the interpolation, and this justifies why we use high-order interpolation in our simulations. In particular, the increase of residual laser noise at high frequencies in fig. 4.12 is the signature of Lagrange interpolation. These issues are discussed in detail in [SWSV04].

As mentioned in the previous sections, the flexing of the constellation is responsible for the non-commutation of delay operators. Such commutators yield a non-vanishing contribution to the noise residuals. Moreover, the antialiasing filters described in section 3.5.5 can couple to the delay operators and leave substantial residuals as well. These two effects are studied and discussed in detail in chapter 5.

Lastly, clock noise couples at various points in the measurement chain, *c.f.* section 3.3.6. In particular, it introduces errors in the measurements provided by the phasemeters that must be corrected for. In chapter 6, we propose an exact calibration algorithm and discuss the limiting noise sources. In conclusion, we show that it is possible to reduce this clock noise to the required levels.

# Chapter 5

# Flexing-Filtering Effect

This chapter is an re-arranged and augmented reproduction of an article [BLPH19] published in *Physical Review D*, 2019. This paper is the result of a work conducted in collaboration with M. Lilley, M. Petiteau, and H. Halloin.

## 5.1 Introduction

We have seen in chapter 3 that, among the multiple sources of noise which enter the measurements made by LISA, laser frequency noise is dominant. In chapter 4, we introduced TDI, an algorithm that aims to reduce the laser frequency noise by 8 orders of magnitude, bringing it below secondary noises and gravitational wave signals. Indeed, one synthesizes virtual equal-arm interferometric measurements by combining time-shifted measurements from LISA.

Laboratory experiments have been performed to study whether TDI can be applied correctly and whether its performance meets mission requirements, in various setups. A first demonstrator was designed at the Jet Propulsion Lab [DWM$^+$10] to reproduce noise couplings and measure TDI noise reduction in a fixed two-arm configuration. It was shown that the laser frequency noise could be reduced to the desired level. The *Hexagon* interferometer [SBP$^+$19] is a metrology test bed developed at the Albert Einstein Institute, and consists of three locked lasers. It was used both to test the performance and feasibility of TDI for heterodyne interferometry and to test phasemeter prototypes. *LISA-On-Table (LOT)* is an electro-optical simulator developed at AstroParticule et Cosmologie Laboratory (APC) [LHB$^+$17, GHP$^+$15]. The results show that in the case of two static unequal

arms, first-generation TDI cancels the laser frequency noise as expected. The *University of Florida LISA Simulator (UFLIS)* uses electronic phase delay units to simulate the time variation of the armlengths. First-generation TDI was successfully tested, reaching the required performance, while TDI 2.0 results were limited by the noise of the electronic phase delay units [CTHM06]. To date, however, no realistic demonstrator using time-varying armlengths was successful in measuring the performance of TDI 2.0. Computer simulations have also been used to check the performance of the laser frequency noise removal performed by TDI. They are described in chapter 2.

In this chapter, we have developed an analytic model that describes both LISA and TDI for a realistic setup in order to determine which instrumental factors play an important role in the laser frequency noise reduction performance. This model reproduces the results of both LISANode and LISACode with great precision. We include the effect of the so-called flexing, *i.e.* time-varying armlengths, and that of the antialiasing filtering applied before the high-frequency measurements are downsampled and telemetered to Earth. The agreement between our theoretical model and our simulations demonstrates that LISACode and LISANode are implemented correctly. Our work also shows that a coupling between the flexing of the constellation and the antialiasing filters can degrade significantly TDI's performance. We show that the effect of this coupling is mitigated with well-designed filters and a specific offline treatment. The remaining laser frequency noise can then be maintained below mission requirements in the frequency band between $10^{-4}$ and $10^{-1}$ Hz, for second-generation TDI.

We first present the LISA mission setup that was modeled analytically and simulated numerically in section 5.2, and the TDI algorithm that was used in section 5.3. In section 5.4, we derive the corresponding analytic model for TDI 1.5 and 2.0. In section 5.5 we describe LISACode and LISANode, and give details about the configuration used to generate the data. Finally, in section 5.6, we compare and discuss the results of the simulators and of the analytic approach. In particular, we study the effect of different types of filters and discuss their potential implementations.

## 5.2 Instrumental Setup

LISA is a constellation of three spacecraft forming a nearly equilateral triangle. The constellation's center of mass trails the Earth in its orbit around the Sun by around 20 deg. [DASpAh$^+$17]. Each spacecraft emits and receives a laser beam along each of the two arms connecting it to its companion spacecraft. All spacecraft host two MOSAs, an on-

board computer, a phasemeter, and two laser sources. A MOSA is composed of a telescope and an optical bench. The telescope sends an outgoing laser beam to its companion spacecraft and collects incoming light. Various conventions are used in the literature to denote the spacecraft, optical benches and arms. In this chapter, we number these components according to fig. 3.4.

The Fourier Transform of a signal $x(t)$ is denoted $\widetilde{x}(\omega)$ and defined here by

$$\widetilde{x}(\omega) = \int_{-\infty}^{\infty} x(t) e^{-j\omega t} \, \mathrm{d}t \,, \tag{5.1}$$

and the Inverse Fourier Transform follows

$$x(t) = \int_{-\infty}^{\infty} \widetilde{x}(\omega) e^{j\omega t} \, \mathrm{d}\omega \,, \tag{5.2}$$

where $j^2 = -1$ is the unit imaginary number.

Usual properties, such as linearity, follow from these definitions.

In this chapter, we consider the latest optical design, often called *split interferometry*. It is extensively described in [OHD12]. Three interferometric measurements are performed on each optical bench $i$: the science $s_i$ (respectively, reference $\tau_i$) signal is the beatnote between the distant (respectively, adjacent) and local beams without any reflection on the test masses. The test mass signal $\epsilon_i$ corresponds to the beatnote formed by the local and adjacent beams after reflection onto the local test mass.

For simplicity, we neglect all secondary noise sources, such as the read-out noise, the optical path noise, and the test mass acceleration noise. The clocks on board each spacecraft are assumed to be perfect and we neglect both the clock noise and the sideband measurements that are used to remove parts of this noise [TH18, OHD12]. We therefore only study laser frequency noise, denoted $p_i(t)$ and $p'_i(t)$, where $i$ is the spacecraft index. For simplicity, we model it here as a white noise with a power spectral density (PSD) of $10^{-26}\,\mathrm{Hz/Hz}$, *c.f.* section 3.3.2. We disregard laser locking and therefore assume that lasers are free-running with independent noise series. Under those assumptions, *split interferometry* reduces to the legacy design described in [Pet08].

The interferometric measurements, defined in eqs. (5.4) and (5.5), are delivered by the phasemeter to the on-board computer at 20 Hz. Due to limitations in the telemetry passband, they must be downsampled to 2 Hz before they are transmitted to Earth [DASpAh$^+$17]. Antialiasing filters are used to prevent power folding in the band of interest during decimation. These filters are assumed to be identical on board all spacecraft, and consist of a convo-

lution with a filter kernel $f(t)$. We define the filter operator $\mathcal{F}$, such that $\mathcal{F}x(t) = (f * x)(t)$ for any signal $x(t)$.

We model all signals as Doppler observables, *i.e.* as the ratio of the instantaneous frequency deviation from the nominal carrier frequency $[\nu(t) - \nu_0]/\nu_0$ [Val05b] over that nominal carrier frequency. We neglect frequency planning [Bar15] and Doppler shifts due to the relative motion of the spacecraft. Therefore, In this chapter, the carrier nominal frequency remains constant and equal for all beams, and interferometric signals are obtained by forming the difference of two incoming Doppler observables.

The propagation of laser beams between two spacecraft is modeled by applying time-varying delays. These delays correspond to the sum of all delays in the optical, analog and digital signal chains, though the main contribution remains the light travel times between the spacecraft. Therefore we suppose here that they are given by the armlengths and the speed of light in vacuum. We denote $\mathcal{D}_i$ the operator associated with traveling along arm $i$, of length $c \times L_i(t)$. For example, the laser frequency noise received by optical bench $2'$ from laser 1, after it has traveled along arm 3, is given by

$$\mathcal{D}_3 p_1(t) = p_1(t - L_3(t)) \,. \tag{5.3}$$

We give the expressions of the measurement signals for the spacecraft 1; others are obtained by circular permutation of the indices. The science signals read

$$\begin{aligned} s_1 &= \mathcal{F}\mathcal{D}_3 p_2' - \mathcal{F} p_1 \,, \\ s_1' &= \mathcal{F}\mathcal{D}_{2'} p_3 - \mathcal{F} p_1' \,. \end{aligned} \tag{5.4}$$

In the absence of secondary noise sources, the expressions for the test mass and reference signals are equal and given by

$$\begin{aligned} \epsilon_1 &= \tau_1 = \mathcal{F} p_1' - \mathcal{F} p_1 \,, \\ \epsilon_1' &= \tau_1' = \mathcal{F} p_1 - \mathcal{F} p_1' \,. \end{aligned} \tag{5.5}$$

## 5.3 Time-Delay Interferometry

TDI is a multi-staged algorithm [Ott15] which is performed off-line, before astrophysical and cosmological source parameters are extracted, cf. fig. 2.1. It is mainly conceived to reduce reduce laser frequency noise, but intermediary steps also cancel other instrumental sources of noise. We shall only consider laser frequency noise, but will nevertheless use the full TDI expressions in this section, for consistency with the literature.

One first uses the measurement signals to form the intermediary variables $\xi_i$, then $Q_i$ and then finally $\eta_i$. These combinations, respectively, cancel out the optical bench displacement noise (here set to zero), reduce the signals to one free-running laser per spacecraft and suppress clock noise (here set to zero). Note that the test mass acceleration and optical measurement system noises, also set to zero in this study, are not suppressed by these combinations. $\xi$, $Q$, and $\eta$ are defined in [Ott15] and can be written under our assumptions as

$$\begin{aligned}
\xi_i &= s_i - \frac{\mathcal{D}_k\epsilon'_j - \mathcal{D}_k\tau'_j}{2}\,,\\
\xi'_i &= s'_i - \frac{\mathcal{D}_{j'}\epsilon_k - \mathcal{D}_{j'}\tau_k}{2}\,,\\
Q_i &= \xi_i + \frac{\mathcal{D}_k\tau'_j - \mathcal{D}_k\tau_j}{2}\,,\\
Q'_i &= \xi'_i + \frac{\tau'_i - \tau_i}{2}\,,\\
\eta_i &= Q_i\,,\\
\eta'_i &= Q'_i\,.
\end{aligned} \tag{5.6}$$

Next, TDI synthesizes virtual equal-arm interferometric measurements in order to reduce laser frequency noise. This is done by applying one of the appropriate sets of nested delays to the $\eta_i$ variables, and by combining the resulting terms. In this chapter, we focus on the Michelson variables $X, Y$ and $Z$, which synthesize pairwise independent Michelson-like interferometers. There exist several generations of Michelson variables, which depend on the complexity of the spacecraft motion. TDI version 1.0 applies to a static configuration. Version 1.5 applies to a rigid but rotating configuration. Finally, TDI version 2.0 applies to a rotating configuration with armlengths varying linearly in time. In this chapter we focus on versions 1.5 and 2.0 of TDI.

The expressions for the $X$ variable for generations 1.5 and 2.0 [VN02] are given by

$$X_1 = \eta_{1'} + \mathcal{D}_{2'}\eta_3 + \mathcal{D}_{2'2}\eta_1 - \mathcal{D}_{2'23}\eta_{2'} - (\eta_1 + \mathcal{D}_3\eta_{2'} + \mathcal{D}_{33'}\eta_{1'} + \mathcal{D}_{33'2'}\eta_3)\,, \tag{5.7}$$

$$\begin{aligned}
X_2 = X_1 &+ \mathcal{D}_{2'233'}\eta_1 + \mathcal{D}_{2'233'3}\eta_{2'} + \mathcal{D}_{2'233'33'}\eta_{1'} + \mathcal{D}_{2'233'33'2'}\eta_3\\
&- (\mathcal{D}_{33'2'2}\eta_{1'} + \mathcal{D}_{33'2'22'}\eta_3 + \mathcal{D}_{33'2'22'2}\eta_1 + \mathcal{D}_{33'2'22'23}\eta_{2'})\,,
\end{aligned} \tag{5.8}$$

where we have used the nested delay notation $\mathcal{D}_{i_1 i_2 \ldots i_n} \equiv \mathcal{D}_{i_1}\mathcal{D}_{i_2}\ldots\mathcal{D}_{i_n}$. The remaining Michelson variables $Y$ and $Z$ can be obtained by circular permutation of the indices.

Substituting in eqs. (5.7) and (5.8) the values for $\eta$ and $\eta'$, given by eq. (5.6), yields expressions which depend on laser frequency noises only. Let us first neglect the filters,

*i.e.* we set $\mathcal{F} = 1$. Because we are dealing with time-varying armlengths, the Michelson variables can be expressed with nonvanishing delay commutators $[A, B] = AB - BA$,

$$X_1 = ([\mathcal{D}_{2'2}, \mathcal{D}_3]\mathcal{D}_{3'} + \mathcal{D}_3[\mathcal{D}_{2'2}, \mathcal{D}_{3'}])p_1\,, \tag{5.9}$$
$$X_2 = ([\mathcal{D}_{2'2}, \mathcal{D}_{33'}]\mathcal{D}_{33'2'2} - \mathcal{D}_{33'2'2}[\mathcal{D}_{2'2}, \mathcal{D}_{33'}])p_1\,. \tag{5.10}$$

If we now include the effect of the filter, delay-filter commutators appear. Indeed, delay operators are used in the definition of these filters, which therefore do not commute with the time-varying delays used by TDI. The residual laser frequency noise now reads

$$\begin{aligned} X_1 = {} & ([\mathcal{D}_{2'2}, \mathcal{D}_3]\mathcal{F}\mathcal{D}_{3'} + \mathcal{D}_3[\mathcal{D}_{2'2}, \mathcal{D}_{3'}]\mathcal{F})p_1 \\ & + \mathcal{D}_3(1 - \mathcal{D}_{2'2})[\mathcal{D}_{3'}, \mathcal{F}]p_1 + (1 - \mathcal{D}_{33'})\mathcal{D}_{2'}[\mathcal{F}, \mathcal{D}_2]p_{1'} \\ & + (1 - \mathcal{D}_{2'2})[\mathcal{D}_3, \mathcal{F}]p_{2'} + (1 - \mathcal{D}_{33'})[\mathcal{D}_{2'}, \mathcal{F}]p_3\,, \end{aligned} \tag{5.11}$$

$$\begin{aligned} X_2 = {} & ([\mathcal{D}_{2'2}, \mathcal{D}_{33'}]\mathcal{D}_{33'2'2}\mathcal{F} + \mathcal{D}_{33'2'2}[\mathcal{D}_{33'}, \mathcal{D}_{2'2}]\mathcal{F})p_1 \\ & + (1 - \mathcal{D}_{2'2} - \mathcal{D}_{2'233'} + \mathcal{D}_{33'2'22'2})\mathcal{D}_3[\mathcal{D}_{3'}, \mathcal{F}]p_1 \\ & + (1 - \mathcal{D}_{33'} - \mathcal{D}_{33'2'2} + \mathcal{D}_{2'233'33'})\mathcal{D}_{2'}[\mathcal{F}, \mathcal{D}_2]p_{1'} \\ & + (1 - \mathcal{D}_{33'} - \mathcal{D}_{2'233'} + \mathcal{D}_{33'2'22'2})[\mathcal{D}_3, \mathcal{F}]p_{2'} \\ & + (1 - \mathcal{D}_{33'} - \mathcal{D}_{33'2'2} + \mathcal{D}_{2'233'33'})[\mathcal{F}, \mathcal{D}_{2'}]p_3\,. \end{aligned} \tag{5.12}$$

In the next section, we use these expressions to derive an analytic model for the residual laser frequency noise after application of TDI. In section 5.5, we numerically simulate the measurement signals, generate the $X$, $Y$, and $Z$ variables, and estimate their PSDs.

## 5.4 Analytic modeling for linear armlengths

### 5.4.1 Modeling Armlengths

For realistic spacecraft orbits computed using Kepler's laws [DNKV05, NKDV06], LISA armlengths are not constant, but modulated with a characteristic time scale of a year. In this section, we expand these armlengths to first order in time. This is a good approximation of the true orbits on a scale of several weeks, *i.e.* to a frequency of the order of $10^{-5}$ Hz, while the lowest frequency in LISA's band of interest is $2 \times 10^{-5}$ Hz [LIS19b]. Therefore, deviations are expected to appear only at low frequencies.

We define the armlengths, in meters, as $c \times L_i(t) = c \times L_i + c \times \dot{L}_i\, t$, where $L_i$ and $\dot{L}_i$ are constant. The delay operators $\mathcal{D}_i$ applied to the laser frequency noise $p(t)$ is now a pure

delay and a time rescaling. It reads

$$\mathcal{D}_i p(t) = p\Big[\Big(1 - \dot{L}_i\Big)t - L_i)\Big]\,. \tag{5.13}$$

The Fourier Transform of a signal $x(at+b)$, which is delayed by $-b$ and whose time is rescaled by $a$, can be expressed as a function of the original signal using a change of variable. The computations follow

$$\widetilde{x(at+b)}(\omega) = \int_{-\infty}^{\infty} x(at+b)e^{-j\omega t}\,\mathrm{d}t = \int_{-\infty}^{\infty} x(\tau)e^{-j\omega\frac{\tau-b}{a}}\frac{\mathrm{d}t}{|a|} = \frac{e^{j\omega b/a}}{|a|}\widetilde{x}\Big(\frac{\omega}{a}\Big)\,. \tag{5.14}$$

We can apply this result to eq. (5.13), with $a = 1 - \dot{L}_i$ and $b = -L_i$. Since $\dot{L}_i \ll 1$, we can get rid of the absolute value and use the simple result

$$\widetilde{\mathcal{D}_i x}(\omega) = \frac{1}{1-\dot{L}_i}\exp\left(-j\omega\frac{L_i}{1-\dot{L}_i}\right)\widetilde{x}\left(\frac{\omega}{1-\dot{L}_i}\right)\,. \tag{5.15}$$

### 5.4.2 Nested Delays

Successive applications of delay operators are called nested delays. In the case of two delays, it follows easily from eq. (5.13) that

$$\mathcal{D}_{ij}x(t) = \mathcal{D}_i x([1-\dot{L}_j]t - L_j) = x([1-\dot{L}_i][1-\dot{L}_j]t - [1-\dot{L}_i]L_j - L_i)\,, \tag{5.16}$$

while, if we apply the same delays in the reverse order we obtain

$$\mathcal{D}_{ji}x(t) = \mathcal{D}_j x([1-\dot{L}_i]t - L_i) = x([1-\dot{L}_j][1-\dot{L}_i]t - [1-\dot{L}_j]L_i - L_j)\,. \tag{5.17}$$

One can note that the time rescaling is, in both cases, identical. Nevertheless, the pure delays are different. This is a good illustration of the non commutation of our delay operators, and we have

$$\mathcal{D}_{ij} \neq \mathcal{D}_{ji}\,. \tag{5.18}$$

Let us now consider the general nested delays $\mathcal{D}_{i_1 i_2 \ldots i_n}$ applied to a signal $x(t)$, denoted $y(t)$. If we apply recursively eq. (5.13) we obtain the compact expression in the time domain

$$y(t) = \mathcal{D}_{i_1 i_2 \ldots i_n}x(t) = x\left(S_n t - \sum_{k=1}^{n} S_{k-1}L_{i_k}\right)\,, \tag{5.19}$$

where we have defined

$$S_k = \prod_{p=1}^{k} \left(1 - \dot{L}_{i_p}\right), \tag{5.20}$$

for $k > 0$ and $S_0 = 1$.

Indeed, eq. (5.19) is trivially valid for a single delay, *i.e.* when $n = 1$ because we have $y(t) = \mathcal{D}_{i_1} x(t) = x([1 - \dot{L}_{i_1}]t - L_{i_1}) = x(S_1 t - S_0 L_{i_1})$. If we assume that the formula holds for $n$ delays, we can apply another delay and find the corresponding version of eq. (5.19). This proves the general formula by mathematical induction.

Applying eq. (5.14) to eq. (5.19), we can derive the Fourier Transform for nested delays as they appear in the TDI residuals, with the same definition of $S_k$,

$$\widetilde{y}(\omega) = \frac{1}{S_n} \exp\left(-j\omega \sum_{k=1}^{n} \frac{L_{i_k}}{S_k}\right) \widetilde{x}\left(\frac{\omega}{S_n}\right). \tag{5.21}$$

The previous equation is not invariant by swapping of delay operators. Indeed, this non-commutation is caused by the terms $S_k$ inside the exponential function. As it is clear in eq. (5.20), these terms are highly dependent on the delay order. As an example, we see in the next section that the commutator of $n$ delays does not vanish.

### 5.4.3 Delay Commutators

#### Analytic Development

Let us consider the commutator of $n$ delay operators, be they propagation or offline delays. We denote its application on a signal $x(t)$

$$y(t) = \left[\mathcal{D}_{i_1 i_2 \ldots i_m}, \mathcal{D}_{i_{m+1} \ldots i_n}\right] x(t) = (\mathcal{D}_{i_1 \ldots i_n} - \mathcal{D}_{j_1 \ldots j_n}) x(t)\,, \tag{5.22}$$

where we have defined the $j_k$ indices such that

$$\begin{cases} j_k = i_{k+m} & \text{for} \quad 1 \leq k \leq n - m\,, \\ j_k = i_{k-n+m} & \text{for} \quad n - m < k \leq n\,. \end{cases} \tag{5.23}$$

Note that, because we only applied an index permutation to obtain the $j$'s from the $i$'s, we have the set equality

$$\{i_k\}_{1 \leq k \leq n} = \{j_k\}_{1 \leq k \leq n}\,. \tag{5.24}$$

Using eq. (5.19), we have in time domain

$$y(t) = x\left(S_n t - \sum_{k=1}^{n} S_{k-1}^i L_{i_k}\right) - x\left(S_n t - \sum_{k=1}^{n} S_{k-1}^j L_{j_k}\right), \tag{5.25}$$

where $S_k^i = \prod_{p=1}^{k}\left(1 - \dot{L}_{i_p}\right)$ and $S_k^j = \prod_{p=1}^{k}\left(1 - \dot{L}_{j_p}\right)$ for $k > 0$, and $S_0^i = S_0^j = 1$. Note that we have $S_n^i = S_n^j = S_n$ because of the set equality eq. (5.24). The difference does not vanish because the two sums use different indices and therefore are not identical. This is the mathematical translation of the non-commutation of our delay operators.

We can massage this equation by trying to write all terms expressed with the $j$'s indices as functions of the $i$'s indices only. We first split the sum $\sum_{k=1}^{n} S_{k-1}^j L_{j_k}$ into two parts.

- The first one is $\sum_{k=1}^{n-m} S_{k-1}^j L_{j_k} = L_{i_{m+1}} + \sum_{k=2}^{n-m} S_{k-1}^j L_{j_k}$. In this sum, we focus on the factors $S_{k-1}^j$, where $1 \le k-1 \le n-m-1$. Using eq. (5.23), we can write

$$S_{k-1}^j = \prod_{p=1}^{k-1}\left(1 - \dot{L}_{i_{p+m}}\right) = \prod_{p=m+1}^{k+m-1}\left(1 - \dot{L}_p\right) = \frac{S_{k+m-1}^i}{S_m^i}\,. \tag{5.26}$$

  Therefore the term of interest reads

$$L_{i_{m+1}} + \frac{1}{S_m^i}\sum_{k=2}^{n-m} S_{k+m-1}^i L_{i_{k+m}} = L_{i_{m+1}} + \frac{1}{S_m^i}\sum_{k=m+2}^{n} S_{k-1}^i L_{i_k} = \frac{1}{S_m^i}\sum_{k=m+1}^{n} S_{k-1}^i L_{i_k}\,. \tag{5.27}$$

- The second part is $\sum_{k=n-m+1}^{n} S_{k-1}^j L_{j_k} = S_{n-m}^j L_{i_1} + \sum_{k=n-m-2}^{n} S_{k-1}^j L_{j_k}$. Once again, we focus on the factors $S_{k-1}^j$, where $n-m < k-1 \le n-1$. Using eq. (5.23), we can write

$$S_{k-1}^j = \prod_{p=1}^{n-m}\left(1 - \dot{L}_{i_{p+m}}\right)\prod_{p=n-m+1}^{k-1}\left(1 - \dot{L}_{i_{p-n+m}}\right) = \frac{S_n^i}{S_m^i} S_{k-n+m-1}^i\,. \tag{5.28}$$

  Similarly, for the extra factor we have

$$S_{n-m}^j = \prod_{p=1}^{n-m}\left(1 - \dot{L}_{i_{p+m}}\right) = \prod_{p=m+1}^{n}\left(1 - \dot{L}_{i_p}\right) = \frac{S_n^i}{S_m^i}\,. \tag{5.29}$$

  Therefore the second term of interest reads

$$\frac{S_n^i}{S_m^i}\left(L_{i_1} + \sum_{k=n-m+2}^{n} S_{k-n+m-1}^i L_{i_{k-n+m}}\right) = \frac{S_n^i}{S_m^i}\sum_{k=1}^{m} S_{k-1}^i L_{i_k}\,. \tag{5.30}$$

Using these results we now have

$$y(t) = x\left(S_n t - \sum_{k=1}^{n} S_{k-1}^i L_{i_k}\right) - x\left(S_n t - \frac{S_n^i}{S_m^i}\sum_{k=1}^{m} S_{k-1}^i L_{i_k} - \frac{1}{S_m^i}\sum_{k=m+1}^{n} S_{k-1}^i L_{i_k}\right). \quad (5.31)$$

which we can Taylor-expand.

If we focus on the first order in powers of the armlength derivatives, $S_k^i \approx 1 - \sum_{p=1}^{k} \dot{L}_{i_p}$, $1/S_k^i \approx 1 + \sum_{p=1}^{k} \dot{L}_{i_p}$ and $S_n^i/S_m^i \approx 1 - \sum_{p=m+1}^{n} \dot{L}_{i_p}$. Plugging these approximations in the expression of $y(t)$, and denoting $\Sigma = \sum_{k=1}^{n} L_{i_k}$ the armlength sum, yields

$$y(t) \approx \left[\left(\sum_{k=1}^{n} L_{i_k}\right)\left(\sum_{k=1}^{m} \dot{L}_{i_k}\right) - \left(\sum_{k=1}^{m} L_{i_k}\right)\left(\sum_{k=1}^{n} \dot{L}_{i_k}\right)\right]\frac{\mathrm{d}x}{\mathrm{d}t}. \quad (5.32)$$

Assuming now that all armlengths at $t = 0$ are almost equal, *i.e.* $L_i \approx L$ for all $i$, we can simplifiy eq. (5.32) to

$$y(t) \approx L\left[(n-m)\left(\sum_{k=1}^{m} \dot{L}_{i_k}\right) - m\left(\sum_{k=m+1}^{n} \dot{L}_{i_k}\right)\right]\frac{\mathrm{d}x}{\mathrm{d}t}. \quad (5.33)$$

The corresponding Fourier transform $\widetilde{y}(\omega)$ is

$$\widetilde{y}(\omega) \approx -j\omega L e^{-j\omega n L}\left[(n-m)\left(\sum_{k=1}^{m} \dot{L}_{i_k}\right) - m\left(\sum_{k=m+1}^{n} \dot{L}_{i_k}\right)\right]\widetilde{x}(\omega), \quad (5.34)$$

and the associated PSD writes

$$S_y(\omega) \approx \omega^2 L^2\left[(n-m)\left(\sum_{k=1}^{m} \dot{L}_{i_k}\right) - m\left(\sum_{k=m+1}^{n} \dot{L}_{i_k}\right)\right]^2 S_x(\omega). \quad (5.35)$$

**Simulations**

Using eq. (5.33), the commutator $[\mathcal{D}_i, \mathcal{D}_j]$ applied to a signal $x(t)$ is approximately, to leading order in the derivative of $x$ and in the powers of the armlength derivatives, and if we assume that armlengths are equal,

$$[\mathcal{D}_i, \mathcal{D}_j]x(t) \approx L\left(\dot{L}_i - \dot{L}_j\right)\frac{\mathrm{d}x}{\mathrm{d}t}(t - 2L). \quad (5.36)$$

Using LISANode, we compute this simple delay commutator using $L_i = L_j = L = 100\,\mathrm{s}$, and $\dot{L}_i = -\dot{L}_j = 10^{-2}\,\mathrm{s/s}$. The input signal $x(t)$ is a simple sinus of amplitude 1, and

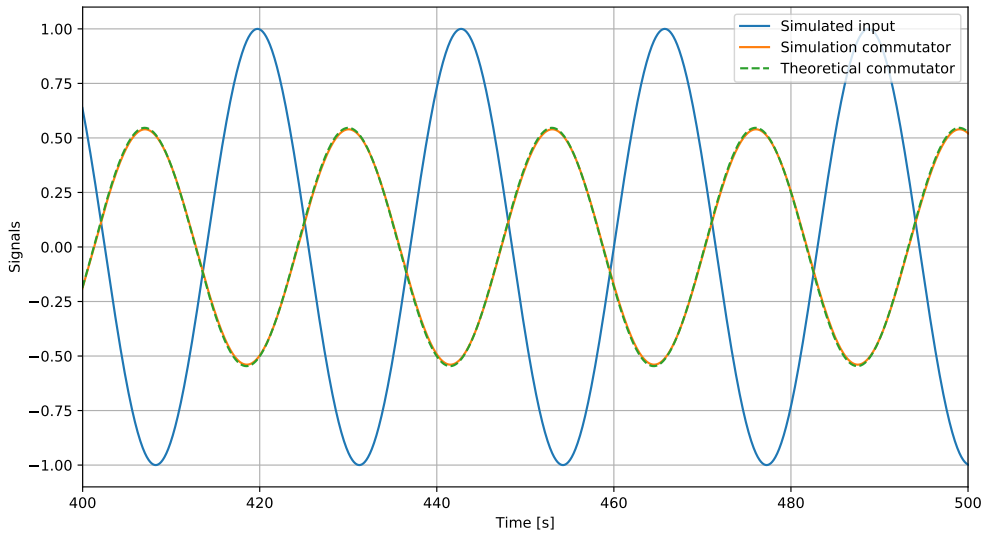


Figure 5.1: Simulated and theoretical time series for a simple delay commutator $[\mathcal{D}_i, \mathcal{D}_j]$ applied to a sinus signal. Parameters used in the simulation are described in the related section.

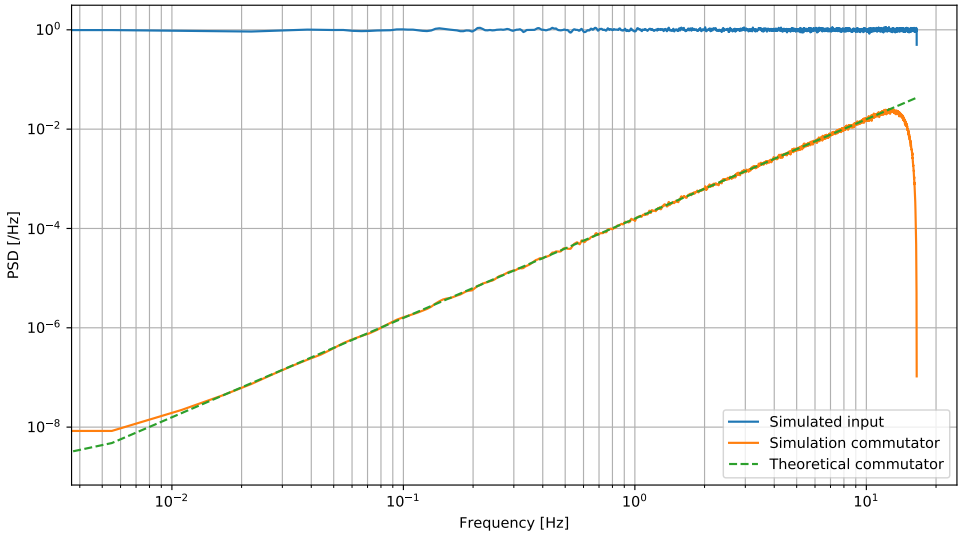


Figure 5.2: Simulated and theoretical PSDs for a simple delay commutator $[\mathcal{D}_i, \mathcal{D}_j]$ applied to a white noise. Parameters used in the simulation are described in the related section.

arbitrary frequency and phase. Figure 5.1 shows a very good match between the simulated data and the theoretical model eq. (5.36).

In the Fourier domain, we use eq. (5.35) to derive the commuator PSD

$$S_{[\mathcal{D}_i,\mathcal{D}_j]x}(\omega) \approx \omega^2 L^2 \left(\dot{L}_i - \dot{L}_j\right)^2 S_x(\omega)\,. \tag{5.37}$$

Using LISANode, we compute this delay commutator using $L = 100\,\mathrm{s}$ and $\dot{L}_i = -\dot{L}_j = \dot{L} = 10^{-5}\,\mathrm{s/s}$ but generate $x(t)$ as a white noise of unit PSD, with an arbitrary sampling frequency. We therefore have the simplified expression for the commutator PSD $\widetilde{[\mathcal{D}_i, \mathcal{D}_j]}x(\omega) \approx 4\omega^2 L^2 \dot{L}^2 S_x$. Figure 5.2 shows that the approximated model matches with good precision the simulated data.

### 5.4.4 Delay-Filter Commutators

#### Analytic Development

The application of the filter operator $\mathcal{F}$ on a signal $x(t)$ is formally written as a convolution of the filter kernel and the signal itself. In the frequency domain, this translates to a simple product of the signal and filter kernel Fourier Transforms

$$\widetilde{\mathcal{F}x}(\omega) = \widetilde{\mathcal{F}}(\omega) \times \widetilde{x}(\omega)\,. \tag{5.38}$$

When delay operators are applied before, *i.e.* when they appear at the right of the $\mathcal{F}$ operator, we simply use eqs. (5.21) and (5.38) and still have a simple product in the Fourier domain. If we define $y(t) = \mathcal{F}\mathcal{D}_{i_1} \dots \mathcal{D}_{i_n} x(t)$, then

$$\widetilde{y}(\omega) = \frac{1}{S_n} \exp\left(-j\omega \sum_{k=1}^{n} \frac{L_{i_k}}{S_k}\right) \widetilde{x}\left(\frac{\omega}{S_n}\right) \widetilde{\mathcal{F}}(\omega)\,. \tag{5.39}$$

When delay operators are applied after the filter, *i.e.* when they appear at the left of the $\mathcal{F}$ operator, we have to apply the frequency rescaling; if $y(t) = \mathcal{D}_{i_1} \dots \mathcal{D}_{i_n} \mathcal{F} x(t)$, we have

$$\widetilde{y}(\omega) = \frac{1}{S_n} \exp\left(-j\omega \sum_{k=1}^{n} \frac{L_{i_k}}{S_k}\right) \widetilde{x}\left(\frac{\omega}{S_n}\right) \widetilde{\mathcal{F}}\left(\frac{\omega}{S_n}\right). \tag{5.40}$$

We can now easily work out the Fourier Transform of the commutator for nested delays and a filter. Let's define, in general,

$$y(t) = [\mathcal{D}_{i_1} \dots \mathcal{D}_{i_n}, \mathcal{F}] x(t) = (\mathcal{D}_{i_1} \dots \mathcal{D}_{i_n} \mathcal{F} - \mathcal{F}\mathcal{D}_{i_1} \dots \mathcal{D}_{i_n}) x(t)\,, \tag{5.41}$$

Using the two previous equations, we have in Fourier domain

$$\widetilde{y}(\omega) = \frac{1}{S_n} \exp\left(-j\omega \sum_{k=1}^{n} \frac{L_{i_k}}{S_k}\right) \widetilde{x}\left(\frac{\omega}{S_n}\right) \left[\widetilde{\mathcal{F}}\left(\frac{\omega}{S_n}\right) - \widetilde{\mathcal{F}}(\omega)\right]. \tag{5.42}$$

Let us expand this last expression to leading order in the armlength derivatives. We use the first order approximation $1/S_n \approx 1 + \sum_{k=1}^{n} \dot{L}_k$, so that eq. (5.42) becomes

$$\widetilde{y}(\omega) \approx \omega \exp\left(-j\omega \sum_{k=1}^{n} L_{i_k}\right) \left(\sum_{k=1}^{n} \dot{L}_{i_k}\right) \frac{\mathrm{d}\widetilde{\mathcal{F}}}{\mathrm{d}\omega}\, \widetilde{x}(\omega)\,. \tag{5.43}$$

One can note the linear dependency on the angular frequency, and the rather small factor $\sum_{k=1}^{n} \dot{L}_{i_k}$. The factor of interest is $\frac{\mathrm{d}\widetilde{\mathcal{F}}}{\mathrm{d}\omega}$, which depends on the filter characteristics. If we denote its square modulus $K_{\mathcal{F}}(\omega) \equiv \left|\frac{\mathrm{d}\widetilde{\mathcal{F}}}{\mathrm{d}\omega}\right|^2$, the corresponding filter commutator PSD can be written as

$$S_y(\omega) \approx \omega^2 K_{\mathcal{F}}(\omega) \left(\sum_{k=1}^{n} \dot{L}_{i_k}\right)^2 S_x(\omega)\,. \tag{5.44}$$

**Simulations**

As an example of eq. (5.43), the PSD of a commutator $[\mathcal{D}_i, \mathcal{F}]$ of a single delay and a filter, applied to a signal $x(t)$ writes

$$S_{[\mathcal{D}_i,\mathcal{F}]}(\omega) \approx \omega^2 K_{\mathcal{F}}(\omega) \dot{L}_i^2 S_x(\omega)\,. \tag{5.45}$$

Using LISANode, we compute this commutator using $L_i = 100\,\mathrm{s}$, and $\dot{L}_i = 10^{-3}\,\mathrm{s/s}$. The input signal $x(t)$ is a white noise of unit PSD $S_x = 1$ and we use a sampling period $T = 1/33\,\mathrm{s}$. We use a simple moving average filter, whose difference equation $y_n = \frac{1}{2}(x_n + x_{n+1})$ gives

$$S_{[\mathcal{D}_i,\mathcal{F}]}(\omega) \approx \omega^2 \frac{S_x}{4} \left(T\dot{L}_i\right)^2 . \tag{5.46}$$

A good match between our approximated model and the simulated data is shown by fig. 5.3.

### 5.4.5 Residual Laser Noise

First, let us neglect the filters; *i.e.* we set $\mathcal{F} = 1$. We substitute in eq. (5.9) the first-order expression for the delay commutator given in eq. (5.34). This yields the approximated Fourier transform of the residual laser noise for $X_1$.

As expected, first-order terms vanish for TDI 2.0. We expand eq. (5.10) to second order, using the exact expression of the delay commutator given in eq. (5.34). This yields the approximated Fourier transform of the residual laser noise for $X_2$.

The corresponding PSDs are obtained by taking the squared modulus and the ensemble average of the Fourier transforms. We use the fact that the laser noises have zero mean, *i.e.* $\langle \widetilde{p}_i(\omega) \rangle = 0$ for all $i$. In addition, we assume that different laser noises are uncorrelated, *i.e.* $\langle \widetilde{p}_i(\omega_1) \widetilde{p}_j(\omega_2) \rangle = 0$ if $i \neq j$. They all are white noises with the same constant PSD,

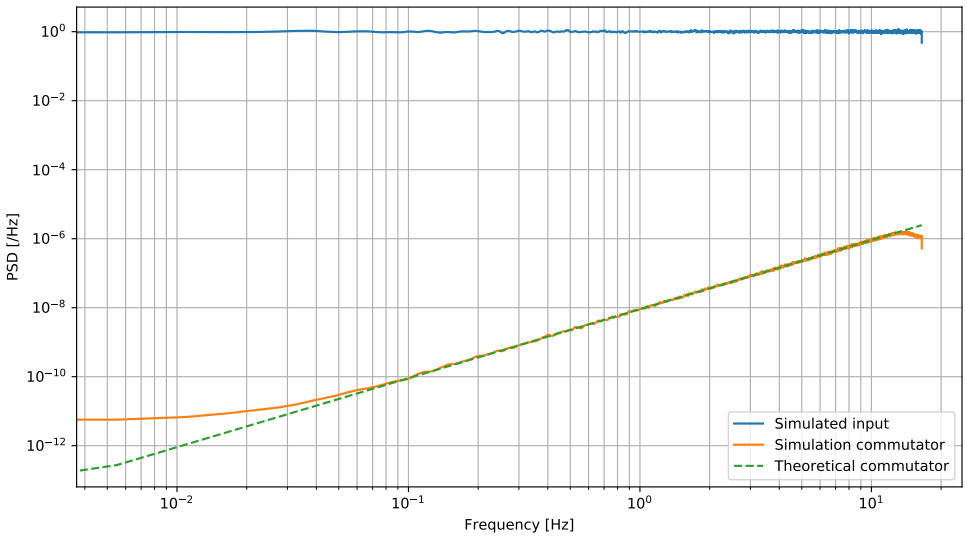


Figure 5.3: Simulated and theoretical time series for a simple filter-delay commutator $[\mathcal{D}_i, \mathcal{F}]$ applied to a white noise signal. Parameters used in the simulation are described in the related section.

denoted $S_p$. We have

$$S_{X_1}(\omega) \approx 16 S_p\, \omega^2 L^2 \Big(\dot{L}_2 - \dot{L}_3\Big)^2 , \tag{5.47}$$

$$S_{X_2}(\omega) \approx 64 S_p\, \omega^2 L^2 \Big(\dot{L}_2{}^2 - \dot{L}_3{}^2\Big)^2 . \tag{5.48}$$

As expected, the residual laser noise scales with the laser frequency noise $S_p$, and vanishes if $\dot{L}_1 = \dot{L}_2$, *i.e.* if the constellation undergoes a homothetic transformation.

We now introduce the effect of the filters. Using eqs. (5.11) and (5.43), we find that the first-order expansion of the laser noise residuals in $X_1$ is given by

$$\begin{aligned} S_{X_1}(\omega) \approx 8 S_p \omega^2 \Big[ & 2L^2 \Big(\dot{L}_2 - \dot{L}_3\Big)^2 S_f(\omega) - L\dot{L}_3 \Big(\dot{L}_2 - \dot{L}_3\Big) D_{\mathcal{F}}(\omega) \\ & + \sin^2(\omega L) \Big(\dot{L}_2^2 + \dot{L}_3^2\Big) K_{\mathcal{F}}(\omega) \Big] , \end{aligned} \tag{5.49}$$

where we have defined the squared modulus of the filter transfer function $S_f(\omega) = \left|\widetilde{f}(\omega)\right|^2$, the filter term $K_{\mathcal{F}}(\omega) = \left|\frac{\mathrm{d}\widetilde{f}}{\mathrm{d}\omega}\right|^2$, and $D_{\mathcal{F}}(\omega) = \mathrm{Im}\Big\{ \big(1 - e^{-j2L\omega}\big) \widetilde{f}(\omega) \frac{\mathrm{d}\widetilde{f}^*}{\mathrm{d}\omega} \Big\}$ can be expressed as

$$D_{\mathcal{F}}(\omega) = [1 - \cos(2L\omega)]\, \mathrm{Im}\left\{ \widetilde{f}(\omega) \frac{\mathrm{d}\widetilde{f}^*}{\mathrm{d}\omega} \right\} - \sin(2L\omega)\, \mathrm{Re}\left\{ \widetilde{f}(\omega) \frac{\mathrm{d}\widetilde{f}^*}{\mathrm{d}\omega} \right\} . \tag{5.50}$$

Comparing this expression with eq. (5.47), we see that an extra term of the same order appears. It corresponds to a coupling between the antialiasing filters and the time-varying armlengths, with a dependance on the filter characteristics expressed by the filter term $K_{\mathcal{F}}(\omega)$ and $D_{\mathcal{F}}(\omega)$, discussed below. This flexing-filtering coupling is however smaller than the previous term by a factor of $1/L$, and eq. (5.47) still gives a good estimate for the residual laser noise in $X_1$.

Similarly, we substitute eq. (5.43) in eq. (5.12) to obtain the approximated expression for the laser noise residuals in $X_2$, which reads

$$S_{X_2}(\omega) \approx 32 S_p \omega^2 \sin^2(\omega L) \sin^2(2\omega L) \Big(\dot{L}_2{}^2 + \dot{L}_3{}^2\Big) K_{\mathcal{F}}(\omega) . \tag{5.51}$$

We see that the flexing-filtering coupling is dominant for second-generation TDI. The level of residual laser frequency noise in $X_2$ is therefore strongly dependent on the filter design. We study various filters in the next paragraphs.

### 5.4.6 Filter Term $K_{\mathcal{F}}(\omega)$

In the current baseline, all antialiasing filters are identical and correspond to a causal symmetrical FIR filter. Its corner frequencies are slightly below 1 Hz, and a high attenuation

must be reached for frequencies higher than 2 Hz.

We can write the filter output $y_n$ as a function of the past input samples $x_{n-k}$ and $2N+1$ coefficients $\alpha_k$

$$y_n = \sum_{k=0}^{2N} \alpha_k x_{n-k} \,. \tag{5.52}$$

Its transfer function reads

$$\widetilde{f}(\omega) = \sum_{k=0}^{2N} \alpha_k e^{-jk\omega/f_s} \,, \tag{5.53}$$

$f_s$ is the sampling frequency. Taking its derivative with respect to the angular frequency $\omega$ immediately yields the associated filter term

$$K_{\mathcal{F}}^{\text{causal}}(\omega) = f_s^{-2} \left| \sum_{k=1}^{2N} k\alpha_k e^{-jk\omega/f_s} \right|^2 . \tag{5.54}$$

This causal filter has a nonvanishing group delay of $Nf_s^{-1}$, which is responsible for the nonvanishing zeroth-order term $K_{\mathcal{F}}^{\text{causal}}(\omega) \approx f_s^{-2} \left| \sum_{k=1}^{2N} k\alpha_k \right|^2$, for $\omega \ll 2\pi f_s$. This filter group delay plays the same role as a pure delay operator, such as those described in section 5.4.3, and which cannot commute with each other.

Noncausal FIR filters are similar to causal filters presented above, but the use of future samples $x_{n+k}$, for $k > 0$, is allowed. We can therefore center the coefficients around the current sample $x_n$, so that the group delay vanishes. We therefore obtain the following relationship between the causal and noncausal coefficients $\alpha_n$ and $\beta_n$ of the same filter,

$$\beta_n = \alpha_{N+n}, \quad -N \leq n \leq N \,. \tag{5.55}$$

The filter term associated with a noncausal filter, whose characteristics are identical to its causal version presented above, reads

$$K_{\mathcal{F}}^{\text{noncausal}}(\omega) = f_s^{-2} \left| \sum_{k=-N}^{N} k\beta_k e^{-j\omega kT} \right|^2 = f_s^{-2} \left| \sum_{k=0}^{N} k\beta_k (e^{-j\omega kT} - e^{j\omega kT}) \right|^2 , \tag{5.56}$$

which can be put in the simple form

$$K_{\mathcal{F}}^{\text{noncausal}}(\omega) = 4f_s^{-2} \left| \sum_{k=1}^{N} k\alpha_{N+k} \sin\left(\frac{k\omega}{f_s}\right) \right|^2 . \tag{5.57}$$

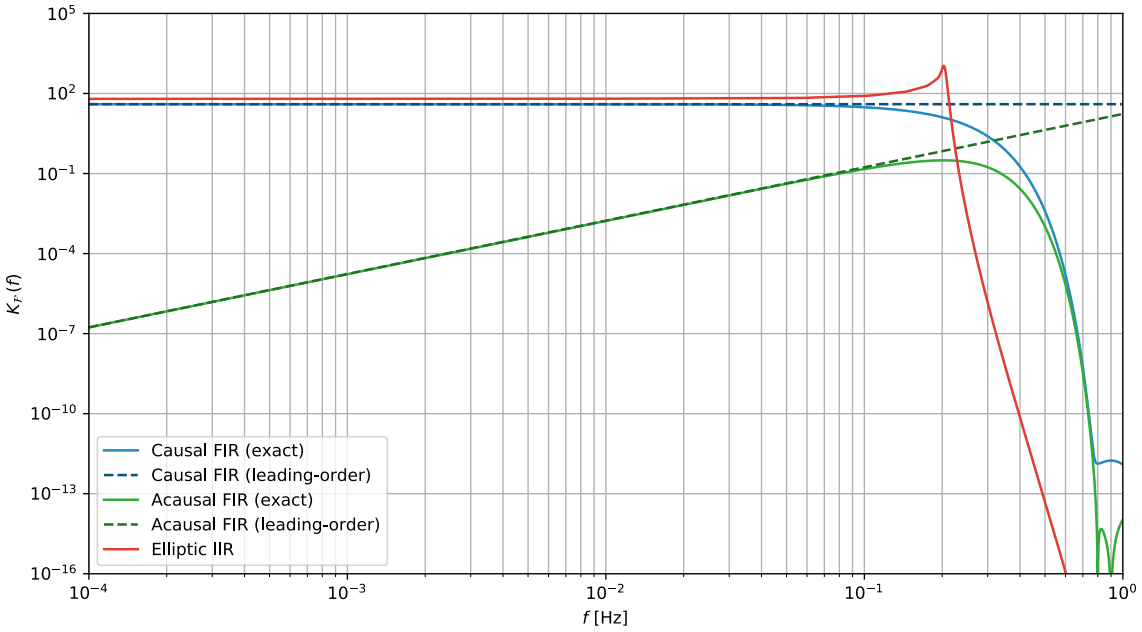


Figure 5.4: Levels for different filter terms $K_{\mathcal{F}}$. Dotted lines correspond to leading-order expansions.

We are now left with a second-order term in $\omega/2\pi f_s$, and $K_{\mathcal{F}}^{\text{noncausal}}(\omega) \approx 4\omega^2 f_s^{-4} \left|\sum_{k=1}^{N} k^2 \alpha_{N+k}\right|^2$. We therefore expect smaller laser noise residuals for noncausal filters in the LISA frequency band of interest, *i.e.* below 1 Hz.

We numerically compute and plot the $K_{\mathcal{F}}^{\text{causal}}(\omega)$ and $K_{\mathcal{F}}^{\text{noncausal}}(\omega)$ terms to compare the causal and noncausal versions of the same realistic filter, used in simulations and described in section 5.5. Results are given in fig. 5.4. We first observe that the approximated expressions at leading order in the low frequency regime are good for a rough estimate. Moreover, we clearly see that the filter term of the noncausal version has a far lower amplitude, which leads to lower residuals, and therefore better performance.

For reference, we also plotted the filter term for an Infinite Impulse Response (IIR), *i.e.* recursive) elliptic filter with the same characteristics[1]. We see that it is larger than that of

[1]The elliptic filter has 6 second-order recursive cells, corner frequencies of $f_1 = 0.1 \times f_{\text{meas}} = 0.2\,\text{Hz}$ and $f_2 = 0.45 \times f_{\text{meas}} = 0.9\,\text{Hz}$, maximum passband ripples of 0.1 dB and an attenuation of at least 240 dB in the stopband. Coefficients of the elliptic filter are as follow. First cell: $\alpha = 4.882 \times 10^{-4}, 7.239 \times 10^{-5}, 4.882 \times 10^{-4}, \beta = -1.969, 9.697 \times 10^{-1}$. Sec-

the noncausal FIR filters, which leads to larger residual noise.

## 5.5 Simulations for Keplerian orbits

LISACode is the simulator currently used by the LISA community to generate realistic data while LISANode is the baseline prototype for an end-to-end mission performance simulator. They both perform computations in time domain and produce time series for any choice of TDI variables. In the following, we only consider the Michelson variables $X$, $Y$, and $Z$.

Two sampling frequencies are used in our simulations. The *physical* sampling frequency applies to the physical subsystems in the simulators: generation of instrumental noise, beam propagation, and optical measurements. It is taken to be equal to $f_{\text{phy}} = 20\,\text{Hz}$ in both simulators. The interferometric signals $s_i$, $\epsilon_i$ and $\tau_i$ are downsampled to the *measurement* frequency $f_{\text{meas}} = 2\,\text{Hz}$ by means of a decimation algorithm. All preprocessing steps, including TDI, are therefore carried out at this measurement frequency. All signals are implemented as doubles (64-bit floating-point numbers).

In both simulators, we use a symmetric FIR antialiasing filter of order 253, designed with a Kaiser window. The coefficients[2] are calculated such that the signal is attenuated by 240 dB

ond cell: $\alpha = 9.765 \times 10^{-4}, -1.487 \times 10^{-3}, 9.765 \times 10^{-4}, \beta = -1.971, 9.719 \times 10^{-1}$. Third cell: $\alpha = 3.125 \times 10^{-2}, -5.997 \times 10^{-2}, 3.125 \times 10^{-2}, \beta = -1.992, 9.961 \times 10^{-1}$. Fourth cell: $\alpha = 7.812 \times 10^{-3}, -1.402 \times 10^{-2}, 7.812 \times 10^{-3}, \beta = -1.974, 9.761 \times 10^{-1}$. Fifth cell: $\alpha = 1.562 \times 10^{-2}, -2.980 \times 10^{-2}, 1.562 \times 10^{-2}, \beta = -1.985, 9.886 \times 10^{-1}$. Sixth cell: $\alpha = 1.866 \times 10^{2}, -3.501 \times 10^{2}, 1.866 \times 10^{2}, \beta = -1.979, 9.818 \times 10^{-1}$. .

[2]The second half of the filter's coefficients are given by: 0.022 503, 0.022 470 8, 0.022 374 4, 0.022 214 6, 0.021 992 6, 0.021 710 1, 0.021 369 2, 0.020 972 6, 0.020 523 3, 0.020 024 6, 0.019 480 1, 0.018 893 9, 0.018 270 1, 0.017 613, 0.016 927 3, 0.016 217 5, 0.015 488 4, 0.014 744 4, 0.013 990 4, 0.013 230 8, 0.012 469 9, 0.011 712 1, 0.010 961 3, 0.010 221 3, 0.009 495 56, 0.008 787 36, 0.008 099 6, 0.007 434 85, 0.006 795 39, 0.006 183 13, 0.005 599 67, 0.005 046 27, 0.004 523 85, 0.004 033 05, 0.003 574 19, 0.003 147 3, 0.002 752 16, 0.002 388 3, 0.002 055 05, 0.001 751 52, 0.001 476 65, 0.001 229 27, 0.001 008 04, 0.000 811 548, 0.000 638 312, 0.000 486 79, 0.000 355 413, 0.000 242 603, 0.000 146 789, $6.642\,34 \times 10^{-5}$, $-3.068\,36 \times 10^{-19}$, $-5.393\,77 \times 10^{-5}$, $-9.678\,36 \times 10^{-5}$, −0.000 129 861, −0.000 154 416, −0.000 171 611, −0.000 182 522, −0.000 188 139, −0.000 189 361, −0.000 187, −0.000 181 782, −0.000 174 349, −0.000 165 266, −0.000 155 02, −0.000 144 028, −0.000 132 644, −0.000 121 158, −0.000 109 81, $-9.878\,85 \times 10^{-5}$, $-8.823\,97 \times 10^{-5}$, $-7.827\,13 \times 10^{-5}$, $-6.895\,86 \times 10^{-5}$, $-6.034\,83 \times 10^{-5}$, $-5.246\,36 \times 10^{-5}$, $-4.530\,84 \times 10^{-5}$, $-3.887\,03 \times 10^{-5}$, $-3.312\,51 \times 10^{-5}$, $-2.803\,88 \times 10^{-5}$, $-2.357\,08 \times 10^{-5}$, $-1.967\,58 \times 10^{-5}$, $-1.630\,62 \times 10^{-5}$, $-1.341\,32 \times 10^{-5}$, $-1.094\,83 \times 10^{-5}$, $-8.864\,23 \times 10^{-6}$, $-7.116\,08 \times 10^{-6}$, $-5.661\,47 \times 10^{-6}$, $-4.461\,13 \times 10^{-6}$, $-3.479\,14 \times 10^{-6}$, $-2.682\,98 \times 10^{-6}$, $-2.043\,59 \times 10^{-6}$, $-1.535\,25 \times 10^{-6}$, $-1.135\,43 \times 10^{-6}$, $-8.246\,23 \times 10^{-7}$, $-5.860\,81 \times 10^{-7}$, $-4.055\,89 \times 10^{-7}$, $-2.711\,98 \times 10^{-7}$, $-1.729\,76 \times 10^{-7}$, $-1.027\,53 \times 10^{-7}$, $-5.388\,86 \times 10^{-8}$, $-2.104\,73 \times 10^{-8}$, $1.670\,89 \times 10^{-22}$, $1.256\,02 \times 10^{-8}$, $1.917\,93 \times 10^{-8}$, $2.178\,35 \times 10^{-8}$, $2.180\,24 \times 10^{-8}$, $2.027\,19 \times 10^{-8}$,

between 0.2 Hz and 0.9 Hz, and we authorize a maximum ripple of 0.1 dB below 0.2 Hz. We implement filters using a direct form I and therefore, account group delays when they are not vanishing.

The propagation of the laser beams between the spacecraft is implemented using time-varying delays. Those delays are computed from the relative positions of the spacecraft, themselves deduced from their Keplerian orbits presented in [NKDV06]. These orbits include the Sagnac effect, as well as first order relativistic corrections.

All delay operators are implemented using Lagrange interpolating polynomials of order 31. This choice is the result of a trade-off: it allows for good precision and limits execution time and numerical errors. As seen above, the TDI algorithm requires the application of multiple delay operators to the interference measurements for the calculation of the Michelson variables $X$, $Y$, and $Z$. In order to minimize the error introduced by the associated interpolations, we use a nested delay algorithm in which a single interpolation is necessary.

### 5.5.1 LISACode

LISACode is based on the original optical design, equivalent, under our assumptions, to the *split interferometry* design described in section 5.2. Each of the three spacecraft of the LISA constellation contains two independent lasers and two optical benches. Each optical bench holds a science and a reference interferometer; the corresponding beatnotes are filtered and decimated to produce the respective measurement signals $s_i(t)$ and $\tau_i(t)$, as presented in fig. 5.5.

The LISACode results use a $10^7$ s time series generated with version 2.12.

### 5.5.2 LISANode

LISANode implements the newest *split interferometry* optical setup described in section 5.2, and presented in fig. 5.6. Three interferometric measurements $s_i$, $\tau_i$ and $\epsilon_i$ (respectively, the science, test mass, and reference signals) are formed and relevant sources of noise are added to the measurements. These signals are then transmitted to the on-board computer, which contains the antialiasing filter and decimation nodes. The results of these operations

$1.792\,19 \times 10^{-8}$, $1.524\,89 \times 10^{-8}$, $1.257\,38 \times 10^{-8}$, $1.008\,99 \times 10^{-8}$, $7.899\,63 \times 10^{-9}$, $6.043\,16 \times 10^{-9}$, $4.520\,36 \times 10^{-9}$, $3.306\,67 \times 10^{-9}$, $2.364\,59 \times 10^{-9}$, $1.651\,59 \times 10^{-9}$, $1.125\,23 \times 10^{-9}$, $7.463\,54 \times 10^{-10}$, $4.807\,13 \times 10^{-10}$, $2.996\,03 \times 10^{-10}$, $1.798\,33 \times 10^{-10}$, $1.032\,79 \times 10^{-10}$, $5.622\,01 \times 10^{-11}$, $2.859\,93 \times 10^{-11}$, $1.328\,41 \times 10^{-11}$, $5.3973 \times 10^{-12}$, $1.737\,05 \times 10^{-12}$ .

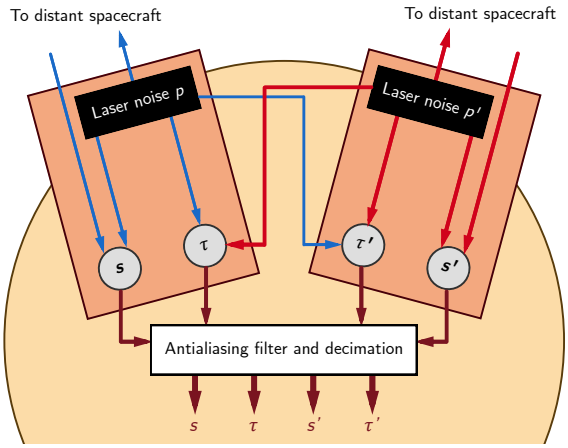


Figure 5.5: Original optical design used in LISACode simulations. Four interferometric measurements per spacecraft are performed: the science signals $s_i$ and $s'_i$, along with the reference signals $\tau_i$ and $\tau'_i$.

are used to form the TDI Michelson variables $X$, $Y$ and $Z$.

The results use a $10^7$ s time series generated with LISANode version 1.1.

## 5.6 Results and discussion

### 5.6.1 Results

In figs. 5.7 and 5.8, we present the PSDs of the residual laser frequency noise for the TDI Michelson variables $X_1$ and $X_2$. We show the results of LISANode simulations for both the causal and the noncausal versions of the same filter, as described in section 5.5 (light and dark blue curves). We plot the results of LISACode simulations for the causal filter only, in order to validate the new simulator (light orange curve). The models derived in section 5.4 are superimposed (dashed light and dark green curves).

For reference, the red solid curves show the residual secondary noises in both $X_1$ and $X_2$ channels, simulated using LISANode and the noncausal antialiasing filter. To generate those signals, we did not change the simulation parameters. However, laser frequency noise is set to zero while the test mass acceleration (TM), optical read-out (RO) and optical path (OP) noise amplitudes were given their nominal LISA instrument noise budget values. The

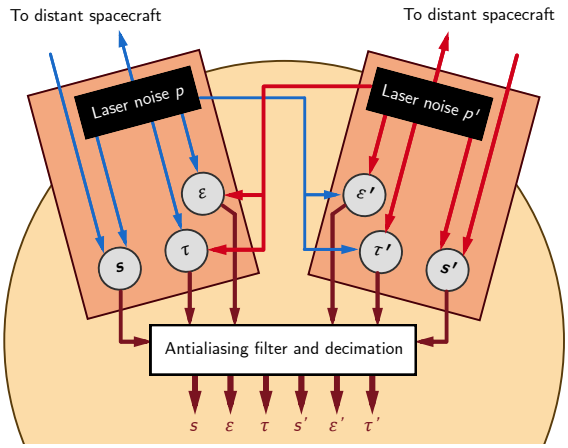


Figure 5.6: New *split interferometry* optical design used in LISANode simulations. Six interferometric measurements per spacecraft are performed: the science signals $s_i$ and $s'_i$, the test mass signals $\epsilon_i$ and $\epsilon'_i$, along with the reference signals $\tau_i$ and $\tau'_i$.

spectral shapes of these three secondary sources of noise are given in [LL18], and read

$$S_{\mathrm{TM}} = \left(2.4 \times 10^{-15}\right)^2 \tag{5.58}$$

$$\times \left[1 + \left(\frac{4 \times 10^{-4}}{f}\right)^2\right] \mathrm{m^2 s^{-4} Hz^{-1}}\,, \tag{5.59}$$

$$S_{\mathrm{RO}} + S_{\mathrm{OP}} = 1 \times 10^{-24}\,\mathrm{m^2 Hz^{-1}}\,. \tag{5.60}$$

Because TDI does not suppress those secondary noises, but only modulates their spectra, they are used as a benchmark.

We use Welch's method to estimate the spectra, implemented with standard Python tools included in the `scipy.signal` module, version 1.1.0. We use segments of 40 000 samples and a Nutall4 window function. The results are presented for the frequency band from $10^{-4}$ Hz to 1 Hz.

We can see that the results of both simulators are in very good agreement. The fact that both simulators give similar results, although they use different implementations, increases our confidence in the results they produce. Note that at frequencies greater than $4 \times 10^{-1}$ Hz, one observes a slight discrepancy between LISANode and LISACode. This discrepancy is due to different implementations of the Lagrange interpolating polynomials in the two simulators.

We can also observe that our analytic models match the simulated data with exquisite

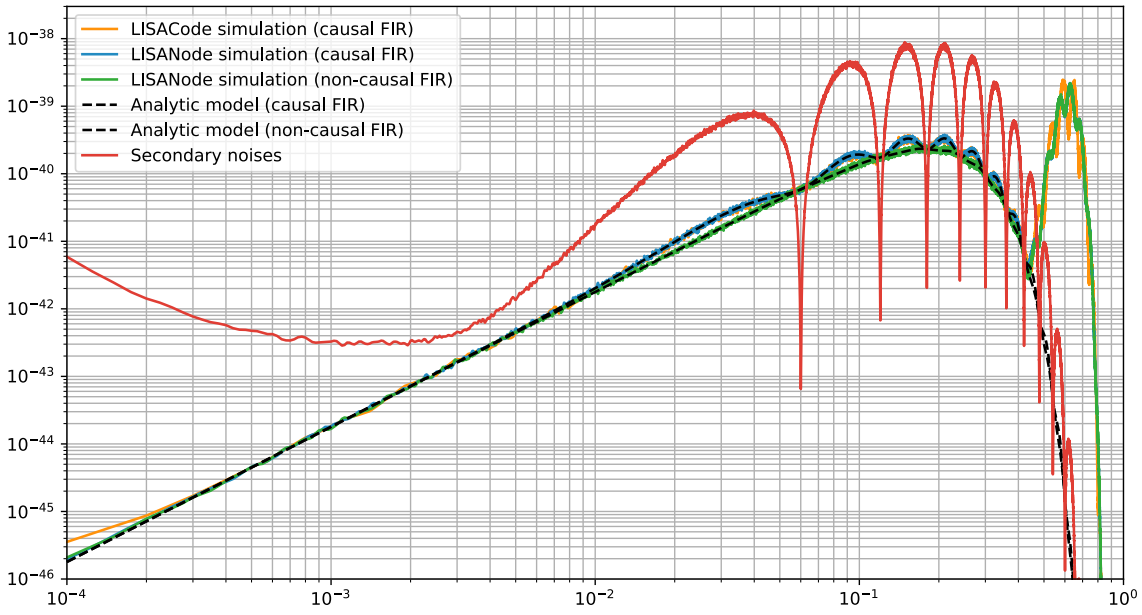


Figure 5.7: Power spectral density of the residual laser frequency noise in the Michelson $X_1$ channel. The LISACode and LISANode simulations use realistic Keplerian orbits, while the theoretical model uses armlengths varying linearly with time. Secondary noises are shown in red and indicate the target level of laser frequency noise suppression.

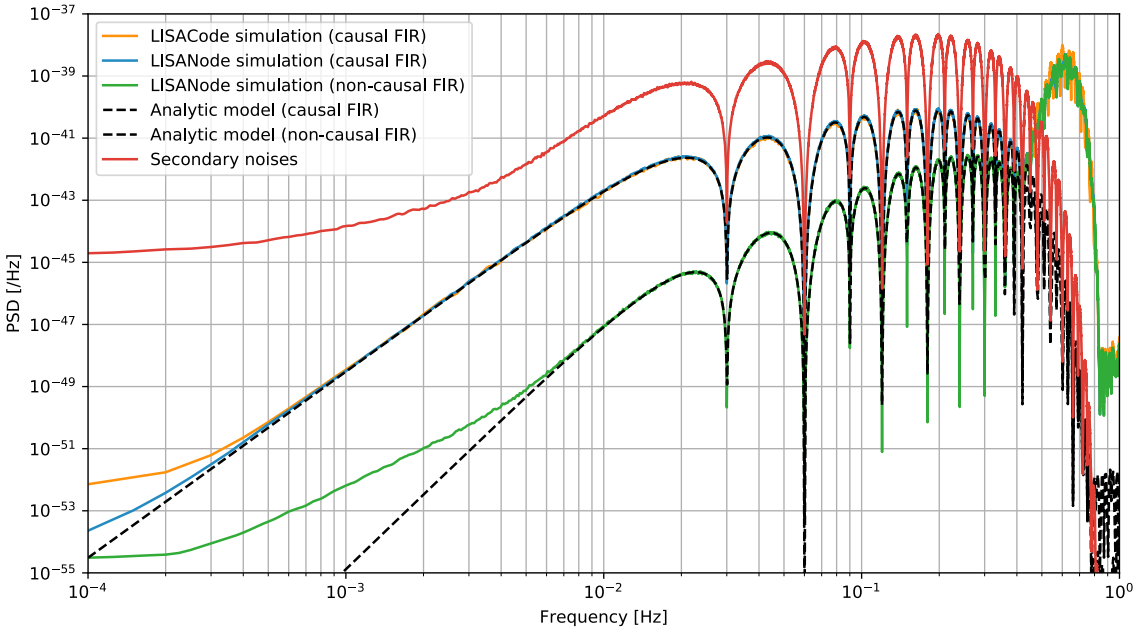


Figure 5.8: Power spectral density of the residual laser frequency noise in the Michelson $X_2$ channel. The LISACode and LISANode simulations use realistic Keplerian orbits, while the theoretical model uses armlengths varying linearly with time. Secondary noises are shown in red and indicate the target level of laser frequency noise suppression.

precision in most of the LISA band. At high frequencies, the model is no longer valid, since it does not include the errors from Lagrange interpolations. These errors, visible in the simulated data, manifest themselves by an increased level of residual laser frequency noise around $6 \times 10^{-1}$ Hz. It can be shown that varying the interpolation order changes the amplitude of this effect. At lower frequencies, the simulated data deviate away from the analytic model. This is because assuming that the armlengths are varying linearly in time is only valid for frequencies higher than 1 mHz. However, we see that at these lower frequencies the residual laser noise is in any case well below mission noise level requirements.

It is also very clear that using a noncausal filter decreases significantly the residual laser noise. This effect is particularly obvious at low frequencies, as the leading-order expansion of the filter term is constant for the causal filter, while being proportional to $\omega^2$ for its noncausal version; see section 5.4.

The fig. 5.7 shows that first-generation Michelson variables reduce the laser frequency noise down to the required level, but only marginally. This is especially true with causal filters. On the contrary, fig. 5.8 shows that second-generation Michelson variables can reduce the laser frequency noise up to 3 orders of magnitude below the secondary noises over the entire frequency range, if we use noncausal filters.

In the case of time varying orbits, and in the presence of antialiasing filters, TDI 2.0 is therefore necessary and sufficient to suppress laser frequency noise levels down to mission requirements [DASpAh$^+$17]. Moreover, using noncausal filters allows for comfortable margins.

### 5.6.2 Filter group delay

TDI uses as inputs the interferometric signals from the six optical benches [$s_i(t)$, $\tau_i(t)$ and $\epsilon_i(t)$], and the ranging estimates $L_i(t)$ for all six links. A causal filter has a nonvanishing group delay $N/f_s$; since it is only applied on the interferometric signals, the latter will be time-shifted while ranging estimates are left untouched. Let us denote the filter group delay operator $\mathcal{D}_\mathcal{F}$. As part of the TDI algorithm, one computes terms of the type $\mathcal{D}_i\mathcal{D}_\mathcal{F}p(t) = p(t - N/f_s - L_i(t))$ when one really wants $\mathcal{D}_\mathcal{F}\mathcal{D}_i p(t) = p(t - N/f_s - L_i(t - N/f_s))$, or, equivalently, $p(t - L_i(t))$.

We recognize here an extra noise proportional to the commutator $[\mathcal{D}_\mathcal{F}, \mathcal{D}_i]p(t) \approx \dot{L}_i(N/f_s)\frac{\mathrm{d}p}{\mathrm{d}t}$; see eq. (5.33). It is non vanishing in the case of time-varying armlengths, which explains this flexing-filtering coupling.

### 5.6.3 Implementation of a Noncausal Filter

We can relate the transfer function $\widetilde{f}^{\text{noncausal}}(\omega)$ of a noncausal filter to that of its causal version $\widetilde{f}^{\text{causal}}(\omega)$,

$$\widetilde{f}^{\text{noncausal}}(\omega) = e^{j\omega N}\,\widetilde{f}^{\text{causal}}(\omega)\,. \tag{5.61}$$

The coefficients of these two versions of the same filter only differ by an integer delay of $N$ samples. We can therefore deduce the output samples of the noncausal filter using future output samples of the causal version,

$$y_n^{\text{noncausal}} = y_{n+N}^{\text{causal}}\,. \tag{5.62}$$

We explore in the following paragraphs solutions to implement, or synthesize offline, such a noncausal version of the antialiasing filter.

#### Online Re-Timestamping

The first solution is to mimic a noncausal antialiasing filter on board. This is achieved by using an actual causal filter, and then re-timestamp the data samples to make up for the corresponding filter group delay, in our case $Nf_s^{-1}$. The re-timestamped data samples are then decimated and transmitted down to Earth.

Although this solution is simple and elegant, it modifies the on-board processing, and applies a transformation to the data before we receive it on Earth, therefore forbidding the access to raw data.

#### Offline Re-Timestamping

We propose in this solution to leave the on-board processing untouched, and only relabel the decimated data once it has been transmitted to Earth.

One caveat is that we might need to use interpolation, and therefore introduce errors in the data, to apply the relevant delay $Nf_s^{-1}$. Indeed, the filter group delay ought not be a multiple of the sampling period after data has been downsampled and telemetered to Earth. Simulations show that good interpolators, such as Lagrange interpolating polynomials of order 15, are good enough for our purpose. Carefully choosing the filter order, or, equivalently, its group delay, so that the downsampled sampling period divides the filter

group delay, may spare us the need to interpolate the data. This is a very light constraint, which must nevertheless be taken into account when designing the on-board filters.

In the simulations presented in sections 5.5 and 5.6, we used the latter solution.

## 5.7 Conclusion

This chapter adapted from [BLPH19] addresses the problem of modeling and simulating the residual laser frequency noise, after TDI has been applied, in a realistic instrumental setup. We have focused our analysis on the first and second-generation Michelson $X$, $Y$ and $Z$ variables, and have included the effect of time-varying armlengths, as well as the effects of the on-board antialiasing filters. In our LISACode and LISANode simulations, the armlengths vary according to Keplerian orbits. In the analytic expressions of the residual laser frequency noise spectrum we derive, armlengths vary linearly with time. This is a very good approximation of Keplerian orbits on the time scales of interest. The resulting expressions are functions of both the varying armlengths and of the filter coefficients, and show at leading-order that a new flexing-filtering coupling noise enters the measurements, degrading the expected TDI performance.

We showed that the simulated data match the analytic model with exquisite precision over a large fraction of the LISA frequency band. As a benchmark for the performance of TDI, we used LISANode simulations that include secondary noise only. In the case of time-varying armlengths, TDI 1.5 is shown not be able to achieve sufficient laser frequency noise reduction over the entire frequency range of interest. On the other hand, TDI 2.0 reduces laser frequency noise to well below the secondary noise level, for the case of a standard finite-impulse response filter. TDI 2.0 is therefore the minimal viable TDI generation for LISA.

As demonstrated In this chapter, our analytic model and simulations help gain insight into TDI and the various parameters that play a key role in its performance. In particular, we were able to demonstrate that a noncausal filter improves TDI performance and helps reduce further the residual laser noise down to 3 extra orders of magnitude in the middle of LISA frequency band. This noncausal filter can be synthesized using its causal version on board and adapt the TDI algorithm by time-shifting the interferometric signals with respect to the ranging estimates. This concept was demonstrated by our simulations.

One could also use the analytic model developed in this study to optimize the filter coefficients, so that the useful frequency band for data analysis (*i.e.* the frequency band over

which the gravitational signal is not attenuated) is maximized, while the residual laser frequency noise level remains below the secondary noise level. Finally, the effect of other instrumental imperfections and artifacts, such as the errors in the absolute ranging or in the interpolation scheme, or even clock noises, remain to be included in both our model and simulations.

# Chapter 6

# Clock-Noise Calibration

This chapter is a draft version of an article that will be submitted to *Physical Review D*. It is the result of a work conducted in collaboration with O. Hartwig.

## 6.1 Introduction

The dominant source of noise in LISA is laser frequency noise, which couples into the measurements many orders of magnitude above the expected gravitational wave signals. TDI is an offline technique used to suppress this laser noise and described in chapter 4. It uses time-shifted combinations of the interferometric signals to synthesize virtual laser-noise-free Michelson-like interferometers. The so-called first generation algorithm assumes that the armlengths are constant in time. A second generation has been proposed, to account for flexing of the constellation, *i.e.* time-varying armlengths. Analytic and numerical studies, as well as laboratory experiments have shown that the second-generation TDI is sufficient to reduce laser noise far below the level of secondary readout noises.

In addition to laser frequency noise, other secondary noise sources are also above the requirements and need to be suppressed as part of the TDI algorithm. In particular, this is envisioned for timing fluctuations of the USOs on-board each spacecraft. An USO provides a unique time reference used to drive all systems of the measurement chain. This clock drives in particular the ADC, the phasemeter, and the on-board computer. It is also used to timestamp the measurement signals at 3 Hz, which are then telemetered down to Earth. To prevent aliasing below 1 Hz [LL18], we filter the signals before they are downsampled.

State-of-the-art oscillators qualified for space typically have an Allan standard deviation of about $10^{-13}$ for averaging times above 1 s [WGR10]. No online synchronization between the three clocks is foreseen, which drift independently over large periods of time. The timestamps of measurements from different spacecraft are therefore inconsistent with each other. The drifting of the clocks also affect the pseudo-ranging measurements used to estimate the absolute distance between the spacecraft, themselves used to produce the TDI variables. In this study, we assume that an on-ground algorithm can synchronize the measurements onto a common time grid and remove the clock offsets from the ranging measurement, such that we can ignore this effect on TDI [Wan17].

In addition to timing and ranging errors due to drifts over large timescales, clock jitter in the measurement band also needs to be considered. The noise introduced into the measurements by three independent oscillators is much higher than the tolerable level to achieve the science objectives. In order to suppress it, we imprint the USO noise onto the laser beam in form of modulation sidebands. This allows an independent measurement of the differential clock noise, which can be used to calibrate it out of the TDI Michelson variables. Technical details on the sideband generation can be found in [Bar15].

A first version of such a calibration algorithm for first-generation TDI was presented in [TA99], which perfectly cancels clock noise assuming constant armlengths. In [TH18], it was shown that this algorithm can be extended for second-generation TDI, where it reduces the USO noise to far below other secondary noises. However, the cancellation is no longer exact for time-varying armlengths. In this article, we propose a new calibration algorithm for both generations, allowing for perfect cancellation of clock noise in the case of time-varying armlengths. We estimate the residual noise from the flexing-filtering effect first described in [BLPH19], as well as the level of other secondary noises and show that numerical simulations match our analytic expressions to a very good precision.

In section 6.2, we introduce the notations and conventions used in this chapter. Then, in section 6.3, we give the equations for the interferometric measurements, and study how clock noise appear in the TDI variables. This allows us to propose a calibration algorithm in section 6.4, and compute the levels of the secondary noises in the clock-calibrated variables. We then present our simulation setup in section 6.6, before discussing the main results in section 6.7.

## 6.2 Notations and Conventions

Various conventions are used in the literature to label the spacecraft, optical benches and light travel times along the links. In this paper, we number these components according to fig. 3.4. We consider the so-called *split-interferometry* optical layout, described in [BLPH19]. Therefore six interferometric measurements are formed on each spacecraft. They are indexed according to associated optical bench. We give here equations for the first spacecraft. The remaining expressions can be deduced by the circular permutation of indices $1 \to 2 \to 3 \to 1$.

In the following, all signals are expressed in terms of frequency deviations from the carrier frequency of the associated beam. Differences in the carrier frequencies are only considered for the calculation of the heterodyne beatnote frequencies, which we assume to be constant. They are given by

$$a_1 = \nu_{2'} - \nu_1 \quad \text{and} \quad a_{1'} = \nu_3 - \nu_{1'}\,, \tag{6.1}$$

$$b_1 = \nu_{1'} - \nu_1 \quad \text{and} \quad b_{1'} = \nu_1 - \nu_{1'} = -b_1\,, \tag{6.2}$$

$$c_1 = (\nu_{2'} + \nu_{2'}^m) - (\nu_1 + \nu_1^m) = a_1 + (\nu_{2'}^m - \nu_1^m)\,, \tag{6.3}$$

$$c_{1'} = (\nu_3 + \nu_3^m) - (\nu_{1'} + \nu_{1'}^m) = a_{1'} + (\nu_3^m - \nu_{1'}^m)\,, \tag{6.4}$$

with $\nu_i \approx 282\,\mathrm{THz}$ as the laser frequencies, and $\nu_i^m \approx 2.5\,\mathrm{GHz}$ as the modulation frequencies used for the clock sideband generation. We only consider the upper sidebands for this study, and neglect the effects of Doppler shifts.

These frequencies are used as coupling coefficients of the USO fluctuations and to determine the sign of the phasemeter measurements. The science and reference beatnote frequencies are denoted by $a_i$ and $b_i$, and their signs are defined as $\theta_i^s$ and $\theta_i^\tau$, respectively. Note that the reference and test-mass interferometers use the same beams, hence they use the same coupling coefficients.

We define $L_i(t)$ as the light travel time along link $i$, in seconds. The propagation of laser beams along this link is modeled using the time-varying delay operator $\mathcal{D}_i$, such that $\mathcal{D}_i x(t) = x(t - L_i(t))$ for any time-dependent function $x(t)$. Multiple delays use the short-hand notation

$$\mathcal{D}_{i_1}\mathcal{D}_{i_2}\ldots\mathcal{D}_{i_n} \equiv \mathcal{D}_{i_1 i_2 \ldots i_n}\,. \tag{6.5}$$

Since the delays $L_i(t)$ are themselves not constant, delay operators do not commute.

Anti-aliasing filters are used on board to downsample the data. They consist of a convolution of the signal with the filter kernel $f(t)$. We can define the filter operator $\mathcal{F}$, such that $\mathcal{F}x(t) \equiv (f * x)(t)$.

We define

$$[\mathcal{F}, \mathcal{D}_i]x(t) = \mathcal{F}\mathcal{D}_i x(t) - \mathcal{D}_i \mathcal{F} x(t)\,. \tag{6.6}$$

as the commutator of the filter operator with a delay. In [BLPH19], it is shown that these terms are non-vanishing and contribute to the residual noise.

If $x(t)$ is a function of time, we denote its Fourier transform $\widetilde{x}(\omega)$ and its PSD $S_x(\omega)$, both functions of the angular frequency $\omega = 2\pi f$. For indexed quantities like e.g. clock noise, we assume that their PSDs are equal, and denote them by $S_q(\omega)$.

## 6.3 Measurement Equations and TDI

For this study, we only include noises which are relevant to the performance of the clock calibration algorithm. These are readout noises $N_i^s$, $N_i^{\mathrm{sb}}$, $N_i^{\epsilon}$, $N_i^{\tau}$, and $N_i^{\mathrm{sb},\tau}$, sideband modulation errors $M_i$, and clock noise $q_i$. Clock noise is defined in terms of fractional frequency deviations, such that it couples into the measurements scaled by the absolute value of the beatnote frequency.

We assume that a pilot tone is used as phase reference on board each spacecraft [Bar15]. In particular, this pilot tone is used to remove any additional clock jitters due to the ADC. As such, $q_i$ are the fractional frequency deviations of that pilot tone and the $M_i$ are additional deviations present in the sidebands relative to that same pilot tone, *e.g.* due to noise added by the fibre amplifiers. Any residual clock jitter due to imperfections in the pilot tone correction is absorbed into the readout noise terms.

All noise signals depend on time, but this time dependency is not stated explicitly in this article, for readability's sake.

### 6.3.1 Interferometric Measurements

The science interferometric measurements $s_1$ and $s_{1'}$ are defined as the beatnotes between the distant and local beams, on spacecraft $i$. They are given by

$$s_1 = \mathcal{F}[-a_1\theta_1^s q_1 + N_1^s]\,, \tag{6.7}$$

$$s_{1'} = \mathcal{F}[-a_{1'}\theta_{1'}^s q_1 + N_{1'}^s]\,. \tag{6.8}$$

The test-mass measurements $\epsilon_i$ and $\epsilon_{i'}$ are the beatnotes between the adjacent beam after

it has bounced onto the local test mass, and the local beam, on spacecraft $i$. They read

$$\epsilon_1 = \mathcal{F}[-b_1\theta_1^\tau q_1 + N_1^\epsilon]\,, \tag{6.9}$$
$$\epsilon_{1'} = \mathcal{F}[-b_{1'}\theta_{1'}^\tau q_1 + N_{1'}^\epsilon]\,. \tag{6.10}$$

Similarly, the reference measurements $\tau_i$ and $\tau_{i'}$ are formed by the beatnote between the adjacent and local beams, without any bouncing on the test mass. They read

$$\tau_1 = \mathcal{F}[-b_1\theta_1^\tau q_1 + N_1^\tau]\,, \tag{6.11}$$
$$\tau_{1'} = \mathcal{F}[-b_{1'}\theta_{1'}^\tau q_1 + N_{1'}^\tau]\,. \tag{6.12}$$

The sideband measurements are defined as the beatnote between the distant and local upper sidebands. Their expressions read

$$s_1^{\rm sb} = \mathcal{F}\big[\theta_1^s(\nu_{2'}^m\mathcal{D}_3(q_2 + M_{2'}) - \nu_1^m(q_1 + M_1) - c_1 q_1) + N_1^{\rm sb}\big]\,, \tag{6.13}$$
$$s_{1'}^{\rm sb} = \mathcal{F}\big[\theta_{1'}^s(\nu_3^m\mathcal{D}_{2'}(q_3 + M_3) - \nu_{1'}^m(q_1 + M_{1'}) - c_{1'} q_1) + N_{1'}^{\rm sb}\big]\,. \tag{6.14}$$

There is also a sideband beatnote present in each reference interferometer, between the sidebands of the adjacent optical benches,

$$\tau_1^{\rm sb} = \mathcal{F}\Big[\theta_1^\tau(\nu_{1'}^m(M_{1'} + q_1) - \nu_1^m(M_1 + q_1) - (b_1 + \nu_1^m - \nu_{1'}^m)q_1) + N_1^{{\rm sb},\tau}\Big]\,, \tag{6.15}$$
$$\tau_{1'}^{\rm sb} = \mathcal{F}\Big[\theta_{1'}^\tau(\nu_1^m(M_1 + q_1) - \nu_{1'}^m(M_{1'} + q_1) - (b_{1'} + \nu_{1'}^m - \nu_1^m)q_1) + N_{1'}^{{\rm sb},\tau}\Big]\,. \tag{6.16}$$

### 6.3.2 TDI Variables

TDI intermediary variables $\xi$ and $\eta$ are constructed to remove primed laser noise, and optical bench displacement noise (here set to zero), respectively. They read [Ott15]

$$\xi_1 = s_1 + \theta_1^s\theta_1^\tau\frac{\epsilon_1 - \tau_1}{2} + \theta_1^s\theta_{2'}^\tau\frac{\mathcal{D}_3(\epsilon_{2'} - \tau_{2'})}{2}\,, \tag{6.17}$$
$$\xi_{1'} = s_{1'} + \theta_{1'}^s\theta_{1'}^\tau\frac{\epsilon_{1'} - \tau_{1'}}{2} + \theta_{1'}^s\theta_3^\tau\frac{\mathcal{D}_{2'}(\epsilon_3 - \tau_3)}{2}\,. \tag{6.18}$$

and

$$\eta_1 = \theta_1^s\xi_1 + \frac{\mathcal{D}_3(\theta_{2'}^\tau\tau_{2'} - \theta_2^\tau\tau_2)}{2}\,, \tag{6.19}$$
$$\eta_{1'} = \theta_{1'}^s\xi_{1'} - \frac{\theta_{1'}^\tau\tau_{1'} - \theta_1^\tau\tau_1}{2}\,. \tag{6.20}$$

Inserting eqs. (6.7) and (6.12) into these expressions yields

$$\eta_1 = -b_{2'}\mathcal{D}_3\mathcal{F}q_2 - a_1\mathcal{F}q_1 + \theta_1^s\mathcal{F}N_1^s + \theta_{1'}^\tau\frac{\mathcal{F}(N_1^\tau - N_1^\epsilon)}{2} + \theta_{2'}^\tau\frac{\mathcal{D}_3\mathcal{F}(N_2^\tau + N_{2'}^\epsilon)}{2}\,, \tag{6.21}$$

$$\eta_{1'} = (b_{1'} - a_{1'})\mathcal{F}q_1 + \theta_{1'}^s\mathcal{F}N_{1'}^s - \theta_{1'}^\tau\mathcal{F}N_{1'}^\tau - \theta_{1'}^\tau\frac{\mathcal{F}(N_1^\tau - N_{1'}^\epsilon)}{2} + \theta_{3'}^\tau\frac{\mathcal{D}_{2'}\mathcal{F}(N_3^\tau - N_3^\epsilon)}{2}\,. \tag{6.22}$$

From these intermediary variables, we can built laser noise-free TDI variables. They can be expressed as polynomials of delay operators $P_i$ and $P_{i'}$, in form

$$\mathrm{TDI} = \sum_{i=1,2,3}\left(P_i\eta_i + P_{i'}\eta_{i'}\right). \tag{6.23}$$

In section 4.2, we give the expressions for the most common TDI variables. In the following, we will focus on first and second-generation Michelson variables $X_1$ and $X_2$ (and their circular permutations $Y$ and $Z$), and first and second-generation Sagnac variables $\alpha_1$ and $\alpha_2$ (and their circular permutations $\beta$ and $\gamma$).

### 6.3.3 Clock Noise Residuals

Inserting eqs. (6.21) and (6.22) and keeping only clock noise, we observe that the clock residual in the variable reads

$$\mathrm{TDI}^q = -\sum_{i=1}^{3}\left(a_iP_i + a_{i'}P_{i'} + b_{i'}[P_{i'} - P_{i-1}\mathcal{D}_{i+1}]\right)q_i\,. \tag{6.24}$$

In this section, we assume that all armlengths are equal and constant[1]. Also, we suppose that all clock noises are uncorrelated but have the same PSD $S_q(\omega)$. Under these assumptions, the clock noise residuals PSD is given by

$$S_{\mathrm{TDI}^q}(\omega) \approx S_q(\omega)\sum_{i=1}^{3}\left|a_i\widetilde{P}_i(\omega) + a_{i'}\widetilde{P}_{i'}(\omega) + b_{i'}[\widetilde{P}_{i'}(\omega) - \widetilde{P}_{i-1}(\omega)\widetilde{\mathcal{D}}_{i+1}(\omega)]\right|^2. \tag{6.25}$$

Here, $\widetilde{\mathcal{D}}_i$ is the Fourier transform of a delay operator, see [BLPH19] for further information.

In the following paragraphs, we apply this formula to give an estimate of the clock noise residuals in the case of the Michelson and Sagnac variables.

[1]Therefore, we can commute delay operators with each other, as well as delay and filter operators. As shown in [BLPH19], these commutators only yield multiplicative terms $\ll 1$.

### Michelson Combinations

Using eq. (6.25), we can work out the clock noise residuals in the Michelson variables. Before calibration, their PSD read

$$\begin{aligned} S_{X_1^q}(\omega) \approx 4\sin^2(\omega L)\big[&(a_1 - a_{1'})^2 + a_{2'}^2 + a_3^2 \\ &+ 4b_{1'}(a_1 - a_{1'} + b_{1'})\sin^2(\omega L)\big] S_f(\omega) S_q(\omega)\,. \end{aligned} \tag{6.26}$$

Here, $S_f(\omega)$ is the transfer function of the anti-aliasing filter.

Because we assume that armlengths are constant, the delays commute and the second-generation Michelson combination $X_2$ has a very simple relationship to the first-generation combination $X_1$,

$$X_2 \approx (\mathcal{D}_{2'233'} - I)X_1\,. \tag{6.27}$$

In particular, for clock noise residuals,

$$S_{X_2^q}(\omega) \approx 4\sin^2(2\omega L) S_{X_1^q}(\omega)\,. \tag{6.28}$$

Observe that this is only valid if the noise in question is not suppressed by TDI, such that additional terms due to delay commutators can be neglected. This approximation does not hold for laser noise, for example, as shown in [BLPH19].

### Sagnac Combinations

Following the same technique and using the same assumptions, we can work out the residual clock noise in the both generations of the Sagnac variables,

$$\begin{aligned} S_{\alpha_1^q}(\omega) = \big[&(a_1 + b_{1'})^2 + (a_2 + b_{2'})^2 + (a_3 + b_{3'})^2 \\ &+ (a_{1'} - b_{1'})^2 + (a_{2'} - b_{2'})^2 + (a_{3'} - b_{3'})^2 - 2a_1 a_{1'} \\ &- 2((a_{2'} - b_{2'})(a_2 + b_{2'}) + (a_{3'} - b_{3'})(a_3 + b_{3'}))\cos(\omega L) \\ &+ 2b_{1'}(a_1 - a_{1'} + b_{1'})\cos(3\omega L)\big] S_f(\omega) S_q(\omega)\,, \end{aligned} \tag{6.29}$$

Again, there exists a simple relationship between the first and second-generation clock noise residuals for the Sagnac variables,

$$S_{\alpha_2^q}(\omega) = 4\sin^2\left(\frac{3\omega L}{2}\right) S_{\alpha_1^q}(\omega) \tag{6.30}$$

## 6.4 Clock Noise Calibration

### 6.4.1 Sideband Measurements

The sideband measurements are used to construct an independent measurement of the differential clock noise between two spacecraft,

$$r_1 = \theta_1^s \frac{s_1 - s_1^{\mathrm{sb}}}{\nu_{2'}^m}\,, \tag{6.31}$$

$$r_{1'} = \theta_{1'}^s \frac{s_{1'} - s_{1'}^{\mathrm{sb}}}{\nu_3^m}\,. \tag{6.32}$$

By inserting eqs. (6.7), (6.8), (6.13) and (6.14) into these expressions, we get

$$r_1 = \mathcal{F}\left(q_1 + \frac{\nu_1^m}{\nu_{2'}^m} M_1\right) - \mathcal{F}\mathcal{D}_3(q_2 + M_{2'}) + \frac{\theta_1^s}{\nu_{2'}^m}\mathcal{F}(N_1^s - N_1^{\mathrm{sb}})\,, \tag{6.33}$$

$$r_{1'} = \mathcal{F}\left(q_1 + \frac{\nu_{1'}^m}{\nu_3^m} M_{1'}\right) - \mathcal{F}\mathcal{D}_{2'}(q_3 + M_3) + \frac{\theta_{1'}^s}{\nu_3^m}\mathcal{F}(N_{1'}^s - N_{1'}^{\mathrm{sb}})\,. \tag{6.34}$$

If we again neglect everything but clock noise, we see that

$$r_1 \approx \mathcal{F}q_1 - \mathcal{F}\mathcal{D}_3 q_2\,, \tag{6.35}$$

$$r_{1'} \approx \mathcal{F}q_1 - \mathcal{F}\mathcal{D}_{2'} q_3\,. \tag{6.36}$$

These terms will be used in section section 6.4.4 to construct calibration expressions, which suppress clock noise.

### 6.4.2 Removal of Primed Modulation Noises

In LISA, the Electro-Optic Modulators (EOMs) on the primed optical benches are running at 2.401 GHz, while the ones on the unprimed optical benches use a modulation frequency of 2.4 GHz. The frequency distribution system ensures that the pilot tone used as phase reference for all phase measurements and the 2.4 GHz signal have a very stable phase relationship. The 2.401 GHz signal, on the other hand, is generated independently and thus contains additional noise compared to the pilot tone.

In our model, this corresponds to a higher value of the $M_{i'}$ compared to the $M_i$. We can remove the primed optical noises by using the sideband-sideband beatnote in the reference

interferometers[2]. Let us define

$$\Delta M_1 = \theta^{\tau}_{1'}\left[\frac{\tau^{\mathrm{sb}}_1 - \tau_1}{2} + \frac{\tau^{\mathrm{sb}}_{1'} - \tau_{1'}}{2}\right]. \tag{6.37}$$

Keeping only modulation error terms, we have

$$\Delta M_1 \approx \mathcal{F}(\nu^m_1 M_1 - \nu^m_{1'} M_{1'})\,. \tag{6.38}$$

We can remove the primed optical bench EOM noise at the expense of adding more readout noise to the calibration variables,

$$r^c_1 = r_1 - \frac{\mathcal{D}_3 \Delta M_2}{\nu^m_{2'}}\,, \tag{6.39}$$

$$r^c_{1'} = r_{1'} + \frac{\Delta M_1}{\nu^m_3}\,. \tag{6.40}$$

If we assume that the modulation frequencies are almost identical on all optical benches $\nu^m_i = \nu^m_{i'} = \nu^m$, we can estimate the residual noise in the calibration variables,

$$\begin{aligned} r^c_1 \approx{}& \mathcal{F}(M_1 + q_1) + \mathcal{D}_3\mathcal{F}(M_{2'} - M_2) - \mathcal{F}\mathcal{D}_3(M_{2'} + q_2) \\ &+ \theta^s_1 \frac{\mathcal{F}(N^s_1 - N^{\mathrm{sb}}_1)}{\nu^m} + \theta^{\tau}_{2'} \frac{\mathcal{D}_3\mathcal{F}(N^{\tau}_2 - N^{\mathrm{sb},\tau}_2 + N^{\tau}_{2'} - N^{\mathrm{sb},\tau}_{2'})}{2\nu^m}\,, \end{aligned} \tag{6.41}$$

$$\begin{aligned} r^c_{1'} \approx{}& \mathcal{F}(M_1 + q_1) - \mathcal{F}\mathcal{D}_{2'}(M_3 + q_3) \\ &+ \theta^s_{1'} \frac{\mathcal{F}(N^s_{1'} - N^{\mathrm{sb}}_{1'})}{\nu^m} - \theta^{\tau}_{1'} \frac{\mathcal{D}_3\mathcal{F}(N^{\tau}_1 - N^{\mathrm{sb},\tau}_1 + N^{\tau}_{1'} - N^{\mathrm{sb},\tau}_{1'})}{2\nu^m}\,. \end{aligned} \tag{6.42}$$

Primed modulation terms do not show up in $r^c_{1'}$, but in $r^c_1$, $M_{2'}$ appears multiplied by a delay-filter commutator. These commutators have a magnitude proportional to the arm-length rate of change $\dot{L} \approx 1 \times 10^{-8}$ [BLPH19]. Neglecting them in the previous expression leads to an approximate calibrating variable, where the primed modulation term $M_{2'}$ has disappeared,

$$\begin{aligned} r^c_1 \approx{}& \mathcal{F}(M_1 + q_1) - \mathcal{D}_3\mathcal{F}(M_2 + q_2) \\ &+ \theta^s_1 \frac{\mathcal{F}(N^s_1 - n^{\mathrm{sb}}_1)}{\nu^m} + \theta^{\tau}_{2'} \frac{\mathcal{D}_3\mathcal{F}(N^{\tau}_2 - N^{\mathrm{sb},\tau}_2 + N^{\tau}_{2'} - N^{\mathrm{sb},\tau}_{2'})}{2\nu^m} \end{aligned} \tag{6.43}$$

[2]Another option would be to use an electronic beatnote between the two modulation signals.

### 6.4.3 Former Calibration Expressions

#### Michelson Combinations

A calibration expression for the first-generation Michelson combination $X_1$ was proposed in [Hel01], and reads

$$\begin{aligned} K_{X_1} = \frac{b_{1'}}{2}&[(1-\mathcal{D}_{33'})(r_{1'}+\mathcal{D}_{2'}r_3)+(1-\mathcal{D}_{2'2})(r_1+\mathcal{D}_3 r_{2'})] \\ &+ a_1(r_{1'}+\mathcal{D}_{2'}r_3) - a_{1'}(r_1+\mathcal{D}_3 r_{2'}) + a_{2'}[r_{1'}-(1-\mathcal{D}_{2'2})r_1+\mathcal{D}_{2'}r_3] \\ &- a_3[r_1-(1-\mathcal{D}_{33'})r_{1'}+\mathcal{D}_3 r_{2'}]\,, \end{aligned} \tag{6.44}$$

such that clock noise is strongly suppressed in $X_1^c = X_1 - K_{X_1}$. In [TH18], it was adapted for second generation under the assumption that delays commute, such that

$$X_2^c = X_2 - K_{X_2} = X_2 - (1-\mathcal{D}_{33'2'2})K_{X_1}\,. \tag{6.45}$$

If we account for time-varying armlengths, these calibration expressions have non-vanishing clock noise residuals for both generations. For the first-generation calibrated $X_1$, and ignoring the filters, these residuals read

$$X_1^{c,q} = \frac{b_{1'}}{2}[\mathcal{D}_{33'},\mathcal{D}_{2'2}]q_1\,, \tag{6.46}$$

while those for the second generation are

$$\begin{aligned} X_2^{c,q} = b_{1'}&\left(\frac{1}{2}[\mathcal{D}_{33'},\mathcal{D}_{2'2}](1+\mathcal{D}_{33'2'2}) + \frac{1}{2}[\mathcal{D}_{33'2'2},\mathcal{D}_{2'233'}] - [\mathcal{D}_{33'},\mathcal{D}_{2'2}]\mathcal{D}_{33'}\right)q_1 \\ &+ (a_{1'}[\mathcal{D}_{33'},\mathcal{D}_{2'2}]\mathcal{D}_{33'} + a_1[\mathcal{D}_{33'},\mathcal{D}_{2'2}])q_1 \\ &+ a_{2'}[\mathcal{D}_{33'},\mathcal{D}_{2'2}]\mathcal{D}_3 q_2 + a_3[\mathcal{D}_{33'},\mathcal{D}_{2'2}]\mathcal{D}_{33'2'}q_3\,. \end{aligned} \tag{6.47}$$

#### Sagnac Combination

Similar to the Michelson combinations, the calibration expression for the first-generation Sagnac combination $\alpha_1$ was first proposed in [Hel01], and reads

$$\begin{aligned} K_{\alpha_1} = \frac{b_{1'}}{2}&[(r_1+\mathcal{D}_3 r_2+\mathcal{D}_{31}r_3)+(r_{1'}+\mathcal{D}_{2'}r_{3'}+\mathcal{D}_{2'1'}r_{2'})] \\ &+ (b_{2'}+a_2)r_1 + (b_{3'}+a_3)(r_1+\mathcal{D}_3 r_2) \\ &+ (b_{3'}-a_{3'})r_{1'} + (b_{2'}-a_{2'})(r_{1'}+\mathcal{D}_{2'}r_{3'})\,, \end{aligned} \tag{6.48}$$

such that $\alpha_1^c = \alpha_1 - K_{\alpha_1}$ is almost free of clock noise. In [TH18], it was adapted for second generation, such that

$$\alpha_2^c = \alpha_2 - K_{\alpha_2} = \alpha_2 - (1 - \mathcal{D}_{312})K_{\alpha_1} \,. \tag{6.49}$$

These calibrated expressions also have non-vanishing clock noise residuals for both generations, if we account for time-varying armlengths. The residuals for the first-generation calibrated $\alpha_1$ are, if one neglects the filters,

$$\alpha_1^{c,q} = \frac{b_{1'}}{2}(\mathcal{D}_{312} - \mathcal{D}_{2'1'3'})q_1 \,, \tag{6.50}$$

while those for the second generation read

$$\begin{aligned}\alpha_2^{c,q} = \frac{b_{1'}}{2}([\mathcal{D}_{2'1'3'}, \mathcal{D}_{312}] + [\mathcal{D}_{2'1'3'} - \mathcal{D}_{312}]\mathcal{D}_{312})]q_1 + \frac{b_{1'} + 2a_1}{2}(\mathcal{D}_{2'1'3'} - \mathcal{D}_{312})q_1 \\ + (b_{2'} + a_2)(\mathcal{D}_{2'1'3'} - \mathcal{D}_{312})\mathcal{D}_3 q_2 + (b_{3'} + a_3)(\mathcal{D}_{2'1'3'} - \mathcal{D}_{312})\mathcal{D}_{31} q_3\end{aligned} \tag{6.51}$$

Here, we used that

$$a_1 + a_2 + a_3 - a_{1'} - a_{2'} - a_{3'} + 2b_{1'} + 2b_{2'} + 2b_{3'} = 0 \,, \tag{6.52}$$

which is not exact, but a good approximation even when Doppler shifts are included in the beatnote definition [TH18].

### 6.4.4 Exact calibration expressions

#### Principle

We recognize that the clock noise terms enter eqs. (6.35) and (6.36) with the same structure as the laser noises in the $\eta_i$ variables. They indeed represent the six one-way interferometric measurements, each containing one local clock noise and one remote clock noise, delayed by the corresponding armlength. From these building blocks, we can apply the reasoning outlined in [Val05a] to synthesize arbitrary virtual photon paths of the form

$$q_B - \mathcal{D}_{i_n i_{n-1} \ldots i_1} q_A \,, \tag{6.53}$$

where the indices $i_1 \ldots i_n$ correspond to a valid path connecting spacecraft $A$ to $B$. Following our indexing convention in fig. 3.4, this means formally that

- The spacecraft pointed to by the link $i_k$ should be the starting point of link $i_{k+1}$, for any $k < n$.

- The first link $i_1$ should start from S/C $A$.
- The last link $i_n$ should point to S/C $B$.

By combining multiple such expressions, we can construct polynomials of delay operators of the form

$$\sum_i P_i q_i \,, \tag{6.54}$$

where the delays in the polynomials $P_i$ pairwise correspond to photon paths.

If the polynomials $P_i, P_{i'}$ in eq. (6.24) are also of this form, we can construct six calibration expressions $R_i, R_{i'}$ out of the $r_i, r_{i'}$ variables such that

$$R_i = P_i q_i, \quad R_{i'} = P_{i'} q_i \,. \tag{6.55}$$

Thus, we find a general expression for exact clock calibration for any TDI variable satisfying the above condition[3]

$$\mathrm{TDI}^c = \mathrm{TDI} - \left( \sum_{i=1}^{3} b_{(i+1)'} P_i r_i^c - (a_i + b_{(i+1)'}) R_i - (a_{i'} - b_{i'}) R_{i'} \right) . \tag{6.56}$$

In the following, we use this principle to find exact calibration expressions for both first and second-generation Michelson variables, as well as the second-generation Sagnac variables. As a counterexample, the first-generation Sagnac variable can't be factored as described above, and thus exact calibration by this method is impossible.

### Michelson Combinations

We recognize that the delay polynomials for the Michelson combinations in eqs. (4.29) and (4.34) correspond to photon paths. As such, we can derive exact calibration expressions,

[3]Here, we used that $P_{i-1}\mathcal{D}_{i+1} q_i = R_{i-1} - P_{i-1} r_{i-1}^c$. This is an immediate consequence of eqs. (6.35) and (6.55).

which can be written as

$$\begin{aligned} X_1^{c,e} = X_1 - \big[ & a_3(1-\mathcal{D}_{33'})r_{1'}^c - a_{2'}(1-\mathcal{D}_{2'2})r_1^c - (a_{1'}+a_3)(r_1^c + \mathcal{D}_3 r_{2'}^c) \\ & + (a_1 + a_{2'} + b_{1'}(1-\mathcal{D}_{33'}))(r_{1'}^c + \mathcal{D}_{2'} r_3^c)\big] , \end{aligned} \tag{6.57}$$

$$\begin{aligned} X_2^{c,e} = X_2 - \big[ & a_3(1-\mathcal{D}_{33'}-\mathcal{D}_{33'2'2}+\mathcal{D}_{2'233'33'})r_{1'}^c \\ & - a_{2'}(1-\mathcal{D}_{2'2}-\mathcal{D}_{2'233'}+\mathcal{D}_{33'2'22'2})r_1^c \\ & - (a_1+a_{2'}+a_{1'}+a_3)(1-\mathcal{D}_{2'2})(r_1^c+\mathcal{D}_3 r_{2'}^c) \\ & + (a_1+a_{2'}+a_{1'}+a_3)(1-\mathcal{D}_{33'})(r_{1'}^c+\mathcal{D}_{2'}r_3^c) \\ & - (a_{1'}+a_3)(1-\mathcal{D}_{2'233'})(r_1^c+\mathcal{D}_3 r_{2'}^c) \\ & + (a_1+a_{2'})(1-\mathcal{D}_{33'2'2})(r_{1'}^c+\mathcal{D}_{2'}r_3^c) \\ & + b_{1'}(1-\mathcal{D}_{33'}-\mathcal{D}_{33'2'2}+\mathcal{D}_{2'233'33'}))(r_{1'}^c+\mathcal{D}_{2'}r_3^c)\big] . \end{aligned} \tag{6.58}$$

Compared to the calibration in [TH18], the calibration expressions that we propose exactly cancel clock noise, even if we account for time-varying armlengths. Besides, they have a reduced number of correction terms. In section 6.5, we study the secondary noises which enter the calibrated expressions and limit the performance of the new algorithm.

### Sagnac Combinations

In [TH18], it is claimed that an exact calibration of clock noise is impossible for second-generation Sagnac combinations. The argument states is that second-generation Sagnac combinations can be related to their first-generation counterparts under the assumptions that delays commute and that Sagnac effect can be neglected for clock noise. Because an exact cancellation of clock noise for first-generation Sagnac variables [Hel01], it was thought that such a calibration is also impossible for the second generation. In this section, we show that an exact calibration for second-generation Sagnac variables is possible and propose a calibration expression.

If we factor the Sagnac variable according to eq. (6.23), we recognize that the delay polynomials correspond to valid photon paths. Thus, we can derive the exact calibration ex-

pression,

$$\begin{aligned}\alpha_2^c = \alpha_2 - \big[&(a_2+a_3+a_{1'}+a_{2'}+a_{3'})r_1^c \\ &-(a_1+a_2+a_3+a_{2'}+a_{3'}+b_{1'})r_{1'}^c \\ &+(a_3+a_{1'}+a_{2'}+a_{3'}-b_{2'})\mathcal{D}_3 r_2^c \\ &-(a_1+a_2+a_3+a_{2'}+b_{1'}+b_{3'})\mathcal{D}_{2'}r_{3'}^c \\ &+(a_{1'}+a_{2'}+a_{3'}-b_{2'}-b_{3'})\mathcal{D}_{31}r_3^c \\ &-(a_1+a_2+a_3+b_{1'}+b_{2'}+b_{3'})\mathcal{D}_{2'1'}r_{2'}^c \\ &+(a_{2'}+a_{3'}-b_{2'}-b_{3'})\mathcal{D}_{312}r_{1'}^c \\ &-(a_2+a_3+b_{1'}+b_{2'}+b_{3'})\mathcal{D}_{2'1'3'}r_1^c \\ &+(a_{2'}-b_{2'})\mathcal{D}_{3122'}r_{3'}^c-(a_3+b_{1'}+b_{3'})\mathcal{D}_{2'1'3'3}r_2^c \\ &-b_{1'}\mathcal{D}_{2'1'3'31}r_3^c\big]\,.\end{aligned} \tag{6.59}$$

## 6.5 Residual Noise in Calibrated Variables

### 6.5.1 Flexing-Filtering Noise

When deriving the exact clock calibration terms, we have neglected the filter-delay commutators in the $r_i$ and $r_{i'}$ variables (*c.f.* eqs. (6.33) and (6.34)). They contribute to the flexing-filtering effect in the calibrated Michelson variables presented in eqs. (6.57) and (6.58). Summing these filter-delay commutators, we find the flexing-filtering coupling in the calibrated Michelson combinations $X_1^{\mathcal{F},c}$ and $X_2^{\mathcal{F},c}$. They are presented in eqs. (6.60) and (6.61).

$$
\begin{aligned}
X_1^{\mathcal{F},c} = & \big[(a_1 + a_{2'} + b_{1'})\mathcal{D}_{2'}[\mathcal{F},\mathcal{D}_2] - (a_{1'} + a_3)\mathcal{D}_3[\mathcal{F},\mathcal{D}_{3'}] - b_{1'}\mathcal{D}_{33'2'}[\mathcal{F},\mathcal{D}_2]\big]q_1 \\
& - [a_{2'}\mathcal{D}_{2'2}[\mathcal{F},\mathcal{D}_3] + (a_{2'} - a_{1'} + a_3)[\mathcal{F},\mathcal{D}_3]]q_2 \\
& - [(a_3 + b_{1'})\mathcal{D}_{33'}[\mathcal{F},\mathcal{D}_{2'}] - (a_1 + a_{2'} + a_3 + b_{1'})[\mathcal{F},\mathcal{D}_{2'}]]q_3\,, \qquad (6.60) \\
X_2^{\mathcal{F},c} \equiv & \big[(2a_1 + a_{1'} + 2a_{2'} + a_3 + b_{1'})\mathcal{D}_{2'}[\mathcal{F},\mathcal{D}_2] - (a_1 + 2a_{1'} + a_{2'} + 2a_3)\mathcal{D}_3[\mathcal{F},\mathcal{D}_{3'}] \\
& + (a_1 + a_{1'} + a_{2'} + a_3)\mathcal{D}_{2'23}[\mathcal{F},\mathcal{D}_{3'}] - (a_1 + a_{1'} + a_{2'} + a_3 + b_{1'})\mathcal{D}_{33'2'}[\mathcal{F},\mathcal{D}_2] \\
& - (a_1 + a_{2'} + b_{1'})\mathcal{D}_{33'2'22'}[\mathcal{F},\mathcal{D}_2] + (a_{1'} + a_3)\mathcal{D}_{2'233'3}[\mathcal{F},\mathcal{D}_{3'}] + b_{1'}\mathcal{D}_{2'233'33'2'}[\mathcal{F},\mathcal{D}_2]\big]q_1 \\
& + \big[(a_1 + a_{1'} + 2a_{2'} + a_3)\mathcal{D}_{2'2}[\mathcal{F},\mathcal{D}_3] - (a_1 + 2a_{1'} + 2a_{2'} + 2a_3)[\mathcal{F},\mathcal{D}_3] \qquad (6.61) \\
& + (a_{1'} + a_{2'} + a_3)\mathcal{D}_{2'233'}[\mathcal{F},\mathcal{D}_3] - a_{1'}\mathcal{D}_{33'2'22'2}[\mathcal{F},\mathcal{D}_3]]q_2 \\
& - [(a_1 + a_{1'} + a_{2'} + 2a_3 + b_{1'})\mathcal{D}_{33'}[\mathcal{F},\mathcal{D}_{2'}] - (2a_1 + a_{1'} + 2a_{2'} + 2a_3 + b_{1'})[\mathcal{F},\mathcal{D}_{2'}] \\
& + (a_1 + a_{2'} + a_3 + b_{1'})\mathcal{D}_{33'2'2}[\mathcal{F},\mathcal{D}_{2'}]]q_3\,.
\end{aligned}
$$

Following the methods used in [BLPH19] to estimate the flexing-filtering for the residual laser noise in the Michelson $X_1$ combination, we find that the flexing-filtering coupling associated with clock noise reads, at first order in powers of the armlength derivatives,

$$S_{X_1^{c,\mathcal{F}}}(\omega) \approx 2\omega^2 K_{\mathcal{F}}(\omega) S_q(\omega) \Big[ (A_1 - B_1 \cos 2\omega L)\dot{L}_2^2 + ((C_1 - D_1 \cos 2\omega L)\dot{L}_3^2 - (E_1 - F_1 \cos 2\omega L)\dot{L}_2 \dot{L}_3 \,. \Big] , \tag{6.62}$$

where we have defined

$$A_1 = (a_1 + a_3)(a_1 + a_3 + 2b_{1'} + a_{2'}) + (a_{2'} + b_{1'})^2 + b_{1'}^2 + a_1 a_{2'} \,, \tag{6.63}$$
$$B_1 = (a_1 + a_3 + a_{2'})(a_3 + 2b_{1'}) + b_{1'}^2 \,, \tag{6.64}$$
$$C_1 = a_{2'}(a_3 + a_{1'} + a_{2'}) + (a_3 + a_{1'})^2 \,, \tag{6.65}$$
$$D_1 = a_{2'}(a_3 + a_{1'} + a_{2'}) \,, \tag{6.66}$$
$$E_1 = (a_3 + a_{1'})(a_1 + a_{2'} + b_{1'}) \,, \tag{6.67}$$
$$F_1 = b_{1'}(a_3 + a_{1'}) \,. \tag{6.68}$$

Similarly, we find for second-generation Michelson combination $X_2$,

$$S_{X_1^{c,\mathcal{F}}}(\omega) \approx 2\omega^2 K_{\mathcal{F}}(\omega) S_q(\omega) [A_2 + b_2 \cos(2\omega L) + C_2 \cos(4\omega L)] \,, \tag{6.69}$$

with

$$A_2 = 2(a_1^2 + a_{1'}^2 + a_3^2 + a_{2'}^2) + 2b_{1'}(a_1 - 2a_{2'}) + 3b_{2'}^2 \,, \tag{6.70}$$
$$B_2 = 4(a_1 + b_{1'})(a_{1'} + b_{1'}) \,, \tag{6.71}$$
$$C_2 = b_{1'}(b_{1'} + 2a_1) \,. \tag{6.72}$$

### 6.5.2 Readout Noise

The readout noise entering the calibration variables appears scaled by the modulation frequency $\nu_m = 2.4\,\mathrm{GHz}$ in eqs. (6.41) and (6.42). Conversely, the calibration terms used in eqs. (6.57) and (6.58) are scaled by the beatnote frequencies $a_i, b_i$, which are all controlled to be smaller than 25 MHz. As such, the additional readout noise due to the calibration step is strongly suppressed by the factors $a_i/m$ or $b_i/m$ and can be neglected. This is also visible in simulations, where the overall noise level after applying the clock calibration is equal to the readout noise in the case that all other noises are turned off.

## 6.6 Simulation

We present here the simulations that are used to generate realistic LISA measurement signals, process them using the TDI algorithm introduced in the previous sections, and calibrate them so as to reduce clock noise. Details about the LISANode simulator and the instrumental model are given below. More details can be found in the dedicated chapters of this thesis, chapters 2 and 3.

### 6.6.1 LISANode

LISANode is the baseline prototype for an end-to-end mission performance simulator. It is a flexible tool that performs computations in the time domain to produce time-series of realistic measurement signals that one expects from LISA, along with raw and corrected TDI Michelson combinations.

It is based on high-level simulation graphs defined in Python scripts. These graphs are composed of atomic computation units chained together, called nodes and written in C++ for computational efficiency. A scheduler triggers the node execution in a specific order and pushes data from one node to the next. In this manner, the execution time is optimized and data flow is synchronized.

All signals are represented as relative frequency deviations, or Doppler variables $\delta\nu/\nu_0$, where $\nu_0$ is the laser frequency. They are implemented as doubles (64-bit floating-point numbers).

Two different sampling frequencies are used in our simulations. The *physical* sampling frequency is used to simulate all physical processes, such as generation of instrumental noise, propagation of laser beams, and optical measurements. It is here set to $f_{\text{phy}} = 30\,\text{Hz}$. The measurement signals are $s_i$, $s_i^{\text{sb}}$, $\epsilon_i$ and $\tau_i$ are downsampled to the *measurement* frequency $f_{\text{meas}} = 3\,\text{Hz}$ by means of a decimation of a factor $f_{\text{phy}}/f_{\text{meas}} = 10$. All pre-processing steps, including TDI and clock noise calibration, are therefore carried out at this measurement frequency.

### 6.6.2 Instrumental modelling

The three spacecraft of the LISA constellation are simulated. Signals imprinted on laser beams are exchanged between the spacecraft. We use time-varying delays to model the propagation of these signals, implemented as Lagrange interpolating polynomials of order

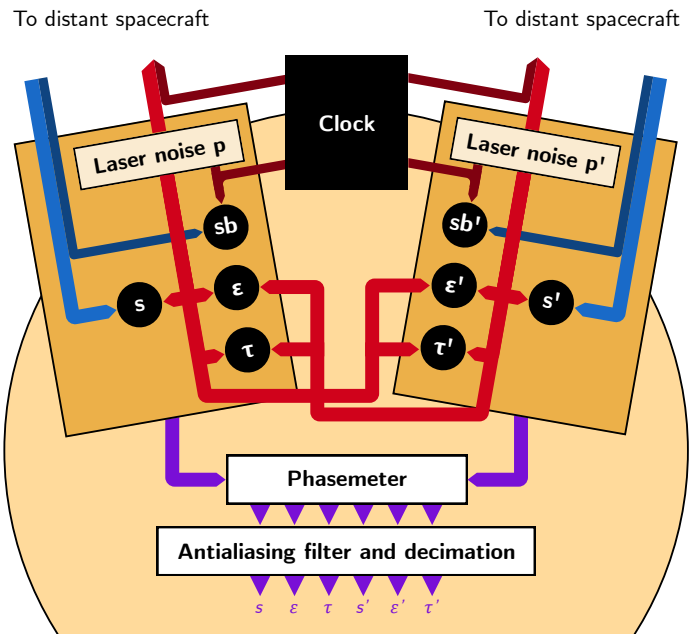


Figure 6.1: Optical design used in LISANode simulations. Eight interferometric measurements are performed for each spacecraft: two science signals $s_i$ and $s_{i'}$, two side-band signals $s_i^{\text{sb}}$ and $s_{i'}^{\text{sb}}$, two test-mass signals $\epsilon_i$ and $\epsilon_{i'}$, along with two reference signals, $\tau_i$ and $\tau_{i'}$.

31. They allow both for good precision and limited execution time and numerical errors.

The Keplerian orbits presented in section 3.2.3 are used in this study. We then deduce the light travel times along each arm from the relative positions and velocities of the spacecraft. These light travel times include contributions from the Sagnac effect, related to the rotation of the constellation, as well as first order relativistic corrections.

Each spacecraft contains two optical benches, a clock, a phasemeter and an on-board computer. Each optical bench implements the latest *split-interferometry* optical setup described in section 6.3.1 and represented in fig. 6.1: four interferometric measurements $s_i$, $s_i^{\text{sb}}$, $\epsilon_i$ and $\tau_i$ (respectively the science, side-band, test-mass and reference signals) are formed. Relevant sources of noise, such as test-mass acceleration noise, optical path noise, readout noise or laser frequency noise are added to the measurements.

These interferometric measurements are then transmitted to the phasemeter, where we add clock noise, in the form of the USO noise scaled by the laser beat note frequency. We model the fractional frequency deviation of each USO by a flicker noise with a power spectrum of $S_y(f) = 6.7 \times 10^{-27}/f$, which is generated using a variant of the infinite RC model,

*c.f.* section 3.3.6. We add to this flicker noise a linear frequency deviation to account for the clock frequency drift.

The other noise sources included in the simulation, as well as the spectral properties that were used to model them, are discussed in great details in section 3.3.

The signals are then fed to the on-board computer, which decimates all signals down to 3 Hz. To prevent power folding, we use a symmetric FIR anti-aliasing filter of order 253, implemented using a direct form I. Its coefficients are computed such that the signal is attenuated by 240 dB in the transition region between 0.2 Hz and 0.9 Hz. The results of these operations are the measurement signals that one can expect from LISA.

### 6.6.3 Pre-processing and Calibration

These measurements are used to form TDI intermediary variables and then Michelson variables $X$, $Y$ and $Z$. The clock noise calibration algorithm presented in Sec. 6.4 is used to reduce the clock noise in the TDI channels. We finally obtain the clock-calibrated Michelson variables $X^c$, $Y^c$, and $Z^c$.

Similarly to what is done to model the propagation of signals between two spacecraft, pre-processing delays are implemented using Lagrange interpolating polynomials of order 31. To form Michelson variables, one must apply multiple delays to the interference measurements for the calculation of the Michelson variables $X$, $Y$, and $Z$. In order to minimize the error introduced by these interpolations, we use a nested delay algorithm in which a single interpolation is necessary.

## 6.7 Results and Discussion

We represent in figs. 6.2 and 6.3 the residual noise in both generations of the Michelson combinations $X_1$ and $X_2$, as well as in the associated clock-calibrated combinations $X_1^c$ and $X_2^c$. Similarly, we show in figs. 6.4 and 6.5 the residual noise in Sagnac combinations $\alpha_1$ and $\alpha_2$, as well as the associated clock-calibrated combinations $\alpha_1^c$ and $\alpha_2^c$. All of these figures show the results of LISANode simulations (*c.f.* section 6.6.1) in the form of PSDs.

We represent the uncalibrated laser noise-free combinations (blue curve) as well as their clock-calibrated counterpart (orange curve) when both laser noise and clock noise are included. We compare these results with the uncalibrated results that one obtains when laser noise is the only noise source included (green curve).

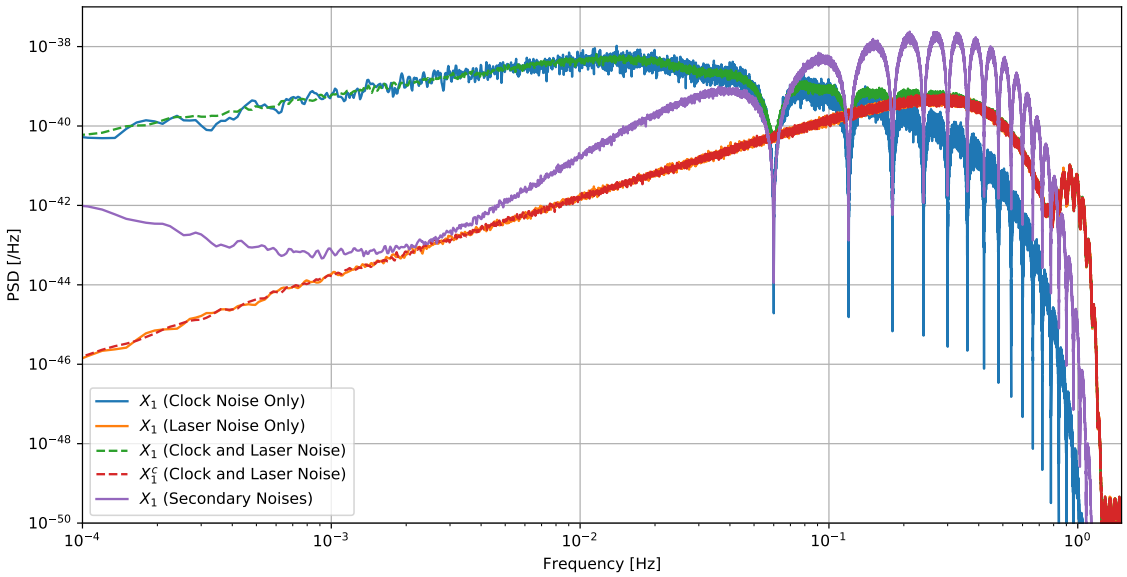


Figure 6.2: Power spectral density of the residual laser frequency noise in the Michelson $X_1$ and clock-calibrated $X_1^c$ channels.

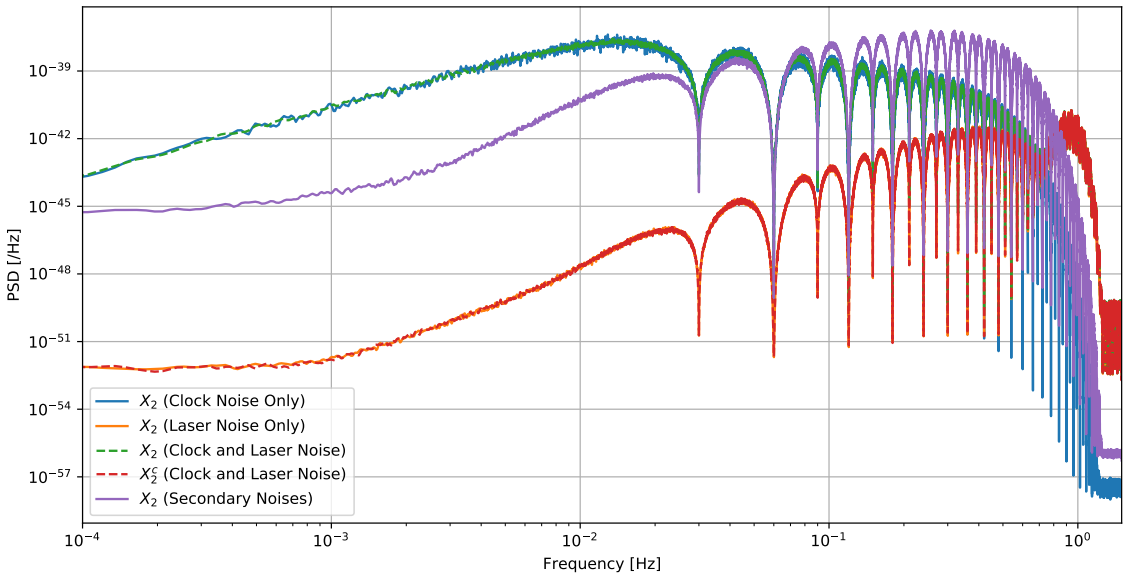


Figure 6.3: Power spectral density of the residual laser frequency noise in the Michelson $X_2$ and clock-calibrated $X_2^c$ channels.

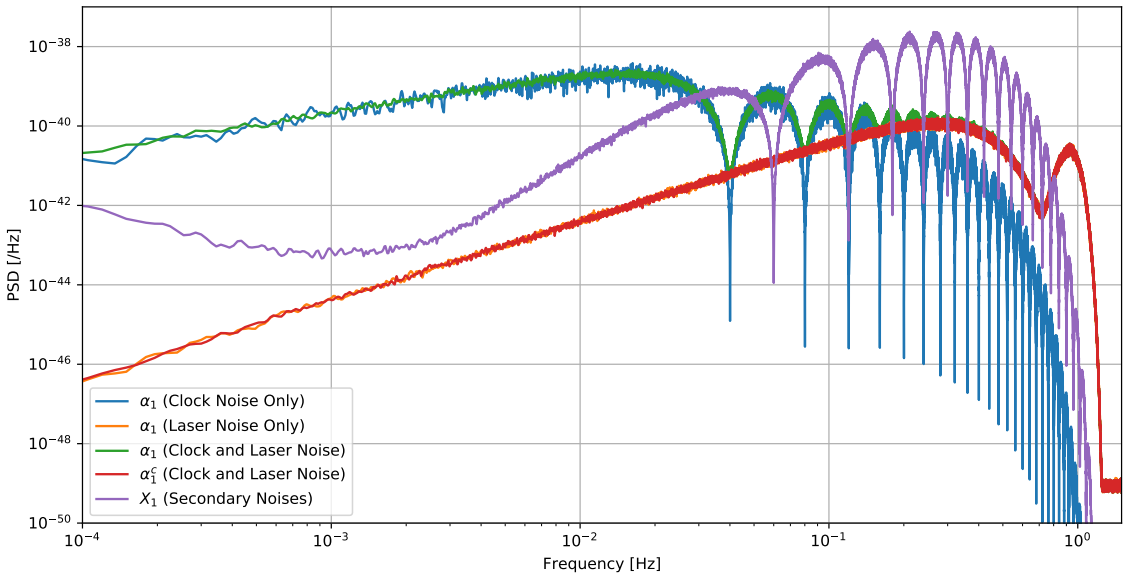


Figure 6.4: Power spectral density of the residual laser frequency noise in the Sagnac $\alpha_1$ and clock-calibrated $\alpha_1^c$ channels.

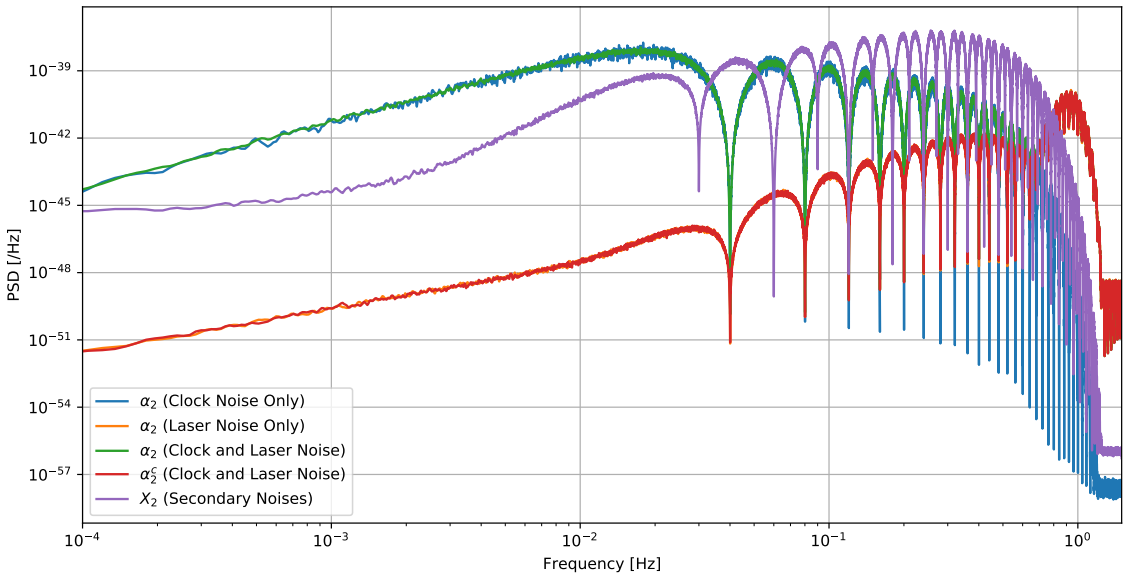


Figure 6.5: Power spectral density of the residual laser frequency noise in the Sagnac $\alpha_2$ and clock-calibrated $\alpha_2^c$ channels.

For reference, the red curves show the residual secondary noises in laser noise-free channels simulated with LISANode. To generate those signals, we did not change the simulation parameters. However, laser frequency noise is set to zero while the test mass acceleration (TM), optical read-out (RO) and optical path (OP) noise amplitudes were given their nominal LISA instrument noise budget values. The spectral shapes of these three secondary sources of noise are given in [**?**], and read

$$S_{\mathrm{TM}} = \left(2.4 \times 10^{-15}\right)^2 \tag{6.73}$$

$$\times \left[1 + \left(\frac{4 \times 10^{-4}}{f}\right)^2\right] \mathrm{m^2 s^{-4} Hz^{-1}}\,, \tag{6.74}$$

$$S_{\mathrm{RO}} + S_{\mathrm{OP}} = 1 \times 10^{-24}\,\mathrm{m^2 Hz^{-1}}\,. \tag{6.75}$$

Because TDI does not suppress those secondary noises but only modulates their spectra, they are used as a benchmark.

We use Welch's method to estimate the spectra, implemented with standard `Python` tools included in the `scipy.signal` module, version 1.1.0. We use segments of 25 000 samples and a `Nutall4` window function. The results are presented for the frequency band from $5 \times 10^{-4}$ Hz to 1 Hz.

We can see that the uncalibrated combinations (blue curves) are above the requirements (red curves). Because of the clock noise model, this is especially true below $10^{-2}$ Hz. This confirm that one must calibrate for clock noise in order to reach the required LISA sensitivity.

It is also clear that calibration expressions proposed in this chapter removes clock noise, as the clock-calibrated channels (orange curves) are significantly superimposed with the uncalibrated channels in the case where clock noise is not included in the simulations (green curves). This enables us to validate the calibration procedure and reduce clock noise to below the requirements, as figs. 6.3 and 6.5 show that the calibrated combinations lie at least three orders of magnitude below the secondary noises (red curves).

# Chapter 7

# Transient Signal Discrimination

In this chapter, we assess the possibility of using machine-learning techniques to discriminate short-lived signals in LISA measurements. The first part of this chapter aims to describe how transient instrumental artifacts, or *glitches*, enter the various interferometric measurements and the TDI combinations. We show these glitches' signatures are different from that of *bursts* gravitational-wave signals, such as cosmic string cusps or kinks (*c.f.* section 1.3.7). In the second part of this chapter, we evaluate the performance of various neuronal-network configurations to discriminate between glitches and bursts. For simple models of signals, we show that some can learn the differences in the way they appear in the Michelson and quasi-orthogonal TDI combinations (*c.f.* section 4.2.4).

This preliminary study has been conducted in collaboration with C. Simpson.

## 7.1 Propagation of Glitches and Bursts

### 7.1.1 Framework

In this section, we use the conventions described in chapter 3. In particular, spacecraft are labeled clockwise from 1 to 3 and links are indexed according to the opposite spacecraft, with primed numbers for links pointing clockwise. Optical benches are denoted by the same index as their host spacecraft, with primed numbers for optical benches receiving light clockwise. Fig. 3.4 illustrates these labelling conventions. Interferometric measurements are labeled accordingly to the optical bench on which they are performed.

The optical-bench design is that of the current mission baseline with telescopes pointing to the distant spacecraft. Test masses are displaced by $\delta_i$ with respect to the optical bench. Sensitive axes are denoted $\mathbf{n}_i$.

All signals are expressed as fractional frequency deviations from the nominal carrier frequency, see section 3.4.2. In this study, we neglect any ranging error, *c.f.* section 3.2.5. Therefore, both TDI and propagation delay operators are equal,

$$\mathbf{D}_i \approx \mathcal{D}_i \,. \tag{7.1}$$

We present equations for signals associated with the first spacecraft, *i.e.* related to the optical benches 1 and 1'. Other expressions can be obtained by a circular permutation of indices $1 \to 2 \to 3 \to 1$.

### 7.1.2 Interferometric Signals

We only consider the following contributions to the interferometric signals described in sections 3.4.6 and 3.4.7:

- Gravitational signals $H_1$ and $H_{1'}$ entering science signals.
- Test-mass displacement noise, expressed using the test-mass velocity vectors $\mathbf{v}_{\delta_1}$ and $\mathbf{v}_{\delta_{1'}}$ projected on the sensitive axis unit vectors $\hat{\mathbf{n}}_{3'}$ and $\hat{\mathbf{n}}_2$.
- Readout noise sources $N_1^\alpha$ and $N_{1'}^\alpha$. They enter each interferometric measurement $\alpha$ including the science signals $s$, the reference signals $\tau$, and the test-mass signals $\epsilon$. We suppose they are uncorrelated.

These noise sources are described in more detail in section 3.3.

The science signals correspond to the beatnote between the distant and local beams, *c.f.* section 3.4.6. They contain the gravitational-wave response of one arm and the readout noise. Using eqs. (3.86) and (3.87), we find

$$s_1 = \theta_1^s H_1 + N_1^s \,, \tag{7.2}$$

$$s_{1'} = \theta_{1'}^s H_{1'} + N_{1'}^s \,. \tag{7.3}$$

The test-mass and reference signals are the beatnotes between the local and adjacent beams, *c.f.* section 3.4.7. In the case of the test-mass signals, the adjacent beam is bounced onto the

local test mass. Therefore, they contain the test-mass displacement noise and the readout noise. The reference signals only contain the latter noise.

$$\epsilon_1 = -2\theta_1^\tau\left(\hat{\mathbf{n}}_{3'}\cdot\frac{\mathbf{v}_{\delta_1}}{c}\right) + N_1^\epsilon\,, \tag{7.4}$$

$$\epsilon_{1'} = -2\theta_{1'}^\tau\left(\hat{\mathbf{n}}_{2}\cdot\frac{\mathbf{v}_{\delta_{1'}}}{c}\right) + N_{1'}^\epsilon\,, \tag{7.5}$$

$$\tau_1 = N_1^\tau\,, \tag{7.6}$$

$$\tau_{1'} = N_{1'}^\tau\,. \tag{7.7}$$

### 7.1.3 Intermediary Variables

Inserting eqs. (7.2) to (7.7) in eqs. (4.13) and (4.14) yields the optical-bench noise-free variables

$$\begin{aligned}\xi_1 = \theta_1^s H_1 - \theta_1^s\left[\hat{\mathbf{n}}_{3'}\cdot\frac{\mathbf{v}_{\delta_1}}{c} + \mathcal{D}_3\left(\hat{\mathbf{n}}_3\cdot\frac{\mathbf{v}_{\delta_{2'}}}{c}\right)\right] + N_1^s \\ + \theta_1^s\theta_1^\tau\frac{N_1^\epsilon - N_1^\tau}{2} + \theta_1^s\theta_{2'}^\tau\frac{\mathcal{D}_3(N_{2'}^\epsilon - N_{2'}^\tau)}{2}\,.\end{aligned} \tag{7.8}$$

$$\begin{aligned}\xi_{1'} = \theta_{1'}^s H_{1'} - \theta_{1'}^s\left[\hat{\mathbf{n}}_{2}\cdot\frac{\mathbf{v}_{\delta_{1'}}}{c} + \mathcal{D}_{2'}\left(\hat{\mathbf{n}}_{2'}\cdot\frac{\mathbf{v}_{\delta_3}}{c}\right)\right] + N_{1'}^s \\ + \theta_{1'}^s\theta_{1'}^\tau\frac{N_{1'}^\epsilon - N_{1'}^\tau}{2} + \theta_{1'}^s\theta_3^\tau\frac{\mathcal{D}_{2'}(N_3^\epsilon - N_3^\tau)}{2}\,.\end{aligned} \tag{7.9}$$

Using these equations in eqs. (4.21) and (4.22), we obtain the $\eta_i$ variables. They reduce the number of free-running lasers to three, and read

$$\begin{aligned}\eta_1 = H_1 - \left[\hat{\mathbf{n}}_{3'}\cdot\frac{\mathbf{v}_{\delta_1}}{c} + \mathcal{D}_3\left(\hat{\mathbf{n}}_3\cdot\frac{\mathbf{v}_{\delta_{2'}}}{c}\right)\right] + \theta_1^s N_1^s \\ + \theta_1^\tau\frac{N_1^\epsilon - N_1^\tau}{2} + \theta_{2'}^\tau\frac{\mathcal{D}_3(N_{2'}^\epsilon + N_2^\tau)}{2}\,,\end{aligned} \tag{7.10}$$

$$\begin{aligned}\eta_{1'} = H_{1'} - \left[\hat{\mathbf{n}}_{2}\cdot\frac{\mathbf{v}_{\delta_{1'}}}{c} + \mathcal{D}_{2'}\left(\hat{\mathbf{n}}_{2'}\cdot\frac{\mathbf{v}_{\delta_3}}{c}\right)\right] + \theta_{1'}^s N_{1'}^s \\ + \theta_{1'}^\tau\frac{N_{1'}^\epsilon - 2N_{1'}^\tau - N_1^\tau}{2} + \theta_3^\tau\frac{\mathcal{D}_{2'}(N_3^\epsilon - N_3^\tau)}{2}\,.\end{aligned} \tag{7.11}$$

### 7.1.4 Michelson Combinations

Michelson combinations are given in section 4.2.4. They synthesize three Michelson-like equal-arm interferometers $X$, $Y$ and $Z$, out of which only two are independent. Geometrically, they correspond to the beatnotes of two photons traveling along both arms in opposite directions, as shown in fig. 4.7.

Different generations account for increasing complexity in the armlength fluctuations. First-generation combinations are given in eqs. (4.28) and (4.29). They assume that armlengths are unequal but constant in time, *i.e.* that the constellation is not flexing. Their second-generation counterparts account for linearly-varying armlengths to first order in the armlength time derivatives. They are given in eqs. (4.33) and (4.34). Because the latter is the baseline, we use it here. Nevertheless, we study first-generation combinations as well, as they allow to understand the results.

### Gravitational Signals

The gravitational signals in first-generation Michelson combination $X_1$ are given by

$$X_1^H = (1 - \mathcal{D}_{33'})(H_{1'} + \mathcal{D}_{2'}H_3) - (1 - \mathcal{D}_{2'2})(H_1 + \mathcal{D}_3 H_{2'})\,. \tag{7.12}$$

For second-generation $X_2$, we obtain

$$\begin{aligned} X_2^H = (1 - \mathcal{D}_{33'} - \mathcal{D}_{33'2'2} + \mathcal{D}_{2'233'33'})(H_{1'} + \mathcal{D}_{2'}H_3) \\ - (1 - \mathcal{D}_{2'2} - \mathcal{D}_{2'233'} + \mathcal{D}_{33'2'22'2})(H_1 + \mathcal{D}_3 H_{2'})\,. \end{aligned} \tag{7.13}$$

We observe that gravitational signals appear multiple times and with various delays in the Michelson combinations. We call these repeated appearances *echos*.

We saw in section 3.2.4 that the light travel time along the six links are not equal because of the constellation's flexing. If these differences matter for data processing, they remain however smaller than 34 ms. In the following study, we consider transient signals with durations of the order $1\,\mathrm{s} \gg 34\,\mathrm{ms}$. Therefore, we can simplify the previous expression by considering delays of a given number $n$ of unspecified links $\mathcal{D}_{nL}$. We have for first-generation $X_1$,

$$X_1^H \approx (1 - \mathcal{D}_{2L})[(H_{1'} - H_1) + \mathcal{D}_{1L}(H_3 - H_{2'})]\,. \tag{7.14}$$

Similarly, for second-generation $X_2$,

$$X_2^H \approx (1 - \mathcal{D}_{2L} - \mathcal{D}_{4L} + \mathcal{D}_{6L})[(H_{1'} - H_1) + \mathcal{D}_{1L}(H_3 - H_{2'})]\,. \tag{7.15}$$

Here, the various echos and the associated delays are clearly visible.

### Test-Mass Glitches

We now only consider glitches in the test-mass displacement. For clarity, let us denote this contribution $\delta_i = \hat{\mathbf{n}}_{(i+2)'} \cdot \mathbf{v}_{\delta_1}/c$. We have

$$X_1^\delta = (1 - \mathcal{D}_{2'2})[(1 + \mathcal{D}_{33'})\delta_1 + 2\mathcal{D}_3\delta_{2'}] - (1 - \mathcal{D}_{33'})[(1 + \mathcal{D}_{2'2})\delta_{1'} + 2\mathcal{D}_{2'}\delta_3]\,. \tag{7.16}$$

Under the assumption that all armlengths are equal, we have

$$X_1^\delta \approx (1-\mathcal{D}_{4L})(\delta_1-\delta_{1'})+2\mathcal{D}_{1L}(1-\mathcal{D}_{2L})(\delta_{2'}-\delta_3)\,. \tag{7.17}$$

A glitch in a single test mass will have two echoes in a Michelson combination. Note that in the case of a distant test mass, we have four echos; however, they disappear if one considers that armlengths are equal.

Conducting the same study for second-generation variables yields

$$\begin{aligned} X_2^\delta = {} & (1-\mathcal{D}_{2'2}-\mathcal{D}_{2'233'}+\mathcal{D}_{33'2'22'2})[(1+\mathcal{D}_{33'})\delta_1+2\mathcal{D}_3\delta_{2'}] \\ & -(1-\mathcal{D}_{33'}-\mathcal{D}_{33'2'2}+\mathcal{D}_{2'233'33'})[(1+\mathcal{D}_{2'2})\delta_{1'}+2\mathcal{D}_{2'}\delta_3]\,, \end{aligned} \tag{7.18}$$

and, in the case of equal armlengths,

$$X_2^\delta \approx (1-2\mathcal{D}_{4L}+\mathcal{D}_{8L})(\delta_1-\delta_{1'})-2\mathcal{D}_{1L}(1-\mathcal{D}_{2L}-\mathcal{D}_{4L}+\mathcal{D}_{6L})(\delta_{2'}-\delta_3)\,. \tag{7.19}$$

We see here that a glitch in a single local test mass has three echoes, while a glitch in a distant test mass has four of them.

### Optical Glitches

We call *optical glitch* a spurious signal in one of the 18 readout systems of the instrument. In each spacecraft, there are two science, two test-mass, and two reference readout systems. We respectively denote the associated glitches $N_i^s$, $N_i^\epsilon$, and $N_i^\tau$. In the following paragraphs, we consider only the propagation of such signals, one after the other.

We observe in eqs. (7.10) and (7.11) that *optical glitches in the science interferometers* propagate identically to gravitational waves. Therefore, we immediately have

$$X_1^{N^s} = (1-\mathcal{D}_{33'})(\theta^s_{1'}N^s_{1'}+\theta^s_3\mathcal{D}_{2'}N^s_3)-(1-\mathcal{D}_{2'2})(\theta^s_1N^s_1+\theta^s_{2'}\mathcal{D}_3N^s_{2'})\,, \tag{7.20}$$

$$\begin{aligned} X_2^{N^s} = {} & (1-\mathcal{D}_{33'}-\mathcal{D}_{33'2'2}+\mathcal{D}_{2'233'33'})(\theta^s_{1'}N^s_{1'}+\theta^s_3\mathcal{D}_{2'}N^s_3) \\ & -(1-\mathcal{D}_{2'2}-\mathcal{D}_{2'233'}+\mathcal{D}_{33'2'22'2})(\theta^s_1N^s_1+\theta^s_{2'}\mathcal{D}_3N^s_{2'})\,. \end{aligned} \tag{7.21}$$

If we suppose that light travel times along all links are equal,

$$X_1^{N^s} \approx (1-\mathcal{D}_{2L})[\theta^s_{1'}(N^s_{1'}-N^s_1)+\mathcal{D}_{1L}(\theta^s_3N^s_3-\theta^s_{2'}N^s_{2'})]\,, \tag{7.22}$$

$$X_2^{N^s} \approx (1-\mathcal{D}_{2L}-\mathcal{D}_{4L}+\mathcal{D}_{6L})[\theta^s_{1'}(N^s_{1'}-N^s_1)+\mathcal{D}_{1L}(\theta^s_3N^s_3-\theta^s_{2'}N^s_{2'})]\,. \tag{7.23}$$

One cannot disentangle glitches in the science interferometers and short-lived gravitational signals by simply studying their echo patterns in the various interferometric signals. The analysis must account for the consistency in the projection of the gravitational signal on the arms, *c.f.* section 3.2.6. As a simple analysis, one could check that $H_1(t) = H_{1'}(t-\tau)$, where $\tau$ is the difference in the light travel time in both directions due to the Sagnac effect (*c.f.* section 3.2.4).

*Optical glitches in the test-mass interferometers* propagate similarly to the test-mass glitches. They pick up an addition factor $-1/2$ as well as a beatnote polarity, yielding the following equations

$$\begin{aligned} X_1^{N^\epsilon} = {} & (1-\mathcal{D}_{33'})\left[\frac{1}{2}(1+\mathcal{D}_{2'2})\theta_{1'}^\tau N_{1'}^\epsilon + \mathcal{D}_{2'}\theta_3^\tau N_3^\epsilon\right] \\ & - (1-\mathcal{D}_{2'2})\left[\frac{1}{2}(1+\mathcal{D}_{33'})\theta_1^\tau N_1^\epsilon + \mathcal{D}_3\theta_{2'}^\tau N_{2'}^\epsilon\right], \end{aligned} \tag{7.24}$$

$$\begin{aligned} X_2^{N^\epsilon} = {} & \frac{1}{2}(1-\mathcal{D}_{33'}-\mathcal{D}_{33'2'2}+\mathcal{D}_{2'233'33'})\left[\frac{1}{2}(1+\mathcal{D}_{2'2})\theta_{1'}^\tau N_{1'}^\epsilon + \mathcal{D}_{2'}\theta_3^\tau N_3^\epsilon\right] \\ & - \frac{1}{2}(1-\mathcal{D}_{2'2}-\mathcal{D}_{2'233'}+\mathcal{D}_{33'2'22'2})\left[\frac{1}{2}(1+\mathcal{D}_{33'})\theta_1^\tau N_1^\epsilon + \mathcal{D}_3\theta_{2'}^\tau N_{2'}^\epsilon\right], \end{aligned} \tag{7.25}$$

If we suppose that light travel times are equal along all links,

$$X_1^{N^\epsilon} \approx \frac{1}{2}(1-\mathcal{D}_{4L})\theta_{1'}^\tau(N_{1'}^\epsilon + N_1^\epsilon) + \mathcal{D}_{1L}(1-\mathcal{D}_{2L})(\theta_3^\tau N_3^\epsilon - \theta_{2'}^\tau N_{2'}^\epsilon), \tag{7.26}$$

$$\begin{aligned} X_2^{N^\epsilon} \approx {} & \frac{1}{2}(1-2\mathcal{D}_{4L}+\mathcal{D}_{8L})\theta_{1'}^\tau(N_{1'}^\epsilon + N_1^\epsilon) \\ & + \mathcal{D}_{1L}(1-\mathcal{D}_{2L}-\mathcal{D}_{4L}+\mathcal{D}_{6L})(\theta_3^\tau N_3^\epsilon - \theta_{2'}^\tau N_{2'}^\epsilon). \end{aligned} \tag{7.27}$$

Therefore one cannot distinguish between a test-mass glitch and an optical glitch in the test-mass interferometers, as both will appear in the measurements with the same echo pattern.

*Optical glitches in the reference interferometer* appear in the first and second-generation Michelson combinations with a specific echo pattern, given by

$$\begin{aligned} X_1^{N^\tau} = {} & (1-\mathcal{D}_{2'2})(\theta_1^\tau N_1^\tau + \mathcal{D}_3\theta_{2'}^\tau N_{2'}^\tau) \\ & - (1-\mathcal{D}_{33'})(\theta_{1'}^\tau N_{1'}^\tau + \mathcal{D}_{2'}\theta_3^\tau N_3^\tau) + \frac{1}{2}\theta_1^\tau[\mathcal{D}_{2'2},\mathcal{D}_{33'}]N_1^\tau, \end{aligned} \tag{7.28}$$

$$\begin{aligned} X_2^{N^\tau} = {} & (1-\mathcal{D}_{2'2}-\mathcal{D}_{2'233'}+\mathcal{D}_{33'2'22'2})(\theta_1^\tau N_1^\tau + \mathcal{D}_3\theta_{2'}^\tau N_{2'}^\tau) \\ & - (1-\mathcal{D}_{33'}-\mathcal{D}_{33'2'2}+\mathcal{D}_{2'233'33'})(\theta_{1'}^\tau N_{1'}^\tau + \mathcal{D}_{2'}\theta_3^\tau N_3^\tau) \\ & + \frac{1}{2}\theta_1^\tau[\mathcal{D}_{33'2'2},\mathcal{D}_{2'233'}]N_1^\tau. \end{aligned} \tag{7.29}$$

Comparing these equations with eqs. (7.12) and (7.13), we see that optical glitches in reference interferometers propagate almost like gravitational signals. Extra delay commutators allow us to distinguish between the two. If we assume that light travel times along all links are equal, these commutators vanish et we are left with eqs. (7.14) and (7.15),

$$X_1^{N\tau} \approx (1 - \mathcal{D}_{2L})[(\theta_1^\tau N_1^\tau - \theta_{1'}^\tau N_{1'}^\tau) + \mathcal{D}_{1L}(\theta_{2'}^\tau N_{2'}^\tau - \theta_3^\tau N_3^\tau)]\,, \tag{7.30}$$

$$X_2^{N\tau} \approx (1 - \mathcal{D}_{2L} - \mathcal{D}_{4L} + \mathcal{D}_{6L})[(\theta_1^\tau N_1^\tau - \theta_{1'}^\tau N_{1'}^\tau) + \mathcal{D}_{1L}(\theta_{2'}^\tau N_{2'}^\tau - \theta_3^\tau N_3^\tau)]\,. \tag{7.31}$$

### 7.1.5 Quasi-Orthogonal Combinations

As discussed in section 4.2.4, it is possible to form TDI combinations from Michelson variables, in which instrumental noises and gravitational signals are strongly decoupled. These quasi-orthogonal combinations $A_i$, $E_i$, and $T_i$ are given by eq. (4.38).

## 7.2 Discrimination with Neural Networks

### 7.2.1 Motivation

We expect LISA to have glitches because its proof-of-concept mission LISA Pathfinder experienced glitches. Their rate was estimated at $0.78 \pm 0.02$ per day [AAB+18], with durations of minutes and occasionally hours. The cause of these glitches is still unclear and LISA could be prone to at least as many glitches, including glitches caused by solar flares, stray electromagnetic fields, and collisions with space debris. Unfortunately, these instrumental artifacts can mimic potential gravitational signals of great interest, *c.f.* section 1.2.1. As a result, one cannot dismiss all short-lived signals.

This work aims to build a neural network that can discriminate burst signals from glitches in LISA data. Because we cannot predict all the types of glitches that will appear, and we want to be able to detect gravitational-wave burst sources of all kinds, we cannot rely on specific signal shapes. Instead, the method needs to classify glitches and bursts based on how they interact with the detector. In the previous sections, we saw that gravitational bursts, test-mass glitches, and some optical glitches propagate differently in the TDI variables. These differences can be exploited to teach a neural network.

We are also interested in differentiating between glitches at different positions in the detector as well. There are three different beam types on each of LISA's optical benches and the same injected signal looks slightly different for each of them, so we have included multiple

glitch categories in every dataset and classification task. It is useful because grouping LISA's glitches by their origins will help us to model them and reduce their impact on the parameter estimates of all the gravitational-wave sources we see in LISA.

If the classifiers can perform well on a dataset of many injection shapes or even on shapes they have never seen before, that indicates that they are learning the patterns we want them to.

### 7.2.2 Generation of Training Samples

I use LISANode (*c.f.* chapter 2) to generate training data. All datasets contain 5000 samples, each one a multi-channel time series with 400 s-worth of data sampled at 3 Hz. The channels correspond to second-generation Michelson combinations $X_2$, $Y_2$, and $Z_2$, as well as the associated quasi-orthogonal $A_2$, $E_2$, and $T_2$ combinations described above.

In all datasets used in this study, we inject exactly one signal per sample – either a gravitational-wave burst or a glitch. We use rectangular injections, parametrized by an amplitude $A$, a duration $\tau$, and an initial time $t_0 = 65\,\mathrm{s}$[1]. We show in fig. 7.1 examples of such training samples.

1. The first datasets are created using rectangles of identical durations $\tau \approx 20\,\mathrm{s}$ for both gravitational-wave bursts and glitches. Instrumental noise is disabled and we choose high amplitudes for all signals so that the neural network can learn about the echo patterns. We also assumed a fixed sky localization for all gravitational burst sources $\theta = 0\,\mathrm{deg}, \phi = 0\,\mathrm{deg}$.

2. This model is refined in a second set of training samples, as signal durations and amplitudes are now drawn from random normal distributions. Glitches amplitudes and durations are respectively chosen centered around $10\,\mathrm{pm\,s^{-1}}$ and 2 s [AAB+18]. We choose similar amplitudes for gravitational-wave bursts while we expect smaller durations of around 10 ms. Instrumental noise remains disabled and burst source sky localization is still fixed.

3. In a third dataset, instrumental noise is turned on while other parameters are kept identical to the second dataset.

4. In a third dataset, instrumental noise is turned off but we randomly and uniformly localize the gravitational-wave burst sources in the sky.

[1] We choose a fixed initial time so that all signals are injected at the same time in the training samples

| | CNN | FCN | Resnet |
|---|---|---|---|
| Layers | 3 | 5 | 11 |
| Convolutions | 2 | 3 | 9 |
| Pooling | Average | None | None |
| Feature | Conv | GAP | GAP |
| Activation | Sigmoid | ReLU | ReLU |
| Optimizer | Adam | Adam | Adam |
| Batch Size | 16 | 16 | 16 |
| Learning Rate | 0.001 | 0.001 | 0.001 |
| Loss | MSE | Entropy | Entropy |

Table 7.1: Details of the hyper-parameters and optimization of `CNN`, `FCN`, and `ResNet`.

The goal in producing these datasets is not to mimic typical burst events for LISA, but instead to create the most adversarial situations possible by simulating bursts and glitches that look very similar.

### 7.2.3 Results and Discussion

With the help of C. Simpson, three deep neural networks were trained with different architectures on the increasingly complicated datasets described in section 7.2.2. Table 7.1 show the hyper-parameters used for these three architectures of neural networks. A more detailed description of the neural network architectures used in this study can be found in [FFW+19].

We report in fig. 7.2 the evolution of the loss function as the training samples are fed to the various types of neural networks. Figure 7.3 presents the confusion matrices for the validation data, in the four cases and for the same three deep neural networks.

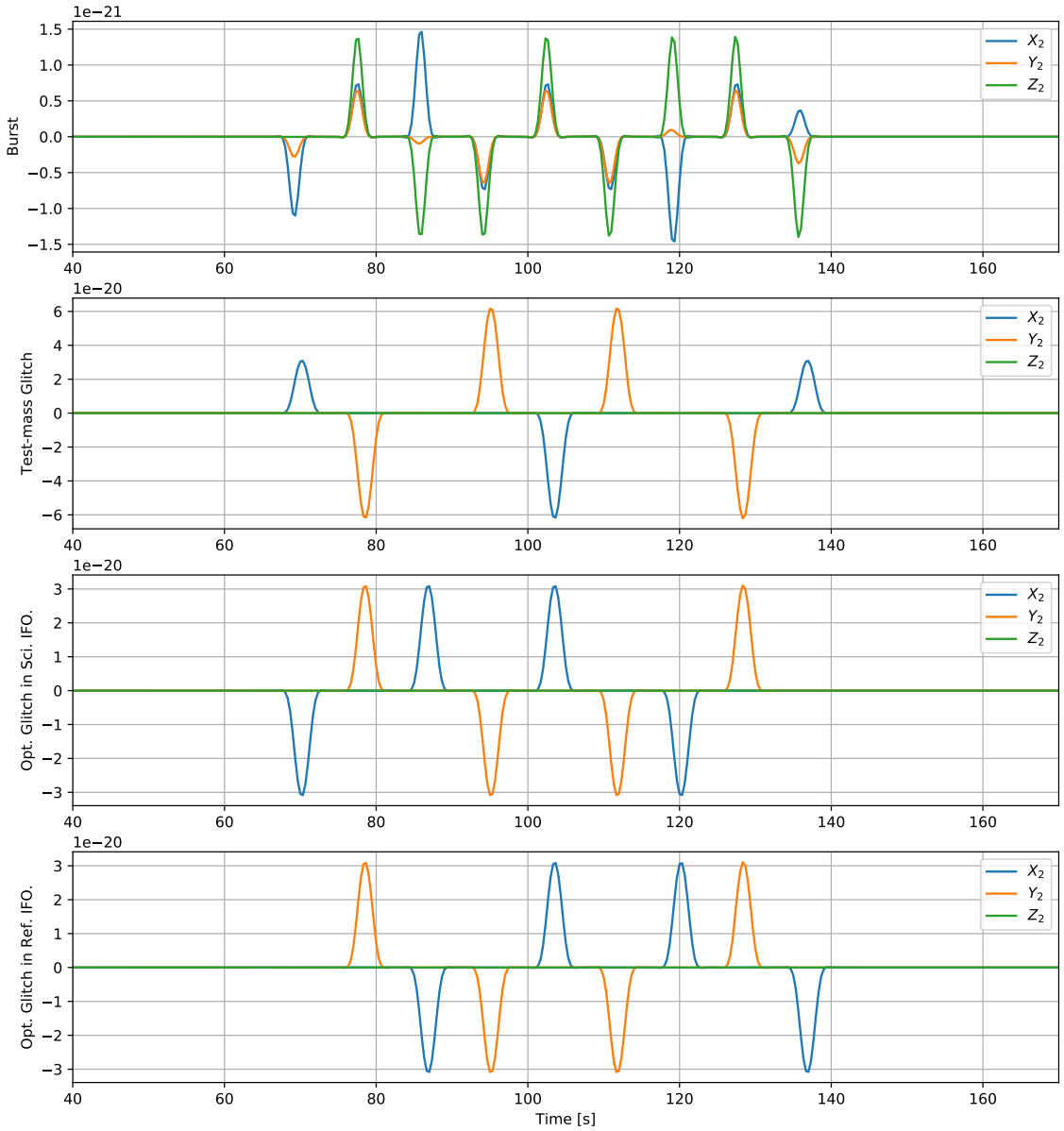


Figure 7.1: Example of training samples for a gravitational-wave burst, a test-mass glitch, an optical glitch in the science interferometer, and an optical glitch in the reference interferometer. Note that in the three last cases, we inject the glitches in the first optical bench.

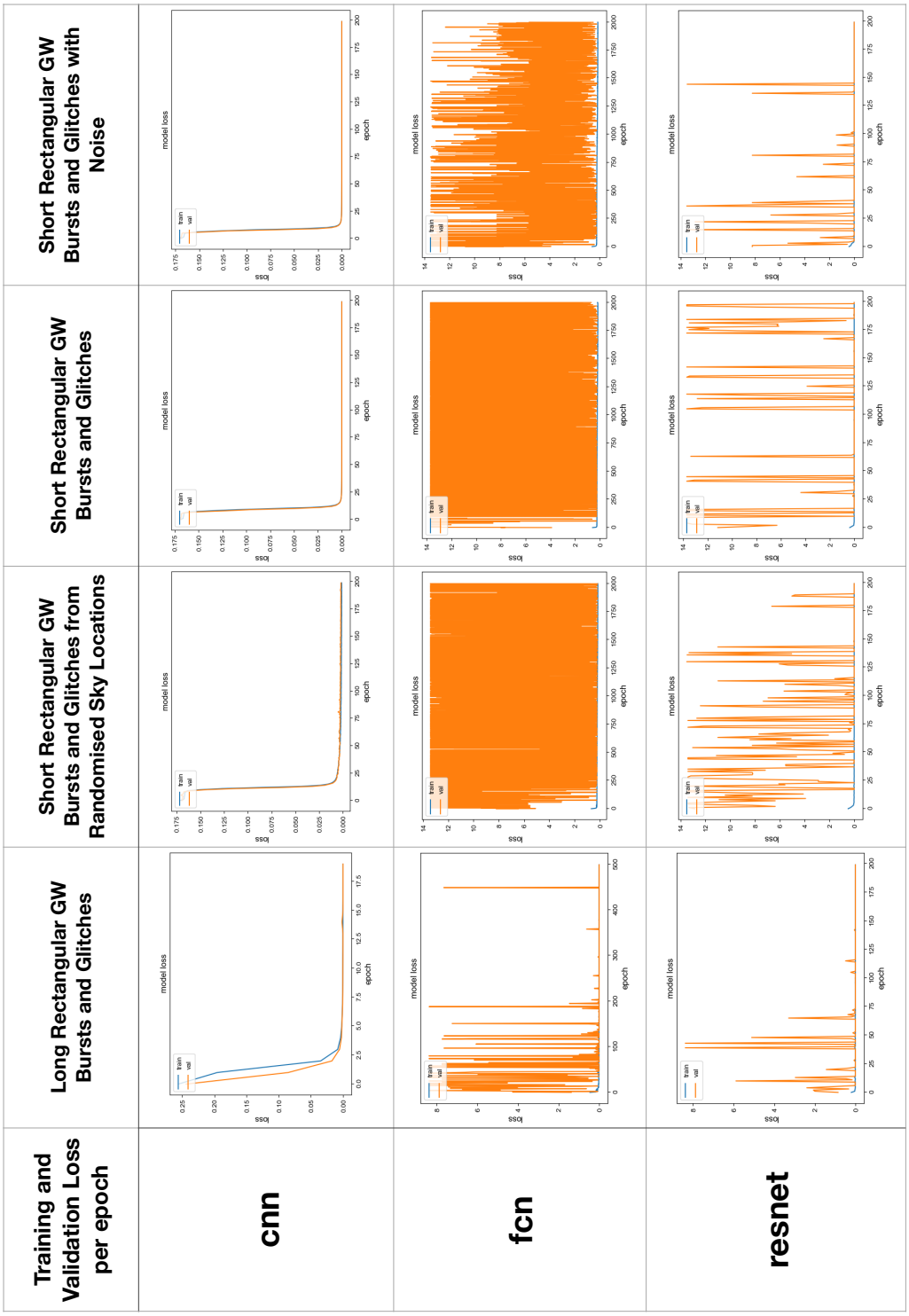


Figure 7.2: Convergence of the loss function for the various types of neural networks.

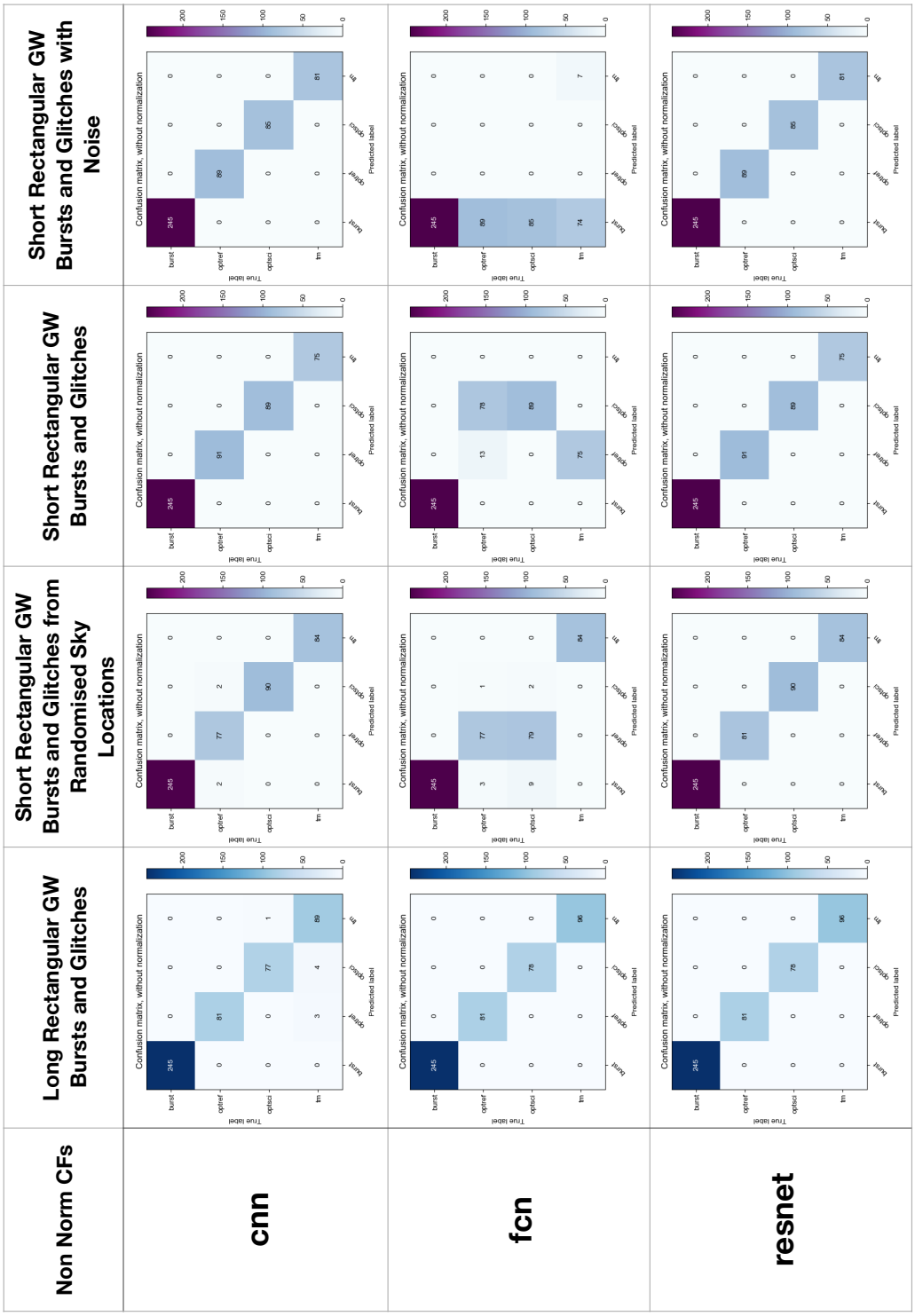


Figure 7.3: Confusion matrices for the various types of neural networks.

`CNN` and `ResNet` were able to achieve near-perfect classification on all of the datasets. `FCN` failed to differentiate between glitch types for short bursts and completely failed to differentiate gravitational-wave bursts from glitches when we added noise. `CNN`'s training and validation loss converged to zero after tens of epochs, whereas `ResNet` converged after hundreds of epochs. This makes sense because `ResNet` is much deeper and therefore has many more parameters to fit. However, if `CNN` is adequate and the problem does not need that many parameters, then we should not use a classifier with an excessive number of layers because it encourages overfitting the network.

### 7.2.4 Future Tasks

We have demonstrated in section 7.2.3 that some neural network architectures can discriminate between the various types of injected signals. Therefore, the first short-term task is now to validate our hypothesis, which is to check that the neural network learns about the signal patterns in the TDI combinations and not about the shapes of the signals. A solution is to work with training datasets containing mixed-shaped injections or validate our results with unseen shapes at all sky positions. Sin-Gaussian bursts or LISA Pathfinder-like glitches could be used. The loss function can also be adapted to favor false-positive gravitational-wave bursts over false negatives.

A more long-term plan would be to create an event trigger and a selection procedure that cut out short-lived excesses of power in the LISA continuous data streams. A similar procedure has already been used in LISA Pathfinder data to exclude instrumental glitches from the scientific analyses. Overlapping glitches and signals must also be handled correctly.

# Chapter 8

# Conclusion and Perspectives

Already with the recent first detections, gravitational-wave astronomy has opened a new and exciting observational window on the Universe. As more ground-based detectors will join LIGO and Virgo, many more detections are to come in the coming years. With them, many questions related to astrophysics, cosmology, and fundamental physics will be addressed. Unfortunately, ground-based detectors are limited to high-frequency gravitational waves. One must rely on other types of observatories to access the low-frequency part of the gravitational spectrum. The space-borne LISA mission is one of such observatories as it will allow us to detect and characterize gravitational-wave sources located at cosmological distances. This includes a large variety of astrophysical objects, from coalescing supermassive black holes, merging black-hole, neutron-star, or white-dwarf binary systems, to EMRIs or cosmological backgrounds.

At first sight, the working principle behind LISA is simple: light interferometry is used to monitor the pico-metric distance changes due to gravitational waves. Therefore, laser beams are exchanged by the three spacecraft of the constellation, bounced onto free-falling test masses, and then interfered on optical benches where readout systems and onboard computers record phase variations. A closer look at the mission specifications reveals a much more complex measurement chain and complicated interplays between the various subsystems. In particular, signals and noises appear strongly correlated in the measurement channels. Non-trivial online and offline processing techniques, such as TDI, must be used to produce data that can then be analyzed.

Such a highly-integrated mission requires a new type of scientific simulator, flexible enough to be easily adapted as the mission specifications evolve and more refined physical mod-

els are to be included. As part of my Ph.D. work, we developed LISANode, a numerical simulator that aims to address these issues. Its modular architecture allows us to implement up-to-date instrumental and noise models so that we obtain realistic simulated data. LISANode is capable of executing the required data processing and calibration steps as well, and in particular, it is used to compute the laser noise-free TDI combinations and their clock-calibrated counterparts.

Based on such a simulation tool, a performance study of the laser-noise reduction algorithms was conducted. An analytic study revealed that the mission-baseline second-generation TDI combinations contain extra noise terms due to the coupling between the antialiasing filters and the flexing of the constellation. This *flexing-filtering* was quantified and a technique to mitigate the effects of the coupling was proposed, so that laser noise is reduced to below the requirements. LISANode simulations were used to validate these results.

Similarly, a study of the clock-noise calibration was conducted. A closer look at state-of-the-art approximate algorithms revealed that it is possible to remove entirely clock noise from most of the TDI combinations. A procedure to derive such exact calibrating expressions was proposed in this thesis, along with a study of the remaining limiting couplings and noises in the Michelson and Sagnac channels. Again, simulations are used to orient and validate these results and we showed that the residual clock noise is reduced to below the requirements.

Besides, LISANode was used to generate realistic data in the context of a pilot study using neural networks for the discrimination of short-lived gravitational-wave signals and instrumental glitches. We showed that both types of signals couple differently in the TDI combinations and that some deep neural networks can learn to distinguish between them.

In the near future, more instrumental effects remain to be implemented in LISANode. In particular, beatnote frequency management (encompassing frequency planning, Doppler shifts due to spacecraft relative motion, and laser locking), absolute ranging errors, tilt-to-length coupling, timestamping errors, and test-mass and spacecraft dynamics should be included in our instrumental model. Also, a study of their propagation in the TDI combinations is necessary to assess their impact on science performance. Note that some of these effects are already being investigated; this is the case of the beatnote frequency management, the ranging errors, and the timestamping errors. Opportunity studies, such as the discrimination of short-lived signals using deep neural networks, should be continued and encouraged. The integration of LISANode in the LDC simulation pipeline is also an important step to promote this tool in the LISA community.

# Appendix A

# Clock Noise Simulation

## A.1 Conventions

We give here the formal definitions and notations for the main entities that we will manipulate in this chapter. This includes time coordinate systems, clock ticks, and clock noise.

### A.1.1 Time Coordinate Systems

Times are measured and expressed with respect to a time coordinate system. In the context of LISA, we distinguish three different types of coordinate systems.

**Barycentric Coordinate Time (TCB) Coordinate System** The TCB (denoted $^{\mathrm{TCB}}$) is defined as the proper time of a perfect clock which would be at rest with respect to the barycenter of the solar system, but not subject to the gravitational time shift caused by the Sun and the rest of the system. Times expressed in TCB coordinates are also often called *god-given*, *perfect* or *natural* times.

**Spacecraft Coordinate Systems** Spacecraft Coordinate Systems 1, 2 and 3 (denoted $^{\mathrm{SC}_i}$) are defined as the proper time of perfect clocks which would be at rest with respect to the barycenters of corresponding spacecraft. They are subject to the gravitational time shifts

relative to the TCB[1]. This is the time that one could read on a perfect clock aboard each spacecraft.

**Clock Coordinate Systems** Clock Coordinate Systems 1, 2 and 3 (denoted $^{\mathrm{C}_i}$) are attached to the USO on board each spacecraft. Relative to the spacecraft coordinate systems, they include the instrumental imperfections (timing jitter and offset).

**Notations** If $e$ is an event, we respectively denote $e^{\mathrm{TCB}}$, $e^{\mathrm{SC}_i}$, and $e^{\mathrm{C}_i}$ its time coordinate in the TCB, spacecraft $i$, and clock $i$ coordinate systems.

**Transformation Operator** The transformation operator converts times from one coordinate system $A$ to another coordinate system $B$. It is denoted $\mathcal{C}_{A\to B}$. We therefore have the following identity

$$\mathcal{C}_{A\to B}\left(e^A\right) = e^B\,. \tag{A.1}$$

In practice, if two coordinate systems are realized by discrete samples in a simulation, the application of this transformation requires an interpolation.

### A.1.2 Sampling Ticks

The times at which the ADC samples a continuous signal to produce one digital value are important events. One must unambiguously designate those events. We call them *ticks* and express them in seconds in a given coordinate system. They are associated with an index: the first tick is indexed 0, the second 1, *etc.*

**Clock Ticks** The ADC is driven by the onboard clocks. Therefore, ticks (denoted $T_i[n]$) are equally spaced when expressed in the associated clock coordinate systems. In the TCB and spacecraft coordinate systems, clock ticks are irregularly spaced.

**Spacecraft Ticks** They are imaginary ticks for a perfect clock that would regularly tick (denoted $\theta_i[n]$) in the associated spacecraft $i$ coordinate system. They have no physical reality but are useful for modeling.

[1]We can derive the time deviation due to the gravitational potential of the Sun $\Delta t = \frac{2GM_\odot}{c^2 d_0^2}\epsilon T_{\mathrm{mission}} \approx 50\,\mathrm{ms}$, after a mission of $T_{\mathrm{mission}} = 10\,\mathrm{yr}$. Special relativity clock shift can be neglected because it is of the order of $1\times10^{-7}\,\mathrm{s}$ after the same mission duration.

**TCB Ticks** They are imaginary ticks (denoted $\tau[n]$) for a perfect clock that would regularly tick in the TCB coordinate system. They are regularly spaced when expressed in TCB coordinates. These ticks are used when gravitational clock shifts are neglected and clocks are assumed to be flawless.

**Proper Coordinate Systems** The sampling ticks expressed in their proper coordinate systems are multiples of the sampling period $T_s = 1/f_s$,

$$\tau[n]^{\mathrm{TCB}} = nT_s\,, \theta_i[n]^{\mathrm{SC}_i} = nT_s\,, \mathcal{T}_i[n]^{\mathrm{C}_i} = nT_s\,. \tag{A.2}$$

For convenience, ticks are expressed in their proper coordinate systems when not otherwise denoted, *i.e.* $\tau[n] = \tau[n]^{\mathrm{TCB}}$. Similar notations are used for all the other types of ticks.

**Decimated Ticks** In reality, different sampling frequencies will occur on the same spacecraft. The phasemeter runs at 80 MHz to retrieve the phase information of all signals. These phase values are provided at a lower rate of 100 Hz for use in the control loops and onboard processing. Eventually, they get further downsampled to 3 Hz before they are telemetered to Earth.

While sampling rates are different, all of these ticks are derived from the same clock signal and thus share the same timing jitter. Therefore, it makes sense to speak of sampling ticks at a certain frequency, *e.g.* high frequency ticks for processing and low frequency ticks for telemetry. In this example, there is a decimation factor $k$ such that the low-frequency ticks can be expressed as a function of the high-frequency ticks

$$\tau[n]^{\mathrm{low}} = \tau[kn]^{\mathrm{high}}\,. \tag{A.3}$$

## A.2 Simulation Schemes

LISANode aims to simulate realistic measurement signals that we expect from the instrument. The most straightforward way to include clock jitter would be to simulate physical behaviour for all three spacecraft using one set of TCB ticks and then interpolate the associated values to the corresponding set of clock ticks. A problem arises when we require an instantaneous feedback from samples associated with clock ticks back to physics simulation, associated with TCB ticks.

Indeed, to compute an order-$n$ interpolated value at a given time $t$, samples of times $kT_s + t, 2k \in [-n, +n]$ are required (where $T_s$ is the sampling period). Therefore the feedback

loop can only affect samples at times $t' > t + nT_s$. Currently we use $n \approx 31$ and $T_s = 0.05\,\mathrm{s}$, which yields an unacceptable delay of $\approx 0.8\,\mathrm{s}$ in our controllers. Since this delay depends on the sampling rate used for the physical simulation, we can hope to reduce it by increasing the sampling rate. Depending on the final sampling rate required for the control loop, this might allow to simulate timestamping errors with this simple scheme.

An obvious solution would be to replace the interpolation by another method, which must be able to generate samples at a any time using past samples only, *i.e.* an extrapolation technique. Other solutions consists in keeping the current interpolation technique, but push the feedback loops entirely to one or the other coordinate system.

In this section, the real measurement chain is presented, along with the current simulation scheme available in LISANode to this date. We then propose three different implementations that might allow to simulate the effects of imperfect clocks on the measurement signals.

### A.2.1 Reality

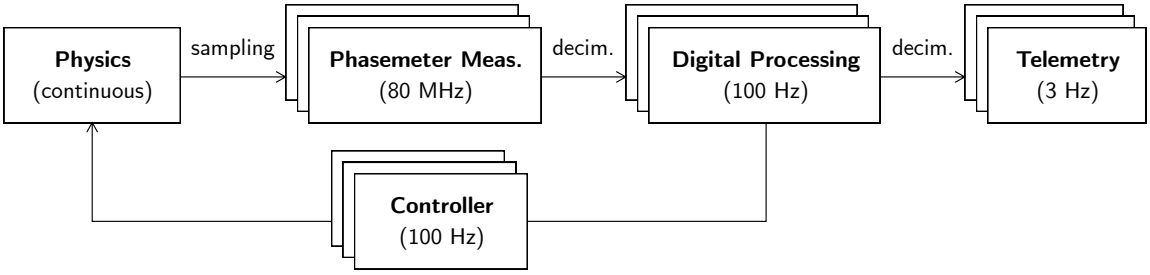


In reality, we sample continuous functions of time describing the physical behaviour of the system to produce phasemeter measurements at high frequency (80 MHz). Those measurements are used to drive the control loop (*e.g.* the DFACS at 100 Hz), which itself influences back the physical behaviour of the system. Controller have therefore no intrinsic delay other than that associated with its sampling rate and electronics.

### A.2.2 Current State

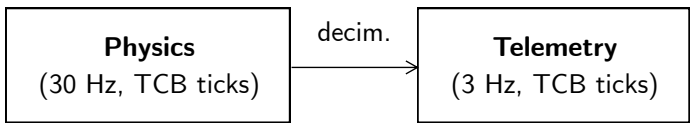

LISANode currently uses one set of TCB ticks sampled at a high frequency sampling rate of 30 Hz to generate the orbits, produce the gravitational waveforms, simulate physics including the propagation of signals between the spacecraft and all digital processes on board each spacecraft. No control loop is yet implemented in this model.

A low frequency sampling rate of 3 Hz is used to deliver telemetry data. The two sampling rates are related by a simple decimation of factor 10. Additional interfaces to external files for orbits and waveforms can have their own decimated versions of TCB ticks.

This model does not account for clock imperfections and relativistic effects (see appendix A.1.1).

### A.2.3 Extrapolation

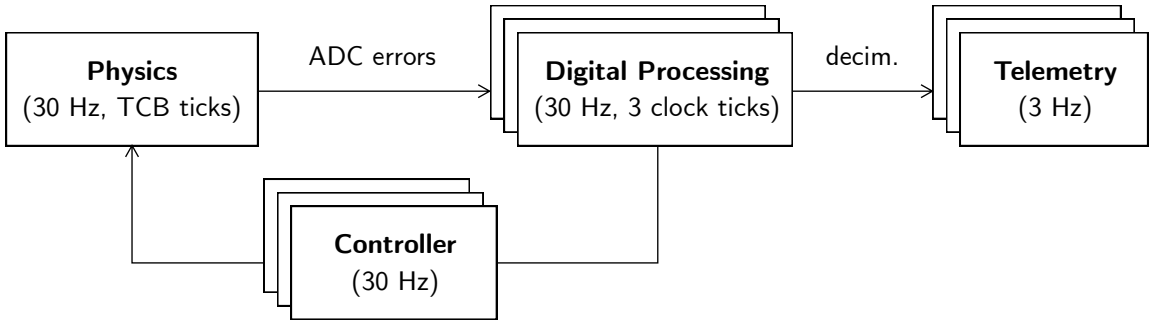


Lagrange interpolation method, used to re-sample the data from TCB to clock ticks, is here replaced by an extrapolation technique. Extrapolation does not need future samples and therefore does not introduce any delay in the feedback loops. In this mode, they are left untouched and the measurement chain is kept as close as possible as they are in reality.

Extrapolation is subjected to a greater uncertainty than interpolation methods. For unconstrained functions, such as the noisy signals that we want to simulate here, polynomial extrapolations are often used, and implemented by means of Lagrange polynomials or Newton series that fit previous samples. Unfortunately the uncertainty grows unbounded with the polynomial order, related to Runge's phenomenon near the end of the equally-spaced interpolation points.

We could use extrapolation only in places where interpolation raises issues, i.e. when we need the re-sampled values as feedback loop inputs.

### A.2.4 Sampling First

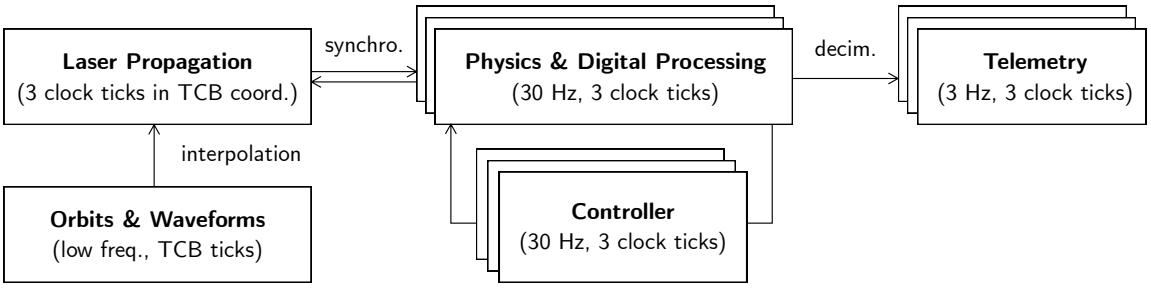


In the *sampling first* scheme, the simulation of both physics and digital processing on board each spacecraft uses the corresponding clock ticks. Almost of the simulation is therefore performed on three different sets of ticks, and only communicate when signals are exchanged. Control loops on board each spacecraft can be implemented without delays, and relativistic effects could also be easily incorporated in this model.

The three sets of clock ticks aforementioned are offset relative to each other, and their frequencies drift with time. When laser beams are propagated from one spacecraft to another, and the effect of passing gravitational waves is accounted for, a synchronization mechanism must take care of transforming the signals from one set of clock ticks (where they were generated) to TCB ticks (where orbits and waveforms are defined), back to another set of clock ticks (where the signals are received and handled). A detailed discussion can be found in appendix A.3.9.

Most physical effects, such as noise generation, are treated as if they were on an equally sampled grid in TCB time.

This scheme requires a change to LISANode's current structure and scheduling algorithms, as we might need to fire nodes associated to one spacecraft multiples times, while nodes associated to other spacecraft are not fired. Indeed, the synchronization mechanism must ensure that all clock ticks are correctly ordered when expressed in TCB coordinates. This can be achieved using three different sets of simulation ticks, *c.f.* appendix A.3.9.

### A.2.5 Sampling Last

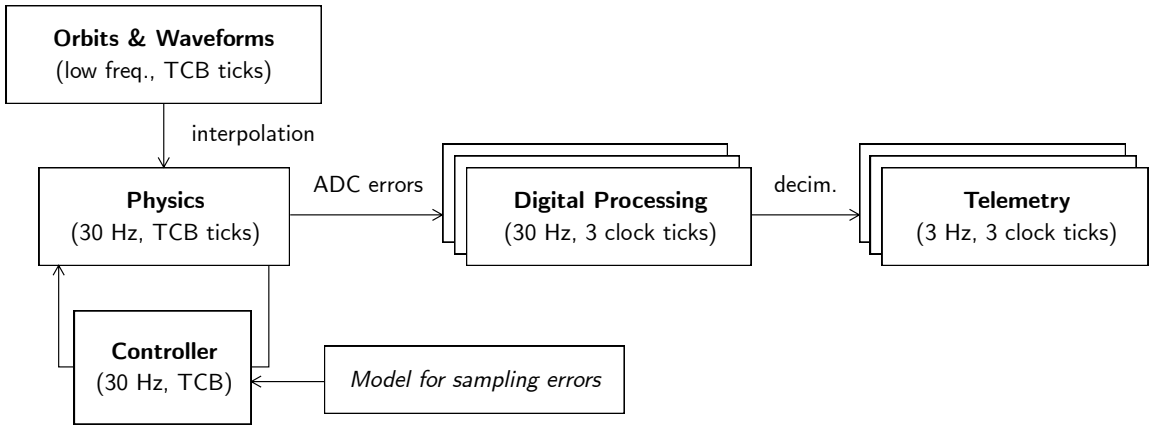


In the *sampling last* scheme, physics simulation, including the propagation of signals between spacecraft, as well as control loops use one unique set of TCB ticks. Any effect sampling errors might have on the control loop must therefore be modeled independently, *e.g.* as an additional noise.

Digital processing simulation and all downstream nodes are bound to the corresponding set of clock ticks. Thus we must interpolate physical variables, associated with TCB ticks, to measurements, expressed at clock ticks. Of course, interpolation requires the availability of input samples at future times. Since there can be no loop between digitally processed measurements and physics simulation, we are able to shift the time origin of the nodes downstream of *ADC errors*, see appendix A.3.10. The same simulation ticks can then be used for both the TCB ticks and all three sets of clock ticks; times associated to each simulation tick are either $\tau[n]$ or $T_i[n]$, depending on the node.

This simulation scheme would not require big changes in LISANode's current structure and scheduling algorithms.

## A.3 Affected Subsystems

In this section, we review each simulated subsystem that might be affected by the choosing either one of the two last simulation schemes. In particular, we describe the coordinate system in which each process really takes place, and then estimate the order of magnitude of the error that we make in both models.

Further studies must be carried out by the corresponding Work Packages, in order to validate the simulation requirements and the rough error estimation.

The control loop, as we understand it now, runs through the spacecraft and test-mass dynamics (appendix A.3.5), the optical simulation (appendix A.3.7), the digital processing (appendix A.3.10) and the controller itself (appendix A.3.6).

In the following study, we neglect relativistic effects, such that the TCB and spacecraft coordinate systems are indistinguishable. We also assume that sample-to-sample time jitter is negligible for most applications, and will be modeled independently if it is not (as is the case for the main phasemeter measurement).

### A.3.1 Orbits

Orbits are either read from a file generated by an external tool, or computed on-the-fly from an analytic model. The required precision on the positions and velocities of the spacecraft and the characteristic time of their evolutions allows for a low-frequency computation of expensive trigonometric formulae (about $5 \times 10^{-5}\,\mathrm{Hz}$, *i.e.* every 6 h). In both schemes we therefore need an interpolation to provide spacecraft positions and velocities at the required times in any case.

It is important that enough values are computed ahead of the rest of the simulation so that it is possible to perform the interpolation. One solution is to **shift the time origin** of this node, w.r.t. all other downstream nodes.

Orbits are naturally computed in the TCB coordinate system; in both simulation schemes we interpolate them to TCB or clock ticks. Thus we make similar interpolation errors. Therefore **no simulation scheme is preferred**.

### A.3.2 Gravitational Waveforms

Similarly to the orbits, waveforms are either read from existing files or generated on-the-fly using an analytic model. They are always expressed, and this is a convention, in the TCB coordinate system. A low frequency (about 5 mHz, i.e. every 15 s) is usually used, and one must interpolate between the available values to retrieve samples at the required times expressed in TCB coordinates.

Therefore the only error is that of the interpolation, and **no simulation scheme is preferred**.

### A.3.3 Arm Response

This system must compute the relative frequency deviation due to passing gravitational waves through each of the arms. It therefore takes as inputs the waveforms (appendix A.3.2), the position of the source and the spacecraft orbits (appendix A.3.1).

As described in the corresponding aforementioned subsections, waveforms and orbits must in any case be interpolated, whether their values are required at clock or TCB ticks. Again, we only make an interpolation error, and **no simulation scheme is preferred**. It is important though that the **low-frequency orbit and waveform samples be equally spaced in the TCB coordinate system** so that simple interpolation techniques can easily be used here.

### A.3.4 Instrumental Noise Generation

Stochastic instrumental noises are generated from a white noises, which are filtered to reproduce the expected spectral shapes. Regularly-spaced white noise samples are drawn from a Gaussian distribution, whose mean and standard deviation are computed as functions of the PSD and the sampling frequency

$$\mathrm{PSD} = 2\sigma^2/f_s\,. \tag{A.4}$$

This really means that the generated noise samples are bound to a coordinate system in which they are regularly spaced.

Since instrumental noises are the results of physical processes, noise samples should be associated with TCB ticks, which are equally spaced in the TCB coordinate system. The *sampling last* simulation scheme follows this prescription (see appendix A.2.5). We therefore make no error in this scheme.

Problems arise in the *sampling first* model, where downstream physical processes are bound to clock ticks. Two solutions can be considered:

- We can either interpolate between the filtered noise samples, attached to TCB ticks, so that they become bound to clock ticks, and can therefore be used by downstream nodes.
- We treat the noises samples as if they were bound to TCB ticks, even though they are really bound to clock ticks when they are generated. In that case, we make an error because TCB and clock ticks do not share the same TCB coordinates (the first ones

are equally spaced while the others are not). The dominant effects are the offsets and the drifts in frequency with respect to TCB ticks, denoted here $\delta f(t)$.

After a time $t$ we compute the PSD of a generated white noise $\mathrm{PSD}(t) = 2\sigma^2/(f_0 + \delta f(t)) \approx \mathrm{PSD}_0(1 - \delta f(t)/f_0)$. The noise was generated using a constant variance, i.e. at $\mathrm{PSD}_0$. We therefore make a relative error in the PSD estimation, after ten years, of

$$\frac{\Delta\mathrm{PSD}}{\mathrm{PSD}_0} = \frac{\delta f(10\,\mathrm{yr})}{f_0} \approx 1 \times 10^{-7}\,. \tag{A.5}$$

This can be considered negligible, and we might not need to interpolate.

Another issue is that of the filters used to give the noise its desired spectral shape. Just like white noise generators, it assumes that the ticks are equally spaced, which is not the case for the TCB ticks in clock coordinate systems. This is probably negligible because the jitter is less than a nanosecond, but this is to be checked.

Another problem comes from clock tick frequency offset and drift. Indeed, digital filters are build using a given value for the sampling period. If the clock tick frequency is offset or shifted along the mission, the nominal and actual sampling periods are not equal, and the filter specifications are no longer correct. The resulting error is hard to estimate since it depends on the filter specifications, but it can be assumed negligible because the relative frequency deviation after a 10-year mission is very small. If needed, one can write a filter node which takes a time-varying sampling period as input.

We conclude that if our assumptions hold, the *sampling first* simulation scheme produce acceptable approximations. However, **the *sampling last* scheme is preferred here, as the model yields exact results**.

### A.3.5 Spacecraft and Test-mass Dynamics

Dynamics is usually expressed in an inertial frame of reference, i.e. in the TCB coordinate system here. It takes as inputs the orbits (appendix A.3.1) and the controller commands (appendix A.3.6) to produce the position and velocities of test-masses and spacecraft. It consists mainly in integrating differential equations, which almost certainly do not depend on absolute values of time. Therefore only time intervals between samples, expressed in TCB coordinates, matter.

Differential equations are really filters. We fall back to the arguments given in appendix A.3.4.

An additional argument is that controllers are specifically designed to produce very stable systems, mostly insensitive to small perturbations of their inputs. Unfortunately, we most certainly want to study the system out-of-loop, and therefore without the stability provided by the controller. One might wonder whether the argument still holds in that case. *Further inputs from the dynamics work package is required here.*

Therefore **the *sampling last* simulation scheme is again preferred in this case** because we do not need any approximation or interpolation. The *sampling first* scheme could also produce good approximated results if our assumptions are valid.

### A.3.6 Controllers and Control Loops

On-board controllers are digital and driven by the clock:imperfections must therefore be included, i.e. samples must be bound to clock ticks. This is naturally the case in the *sampling first* simulation scheme.

For "sampling last", the argument used in appendix A.3.4 and appendix A.3.5 applies to integration of the controller laws: small changes in inputs should not have significant effects, given that the controller are designed for stability. This is an assumption that should be checked, and we can fall back to modeling any effects independently as an additional noise in the commanded forces delivered by the controller, similarly to what we do for the phasemeter.

Therefore we have inverted the situation studied in appendix A.3.5: **the *sampling first* simulation scheme is preferred** because clock noise is already included. The *sampling last* scheme could produce valid results if clock noise can be neglected for the controllers, or if we can model it by an additional noise.

### A.3.7 Optical Simulation

We gather under the terms *Optical Simulation* all computations to compute the relative beatnote frequency deviations of the various beams on the optical benches, mix the different noises, and compute the signal delivered by the photodiodes. It is composed of basic mathematical operations (addition, subtraction, etc.), as well as derivatives and integrals.

All basic mathematical operations require that the operands are attached to the same ticks, so that the results are correctly computed and clearly attached to the same set of ticks. This is the case in both simulation schemes.

Time-derivation operators that simulate physical processes use the tick frequency computed in the TCB coordinate system, and assume, in the current state of the simulator, that it is constant. This is correct in the *sampling last* scheme, since samples are attached to TCB ticks which are indeed equally spaced in the TCP coordinate system. This is wrong in the *sampling first* scheme, as the TCB frequency of clock ticks drifts with time. Therefore after $t$, we estimate the time-derivative of a signal $\tilde{x'_n} = (x_n - x_{n-1})f_0$ when in fact the true derivative is really $x'_n = (x_n - x_{n-1})(f_0 + \delta f(t))$. The relative error on the time-derivative estimate that we make after 10 years is therefore

$$\frac{\Delta x'_n}{x'_n} = \frac{\delta f(t)}{f_0} \approx 1 \times 10^{-7}\,. \tag{A.6}$$

If we assume that this is negligible, we can then safely use the *sampling first* simulation scheme. If not, we might want to write a node to estimate time-derivatives with a variable sampling frequency, i.e. a node with the sampling frequency as input and not as parameter.

For integral operators, we again make an accumulated error in the *sampling first* simulation scheme. Estimating its magnitude is not as straight forward as that of derivatives, as the result depends on the integrand. In any case, it could again be circumvented by using a node which takes the current sampling frequency $f(t)$ as input, and use it to compute the integral: $y_n = y_{n-1} + x_n/f(t)$.

To get a rough estimate of the error, we can look at the special case of integrating a constant function over the mission duration. The error becomes proportional to the accumulated timing error over 10 years, which was estimated to be up to 25 seconds given a relative frequency drift of $\approx 1 \times 10^{-16}$. Compared to 10 years, this again gives a relative error of $\approx 1 \times 10^{-7}$. Therefore **the *sampling last* simulation scheme is preferred here**, although the *sampling first* could be viable under some assumptions.

### A.3.8 Non Stationarities and Systematics

We consider here all the noises that are not purely stochastic, or whose statistical properties vary with time or are functions of other parameters. Environmental effects, thermo-elastic couplings, etc. are examples of such non-stationary noises. They most probably have characteristic times much bigger than a few dozens of seconds, and clock errors, even accumulated over 10 yr, probably do not matter.

The argument developed here are similar to those in appendix A.3.7, but **a clear list of requirements from the non stationarity work package is required**.

### A.3.9 Laser Propagation

Light travel times along each arm are computed from the position and velocities of the spacecraft, themselves computed from the orbits. They are thus associated to TCB ticks. Outgoing beam signals are originally bound to a given set of ticks; they must be delayed and attached to a potentially different set of ticks, which correspond to that of the receiving spacecraft. Therefore the samples must be buffered in memory and timestamped using a common coordinate system. We naturally choose the TCB coordinate system.

#### Sampling Last

In the *sampling last* simulation scheme, outgoing beam signals on each spacecraft are all bound to TCB ticks, which is common to all spacecraft. Moreover the incoming beam signals in the receiving spacecraft are expected to be bound to the same set of TCB ticks. There is no synchronization problem and we can safely use the common TCB coordinate system, in which TCB ticks are regularly spaced. Interpolation between regularly spaced samples, to random times (depending here on the light travel times) also expressed in TCB coordinates, is easy to implement. One must yet ensure that $(n+1)/2 \approx 16 \ll Lf_s \approx 160$, where $n$ is the interpolation order and $L$ the order of magnitude of the light travel time. This seems to be verified given the current baseline values that we are aware of.

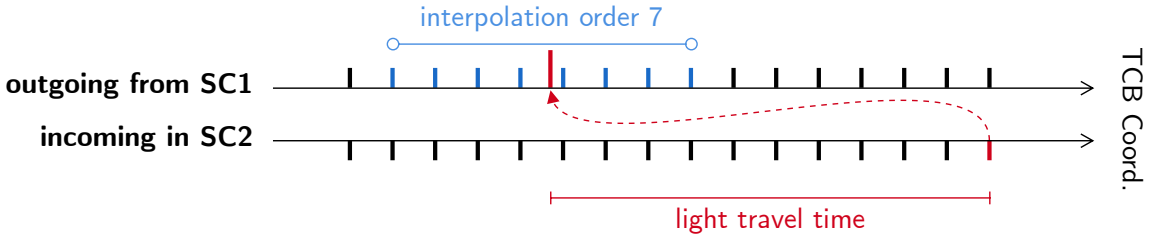


#### Clock Jitter

In the *sampling first* simulation scheme, outgoing and incoming beam signals are bound to different sets of clock ticks $T_i[n]$ and $T_j[n]$. A conversion system must play the role of the transformation operators $\mathcal{C}_{\mathrm{TCB}\to\mathrm{C}_i}$ and $\mathcal{C}_{\mathrm{C}_j\to\mathrm{TCB}}$ (see appendix A.1.1), and retrieve the TCB coordinates associated with clock ticks $T_i[n]^{\mathrm{TCB}}$ and $T_j[n]^{\mathrm{TCB}}$. One must here consider several effects of clock noise.

Clock jitter results in irregularly-spaced clock ticks when they are expressed in TCB coor-

dinates. This effect is very small (less than a nanosecond) and we make the assumptions that is can be neglected in the interpolation process, i.e. we perform a simple interpolation scheme with regularly sampled inputs. The figure below shows in black the real clock ticks, and in blue the time coordinates that the interpolation scheme assumes to compute the incoming beam signal.

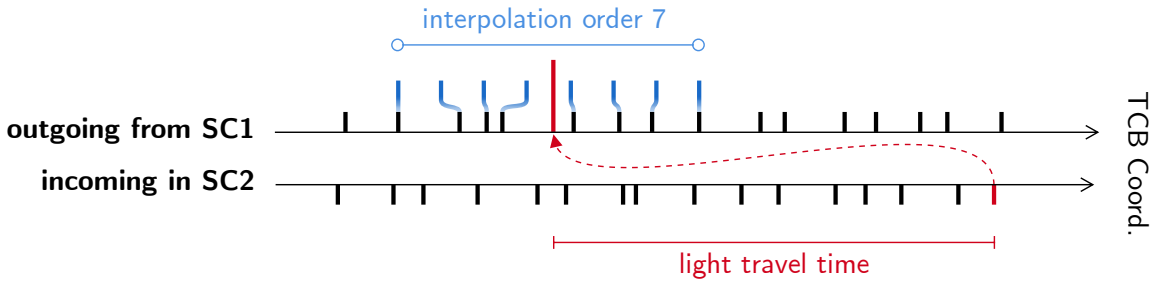


### Clock Offset

The absolute time showed by the clocks might be have a significant offset w.r.t. each other. This offset must be accounted for when converting between clock and TCB coordinates. Problems arise when this offset $\Delta t_0$ is such that $L < \Delta t_0 + (n+1)/2$. In this case, interpolation becomes impossible, c.f. figure below.

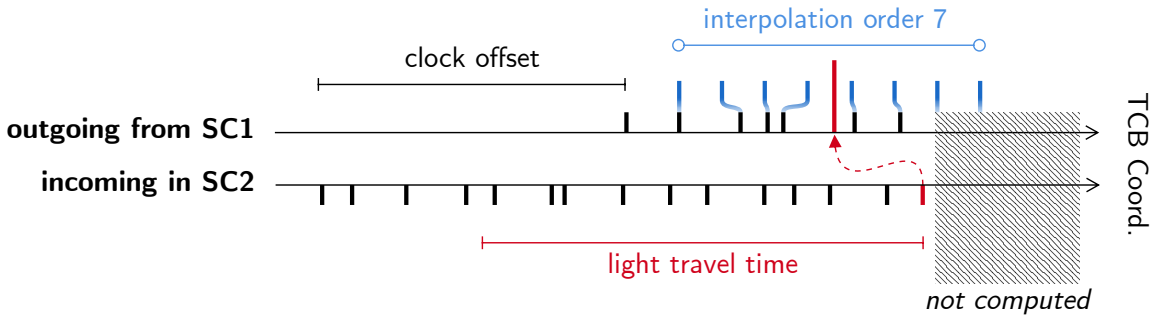


Clock offsets should be drawn from a to-be-defined random distribution before simulation begins. A synchronization mechanism must ensure that the offset is compensated by a shift in the time origin of the relevant nodes. This is illustrated on the figure below.

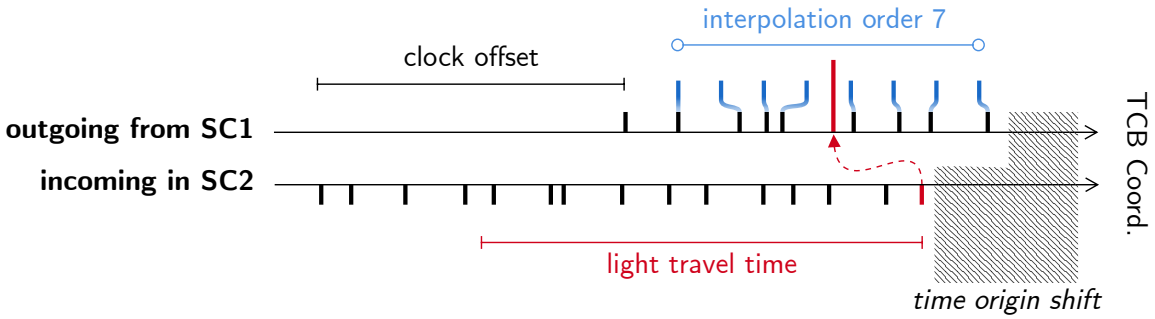


### Frequency Offset and Drift

A last effect is the offset and the drift with time of the three clock tick frequencies, as measured in the TCB coordinate system. We already encountered this issue in appendix A.3.4 and in appendix A.3.7. In this case, one cannot easily estimate the error as it depends on the signal, the sampling frequency, the interpolation order, and the value of the delay. However, if this error cannot be neglected, one can write a new interpolation node that takes the time-varying sampling frequency as an input.

This different clock tick frequencies, as measured in TCB coordinates, can have a last effect that must be accounted for. With time, they can significantly offset the ticks w.r.t each other, i.e. $\left|T_i[n]^{\mathrm{TCB}} - T_j[n]^{\mathrm{TCB}}\right|$ can become very big for $n$ big enough. The problems described in appendix A.3.9 arise again, and one cannot know this stochastic relative offset when the simulation begins. Therefore the synchronization mechanism must be adapted so that it runs continuously during the simulation, in order to keep all clocks synchronized. More precisely, the scheduler must make sure that the executions of the nodes bound to one of the three sets of clock ticks are ordered accordingly to the TCB coordinates of those clock ticks. This is of course a major change in the current LISANode's structure and scheduling algorithms.

### Conclusion

Laser propagation is a major issue when simulating clock noise errors. This is indeed the contact point of the three spacecraft, and therefore where three potentially different sets of ticks interact. **The *sampling last* simulation scheme is largely preferred** since it would not require any change in the current LISANode's structure. Conversely, the *sampling first* scheme would require major additions and changes to the scheduling algorithms, so that conversion and synchronization can occur during the simulation. The last section of

this document attempt to give an example of such a synchronization algorithm.

### A.3.10 Digital Processing

Digital processing includes all operations of the digital measurement chain: phasemeter, ADCs, onboard computer (filtering or decimation), etc. These processes are driven by the onboard clocks, and are therefore submitted to clock noise. The real measurement chain on board a single spacecraft is represented in the figure below. Dotted lines represents measurements submitted to clock noise.

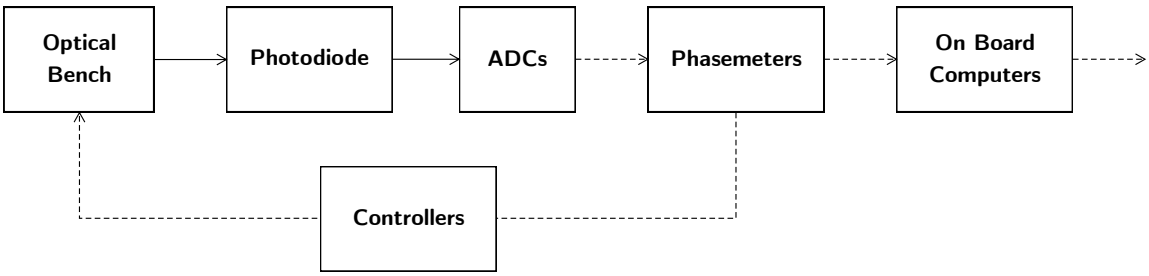


No issue is foreseen with the *sampling first* simulation scheme, as all inputs (clocks, beams, etc.) are computed for clock ticks. They can be used as-is to generate outputs attached to the same expected clock ticks.

The measurement chain in the *sampling last* scheme is represented in the figure below. Again, dotted lines represents measurements submitted to clock noise, i.e. bound to clock ticks. In this simulation scheme, the optical bench, the phasemeter and the controllers are all bound to TCB ticks. To simulate the effects of the ADC, and go to clock ticks, we interpolate the phasemeter measurements at high frequency. Then we apply the anti-aliasing filters and the decimation, which are subjected to clock errors, as expected. The results are passed on to telemetry, see appendix A.3.11.

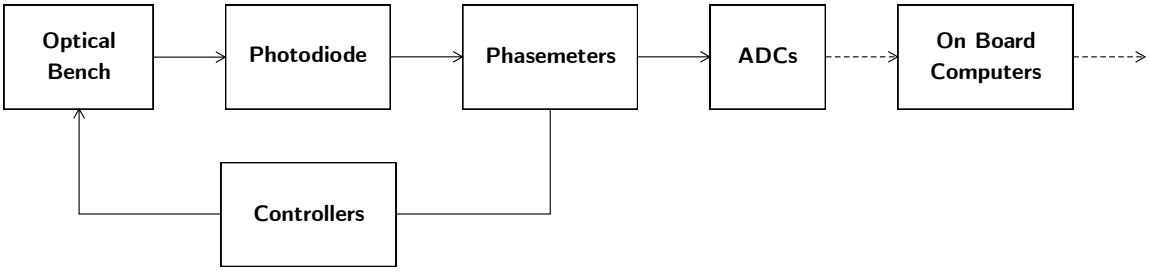

Interpolation mut be carried out at high frequency, so that clock effects are included in the filtering and decimation processes. Although it is computationally expensive, interpolating at high frequency introduces artifacts in the high-frequency part of the spectrum that are suppressed later on by the anti-aliasing filters. If we were to interpolate at lower frequency, these artifact would appear in a lower-frequency part of the spectrum and would not be removed when filtering.

Interpolating from TCB to clock ticks requires input samples at future times, since there is no big delay to apply. This is not a problem here, since we can adjust the time origins of the downstream nodes by a big enough value, so that interpolation remains possible during the whole simulation. These time origins should be greater than the maximum expected clock shift w.r.t. TCB at the end of the mission, plus the required offset for the interpolation $(n+1)T_s/2$, where $n$ is the interpolation order.

In conclusion, ***sampling first* simulation scheme is here preferred**, as no interpolation is required and it naturally uses clock ticks driving the digital computation units. The alternative *sampling last* scheme can also be used with a bit more work, but no changes in LISANode's current structure is expected.

### A.3.11 Telemetry

We focus here on the handling of gaps or errors in the transmission of data, as well as Doppler shifts of the radio signals that we might want to simulate, since they might be used to estimate the satellite positions. We have to get precise requirements from the associated Work Package.

In both schemes, the samples are attached to the clock ticks and therefore **no simulation scheme is preferred**. Gaps or Doppler might be transformed from TCB to clock ticks, though.

### A.3.12 Relativistic Effects

At first sight, the *sampling first* simulation scheme and its associated synchronization mechanism would allow for an easy implementation of relativistic effects. Indeed, each spacecraft already uses its own clock ticks for all computations. Further study should be carried out to check whether *sampling last* scheme can be used as well.

## A.4 Clock Noise Implementation

### A.4.1 Simulation Ticks

The time coordinate systems defined in subsection A.1.1 describe a continuum of values. In a simulation, we can only use discrete time steps to simulate physical events, *i.e.* LISANode computes discrete samples for the measurement signals. We keep track of these time steps with the counters used to iterate through the simulation.

We call simulation ticks the events associated with incrementing one of these counters. Each node `i` has an associated timestamp $\mathtt{T_i}[n]$ for each simulation tick $n$, which can be expressed in any coordinate system. In practice, physical simulations are usually attached to TCB or spacecraft ticks, whereas digital processing uses clock ticks. Some nodes need to have knowledge of the absolute timestamps associated with a given simulation tick, in some coordinate system[2]. It is the responsibility of these nodes to use the required timestamps.

### A.4.2 Current Implementation

Currently, there is only one counter for all nodes, denoted $n$. We still allow nodes to have different sampling rates $f_s$, but they must all be on the same time grid. The node sampling rates must be chosen such that they all divide the simulation sampling rate $f_s$. It is defined as the Least Common Multiple (LCM) of all node sampling rates, and is the highest of the them if they are all multiples of each other.

Example: In the current version, we have two sets of nodes in the simulation, one at a high-frequency sampling rate of 30 Hz and one at a low-frequency rate of 3 Hz. The high-frequency nodes are executed each tick $n$, with associated times $\tau[n]$, $n \in \{0, 1, 2, \dots\}$.

The low-frequency nodes are only executed every tenth tick, such that the associated times are still $\tau[n]$, but with $n \in \{0, 10, 20, \dots\}$. Since we assume all clocks to be perfect in the current version, the times associated to the high-frequency and low-frequency nodes are identical to the physical clock ticks down-sampled to 30 Hz and 3 Hz, respectively.

### A.4.3 Different Clocks in Sampling Last

If we have three different clocks taking samples at clock times $T_i[n]$, we could also use a single counter $n$ to iterate through all of them. The associated physical times, $T_i[n]^{\mathrm{TCB}}$,

[2]Nodes that generate waveforms, or which write data to file are examples of such nodes.

would no longer be multiples of any sampling rate. If we only want a single counter $n$ in our simulation, we also need to use it for the physical simulation corresponding to time steps at $\tau[n]$ (assuming we still want to simulate physics on an equal grid). Define the differences $\Delta T_i[n] = T_i[n]^{\mathrm{TCB}} - \tau[n]$ and $\Delta T_i^j[n] = T_i[n]^{\mathrm{TCB}} - T_j[n]^{\mathrm{TCB}}$.

In the *sampling last* simulation scheme, there is no interaction of nodes associated to different ticks after the initial sampling. Therefore, offsets between different clocks described by $\Delta T_i^j[n]$ are not a problem.

If $\Delta T_i[n] > 0$, the physical time associated with the $n$'th simulation tick of the clock-associated nodes is larger than the corresponding time of the physics nodes. This is a problem since the clock-associated nodes need the physical measurements as input, as described in subsection A.3.10. Since we need to interpolate, we actually need $\Delta T_i[n] < T_{int}$, where $T_{int}$ is a constant depending on the interpolation order. This problem can be remedied by adding a large constant offset to the clock-associated nodes, e.g. by replacing $T_i[n]$ with $T_i[n]' = T_i[n-k]$ , such that $\Delta T_i[n]' < T_{int}\ \forall n$. Again, this is possible in *sampling last*, since the clock-associated nodes can simply wait for the physical simulation; there is no loop back.

### A.4.4 Different Clocks in Sampling First

In the *sampling first* scheme, the situation is different. Physical simulation on board a single spacecraft is done using the corresponding clock ticks, *i.e.* there are no TCB ticks. Thus, $\Delta T_i[n]$ is not a problem.

If we would only use a single counter $n$, $\Delta T_i^j[n]$ could potentially become too large to allow for interpolation required for laser propagation, as explained in subsection A.3.9. We need $\|\Delta T_i^j[n]\| < T_{\text{light travel}} + T_{\text{int}} \approx 8\,\mathrm{s}$. Initial offsets could again be removed by shifting the time origins of the clock-associated nodes such that $\|\Delta T_i^j[0]\| \approx 0\ \forall i, j$.

This does not work if the clocks are allowed to drift in time with a rate that is large enough to reach $\approx 8\,\mathrm{s}$ over the course of the simulation. Realistic parameters measured for USOs for the GRAIL mission (which should be comparable in quality to once used for LISA) suggest that they can have an average fractional frequency drift of $y_d \approx 5 \times 10^{-16}\,\mathrm{s}^{-1}$, which corresponds to 25 s after 10 yr.

One possible algorithm to keep the physical times of all nodes synchronized is outlined in the following. It relies on having different counters $n_i$ for all three spacecraft (using a sampling rate of $f_{s,i}$ in the corresponding clock frame) as well as one counter $n$ to iterate

through physical time at a potentially different rate $f_s$ in the TCB frame. The main idea is to check at each physical time step $n$ if each of the clocks has reached its next time step. If it has, execute all associated nodes and increment the clock counter $n_i$. This is continued until $T_i[n_i]^{\mathrm{TCB}} > \tau[n]$ for all clocks, at which point $n$ is incremented and the loop continues.

$n_i \leftarrow 0$
**for** $n = 0$ to $T_{\mathrm{end}}$ **do** ▷ Main simulation loop
  **for** $i = 1, 2, 3$ **do** ▷ Iterate through all clocks
    **while** $\tau[n] > T_i[n_i]^{\mathrm{TCB}}$ **do** ▷ While last clock tick happened
      Execute all nodes associated to time $T_i[n]^{\mathrm{TCB}}$
      $n_i \leftarrow n_i + 1$
    **end while**
  **end for**
**end for**

By choosing $f_s > f_{s,i}$, we could make sure that for each physical tick $n$ there can be at most one clock tick $n_i$. This would reduce the inner **while** loop in the above algorithm to an **if** statement.

### A.4.5 USO and Clock Nodes

The current version of LISANode models clock errors as a simple additive phase error in the phasemeter measurements and neglects any other effect it has on the measurement times. There is one USO node per spacecraft providing a noise series, which represents the USO fractional frequency variations, including a deterministic frequency drift. This noise series is subtracted from all phasemeter measurements (scaled by the corresponding beatnote frequency) and added to the sideband laser beams frequency deviations (scaled by the modulation frequency).

This USO noise series must also be utilized in a clock node to calculate the time shown by the local clock at a given TCB tick. In order to simulate imperfect sampling times, such a clock node needs to provide the inverse of the clock times, *i.e.* $T_i[n_i]^{\mathrm{TCB}}$. This can either be achieved by an analytical estimate of the inverse or by first generating a series of clock times at TCB ticks and then interpolating this series to a desired clock tick value.

In the *sampling last* scheme, the times provided by this clock node can then be used in the phasemeter node to interpolate all measurements to the correct sampling times.

In the *sampling first* scheme, $T_i[n_i]^{\mathrm{TCB}}$ is already required for the synchronization algorithm outlined above. Thus, clock noise needs to be treated differently from other noises in this

scheme.

## A.5 Conclusion

### A.5.1 Summary

We presented in this document the main issues associated with the simulation of LISA's measurement chain, including clock errors. We proposed three simulations schemes circumventing the problems associated with the simulation of different time grids in LISANode. Two make use of interpolation while one replaces it by extrapolation. We then studied the impact of these different models on the simulation of the different subsystems, along with the amount of structural changes they imply for LISANode.

Preliminary analysis indicates that both schemes using interpolation could be valid. Further study is required to evaluate extrapolation as an alternative. One should note that the *sampling last* scheme would be much easier to implement in the current framework since it does not imply any changes of the scheduling algorithms. It also impacts fewer subsystems, thus making the task of estimating the associated errors more manageable.

### A.5.2 Recommendations

**It is therefore our recommendation to use the *sampling last* scheme for the moment. Any feedback from other work packages on subsystem requirements that would favor one of the schemes would be highly appreciated and might help refine this recommendation.**

# Appendix B

# LISANode Library

We give here the list of atomic nodes provided as part of the LISANode library. Atomic nodes are defined as header-only C++ subclasses of Node, and placed in their own file. Atomic nodes provided in the LISANode library are located under `lisanode/toolbox/nodes/` and organized by category.

## B.1 Math

This category defines elementary mathematical operations.

### B.1.1 Addition<T>

Compute the sum of two signals.

**Model**

$$\text{result}_n = \text{a}_n + \text{b}_n \,. \tag{B.1}$$

**Inputs**

- a (T), first signal.
- b (T), second signal.

**Outputs**

- result (T), sum of the two signals.

### B.1.2 Sum<T>

Compute the sum of an arbitrary number of signals.

**Model**

$$\text{result}_n = \sum_{k=1}^{\text{input\_count}} \text{inputs[k]}_n \,. \tag{B.2}$$

**Parameters**

- input_count (int), number of inputs.

**Inputs**

- inputs (vector<T>), vector of inputs.

**Outputs**

- result (T), sum of signals.

### B.1.3 LinearCombination<T>

Compute a linear combination of an arbitrary number of signals.

**Model**

$$\text{result}_n = \sum_{k=1}^{\text{input\_count}} \text{coeffs[k]}_n \times \text{inputs[k]}_n \,. \tag{B.3}$$

**Parameters**

- input_count (int), number of inputs.

**Inputs**

- inputs (vector<T>), vector of inputs.

- coeffs (std :: vector<double>), vector of coefficients.

**Outputs**

- result (T), linear combination of all inputs.

### B.1.4 Difference<T>

Compute the sum of two signals.

**Model**

$$\text{result}_n = \text{a}_n - \text{b}_n \,. \tag{B.4}$$

**Inputs**

- a (T), first signal.
- b (T), second signal.

**Outputs**

- result (T), difference of the two signals.

### B.1.5 Constant<T>

Return a constant value.

This node can be used to convert a parameter to a signal.

**Model**

$$\text{result}_n = \text{value} \,. \tag{B.5}$$

**Parameters**

- value (T), constant value.

**Outputs**

- result (T), constant value.

### B.1.6 Sign<T>

Return the signal of a signal.

The C++ function copysign(), defined in <cmath>, is used.

**Model**

$$\text{result}_n = \text{sign}(\text{input}_n)\,. \tag{B.6}$$

**Inputs**

- input (T), input signal.

**Outputs**

- result (T), sign of input as $+1$ or $-1$.

### B.1.7 Gain<T>

Multiply a signal by a constant gain.

**Model**

$$\text{result}_n = \text{gain} \times \text{input}_n\,. \tag{B.7}$$

**Parameters**

- gain (double), constant gain or multiplication factor.

**Inputs**

- input (T), input signal.

**Outputs**

- result (T), gained input.

### B.1.8 Abs<T>

Return the absolute value of a signal.

The C++ function abs(), defined in <cmath>, is used.

**Model**

$$\text{result}_n = |\text{input}_n| \,. \tag{B.8}$$

**Inputs**

- input (T), input signal.

**Outputs**

- result (T), absolute value of input.

### B.1.9 Product<T>

Compute the product of two signals.

**Model**

$$\text{result}_n = \text{a}_n \times \text{b}_n \,. \tag{B.9}$$

**Inputs**

- a (T), first signal.
- b (T), second signal.

**Outputs**

- result (T), product of the signals.

### B.1.10 Power<T>

Compute the mathematical power of a signal.

**Model**

$$\text{result}_n = \text{input}_n^{\text{exponent}} \,. \tag{B.10}$$

The C++ function pow(), defined in <cmath>, is used here.

**Parameters**

- exponent (double), constant exponent.

**Inputs**

- input (T), input signal.

**Outputs**

- result (T), power of the input.

### B.1.11 VariablePower<T>

Compute the integer and variable power of a signal.

**Model**

$$\text{result}_n = \text{input}_n{}^{\text{exponent}_n} . \tag{B.11}$$

The C++ function pow(), defined in <cmath>, is used here.

**Inputs**

- input (T), input signal.
- exponent (int), constant exponent.

**Outputs**

- result (T), power of the input.

### B.1.12 Expression<T>

Parse and compute a mathematical expression with multiple inputs.

This node takes as parameter a number of input names and a mathematical expression, which is function of these inputs and the current time t. The expression is parsed using the library exprtk and the result is computed.

Refer to `http://www.partow.net/programming/exprtk/index.html` for more info.

**Model**

$$\text{result}_n = \text{expression}\big(\text{input\_name}[0]_n, \ldots, \text{input\_name}[\text{input\_name.size}()]_n\big)\,. \tag{B.12}$$

**Parameters**

- expression (std :: string), mathematical expression.
- input_names (vector<string>), vector of input names.

**Inputs**

- inputs (map<string, T>), dictionary of inputs.

**Outputs**

- result (T), result of mathematical expression.

### B.1.13 Clip<T>

Clip signal between a minimum and maximum values.

**Model**

$$\text{result}_n = \max\big(\text{min}, \min\big(\text{max}, \text{input}_n\big)\big)\,. \tag{B.13}$$

**Parameters**

- min (T), minimal value.
- max (T), maximal value.

**Inputs**

- input (T), input signal.

**Outputs**

- result (T), clipped signal.

## B.2 Logic

This category defines elementary logical operations.

### B.2.1 Not

Compute logical negation (not).

**Model**

$$\text{result}_n = \neg \text{input}_n \,. \tag{B.14}$$

**Inputs**

- input (bool), input signal.

**Outputs**

- result (bool), negated input signal.

### B.2.2 And

Compute logical conjunction (and).

**Model**

$$\text{result}_n = \text{a}_n \wedge \text{b}_n \,. \tag{B.15}$$

**Inputs**

- a (bool), first signal.
- b (bool), second signal.

**Outputs**

- result (bool), conjunction of two signals.

### B.2.3 Or

Compute logical disjunction (or).

**Model**

$$\text{result}_n = \text{a}_n \vee \text{b}_n \,. \tag{B.16}$$

**Inputs**

- a (bool), first signal.
- b (bool), second signal.

**Outputs**

- result (bool), disjunction of two signals.

### B.2.4 Xor

Compute logical exclusive disjunction (xor).

**Model**

$$\text{result}_n = \text{a}_n \oplus \text{b}_n \,. \tag{B.17}$$

**Inputs**

- a (bool), first signal.
- b (bool), second signal.

**Outputs**

- result (bool), exclusive disjunction of two signals.

## B.3 Sampling

This category defines nodes used to adjust or modify the sampling frequency of downstream nodes.

### B.3.1 Dummy<T>

Does not change the signal, passthrough no-operation node.

This node is used in the former FPGA-like scheduling algorithm to increase latency of some nodes during graph analysis. Dummy nodes were automatically inserted in the simulation graph during graph analysis, and more specifically during latency balancing.

**Model**

$$\text{result}_n = \text{input}_n \,. \tag{B.18}$$

**Inputs**

- input (T), input signal.

**Outputs**

- result (T), output signal.

### B.3.2 Decimation<T>

RESAmple a signal using decimation.

Decimation takes only one sample every $n$ samples, where $n$ is the downsampling factor.

**Model**

$$\text{result}_n = \text{input}_n \,. \tag{B.19}$$

**Inputs**

- input (T), input signal.

**Outputs**

- result (T), decimated signal.

### B.3.3 HoldValue<T>

Upsample a signal holding previous known value.

**Model**

$$\text{result}_n = \text{input}_n \,. \tag{B.20}$$

**Inputs**

- input (T), input signal.

**Outputs**

- result (T), hold value.

### B.3.4 LastSamples<T>

Offer a way to access a number of last samples of a signal.

**Model**

$$\text{samples[k]}_n = \text{input}_{n+\text{sample\_count}-(k+1)} \,. \tag{B.21}$$

**Parameters**

- sample_count (int), number of samples to remember.

**Inputs**

- input (T), input signal.

**Outputs**

- samples (vector<T>), vector of last samples, most recent at the end.

### B.3.5 SlidingAverage<T>

Compute a moving average on a arbitrary number of last samples.

**Model**

$$\text{result}_n = \frac{1}{\text{sample\_count}} \sum_{k=0}^{\text{sample\_count}\,-\,1} \text{input}_{n-k} \,. \tag{B.22}$$

**Parameters**

- sample_count (int), number of samples to average.

**Inputs**

- input (T), input signal.

**Outputs**

- result (T), average of last samples.

## B.4 Delays

This category defines nodes that are used to delay a signal.

### B.4.1 IntegerDelay<T>

Delay a signal by a constant integer number of samples.

**Model**

$$\text{result}_n = \text{input}_{n-\text{delay}} \,. \tag{B.23}$$

**Parameters**

- delay (int), number of samples used as delay. Must be a positive integer.

**Inputs**

- input (T), input signal.

**Outputs**

- result (T), delayed signal.

### B.4.2 VariableIntegerDelay<T>

Delay a signal by a varying integer number of samples.

**Model**

$$\text{result}_n = \text{input}_{n-\text{delay}_n} . \tag{B.24}$$

**Parameters**

- max_delay (int), maximum delay, in number of samples. Must be a positive integer.

**Inputs**

- input (T), input signal.
- delay (int), delay, in number of samples. Must be a positive integer less than max_delay.

**Outputs**

- result (T), delayed signal.

### B.4.3 FractionalDelay<T>

Delay a signal by an arbitrary but constant delay using Lagrange interpolation.

We use the centered Lagrange interpolating polynomials, applied on past samples of the input signal, to compute a new value between two past samples. A high interpolation order increase the quality of the interpolation and allows to keep the high-frequency content of the signal, but simultaneously increase the computation time, and the minimum authorized delay.

The minimum authorized delay is defined by the number of input samples required in the Lagrange polynomials, at the right of the desired new sample. These input samples must exist, *i.e.* they must be at times smaller than the current time. Therefore, the minimum authorized delay is defined by

$$\text{min\_delay} = \frac{\text{order} + 1}{2\text{sampling\_frequency}} . \tag{B.25}$$

The expression for the Lagrange polynomials are extracted from [Hal18], equation (56), and are given in the model below.

**Model**

We first define the half point count $p = \frac{\text{order}+1}{2}$, which is a positive integer, the integer part of the delay $d = \text{ceil}(\text{delay} * \text{sampling\_frequency}) - 1$, and the fractional part of the delay $\epsilon = 1 + d - \text{delay} * \text{sampling\_frequency}$.

We can then define the following variables,

$$\text{A} = \frac{1}{h} \prod_{i=1}^{h-1} (1 + \frac{\epsilon}{i})(1 + \frac{1-\epsilon}{i}) \,, \tag{B.26}$$

$$\text{B} = 1 - \epsilon \,, \tag{B.27}$$

$$\text{C} = \epsilon \,, \tag{B.28}$$

$$\text{D} = \epsilon(1 - \epsilon) \,, \tag{B.29}$$

$$\text{E[j]} = (-1)^j \frac{(p-1)!}{(p-1-j)!} \frac{p!}{(p+j)!} \,, \tag{B.30}$$

$$\text{F[j]} = j + \epsilon \,, \tag{B.31}$$

$$\text{G[j]} = j + (1 - \epsilon) \,. \tag{B.32}$$

Then the model reads

$$\text{result}_n = \text{A} \left[ \text{B}\, \text{input}_{d+1} + \text{C}\, \text{input}_d + \text{D} \sum_{j=1}^{p-1} \text{E[j]} \left( \frac{\text{input}_{d+1+j}}{\text{F[j]}} + \frac{\text{input}_{d-j}}{\text{G[j]}} \right) \right] . \tag{B.33}$$

### Parameters

- delay (double), delay, in seconds. Must be greater than the minimum authorized delay min_delay.
- order (int), order of interpolation. Must be an odd positive integer.

### Inputs

- input (T), input signal.

### Outputs

- result (T), delayed signal.

### B.4.4 VariableFractionalDelay<T>

Delay a signal by an arbitrary and time-varying delay using Lagrange interpolation.

We use the centered Lagrange interpolating polynomials, applied on past samples of the input signal, to compute a new value between two past samples. A high interpolation order increase the quality of the interpolation and allows to keep the high-frequency content of the signal, but simultaneously increase the computation time, and the minimum authorized delay.

The Lagrange polynomial coefficients must be recalculated at each step, because the delays are time-varying. If you wish yo delay your signal by an arbitrary but constant delay, use the dedicated VariableDelay<T> node instead.

You must specify the maximum delay that will be used to clip the delay signal during the simulation. A high value allows for a larger dynamical range for the delays, but increase the memory usage. The minimum authorized delay is defined by the number of input samples required in the Lagrange polynomials, at the right of the desired new sample. These input samples must exist, *i.e.* they must be at times smaller than the current time. Therefore, the minimum authorized delay is defined by

$$\text{min\_delay} = \frac{\text{order} + 1}{2 \times \text{sampling\_frequency}} \,. \tag{B.34}$$

The delay signal is always clipped to the minimum and maximum authorized delays, in which case a warning is issued.

The expression for the Lagrange polynomials are extracted from [Hal18], equation (56), and are given in the model below.

**Model** We first define the half point count $p = \frac{\text{order}+1}{2}$, which is a positive integer, the integer part of the delay $d = \text{ceil}(\text{delay} * \text{sampling\_frequency}) - 1$, and the fractional part of the delay $\epsilon = 1 + d - \text{delay} * \text{sampling\_frequency}$.

We can then define the following variables,

$$\mathrm{A} = \frac{1}{h}\prod_{i=1}^{h-1}(1+\frac{\epsilon}{i})(1+\frac{1-\epsilon}{i})\,, \tag{B.35}$$

$$\mathrm{B} = 1-\epsilon\,, \tag{B.36}$$

$$\mathrm{C} = \epsilon\,, \tag{B.37}$$

$$\mathrm{D} = \epsilon(1-\epsilon)\,, \tag{B.38}$$

$$\mathrm{E[j]} = (-1)^j \frac{(p-1)!}{(p-1-j)!}\frac{p!}{(p+j)!}\,, \tag{B.39}$$

$$\mathrm{F[j]} = j+\epsilon\,, \tag{B.40}$$

$$\mathrm{G[j]} = j+(1-\epsilon)\,. \tag{B.41}$$

Then the model reads

$$\mathrm{result}_n = \mathrm{A}\left[\mathrm{B}\,\mathrm{input}_{d+1} + \mathrm{C}\,\mathrm{input}_d + \mathrm{D}\sum_{j=1}^{p-1}\mathrm{E[j]}\left(\frac{\mathrm{input}_{d+1+j}}{\mathrm{F[j]}} + \frac{\mathrm{input}_{d-j}}{\mathrm{G[j]}}\right)\right]. \tag{B.42}$$

### Parameters

- max_delay (double), maximum delay, in seconds. Must be greater than the minimum authorized delay min_delay.
- order (int), order of interpolation. Must be an odd positive integer.

### Inputs

- input (T), input signal.
- delay (double), delay, in seconds. Clipped to within [min_delay, max_delay].

### Outputs

- result (T), delayed signal.

### B.4.5 FarrowFractionalDelay<T>

### B.4.6 FarrowVariableFractionalDelay<T>

## B.5 Calculus

This category defines nodes that compute the time derivative and the integral of signals.

### B.5.1 Derivator<T>

Compute the time derivative of a signal using first-order difference equation.

**Model**

$$\text{result}_n = \text{sampling\_frequency}\big(\text{input}_n - \text{input}_{n-1}\big)\,. \tag{B.43}$$

**Inputs**

- input (T), input signal.

**Outputs**

- result (T), derivative of signal.

### B.5.2 Derivator<T>

Integrate a signal using first-order difference equation.

**Model**

$$\text{result}_n = \text{init\_value} + \frac{1}{\text{sampling\_frequency}} \sum_{k=0}^{n} \text{input}_k\,. \tag{B.44}$$

**Parameters**

- init_value (T), initial value.

**Inputs**

- input (T), input signal.

**Outputs**

- result (T), integral of signal.

## B.6 Generators

This category defines nodes that are used to generate deterministic signals.

### B.6.1 Sinus

Generate sinus signal.

**Model**

$$\text{result}_n = \text{offset} + \text{amplitude} \times \sin\left(\frac{2\pi}{\text{period}} t + \text{phase}\right). \tag{B.45}$$

**Parameters**

- period (double), sinus period, in seconds.
- phase (double), initial phase, in radians.
- amplitude (double), wave amplitude.
- offset (double), wave offset.

**Outputs**

- result (double), generated sinus wave.

### B.6.2 Ramp

Generate a linear function.

**Model**

$$\text{result}_n = \text{b} + \text{a} \times t\,. \tag{B.46}$$

**Parameters**

- a (double), ramp slope, in $s^{-}1$.
- b (double), initial value at $t = 0\,s$.

**Outputs**

- result (double), generated ramp.

### B.6.3 Step

Generate a step, or Heavyside function.

**Model**

$$\text{result}_n = \text{amplitude} \times \Theta(t)\,. \tag{B.47}$$

**Parameters**

- amplitude (double), amplitude of the step.

**Outputs**

- result (double), generated step.

### B.6.4 Pulse

Generate a pulse signal, or Dirac delta function.

**Model**

$$\text{result}_n = \text{amplitude} \times \delta(t)\,. \tag{B.48}$$

**Parameters**

- amplitude (double), amplitude of the pulse.

**Outputs**

- result (double), generated pulse.

### B.6.5 LogicalOscillator

Generate a logical signal oscillating between 0 and 1.

**Model**

**Parameters**

- period (int), period of oscillation, in number of samples.

**Outputs**

- result (bool), oscillating logical signal.

### B.6.6 CurrentTime

Return current time.

**Model**

$$\text{result}_n = t\,. \tag{B.49}$$

**Outputs**

- result (double), current time, in seconds.

## B.7 Random

This category gathers random number generators.

### B.7.1 NormalGenerator

Draw random numbers from a normal (Gaussian) distribution.

The standard library std::mt19937 class is used to generate random numbers.

**Model**

$$\text{prob}(\text{result}_n) = \frac{1}{\sqrt{2\pi}\text{standard\_deviation}} \exp\left(-\frac{(\text{result}_n - \text{mean})^2}{2\text{standard\_deviation}^2}\right). \tag{B.50}$$

**Parameters**

- mean (double), mean of the distribution.
- standard_deviation (double), standard deviation of the distribution.
- seed (int), random seed for reproducible results. Note that you must set random_seed to false for the seed to be taken into account.
- random_seed (bool), use random seed. If set to true the seed will be overridden by a random number.

**Outputs**

- result (double), generated number.

### B.7.2 UniformGenerator

Draw random numbers from a uniform distribution.

The standard library std::mt19937 class is used to generate random numbers.

**Model**

$$\text{prob}(\text{result}_n) = \frac{1}{\text{max} - \text{min}} \,. \tag{B.51}$$

**Parameters**

- min (double), minimum of the distribution.
- max (double), maximum of the distribution.
- seed (int), random seed for reproducible results. Note that you must set random_seed to false for the seed to be taken into account.
- random_seed (bool), use random seed. If set to true the seed will be overridden by a random number.

**Outputs**

- result (double), generated number.

### B.7.3 WhiteNoise

Generate a Gaussian white noise.

This node generates a Gaussian white noise for a given amplitude spectral density and sampling frequency. The noise samples are drawn from a zero-mean Gaussian distribution, such that the energy is evenly distributed in each frequency bin.

The standard library std::mt19937 class is used to generate random numbers.

#### Model

The amplitude spectral density is used to compute the standard deviation of the normal distribution

$$\sigma = \mathrm{asd}\sqrt{\frac{\mathrm{sampling\_frequency}}{2}}\,, \tag{B.52}$$

and we have the following statistical model for the noise, if enabled is true,

$$\mathrm{prob}(\,\mathrm{result}_n) = \frac{1}{\sqrt{2\pi}\sigma}\exp\left(-\frac{\mathrm{result}_n^2}{2\sigma^2}\right). \tag{B.53}$$

If enabled is false, then $\mathrm{result}_n = 0$.

#### Parameters

- enabled (bool), on-off switch for the noise.
- asd (double), amplitude spectral density, in Hz$^-$1.
- seed (int), seed used to initialize the sequence of random numbers. If the seed is set to its default value 0, a random seed is drawn instead. Setting it to another value allows for reproducible results.

#### Outputs

- result (double), generated noise.

### B.7.4 NonStationaryWhiteNoise

Generate a non-stationary Gaussian white noise.

This node generates a Gaussian white noise for a time-varying amplitude spectral density and sampling frequency. Because the generated signal is non-stationary, one cannot compute its spectral density.

The standard library std::mt19937 class is used to generate random numbers.

**Model**

The amplitude spectral density is used to compute the standard deviation of the normal distribution. Here, it is time-dependent so that we define a time series

$$\sigma_n = \text{asd}_n \sqrt{\frac{\text{sampling\_frequency}}{2}}\,, \tag{B.54}$$

and we have the following statistical model for the noise, if enabled is true,

$$\text{prob}(\text{result}_n) = \frac{1}{\sqrt{2\pi}\sigma_n} \exp\left(-\frac{\text{result}_n^2}{2\sigma_n^2}\right). \tag{B.55}$$

If enabled is false, then $\text{result}_n = 0$.

**Parameters**

- enabled (bool), on-off switch for the noise.
- seed (int), seed used to initialize the sequence of random numbers. If the seed is set to its default value 0, a random seed is drawn instead. Setting it to another value allows for reproducible results.

**Inputs**

- asd (double), time-dependent amplitude spectral density, in Hz$^-$1.

**Outputs**

- result (double), generated noise.

## B.8 Filters

This category defines digital filters.

### B.8.1 Filter<T>

Implement a digital filter.

Use an empty vector for feedback coefficients to implement a finite-impulse response (FIR) filter.

### Model

$$\text{result}_n = \sum_{k=0}^{\text{direct\_coeffs . size ()}} \text{direct\_coeffs [k]} \times \text{input}_{n-k} - \sum_{k=0}^{\text{feedback\_coeffs. size ()}} \text{feedback\_coeffs[k]} \times \text{input}_{n-k-1} \,. \tag{B.56}$$

Note the minus sign in front of the recursive (feedback) terms, and the fact that the first feedback coefficient is associated with $\text{input}_{n-1}$, and not $\text{input}_n$. This is because the associated discrete transfer function is

$$H(z) = \frac{\sum_{k=0}^{\text{direct\_coeffs . size ()}} \text{direct\_coeffs [k]}\, z^{-k}}{1 + \sum_{k=0}^{\text{feedback\_coeffs. size ()}} \text{feedback\_coeffs[k]}\, z^{-k-1}} \,. \tag{B.57}$$

### Parameters

- direct_coeffs (std :: vector<double>), vector of direct coefficients.
- feedback_coeffs (std :: vector<double>), vector of recursive coefficients.

### Inputs

- input (T), input signal.

### Outputs

- result (T), filtered signal.

### B.8.2 EllipticFilter

### B.8.3 PinkFilter

### B.8.4 KaiserFilter

## B.9 I/O

This category defines nodes that can read or write data. They enable an interface between LISANode and other external tools.

### B.9.1 WriteText<T>

Write a signal to text file, using ASCII encoding.

In particular, this node is automatically added and connected by LISANode to every published outputs, so that they are written to file as the simulation products.

**Parameters**

- path (std :: string), absolute or relative path to text file.
- print_time (bool), whether a first column with timestamps should be printed.
- precision (int), number of printed decimals.

**Inputs**

- input (T), input signal.

### B.9.2 WriteStream<T>

Insert a signal into a stream, such as the standard output.

Use this node with standard output for debugging.

**Parameters**

- stream (std :: ostream), pointer to stream, default to standard output.
- print_name (bool), whether name of the node should be printed.
- print_time (bool), whether a first column with timestamps should be printed.
- precision (int), number of printed decimals.

**Inputs**

- input (T), input signal.

### B.9.3 ReadText<T>

Read a signal from text file, encoded in ASCII.

**Parameters**

- path (std :: string), absolute or relative path to text file.
- column_count (int), number of columns in the text file.
- header_count (int), number of header lines to be ignored.
- precision (int), number of printed decimals.

**Outputs:**

- data (vector<T>), read data, as a vector of columns.

# Appendix C

# LISA Simulation Graphs and Nodes

We give here the documentation for the LISA-specific simulation graphs and atomic nodes.

Simulation graphs are defined as Python subclasses of Graph, and placed in various files under `/lisanode/lisa/`. See section 3.2.1 for more information about the architecture of the project. Atomic nodes are defined as header-only C++ subclasses of Node, and placed in their own file. Atomic nodes specific to LISA are located under `lisanode/toolbox/nodes/lisa/`.

## C.1 Instrumental Subsystems

The module `instrument.py` defines graphs for the main instrument systems and subsystems, including the optical bench, interferometer, phasemeter, on-board computer, spacecraft, laser links, and most importantly, the high-level graph for LISA.

### C.1.1 LISA

Simulate the LISA constellation.

The measurements are output at the frequency LOW_SAMPLING_FREQ (in Hz, defined in the simulation configuration), and the physics is simulated at HIGH_SAMPLING_FREQ (in Hz). The orbits are read or simulated depending on the configuration option ORBIT_TYPE, at a sampling frequency of ORBIT_SAMPLING_FREQ (in Hz).

PUBLISH_MEASUREMENTS and PUBLISH_TRAVEL_TIMES configuration options are used

to enable or disable respectively the publication of the all interferometric measurements and the estimated light travel times.

**Model**

*C.f.* section 3.2.2.

**Parameters**

- Laser Noises
  - lasernoise_on_off (int), on/off switch for laser frequency noise, must be 0 or 1.
  - laser_asd1 (double), laser noise ASD of MOSA 1, in $s/\sqrt{Hz}$.
  - laser_asd1_p (double), laser noise ASD of MOSA 1', in $s/\sqrt{Hz}$.
  - laser_asd2 (double), laser noise ASD of MOSA 2, in $s/\sqrt{Hz}$.
  - laser_asd2_p (double), laser noise ASD of MOSA 2', in $s/\sqrt{Hz}$.
  - laser_asd3 (double), laser noise ASD of MOSA 3, in $s/\sqrt{Hz}$.
  - laser_asd3_p (double), laser noise ASD of MOSA 3', in $s/\sqrt{Hz}$.
  - laser_seed1 (int), seed for generation of random samples for laser noise of MOSA 1, default to 0 (a seed is randomly chosen when the simulation starts).
  - laser_seed1_p (int), seed for generation of random samples for laser noise of MOSA 1', default to 0 (a seed is randomly chosen when the simulation starts).
  - laser_seed2 (int), seed for generation of random samples for laser noise of MOSA 2, default to 0 (a seed is randomly chosen when the simulation starts).
  - laser_seed2_p (int), seed for generation of random samples for laser noise of MOSA 2', default to 0 (a seed is randomly chosen when the simulation starts).
  - laser_seed3 (int), seed for generation of random samples for laser noise of MOSA 3, default to 0 (a seed is randomly chosen when the simulation starts).
  - laser_seed3_p (int), seed for generation of random samples for laser noise of MOSA 3', default to 0 (a seed is randomly chosen when the simulation starts).

- Readout Noises
  - readoutnoise_on_off (int), on/off switch for readout noise, must be 0 or 1.
- Optical Noises
  - opticalnoise_on_off (int), on/off switch for optical noise, must be 0 or 1.
- Test-mass Acceleration Noises in GRS
  - accelnoise_on_off (int), on/off switch for test-mass acceleration noise, must be 0 or 1.
- Clock noises
  - usonoise_on_off (int), on/off switch for USO frequency fluctuations and drift.
  - uso_asd (double), ASD of the USO flicker noise, in fractional frequency deviation $/\sqrt{\text{Hz}}$.
  - uso_seed1 (int), seed for generation of random samples for USO noise for spacecraft 1, default to 0 (random seed).
  - uso_seed2 (int), seed for generation of random samples for USO noise for spacecraft 2, default to 0 (random seed).
  - uso_seed3 (int), seed for generation of random samples for USO noise for spacecraft 3, default to 0 (random seed).
- Absolute Ranging Errors
  - rangingnoise_on_off (int), on/off switch for absolute ranging error, must be 0 or 1.
  - ranging_systematic (double), constant systematic error on travel time estimation, in s.
  - ranging_asd: amplitude spectral density of the error on travel times, in $\text{s}/\sqrt{\text{Hz}}$.
- Linear Armlengths (only applies when using linearly-evolving armlengths, *i.e.* when ORBIT_TYPE = 'linear_armlengths')

  - L1 (double), armlength 1 at initial time, in m.
  - L2 (double), armlength 2 at initial time, in m.
  - L3 (double), armlength 3 at initial time, in m.
  - dL1 (double), armlength 1 first time derivative, in m/s.
  - dL2 (double), armlength 2 first time derivative, in m/s.
  - dL3 (double), armlength 3 first time derivative, in m/s.

- Interpolations

  - order (int), interpolation order for simulating beam propagation, must be an odd integer greater or equal to 1.

**Inputs**

- Beatnote Frequencies

  - sci_f1 (double), science beatnote frequencies in MOSA 1, in MHz.
  - sci_f1_p (double), science beatnote frequencies in MOSA 1', in MHz.
  - sci_f2 (double), science beatnote frequencies in MOSA 2, in MHz.
  - sci_f2_p (double), science beatnote frequencies in MOSA 2', in MHz.
  - sci_f3 (double), science beatnote frequencies in MOSA 3, in MHz.
  - sci_f3_p (double), science beatnote frequencies in MOSA 3', in MHz.
  - ref_f1 (double), reference and test-mass beatnote frequencies in MOSA 1, in MHz.
  - ref_f1_p (double), reference and test-mass beatnote frequencies in MOSA 1', in MHz.
  - ref_f2 (double), reference and test-mass beatnote frequencies in MOSA 2, in MHz.
  - ref_f2_p (double), reference and test-mass beatnote frequencies in MOSA 2', in MHz.

  - ref_f3 (double), reference and test-mass beatnote frequencies in MOSA 3, in MHz.
  - ref_f3_p (double), reference and test-mass beatnote frequencies in MOSA 3', in MHz.
  - sb_f1 (double), sideband beatnote frequencies in MOSA 1, in MHz.
  - sb_f1_p (double), sideband beatnote frequencies in MOSA 1', in MHz.
  - sb_f2 (double), sideband beatnote frequencies in MOSA 2, in MHz.
  - sb_f2_p (double), sideband beatnote frequencies in MOSA 2', in MHz.
  - sb_f3 (double), sideband beatnote frequencies in MOSA 3, in MHz.
  - sb_f3_p (double), sideband beatnote frequencies in MOSA 3', in MHz.

- Clock Noises
  - uso_drift1 (double), fractional frequency time drift of USO onboard spacecraft 1, in /s.
  - uso_drift2 (double), fractional frequency time drift of USO onboard spacecraft 2, in /s.
  - uso_drift3 (double), fractional frequency time drift of USO onboard spacecraft 3, in /s.

**Outputs**

- Measurement Channels (only applied if PUBLISH_MEASUREMENTS = True)
  - s1 (double), science interferometric measurement in MOSA 1, in fractional frequency deviation.
  - s1_p (double), science interferometric measurement in MOSA 1', in fractional frequency deviation.
  - s2 (double), science interferometric measurement in MOSA 2, in fractional frequency deviation.
  - s2_p (double), science interferometric measurement in MOSA 2', in fractional

frequency deviation.

- s3 (double), science interferometric measurement in MOSA 3, in fractional frequency deviation.
- s3_p (double), science interferometric measurement in MOSA 3', in fractional frequency deviation.
- sb1 (double), sideband interferometric measurement in MOSA 1, in fractional frequency deviation.
- sb1_p (double), sideband interferometric measurement in MOSA 1', in fractional frequency deviation.
- sb2 (double), sideband interferometric measurement in MOSA 2, in fractional frequency deviation.
- sb2_p (double), sideband interferometric measurement in MOSA 2', in fractional frequency deviation.
- sb3 (double), sideband interferometric measurement in MOSA 3, in fractional frequency deviation.
- sb3_p (double), sideband interferometric measurement in MOSA 3', in fractional frequency deviation.
- tau1 (double), reference interferometric measurement in MOSA 1, in fractional frequency deviation.
- tau1_p (double), reference interferometric measurement in MOSA 1', in fractional frequency deviation.
- tau2 (double), reference interferometric measurement in MOSA 2, in fractional frequency deviation.
- tau2_p (double), reference interferometric measurement in MOSA 2', in fractional frequency deviation.
- tau3 (double), reference interferometric measurement in MOSA 3, in fractional frequency deviation.
- tau3_p (double), reference interferometric measurement in MOSA 3', in fractional

frequency deviation.

- epsilon1 (double), test-mass interferometric measurement in MOSA 1, in fractional frequency deviation.
- epsilon1_p (double), test-mass interferometric measurement in MOSA 1', in fractional frequency deviation.
- epsilon2 (double), test-mass interferometric measurement in MOSA 2, in fractional frequency deviation.
- epsilon2_p (double), test-mass interferometric measurement in MOSA 2', in fractional frequency deviation.
- epsilon3 (double), test-mass interferometric measurement in MOSA 3, in fractional frequency deviation.
- epsilon3_p (double), test-mass interferometric measurement in MOSA 3', in fractional frequency deviation.

- Absolute Ranging Estimates (only applies if PUBLISH_TRAVEL_TIMES = True)
  - tt1 (double), estimated travel times along link 1, in s.
  - tt1_p (double), estimated travel times along link 1', in s.
  - tt2 (double), estimated travel times along link 2, in s.
  - tt2_p (double), estimated travel times along link 2', in s.
  - tt3 (double), estimated travel times along link 3, in s.
  - tt3_p (double), estimated travel times along link 3', in s.

### C.1.2 Spacecraft

Contains two MOSA units, as USO, a phasemeter, and an onboard computer. See section 3.2.2.

The measurements are output at the frequency LOW_SAMPLING_FREQ (in Hz, defined in the simulation configuration), and the physics is simulated at HIGH_SAMPLING_FREQ (in

Hz).

**Model**

*C.f.* section 3.2.2 and section 3.4.1.

**Parameters**

- Laser Noises
  - lasernoise_on_off (int), on/off switch for laser frequency noise, must be 0 or 1.
  - laser_asd (double), laser noise ASD of unprimed MOSA, in $\mathrm{s}/\sqrt{\mathrm{Hz}}$.
  - laser_asd_p (double), laser noise ASD of primed MOSA, in $\mathrm{s}/\sqrt{\mathrm{Hz}}$.
  - laser_seed (int), seed for generation of random samples for laser noise of unprimed MOSA, default to 0 (a seed is randomly chosen when the simulation starts).
  - laser_seed_p (int), seed for generation of random samples for laser noise of primed MOSA, default to 0 (a seed is randomly chosen when the simulation starts).
- Readout Noises
  - readoutnoise_on_off (int), on/off switch for readout noise, must be 0 or 1.
- Optical Noises
  - opticalnoise_on_off (int), on/off switch for optical noise, must be 0 or 1.
- Test-mass Acceleration Noises in GRS
  - accelnoise_on_off (int), on/off switch for test-mass acceleration noise, must be 0 or 1.
- Clock noises
  - usonoise_on_off (int), on/off switch for USO frequency fluctuations and drift.
  - uso_asd (double), ASD of the USO flicker noise, in fractional frequency deviation $/\sqrt{\mathrm{Hz}}$.

  - uso_seed (int), seed for generation of random samples for USO noise, default to 0 (random seed).

**Inputs**

- Incoming Laser Beams
  - incoming_laser (double), main signal from distant spacecraft to unprimed MOSA, in fractional frequency deviations.
  - incoming_laser_p (double), main signal from distant spacecraft to primed MOSA, in fractional frequency deviations.
  - incoming_sb (double), sideband signal from distant spacecraft to unprimed MOSA, in fractional frequency deviations.
  - incoming_sb_p (double), sideband signal from distant spacecraft to primed MOSA, in fractional frequency deviations.
- Beatnote Frequencies
  - sci_f (double), science beatnote frequencies in unprimed MOSA, in MHz.
  - sci_f_p (double), science beatnote frequencies in primed MOSA, in MHz.
  - sb_f (double), sideband beatnote frequencies in unprimed MOSA, in MHz.
  - sb_f_p (double), sideband beatnote frequencies in primed MOSA, in MHz.
  - tm_f (double), test-mass beatnote frequencies in unprimed MOSA, in MHz.
  - tm_f_p (double), test-mass beatnote frequencies in primed MOSA, in MHz.
  - ref_f (double), reference beatnote frequencies in unprimed MOSA, in MHz.
  - ref_f_p (double), reference beatnote frequencies in primed MOSA, in MHz.
- Clock Noises
  - uso_drift (double), USO fractional frequency drift with time, in /s.

**Outputs**

- Measurement Channels
  - s (double), science interferometric measurement in unprimed MOSA, in fractional frequency deviation.
  - s_p (double), science interferometric measurement in primed MOSA, in fractional frequency deviation.
  - sb (double), sideband interferometric measurement in unprimed MOSA, in fractional frequency deviation.
  - sb_p (double), sideband interferometric measurement in primed MOSA, in fractional frequency deviation.
  - tau (double), reference interferometric measurement in unprimed MOSA, in fractional frequency deviation.
  - tau_p (double), reference interferometric measurement in primed MOSA, in fractional frequency deviation.
  - epsilon (double), test-mass interferometric measurement in unprimed MOSA, in fractional frequency deviation.
  - epsilon_p (double), test-mass interferometric measurement in primed MOSA, in fractional frequency deviation.

- Outgoing Laser Beams
  - outgoing_laser (double), main signal from unprimed MOSA to distance spacecraft, in fractional frequency deviations.
  - outgoing_laser_p (double), main signal from primed MOSA to distance spacecraft, in fractional frequency deviations.
  - outgoing_sb (double), sideband signal from unprimed MOSA to distance spacecraft, in fractional frequency deviations.
  - outgoing_sb_p (double), sideband signal from primed MOSA to distance spacecraft, in fractional frequency deviations.

### C.1.3 MOSA

Movable optical sub-assembly. Only hosts one optical bench, receives laser beams from the distant and adjacent MOSAs, and send the local laser beam to the distant MOSA.

The measurements are output at the frequency LOW_SAMPLING_FREQ (in Hz, defined in the simulation configuration), and the physics is simulated at HIGH_SAMPLING_FREQ (in Hz).

**Model**

*C.f.* section 3.4.1.

**Parameters**

- Laser Noises
  - lasernoise_on_off (int), on/off switch for laser frequency noise, must be 0 or 1.
  - laser_asd (double), laser noise ASD, in $\mathrm{s}/\sqrt{\mathrm{Hz}}$.
  - laser_seed (int), seed for generation of random samples for laser noise, default to 0 (a seed is randomly chosen when the simulation starts).
- Other Noises
  - readoutnoise_on_off (int), on/off switch for readout noise, must be 0 or 1.
  - opticalnoise_on_off (int), on/off switch for optical noise, must be 0 or 1.
  - accelnoise_on_off (int), on/off switch for test-mass acceleration noise, must be 0 or 1.

**Inputs**

- Incoming Laser Beams
  - distant_beam (double), main signal from distant optical bench, in fractional frequency deviations.
  - distant_sb (double), sideband signal from distant optical bench, in fractional frequency deviations.

  - adjacent_beam (double), main signal from twin optical bench hosted in the same spacecraft, in fractional frequency deviations.

- Beatnote Frequencies

  - sci_f (double), beatnote frequency for the science interferometer, in MHz.
  - sb_f (double), beatnote frequency for the sideband interferometer, in MHz.
  - tm_f (double), beatnote frequency for the test-mass interferometer, in MHz.
  - ref_f (double), beatnote frequency for the reference interferometer, in MHz.

- Clock Noises

  - modulation_factor (int), sideband scaling for the sideband.
  - uso_noise (double), USO noise used for the sideband, in normalized fractional frequency deviation.

**Outputs**

- Measurement Channels

  - s (double), data from science interferometer, in fractional frequency deviation.
  - sb (double), data from sideband interferometer, in fractional frequency deviation.
  - tau (double), data from reference interferometer, in fractional frequency deviation.
  - epsilon (double), data from test-mass interferometer, in fractional frequency deviation.

- Outgoing Laser Beams

  - beam_to_distant (double), main signal from local laser to distant optical bench, in fractional frequency deviations.
  - sb_to_distant (double), sideband signal from local laser to distant optical bench, in fractional frequency deviations.

- beam_to_adjacent (double), main signal from local laser to adjacent optical bench.

### C.1.4 OpticalBench

LISA optical bench. The optical bench defines a local laser, and feed four interferometers with the beam from the local laser, the adjacent and the remote optical benches. The fourth interferometer use the sideband signal from the distant optical bench and the local clock.

The physics is simulated at HIGH_SAMPLING_FREQ (in Hz).

**Model**

*C.f.* section 3.4.1.

**Parameters**

- Laser Noises
  - lasernoise_on_off (int), on/off switch for laser frequency noise, must be 0 or 1.
  - laser_asd (double), laser noise ASD, in $\mathrm{s}/\sqrt{\mathrm{Hz}}$.
  - laser_seed (int), seed for generation of random samples for laser noise, default to 0 (a seed is randomly chosen when the simulation starts).
- Other Noises
  - readoutnoise_on_off (int), on/off switch for readout noise, must be 0 or 1.
  - opticalnoise_on_off (int), on/off switch for optical noise, must be 0 or 1.
  - accelnoise_on_off (int), on/off switch for test-mass acceleration noise, must be 0 or 1.

**Inputs**

- Incoming Laser Beams
  - distant_beam (double), main signal from distant optical bench, in fractional frequency deviations.

  - distant_sb (double), sideband signal from distant optical bench, in fractional frequency deviations.
  - adjacent_beam (double), main signal from twin optical bench hosted in the same spacecraft, in fractional frequency deviations.

- Beatnote Frequencies
  - sci_f (double), beatnote frequency for the science interferometer, in MHz.
  - sb_f (double), beatnote frequency for the sideband interferometer, in MHz.
  - tm_f (double), beatnote frequency for the test-mass interferometer, in MHz.
  - ref_f (double), beatnote frequency for the reference interferometer, in MHz.

- Clock Noises
  - modulation_factor (int), sideband scaling for the sideband.
  - uso_noise (double), USO noise used for the sideband, in normalized fractional frequency deviation.

**Outputs**

- Interferometric Optical Signals
  - s (double), data from science interferometer, in fractional frequency deviation.
  - sb (double), data from sideband interferometer, in fractional frequency deviation.
  - tau (double), data from reference interferometer, in fractional frequency deviation.
  - epsilon (double), data from test-mass interferometer, in fractional frequency deviation.

- Outgoing Laser Beams
  - beam_to_distant (double), main signal from local laser to distant optical bench, in fractional frequency deviations.

  - sb_to_distant (double), sideband signal from local laser to distant optical bench, in fractional frequency deviations.
  - beam_to_adjacent (double), main signal from local laser to adjacent optical bench.

### C.1.5 SingleSignalOMS

Add the optical metrology system noise contributions for a single signal.

This node contains an interferometer, and sums to add noises to both incoming beams, as well as the resulting beatnote signal. It also contains an OMSDisplacementNoise, adding contributions such as shot noise after the beatnote has been formed.

The physics is simulated at HIGH_SAMPLING_FREQ (in Hz).

#### Model

*C.f.* section 3.4.

#### Parameters

- omsnoise_on_off (int), on/off switch for OMS noise, must be 0 or 1.

#### Inputs

- beam1 (double), first beam, in fractional frequency deviation.
- beam2 (double), second beam, in fractional frequency deviation.
- unallocated_noise (double), different noise contributions from [LIS18b], see documentation for UnallocatedNoise graph, in fractional frequency deviation.
- f (double), signed beatnote frequency, in MHz.
- Acceleration, for test-mass interferometer only
  - accel_noise (double), test-mass acceleration noise, in fractional frequency deviation.

#### Outputs

- result (double), beatnote, in fractional frequency variations

### C.1.6 Interferometer

Define a simple interferometer. This interferometer computes the measured normalized heterodyne beatnote frequency from the fractional frequency deviations of the two input signals, adjusting the sign according to the beatnote polarity.

This node contains an interferometer, and sums to add noises to both incoming beams, as well as the resulting beatnote signal. It also contains an OMSDisplacementNoise, adding contributions such as shot noise after the beatnote has been formed.

The physics is simulated at HIGH_SAMPLING_FREQ (in Hz).

#### Model

*C.f.* section 3.4.2.

$$\text{result} = \text{sign}(\text{f}) \times (\text{a} - \text{b})\,. \tag{C.1}$$

#### Inputs

- f (double), signed beatnote frequency, in MHz.
- a (double), first optical signal, in relative relative frequency shift.
- b (double),second optical signal, in relative relative frequency shift.

#### Outputs

- result (double), signed beatnote, in fractional frequency variations

### C.1.7 Phasemeter

Model timing error in the measurements by interpolation to times provided by clock noise. It currently only adds to the optical signals an error due to USO noise, scaled by beatnote frequency. This yields the high frequency measurement signals.

The physics is simulated at HIGH_SAMPLING_FREQ (in Hz).

#### Model

*C.f.* section 3.5.1 and chapter 6.

#### Inputs

- Interferometric Optical Signals
  - sci_ifo (double), science interferometric measurement from unprimed MOSA, in fractional frequency deviation.
  - sci_ifo_p (double), science interferometric measurement from primed MOSA, in fractional frequency deviation.
  - sb_ifo (double), sideband interferometric measurement from unprimed MOSA, in fractional frequency deviation.
  - sb_ifo_p (double), sideband interferometric measurement from primed MOSA, in fractional frequency deviation.
  - ref_ifo (double), reference interferometric measurement from unprimed MOSA, in fractional frequency deviation.
  - ref_ifo_p (double), reference interferometric measurement from primed MOSA, in fractional frequency deviation.
  - tm_ifo (double), test-mass interferometric measurement from unprimed MOSA, in fractional frequency deviation.
  - tm_ifo_p (double), test-mass interferometric measurement from primed MOSA, in fractional frequency deviation.
- Beatnote Frequencies
  - sci_f (double), science beatnote frequencies in unprimed MOSA, in MHz.
  - sci_f_p (double), science beatnote frequencies in primed MOSA, in MHz.
  - sb_f (double), sideband beatnote frequencies in unprimed MOSA, in MHz.
  - sb_f_p (double), sideband beatnote frequencies in primed MOSA, in MHz.
  - tm_f (double), test-mass beatnote frequencies in unprimed MOSA, in MHz.
  - tm_f_p (double), test-mass beatnote frequencies in primed MOSA, in MHz.
  - ref_f (double), reference beatnote frequencies in unprimed MOSA, in MHz.

  - ref_f_p (double), reference beatnote frequencies in primed MOSA, in MHz.

- Clock Noises

  - uso_noise (double), USO noise, in normalized fractional frequency deviation.

**Outputs**

- High Frequency Measurement Channels

  - hf_sci (double), high frequency science signal, in fractional frequency deviation.
  - hf_sci_p (double), high frequency science signal, in fractional frequency deviation.
  - hf_sb (double), high frequency sideband signal, in fractional frequency deviation.
  - hf_sb_p (double), high frequency sideband signal, in fractional frequency deviation.
  - hf_ref (double), high frequency reference signal, in fractional frequency deviation.
  - hf_ref_p (double), high frequency reference signal, in fractional frequency deviation.
  - hf_tm (double), high frequency test-mass signal, in fractional frequency deviation.
  - hf_tm_p (double), high frequency test-mass signal, in fractional frequency deviation.

### C.1.8 OnboardComputer

Define a simple onboard computer. This version takes in the measurement signals from the phasemeter, applies an antialiasing filter, and downsamples each of these signals.

The measurements generated by the phasemeter have the sampling frequency of HIGH_SAMPLING_FREQ (in Hz, defined in the simulation configuration), and are downsampled to HIGH_SAMPLING_FREQ (in Hz).

**Model**

*C.f.* section 3.5.5.

**Inputs**

- High Frequency Measurement Channels
  - hf_sci (double), high frequency science signal, in fractional frequency deviation.
  - hf_sci_p (double), high frequency science signal, in fractional frequency deviation.
  - hf_sb (double), high frequency sideband signal, in fractional frequency deviation.
  - hf_sb_p (double), high frequency sideband signal, in fractional frequency deviation.
  - hf_ref (double), high frequency reference signal, in fractional frequency deviation.
  - hf_ref_p (double), high frequency reference signal, in fractional frequency deviation.
  - hf_tm (double), high frequency test-mass signal, in fractional frequency deviation.
  - hf_tm_p (double), high frequency test-mass signal, in fractional frequency deviation.

**Outputs**

- Measurement Channels
  - s (double), low frequency science signal, in fractional frequency deviation.
  - s_p (double), low frequency science signal, in fractional frequency deviation.
  - sb (double), low frequency sideband signal, in fractional frequency deviation.
  - sb_p (double), low frequency sideband signal, in fractional frequency deviation.
  - tau (double), low frequency reference signal, in fractional frequency deviation.
  - tau_p (double), low frequency reference signal, in fractional frequency deviation.
  - epsilon (double), low frequency test-mass signal, in fractional frequency deviation.
  - epsilon_p (double), low frequency test-mass signal, in fractional frequency deviation.

### C.1.9 AntiAliasingDecimation

Filter and decimate a single measurement signal.

We filter the signal using a finite impulse response filter, designed using a Kaiser window and the following specifications: corner frequencies at 10 % and 45 % the decimated (low) sampling frequency, a minimum attenuation in the stopband of 240 dB, and a maximum attenuation of 0.1 dB in the passband. Then the signal is downsampled using a simple decimation process.

The measurements generated by the phasemeter have the sampling frequency of HIGH_SAMPLING_FREQ (in Hz, defined in the simulation configuration), and are downsampled to HIGH_SAMPLING_FREQ (in Hz).

#### Model

*C.f.* section 3.5.5

#### Inputs

- input (double), input signal, in relative frequency deviation.

#### Outputs

- result (double), filtered and decimated signal, in relative frequency deviation.

### C.1.10 LaserNoise

## C.2 Noise Sources

The module `noises.py` defines graphs for the instrumental noise sources. These graphs generate the samples for the each noise time series used for the instrumental simulation.

### C.2.1 LaserNoise

Simulate a noisy laser beam.

Generates a white noise series using an amplitude spectral density of $10^{-13}/\sqrt{\text{Hz}}$, which corresponds to $28.2\,\text{Hz}/\sqrt{\text{Hz}}$ in terms of absolute frequency stability. This is the state-of-the-art performance for a space-qualified laser source [**?**].

The noise samples are generated at a sampling frequency of HIGH_SAMPLING_FREQ (in Hz, defined in the simulation configuration).

**Model**

White noise with an amplitude spectral density of $10^{-13}\,/\sqrt{\text{Hz}}$.

**Parameters**

- on_off (int), on/off switch for laser frequency noise, must be 0 or 1.
- asd (double), amplitude spectral density for laser frequency shift noise, in $/\sqrt{\text{Hz}}$.
- seed (int), seed for generation of random samples, default to 0 (a seed is randomly chosen when the simulation starts).

**Outputs**

- **beam** (double), relative frequency deviation of the laser beam.

### C.2.2 TestMassAccelerationNoise

Test-mass acceleration noise.

The acceleration noise is built from two white noise signals and infinite impulse response filters.

The noise samples are generated at a sampling frequency of HIGH_SAMPLING_FREQ (in Hz, defined in the simulation configuration).

**Model**

The test-mass acceleration noise is given by its PSD

$$S_{\text{result}}(f) = A^2\left[1 + \left(\frac{f_{\text{knee}}}{f}\right)^2\right]. \tag{C.2}$$

The values of $A$ and $f_{\text{knee}}$ are taken from [LIS18b],

$$A = 2.4 \times 10^{-15}\,\text{m/s}^2/\sqrt{\text{Hz}}, \quad f_{\text{knee}} = 0.4 \times 10^{-3}\,\text{Hz}\,. \tag{C.3}$$

The generated noise accounts for the beam reflection onto the test mass. Thus, it is scaled by another factor of 2 compared to the definition above.

We whiten the noise at below $f_{\text{sat}} = 10^{-14}\,\text{Hz}$, to prevent numerical overflows. We neglect the high-frequency components given in [LIS18b], because they are far smaller than the optical metrology displacement noise.

**Parameters**

- on_off (int), on/off switch for test-mass acceleration noise, must be 0 or 1.

**Outputs**

- result (double), test-mass acceleration noise, in relative frequency deviation.

### C.2.3 UnallocatedNoise

Sum of different noise contributions from [LIS18b].

Its amplitude corresponds to the sum of various noise contributions in [LIS18b], such as thermo-mechanical coupling, spacecraft-IFO coupling, and unallocated noises.

A clear naming and definition of these noises remains to be found. Some of them need better, dedicated models.

The noise samples are generated at a sampling frequency of HIGH_SAMPLING_FREQ (in Hz, defined in the simulation configuration).

**Model**

This is a white noise which in displacement (in meters), with a constant amplitude spectral density denoted $\text{ASD}_m$. Therefore, the amplitude spectral density $\text{ASD}_y$ of the noise expressed as a relative frequency deviation (dimensionless) is proportional to $f$, and given by

$$\text{ASD}_y(f) = \frac{2\pi}{c} \times \text{ASD}_m \times f\,. \tag{C.4}$$

The various contributions, and therefore the level of this noise, depends on the type of interferometer. The type of interferometer is passed as an argument when one creates an instance of this graph:

- sci for the science and sideband interferometers, contains thermo-mechanical noise, and TDI errors in a single link (to be removed), so that $\text{ASD}_m = 5 \times 10^{-12}\,\text{m}$.

- tm for the test-mass interferometer, contains spacecraft-interferometer cross-coupling noise, so that $\mathrm{ASD}_m = 4.24 \times 10^{-12}\,\mathrm{m}$.
- ref for the reference interferometer, contains the unallocated OMS contingency, so that $\mathrm{ASD}_m = 2 \times 10^{-12}\,\mathrm{m}$.

**Parameters**

- on_off (int), on/off switch for unallocated noise, must be 0 or 1.

**Outputs**

- result (double), unallocated noise, in relative frequency deviation.

### C.2.4 OMSDisplacementNoise

Optical metrology displacement noise at photodiode.

Its amplitude corresponds to the overall allocation for the LISA OMS displacement noise in [LIS18b], at each of the interferometers.

The noise samples are generated at a sampling frequency of HIGH_SAMPLING_FREQ (in Hz, defined in the simulation configuration).

**Model**

This is a white noise which in displacement (in meters), with a constant amplitude spectral density denoted $\mathrm{ASD}_m$. Therefore, the amplitude spectral density $\mathrm{ASD}_y$ of the noise expressed as a relative frequency deviation (dimensionless) is proportional to $f$, and given by

$$\mathrm{ASD}_y(f) = \frac{2\pi}{c} \times \mathrm{ASD}_m \times f\,. \tag{C.5}$$

The type of interferometer is passed as an argument when one creates an instance of this graph:

- sci for the science interferometer, contains the long-arm noise, so that $\mathrm{ASD}_m = 6.35 \times 10^{-12}\,\mathrm{m}$.
- sb for the sideband interferometer, contains the long-arm noise rescaled by $\sqrt{0.85/0.15}$ to account for different beam powers, so that $\mathrm{ASD}_m = 1.51 \times 10^{-12}\,\mathrm{m}$.

- tm for the test-mass interferometer, contains test-mass IFO noise, so that $\mathrm{ASD}_m = 1.42 \times 10^{-12}\,\mathrm{m}$.
- ref for the reference interferometer, contains the reference IFO noise, so that $\mathrm{ASD}_m = 3.32 \times 10^{-12}\,\mathrm{m}$.

**Parameters**

- on_off (int), on/off switch for OMS displacement noise, must be 0 or 1.

**Outputs**

- result (double), OMS displacement noise, in relative frequency deviation.

### C.2.5 ClockNoise

Provides a noise series for the onboard reference ultra stable oscillator (USO).

The noise samples are generated at a sampling frequency of HIGH_SAMPLING_FREQ (in Hz, defined in the simulation configuration).

**Model**

The USO noise is expressed in fractional frequency deviations, normalized by the nominal laser frequency in MHz (which defaults here to $2.818 \times 10^8\,\mathrm{MHz}$).

The noise is the sum of a deterministic frequency drift with time, and a stochastic flicker noise whose power spectrum is in the form of $A^2/f$, where $A$ is the amplitude spectral density of the clock flicker noise. Cutoff frequencies at $1 \times 10^{-5}\,\mathrm{Hz}$ and Nyquist frequency are used to prevent numerical issues.

$$\mathrm{result}_n = \frac{\mathrm{flicker}_n + t_n \times \mathrm{drift}_n}{\mathrm{laser\_frequency}_n}\,. \tag{C.6}$$

This is an ad-hoc model, based on [Spe17].

**Parameters**

- on_off (int), on/off switch for USO noise, must be 0 or 1.
- asd (double), ASD of the USO flicker noise, in fractional frequency deviation $/\sqrt{\mathrm{Hz}}$.

- seed (int), seed for generation of random samples for USO noise, default to 0 (random seed).

**Inputs**

- drift (double), fractional frequency drift with time, in /s.
- laser_frequency (double), nominal laser frequency, in MHz.

**Outputs**

- uso_noise (double), USO noise, in normalized fractional frequency deviation.

### C.2.6 RangingError

Model ranging estimation errors for a single link.

Absolute ranging is determined off-line using Kalman filters. We model the imperfection of these algorithms as noise on the estimated travel times. More specifically, we model the ranging errors by a constant systematic bias plus zero-mean stochastic white noise.

**Model**

$$\text{result}_n = \text{stochastic}_n + \text{systematic}_n \,. \tag{C.7}$$

**Parameters**

- asd (double), stochastic error amplitude spectral density, in $\text{s}/\sqrt{\text{Hz}}$.

**Inputs**

- on_off (int), on/off switch for ranging errors, must be 0 or 1.
- systematic (double), systematic bias on travel times, in s.

**Outputs**

- result (double), ranging error, in s.

## C.3 Absolute Ranging Estimation

The module `ranging.py` defines graphs for absolute ranging estimation with Kalman filters. This is currently achieved by using the god-given ranging information, and adding a noise to account for imperfection of the algorithms.

### C.3.1 AbsoluteRanging

Model absolute the ranging estimation and its errors.

Absolute ranging is determined off-line using Kalman filters. We model the errors of these algorithms for each link, by adding the ranging errors generated by the node RangingError to the god-given ranging data.

**Parameters**

- on_off (int), on/off switch for ranging errors, must be 0 or 1.
- systematic (double), systematic bias on travel times, in s.
- asd (double), stochastic error amplitude spectral density, in $s/\sqrt{Hz}$.

**Inputs**

- tt1 (double), god-given travel times along link 1, in s.
- tt1_p (double), god-given travel times along link 1', in s.
- tt2 (double), god-given travel times along link 2, in s.
- tt2_p (double), god-given travel times along link 2', in s.
- tt3 (double), god-given travel times along link 3, in s.
- tt3_p (double), god-given travel times along link 3', in s.

**Outputs**

- tt1 (double), estimated travel times along link 1, in s.
- tt1_p (double), estimated travel times along link 1', in s.

- tt2 (double), estimated travel times along link 2, in s.
- tt2_p (double), estimated travel times along link 2', in s.
- tt3 (double), estimated travel times along link 3, in s.
- tt3_p (double), estimated travel times along link 3', in s.

### C.3.2 RangingEstimation

Model absolute ranging estimation for a single link.

This nodes adds the ranging error generated by RangingError nodes to the god-given ranging information, to produce the ranging estimates. Cf. AbsoluteRanging graph documentation.

**Parameters**

- asd (double), stochastic error amplitude spectral density, in $s/\sqrt{Hz}$.

**Inputs**

- tt (double), god-given travel times, in s.
- on_off (int), on/off switch for ranging errors, must be 0 or 1.
- systematic (double), systematic bias on travel times, in s.

**Outputs**

- result (double), estimated travel times, in s.

## C.4 Propagation and Instrument Response

The module `propag.py` defines graphs for propagating beams between LISA spacecraft. This includes the computation of the orbits, the addition of the gravitational waves effect, the delaying of the beams to account for the limited speed of light and Doppler effect.

In this section, we also document the nodes that are used for the simulation of the orbits. The corresponding header files are located under `lisanode/toolbox/lisa/orbits/`.

Similarly, nodes used to simulate waveforms and compute the instrument response are located, respectively, under `lisanode/toolbox/lisa/waveforms/` and `lisanode/toolbox/lisa/response`.

### C.4.1 LaserLinks

Simulate the six laser links between the LISA spacecraft, and propagate all laser beams along them.

This graph takes as inputs all signals that are exchanged between the three LISA spacecraft, and propagate them along the six laser links, using SingleSignalPropagation nodes. The propagation is performed by delaying signals, with delays matching the light travel times between the spacecraft.

The type of orbits is determined by the configuration option ORBIT_TYPE, which can be

- keplerian for analytic Keplerian orbits (see node KeplerianOrbits, and section 3.2.3).
- linear_armlengths to simulate armlengths evolving linearly with time.
- from_file to read the orbits from an external file.

This graph is instantiated with a list of signals which must be propagated, laser or sideband.

**Model**

*C.f.* section 3.2.3.

**Parameters**

- Linear Armlengths (only applies when using linearly-evolving armlengths, *i.e.* when ORBIT_TYPE = 'linear_armlengths')
  - L1 (double), armlength 1 at initial time, in m.
  - L2 (double), armlength 2 at initial time, in m.
  - L3 (double), armlength 3 at initial time, in m.
  - dL1 (double), armlength 1 first time derivative, in m/s.
  - dL2 (double), armlength 2 first time derivative, in m/s.

  - dL3 (double), armlength 3 first time derivative, in m/s.

- Interpolations

  - order (int), interpolation order for simulating beam propagation, must be an odd integer greater or equal to 1.

  - max_tt (double), maximum accepted travel times, in s.

**Inputs**

- Main Signals

  - laser_in_from_1_to_2 (double), main signal propagating from spacecraft 1 to 2, in fractional frequency deviation.

  - laser_in_from_1_to_3 (double), main signal propagating from spacecraft 1 to 3, in fractional frequency deviation.

  - laser_in_from_2_to_1 (double), main signal propagating from spacecraft 2 to 1, in fractional frequency deviation.

  - laser_in_from_2_to_3 (double), main signal propagating from spacecraft 2 to 3, in fractional frequency deviation.

  - laser_in_from_3_to_1 (double), main signal propagating from spacecraft 3 to 1, in fractional frequency deviation.

  - laser_in_from_3_to_2 (double), main signal propagating from spacecraft 3 to 2, in fractional frequency deviation.

- Sideband Signals

  - sideband_in_from_1_to_2 (double), sideband signal propagating from spacecraft 1 to 2, in fractional frequency deviation.

  - sideband_in_from_1_to_3 (double), sideband signal propagating from spacecraft 1 to 3, in fractional frequency deviation.

  - sideband_in_from_2_to_1 (double), sideband signal propagating from spacecraft 2 to 1, in fractional frequency deviation.

  - sideband_in_from_2_to_3 (double), sideband signal propagating from spacecraft 2 to 3, in fractional frequency deviation.
  - sideband_in_from_3_to_1 (double), sideband signal propagating from spacecraft 3 to 1, in fractional frequency deviation.
  - sideband_in_from_3_to_2 (double), sideband signal propagating from spacecraft 3 to 2, in fractional frequency deviation.

Outputs

- Main Signals
  - laser_out_from_1_to_2 (double), main signal propagated from spacecraft 1 to 2, in fractional frequency deviation.
  - laser_out_from_1_to_3 (double), main signal propagated from spacecraft 1 to 3, in fractional frequency deviation.
  - laser_out_from_2_to_1 (double), main signal propagated from spacecraft 2 to 1, in fractional frequency deviation.
  - laser_out_from_2_to_3 (double), main signal propagated from spacecraft 2 to 3, in fractional frequency deviation.
  - laser_out_from_3_to_1 (double), main signal propagated from spacecraft 3 to 1, in fractional frequency deviation.
  - laser_out_from_3_to_2 (double), main signal propagated from spacecraft 3 to 2, in fractional frequency deviation.
- Sideband Signals
  - sideband_out_from_1_to_2 (double), sideband signal propagated from spacecraft 1 to 2, in fractional frequency deviation.
  - sideband_out_from_1_to_3 (double), sideband signal propagated from spacecraft 1 to 3, out fractional frequency deviation.
  - sideband_out_from_2_to_1 (double), sideband signal propagated from spacecraft 2 to 1, in fractional frequency deviation.

  - sideband_out_from_2_to_3 (double), sideband signal propagated from spacecraft 2 to 3, in fractional frequency deviation.
  - sideband_out_from_3_to_1 (double), sideband signal propagated from spacecraft 3 to 1, in fractional frequency deviation.
  - sideband_out_from_3_to_2 (double), sideband signal propagated from spacecraft 3 to 2, in fractional frequency deviation.

- Absolute Ranging Estimates
  - tt1 (double), estimated travel times along link 1, in s.
  - tt1_p (double), estimated travel times along link 1', in s.
  - tt2 (double), estimated travel times along link 2, in s.
  - tt2_p (double), estimated travel times along link 2', in s.
  - tt3 (double), estimated travel times along link 3, in s.
  - tt3_p (double), estimated travel times along link 3', in s.

### C.4.2 SingleSignalPropagation

Propagate a single signal across all laser links, *i.e.* between all spacecraft.

This graph is internally used in LaserLinks, itself used in LISA.

The graph delays signals exchanged by spacecraft. The estimated travel times, or absolute ranging, used are published as inputs. Note that a single SingleSignalPropagation handles the propagation of one signal signal along all six laser links of the constellation.

#### Model

*C.f.* section 3.2.3.

#### Parameters

- order (int), interpolation order for simulating beam propagation, must be an odd integer greater or equal to 1.
- max_tt (double), maximum accepted travel times, in s.

**Inputs**

- Signals
  - in_from_1_to_2 (double), signal propagating from spacecraft 1 to 2, in fractional frequency deviation.
  - in_from_1_to_3 (double), signal propagating from spacecraft 1 to 3, in fractional frequency deviation.
  - in_from_2_to_1 (double), signal propagating from spacecraft 2 to 1, in fractional frequency deviation.
  - in_from_2_to_3 (double), signal propagating from spacecraft 2 to 3, in fractional frequency deviation.
  - in_from_3_to_1 (double), signal propagating from spacecraft 3 to 1, in fractional frequency deviation.
  - in_from_3_to_2 (double), signal propagating from spacecraft 3 to 2, in fractional frequency deviation.
- Delays
  - delay_from_1_to_2 (double), delay to be applied on signal propagating from spacecraft 1 to 2, in s.
  - delay_from_1_to_3 (double), delay to be applied on signal propagating from spacecraft 1 to 3, in s.
  - delay_from_2_to_1 (double), delay to be applied on signal propagating from spacecraft 2 to 1, in s.
  - delay_from_2_to_3 (double), delay to be applied on signal propagating from spacecraft 2 to 3, in s.
  - delay_from_3_to_1 (double), delay to be applied on signal propagating from spacecraft 3 to 1, in s.
  - delay_from_3_to_2 (double), delay to be applied on signal propagating from spacecraft 3 to 2, in s.

**Outputs**

- out_from_1_to_2 (double), signal propagated from spacecraft 1 to 2, in fractional frequency deviation.
- out_from_1_to_3 (double), signal propagated from spacecraft 1 to 3, in fractional frequency deviation.
- out_from_2_to_1 (double), signal propagated from spacecraft 2 to 1, in fractional frequency deviation.
- out_from_2_to_3 (double), signal propagated from spacecraft 2 to 3, in fractional frequency deviation.
- out_from_3_to_1 (double), signal propagated from spacecraft 3 to 1, in fractional frequency deviation.
- out_from_3_to_2 (double), signal propagated from spacecraft 3 to 2, in fractional frequency deviation.

### C.4.3 KeplerianOrbits

Compute Keplerian orbits for a LISA three-spacecraft constellation.

Keplerian orbits for a constellation of three spacecraft based on [NKDV06], for a LISA stable flight formation that reduced flexing, to second order in the characteristic ration. *C.f.* section 3.2.3.

**Model**

We compute the characteristic ration $\alpha$, the constellation plane inclination $\mu$, and the orbit eccentricity $e$ when the node is prepared,

$$\alpha = \frac{\text{spacecraft\_separation}}{2 \times \text{distance\_to\_sun}}\,, \tag{C.8}$$

$$e = \frac{\alpha}{\sqrt{3}} + \left(\frac{1}{2} - \text{tilt\_perturbation}\right)\alpha^2\,, \tag{C.9}$$

$$\mu = \alpha - \frac{\text{tilt\_perturbation} - 1}{\sqrt{3}}\alpha^2\,. \tag{C.10}$$

At each timestep, we loop on the spacecraft index k, for $\mathtt{k} = 0, 1, 2$. We first compute the

sinus and cosinus of the eccentric anomaly, using the formula

$$\begin{aligned}\text{anomaly[k]}_n = \text{ rotation[k]}_n - \frac{\alpha \sin(\text{rotation[k]}_n)}{\sqrt{3}} \\ + \frac{6\text{tilt\_perturbation} - 3 + 2\cos(\text{rotation[k]}_n)}{6} \sin(\text{rotation[k]}_n)\alpha^2 \,,\end{aligned} \tag{C.11}$$

where the k-th time-dependent spacecraft rotation is given by

$$\text{rotation}_n = \Omega \times \text{t}_n - \text{k} \times \frac{2\pi}{3} + \text{ initial\_rotation} \,. \tag{C.12}$$

The intermediary variables

$$\begin{aligned}\text{inter\_x[k]}_n = \text{distance\_to\_sun} \times [\cos(\text{anomaly[k]}_n) - \text{ eccentricity}\,] \\ \times \cos(\text{ inclination}) \,,\end{aligned} \tag{C.13}$$

$$\text{inter\_y[k]}_n = \text{distance\_to\_sun} \times \sqrt{1 - \text{ eccentricity}^{\,2}} \times \sin(\text{anomaly[k]}_n) \,, \tag{C.14}$$

$$\begin{aligned}\text{inter\_z[k]}_n = -\text{distance\_to\_sun} \times [\cos(\text{anomaly[k]}_n) - \text{ eccentricity}\,] \\ \times \sin(\text{ inclination}) \,,\end{aligned} \tag{C.15}$$

let us easily compute the spacecraft position

$$\text{x[k]}_n = \text{inter\_x[k]}_n \times \cos(\text{rotation[k]}) - \text{inter\_y[k]}_n \times \sin(\text{rotation[k]}) \,, \tag{C.16}$$

$$\text{y[k]}_n = \text{inter\_x[k]}_n \times \sin(\text{rotation[k]}) + \text{inter\_y[k]}_n \times \cos(\text{rotation[k]}) \,, \tag{C.17}$$

$$\text{z[k]}_n = \text{inter\_z[k]}_n \,, \tag{C.18}$$

where the k-th spacecraft initial rotation is

$$\text{rotation[k]} = \text{k} \times \frac{2\pi}{3} + \text{ initial\_rotation} \,. \tag{C.19}$$

The derivative of the eccentric anomaly for the k-th spacecraft reads

$$\text{anomaly\_derivative[k]}_n = \frac{\Omega}{1 - \text{ eccentricity } \cos(\text{anomaly[k]})} \,. \tag{C.20}$$

The intermediary variables

$$\begin{aligned}\text{inter\_vx[k]}_n = -\text{distance\_to\_sun} \times \text{anomaly\_derivative[k]}_n \\ \times \cos(\text{ inclination}) \times \sin(\text{anomaly[k]}_n) \,,\end{aligned} \tag{C.21}$$

$$\begin{aligned}\text{inter\_vy[k]}_n = \text{distance\_to\_sun} \times \text{anomaly\_derivative[k]}_n \\ \times \sqrt{1 - \text{ eccentricity}^{\,2}} \times \cos(\text{anomaly[k]}_n) \,,\end{aligned} \tag{C.22}$$

$$\begin{aligned}\text{inter\_vz[k]}_n = \text{distance\_to\_sun} \times \text{anomaly\_derivative[k]}_n \\ \times \sin(\text{ inclination}) \times \sin(\text{anomaly[k]}_n) \,,\end{aligned} \tag{C.23}$$

let us easily compute the spacecraft velocity

$$\mathrm{vx[k]}_n = \mathrm{bary\_vx[k]}_n \times \cos(\mathrm{rotation\,[k]}) - \mathrm{bary\_vy[k]}_n \times \sin(\mathrm{rotation\,[k]})\,, \tag{C.24}$$

$$\mathrm{vy[k]}_n = \mathrm{bary\_vx[k]}_n \times \sin(\mathrm{rotation\,[k]}) + \mathrm{bary\_vy[k]}_n \times \cos(\mathrm{rotation\,[k]})\,, \tag{C.25}$$

$$\mathrm{vz[k]}_n = \mathrm{bary\_vz[k]}_n\,, \tag{C.26}$$

where the k-th spacecraft initial rotation is

$$\mathrm{rotation\,[k]} = \mathrm{k} \times \frac{2\pi}{3} + \mathrm{initial\_rotation}\ . \tag{C.27}$$

**Parameters**

- distance_to_sun (double), mean distance between the Sun and constellation barycenter, in m (default to 1 a u ).
- spacecraft_separation (double), mean distance between spacecraft, in m (default to $2.9 \times 10^6$ km).
- initial_rotation (double), initial constellation rotation angle, in rad (default to 0).
- tilt_perturbation (double), small perturbation to LISA plane tilt, in rad (default to the optimal value of 5/8 to reduce the flexing of the constellation).

**Outputs**

- x (std :: array<double, 3>), spacecraft positions along $X$, in m.
- y (std :: array<double, 3>), spacecraft positions along $Y$, in m.
- z (std :: array<double, 3>), spacecraft positions along $Z$, in m.
- vx (std :: array<double, 3>), spacecraft velocities along $X$, in m/s.
- vy (std :: array<double, 3>), spacecraft velocities along $Y$, in m/s.
- vz (std :: array<double, 3>), spacecraft velocities along $Z$, in m/s.

### C.4.4 ArbitraryOrbits

Orbits for a fixed constellation but arbitrary armlengths evolving with time.

Armlengths are given as inputs, and must satisfy the triangular inequalities. Then the node deduces one set of spacecraft positions and velocities matching these armlengths. *C.f.* section 3.2.3.

**Model**

We use the constellation configuration and parametrization illustrated in fig. 3.8.

The following triangular inequalities must be verified at all times,

$$\mathrm{L1}_n > \mathrm{L2}_n + \mathrm{L3}_n, \quad \mathrm{L2}_n > \mathrm{L3}_n + \mathrm{L1}_n, \quad \mathrm{L3}_n > \mathrm{L1}_n + \mathrm{L2}_n \,. \tag{C.28}$$

We define the angle $\alpha_n$, such as

$$\cos\alpha_n = \frac{\mathrm{L1}_n^2 + \mathrm{L3}_n^2 - \mathrm{L2}_n^2}{2 \times \mathrm{L1}_n \times \mathrm{L3}_n} \,, \tag{C.29}$$

and we have

$$\mathrm{x}[0]_n = \mathrm{L3}_n \,, \qquad \mathrm{y}[0]_n = 0 \,, \qquad \mathrm{z}[0]_n = 0 \,, \tag{C.30}$$

$$\mathrm{x}[1]_n = 0 \,, \qquad \mathrm{y}[1]_n = 0 \,, \qquad \mathrm{z}[1]_n = 0 \,, \tag{C.31}$$

$$\mathrm{x}[2]_n = \mathrm{L1}_n \times \cos\alpha_n \,, \qquad \mathrm{y}[2]_n = \mathrm{L1}_n \times \sin\alpha_n \,, \qquad \mathrm{z}[2]_n = 0 \,. \tag{C.32}$$

Most velocities are identically zero. The non-vanishing spacecraft velocities are computed using a first-order backward Newton difference equation,

$$\mathrm{vx}[0]_n = \big(\mathrm{x}[0]_n - \mathrm{x}[0]_{n-1}\big) f_s \,, \tag{C.33}$$

$$\mathrm{vx}[2]_n = \big(\mathrm{x}[2]_n - \mathrm{x}[2]_{n-1}\big) f_s \,, \tag{C.34}$$

$$\mathrm{vy}[2]_n = \big(\mathrm{y}[2]_n - \mathrm{y}[2]_{n-1}\big) f_s \,. \tag{C.35}$$

**Inputs**

- L1 (double), armlength between spacecraft 2 and 3, in m.
- L2 (double), armlength between spacecraft 1 and 3, in m.
- L3 (double), armlength between spacecraft 1 and 2, in m.

**Outputs**

- x (std::array<double, 3>), spacecraft positions along $X$, in m.

- y (std::array<double, 3>), spacecraft positions along $Y$, in m.
- z (std::array<double, 3>), spacecraft positions along $Z$, in m.
- vx (std::array<double, 3>), spacecraft velocities along $X$, in m/s.
- vy (std::array<double, 3>), spacecraft velocities along $Y$, in m/s.
- vz (std::array<double, 3>), spacecraft velocities along $Z$, in m/s.

### C.4.5 TravelTimes

Compute the light travel times between each pair of spacecraft of the LISA constellation.

This nodes computes the travel times of light between each spacecraft of the three-spacecraft LISA constellation, at a given order of computation.

#### Model

See section 3.2.3, section 3.2.4, and section 3.2.5.

#### Parameters

- order (int), order of computation. Choose 0 for no effect, 1 to include Sagnac effect, and 2 to include in addition relativistic effects of first order (default to 0 for no effect).

#### Inputs

- x (std::array<double, 3>), spacecraft positions along $X$, in m.
- y (std::array<double, 3>), spacecraft positions along $Y$, in m.
- z (std::array<double, 3>), spacecraft positions along $Z$, in m.
- vx (std::array<double, 3>), spacecraft velocities along $X$, in m/s.
- vy (std::array<double, 3>), spacecraft velocities along $Y$, in m/s.
- vz (std::array<double, 3>), spacecraft velocities along $Z$, in m/s.

#### Outputs

- travel_times (std::array<array<double, 3>, 3>), matrix of travel times, in s.

### C.4.6 GravitationalContributions

Add the gravitational contribution of a compact binary to all links.

This graph uses SingleLinkGravitationalContribution nodes to add the gravitational contribution to each beam propagating along each link. It is used in LaserLinks.

#### Model

See section 3.2.6.

#### Parameters

- amplitude (double), gravitational-wave strain amplitude.
- frequency (double), gravitational-wave frequency $f_0$, in Hz.
- dot_freq (double), time derivative of the gravitational-wave frequency $\mathrm{d}f_0/\mathrm{d}t$, in Hz/s.
- init_phase (double), observer initial phase $\varphi$, in rad.
- inclination (double), inclination angle $\iota_0$, in rad.
- polarization (double), polarization angle $\iota_0$, in rad.
- position_lambda (double), source ecliptic longitude $\lambda$, un rad.
- position_beta (double), source ecliptic latitude $\beta$, un rad.
- order (int), interpolation order for the gravitational waveform at emission, must be an odd integer greater or equal to 1.
- max_tt (double), maximum accepted travel times, in s.

#### Inputs

- Signals
  - in_from_1_to_2 (double), signal propagating from spacecraft 1 to 2, in fractional frequency deviation.
  - in_from_1_to_3 (double), signal propagating from spacecraft 1 to 3, in fractional frequency deviation.

  - in_from_2_to_1 (double), signal propagating from spacecraft 2 to 1, in fractional frequency deviation.
  - in_from_2_to_3 (double), signal propagating from spacecraft 2 to 3, in fractional frequency deviation.
  - in_from_3_to_1 (double), signal propagating from spacecraft 3 to 1, in fractional frequency deviation.
  - in_from_3_to_2 (double), signal propagating from spacecraft 3 to 2, in fractional frequency deviation.

- Spacecraft 1 Position
  - x1 (double), spacecraft 1 position along the $x$-axis, in m.
  - y1 (double), spacecraft 1 position along the $y$-axis, in m.
  - z1 (double), spacecraft 1 position along the $z$-axis, in m.

- Spacecraft 2 Position
  - x2 (double), spacecraft 2 position along the $x$-axis, in m.
  - y2 (double), spacecraft 2 position along the $y$-axis, in m.
  - z2 (double), spacecraft 2 position along the $z$-axis, in m.

- Spacecraft 3 Position
  - x3 (double), spacecraft 3 position along the $x$-axis, in m.
  - y3 (double), spacecraft 3 position along the $y$-axis, in m.
  - z3 (double), spacecraft 3 position along the $z$-axis, in m.

- Light Travel Times
  - tt1 (double), light travel time between spacecraft 3 to 2, in s.
  - tt2 (double), light travel time between spacecraft 1 to 3, in s.

  - tt3 (double), light travel time between spacecraft 2 to 3, in s.
  - tt1_p (double), light travel time between spacecraft 2 to 3, in s.
  - tt2_p (double), light travel time between spacecraft 3 to 1, in s.
  - tt3_p (double), light travel time between spacecraft 3 to 2, in s.

**Outputs**

- out_from_1_to_2 (double), signal propagated from spacecraft 1 to 2, in fractional frequency deviation.
- out_from_1_to_3 (double), signal propagated from spacecraft 1 to 3, in fractional frequency deviation.
- out_from_2_to_1 (double), signal propagated from spacecraft 2 to 1, in fractional frequency deviation.
- out_from_2_to_3 (double), signal propagated from spacecraft 2 to 3, in fractional frequency deviation.
- out_from_3_to_1 (double), signal propagated from spacecraft 3 to 1, in fractional frequency deviation.
- out_from_3_to_2 (double), signal propagated from spacecraft 3 to 2, in fractional frequency deviation.

### C.4.7 SingleLinkGravitationalContribution

Add the gravitational contribution of a compact binary to a single link. This graph is used in GravitationalContributions.

**Model**

See section 3.2.6.

**Parameters**

- amplitude (double), gravitational-wave strain amplitude.
- frequency (double), gravitational-wave frequency $f_0$, in Hz.

- dot_freq (double), time derivative of the gravitational-wave frequency $\mathrm{d}f_0/\mathrm{d}t$, in Hz/s.
- init_phase (double), observer initial phase $\varphi$, in rad.
- inclination (double), inclination angle $\iota_0$, in rad.
- polarization (double), polarization angle $\iota_0$, in rad.
- position_lambda (double), source ecliptic longitude $\lambda$, un rad.
- position_beta (double), source ecliptic latitude $\beta$, un rad.
- order (int), interpolation order for the gravitational waveform at emission, must be an odd integer greater or equal to 1.
- max_tt (double), maximum accepted travel times, in s.

**Inputs**

- input (double), propagating laser beam, in fractional frequency deviation.
- Emitter Position
  - emitter_x (double), emitter spacecraft position along the $x$-axis at reception time, in m.
  - emitter_y (double), emitter spacecraft position along the $y$-axis at reception time, in m.
  - emitter_z (double), emitter spacecraft position along the $z$-axis at reception time, in m.
- Receiver Position
  - receiver_x (double), receiver spacecraft position along the $x$-axis at reception time, in m.
  - receiver_y (double), receiver spacecraft position along the $y$-axis at reception time, in m.
  - receiver_z (double), receiver spacecraft position along the $z$-axis at reception time, in m.

- travel_time (double), light travel time between emitter and receiver, in s.

**Outputs**

- result (double), propagating laser beam with gravitational contribution, in fractional frequency deviation.

### C.4.8 LinkResponse

Compute the response of one LISA link to a gravitational signal given by its time series.

This node computes the contribution of one gravitational signal for one of the six LISA arms. The gravitational signal is an input of the node, and is internally interpolated back in time using Lagrange interpolating polynomials.

**Model**

The function of single arm response is given in [LIS19a] by

$$\text{result}_n = \frac{1}{2(\mathbf{k}\cdot\hat{\mathbf{n}})}\left[H\left(t - \text{travel\_time} - \frac{\mathbf{k}\cdot\mathbf{x}_0(t)}{c}\right) - H\left(t - \frac{\mathbf{k}\cdot\mathbf{x}_1(t)}{c}\right)\right], \tag{C.36}$$

where $\hat{\mathbf{n}} = (\mathbf{x}_1 - \mathbf{x}_0)/\|\mathbf{x}_1 - \mathbf{x}_0\|$ is the link unit vector, $\mathbf{k}$ is the wave propagation direction unit vector, $\mathbf{x}_0(t)$ the emitter position, $\mathbf{x}_1(t)$ the receiver position, and $H(t)$ is the gravitational deformation in the link direction.

We define the spacecraft position vectors with the coordinates

$$\mathbf{x}_0 = (\text{emitter\_x}_n, \text{emitter\_y}_n, \text{emitter\_z}_n)\,, \tag{C.37}$$

$$\mathbf{x}_1 = (\text{receiver\_x}_n, \text{receiver\_y}_n, \text{receiver\_z}_n)\,. \tag{C.38}$$

This deformation is given by

$$H(t) = \text{hSSB\_plus} \times \xi_+(\mathbf{u},\mathbf{v},\mathbf{n}) + \text{hSSB\_cross} \times \xi_\times(\mathbf{u},\mathbf{v},\mathbf{n})\,, \tag{C.39}$$

where we define the antenna pattern functions

$$\xi_+(\mathbf{u},\mathbf{v},\mathbf{n}) = (\mathbf{u}\cdot\hat{\mathbf{n}})^2 - (\mathbf{v}\cdot\hat{\mathbf{n}})^2\,, \tag{C.40}$$

$$\xi_\times(\mathbf{u},\mathbf{v},\mathbf{n}) = 2(\mathbf{u}\cdot\hat{\mathbf{n}})(\mathbf{v}\cdot\hat{\mathbf{n}})\,. \tag{C.41}$$

Here, $(\mathbf{u}, \mathbf{v}, \mathbf{k})$ is a direct orthonormal basis obtained from the source sky localization $(\beta, \lambda)$,

$$\mathbf{k} = (-\cos(\text{position\_beta})\cos(\text{position\_lambda}), -\cos(\text{position\_beta})\sin(\text{position\_lambda}), -\sin(\text{position\_beta}))\,, \tag{C.42}$$

$$\mathbf{u} = (\sin(\text{position\_lambda}), -\cos(\text{position\_lambda}), 0)\,, \tag{C.43}$$

$$\mathbf{v} = (-\sin(\text{position\_beta})\cos(\text{position\_lambda}), -\sin(\text{position\_beta})\sin(\text{position\_lambda}), \cos(\text{position\_beta}))\,. \tag{C.44}$$

See section 3.2.6 for details.

**Parameters**

- position_lambda (double), source ecliptic longitude $\lambda$, un rad.
- position_beta (double), source ecliptic latitude $\beta$, un rad.
- order (int), interpolation order for the gravitational waveform at emission, must be an odd integer greater or equal to 1.
- max_tt (double), maximum accepted travel times, in s.

**Inputs**

- Gravitational Waveform
  - hSSB_plus (double), plus-polarized strain amplitude in the SSB frame.
  - hSSB_cross (double), cross-polarized strain amplitude in the SSB frame.
- Emitter Position
  - emitter_x (double), emitter spacecraft position along the $x$-axis at reception time, in m.
  - emitter_y (double), emitter spacecraft position along the $y$-axis at reception time, in m.
  - emitter_z (double), emitter spacecraft position along the $z$-axis at reception time, in m.
- Receiver Position

  - receiver_x (double), receiver spacecraft position along the $x$-axis at reception time, in m.
  - receiver_y (double), receiver spacecraft position along the $y$-axis at reception time, in m.
  - receiver_z (double), receiver spacecraft position along the $z$-axis at reception time, in m.

- travel_time (double), light travel time between emitter and receiver, in s.

**Outputs**

- result (double), gravitational contribution to the fractional frequency deviation of the beam.

### C.4.9 AnalyticLinkResponse

Compute the response of one LISA link to a gravitational signal given by its analytic expression.

This node computes the contribution of one gravitational signal for one of the six LISA arms. The gravitational signal must be given as an explicit function of time, for the plus and cross polarizations.

**Model**

*C.f.* documentation of AnalyticLink.

**Parameters**

- hSSB_plus (std :: string), expression of plus-polarized strain amplitude in the SSB frame.
- hSSB_cross (std :: string), expression of cross-polarized strain amplitude in the SSB frame.
- inclination (double), inclination angle, in rad.
- polarization (double), polarization angle, in rad.
- position_lambda (double), source ecliptic longitude $\lambda$, un rad.

- position_beta (double), source ecliptic latitude $\beta$, un rad.

**Inputs**

- Emitter Position
  - emitter_x (double), emitter spacecraft position along the $x$-axis at reception time, in m.
  - emitter_y (double), emitter spacecraft position along the $y$-axis at reception time, in m.
  - emitter_z (double), emitter spacecraft position along the $z$-axis at reception time, in m.
- Receiver Position
  - receiver_x (double), receiver spacecraft position along the $x$-axis at reception time, in m.
  - receiver_y (double), receiver spacecraft position along the $y$-axis at reception time, in m.
  - receiver_z (double), receiver spacecraft position along the $z$-axis at reception time, in m.
- travel_time (double), light travel time between emitter and receiver, in s.

**Outputs**

- result (double), gravitational contribution to the fractional frequency deviation of the beam.

### C.4.10 SolarSystemBarycenterFrame

Convert the gravitational-wave strain from the source frame to the SSB frame, *c.f.* section 3.2.6.

**Model**

First, the gravitational-wave signal in source frame is projected onto the observational plane via

$$\text{hS\_plus}_n = [1 + \cos^2(\text{ inclination })] \times \text{h\_plus}_n \,, \tag{C.45}$$

$$\text{hS\_cross}_n = -2\cos(\text{ inclination }) \times \text{h\_cross}_n \,. \tag{C.46}$$

Then, it is rotated in the observational plane to get the gravitational wave strain in the SSB frame:

$$\text{hSSB\_plus}_n = -\text{hS\_plus}_n \times \cos(2 \times \text{ polarization }) - \text{hS\_cross}_n \times \sin(2 \times \text{ polarization }) \,, \tag{C.47}$$

$$\text{hSSB\_cross}_n = \text{hS\_plus}_n \times \sin(2 \times \text{ polarization }) - \text{hS\_cross}_n \times \cos(2 \times \text{ polarization }) \,. \tag{C.48}$$

**Parameters**

- inclination (double), inclination angle, in rad.
- polarization (double), polarization angle, in rad.

**Inputs**

- h_plus (double), plus-polarization strain amplitude in source frame.
- h_cross (double), cross-polarization strain amplitude in source frame.

**Outputs**

- h_plus (double), plus-polarization strain amplitude in source frame.
- h_cross (double), cross-polarization strain amplitude in source frame.

### C.4.11 GalacticBinary

Generate gravitational wave strain for a chirping galactic binary.

**Model**

The gravitational wave signal computed in the source frame [LIS19a], as

$$\text{h\_plus}_n = \text{amplitude}\cos\big(2\pi \times \text{frequency} \times t_n + \pi \times \text{frequency\_derivative} \times t_n^2 + \text{initial\_phase}\big) \,, \tag{C.49}$$

$$\text{h\_cross}_n = \text{amplitude}\sin\big(2\pi \times \text{frequency} \times t_n + \pi \times \text{frequency\_derivative} \times t_n^2 + \text{initial\_phase}\big) \,. \tag{C.50}$$

**Parameters**

- amplitude (double), gravitational-wave strain amplitude.
- frequency (double), gravitational-wave frequency $f_0$, in Hz.
- frequency_derivative (double), time derivative of the gravitational-wave frequency $\mathrm{d}f_0/\mathrm{d}t$, in Hz/s.
- initial_phase (double), observer initial phase $\varphi$, in rad.

**Outputs**

- h_plus (double), plus-polarization strain amplitude.
- h_cross (double), cross-polarization strain amplitude.

## C.5 Calibration Chain

The module `tdi.py` gathers the top-level and convenience TDI-related graphs. In `intervar.py`, graphs are defined, that computes the intermediary variables described in sections 4.2.1 and 4.2.2. In `tdivar.py`, graphs that form the laser noise-suppressing combinations are defined. Lastly, clock noise-calibrated combinations are computed in `clockcal.py`.

### C.5.1 TDI

Standalone TDI intermediary variables and laser noise-suppressing combinations.

Most of the users may want to use the off-the-shelf LISAWithTDI or TDIFromText graphs, which embed this graph and connect it to either LISA or ReadText nodes.

**Model**

*C.f.* sections 4.2 and 4.3.

**Parameters**

- Synthesizing Acausal Filter
  - ttshift (double), time-shift for travel times, must match filter group delay, in s.

  - ttshift_order (int), interpolation order to time-shift travel times, must be an odd integer greater or equal to 1.

- Interpolations

  - tdi_order (int), interpolation order for TDI delays, must be an odd integer greater or equal to 1.

  - max_delay (double), maximum accepted delays for TDI, in s.

**Inputs**

- Measurement Channels

  - s1 (double), science interferometric measurement in MOSA 1, in fractional frequency deviation.

  - s1_p (double), science interferometric measurement in MOSA 1', in fractional frequency deviation.

  - s2 (double), science interferometric measurement in MOSA 2, in fractional frequency deviation.

  - s2_p (double), science interferometric measurement in MOSA 2', in fractional frequency deviation.

  - s3 (double), science interferometric measurement in MOSA 3, in fractional frequency deviation.

  - s3_p (double), science interferometric measurement in MOSA 3', in fractional frequency deviation.

  - sb1 (double), sideband interferometric measurement in MOSA 1, in fractional frequency deviation.

  - sb1_p (double), sideband interferometric measurement in MOSA 1', in fractional frequency deviation.

  - sb2 (double), sideband interferometric measurement in MOSA 2, in fractional frequency deviation.

- sb2_p (double), sideband interferometric measurement in MOSA 2', in fractional frequency deviation.
- sb3 (double), sideband interferometric measurement in MOSA 3, in fractional frequency deviation.
- sb3_p (double), sideband interferometric measurement in MOSA 3', in fractional frequency deviation.
- tau1 (double), reference interferometric measurement in MOSA 1, in fractional frequency deviation.
- tau1_p (double), reference interferometric measurement in MOSA 1', in fractional frequency deviation.
- tau2 (double), reference interferometric measurement in MOSA 2, in fractional frequency deviation.
- tau2_p (double), reference interferometric measurement in MOSA 2', in fractional frequency deviation.
- tau3 (double), reference interferometric measurement in MOSA 3, in fractional frequency deviation.
- tau3_p (double), reference interferometric measurement in MOSA 3', in fractional frequency deviation.
- epsilon1 (double), test-mass interferometric measurement in MOSA 1, in fractional frequency deviation.
- epsilon1_p (double), test-mass interferometric measurement in MOSA 1', in fractional frequency deviation.
- epsilon2 (double), test-mass interferometric measurement in MOSA 2, in fractional frequency deviation.
- epsilon2_p (double), test-mass interferometric measurement in MOSA 2', in fractional frequency deviation.
- epsilon3 (double), test-mass interferometric measurement in MOSA 3, in fractional frequency deviation.

  - epsilon3_p (double), test-mass interferometric measurement in MOSA 3', in fractional frequency deviation.

- Absolute Ranging Estimates

  - tt1 (double), estimated travel times along link 1, in s.
  - tt1_p (double), estimated travel times along link 1', in s.
  - tt2 (double), estimated travel times along link 2, in s.
  - tt2_p (double), estimated travel times along link 2', in s.
  - tt3 (double), estimated travel times along link 3, in s.
  - tt3_p (double), estimated travel times along link 3', in s.

- Beatnote Frequencies

  - sci_f1 (double), science beatnote frequencies in MOSA 1, in MHz.
  - sci_f1_p (double), science beatnote frequencies in MOSA 1', in MHz.
  - sci_f2 (double), science beatnote frequencies in MOSA 2, in MHz.
  - sci_f2_p (double), science beatnote frequencies in MOSA 2', in MHz.
  - sci_f3 (double), science beatnote frequencies in MOSA 3, in MHz.
  - sci_f3_p (double), science beatnote frequencies in MOSA 3', in MHz.
  - ref_f1 (double), reference and test-mass beatnote frequencies in MOSA 1, in MHz.
  - ref_f1_p (double), reference and test-mass beatnote frequencies in MOSA 1', in MHz.
  - ref_f2 (double), reference and test-mass beatnote frequencies in MOSA 2, in MHz.
  - ref_f2_p (double), reference and test-mass beatnote frequencies in MOSA 2', in MHz.
  - ref_f3 (double), reference and test-mass beatnote frequencies in MOSA 3, in MHz.

  - ref_f3_p (double), reference and test-mass beatnote frequencies in MOSA 3', in MHz.
  - sb_f1 (double), sideband beatnote frequencies in MOSA 1, in MHz.
  - sb_f1_p (double), sideband beatnote frequencies in MOSA 1', in MHz.
  - sb_f2 (double), sideband beatnote frequencies in MOSA 2, in MHz.
  - sb_f2_p (double), sideband beatnote frequencies in MOSA 2', in MHz.
  - sb_f3 (double), sideband beatnote frequencies in MOSA 3, in MHz.
  - sb_f3_p (double), sideband beatnote frequencies in MOSA 3', in MHz.

**Outputs**

- Michelson Combinations (generation $i$ is defined in simulation configuration)
  - X (double), Michelson $X_i$ combination.
  - Y (double), Michelson $Y_i$ combination.
  - Z (double), Michelson $Z_i$ combination.
  - Xc (double), clock noise-calibrated Michelson $X_i$ combination.
  - Yc (double), clock noise-calibrated Michelson $Y_i$ combination.
  - Zc (double), clock noise-calibrated Michelson $Z_i$ combination.
- Quasi-Orthogonal Combinations (generation $i$ is defined in simulation configuration)
  - A (double), Michelson $A_i$ combination.
  - E (double), Michelson $E_i$ combination.
  - T (double), Michelson $T_i$ combination.
  - Ac (double), clock noise-calibrated Michelson $A_i$ combination.
  - Ec (double), clock noise-calibrated Michelson $E_i$ combination.

  - Tc (double), clock noise-calibrated Michelson $T_i$ combination.

- Sagnac Combinations (generation $i$ is defined in simulation configuration)
  - alpha (double), Sagnac $\alpha_i$ combination.
  - beta (double), Sagnac $\beta_i$ combination.
  - gamma (double), Sagnac $\gamma_i$ combination.
  - zeta (double), fully symmetric $\zeta$ Sagnac combination for first generation.
  - zeta1 (double), first permutation of fully symmetric $\zeta$ combination for second generation.
  - zeta2 (double), second permutation of fully symmetric $\zeta$ combination for second generation.
  - zeta3 (double), third permutation of fully symmetric $\zeta$ combination for second generation.

- Intermediary Variables
  - xi1 (double), intermediary variable for optical-bench displacement noise removal $\xi_1$.
  - xi2 (double), intermediary variable for optical-bench displacement noise removal $\xi_2$.
  - xi3 (double), intermediary variable for optical-bench displacement noise removal $\xi_3$.
  - xi1_p (double), intermediary variable for optical-bench displacement noise removal $\xi_{1'}$.
  - xi2_p (double), intermediary variable for optical-bench displacement noise removal $\xi_{2'}$.
  - xi3_p (double), intermediary variable for optical-bench displacement noise removal $\xi_{3'}$.
  - eta1 (double), intermediary variable to reduce the number of free-running lasers

to three $\eta_1$.

- eta2 (double), intermediary variable to reduce the number of free-running lasers to three $\eta_2$.
- eta3 (double), intermediary variable to reduce the number of free-running lasers to three $\eta_3$.
- eta1_p (double), intermediary variable to reduce the number of free-running lasers to three $\eta_{1'}$.
- eta2_p (double), intermediary variable to reduce the number of free-running lasers to three $\eta_{2'}$.
- eta3_p (double), intermediary variable to reduce the number of free-running lasers to three $\eta_{3'}$.
- R1 (double), clock noise-calibrating expression $r_1^c$.
- R2 (double), clock noise-calibrating expression $r_2^c$.
- R3 (double), clock noise-calibrating expression $r_3^c$.
- R1_p (double), clock noise-calibrating expression $r_{1'}^c$.
- R2_p (double), clock noise-calibrating expression $r_{2'}^c$.
- R3_p (double), clock noise-calibrating expression $r_{3'}^c$.

- Time-Shifted Ranging Estimates

  - shift_tt1 (double), time-shifted travel times along link 1, in s.
  - shift_tt1_p (double), time-shifted travel times along link 1', in s.
  - shift_tt2 (double), time-shifted travel times along link 2, in s.
  - shift_tt2_p (double), time-shifted travel times along link 2', in s.
  - shift_tt3 (double), time-shifted travel times along link 3, in s.
  - shift_tt3_p (double), time-shifted travel times along link 3', in s.

### C.5.2 TDIFromText

TDI algorithms with inputs read from text files.

This graph reads all inputs from text files, and compute the TDI combinations. You must therefore generate the data with LISA or LISAWithTDI and make sure that PUBLISH_MEASUREMENTS and PUBLISH_TRAVEL_TIMES are set to True in `config.py`.

**Model**

*C.f.* sections 4.2 and 4.3.

**Parameters**

- Input File Basepath
  - basepath (str), basepath for input text files.
- Synthesizing Acausal Filter
  - ttshift (double), time-shift for travel times, must match filter group delay, in s.
  - ttshift_order (int), interpolation order to time-shift travel times, must be an odd integer greater or equal to 1.
- Interpolations
  - tdi_order (int), interpolation order for TDI delays, must be an odd integer greater or equal to 1.
  - max_delay (double), maximum accepted delays for TDI, in s.

**Inputs**

- Beatnote Frequencies
  - sci_f1 (double), science beatnote frequencies in MOSA 1, in MHz.
  - sci_f1_p (double), science beatnote frequencies in MOSA 1', in MHz.
  - sci_f2 (double), science beatnote frequencies in MOSA 2, in MHz.

- sci_f2_p (double), science beatnote frequencies in MOSA 2', in MHz.
- sci_f3 (double), science beatnote frequencies in MOSA 3, in MHz.
- sci_f3_p (double), science beatnote frequencies in MOSA 3', in MHz.
- ref_f1 (double), reference and test-mass beatnote frequencies in MOSA 1, in MHz.
- ref_f1_p (double), reference and test-mass beatnote frequencies in MOSA 1', in MHz.
- ref_f2 (double), reference and test-mass beatnote frequencies in MOSA 2, in MHz.
- ref_f2_p (double), reference and test-mass beatnote frequencies in MOSA 2', in MHz.
- ref_f3 (double), reference and test-mass beatnote frequencies in MOSA 3, in MHz.
- ref_f3_p (double), reference and test-mass beatnote frequencies in MOSA 3', in MHz.
- sb_f1 (double), sideband beatnote frequencies in MOSA 1, in MHz.
- sb_f1_p (double), sideband beatnote frequencies in MOSA 1', in MHz.
- sb_f2 (double), sideband beatnote frequencies in MOSA 2, in MHz.
- sb_f2_p (double), sideband beatnote frequencies in MOSA 2', in MHz.
- sb_f3 (double), sideband beatnote frequencies in MOSA 3, in MHz.
- sb_f3_p (double), sideband beatnote frequencies in MOSA 3', in MHz.

**Outputs**

- Michelson Combinations (generation $i$ is defined in simulation configuration)
  - X (double), Michelson $X_i$ combination.
  - Y (double), Michelson $Y_i$ combination.
  - Z (double), Michelson $Z_i$ combination.
  - Xc (double), clock noise-calibrated Michelson $X_i$ combination.

  - Yc (double), clock noise-calibrated Michelson $Y_i$ combination.
  - Zc (double), clock noise-calibrated Michelson $Z_i$ combination.

- Quasi-Orthogonal Combinations (generation $i$ is defined in simulation configuration)
  - A (double), Michelson $A_i$ combination.
  - E (double), Michelson $E_i$ combination.
  - T (double), Michelson $T_i$ combination.
  - Ac (double), clock noise-calibrated Michelson $A_i$ combination.
  - Ec (double), clock noise-calibrated Michelson $E_i$ combination.
  - Tc (double), clock noise-calibrated Michelson $T_i$ combination.

- Sagnac Combinations (generation $i$ is defined in simulation configuration)
  - alpha (double), Sagnac $\alpha_i$ combination.
  - beta (double), Sagnac $\beta_i$ combination.
  - gamma (double), Sagnac $\gamma_i$ combination.
  - zeta (double), fully symmetric $\zeta$ Sagnac combination for first generation.
  - zeta1 (double), first permutation of fully symmetric $\zeta$ combination for second generation.
  - zeta2 (double), second permutation of fully symmetric $\zeta$ combination for second generation.
  - zeta3 (double), third permutation of fully symmetric $\zeta$ combination for second generation.

- Intermediary Variables
  - xi1 (double), intermediary variable for optical-bench displacement noise removal $\xi_1$.

- xi2 (double), intermediary variable for optical-bench displacement noise removal $\xi_2$.
- xi3 (double), intermediary variable for optical-bench displacement noise removal $\xi_3$.
- xi1_p (double), intermediary variable for optical-bench displacement noise removal $\xi_{1'}$.
- xi2_p (double), intermediary variable for optical-bench displacement noise removal $\xi_{2'}$.
- xi3_p (double), intermediary variable for optical-bench displacement noise removal $\xi_{3'}$.
- eta1 (double), intermediary variable to reduce the number of free-running lasers to three $\eta_1$.
- eta2 (double), intermediary variable to reduce the number of free-running lasers to three $\eta_2$.
- eta3 (double), intermediary variable to reduce the number of free-running lasers to three $\eta_3$.
- eta1_p (double), intermediary variable to reduce the number of free-running lasers to three $\eta_{1'}$.
- eta2_p (double), intermediary variable to reduce the number of free-running lasers to three $\eta_{2'}$.
- eta3_p (double), intermediary variable to reduce the number of free-running lasers to three $\eta_{3'}$.
- R1 (double), clock noise-calibrating expression $r_1^c$.
- R2 (double), clock noise-calibrating expression $r_2^c$.
- R3 (double), clock noise-calibrating expression $r_3^c$.
- R1_p (double), clock noise-calibrating expression $r_{1'}^c$.
- R2_p (double), clock noise-calibrating expression $r_{2'}^c$.

  - R3_p (double), clock noise-calibrating expression $r^{c}_{3'}$.

- Time-Shifted Ranging Estimates

  - shift_tt1 (double), time-shifted travel times along link 1, in s.
  - shift_tt1_p (double), time-shifted travel times along link 1', in s.
  - shift_tt2 (double), time-shifted travel times along link 2, in s.
  - shift_tt2_p (double), time-shifted travel times along link 2', in s.
  - shift_tt3 (double), time-shifted travel times along link 3, in s.
  - shift_tt3_p (double), time-shifted travel times along link 3', in s.

### C.5.3 LISAWithTDI

Simulation of the LISA instrument with TDI algorithms.

This graph produces the interferometric measurements and ranging estimates as they are generated and transmitted from LISA, and feed them to the TDI graph.

**Model**

*C.f.* sections 3.2, 4.2 and 4.3.

**Parameters**

- Laser Noises

  - lasernoise_on_off (int), on/off switch for laser frequency noise, must be 0 or 1.
  - laser_asd1 (double), laser noise ASD of MOSA 1, in $\mathrm{s}/\sqrt{\mathrm{Hz}}$.
  - laser_asd1_p (double), laser noise ASD of MOSA 1', in $\mathrm{s}/\sqrt{\mathrm{Hz}}$.
  - laser_asd2 (double), laser noise ASD of MOSA 2, in $\mathrm{s}/\sqrt{\mathrm{Hz}}$.
  - laser_asd2_p (double), laser noise ASD of MOSA 2', in $\mathrm{s}/\sqrt{\mathrm{Hz}}$.
  - laser_asd3 (double), laser noise ASD of MOSA 3, in $\mathrm{s}/\sqrt{\mathrm{Hz}}$.

  - laser_asd3_p (double), laser noise ASD of MOSA 3', in s/$\sqrt{\text{Hz}}$.
  - laser_seed1 (int), seed for generation of random samples for laser noise of MOSA 1, default to 0 (a seed is randomly chosen when the simulation starts).
  - laser_seed1_p (int), seed for generation of random samples for laser noise of MOSA 1', default to 0 (a seed is randomly chosen when the simulation starts).
  - laser_seed2 (int), seed for generation of random samples for laser noise of MOSA 2, default to 0 (a seed is randomly chosen when the simulation starts).
  - laser_seed2_p (int), seed for generation of random samples for laser noise of MOSA 2', default to 0 (a seed is randomly chosen when the simulation starts).
  - laser_seed3 (int), seed for generation of random samples for laser noise of MOSA 3, default to 0 (a seed is randomly chosen when the simulation starts).
  - laser_seed3_p (int), seed for generation of random samples for laser noise of MOSA 3', default to 0 (a seed is randomly chosen when the simulation starts).

- Readout Noises
  - readoutnoise_on_off (int), on/off switch for readout noise, must be 0 or 1.

- Optical Noises
  - opticalnoise_on_off (int), on/off switch for optical noise, must be 0 or 1.

- Test-mass Acceleration Noises in GRS
  - accelnoise_on_off (int), on/off switch for test-mass acceleration noise, must be 0 or 1.

- Clock noises
  - usonoise_on_off (int), on/off switch for USO frequency fluctuations and drift.
  - uso_asd (double), ASD of the USO flicker noise, in fractional frequency deviation /$\sqrt{\text{Hz}}$.

  - uso_seed1 (int), seed for generation of random samples for USO noise for spacecraft 1, default to 0 (random seed).
  - uso_seed2 (int), seed for generation of random samples for USO noise for spacecraft 2, default to 0 (random seed).
  - uso_seed3 (int), seed for generation of random samples for USO noise for spacecraft 3, default to 0 (random seed).

- Absolute Ranging Errors
  - rangingnoise_on_off (int), on/off switch for absolute ranging error, must be 0 or 1.
  - ranging_systematic (double), constant systematic error on travel time estimation, in s.
  - ranging_asd: amplitude spectral density of the error on travel times, in $s/\sqrt{Hz}$.

- Synthesizing Acausal Filter
  - ttshift (double), time-shift for travel times, must match filter group delay, in s.
  - ttshift_order (int), interpolation order to time-shift travel times, must be an odd integer greater or equal to 1.

- Linear Armlengths (only applies when using linearly-evolving armlengths, *i.e.* when ORBIT_TYPE = 'linear_armlengths')
  - L1 (double), armlength 1 at initial time, in m.
  - L2 (double), armlength 2 at initial time, in m.
  - L3 (double), armlength 3 at initial time, in m.
  - dL1 (double), armlength 1 first time derivative, in m/s.
  - dL2 (double), armlength 2 first time derivative, in m/s.
  - dL3 (double), armlength 3 first time derivative, in m/s.

- Interpolations

  - lisa_order (int), interpolation order for simulating beam propagation in LISA, must be an odd integer greater or equal to 1.
  - tdi_order (int), interpolation order for TDI delays, must be an odd integer greater or equal to 1.
  - max_delay (double), maximum accepted delays for TDI, in s.

**Inputs**

- Beatnote Frequencies
  - sci_f1 (double), science beatnote frequencies in MOSA 1, in MHz.
  - sci_f1_p (double), science beatnote frequencies in MOSA 1', in MHz.
  - sci_f2 (double), science beatnote frequencies in MOSA 2, in MHz.
  - sci_f2_p (double), science beatnote frequencies in MOSA 2', in MHz.
  - sci_f3 (double), science beatnote frequencies in MOSA 3, in MHz.
  - sci_f3_p (double), science beatnote frequencies in MOSA 3', in MHz.
  - ref_f1 (double), reference and test-mass beatnote frequencies in MOSA 1, in MHz.
  - ref_f1_p (double), reference and test-mass beatnote frequencies in MOSA 1', in MHz.
  - ref_f2 (double), reference and test-mass beatnote frequencies in MOSA 2, in MHz.
  - ref_f2_p (double), reference and test-mass beatnote frequencies in MOSA 2', in MHz.
  - ref_f3 (double), reference and test-mass beatnote frequencies in MOSA 3, in MHz.
  - ref_f3_p (double), reference and test-mass beatnote frequencies in MOSA 3', in MHz.
  - sb_f1 (double), sideband beatnote frequencies in MOSA 1, in MHz.
  - sb_f1_p (double), sideband beatnote frequencies in MOSA 1', in MHz.

  - sb_f2 (double), sideband beatnote frequencies in MOSA 2, in MHz.
  - sb_f2_p (double), sideband beatnote frequencies in MOSA 2', in MHz.
  - sb_f3 (double), sideband beatnote frequencies in MOSA 3, in MHz.
  - sb_f3_p (double), sideband beatnote frequencies in MOSA 3', in MHz.

- Clock Noises
  - uso_drift1 (double), fractional frequency time drift of USO onboard spacecraft 1, in /s.
  - uso_drift2 (double), fractional frequency time drift of USO onboard spacecraft 2, in /s.
  - uso_drift3 (double), fractional frequency time drift of USO onboard spacecraft 3, in /s.

**Outputs**

- Michelson Combinations (generation $i$ is defined in simulation configuration)
  - X (double), Michelson $X_i$ combination.
  - Y (double), Michelson $Y_i$ combination.
  - Z (double), Michelson $Z_i$ combination.
  - Xc (double), clock noise-calibrated Michelson $X_i$ combination.
  - Yc (double), clock noise-calibrated Michelson $Y_i$ combination.
  - Zc (double), clock noise-calibrated Michelson $Z_i$ combination.

- Quasi-Orthogonal Combinations (generation $i$ is defined in simulation configuration)
  - A (double), Michelson $A_i$ combination.
  - E (double), Michelson $E_i$ combination.
  - T (double), Michelson $T_i$ combination.

  - Ac (double), clock noise-calibrated Michelson $A_i$ combination.
  - Ec (double), clock noise-calibrated Michelson $E_i$ combination.
  - Tc (double), clock noise-calibrated Michelson $T_i$ combination.

- Sagnac Combinations (generation $i$ is defined in simulation configuration)
  - alpha (double), Sagnac $\alpha_i$ combination.
  - beta (double), Sagnac $\beta_i$ combination.
  - gamma (double), Sagnac $\gamma_i$ combination.
  - zeta (double), fully symmetric $\zeta$ Sagnac combination for first generation.
  - zeta1 (double), first permutation of fully symmetric $\zeta$ combination for second generation.
  - zeta2 (double), second permutation of fully symmetric $\zeta$ combination for second generation.
  - zeta3 (double), third permutation of fully symmetric $\zeta$ combination for second generation.

- Intermediary Variables
  - xi1 (double), intermediary variable for optical-bench displacement noise removal $\xi_1$.
  - xi2 (double), intermediary variable for optical-bench displacement noise removal $\xi_2$.
  - xi3 (double), intermediary variable for optical-bench displacement noise removal $\xi_3$.
  - xi1_p (double), intermediary variable for optical-bench displacement noise removal $\xi_{1'}$.
  - xi2_p (double), intermediary variable for optical-bench displacement noise removal $\xi_{2'}$.

  - xi3_p (double), intermediary variable for optical-bench displacement noise removal $\xi_{3'}$.
  - eta1 (double), intermediary variable to reduce the number of free-running lasers to three $\eta_1$.
  - eta2 (double), intermediary variable to reduce the number of free-running lasers to three $\eta_2$.
  - eta3 (double), intermediary variable to reduce the number of free-running lasers to three $\eta_3$.
  - eta1_p (double), intermediary variable to reduce the number of free-running lasers to three $\eta_{1'}$.
  - eta2_p (double), intermediary variable to reduce the number of free-running lasers to three $\eta_{2'}$.
  - eta3_p (double), intermediary variable to reduce the number of free-running lasers to three $\eta_{3'}$.
  - R1 (double), clock noise-calibrating expression $r_1^c$.
  - R2 (double), clock noise-calibrating expression $r_2^c$.
  - R3 (double), clock noise-calibrating expression $r_3^c$.
  - R1_p (double), clock noise-calibrating expression $r_{1'}^c$.
  - R2_p (double), clock noise-calibrating expression $r_{2'}^c$.
  - R3_p (double), clock noise-calibrating expression $r_{3'}^c$.

- Time-Shifted Ranging Estimates

  - tt1 (double), estimated travel times along link 1, in s.
  - tt1_p (double), estimated travel times along link 1', in s.
  - tt2 (double), estimated travel times along link 2, in s.
  - tt2_p (double), estimated travel times along link 2', in s.

- tt3 (double), estimated travel times along link 3, in s.
- tt3_p (double), time-shifted travel times along link 3', in s.
- shift_tt1 (double), time-shifted travel times along link 1, in s.
- shift_tt1_p (double), time-shifted travel times along link 1', in s.
- shift_tt2 (double), time-shifted travel times along link 2, in s.
- shift_tt2_p (double), time-shifted travel times along link 2', in s.
- shift_tt3 (double), time-shifted travel times along link 3, in s.
- shift_tt3_p (double), time-shifted travel times along link 3', in s.

### C.5.4 TravelTimeShift

Time-shift the travel times by a constant fractional delay to synthesize an acausal filter.

Causal anti-aliasing filters are used on board the spacecraft to prevent power folding before interferometric measurement are decimated and telemetered down to Earth. These filters have a non-vanishing group delay, which decreases TDI's ability to reduce laser noise [BLPH19]. This effect can be mitigated by synthesizing an offline non-causal filter, *i.e.* by time-shifting the ranging estimates with respect to the interferometric measurements by exactly the same filter group delay. This node is used to apply this constant time-shift.

*C.f.* section 4.3.

**Model**

$$\text{shift\_tt1}(t_n) = \text{tt1}(t_n - \text{delay}_n)\,, \tag{C.51}$$
$$\text{shift\_tt2}(t_n) = \text{tt2}(t_n - \text{delay}_n)\,, \tag{C.52}$$
$$\text{shift\_tt3}(t_n) = \text{tt3}(t_n - \text{delay}_n)\,, \tag{C.53}$$
$$\text{shift\_tt1\_p}(t_n) = \text{tt1\_p}(t_n - \text{delay}_n)\,, \tag{C.54}$$
$$\text{shift\_tt2\_p}(t_n) = \text{tt2\_p}(t_n - \text{delay}_n)\,, \tag{C.55}$$
$$\text{shift\_tt3\_p}(t_n) = \text{tt3\_p}(t_n - \text{delay}_n)\,. \tag{C.56}$$

**Parameters**

- order (int), interpolation order to time-shift travel times, must be an odd integer greater or equal to 1.
- delay (double), antialiasing filter group delay, in s.

**Inputs**

- tt1 (double), estimated travel times along link 1, in s.
- tt1_p (double), estimated travel times along link 1', in s.
- tt2 (double), estimated travel times along link 2, in s.
- tt2_p (double), estimated travel times along link 2', in s.
- tt3 (double), estimated travel times along link 3, in s.
- tt3_p (double), estimated travel times along link 3', in s.

**Outputs**

- shift_tt1 (double), time-shifted travel times along link 1, in s.
- shift_tt1_p (double), time-shifted travel times along link 1', in s.
- shift_tt2 (double), time-shifted travel times along link 2, in s.
- shift_tt2_p (double), time-shifted travel times along link 2', in s.
- shift_tt3 (double), time-shifted travel times along link 3, in s.
- shift_tt3_p (double), time-shifted travel times along link 3', in s.

### C.5.5 xi

Compute $\xi$ intermediary variables for unprimed optical benches.

**Model**

The $\xi$ variable removes the optical-bench displacement noise, and is given in [Ott15] by

$$\begin{aligned}\text{result}_n = \text{s1}_n + \text{theta1s}_n \times \text{theta1tau}_n \times \frac{\text{epsilon1}_n - \text{tau1}_n}{2} \\ + \text{theta1s}_n \times \text{theta2\_ptau}_n \times \frac{\text{epsilon2\_p}(t_n - \text{tt3}_n) - \text{tau2\_p}(t_n - \text{tt3}_n)}{2}\,.\end{aligned} \tag{C.57}$$

The names of inputs and outputs match the $\xi_1$ variable, but the node can be used to form $\xi_2$ and $\xi_3$ by simply connecting the correct inputs. They are obtained by a circular permutation of indices.

**Parameters**

- max_delay (double), max delay, in s.
- order (int), interpolation order for delays, must be an odd integer greater or equal to 1.

**Inputs**

- s1 (double), science signal on optical bench 1.
- epsilon1 (double), test-mass signal on optical bench 1.
- tau1 (double), reference signal on optical bench 1.
- epsilon2_p (double), test-mass signal on optical bench 2'.
- tau2_p (double), reference signal on optical bench 2'.
- theta1s (double), science beatnote polarity on optical bench 1, is +/- 1.
- theta1tau (double), reference beatnote polarity on optical bench 1, is +/- 1.
- theta2_ptau (double), reference beatnote polarity on optical bench 2', is +/- 1.
- lambda1_p (double), laser frequency on optical bench 1', in Hz.
- lambda2_p (double), laser frequency on optical bench 2', in Hz.
- lambda2 (double), laser frequency on optical bench 2, in Hz.
- tt3 (double), light travel time along link 3, in s.

**Outputs**

- result (double), $\xi_1$ intermediary variable.

### C.5.6 Xi_p

Compute $\xi$ intermediary variables for primed optical benches.

**Model**

The $\xi$ variable removes the optical-bench displacement noise, and is given in [Ott15] by

$$\begin{aligned}\text{result}_n = \text{s1\_p}_n + \text{theta1\_ps}_n \times \text{theta1\_ptau}_n \times \frac{\text{epsilon1\_p}_n - \text{tau1\_p}_n}{2} \\ + \text{theta1\_ps}_n \times \text{theta3tau}_n \times \frac{\text{epsilon3}(t_n - \text{tt2\_p}_n) - \text{tau3}(t_n - \text{tt2\_p}_n)}{2}\,.\end{aligned} \tag{C.58}$$

The names of inputs and outputs match the $\xi_{1'}$ variable, but the node can be used to form $\xi_{2'}$ and $\xi_{3'}$ by simply connecting the correct inputs. They are obtained by a circular permutation of indices.

**Parameters**

- max_delay (double), max delay, in s.
- order (int), interpolation order for delays, must be an odd integer greater or equal to 1.

**Inputs**

- s1_p (double), science signal on optical bench 1'.
- epsilon1_p (double), test-mass signal on optical bench 1'.
- tau1_p (double), reference signal on optical bench 1'.
- epsilon2_p (double), test-mass signal on optical bench 2'.
- tau2_p (double), reference signal on optical bench 2'.
- theta1_ps (double), science beatnote polarity on optical bench 1', is +/- 1.
- theta1_ptau (double), reference beatnote polarity on optical bench 1', is +/- 1.

- theta3tau (double), reference beatnote polarity on optical bench 3, is +/- 1.
- lambda1 (double), laser frequency on optical bench 1, in Hz.
- lambda3 (double), laser frequency on optical bench 3, in Hz.
- lambda3_p (double), laser frequency on optical bench 3', in Hz.
- tt2_p (double), light travel time along link 2', in s.

**Outputs**

- result (double), $\xi_{1'}$ intermediary variable.

### C.5.7 Eta

Compute $\eta$ intermediary variables for unprimed optical benches.

**Model**

The $\eta$ variable reduces the number of free-running lasers to three, and is given in [Ott15] by

$$\text{result}_n = \text{theta1s}_n \times \text{xi1}_n + \text{theta2\_ptau} \times \frac{\text{tau2\_p}(t_n - \text{tt3}_n) + \text{tau2}(t_n - \text{tt3}_n)}{2}. \tag{C.59}$$

The names of inputs and outputs match the $\eta_1$ variable, but the node can be used to form $\eta_2$ and $\eta_3$ by simply connecting the correct inputs. They are obtained by a circular permutation of indices.

**Parameters**

- max_delay (double), max delay, in s.
- order (int), interpolation order for delays, must be an odd integer greater or equal to 1.

**Inputs**

- xi1 (double), $\xi_1$ intermediary variable.
- tau2 (double), reference signal on optical bench 2.

- tau2_p (double), reference signal on optical bench 2'.
- theta1s (double), science beatnote polarity on optical bench 1, is +/- 1.
- theta2_ptau (double), reference beatnote polarity on optical bench 2', is +/- 1.
- tt3 (double), light travel time along link 3, in s.

**Outputs**

- result (double), $\eta_1$ intermediary variable.

### C.5.8 Eta_p

Compute $\eta$ intermediary variables for primed optical benches.

**Model**

The $\eta$ variable reduces the number of free-running lasers to three, and is given in [Ott15] by

$$\text{result}_n = \text{theta1\_ps}_n \times \text{xi1\_p}_n + \text{theta1\_ptau} \times \frac{\text{tau1\_p}_n + \text{tau1}_n}{2} \,. \tag{C.60}$$

The names of inputs and outputs match the $\eta_{1'}$ variable, but the node can be used to form $\eta_{2'}$ and $\eta_{3'}$ by simply connecting the correct inputs. They are obtained by a circular permutation of indices.

**Parameters**

- max_delay (double), max delay, in s.
- order (int), interpolation order for delays, must be an odd integer greater or equal to 1.

**Inputs**

- xi1_p (double), $\xi_{1'}$ intermediary variable.
- tau1 (double), reference signal on optical bench 1.
- tau1_p (double), reference signal on optical bench 1'.

- theta1_ps (double), science beatnote polarity on optical bench 1', is +/- 1.
- theta1_ptau (double), reference beatnote polarity on optical bench 1', is +/- 1.

**Outputs**

- result (double), $\eta_{1'}$ intermediary variable.

### C.5.9 IntermediaryVariables

Build $\xi$'s and $\eta$'s intermediary variables for all optical benches.

**Model**

This graph embeds three instances of Xi, Xi_p, Eta, and Eta_p. Refer to the documentation of these graphs for further information.

**Parameters**

- max_delay (double), max delay, in s.
- order (int), interpolation order for delays, must be an odd integer greater or equal to 1.

**Inputs**

- Measurement Channels
  - s1 (double), science interferometric measurement in MOSA 1, in fractional frequency deviation.
  - s1_p (double), science interferometric measurement in MOSA 1', in fractional frequency deviation.
  - s2 (double), science interferometric measurement in MOSA 2, in fractional frequency deviation.
  - s2_p (double), science interferometric measurement in MOSA 2', in fractional frequency deviation.
  - s3 (double), science interferometric measurement in MOSA 3, in fractional frequency deviation.

- s3_p (double), science interferometric measurement in MOSA 3', in fractional frequency deviation.
- tau1 (double), reference interferometric measurement in MOSA 1, in fractional frequency deviation.
- tau1_p (double), reference interferometric measurement in MOSA 1', in fractional frequency deviation.
- tau2 (double), reference interferometric measurement in MOSA 2, in fractional frequency deviation.
- tau2_p (double), reference interferometric measurement in MOSA 2', in fractional frequency deviation.
- tau3 (double), reference interferometric measurement in MOSA 3, in fractional frequency deviation.
- tau3_p (double), reference interferometric measurement in MOSA 3', in fractional frequency deviation.
- epsilon1 (double), test-mass interferometric measurement in MOSA 1, in fractional frequency deviation.
- epsilon1_p (double), test-mass interferometric measurement in MOSA 1', in fractional frequency deviation.
- epsilon2 (double), test-mass interferometric measurement in MOSA 2, in fractional frequency deviation.
- epsilon2_p (double), test-mass interferometric measurement in MOSA 2', in fractional frequency deviation.
- epsilon3 (double), test-mass interferometric measurement in MOSA 3, in fractional frequency deviation.
- epsilon3_p (double), test-mass interferometric measurement in MOSA 3', in fractional frequency deviation.

- Light Travel Times

  - tt1 (double), light travel times along link 1, in s.
  - tt1_p (double), light travel times along link 1', in s.
  - tt2 (double), light travel times along link 2, in s.
  - tt2_p (double), light travel times along link 2', in s.
  - tt3 (double), light travel times along link 3, in s.
  - tt3_p (double), light travel times along link 3', in s.

- Beatnote Frequencies

  - sci_f1 (double), science beatnote frequencies in MOSA 1, in MHz.
  - sci_f1_p (double), science beatnote frequencies in MOSA 1', in MHz.
  - sci_f2 (double), science beatnote frequencies in MOSA 2, in MHz.
  - sci_f2_p (double), science beatnote frequencies in MOSA 2', in MHz.
  - sci_f3 (double), science beatnote frequencies in MOSA 3, in MHz.
  - sci_f3_p (double), science beatnote frequencies in MOSA 3', in MHz.
  - ref_f1 (double), reference and test-mass beatnote frequencies in MOSA 1, in MHz.
  - ref_f1_p (double), reference and test-mass beatnote frequencies in MOSA 1', in MHz.
  - ref_f2 (double), reference and test-mass beatnote frequencies in MOSA 2, in MHz.
  - ref_f2_p (double), reference and test-mass beatnote frequencies in MOSA 2', in MHz.
  - ref_f3 (double), reference and test-mass beatnote frequencies in MOSA 3, in MHz.
  - ref_f3_p (double), reference and test-mass beatnote frequencies in MOSA 3', in MHz.

**Outputs**

- xi1 (double), $\xi_1$ intermediary variable.
- xi2 (double), $\xi_2$ intermediary variable.
- xi3 (double), $\xi_3$ intermediary variable.
- xi1_p (double), $\xi_{1'}$ intermediary variable.
- xi2_p (double), $\xi_{2'}$ intermediary variable.
- xi3_p (double), $\xi_{3'}$ intermediary variable.
- eta1 (double), $\eta_1$ intermediary variable.
- eta2 (double), $\eta_2$ intermediary variable.
- eta3 (double), $\eta_3$ intermediary variable.
- eta1_p (double), $\eta_{1'}$ intermediary variable.
- eta2_p (double), $\eta_{2'}$ intermediary variable.
- eta3_p (double), $\eta_{3'}$ intermediary variable.

## C.6 Simulation Configuration

The simulation can be configured in `config.py`. In this section, we document the various configuration options.

- Sampling Frequencies
  - LOW_SAMPLING_FREQ (float), sampling frequency at which interferometric measurements are delivered by the onboard computer, in Hz. The current default value is 3 Hz.
  - DOWNSAMPLING (int), downsampling rate to go from HIGH_SAMPLING_FREQ to LOW_SAMPLING_FREQ. This downsampling rate must be an integer, since signals are decimated by the onboard computer. The current default value is 10.
  - HIGH_SAMPLING_FREQ (float, read-only), sampling frequency used to simulate all physical behaviour as well as the interferometric measurements before they

are downsampled by the onboard computer, in Hz. This parameter is deduced from LOW_SAMPLING_FREQ and DOWNSAMPLING, and defaults to 10 Hz.

- ORBIT_UPSAMPLING (int), upsampling rate use to compute the orbits. The spacecraft positions and velocities can be modeled, or read from a file, at a sampling frequency lower than HIGH_SAMPLING_FREQ. This defaults to 1.

- ORBIT_SAMPLING_FREQ (float, read-only), very low sampling frequency, used for the orbits, in Hz. This parameter is deduced from HIGH_SAMPLING_FREQ and ORBIT_UPSAMPLING, and default to 30 Hz.

- Orbits and TDI Generation

  - ORBIT_TYPE (str), defines the type of orbits used to compute the spacecraft positions and velocities in the graph LaserLinks. Its value must be one of the following: keplerian for analytic Keplerian orbits (*c.f.* KeplerianOrbits and section 3.2.3), linear_armlengths to simulate armlengths evolving linearly with time (*c.f.* section 3.2.3), or from_file to read the orbits from an external file (*c.f.* section 3.2.3). Please note that this option does not set the TDI generation. The default value is keplerian.

  - TDI_GENERATION (int), TDI generation used in TDI. Must be 1.5 or 2, defaults to 2.

- Publication of Outputs

  - PUBLISH_MEASUREMENTS (bool), whether interferometric measurements should be published, defaults to True.

  - PUBLISH_TRAVEL_TIMES (bool), whether the estimated light travel times along the arms should be published, defaults to True.

  - PUBLISH_INTERVAR (bool), whether the TDI intermediary variables should be published (*c.f.* chapter 4), defaults to True.

  - PUBLISH_MICHELSON (bool), whether TDI Michelson $X$, $Y$, and $Z$ variables should be published (*c.f.* chapter 4), defaults to True.

  - PUBLISH_ORTHVAR (bool), whether TDI quasi-orthogonal $A$, $E$, and $T$ variables should be published (*c.f.* chapter 4), defaults to True.

- PUBLISH_SAGNAC (bool), whether TDI Sagnac $\alpha$, $\beta$, and $\gamma$ variables should be published (*c.f.* chapter 4), defaults to False.
- CLOCKCAL_MICHELSON (bool), whether clock calibration should be carried out on Michelson variables (*c.f.* chapter 6), defaults to True.
- CLOCKCAL_ORTHVAR (bool), whether clock calibration should be carried out on quasi-orthogonal variables (*c.f.* chapter 6), defaults to True.

# Bibliography

[AAA+13] J. Aasi, J. Abadie, B. P. Abbott, R. Abbott, T. D. Abbott, M. R. Abernathy, C. Adams, T. Adams, P. Addesso, R. X. Adhikari, C. Affeldt, O. D. Aguiar, P. Ajith, B. Allen, E. Amador Ceron, D. Amariutei, S. B. Anderson, W. G. Anderson, K. Arai, M. C. Araya, C. Arceneaux, S. Ast, S. M. Aston, D. Atkinson, P. Aufmuth, C. Aulbert, L. Austin, B. E. Aylott, S. Babak, P. T. Baker, S. Ballmer, Y. Bao, J. C. Barayoga, D. Barker, B. Barr, L. Barsotti, M. A. Barton, I. Bartos, R. Bassiri, J. Batch, J. Bauchrowitz, B. Behnke, A. S. Bell, C. Bell, G. Bergmann, J. M. Berliner, A. Bertolini, J. Betzwieser, N. Beveridge, P. T. Beyersdorf, T. Bhadbhade, I. A. Bilenko, G. Billingsley, J. Birch, S. Biscans, E. Black, J. K. Blackburn, L. Blackburn, D. Blair, B. Bland, O. Bock, T. P. Bodiya, C. Bogan, C. Bond, R. Bork, M. Born, S. Bose, J. Bowers, P. R. Brady, V. B. Braginsky, J. E. Brau, J. Breyer, D. O. Bridges, M. Brinkmann, M. Britzger, A. F. Brooks, D. A. Brown, D. D. Brown, K. Buckland, F. Brückner, B. C. Buchler, A. Buonanno, J. Burguet-Castell, R. L. Byer, L. Cadonati, J. B. Camp, P. Campsie, K. Cannon, J. Cao, C. D. Capano, L. Carbone, S. Caride, A. D. Castiglia, S. Caudill, M. Cavaglià, C. Cepeda, T. Chalermsongsak, S. Chao, P. Charlton, X. Chen, Y. Chen, H. S. Cho, J. H. Chow, N. Christensen, Q. Chu, S. S.Y. Chua, C. T.Y. Chung, G. Ciani, F. Clara, D. E. Clark, J. A. Clark, M. Constancio, D. Cook, T. R. Corbitt, M. Cordier, N. Cornish, A. Corsi, C. A. Costa, M. W. Coughlin, S. Countryman, P. Couvares, D. M. Coward, M. Cowart, D. C. Coyne, K. Craig, J. D.E. Creighton, T. D. Creighton, A. Cumming, L. Cunningham, K. Dahl, M. Damjanic, S. L. Danilishin, K. Danzmann, B. Daudert, H. Daveloza, G. S. Davies, E. J. Daw, T. Dayanga, E. Deleeuw, T. Denker, T. Dent, V. Dergachev, R. DeRosa, R. DeSalvo, S. Dhurandhar, I. Di Palma, M. Díaz, A. Dietz, F. Donovan, K. L. Dooley, S. Doravari, S. Drasco, R. W.P. Drever, J. C.

Driggers, Z. Du, J. C. Dumas, S. Dwyer, T. Eberle, M. Edwards, A. Effler, P. Ehrens, S. S. Eikenberry, R. Engel, R. Essick, T. Etzel, K. Evans, M. Evans, T. Evans, M. Factourovich, S. Fairhurst, Q. Fang, B. F. Farr, W. Farr, M. Favata, D. Fazi, H. Fehrmann, D. Feldbaum, L. S. Finn, R. P. Fisher, S. Foley, E. Forsi, N. Fotopoulos, M. Frede, M. A. Frei, Z. Frei, A. Freise, R. Frey, T. T. Fricke, D. Friedrich, P. Fritschel, V. V. Frolov, M. K. Fujimoto, P. J. Fulda, M. Fyffe, J. Gair, J. Garcia, N. Gehrels, G. Gelencser, L. Á Gergely, S. Ghosh, J. A. Giaime, S. Giampanis, K. D. Giardina, S. Gil-Casanova, C. Gill, J. Gleason, E. Goetz, G. González, N. Gordon, M. L. Gorodetsky, S. Gossan, S. Goßler, C. Graef, P. B. Graff, A. Grant, S. Gras, C. Gray, R. J.S. Greenhalgh, A. M. Gretarsson, C. Griffo, H. Grote, K. Grover, S. Grunewald, C. Guido, E. K. Gustafson, R. Gustafson, D. Hammer, G. Hammond, J. Hanks, C. Hanna, J. Hanson, K. Haris, J. Harms, G. M. Harry, I. W. Harry, E. D. Harstad, M. T. Hartman, K. Haughian, K. Hayama, J. Heefner, M. C. Heintze, M. A. Hendry, I. S. Heng, A. W. Heptonstall, M. Heurs, M. Hewitson, S. Hild, D. Hoak, K. A. Hodge, K. Holt, M. Holtrop, T. Hong, S. Hooper, J. Hough, E. J. Howell, V. Huang, E. A. Huerta, B. Hughey, S. H. Huttner, M. Huynh, T. Huynh-Dinh, D. R. Ingram, R. Inta, T. Isogai, A. Ivanov, B. R. Iyer, K. Izumi, M. Jacobson, E. James, H. Jang, Y. J. Jang, E. Jesse, W. W. Johnson, D. Jones, D. I. Jones, R. Jones, L. Ju, P. Kalmus, V. Kalogera, S. Kandhasamy, G. Kang, J. B. Kanner, R. Kasturi, E. Katsavounidis, W. Katzman, H. Kaufer, K. Kawabe, S. Kawamura, F. Kawazoe, D. Keitel, D. B. Kelley, W. Kells, D. G. Keppel, A. Khalaidovski, F. Y. Khalili, E. A. Khazanov, B. K. Kim, C. Kim, K. Kim, N. Kim, Y. M. Kim, P. J. King, D. L. Kinzel, J. S. Kissel, S. Klimenko, J. Kline, K. Kokeyama, V. Kondrashov, S. Koranda, W. Z. Korth, D. Kozak, C. Kozameh, A. Kremin, V. Kringel, B. Krishnan, C. Kucharczyk, G. Kuehn, P. Kumar, R. Kumar, B. J. Kuper, R. Kurdyumov, P. Kwee, P. K. Lam, M. Landry, B. Lantz, P. D. Lasky, C. Lawrie, A. Lazzarini, A. Le Roux, P. Leaci, C. H. Lee, H. K. Lee, H. M. Lee, J. Lee, J. R. Leong, B. Levine, V. Lhuillier, A. C. Lin, V. Litvine, Y. Liu, Z. Liu, N. A. Lockerbie, D. Lodhia, K. Loew, J. Logue, A. L. Lombardi, M. Lormand, J. Lough, M. Lubinski, H. Lück, A. P. Lundgren, J. Macarthur, E. Macdonald, B. Machenschalk, M. MacInnis, D. M. Macleod, F. Magaña-Sandoval, M. Mageswaran, K. Mailand, G. Manca, I. Mandel, V. Mandic, S. Márka, Z. Márka, A. S. Markosyan, E. Maros, I. W. Martin, R. M. Martin, D. Martinov, J. N. Marx, K. Mason, F. Matichard,

L. Matone, R. A. Matzner, N. Mavalvala, G. May, G. Mazzolo, K. McAuley, R. McCarthy, D. E. McClelland, S. C. McGuire, G. McIntyre, J. McIver, G. D. Meadors, M. Mehmet, T. Meier, A. Melatos, G. Mendell, R. A. Mercer, S. Meshkov, C. Messenger, M. S. Meyer, H. Miao, J. Miller, C. M.F. Mingarelli, S. Mitra, V. P. Mitrofanov, G. Mitselmakher, R. Mittleman, B. Moe, F. Mokler, S. R.P. Mohapatra, D. Moraru, G. Moreno, T. Mori, S. R. Morriss, K. Mossavi, C. M. Mow-Lowry, C. L. Mueller, G. Mueller, S. Mukherjee, A. Mullavey, J. Munch, D. Murphy, P. G. Murray, A. Mytidis, D. Nanda Kumar, T. Nash, R. Nayak, V. Necula, G. Newton, T. Nguyen, E. Nishida, A. Nishizawa, A. Nitz, D. Nolting, M. E. Normandin, L. K. Nuttall, J. O'Dell, B. O'Reilly, R. O'Shaughnessy, E. Ochsner, E. Oelker, G. H. Ogin, J. J. Oh, S. H. Oh, F. Ohme, P. Oppermann, C. Osthelder, C. D. Ott, D. J. Ottaway, R. S. Ottens, J. Ou, H. Overmier, B. J. Owen, C. Padilla, A. Pai, Y. Pan, C. Pankow, M. A. Papa, H. Paris, W. Parkinson, M. Pedraza, S. Penn, C. Peralta, A. Perreca, M. Phelps, M. Pickenpack, V. Pierro, I. M. Pinto, M. Pitkin, H. J. Pletsch, J. Pöld, F. Postiglione, C. Poux, V. Predoi, T. Prestegard, L. R. Price, M. Prijatelj, S. Privitera, L. G. Prokhorov, O. Puncken, V. Quetschke, E. Quintero, R. Quitzow-James, F. J. Raab, H. Radkins, P. Raffai, S. Raja, M. Rakhmanov, C. Ramet, V. Raymond, C. M. Reed, T. Reed, S. Reid, D. H. Reitze, R. Riesen, K. Riles, M. Roberts, N. A. Robertson, E. L. Robinson, S. Roddy, C. Rodriguez, L. Rodriguez, M. Rodruck, J. G. Rollins, J. H. Romie, C. Röver, S. Rowan, A. Rüdiger, K. Ryan, F. Salemi, L. Sammut, V. Sandberg, J. Sanders, S. Sankar, V. Sannibale, L. Santamaría, I. Santiago-Prieto, G. Santostasi, B. S. Sathyaprakash, P. R. Saulson, R. L. Savage, R. Schilling, R. Schnabel, R. M.S. Schofield, D. Schuette, B. Schulz, B. F. Schutz, P. Schwinberg, J. Scott, S. M. Scott, F. Seifert, D. Sellers, A. S. Sengupta, A. Sergeev, D. A. Shaddock, M. S. Shahriar, M. Shaltev, Z. Shao, B. Shapiro, P. Shawhan, D. H. Shoemaker, T. L. Sidery, X. Siemens, D. Sigg, D. Simakov, A. Singer, L. Singer, A. M. Sintes, G. R. Skelton, B. J.J. Slagmolen, J. Slutsky, J. R. Smith, M. R. Smith, R. J.E. Smith, N. D. Smith-Lefebvre, E. J. Son, B. Sorazu, T. Souradeep, M. Stefszky, E. Steinert, J. Steinlechner, S. Steinlechner, S. Steplewski, D. Stevens, A. Stochino, R. Stone, K. A. Strain, S. E. Strigin, A. S. Stroeer, A. L. Stuver, T. Z. Summerscales, S. Susmithan, P. J. Sutton, G. Szeifert, D. Talukder, D. B. Tanner, S. P. Tarabrin, R. Taylor, M. Thomas, P. Thomas, K. A. Thorne, K. S. Thorne, E. Thrane, V. Tiwari, K. V. Tokmakov, C. Tomlinson, C. V. Torres, C. I. Torrie, G. Traylor,

M. Tse, D. Ugolini, C. S. Unnikrishnan, H. Vahlbruch, M. Vallisneri, M. V. Van Der Sluys, A. A. Van Veggel, S. Vass, R. Vaulin, A. Vecchio, P. J. Veitch, J. Veitch, K. Venkateswara, S. Verma, R. Vincent-Finley, S. Vitale, T. Vo, C. Vorvick, W. D. Vousden, S. P. Vyatchanin, A. Wade, L. Wade, M. Wade, S. J. Waldman, L. Wallace, Y. Wan, M. Wang, J. Wang, X. Wang, A. Wanner, R. L. Ward, M. Was, M. Weinert, A. J. Weinstein, R. Weiss, T. Welborn, L. Wen, P. Wessels, M. West, T. Westphal, K. Wette, J. T. Whelan, S. E. Whitcomb, A. G. Wiseman, D. J. White, B. F. Whiting, K. Wiesner, C. Wilkinson, P. A. Willems, L. Williams, R. Williams, T. Williams, J. L. Willis, B. Willke, M. Wimmer, L. Winkelmann, W. Winkler, C. C. Wipf, H. Wittel, G. Woan, R. Wooley, J. Worden, J. Yablon, I. Yakushin, H. Yamamoto, C. C. Yancey, H. Yang, D. Yeaton-Massey, S. Yoshida, H. Yum, M. Zanolin, F. Zhang, L. Zhang, C. Zhao, H. Zhu, X. J. Zhu, N. Zotov, M. E. Zucker, and J. Zweizig. Enhanced sensitivity of the LIGO gravitational wave detector by using squeezed states of light. *Nature Photonics*, 2013.

[AAA+16a] B. P. Abbott, R. Abbott, T. D. Abbott, M. R. Abernathy, F. Acernese, K. Ackley, C. Adams, T. Adams, P. Addesso, R. X. Adhikari, V. B. Adya, C. Affeldt, M. Agathos, K. Agatsuma, N. Aggarwal, O. D. Aguiar, L. Aiello, A. Ain, P. Ajith, B. Allen, A. Allocca, P. A. Altin, S. B. Anderson, W. G. Anderson, K. Arai, M. A. Arain, M. C. Araya, C. C. Arceneaux, J. S. Areeda, N. Arnaud, K. G. Arun, S. Ascenzi, G. Ashton, M. Ast, S. M. Aston, P. Astone, P. Aufmuth, C. Aulbert, S. Babak, P. Bacon, M. K. M. Bader, P. T. Baker, F. Baldaccini, G. Ballardin, S. W. Ballmer, J. C. Barayoga, S. E. Barclay, B. C. Barish, D. Barker, F. Barone, B. Barr, L. Barsotti, M. Barsuglia, D. Barta, J. Bartlett, M. A. Barton, I. Bartos, R. Bassiri, A. Basti, J. C. Batch, C. Baune, V. Bavigadda, M. Bazzan, B. Behnke, M. Bejger, C. Belczynski, A. S. Bell, C. J. Bell, B. K. Berger, J. Bergman, G. Bergmann, C. P. L. Berry, D. Bersanetti, A. Bertolini, J. Betzwieser, S. Bhagwat, R. Bhandare, I. A. Bilenko, G. Billingsley, J. Birch, R. Birney, O. Birnholtz, S. Biscans, A. Bisht, M. Bitossi, C. Biwer, M. A. Bizouard, J. K. Blackburn, C. D. Blair, D. G. Blair, R. M. Blair, S. Bloemen, O. Bock, T. P. Bodiya, M. Boer, G. Bogaert, C. Bogan, A. Bohe, P. Bojtos, C. Bond, F. Bondu, R. Bonnand, B. A. Boom, R. Bork, V. Boschi, S. Bose, Y. Bouffanais, A. Bozzi, C. Bradaschia, P. R. Brady, V. B. Braginsky, M. Branchesi, J. E. Brau, T. Briant, A. Brillet, M. Brinkmann, V. Bris-

son, P. Brockill, A. F. Brooks, D. A. Brown, D. D. Brown, N. M. Brown, C. C. Buchanan, A. Buikema, T. Bulik, H. J. Bulten, A. Buonanno, D. Buskulic, C. Buy, R. L. Byer, M. Cabero, L. Cadonati, G. Cagnoli, C. Cahillane, J. Calderón Bustillo, T. Callister, E. Calloni, J. B. Camp, K. C. Cannon, J. Cao, C. D. Capano, E. Capocasa, F. Carbognani, S. Caride, J. Casanueva Diaz, C. Casentini, S. Caudill, M. Cavaglià, F. Cavalier, R. Cavalieri, G. Cella, C. B. Cepeda, L. Cerboni Baiardi, G. Cerretani, E. Cesarini, R. Chakraborty, T. Chalermsongsak, S. J. Chamberlin, M. Chan, S. Chao, P. Charlton, E. Chassande-Mottin, H. Y. Chen, Y. Chen, C. Cheng, A. Chincarini, A. Chiummo, H. S. Cho, M. Cho, J. H. Chow, N. Christensen, Q. Chu, S. Chua, S. Chung, G. Ciani, F. Clara, J. A. Clark, F. Cleva, E. Coccia, P.-F. Cohadon, A. Colla, C. G. Collette, L. Cominsky, M. Constancio, A. Conte, L. Conti, D. Cook, T. R. Corbitt, N. Cornish, A. Corsi, S. Cortese, C. A. Costa, M. W. Coughlin, S. B. Coughlin, J.-P. Coulon, S. T. Countryman, P. Couvares, E. E. Cowan, D. M. Coward, M. J. Cowart, D. C. Coyne, R. Coyne, K. Craig, J. D. E. Creighton, T. D. Creighton, J. Cripe, S. G. Crowder, A. M. Cruise, A. Cumming, L. Cunningham, E. Cuoco, T. Dal Canton, S. L. Danilishin, S. D'Antonio, K. Danzmann, N. S. Darman, C. F. Da Silva Costa, V. Dattilo, I. Dave, H. P. Daveloza, M. Davier, G. S. Davies, E. J. Daw, R. Day, S. De, D. DeBra, G. Debreczeni, J. Degallaix, M. De Laurentis, S. Deléglise, W. Del Pozzo, T. Denker, T. Dent, H. Dereli, V. Dergachev, R. T. DeRosa, R. De Rosa, R. DeSalvo, S. Dhurandhar, M. C. Díaz, L. Di Fiore, M. Di Giovanni, A. Di Lieto, S. Di Pace, I. Di Palma, A. Di Virgilio, G. Dojcinoski, V. Dolique, F. Donovan, K. L. Dooley, S. Doravari, R. Douglas, T. P. Downes, M. Drago, R. W. P. Drever, J. C. Driggers, Z. Du, M. Ducrot, S. E. Dwyer, T. B. Edo, M. C. Edwards, A. Effler, H.-B. Eggenstein, P. Ehrens, J. Eichholz, S. S. Eikenberry, W. Engels, R. C. Essick, T. Etzel, M. Evans, T. M. Evans, R. Everett, M. Factourovich, V. Fafone, H. Fair, S. Fairhurst, X. Fan, Q. Fang, S. Farinon, B. Farr, W. M. Farr, M. Favata, M. Fays, H. Fehrmann, M. M. Fejer, D. Feldbaum, I. Ferrante, E. C. Ferreira, F. Ferrini, F. Fidecaro, L. S. Finn, I. Fiori, D. Fiorucci, R. P. Fisher, R. Flaminio, M. Fletcher, H. Fong, J.-D. Fournier, S. Franco, S. Frasca, F. Frasconi, M. Frede, Z. Frei, A. Freise, R. Frey, V. Frey, T. T. Fricke, P. Fritschel, V. V. Frolov, P. Fulda, M. Fyffe, H. A. G. Gabbard, J. R. Gair, L. Gammaitoni, S. G. Gaonkar, F. Garufi, A. Gatto, G. Gaur, N. Gehrels, G. Gemme, B. Gendre, E. Genin, A. Gennai, J. George, L. Gergely, V. Germain, Abhirup Ghosh, Archisman Ghosh, S. Ghosh, J. A. Giaime,

K. D. Giardina, A. Giazotto, K. Gill, A. Glaefke, J. R. Gleason, E. Goetz, R. Goetz, L. Gondan, G. González, J. M. Gonzalez Castro, A. Gopakumar, N. A. Gordon, M. L. Gorodetsky, S. E. Gossan, M. Gosselin, R. Gouaty, C. Graef, P. B. Graff, M. Granata, A. Grant, S. Gras, C. Gray, G. Greco, A. C. Green, R. J. S. Greenhalgh, P. Groot, H. Grote, S. Grunewald, G. M. Guidi, X. Guo, A. Gupta, M. K. Gupta, K. E. Gushwa, E. K. Gustafson, R. Gustafson, J. J. Hacker, B. R. Hall, E. D. Hall, G. Hammond, M. Haney, M. M. Hanke, J. Hanks, C. Hanna, M. D. Hannam, J. Hanson, T. Hardwick, J. Harms, G. M. Harry, I. W. Harry, M. J. Hart, M. T. Hartman, C.-J. Haster, K. Haughian, J. Healy, J. Heefner, A. Heidmann, M. C. Heintze, G. Heinzel, H. Heitmann, P. Hello, G. Hemming, M. Hendry, I. S. Heng, J. Hennig, A. W. Heptonstall, M. Heurs, S. Hild, D. Hoak, K. A. Hodge, D. Hofman, S. E. Hollitt, K. Holt, D. E. Holz, P. Hopkins, D. J. Hosken, J. Hough, E. A. Houston, E. J. Howell, Y. M. Hu, S. Huang, E. A. Huerta, D. Huet, B. Hughey, S. Husa, S. H. Huttner, T. Huynh-Dinh, A. Idrisy, N. Indik, D. R. Ingram, R. Inta, H. N. Isa, J.-M. Isac, M. Isi, G. Islas, T. Isogai, B. R. Iyer, K. Izumi, M. B. Jacobson, T. Jacqmin, H. Jang, K. Jani, P. Jaranowski, S. Jawahar, F. Jiménez-Forteza, W. W. Johnson, N. K. Johnson-McDaniel, D. I. Jones, R. Jones, R. J. G. Jonker, L. Ju, K. Haris, C. V. Kalaghatgi, V. Kalogera, S. Kandhasamy, G. Kang, J. B. Kanner, S. Karki, M. Kasprzack, E. Katsavounidis, W. Katzman, S. Kaufer, T. Kaur, K. Kawabe, F. Kawazoe, F. Kéfélian, M. S. Kehl, D. Keitel, D. B. Kelley, W. Kells, R. Kennedy, D. G. Keppel, J. S. Key, A. Khalaidovski, F. Y. Khalili, I. Khan, S. Khan, Z. Khan, E. A. Khazanov, N. Kijbunchoo, C. Kim, J. Kim, K. Kim, Nam-Gyu Kim, Namjun Kim, Y.-M. Kim, E. J. King, P. J. King, D. L. Kinzel, J. S. Kissel, L. Kleybolte, S. Klimenko, S. M. Koehlenbeck, K. Kokeyama, S. Koley, V. Kondrashov, A. Kontos, S. Koranda, M. Korobko, W. Z. Korth, I. Kowalska, D. B. Kozak, V. Kringel, B. Krishnan, A. Królak, C. Krueger, G. Kuehn, P. Kumar, R. Kumar, L. Kuo, A. Kutynia, P. Kwee, B. D. Lackey, M. Landry, J. Lange, B. Lantz, P. D. Lasky, A. Lazzarini, C. Lazzaro, P. Leaci, S. Leavey, E. O. Lebigot, C. H. Lee, H. K. Lee, H. M. Lee, K. Lee, A. Lenon, M. Leonardi, J. R. Leong, N. Leroy, N. Letendre, Y. Levin, B. M. Levine, T. G. F. Li, A. Libson, T. B. Littenberg, N. A. Lockerbie, J. Logue, A. L. Lombardi, L. T. London, J. E. Lord, M. Lorenzini, V. Loriette, M. Lormand, G. Losurdo, J. D. Lough, C. O. Lousto, G. Lovelace, H. Lück, A. P. Lundgren, J. Luo, R. Lynch, Y. Ma, T. MacDonald, B. Machenschalk, M. MacInnis, D. M. Macleod, F. Magaña-Sandoval, R. M.

Magee, M. Mageswaran, E. Majorana, I. Maksimovic, V. Malvezzi, N. Man, I. Mandel, V. Mandic, V. Mangano, G. L. Mansell, M. Manske, M. Mantovani, F. Marchesoni, F. Marion, S. Márka, Z. Márka, A. S. Markosyan, E. Maros, F. Martelli, L. Martellini, I. W. Martin, R. M. Martin, D. V. Martynov, J. N. Marx, K. Mason, A. Masserot, T. J. Massinger, M. Masso-Reid, F. Matichard, L. Matone, N. Mavalvala, N. Mazumder, G. Mazzolo, R. McCarthy, D. E. McClelland, S. McCormick, S. C. McGuire, G. McIntyre, J. McIver, D. J. McManus, S. T. McWilliams, D. Meacher, G. D. Meadors, J. Meidam, A. Melatos, G. Mendell, D. Mendoza-Gandara, R. A. Mercer, E. Merilh, M. Merzougui, S. Meshkov, C. Messenger, C. Messick, P. M. Meyers, F. Mezzani, H. Miao, C. Michel, H. Middleton, E. E. Mikhailov, L. Milano, J. Miller, M. Millhouse, Y. Minenkov, J. Ming, S. Mirshekari, C. Mishra, S. Mitra, V. P. Mitrofanov, G. Mitselmakher, R. Mittleman, A. Moggi, M. Mohan, S. R. P. Mohapatra, M. Montani, B. C. Moore, C. J. Moore, D. Moraru, G. Moreno, S. R. Morriss, K. Mossavi, B. Mours, C. M. Mow-Lowry, C. L. Mueller, G. Mueller, A. W. Muir, Arunava Mukherjee, D. Mukherjee, S. Mukherjee, N. Mukund, A. Mullavey, J. Munch, D. J. Murphy, P. G. Murray, A. Mytidis, I. Nardecchia, L. Naticchioni, R. K. Nayak, V. Necula, K. Nedkova, G. Nelemans, M. Neri, A. Neunzert, G. Newton, T. T. Nguyen, A. B. Nielsen, S. Nissanke, A. Nitz, F. Nocera, D. Nolting, M. E. N. Normandin, L. K. Nuttall, J. Oberling, E. Ochsner, J. O'Dell, E. Oelker, G. H. Ogin, J. J. Oh, S. H. Oh, F. Ohme, M. Oliver, P. Oppermann, Richard J. Oram, B. O'Reilly, R. O'Shaughnessy, C. D. Ott, D. J. Ottaway, R. S. Ottens, H. Overmier, B. J. Owen, A. Pai, S. A. Pai, J. R. Palamos, O. Palashov, C. Palomba, A. Pal-Singh, H. Pan, Y. Pan, C. Pankow, F. Pannarale, B. C. Pant, F. Paoletti, A. Paoli, M. A. Papa, H. R. Paris, W. Parker, D. Pascucci, A. Pasqualetti, R. Passaquieti, D. Passuello, B. Patricelli, Z. Patrick, B. L. Pearlstone, M. Pedraza, R. Pedurand, L. Pekowsky, A. Pele, S. Penn, A. Perreca, H. P. Pfeiffer, M. Phelps, O. Piccinni, M. Pichot, M. Pickenpack, F. Piergiovanni, V. Pierro, G. Pillant, L. Pinard, I. M. Pinto, M. Pitkin, J. H. Poeld, R. Poggiani, P. Popolizio, A. Post, J. Powell, J. Prasad, V. Predoi, S. S. Premachandra, T. Prestegard, L. R. Price, M. Prijatelj, M. Principe, S. Privitera, R. Prix, G. A. Prodi, L. Prokhorov, O. Puncken, M. Punturo, P. Puppo, M. Pürrer, H. Qi, J. Qin, V. Quetschke, E. A. Quintero, R. Quitzow-James, F. J. Raab, D. S. Rabeling, H. Radkins, P. Raffai, S. Raja, M. Rakhmanov, C. R. Ramet, P. Rapagnani, V. Raymond, M. Razzano, V. Re, J. Read, C. M. Reed,

T. Regimbau, L. Rei, S. Reid, D. H. Reitze, H. Rew, S. D. Reyes, F. Ricci, K. Riles, N. A. Robertson, R. Robie, F. Robinet, A. Rocchi, L. Rolland, J. G. Rollins, V. J. Roma, J. D. Romano, R. Romano, G. Romanov, J. H. Romie, D. Rosińska, S. Rowan, A. Rüdiger, P. Ruggi, K. Ryan, S. Sachdev, T. Sadecki, L. Sadeghian, L. Salconi, M. Saleem, F. Salemi, A. Samajdar, L. Sammut, L. M. Sampson, E. J. Sanchez, V. Sandberg, B. Sandeen, G. H. Sanders, J. R. Sanders, B. Sassolas, B. S. Sathyaprakash, P. R. Saulson, O. Sauter, R. L. Savage, A. Sawadsky, P. Schale, R. Schilling, J. Schmidt, P. Schmidt, R. Schnabel, R. M. S. Schofield, A. Schönbeck, E. Schreiber, D. Schuette, B. F. Schutz, J. Scott, S. M. Scott, D. Sellers, A. S. Sengupta, D. Sentenac, V. Sequino, A. Sergeev, G. Serna, Y. Setyawati, A. Sevigny, D. A. Shaddock, T. Shaffer, S. Shah, M. S. Shahriar, M. Shaltev, Z. Shao, B. Shapiro, P. Shawhan, A. Sheperd, D. H. Shoemaker, D. M. Shoemaker, K. Siellez, X. Siemens, D. Sigg, A. D. Silva, D. Simakov, A. Singer, L. P. Singer, A. Singh, R. Singh, A. Singhal, A. M. Sintes, B. J. J. Slagmolen, J. R. Smith, M. R. Smith, N. D. Smith, R. J. E. Smith, E. J. Son, B. Sorazu, F. Sorrentino, T. Souradeep, A. K. Srivastava, A. Staley, M. Steinke, J. Steinlechner, S. Steinlechner, D. Steinmeyer, B. C. Stephens, S. P. Stevenson, R. Stone, K. A. Strain, N. Straniero, G. Stratta, N. A. Strauss, S. Strigin, R. Sturani, A. L. Stuver, T. Z. Summerscales, L. Sun, P. J. Sutton, B. L. Swinkels, M. J. Szczepańczyk, M. Tacca, D. Talukder, D. B. Tanner, M. Tápai, S. P. Tarabrin, A. Taracchini, R. Taylor, T. Theeg, M. P. Thirugnanasambandam, E. G. Thomas, M. Thomas, P. Thomas, K. A. Thorne, K. S. Thorne, E. Thrane, S. Tiwari, V. Tiwari, K. V. Tokmakov, C. Tomlinson, M. Tonelli, C. V. Torres, C. I. Torrie, D. Töyrä, F. Travasso, G. Traylor, D. Trifirò, M. C. Tringali, L. Trozzo, M. Tse, M. Turconi, D. Tuyenbayev, D. Ugolini, C. S. Unnikrishnan, A. L. Urban, S. A. Usman, H. Vahlbruch, G. Vajente, G. Valdes, M. Vallisneri, N. van Bakel, M. van Beuzekom, J. F. J. van den Brand, C. Van Den Broeck, D. C. Vander-Hyde, L. van der Schaaf, J. V. van Heijningen, A. A. van Veggel, M. Vardaro, S. Vass, M. Vasúth, R. Vaulin, A. Vecchio, G. Vedovato, J. Veitch, P. J. Veitch, K. Venkateswara, D. Verkindt, F. Vetrano, A. Viceré, S. Vinciguerra, D. J. Vine, J.-Y. Vinet, S. Vitale, T. Vo, H. Vocca, C. Vorvick, D. Voss, W. D. Vousden, S. P. Vyatchanin, A. R. Wade, L. E. Wade, M. Wade, S. J. Waldman, M. Walker, L. Wallace, S. Walsh, G. Wang, H. Wang, M. Wang, X. Wang, Y. Wang, H. Ward, R. L. Ward, J. Warner, M. Was, B. Weaver, L.-W. Wei, M. Weinert, A. J. Weinstein, R. Weiss, T. Welborn, L. Wen, P. Weßels, T. West-

phal, K. Wette, J. T. Whelan, S. E. Whitcomb, D. J. White, B. F. Whiting, K. Wiesner, C. Wilkinson, P. A. Willems, L. Williams, R. D. Williams, A. R. Williamson, J. L. Willis, B. Willke, M. H. Wimmer, L. Winkelmann, W. Winkler, C. C. Wipf, A. G. Wiseman, H. Wittel, G. Woan, J. Worden, J. L. Wright, G. Wu, J. Yablon, I. Yakushin, W. Yam, H. Yamamoto, C. C. Yancey, M. J. Yap, H. Yu, M. Yvert, A. Zadrożny, L. Zangrando, M. Zanolin, J.-P. Zendri, M. Zevin, F. Zhang, L. Zhang, M. Zhang, Y. Zhang, C. Zhao, M. Zhou, Z. Zhou, X. J. Zhu, M. E. Zucker, S. E. Zuraw, and J. Zweizig. Observation of Gravitational Waves from a Binary Black Hole Merger. *Physical Review Letters*, 116(6):061102, feb 2016.

[AAA+16b] B. P. Abbott, R. Abbott, T. D. Abbott, M. R. Abernathy, F. Acernese, K. Ackley, C. Adams, T. Adams, P. Addesso, R. X. Adhikari, V. B. Adya, C. Affeldt, M. Agathos, K. Agatsuma, N. Aggarwal, O. D. Aguiar, L. Aiello, A. Ain, P. Ajith, B. Allen, A. Allocca, P. A. Altin, S. B. Anderson, W. G. Anderson, K. Arai, M. C. Araya, C. C. Arceneaux, J. S. Areeda, N. Arnaud, K. G. Arun, S. Ascenzi, G. Ashton, M. Ast, S. M. Aston, P. Astone, P. Aufmuth, C. Aulbert, S. Babak, P. Bacon, M. K. M. Bader, P. T. Baker, F. Baldaccini, G. Ballardin, S. W. Ballmer, J. C. Barayoga, S. E. Barclay, B. C. Barish, D. Barker, F. Barone, B. Barr, L. Barsotti, M. Barsuglia, D. Barta, J. Bartlett, I. Bartos, R. Bassiri, A. Basti, J. C. Batch, C. Baune, V. Bavigadda, M. Bazzan, M. Bejger, A. S. Bell, B. K. Berger, G. Bergmann, C. P. L. Berry, D. Bersanetti, A. Bertolini, J. Betzwieser, S. Bhagwat, R. Bhandare, I. A. Bilenko, G. Billingsley, J. Birch, R. Birney, O. Birnholtz, S. Biscans, A. Bisht, M. Bitossi, C. Biwer, M. A. Bizouard, J. K. Blackburn, C. D. Blair, D. G. Blair, R. M. Blair, S. Bloemen, O. Bock, M. Boer, G. Bogaert, C. Bogan, A. Bohe, C. Bond, F. Bondu, R. Bonnand, B. A. Boom, R. Bork, V. Boschi, S. Bose, Y. Bouffanais, A. Bozzi, C. Bradaschia, P. R. Brady, V. B. Braginsky, M. Branchesi, J. E. Brau, T. Briant, A. Brillet, M. Brinkmann, V. Brisson, P. Brockill, J. E. Broida, A. F. Brooks, D. A. Brown, D. D. Brown, N. M. Brown, S. Brunett, C. C. Buchanan, A. Buikema, T. Bulik, H. J. Bulten, A. Buonanno, D. Buskulic, C. Buy, R. L. Byer, M. Cabero, L. Cadonati, G. Cagnoli, C. Cahillane, J. Calderón Bustillo, T. Callister, E. Calloni, J. B. Camp, K. C. Cannon, J. Cao, C. D. Capano, E. Capocasa, F. Carbognani, S. Caride, J. Casanueva Diaz, C. Casentini, S. Caudill, M. Cavaglià, F. Cavalier, R. Cavalieri, G. Cella, C. B. Cepeda, L. Cerboni Baiardi, G. Cerretani, E. Cesarini, S. J. Chamberlin, M. Chan, S. Chao,

P. Charlton, E. Chassande-Mottin, B. D. Cheeseboro, H. Y. Chen, Y. Chen, C. Cheng, A. Chincarini, A. Chiummo, H. S. Cho, M. Cho, J. H. Chow, N. Christensen, Q. Chu, S. Chua, S. Chung, G. Ciani, F. Clara, J. A. Clark, F. Cleva, E. Coccia, P.-F. Cohadon, A. Colla, C. G. Collette, L. Cominsky, M. Constancio, A. Conte, L. Conti, D. Cook, T. R. Corbitt, N. Cornish, A. Corsi, S. Cortese, C. A. Costa, M. W. Coughlin, S. B. Coughlin, J.-P. Coulon, S. T. Countryman, P. Couvares, E. E. Cowan, D. M. Coward, M. J. Cowart, D. C. Coyne, R. Coyne, K. Craig, J. D. E. Creighton, J. Cripe, S. G. Crowder, A. Cumming, L. Cunningham, E. Cuoco, T. Dal Canton, S. L. Danilishin, S. D'Antonio, K. Danzmann, N. S. Darman, A. Dasgupta, C. F. Da Silva Costa, V. Dattilo, I. Dave, M. Davier, G. S. Davies, E. J. Daw, R. Day, S. De, D. DeBra, G. Debreczeni, J. Degallaix, M. De Laurentis, S. Deléglise, W. Del Pozzo, T. Denker, T. Dent, V. Dergachev, R. De Rosa, R. T. DeRosa, R. DeSalvo, R. C. Devine, S. Dhurandhar, M. C. Díaz, L. Di Fiore, M. Di Giovanni, T. Di Girolamo, A. Di Lieto, S. Di Pace, I. Di Palma, A. Di Virgilio, V. Dolique, F. Donovan, K. L. Dooley, S. Doravari, R. Douglas, T. P. Downes, M. Drago, R. W. P. Drever, J. C. Driggers, M. Ducrot, S. E. Dwyer, T. B. Edo, M. C. Edwards, A. Effler, H.-B. Eggenstein, P. Ehrens, J. Eichholz, S. S. Eikenberry, W. Engels, R. C. Essick, T. Etzel, M. Evans, T. M. Evans, R. Everett, M. Factourovich, V. Fafone, H. Fair, S. Fairhurst, X. Fan, Q. Fang, S. Farinon, B. Farr, W. M. Farr, M. Favata, M. Fays, H. Fehrmann, M. M. Fejer, E. Fenyvesi, I. Ferrante, E. C. Ferreira, F. Ferrini, F. Fidecaro, I. Fiori, D. Fiorucci, R. P. Fisher, R. Flaminio, M. Fletcher, H. Fong, J.-D. Fournier, S. Frasca, F. Frasconi, Z. Frei, A. Freise, R. Frey, V. Frey, P. Fritschel, V. V. Frolov, P. Fulda, M. Fyffe, H. A. G. Gabbard, J. R. Gair, L. Gammaitoni, S. G. Gaonkar, F. Garufi, G. Gaur, N. Gehrels, G. Gemme, P. Geng, E. Genin, A. Gennai, J. George, L. Gergely, V. Germain, Abhirup Ghosh, Archisman Ghosh, S. Ghosh, J. A. Giaime, K. D. Giardina, A. Giazotto, K. Gill, A. Glaefke, E. Goetz, R. Goetz, L. Gondan, G. González, J. M. Gonzalez Castro, A. Gopakumar, N. A. Gordon, M. L. Gorodetsky, S. E. Gossan, M. Gosselin, R. Gouaty, A. Grado, C. Graef, P. B. Graff, M. Granata, A. Grant, S. Gras, C. Gray, G. Greco, A. C. Green, P. Groot, H. Grote, S. Grunewald, G. M. Guidi, X. Guo, A. Gupta, M. K. Gupta, K. E. Gushwa, E. K. Gustafson, R. Gustafson, J. J. Hacker, B. R. Hall, E. D. Hall, H. Hamilton, G. Hammond, M. Haney, M. M. Hanke, J. Hanks, C. Hanna, M. D. Hannam, J. Hanson, T. Hardwick, J. Harms, G. M. Harry, I. W. Harry,

M. J. Hart, M. T. Hartman, C.-J. Haster, K. Haughian, J. Healy, A. Heidmann, M. C. Heintze, H. Heitmann, P. Hello, G. Hemming, M. Hendry, I. S. Heng, J. Hennig, J. Henry, A. W. Heptonstall, M. Heurs, S. Hild, D. Hoak, D. Hofman, K. Holt, D. E. Holz, P. Hopkins, J. Hough, E. A. Houston, E. J. Howell, Y. M. Hu, S. Huang, E. A. Huerta, D. Huet, B. Hughey, S. Husa, S. H. Huttner, T. Huynh-Dinh, N. Indik, D. R. Ingram, R. Inta, H. N. Isa, J.-M. Isac, M. Isi, T. Isogai, B. R. Iyer, K. Izumi, T. Jacqmin, H. Jang, K. Jani, P. Jaranowski, S. Jawahar, L. Jian, F. Jiménez-Forteza, W. W. Johnson, N. K. Johnson-McDaniel, D. I. Jones, R. Jones, R. J. G. Jonker, L. Ju, Haris K, C. V. Kalaghatgi, V. Kalogera, S. Kandhasamy, G. Kang, J. B. Kanner, S. J. Kapadia, S. Karki, K. S. Karvinen, M. Kasprzack, E. Katsavounidis, W. Katzman, S. Kaufer, T. Kaur, K. Kawabe, F. Kéfélian, M. S. Kehl, D. Keitel, D. B. Kelley, W. Kells, R. Kennedy, J. S. Key, F. Y. Khalili, I. Khan, S. Khan, Z. Khan, E. A. Khazanov, N. Kijbunchoo, Chi-Woong Kim, Chunglee Kim, J. Kim, K. Kim, N. Kim, W. Kim, Y.-M. Kim, S. J. Kimbrell, E. J. King, P. J. King, J. S. Kissel, B. Klein, L. Kleybolte, S. Klimenko, S. M. Koehlenbeck, S. Koley, V. Kondrashov, A. Kontos, M. Korobko, W. Z. Korth, I. Kowalska, D. B. Kozak, V. Kringel, B. Krishnan, A. Królak, C. Krueger, G. Kuehn, P. Kumar, R. Kumar, L. Kuo, A. Kutynia, B. D. Lackey, M. Landry, J. Lange, B. Lantz, P. D. Lasky, M. Laxen, A. Lazzarini, C. Lazzaro, P. Leaci, S. Leavey, E. O. Lebigot, C. H. Lee, H. K. Lee, H. M. Lee, K. Lee, A. Lenon, M. Leonardi, J. R. Leong, N. Leroy, N. Letendre, Y. Levin, J. B. Lewis, T. G. F. Li, A. Libson, T. B. Littenberg, N. A. Lockerbie, A. L. Lombardi, L. T. London, J. E. Lord, M. Lorenzini, V. Loriette, M. Lormand, G. Losurdo, J. D. Lough, C. O. Lousto, H. Lück, A. P. Lundgren, R. Lynch, Y. Ma, B. Machenschalk, M. MacInnis, D. M. Macleod, F. Magaña-Sandoval, L. Magaña Zertuche, R. M. Magee, E. Majorana, I. Maksimovic, V. Malvezzi, N. Man, I. Mandel, V. Mandic, V. Mangano, G. L. Mansell, M. Manske, M. Mantovani, F. Marchesoni, F. Marion, S. Márka, Z. Márka, A. S. Markosyan, E. Maros, F. Martelli, L. Martellini, I. W. Martin, D. V. Martynov, J. N. Marx, K. Mason, A. Masserot, T. J. Massinger, M. Masso-Reid, S. Mastrogiovanni, F. Matichard, L. Matone, N. Mavalvala, N. Mazumder, R. McCarthy, D. E. McClelland, S. McCormick, S. C. McGuire, G. McIntyre, J. McIver, D. J. McManus, T. McRae, S. T. McWilliams, D. Meacher, G. D. Meadors, J. Meidam, A. Melatos, G. Mendell, R. A. Mercer, E. L. Merilh, M. Merzougui, S. Meshkov, C. Messenger, C. Messick, R. Metzdorff, P. M.

Meyers, F. Mezzani, H. Miao, C. Michel, H. Middleton, E. E. Mikhailov, L. Milano, A. L. Miller, A. Miller, B. B. Miller, J. Miller, M. Millhouse, Y. Minenkov, J. Ming, S. Mirshekari, C. Mishra, S. Mitra, V. P. Mitrofanov, G. Mitselmakher, R. Mittleman, A. Moggi, M. Mohan, S. R. P. Mohapatra, M. Montani, B. C. Moore, C. J. Moore, D. Moraru, G. Moreno, S. R. Morriss, K. Mossavi, B. Mours, C. M. Mow-Lowry, G. Mueller, A. W. Muir, Arunava Mukherjee, D. Mukherjee, S. Mukherjee, N. Mukund, A. Mullavey, J. Munch, D. J. Murphy, P. G. Murray, A. Mytidis, I. Nardecchia, L. Naticchioni, R. K. Nayak, K. Nedkova, G. Nelemans, T. J. N. Nelson, M. Neri, A. Neunzert, G. Newton, T. T. Nguyen, A. B. Nielsen, S. Nissanke, A. Nitz, F. Nocera, D. Nolting, M. E. N. Normandin, L. K. Nuttall, J. Oberling, E. Ochsner, J. O'Dell, E. Oelker, G. H. Ogin, J. J. Oh, S. H. Oh, F. Ohme, M. Oliver, P. Oppermann, Richard J. Oram, B. O'Reilly, R. O'Shaughnessy, D. J. Ottaway, H. Overmier, B. J. Owen, A. Pai, S. A. Pai, J. R. Palamos, O. Palashov, C. Palomba, A. Pal-Singh, H. Pan, C. Pankow, F. Pannarale, B. C. Pant, F. Paoletti, A. Paoli, M. A. Papa, H. R. Paris, W. Parker, D. Pascucci, A. Pasqualetti, R. Passaquieti, D. Passuello, B. Patricelli, Z. Patrick, B. L. Pearlstone, M. Pedraza, R. Pedurand, L. Pekowsky, A. Pele, S. Penn, A. Perreca, L. M. Perri, H. P. Pfeiffer, M. Phelps, O. J. Piccinni, M. Pichot, F. Piergiovanni, V. Pierro, G. Pillant, L. Pinard, I. M. Pinto, M. Pitkin, M. Poe, R. Poggiani, P. Popolizio, A. Post, J. Powell, J. Prasad, V. Predoi, T. Prestegard, L. R. Price, M. Prijatelj, M. Principe, S. Privitera, R. Prix, G. A. Prodi, L. Prokhorov, O. Puncken, M. Punturo, P. Puppo, M. Pürrer, H. Qi, J. Qin, S. Qiu, V. Quetschke, E. A. Quintero, R. Quitzow-James, F. J. Raab, D. S. Rabeling, H. Radkins, P. Raffai, S. Raja, C. Rajan, M. Rakhmanov, P. Rapagnani, V. Raymond, M. Razzano, V. Re, J. Read, C. M. Reed, T. Regimbau, L. Rei, S. Reid, D. H. Reitze, H. Rew, S. D. Reyes, F. Ricci, K. Riles, M. Rizzo, N. A. Robertson, R. Robie, F. Robinet, A. Rocchi, L. Rolland, J. G. Rollins, V. J. Roma, J. D. Romano, R. Romano, G. Romanov, J. H. Romie, D. Rosińska, S. Rowan, A. Rüdiger, P. Ruggi, K. Ryan, S. Sachdev, T. Sadecki, L. Sadeghian, M. Sakellariadou, L. Salconi, M. Saleem, F. Salemi, A. Samajdar, L. Sammut, E. J. Sanchez, V. Sandberg, B. Sandeen, J. R. Sanders, B. Sassolas, B. S. Sathyaprakash, P. R. Saulson, O. E. S. Sauter, R. L. Savage, A. Sawadsky, P. Schale, R. Schilling, J. Schmidt, P. Schmidt, R. Schnabel, R. M. S. Schofield, A. Schönbeck, E. Schreiber, D. Schuette, B. F. Schutz, J. Scott, S. M. Scott, D. Sellers, A. S. Sengupta, D. Sentenac, V. Sequino, A. Sergeev, Y. Setyawati, D. A.

Shaddock, T. Shaffer, M. S. Shahriar, M. Shaltev, B. Shapiro, P. Shawhan, A. Sheperd, D. H. Shoemaker, D. M. Shoemaker, K. Siellez, X. Siemens, M. Sieniawska, D. Sigg, A. D. Silva, A. Singer, L. P. Singer, A. Singh, R. Singh, A. Singhal, A. M. Sintes, B. J. J. Slagmolen, J. R. Smith, N. D. Smith, R. J. E. Smith, E. J. Son, B. Sorazu, F. Sorrentino, T. Souradeep, A. K. Srivastava, A. Staley, M. Steinke, J. Steinlechner, S. Steinlechner, D. Steinmeyer, B. C. Stephens, S. P. Stevenson, R. Stone, K. A. Strain, N. Straniero, G. Stratta, N. A. Strauss, S. Strigin, R. Sturani, A. L. Stuver, T. Z. Summerscales, L. Sun, S. Sunil, P. J. Sutton, B. L. Swinkels, M. J. Szczepańczyk, M. Tacca, D. Talukder, D. B. Tanner, M. Tápai, S. P. Tarabrin, A. Taracchini, R. Taylor, T. Theeg, M. P. Thirugnanasambandam, E. G. Thomas, M. Thomas, P. Thomas, K. A. Thorne, E. Thrane, S. Tiwari, V. Tiwari, K. V. Tokmakov, K. Toland, C. Tomlinson, M. Tonelli, Z. Tornasi, C. V. Torres, C. I. Torrie, D. Töyrä, F. Travasso, G. Traylor, D. Trifirò, M. C. Tringali, L. Trozzo, M. Tse, M. Turconi, D. Tuyenbayev, D. Ugolini, C. S. Unnikrishnan, A. L. Urban, S. A. Usman, H. Vahlbruch, G. Vajente, G. Valdes, M. Vallisneri, N. van Bakel, M. van Beuzekom, J. F. J. van den Brand, C. Van Den Broeck, D. C. Vander-Hyde, L. van der Schaaf, J. V. van Heijningen, A. A. van Veggel, M. Vardaro, S. Vass, M. Vasúth, R. Vaulin, A. Vecchio, G. Vedovato, J. Veitch, P. J. Veitch, K. Venkateswara, D. Verkindt, F. Vetrano, A. Viceré, S. Vinciguerra, D. J. Vine, J.-Y. Vinet, S. Vitale, T. Vo, H. Vocca, C. Vorvick, D. V. Voss, W. D. Vousden, S. P. Vyatchanin, A. R. Wade, L. E. Wade, M. Wade, M. Walker, L. Wallace, S. Walsh, G. Wang, H. Wang, M. Wang, X. Wang, Y. Wang, R. L. Ward, J. Warner, M. Was, B. Weaver, L.-W. Wei, M. Weinert, A. J. Weinstein, R. Weiss, L. Wen, P. Weßels, T. Westphal, K. Wette, J. T. Whelan, B. F. Whiting, R. D. Williams, A. R. Williamson, J. L. Willis, B. Willke, M. H. Wimmer, W. Winkler, C. C. Wipf, H. Wittel, G. Woan, J. Woehler, J. Worden, J. L. Wright, D. S. Wu, G. Wu, J. Yablon, W. Yam, H. Yamamoto, C. C. Yancey, H. Yu, M. Yvert, A. Zadrożny, L. Zangrando, M. Zanolin, J.-P. Zendri, M. Zevin, L. Zhang, M. Zhang, Y. Zhang, C. Zhao, M. Zhou, Z. Zhou, X. J. Zhu, M. E. Zucker, S. E. Zuraw, J. Zweizig, M. Boyle, D. Hemberger, L. E. Kidder, G. Lovelace, S. Ossokine, M. Scheel, B. Szilagyi, and S. Teukolsky. GW151226: Observation of Gravitational Waves from a 22-Solar-Mass Binary Black Hole Coalescence. *Physical Review Letters*, 116(24):241103, jun 2016.

[AAA+16c] M. Armano, H. Audley, G. Auger, J. T. Baird, M. Bassan, P. Binetruy, M. Born, D. Bortoluzzi, N. Brandt, M. Caleno, L. Carbone, A. Cavalleri, A. Cesarini, G. Ciani, G. Congedo, A. M. Cruise, K. Danzmann, M. de Deus Silva, R. De Rosa, M. Diaz-Aguiló, L. Di Fiore, I. Diepholz, G. Dixon, R. Dolesi, N. Dunbar, L. Ferraioli, V. Ferroni, W. Fichter, E. D. Fitzsimons, R. Flatscher, M. Freschi, A. F. García Marín, C. García Marirrodriga, R. Gerndt, L. Gesa, F. Gibert, D. Giardini, R. Giusteri, F. Guzmán, A. Grado, C. Grimani, A. Grynagier, J. Grzymisch, I. Harrison, G. Heinzel, M. Hewitson, D. Hollington, D. Hoyland, M. Hueller, H. Inchauspé, O. Jennrich, P. Jetzer, U. Johann, B. Johlander, N. Karnesis, B. Kaune, N. Korsakova, C. J. Killow, J. A. Lobo, I. Lloro, L. Liu, J. P. López-Zaragoza, R. Maarschalkerweerd, D. Mance, V. Martín, L. Martin-Polo, J. Martino, F. Martin-Porqueras, S. Madden, I. Mateos, P. W. McNamara, J. Mendes, L. Mendes, A. Monsky, D. Nicolodi, M. Nofrarias, S. Paczkowski, M. Perreur-Lloyd, A. Petiteau, P. Pivato, E. Plagnol, P. Prat, U. Ragnit, B. Raïs, J. Ramos-Castro, J. Reiche, D. I. Robertson, H. Rozemeijer, F. Rivas, G. Russano, J. Sanjuán, P. Sarra, A. Schleicher, D. Shaul, J. Slutsky, C. F. Sopuerta, R. Stanga, F. Steier, T. Sumner, D. Texier, J. I. Thorpe, C. Trenkel, M. Tröbs, H. B. Tu, D. Vetrugno, S. Vitale, V. Wand, G. Wanner, H. Ward, C. Warren, P. J. Wass, D. Wealthy, W. J. Weber, L. Wissel, A. Wittchen, A. Zambotti, C. Zanoni, T. Ziegler, and P. Zweifel. Sub-Femto-g Free Fall for Space-Based Gravitational Wave Observatories: LISA Pathfinder Results. *Physical Review Letters*, 116(23):231101, jun 2016.

[AAA+17a] B. P. Abbott, R. Abbott, T. D. Abbott, F. Acernese, K. Ackley, C. Adams, T. Adams, P. Addesso, R. X. Adhikari, V. B. Adya, C. Affeldt, M. Afrough, B. Agarwal, M. Agathos, K. Agatsuma, N. Aggarwal, O. D. Aguiar, L. Aiello, A. Ain, P. Ajith, B. Allen, G. Allen, A. Allocca, P. A. Altin, A. Amato, A. Ananyeva, S. B. Anderson, W. G. Anderson, S. V. Angelova, S. Antier, S. Appert, K. Arai, M. C. Araya, J. S. Areeda, N. Arnaud, K. G. Arun, S. Ascenzi, G. Ashton, M. Ast, S. M. Aston, P. Astone, D. V. Atallah, P. Aufmuth, C. Aulbert, K. AultONeal, C. Austin, A. Avila-Alvarez, S. Babak, P. Bacon, M. K. M. Bader, S. Bae, P. T. Baker, F. Baldaccini, G. Ballardin, S. W. Ballmer, S. Banagiri, J. C. Barayoga, S. E. Barclay, B. C. Barish, D. Barker, K. Barkett, F. Barone, B. Barr, L. Barsotti, M. Barsuglia, D. Barta, J. Bartlett, I. Bartos, R. Bassiri, A. Basti, J. C. Batch, M. Bawaj, J. C. Bayley, M. Bazzan, B. Bécsy, C. Beer, M. Bejger, I. Be-

lahcene, A. S. Bell, B. K. Berger, G. Bergmann, J. J. Bero, C. P. L. Berry, D. Bersanetti, A. Bertolini, J. Betzwieser, S. Bhagwat, R. Bhandare, I. A. Bilenko, G. Billingsley, C. R. Billman, J. Birch, R. Birney, O. Birnholtz, S. Biscans, S. Biscoveanu, A. Bisht, M. Bitossi, C. Biwer, M. A. Bizouard, J. K. Blackburn, J. Blackman, C. D. Blair, D. G. Blair, R. M. Blair, S. Bloemen, O. Bock, N. Bode, M. Boer, G. Bogaert, A. Bohe, F. Bondu, E. Bonilla, R. Bonnand, B. A. Boom, R. Bork, V. Boschi, S. Bose, K. Bossie, Y. Bouffanais, A. Bozzi, C. Bradaschia, P. R. Brady, M. Branchesi, J. E. Brau, T. Briant, A. Brillet, M. Brinkmann, V. Brisson, P. Brockill, J. E. Broida, A. F. Brooks, D. A. Brown, D. D. Brown, S. Brunett, C. C. Buchanan, A. Buikema, T. Bulik, H. J. Bulten, A. Buonanno, D. Buskulic, C. Buy, R. L. Byer, M. Cabero, L. Cadonati, G. Cagnoli, C. Cahillane, J. Calderón Bustillo, T. A. Callister, E. Calloni, J. B. Camp, M. Canepa, P. Canizares, K. C. Cannon, H. Cao, J. Cao, C. D. Capano, E. Capocasa, F. Carbognani, S. Caride, M. F. Carney, J. Casanueva Diaz, C. Casentini, S. Caudill, M. Cavaglià, F. Cavalier, R. Cavalieri, G. Cella, C. B. Cepeda, P. Cerdá-Durán, G. Cerretani, E. Cesarini, S. J. Chamberlin, M. Chan, S. Chao, P. Charlton, E. Chase, E. Chassande-Mottin, D. Chatterjee, K. Chatziioannou, B. D. Cheeseboro, H. Y. Chen, X. Chen, Y. Chen, H.-P. Cheng, H. Chia, A. Chincarini, A. Chiummo, T. Chmiel, H. S. Cho, M. Cho, J. H. Chow, N. Christensen, Q. Chu, A. J. K. Chua, S. Chua, A. K. W. Chung, S. Chung, G. Ciani, R. Ciolfi, C. E. Cirelli, A. Cirone, F. Clara, J. A. Clark, P. Clearwater, F. Cleva, C. Cocchieri, E. Coccia, P.-F. Cohadon, D. Cohen, A. Colla, C. G. Collette, L. R. Cominsky, M. Constancio, L. Conti, S. J. Cooper, P. Corban, T. R. Corbitt, I. Cordero-Carrión, K. R. Corley, N. Cornish, A. Corsi, S. Cortese, C. A. Costa, M. W. Coughlin, S. B. Coughlin, J.-P. Coulon, S. T. Countryman, P. Couvares, P. B. Covas, E. E. Cowan, D. M. Coward, M. J. Cowart, D. C. Coyne, R. Coyne, J. D. E. Creighton, T. D. Creighton, J. Cripe, S. G. Crowder, T. J. Cullen, A. Cumming, L. Cunningham, E. Cuoco, T. Dal Canton, G. Dálya, S. L. Danilishin, S. D'Antonio, K. Danzmann, A. Dasgupta, C. F. Da Silva Costa, V. Dattilo, I. Dave, M. Davier, D. Davis, E. J. Daw, B. Day, S. De, D. DeBra, J. Degallaix, M. De Laurentis, S. Deléglise, W. Del Pozzo, N. Demos, T. Denker, T. Dent, R. De Pietri, V. Dergachev, R. De Rosa, R. T. DeRosa, C. De Rossi, R. DeSalvo, O. de Varona, J. Devenson, S. Dhurandhar, M. C. Díaz, L. Di Fiore, M. Di Giovanni, T. Di Girolamo, A. Di Lieto, S. Di Pace, I. Di Palma, F. Di Renzo, Z. Doctor, V. Dolique, F. Donovan, K. L. Dooley,

S. Doravari, I. Dorrington, R. Douglas, M. Dovale Álvarez, T. P. Downes, M. Drago, C. Dreissigacker, J. C. Driggers, Z. Du, M. Ducrot, P. Dupej, S. E. Dwyer, T. B. Edo, M. C. Edwards, A. Effler, H.-B. Eggenstein, P. Ehrens, J. Eichholz, S. S. Eikenberry, R. A. Eisenstein, R. C. Essick, D. Estevez, Z. B. Etienne, T. Etzel, M. Evans, T. M. Evans, M. Factourovich, V. Fafone, H. Fair, S. Fairhurst, X. Fan, S. Farinon, B. Farr, W. M. Farr, E. J. Fauchon-Jones, M. Favata, M. Fays, C. Fee, H. Fehrmann, J. Feicht, M. M. Fejer, A. Fernandez-Galiana, I. Ferrante, E. C. Ferreira, F. Ferrini, F. Fidecaro, D. Finstad, I. Fiori, D. Fiorucci, M. Fishbach, R. P. Fisher, M. Fitz-Axen, R. Flaminio, M. Fletcher, H. Fong, J. A. Font, P. W. F. Forsyth, S. S. Forsyth, J.-D. Fournier, S. Frasca, F. Frasconi, Z. Frei, A. Freise, R. Frey, V. Frey, E. M. Fries, P. Fritschel, V. V. Frolov, P. Fulda, M. Fyffe, H. Gabbard, B. U. Gadre, S. M. Gaebel, J. R. Gair, L. Gammaitoni, M. R. Ganija, S. G. Gaonkar, C. Garcia-Quiros, F. Garufi, B. Gateley, S. Gaudio, G. Gaur, V. Gayathri, N. Gehrels, G. Gemme, E. Genin, A. Gennai, D. George, J. George, L. Gergely, V. Germain, S. Ghonge, Abhirup Ghosh, Archisman Ghosh, S. Ghosh, J. A. Giaime, K. D. Giardina, A. Giazotto, K. Gill, L. Glover, E. Goetz, R. Goetz, S. Gomes, B. Goncharov, G. González, J. M. Gonzalez Castro, A. Gopakumar, M. L. Gorodetsky, S. E. Gossan, M. Gosselin, R. Gouaty, A. Grado, C. Graef, M. Granata, A. Grant, S. Gras, C. Gray, G. Greco, A. C. Green, E. M. Gretarsson, P. Groot, H. Grote, S. Grunewald, P. Gruning, G. M. Guidi, X. Guo, A. Gupta, M. K. Gupta, K. E. Gushwa, E. K. Gustafson, R. Gustafson, O. Halim, B. R. Hall, E. D. Hall, E. Z. Hamilton, G. Hammond, M. Haney, M. M. Hanke, J. Hanks, C. Hanna, M. D. Hannam, O. A. Hannuksela, J. Hanson, T. Hardwick, J. Harms, G. M. Harry, I. W. Harry, M. J. Hart, C.-J. Haster, K. Haughian, J. Healy, A. Heidmann, M. C. Heintze, H. Heitmann, P. Hello, G. Hemming, M. Hendry, I. S. Heng, J. Hennig, A. W. Heptonstall, M. Heurs, S. Hild, T. Hinderer, D. Hoak, D. Hofman, K. Holt, D. E. Holz, P. Hopkins, C. Horst, J. Hough, E. A. Houston, E. J. Howell, A. Hreibi, Y. M. Hu, E. A. Huerta, D. Huet, B. Hughey, S. Husa, S. H. Huttner, T. Huynh-Dinh, N. Indik, R. Inta, G. Intini, H. N. Isa, J.-M. Isac, M. Isi, B. R. Iyer, K. Izumi, T. Jacqmin, K. Jani, P. Jaranowski, S. Jawahar, F. Jiménez-Forteza, W. W. Johnson, N. K. Johnson-McDaniel, D. I. Jones, R. Jones, R. J. G. Jonker, L. Ju, J. Junker, C. V. Kalaghatgi, V. Kalogera, B. Kamai, S. Kandhasamy, G. Kang, J. B. Kanner, S. J. Kapadia, S. Karki, K. S. Karvinen, M. Kasprzack, M. Kato-

lik, E. Katsavounidis, W. Katzman, S. Kaufer, K. Kawabe, F. Kéfélian, D. Keitel, A. J. Kemball, R. Kennedy, C. Kent, J. S. Key, F. Y. Khalili, I. Khan, S. Khan, Z. Khan, E. A. Khazanov, N. Kijbunchoo, Chunglee Kim, J. C. Kim, K. Kim, W. Kim, W. S. Kim, Y.-M. Kim, S. J. Kimbrell, E. J. King, P. J. King, M. Kinley-Hanlon, R. Kirchhoff, J. S. Kissel, L. Kleybolte, S. Klimenko, T. D. Knowles, P. Koch, S. M. Koehlenbeck, S. Koley, V. Kondrashov, A. Kontos, M. Korobko, W. Z. Korth, I. Kowalska, D. B. Kozak, C. Krämer, V. Kringel, B. Krishnan, A. Królak, G. Kuehn, P. Kumar, R. Kumar, S. Kumar, L. Kuo, A. Kutynia, S. Kwang, B. D. Lackey, K. H. Lai, M. Landry, R. N. Lang, J. Lange, B. Lantz, R. K. Lanza, A. Lartaux-Vollard, P. D. Lasky, M. Laxen, A. Lazzarini, C. Lazzaro, P. Leaci, S. Leavey, C. H. Lee, H. K. Lee, H. M. Lee, H. W. Lee, K. Lee, J. Lehmann, A. Lenon, M. Leonardi, N. Leroy, N. Letendre, Y. Levin, T. G. F. Li, S. D. Linker, T. B. Littenberg, J. Liu, R. K. L. Lo, N. A. Lockerbie, L. T. London, J. E. Lord, M. Lorenzini, V. Loriette, M. Lormand, G. Losurdo, J. D. Lough, C. O. Lousto, G. Lovelace, H. Lück, D. Lumaca, A. P. Lundgren, R. Lynch, Y. Ma, R. Macas, S. Macfoy, B. Machenschalk, M. MacInnis, D. M. Macleod, I. Magaña Hernandez, F. Magaña-Sandoval, L. Magaña Zertuche, R. M. Magee, E. Majorana, I. Maksimovic, N. Man, V. Mandic, V. Mangano, G. L. Mansell, M. Manske, M. Mantovani, F. Marchesoni, F. Marion, S. Márka, Z. Márka, C. Markakis, A. S. Markosyan, A. Markowitz, E. Maros, A. Marquina, F. Martelli, L. Martellini, I. W. Martin, R. M. Martin, D. V. Martynov, K. Mason, E. Massera, A. Masserot, T. J. Massinger, M. Masso-Reid, S. Mastrogiovanni, A. Matas, F. Matichard, L. Matone, N. Mavalvala, N. Mazumder, R. McCarthy, D. E. McClelland, S. McCormick, L. McCuller, S. C. McGuire, G. McIntyre, J. McIver, D. J. McManus, L. McNeill, T. McRae, S. T. McWilliams, D. Meacher, G. D. Meadors, M. Mehmet, J. Meidam, E. Mejuto-Villa, A. Melatos, G. Mendell, R. A. Mercer, E. L. Merilh, M. Merzougui, S. Meshkov, C. Messenger, C. Messick, R. Metzdorff, P. M. Meyers, H. Miao, C. Michel, H. Middleton, E. E. Mikhailov, L. Milano, A. L. Miller, B. B. Miller, J. Miller, M. Millhouse, M. C. Milovich-Goff, O. Minazzoli, Y. Minenkov, J. Ming, C. Mishra, S. Mitra, V. P. Mitrofanov, G. Mitselmakher, R. Mittleman, D. Moffa, A. Moggi, K. Mogushi, M. Mohan, S. R. P. Mohapatra, M. Montani, C. J. Moore, D. Moraru, G. Moreno, S. R. Morriss, B. Mours, C. M. Mow-Lowry, G. Mueller, A. W. Muir, Arunava Mukherjee, D. Mukherjee, S. Mukherjee, N. Mukund, A. Mullavey, J. Munch, E. A. Muñiz, M. Muratore, P. G.

Murray, K. Napier, I. Nardecchia, L. Naticchioni, R. K. Nayak, J. Neilson, G. Nelemans, T. J. N. Nelson, M. Nery, A. Neunzert, L. Nevin, J. M. Newport, G. Newton, K. K. Y. Ng, T. T. Nguyen, D. Nichols, A. B. Nielsen, S. Nissanke, A. Nitz, A. Noack, F. Nocera, D. Nolting, C. North, L. K. Nuttall, J. Oberling, G. D. O'Dea, G. H. Ogin, J. J. Oh, S. H. Oh, F. Ohme, M. A. Okada, M. Oliver, P. Oppermann, Richard J. Oram, B. O'Reilly, R. Ormiston, L. F. Ortega, R. O'Shaughnessy, S. Ossokine, D. J. Ottaway, H. Overmier, B. J. Owen, A. E. Pace, J. Page, M. A. Page, A. Pai, S. A. Pai, J. R. Palamos, O. Palashov, C. Palomba, A. Pal-Singh, Howard Pan, Huang-Wei Pan, B. Pang, P. T. H. Pang, C. Pankow, F. Pannarale, B. C. Pant, F. Paoletti, A. Paoli, M. A. Papa, A. Parida, W. Parker, D. Pascucci, A. Pasqualetti, R. Passaquieti, D. Passuello, M. Patil, B. Patricelli, B. L. Pearlstone, M. Pedraza, R. Pedurand, L. Pekowsky, A. Pele, S. Penn, C. J. Perez, A. Perreca, L. M. Perri, H. P. Pfeiffer, M. Phelps, O. J. Piccinni, M. Pichot, F. Piergiovanni, V. Pierro, G. Pillant, L. Pinard, I. M. Pinto, M. Pirello, M. Pitkin, M. Poe, R. Poggiani, P. Popolizio, E. K. Porter, A. Post, J. Powell, J. Prasad, J. W. W. Pratt, G. Pratten, V. Predoi, T. Prestegard, M. Prijatelj, M. Principe, S. Privitera, G. A. Prodi, L. G. Prokhorov, O. Puncken, M. Punturo, P. Puppo, M. Pürrer, H. Qi, V. Quetschke, E. A. Quintero, R. Quitzow-James, F. J. Raab, D. S. Rabeling, H. Radkins, P. Raffai, S. Raja, C. Rajan, B. Rajbhandari, M. Rakhmanov, K. E. Ramirez, A. Ramos-Buades, P. Rapagnani, V. Raymond, M. Razzano, J. Read, T. Regimbau, L. Rei, S. Reid, D. H. Reitze, W. Ren, S. D. Reyes, F. Ricci, P. M. Ricker, S. Rieger, K. Riles, M. Rizzo, N. A. Robertson, R. Robie, F. Robinet, A. Rocchi, L. Rolland, J. G. Rollins, V. J. Roma, R. Romano, C. L. Romel, J. H. Romie, D. Rosińska, M. P. Ross, S. Rowan, A. Rüdiger, P. Ruggi, G. Rutins, K. Ryan, S. Sachdev, T. Sadecki, L. Sadeghian, M. Sakellariadou, L. Salconi, M. Saleem, F. Salemi, A. Samajdar, L. Sammut, L. M. Sampson, E. J. Sanchez, L. E. Sanchez, N. Sanchis-Gual, V. Sandberg, J. R. Sanders, B. Sassolas, B. S. Sathyaprakash, P. R. Saulson, O. Sauter, R. L. Savage, A. Sawadsky, P. Schale, M. Scheel, J. Scheuer, J. Schmidt, P. Schmidt, R. Schnabel, R. M. S. Schofield, A. Schönbeck, E. Schreiber, D. Schuette, B. W. Schulte, B. F. Schutz, S. G. Schwalbe, J. Scott, S. M. Scott, E. Seidel, D. Sellers, A. S. Sengupta, D. Sentenac, V. Sequino, A. Sergeev, D. A. Shaddock, T. J. Shaffer, A. A. Shah, M. S. Shahriar, M. B. Shaner, L. Shao, B. Shapiro, P. Shawhan, A. Sheperd, D. H. Shoemaker, D. M. Shoemaker,

K. Siellez, X. Siemens, M. Sieniawska, D. Sigg, A. D. Silva, L. P. Singer, A. Singh, A. Singhal, A. M. Sintes, B. J. J. Slagmolen, B. Smith, J. R. Smith, R. J. E. Smith, S. Somala, E. J. Son, J. A. Sonnenberg, B. Sorazu, F. Sorrentino, T. Souradeep, A. P. Spencer, A. K. Srivastava, K. Staats, A. Staley, M. Steinke, J. Steinlechner, S. Steinlechner, D. Steinmeyer, S. P. Stevenson, R. Stone, D. J. Stops, K. A. Strain, G. Stratta, S. E. Strigin, A. Strunk, R. Sturani, A. L. Stuver, T. Z. Summerscales, L. Sun, S. Sunil, J. Suresh, P. J. Sutton, B. L. Swinkels, M. J. Szczepańczyk, M. Tacca, S. C. Tait, C. Talbot, D. Talukder, D. B. Tanner, M. Tápai, A. Taracchini, J. D. Tasson, J. A. Taylor, R. Taylor, S. V. Tewari, T. Theeg, F. Thies, E. G. Thomas, M. Thomas, P. Thomas, K. A. Thorne, E. Thrane, S. Tiwari, V. Tiwari, K. V. Tokmakov, K. Toland, M. Tonelli, Z. Tornasi, A. Torres-Forné, C. I. Torrie, D. Töyrä, F. Travasso, G. Traylor, J. Trinastic, M. C. Tringali, L. Trozzo, K. W. Tsang, M. Tse, R. Tso, L. Tsukada, D. Tsuna, D. Tuyenbayev, K. Ueno, D. Ugolini, C. S. Unnikrishnan, A. L. Urban, S. A. Usman, H. Vahlbruch, G. Vajente, G. Valdes, N. van Bakel, M. van Beuzekom, J. F. J. van den Brand, C. Van Den Broeck, D. C. Vander-Hyde, L. van der Schaaf, J. V. van Heijningen, A. A. van Veggel, M. Vardaro, V. Varma, S. Vass, M. Vasúth, A. Vecchio, G. Vedovato, J. Veitch, P. J. Veitch, K. Venkateswara, G. Venugopalan, D. Verkindt, F. Vetrano, A. Viceré, A. D. Viets, S. Vinciguerra, D. J. Vine, J.-Y. Vinet, S. Vitale, T. Vo, H. Vocca, C. Vorvick, S. P. Vyatchanin, A. R. Wade, L. E. Wade, M. Wade, R. Walet, M. Walker, L. Wallace, S. Walsh, G. Wang, H. Wang, J. Z. Wang, W. H. Wang, Y. F. Wang, R. L. Ward, J. Warner, M. Was, J. Watchi, B. Weaver, L.-W. Wei, M. Weinert, A. J. Weinstein, R. Weiss, L. Wen, E. K. Wessel, P. Weßels, J. Westerweck, T. Westphal, K. Wette, J. T. Whelan, B. F. Whiting, C. Whittle, D. Wilken, D. Williams, R. D. Williams, A. R. Williamson, J. L. Willis, B. Willke, M. H. Wimmer, W. Winkler, C. C. Wipf, H. Wittel, G. Woan, J. Woehler, J. Wofford, K. W. K. Wong, J. Worden, J. L. Wright, D. S. Wu, D. M. Wysocki, S. Xiao, H. Yamamoto, C. C. Yancey, L. Yang, M. J. Yap, M. Yazback, Hang Yu, Haocun Yu, M. Yvert, A. Zadrożny, M. Zanolin, T. Zelenova, J.-P. Zendri, M. Zevin, L. Zhang, M. Zhang, T. Zhang, Y.-H. Zhang, C. Zhao, M. Zhou, Z. Zhou, S. J. Zhu, X. J. Zhu, A. B. Zimmerman, M. E. Zucker, J. Zweizig, (LIGO Scientific Collaboration Collaboration), and Virgo. GW170608: Observation of a 19 Solar-mass Binary Black Hole Coalescence. *The Astrophysical Journal*, 851(2):L35, dec 2017.

[AAA+17b] B. P. Abbott, R. Abbott, T. D. Abbott, F. Acernese, K. Ackley, C. Adams, T. Adams, P. Addesso, R. X. Adhikari, V. B. Adya, C. Affeldt, M. Afrough, B. Agarwal, M. Agathos, K. Agatsuma, N. Aggarwal, O. D. Aguiar, L. Aiello, A. Ain, P. Ajith, B. Allen, G. Allen, A. Allocca, P. A. Altin, A. Amato, A. Ananyeva, S. B. Anderson, W. G. Anderson, S. V. Angelova, S. Antier, S. Appert, K. Arai, M. C. Araya, J. S. Areeda, N. Arnaud, K. G. Arun, S. Ascenzi, G. Ashton, M. Ast, S. M. Aston, P. Astone, D. V. Atallah, P. Aufmuth, C. Aulbert, K. AultONeal, C. Austin, A. Avila-Alvarez, S. Babak, P. Bacon, M. K. M. Bader, S. Bae, P. T. Baker, F. Baldaccini, G. Ballardin, S. W. Ballmer, S. Banagiri, J. C. Barayoga, S. E. Barclay, B. C. Barish, D. Barker, K. Barkett, F. Barone, B. Barr, L. Barsotti, M. Barsuglia, D. Barta, S. D. Barthelmy, J. Bartlett, I. Bartos, R. Bassiri, A. Basti, J. C. Batch, M. Bawaj, J. C. Bayley, M. Bazzan, B. Bécsy, C. Beer, M. Bejger, I. Belahcene, A. S. Bell, B. K. Berger, G. Bergmann, J. J. Bero, C. P. L. Berry, D. Bersanetti, A. Bertolini, J. Betzwieser, S. Bhagwat, R. Bhandare, I. A. Bilenko, G. Billingsley, C. R. Billman, J. Birch, R. Birney, O. Birnholtz, S. Biscans, S. Biscoveanu, A. Bisht, M. Bitossi, C. Biwer, M. A. Bizouard, J. K. Blackburn, J. Blackman, C. D. Blair, D. G. Blair, R. M. Blair, S. Bloemen, O. Bock, N. Bode, M. Boer, G. Bogaert, A. Bohe, F. Bondu, E. Bonilla, R. Bonnand, B. A. Boom, R. Bork, V. Boschi, S. Bose, K. Bossie, Y. Bouffanais, A. Bozzi, C. Bradaschia, P. R. Brady, M. Branchesi, J. E. Brau, T. Briant, A. Brillet, M. Brinkmann, V. Brisson, P. Brockill, J. E. Broida, A. F. Brooks, D. A. Brown, D. D. Brown, S. Brunett, C. C. Buchanan, A. Buikema, T. Bulik, H. J. Bulten, A. Buonanno, D. Buskulic, C. Buy, R. L. Byer, M. Cabero, L. Cadonati, G. Cagnoli, C. Cahillane, J. Calderón Bustillo, T. A. Callister, E. Calloni, J. B. Camp, M. Canepa, P. Canizares, K. C. Cannon, H. Cao, J. Cao, C. D. Capano, E. Capocasa, F. Carbognani, S. Caride, M. F. Carney, J. Casanueva Diaz, C. Casentini, S. Caudill, M. Cavaglià, F. Cavalier, R. Cavalieri, G. Cella, C. B. Cepeda, P. Cerdá-Durán, G. Cerretani, E. Cesarini, S. J. Chamberlin, M. Chan, S. Chao, P. Charlton, E. Chase, E. Chassande-Mottin, D. Chatterjee, K. Chatziioannou, B. D. Cheeseboro, H. Y. Chen, X. Chen, Y. Chen, H.-P. Cheng, H. Chia, A. Chincarini, A. Chiummo, T. Chmiel, H. S. Cho, M. Cho, J. H. Chow, N. Christensen, Q. Chu, A. J. K. Chua, S. Chua, A. K. W. Chung, S. Chung, G. Ciani, R. Ciolfi, C. E. Cirelli, A. Cirone, F. Clara, J. A. Clark, P. Clearwater, F. Cleva, C. Cocchieri, E. Coccia, P.-F. Cohadon, D. Cohen, A. Colla, C. G. Collette, L. R. Cominsky, M. Constancio, L. Conti, S. J.

Cooper, P. Corban, T. R. Corbitt, I. Cordero-Carrión, K. R. Corley, N. Cornish, A. Corsi, S. Cortese, C. A. Costa, M. W. Coughlin, S. B. Coughlin, J.-P. Coulon, S. T. Countryman, P. Couvares, P. B. Covas, E. E. Cowan, D. M. Coward, M. J. Cowart, D. C. Coyne, R. Coyne, J. D. E. Creighton, T. D. Creighton, J. Cripe, S. G. Crowder, T. J. Cullen, A. Cumming, L. Cunningham, E. Cuoco, T. Dal Canton, G. Dálya, S. L. Danilishin, S. D'Antonio, K. Danzmann, A. Dasgupta, C. F. Da Silva Costa, V. Dattilo, I. Dave, M. Davier, D. Davis, E. J. Daw, B. Day, S. De, D. DeBra, J. Degallaix, M. De Laurentis, S. Deléglise, W. Del Pozzo, N. Demos, T. Denker, T. Dent, R. De Pietri, V. Dergachev, R. De Rosa, R. T. DeRosa, C. De Rossi, R. DeSalvo, O. de Varona, J. Devenson, S. Dhurandhar, M. C. Díaz, L. Di Fiore, M. Di Giovanni, T. Di Girolamo, A. Di Lieto, S. Di Pace, I. Di Palma, F. Di Renzo, Z. Doctor, V. Dolique, F. Donovan, K. L. Dooley, S. Doravari, I. Dorrington, R. Douglas, M. Dovale Álvarez, T. P. Downes, M. Drago, C. Dreissigacker, J. C. Driggers, Z. Du, M. Ducrot, P. Dupej, S. E. Dwyer, T. B. Edo, M. C. Edwards, A. Effler, H.-B. Eggenstein, P. Ehrens, J. Eichholz, S. S. Eikenberry, R. A. Eisenstein, R. C. Essick, D. Estevez, Z. B. Etienne, T. Etzel, M. Evans, T. M. Evans, M. Factourovich, V. Fafone, H. Fair, S. Fairhurst, X. Fan, S. Farinon, B. Farr, W. M. Farr, E. J. Fauchon-Jones, M. Favata, M. Fays, C. Fee, H. Fehrmann, J. Feicht, M. M. Fejer, A. Fernandez-Galiana, I. Ferrante, E. C. Ferreira, F. Ferrini, F. Fidecaro, D. Finstad, I. Fiori, D. Fiorucci, M. Fishbach, R. P. Fisher, M. Fitz-Axen, R. Flaminio, M. Fletcher, H. Fong, J. A. Font, P. W. F. Forsyth, S. S. Forsyth, J.-D. Fournier, S. Frasca, F. Frasconi, Z. Frei, A. Freise, R. Frey, V. Frey, E. M. Fries, P. Fritschel, V. V. Frolov, P. Fulda, M. Fyffe, H. Gabbard, B. U. Gadre, S. M. Gaebel, J. R. Gair, L. Gammaitoni, M. R. Ganija, S. G. Gaonkar, C. Garcia-Quiros, F. Garufi, B. Gateley, S. Gaudio, G. Gaur, V. Gayathri, N. Gehrels, G. Gemme, E. Genin, A. Gennai, D. George, J. George, L. Gergely, V. Germain, S. Ghonge, Abhirup Ghosh, Archisman Ghosh, S. Ghosh, J. A. Giaime, K. D. Giardina, A. Giazotto, K. Gill, L. Glover, E. Goetz, R. Goetz, S. Gomes, B. Goncharov, G. González, J. M. Gonzalez Castro, A. Gopakumar, M. L. Gorodetsky, S. E. Gossan, M. Gosselin, R. Gouaty, A. Grado, C. Graef, M. Granata, A. Grant, S. Gras, C. Gray, G. Greco, A. C. Green, E. M. Gretarsson, P. Groot, H. Grote, S. Grunewald, P. Gruning, G. M. Guidi, X. Guo, A. Gupta, M. K. Gupta, K. E. Gushwa, E. K. Gustafson, R. Gustafson, O. Halim, B. R. Hall, E. D. Hall, E. Z. Hamilton, G. Hammond, M. Haney, M. M. Hanke, J. Hanks, C. Hanna, M. D. Han-

nam, O. A. Hannuksela, J. Hanson, T. Hardwick, J. Harms, G. M. Harry, I. W. Harry, M. J. Hart, C.-J. Haster, K. Haughian, J. Healy, A. Heidmann, M. C. Heintze, H. Heitmann, P. Hello, G. Hemming, M. Hendry, I. S. Heng, J. Hennig, A. W. Heptonstall, M. Heurs, S. Hild, T. Hinderer, D. Hoak, D. Hofman, K. Holt, D. E. Holz, P. Hopkins, C. Horst, J. Hough, E. A. Houston, E. J. Howell, Y. M. Hu, E. A. Huerta, D. Huet, B. Hughey, S. Husa, S. H. Huttner, T. Huynh-Dinh, N. Indik, R. Inta, G. Intini, H. N. Isa, J.-M. Isac, M. Isi, B. R. Iyer, K. Izumi, T. Jacqmin, K. Jani, P. Jaranowski, S. Jawahar, F. Jiménez-Forteza, W. W. Johnson, N. K. Johnson-McDaniel, D. I. Jones, R. Jones, R. J. G. Jonker, L. Ju, J. Junker, C. V. Kalaghatgi, V. Kalogera, B. Kamai, S. Kandhasamy, G. Kang, J. B. Kanner, S. J. Kapadia, S. Karki, K. S. Karvinen, M. Kasprzack, M. Katolik, E. Katsavounidis, W. Katzman, S. Kaufer, K. Kawabe, F. Kéfélian, D. Keitel, A. J. Kemball, R. Kennedy, C. Kent, J. S. Key, F. Y. Khalili, I. Khan, S. Khan, Z. Khan, E. A. Khazanov, N. Kijbunchoo, Chunglee Kim, J. C. Kim, K. Kim, W. Kim, W. S. Kim, Y.-M. Kim, S. J. Kimbrell, E. J. King, P. J. King, M. Kinley-Hanlon, R. Kirchhoff, J. S. Kissel, L. Kleybolte, S. Klimenko, T. D. Knowles, P. Koch, S. M. Koehlenbeck, S. Koley, V. Kondrashov, A. Kontos, M. Korobko, W. Z. Korth, I. Kowalska, D. B. Kozak, C. Krämer, V. Kringel, B. Krishnan, A. Królak, G. Kuehn, P. Kumar, R. Kumar, S. Kumar, L. Kuo, A. Kutynia, S. Kwang, B. D. Lackey, K. H. Lai, M. Landry, R. N. Lang, J. Lange, B. Lantz, R. K. Lanza, A. Lartaux-Vollard, P. D. Lasky, M. Laxen, A. Lazzarini, C. Lazzaro, P. Leaci, S. Leavey, C. H. Lee, H. K. Lee, H. M. Lee, H. W. Lee, K. Lee, J. Lehmann, A. Lenon, M. Leonardi, N. Leroy, N. Letendre, Y. Levin, T. G. F. Li, S. D. Linker, T. B. Littenberg, J. Liu, R. K. L. Lo, N. A. Lockerbie, L. T. London, J. E. Lord, M. Lorenzini, V. Loriette, M. Lormand, G. Losurdo, J. D. Lough, C. O. Lousto, G. Lovelace, H. Lück, D. Lumaca, A. P. Lundgren, R. Lynch, Y. Ma, R. Macas, S. Macfoy, B. Machenschalk, M. MacInnis, D. M. Macleod, I. Magaña Hernandez, F. Magaña-Sandoval, L. Magaña Zertuche, R. M. Magee, E. Majorana, I. Maksimovic, N. Man, V. Mandic, V. Mangano, G. L. Mansell, M. Manske, M. Mantovani, F. Marchesoni, F. Marion, S. Márka, Z. Márka, C. Markakis, A. S. Markosyan, A. Markowitz, E. Maros, A. Marquina, P. Marsh, F. Martelli, L. Martellini, I. W. Martin, R. M. Martin, D. V. Martynov, K. Mason, E. Massera, A. Masserot, T. J. Massinger, M. Masso-Reid, S. Mastrogiovanni, A. Matas, F. Matichard, L. Matone, N. Mavalvala, N. Mazumder, R. McCarthy, D. E. McClelland, S. McCormick, L. Mc-

Culler, S. C. McGuire, G. McIntyre, J. McIver, D. J. McManus, L. McNeill, T. McRae, S. T. McWilliams, D. Meacher, G. D. Meadors, M. Mehmet, J. Meidam, E. Mejuto-Villa, A. Melatos, G. Mendell, R. A. Mercer, E. L. Merilh, M. Merzougui, S. Meshkov, C. Messenger, C. Messick, R. Metzdorff, P. M. Meyers, H. Miao, C. Michel, H. Middleton, E. E. Mikhailov, L. Milano, A. L. Miller, B. B. Miller, J. Miller, M. Millhouse, M. C. Milovich-Goff, O. Minazzoli, Y. Minenkov, J. Ming, C. Mishra, S. Mitra, V. P. Mitrofanov, G. Mitselmakher, R. Mittleman, D. Moffa, A. Moggi, K. Mogushi, M. Mohan, S. R. P. Mohapatra, M. Montani, C. J. Moore, D. Moraru, G. Moreno, S. Morisaki, S. R. Morriss, B. Mours, C. M. Mow-Lowry, G. Mueller, A. W. Muir, A. Mukherjee, D. Mukherjee, S. Mukherjee, N. Mukund, A. Mullavey, J. Munch, E. A. Muñiz, M. Muratore, P. G. Murray, K. Napier, I. Nardecchia, L. Naticchioni, R. K. Nayak, J. Neilson, G. Nelemans, T. J. N. Nelson, M. Nery, A. Neunzert, L. Nevin, J. M. Newport, G. Newton, K. K. Y. Ng, T. T. Nguyen, D. Nichols, A. B. Nielsen, S. Nissanke, A. Nitz, A. Noack, F. Nocera, D. Nolting, C. North, L. K. Nuttall, J. Oberling, G. D. O'Dea, G. H. Ogin, J. J. Oh, S. H. Oh, F. Ohme, M. A. Okada, M. Oliver, P. Oppermann, R. J. Oram, B. O'Reilly, R. Ormiston, L. F. Ortega, R. O'Shaughnessy, S. Ossokine, D. J. Ottaway, H. Overmier, B. J. Owen, A. E. Pace, J. Page, M. A. Page, A. Pai, S. A. Pai, J. R. Palamos, O. Palashov, C. Palomba, A. Pal-Singh, Howard Pan, Huang-Wei Pan, B. Pang, P. T. H. Pang, C. Pankow, F. Pannarale, B. C. Pant, F. Paoletti, A. Paoli, M. A. Papa, A. Parida, W. Parker, D. Pascucci, A. Pasqualetti, R. Passaquieti, D. Passuello, M. Patil, B. Patricelli, B. L. Pearlstone, M. Pedraza, R. Pedurand, L. Pekowsky, A. Pele, S. Penn, C. J. Perez, A. Perreca, L. M. Perri, H. P. Pfeiffer, M. Phelps, O. J. Piccinni, M. Pichot, F. Piergiovanni, V. Pierro, G. Pillant, L. Pinard, I. M. Pinto, M. Pirello, M. Pitkin, M. Poe, R. Poggiani, P. Popolizio, E. K. Porter, A. Post, J. Powell, J. Prasad, J. W. W. Pratt, G. Pratten, V. Predoi, T. Prestegard, M. Prijatelj, M. Principe, S. Privitera, R. Prix, G. A. Prodi, L. G. Prokhorov, O. Puncken, M. Punturo, P. Puppo, M. Pürrer, H. Qi, V. Quetschke, E. A. Quintero, R. Quitzow-James, F. J. Raab, D. S. Rabeling, H. Radkins, P. Raffai, S. Raja, C. Rajan, B. Rajbhandari, M. Rakhmanov, K. E. Ramirez, A. Ramos-Buades, P. Rapagnani, V. Raymond, M. Razzano, J. Read, T. Regimbau, L. Rei, S. Reid, D. H. Reitze, W. Ren, S. D. Reyes, F. Ricci, P. M. Ricker, S. Rieger, K. Riles, M. Rizzo, N. A. Robertson, R. Robie, F. Robinet, A. Rocchi, L. Rolland,

J. G. Rollins, V. J. Roma, J. D. Romano, R. Romano, C. L. Romel, J. H. Romie, D. Rosińska, M. P. Ross, S. Rowan, A. Rüdiger, P. Ruggi, G. Rutins, K. Ryan, S. Sachdev, T. Sadecki, L. Sadeghian, M. Sakellariadou, L. Salconi, M. Saleem, F. Salemi, A. Samajdar, L. Sammut, L. M. Sampson, E. J. Sanchez, L. E. Sanchez, N. Sanchis-Gual, V. Sandberg, J. R. Sanders, B. Sassolas, B. S. Sathyaprakash, P. R. Saulson, O. Sauter, R. L. Savage, A. Sawadsky, P. Schale, M. Scheel, J. Scheuer, J. Schmidt, P. Schmidt, R. Schnabel, R. M. S. Schofield, A. Schönbeck, E. Schreiber, D. Schuette, B. W. Schulte, B. F. Schutz, S. G. Schwalbe, J. Scott, S. M. Scott, E. Seidel, D. Sellers, A. S. Sengupta, D. Sentenac, V. Sequino, A. Sergeev, D. A. Shaddock, T. J. Shaffer, A. A. Shah, M. S. Shahriar, M. B. Shaner, L. Shao, B. Shapiro, P. Shawhan, A. Sheperd, D. H. Shoemaker, D. M. Shoemaker, K. Siellez, X. Siemens, M. Sieniawska, D. Sigg, A. D. Silva, L. P. Singer, A. Singh, A. Singhal, A. M. Sintes, B. J. J. Slagmolen, B. Smith, J. R. Smith, R. J. E. Smith, S. Somala, E. J. Son, J. A. Sonnenberg, B. Sorazu, F. Sorrentino, T. Souradeep, A. P. Spencer, A. K. Srivastava, K. Staats, A. Staley, M. Steinke, J. Steinlechner, S. Steinlechner, D. Steinmeyer, S. P. Stevenson, R. Stone, D. J. Stops, K. A. Strain, G. Stratta, S. E. Strigin, A. Strunk, R. Sturani, A. L. Stuver, T. Z. Summerscales, L. Sun, S. Sunil, J. Suresh, P. J. Sutton, B. L. Swinkels, M. J. Szczepańczyk, M. Tacca, S. C. Tait, C. Talbot, D. Talukder, D. B. Tanner, M. Tápai, A. Taracchini, J. D. Tasson, J. A. Taylor, R. Taylor, S. V. Tewari, T. Theeg, F. Thies, E. G. Thomas, M. Thomas, P. Thomas, K. A. Thorne, E. Thrane, S. Tiwari, V. Tiwari, K. V. Tokmakov, K. Toland, M. Tonelli, Z. Tornasi, A. Torres-Forné, C. I. Torrie, D. Töyrä, F. Travasso, G. Traylor, J. Trinastic, M. C. Tringali, L. Trozzo, K. W. Tsang, M. Tse, R. Tso, L. Tsukada, D. Tsuna, D. Tuyenbayev, K. Ueno, D. Ugolini, C. S. Unnikrishnan, A. L. Urban, S. A. Usman, H. Vahlbruch, G. Vajente, G. Valdes, M. Vallisneri, N. van Bakel, M. van Beuzekom, J. F. J. van den Brand, C. Van Den Broeck, D. C. Vander-Hyde, L. van der Schaaf, J. V. van Heijningen, A. A. van Veggel, M. Vardaro, V. Varma, S. Vass, M. Vasúth, A. Vecchio, G. Vedovato, J. Veitch, P. J. Veitch, K. Venkateswara, G. Venugopalan, D. Verkindt, F. Vetrano, A. Viceré, A. D. Viets, S. Vinciguerra, D. J. Vine, J.-Y. Vinet, S. Vitale, T. Vo, H. Vocca, C. Vorvick, S. P. Vyatchanin, A. R. Wade, L. E. Wade, M. Wade, R. Walet, M. Walker, L. Wallace, S. Walsh, G. Wang, H. Wang, J. Z. Wang, W. H. Wang, Y. F. Wang, R. L. Ward, J. Warner, M. Was, J. Watchi, B. Weaver, L.-W. Wei, M. Weinert, A. J. Weinstein, R. Weiss,

L. Wen, E. K. Wessel, P. Weßels, J. Westerweck, T. Westphal, K. Wette, J. T. Whelan, S. E. Whitcomb, B. F. Whiting, C. Whittle, D. Wilken, D. Williams, R. D. Williams, A. R. Williamson, J. L. Willis, B. Willke, M. H. Wimmer, W. Winkler, C. C. Wipf, H. Wittel, G. Woan, J. Woehler, J. Wofford, K. W. K. Wong, J. Worden, J. L. Wright, D. S. Wu, D. M. Wysocki, S. Xiao, H. Yamamoto, C. C. Yancey, L. Yang, M. J. Yap, M. Yazback, Hang Yu, Haocun Yu, M. Yvert, A. Zadrożny, M. Zanolin, T. Zelenova, J.-P. Zendri, M. Zevin, L. Zhang, M. Zhang, T. Zhang, Y.-H. Zhang, C. Zhao, M. Zhou, Z. Zhou, S. J. Zhu, X. J. Zhu, A. B. Zimmerman, M. E. Zucker, and J. Zweizig. GW170814: A Three-Detector Observation of Gravitational Waves from a Binary Black Hole Coalescence. *Physical Review Letters*, 119(14):141101, oct 2017.

[AAA+17c] B. P. Abbott, R. Abbott, T. D. Abbott, F. Acernese, K. Ackley, C. Adams, T. Adams, P. Addesso, R. X. Adhikari, V. B. Adya, C. Affeldt, M. Afrough, B. Agarwal, M. Agathos, K. Agatsuma, N. Aggarwal, O. D. Aguiar, L. Aiello, A. Ain, P. Ajith, B. Allen, G. Allen, A. Allocca, P. A. Altin, A. Amato, A. Ananyeva, S. B. Anderson, W. G. Anderson, S. V. Angelova, S. Antier, S. Appert, K. Arai, M. C. Araya, J. S. Areeda, N. Arnaud, K. G. Arun, S. Ascenzi, G. Ashton, M. Ast, S. M. Aston, P. Astone, D. V. Atallah, P. Aufmuth, C. Aulbert, K. AultONeal, C. Austin, A. Avila-Alvarez, S. Babak, P. Bacon, M. K. M. Bader, S. Bae, M. Bailes, P. T. Baker, F. Baldaccini, G. Ballardin, S. W. Ballmer, S. Banagiri, J. C. Barayoga, S. E. Barclay, B. C. Barish, D. Barker, K. Barkett, F. Barone, B. Barr, L. Barsotti, M. Barsuglia, D. Barta, S. D. Barthelmy, J. Bartlett, I. Bartos, R. Bassiri, A. Basti, J. C. Batch, M. Bawaj, J. C. Bayley, M. Bazzan, B. Bécsy, C. Beer, M. Bejger, I. Belahcene, A. S. Bell, B. K. Berger, G. Bergmann, S. Bernuzzi, J. J. Bero, C. P. L. Berry, D. Bersanetti, A. Bertolini, J. Betzwieser, S. Bhagwat, R. Bhandare, I. A. Bilenko, G. Billingsley, C. R. Billman, J. Birch, R. Birney, O. Birnholtz, S. Biscans, S. Biscoveanu, A. Bisht, M. Bitossi, C. Biwer, M. A. Bizouard, J. K. Blackburn, J. Blackman, C. D. Blair, D. G. Blair, R. M. Blair, S. Bloemen, O. Bock, N. Bode, M. Boer, G. Bogaert, A. Bohe, F. Bondu, E. Bonilla, R. Bonnand, B. A. Boom, R. Bork, V. Boschi, S. Bose, K. Bossie, Y. Bouffanais, A. Bozzi, C. Bradaschia, P. R. Brady, M. Branchesi, J. E. Brau, T. Briant, A. Brillet, M. Brinkmann, V. Brisson, P. Brockill, J. E. Broida, A. F. Brooks, D. A. Brown, D. D. Brown, S. Brunett, C. C. Buchanan, A. Buikema, T. Bulik,

H. J. Bulten, A. Buonanno, D. Buskulic, C. Buy, R. L. Byer, M. Cabero, L. Cadonati, G. Cagnoli, C. Cahillane, J. Calderón Bustillo, T. A. Callister, E. Calloni, J. B. Camp, M. Canepa, P. Canizares, K. C. Cannon, H. Cao, J. Cao, C. D. Capano, E. Capocasa, F. Carbognani, S. Caride, M. F. Carney, G. Carullo, J. Casanueva Diaz, C. Casentini, S. Caudill, M. Cavaglià, F. Cavalier, R. Cavalieri, G. Cella, C. B. Cepeda, P. Cerdá-Durán, G. Cerretani, E. Cesarini, S. J. Chamberlin, M. Chan, S. Chao, P. Charlton, E. Chase, E. Chassande-Mottin, D. Chatterjee, K. Chatziioannou, B. D. Cheeseboro, H. Y. Chen, X. Chen, Y. Chen, H.-P. Cheng, H. Chia, A. Chincarini, A. Chiummo, T. Chmiel, H. S. Cho, M. Cho, J. H. Chow, N. Christensen, Q. Chu, A. J. K. Chua, S. Chua, A. K. W. Chung, S. Chung, G. Ciani, R. Ciolfi, C. E. Cirelli, A. Cirone, F. Clara, J. A. Clark, P. Clearwater, F. Cleva, C. Cocchieri, E. Coccia, P.-F. Cohadon, D. Cohen, A. Colla, C. G. Collette, L. R. Cominsky, M. Constancio, L. Conti, S. J. Cooper, P. Corban, T. R. Corbitt, I. Cordero-Carrión, K. R. Corley, N. Cornish, A. Corsi, S. Cortese, C. A. Costa, M. W. Coughlin, S. B. Coughlin, J.-P. Coulon, S. T. Countryman, P. Couvares, P. B. Covas, E. E. Cowan, D. M. Coward, M. J. Cowart, D. C. Coyne, R. Coyne, J. D. E. Creighton, T. D. Creighton, J. Cripe, S. G. Crowder, T. J. Cullen, A. Cumming, L. Cunningham, E. Cuoco, T. Dal Canton, G. Dálya, S. L. Danilishin, S. D'Antonio, K. Danzmann, A. Dasgupta, C. F. Da Silva Costa, V. Dattilo, I. Dave, M. Davier, D. Davis, E. J. Daw, B. Day, S. De, D. DeBra, J. Degallaix, M. De Laurentis, S. Deléglise, W. Del Pozzo, N. Demos, T. Denker, T. Dent, R. De Pietri, V. Dergachev, R. De Rosa, R. T. DeRosa, C. De Rossi, R. DeSalvo, O. de Varona, J. Devenson, S. Dhurandhar, M. C. Díaz, T. Dietrich, L. Di Fiore, M. Di Giovanni, T. Di Girolamo, A. Di Lieto, S. Di Pace, I. Di Palma, F. Di Renzo, Z. Doctor, V. Dolique, F. Donovan, K. L. Dooley, S. Doravari, I. Dorrington, R. Douglas, M. Dovale Álvarez, T. P. Downes, M. Drago, C. Dreissigacker, J. C. Driggers, Z. Du, M. Ducrot, R. Dudi, P. Dupej, S. E. Dwyer, T. B. Edo, M. C. Edwards, A. Effler, H.-B. Eggenstein, P. Ehrens, J. Eichholz, S. S. Eikenberry, R. A. Eisenstein, R. C. Essick, D. Estevez, Z. B. Etienne, T. Etzel, M. Evans, T. M. Evans, M. Factourovich, V. Fafone, H. Fair, S. Fairhurst, X. Fan, S. Farinon, B. Farr, W. M. Farr, E. J. Fauchon-Jones, M. Favata, M. Fays, C. Fee, H. Fehrmann, J. Feicht, M. M. Fejer, A. Fernandez-Galiana, I. Ferrante, E. C. Ferreira, F. Ferrini, F. Fidecaro, D. Finstad, I. Fiori, D. Fiorucci, M. Fishbach, R. P. Fisher, M. Fitz-Axen, R. Flaminio, M. Fletcher, H. Fong, J. A. Font, P. W. F. Forsyth, S. S.

Forsyth, J.-D. Fournier, S. Frasca, F. Frasconi, Z. Frei, A. Freise, R. Frey, V. Frey, E. M. Fries, P. Fritschel, V. V. Frolov, P. Fulda, M. Fyffe, H. Gabbard, B. U. Gadre, S. M. Gaebel, J. R. Gair, L. Gammaitoni, M. R. Ganija, S. G. Gaonkar, C. Garcia-Quiros, F. Garufi, B. Gateley, S. Gaudio, G. Gaur, V. Gayathri, N. Gehrels, G. Gemme, E. Genin, A. Gennai, D. George, J. George, L. Gergely, V. Germain, S. Ghonge, Abhirup Ghosh, Archisman Ghosh, S. Ghosh, J. A. Giaime, K. D. Giardina, A. Giazotto, K. Gill, L. Glover, E. Goetz, R. Goetz, S. Gomes, B. Goncharov, G. González, J. M. Gonzalez Castro, A. Gopakumar, M. L. Gorodetsky, S. E. Gossan, M. Gosselin, R. Gouaty, A. Grado, C. Graef, M. Granata, A. Grant, S. Gras, C. Gray, G. Greco, A. C. Green, E. M. Gretarsson, P. Groot, H. Grote, S. Grunewald, P. Gruning, G. M. Guidi, X. Guo, A. Gupta, M. K. Gupta, K. E. Gushwa, E. K. Gustafson, R. Gustafson, O. Halim, B. R. Hall, E. D. Hall, E. Z. Hamilton, G. Hammond, M. Haney, M. M. Hanke, J. Hanks, C. Hanna, M. D. Hannam, O. A. Hannuksela, J. Hanson, T. Hardwick, J. Harms, G. M. Harry, I. W. Harry, M. J. Hart, C.-J. Haster, K. Haughian, J. Healy, A. Heidmann, M. C. Heintze, H. Heitmann, P. Hello, G. Hemming, M. Hendry, I. S. Heng, J. Hennig, A. W. Heptonstall, M. Heurs, S. Hild, T. Hinderer, W. C. G. Ho, D. Hoak, D. Hofman, K. Holt, D. E. Holz, P. Hopkins, C. Horst, J. Hough, E. A. Houston, E. J. Howell, A. Hreibi, Y. M. Hu, E. A. Huerta, D. Huet, B. Hughey, S. Husa, S. H. Huttner, T. Huynh-Dinh, N. Indik, R. Inta, G. Intini, H. N. Isa, J.-M. Isac, M. Isi, B. R. Iyer, K. Izumi, T. Jacqmin, K. Jani, P. Jaranowski, S. Jawahar, F. Jiménez-Forteza, W. W. Johnson, N. K. Johnson-McDaniel, D. I. Jones, R. Jones, R. J. G. Jonker, L. Ju, J. Junker, C. V. Kalaghatgi, V. Kalogera, B. Kamai, S. Kandhasamy, G. Kang, J. B. Kanner, S. J. Kapadia, S. Karki, K. S. Karvinen, M. Kasprzack, W. Kastaun, M. Katolik, E. Katsavounidis, W. Katzman, S. Kaufer, K. Kawabe, F. Kéfélian, D. Keitel, A. J. Kemball, R. Kennedy, C. Kent, J. S. Key, F. Y. Khalili, I. Khan, S. Khan, Z. Khan, E. A. Khazanov, N. Kijbunchoo, Chunglee Kim, J. C. Kim, K. Kim, W. Kim, W. S. Kim, Y.-M. Kim, S. J. Kimbrell, E. J. King, P. J. King, M. Kinley-Hanlon, R. Kirchhoff, J. S. Kissel, L. Kleybolte, S. Klimenko, T. D. Knowles, P. Koch, S. M. Koehlenbeck, S. Koley, V. Kondrashov, A. Kontos, M. Korobko, W. Z. Korth, I. Kowalska, D. B. Kozak, C. Krämer, V. Kringel, B. Krishnan, A. Królak, G. Kuehn, P. Kumar, R. Kumar, S. Kumar, L. Kuo, A. Kutynia, S. Kwang, B. D. Lackey, K. H. Lai, M. Landry, R. N. Lang, J. Lange, B. Lantz, R. K. Lanza, S. L. Larson, A. Lartaux-Vollard, P. D.

Lasky, M. Laxen, A. Lazzarini, C. Lazzaro, P. Leaci, S. Leavey, C. H. Lee, H. K. Lee, H. M. Lee, H. W. Lee, K. Lee, J. Lehmann, A. Lenon, E. Leon, M. Leonardi, N. Leroy, N. Letendre, Y. Levin, T. G. F. Li, S. D. Linker, T. B. Littenberg, J. Liu, X. Liu, R. K. L. Lo, N. A. Lockerbie, L. T. London, J. E. Lord, M. Lorenzini, V. Loriette, M. Lormand, G. Losurdo, J. D. Lough, C. O. Lousto, G. Lovelace, H. Lück, D. Lumaca, A. P. Lundgren, R. Lynch, Y. Ma, R. Macas, S. Macfoy, B. Machenschalk, M. MacInnis, D. M. Macleod, I. Magaña Hernandez, F. Magaña-Sandoval, L. Magaña Zertuche, R. M. Magee, E. Majorana, I. Maksimovic, N. Man, V. Mandic, V. Mangano, G. L. Mansell, M. Manske, M. Mantovani, F. Marchesoni, F. Marion, S. Márka, Z. Márka, C. Markakis, A. S. Markosyan, A. Markowitz, E. Maros, A. Marquina, P. Marsh, F. Martelli, L. Martellini, I. W. Martin, R. M. Martin, D. V. Martynov, J. N. Marx, K. Mason, E. Massera, A. Masserot, T. J. Massinger, M. Masso-Reid, S. Mastrogiovanni, A. Matas, F. Matichard, L. Matone, N. Mavalvala, N. Mazumder, R. McCarthy, D. E. McClelland, S. McCormick, L. McCuller, S. C. McGuire, G. McIntyre, J. McIver, D. J. McManus, L. McNeill, T. McRae, S. T. McWilliams, D. Meacher, G. D. Meadors, M. Mehmet, J. Meidam, E. Mejuto-Villa, A. Melatos, G. Mendell, R. A. Mercer, E. L. Merilh, M. Merzougui, S. Meshkov, C. Messenger, C. Messick, R. Metzdorff, P. M. Meyers, H. Miao, C. Michel, H. Middleton, E. E. Mikhailov, L. Milano, A. L. Miller, B. B. Miller, J. Miller, M. Millhouse, M. C. Milovich-Goff, O. Minazzoli, Y. Minenkov, J. Ming, C. Mishra, S. Mitra, V. P. Mitrofanov, G. Mitselmakher, R. Mittleman, D. Moffa, A. Moggi, K. Mogushi, M. Mohan, S. R. P. Mohapatra, I. Molina, M. Montani, C. J. Moore, D. Moraru, G. Moreno, S. Morisaki, S. R. Morriss, B. Mours, C. M. Mow-Lowry, G. Mueller, A. W. Muir, Arunava Mukherjee, D. Mukherjee, S. Mukherjee, N. Mukund, A. Mullavey, J. Munch, E. A. Muñiz, M. Muratore, P. G. Murray, A. Nagar, K. Napier, I. Nardecchia, L. Naticchioni, R. K. Nayak, J. Neilson, G. Nelemans, T. J. N. Nelson, M. Nery, A. Neunzert, L. Nevin, J. M. Newport, G. Newton, K. K. Y. Ng, P. Nguyen, T. T. Nguyen, D. Nichols, A. B. Nielsen, S. Nissanke, A. Nitz, A. Noack, F. Nocera, D. Nolting, C. North, L. K. Nuttall, J. Oberling, G. D. O'Dea, G. H. Ogin, J. J. Oh, S. H. Oh, F. Ohme, M. A. Okada, M. Oliver, P. Oppermann, Richard J. Oram, B. O'Reilly, R. Ormiston, L. F. Ortega, R. O'Shaughnessy, S. Ossokine, D. J. Ottaway, H. Overmier, B. J. Owen, A. E. Pace, J. Page, M. A. Page, A. Pai, S. A. Pai, J. R. Palamos, O. Palashov, C. Palomba, A. Pal-Singh, Howard Pan, Huang-Wei Pan, B. Pang, P. T. H. Pang,

C. Pankow, F. Pannarale, B. C. Pant, F. Paoletti, A. Paoli, M. A. Papa, A. Parida, W. Parker, D. Pascucci, A. Pasqualetti, R. Passaquieti, D. Passuello, M. Patil, B. Patricelli, B. L. Pearlstone, M. Pedraza, R. Pedurand, L. Pekowsky, A. Pele, S. Penn, C. J. Perez, A. Perreca, L. M. Perri, H. P. Pfeiffer, M. Phelps, O. J. Piccinni, M. Pichot, F. Piergiovanni, V. Pierro, G. Pillant, L. Pinard, I. M. Pinto, M. Pirello, M. Pitkin, M. Poe, R. Poggiani, P. Popolizio, E. K. Porter, A. Post, J. Powell, J. Prasad, J. W. W. Pratt, G. Pratten, V. Predoi, T. Prestegard, M. Prijatelj, M. Principe, S. Privitera, R. Prix, G. A. Prodi, L. G. Prokhorov, O. Puncken, M. Punturo, P. Puppo, M. Pürrer, H. Qi, V. Quetschke, E. A. Quintero, R. Quitzow-James, F. J. Raab, D. S. Rabeling, H. Radkins, P. Raffai, S. Raja, C. Rajan, B. Rajbhandari, M. Rakhmanov, K. E. Ramirez, A. Ramos-Buades, P. Rapagnani, V. Raymond, M. Razzano, J. Read, T. Regimbau, L. Rei, S. Reid, D. H. Reitze, W. Ren, S. D. Reyes, F. Ricci, P. M. Ricker, S. Rieger, K. Riles, M. Rizzo, N. A. Robertson, R. Robie, F. Robinet, A. Rocchi, L. Rolland, J. G. Rollins, V. J. Roma, J. D. Romano, R. Romano, C. L. Romel, J. H. Romie, D. Rosińska, M. P. Ross, S. Rowan, A. Rüdiger, P. Ruggi, G. Rutins, K. Ryan, S. Sachdev, T. Sadecki, L. Sadeghian, M. Sakellariadou, L. Salconi, M. Saleem, F. Salemi, A. Samajdar, L. Sammut, L. M. Sampson, E. J. Sanchez, L. E. Sanchez, N. Sanchis-Gual, V. Sandberg, J. R. Sanders, B. Sassolas, B. S. Sathyaprakash, P. R. Saulson, O. Sauter, R. L. Savage, A. Sawadsky, P. Schale, M. Scheel, J. Scheuer, J. Schmidt, P. Schmidt, R. Schnabel, R. M. S. Schofield, A. Schönbeck, E. Schreiber, D. Schuette, B. W. Schulte, B. F. Schutz, S. G. Schwalbe, J. Scott, S. M. Scott, E. Seidel, D. Sellers, A. S. Sengupta, D. Sentenac, V. Sequino, A. Sergeev, D. A. Shaddock, T. J. Shaffer, A. A. Shah, M. S. Shahriar, M. B. Shaner, L. Shao, B. Shapiro, P. Shawhan, A. Sheperd, D. H. Shoemaker, D. M. Shoemaker, K. Siellez, X. Siemens, M. Sieniawska, D. Sigg, A. D. Silva, L. P. Singer, A. Singh, A. Singhal, A. M. Sintes, B. J. J. Slagmolen, B. Smith, J. R. Smith, R. J. E. Smith, S. Somala, E. J. Son, J. A. Sonnenberg, B. Sorazu, F. Sorrentino, T. Souradeep, A. P. Spencer, A. K. Srivastava, K. Staats, A. Staley, M. Steinke, J. Steinlechner, S. Steinlechner, D. Steinmeyer, S. P. Stevenson, R. Stone, D. J. Stops, K. A. Strain, G. Stratta, S. E. Strigin, A. Strunk, R. Sturani, A. L. Stuver, T. Z. Summerscales, L. Sun, S. Sunil, J. Suresh, P. J. Sutton, B. L. Swinkels, M. J. Szczepańczyk, M. Tacca, S. C. Tait, C. Talbot, D. Talukder, D. B. Tanner, M. Tápai, A. Taracchini, J. D. Tasson, J. A. Taylor, R. Taylor, S. V. Tewari, T. Theeg, F. Thies, E. G. Thomas,

M. Thomas, P. Thomas, K. A. Thorne, K. S. Thorne, E. Thrane, S. Tiwari, V. Tiwari, K. V. Tokmakov, K. Toland, M. Tonelli, Z. Tornasi, A. Torres-Forné, C. I. Torrie, D. Töyrä, F. Travasso, G. Traylor, J. Trinastic, M. C. Tringali, L. Trozzo, K. W. Tsang, M. Tse, R. Tso, L. Tsukada, D. Tsuna, D. Tuyenbayev, K. Ueno, D. Ugolini, C. S. Unnikrishnan, A. L. Urban, S. A. Usman, H. Vahlbruch, G. Vajente, G. Valdes, M. Vallisneri, N. van Bakel, M. van Beuzekom, J. F. J. van den Brand, C. Van Den Broeck, D. C. Vander-Hyde, L. van der Schaaf, J. V. van Heijningen, A. A. van Veggel, M. Vardaro, V. Varma, S. Vass, M. Vasúth, A. Vecchio, G. Vedovato, J. Veitch, P. J. Veitch, K. Venkateswara, G. Venugopalan, D. Verkindt, F. Vetrano, A. Viceré, A. D. Viets, S. Vinciguerra, D. J. Vine, J.-Y. Vinet, S. Vitale, T. Vo, H. Vocca, C. Vorvick, S. P. Vyatchanin, A. R. Wade, L. E. Wade, M. Wade, R. Walet, M. Walker, L. Wallace, S. Walsh, G. Wang, H. Wang, J. Z. Wang, W. H. Wang, Y. F. Wang, R. L. Ward, J. Warner, M. Was, J. Watchi, B. Weaver, L.-W. Wei, M. Weinert, A. J. Weinstein, R. Weiss, L. Wen, E. K. Wessel, P. Weßels, J. Westerweck, T. Westphal, K. Wette, J. T. Whelan, S. E. Whitcomb, B. F. Whiting, C. Whittle, D. Wilken, D. Williams, R. D. Williams, A. R. Williamson, J. L. Willis, B. Willke, M. H. Wimmer, W. Winkler, C. C. Wipf, H. Wittel, G. Woan, J. Woehler, J. Wofford, K. W. K. Wong, J. Worden, J. L. Wright, D. S. Wu, D. M. Wysocki, S. Xiao, H. Yamamoto, C. C. Yancey, L. Yang, M. J. Yap, M. Yazback, Hang Yu, Haocun Yu, M. Yvert, A. Zadrożny, M. Zanolin, T. Zelenova, J.-P. Zendri, M. Zevin, L. Zhang, M. Zhang, T. Zhang, Y.-H. Zhang, C. Zhao, M. Zhou, Z. Zhou, S. J. Zhu, X. J. Zhu, A. B. Zimmerman, M. E. Zucker, and J. Zweizig. GW170817: Observation of Gravitational Waves from a Binary Neutron Star Inspiral. *Physical Review Letters*, 119(16):161101, oct 2017.

[AAA+19] Kazunori Akiyama, Antxon Alberdi, Walter Alef, Keiichi Asada, Rebecca Azulay, Anne-Kathrin Baczko, David Ball, Mislav Baloković, John Barrett, Dan Bintley, Lindy Blackburn, Wilfred Boland, Katherine L. Bouman, Geoffrey C. Bower, Michael Bremer, Christiaan D. Brinkerink, Roger Brissenden, Silke Britzen, Avery E. Broderick, Dominique Broguiere, Thomas Bronzwaer, Do-Young Byun, John E. Carlstrom, Andrew Chael, Chi-kwan Chan, Shami Chatterjee, Koushik Chatterjee, Ming-Tang Chen, Yongjun Chen, Ilje Cho, Pierre Christian, John E. Conway, James M. Cordes, Geoffrey B. Crew, Yuzhu Cui, Jordy Davelaar, Mariafelicia De Laurentis, Roger Deane, Jessica Dempsey, Gregory Desvignes, Jason Dexter, Shep-

erd S. Doeleman, Ralph P. Eatough, Heino Falcke, Vincent L. Fish, Ed Fomalont, Raquel Fraga-Encinas, Per Friberg, Christian M. Fromm, José L. Gómez, Peter Galison, Charles F. Gammie, Roberto García, Olivier Gentaz, Boris Georgiev, Ciriaco Goddi, Roman Gold, Minfeng Gu, Mark Gurwell, Kazuhiro Hada, Michael H. Hecht, Ronald Hesper, Luis C. Ho, Paul Ho, Mareki Honma, Chih-Wei L. Huang, Lei Huang, David H. Hughes, Shiro Ikeda, Makoto Inoue, Sara Issaoun, David J. James, Buell T. Jannuzi, Michael Janssen, Britton Jeter, Wu Jiang, Michael D. Johnson, Svetlana Jorstad, Taehyun Jung, Mansour Karami, Ramesh Karuppusamy, Tomohisa Kawashima, Garrett K. Keating, Mark Kettenis, Jae-Young Kim, Junhan Kim, Jongsoo Kim, Motoki Kino, Jun Yi Koay, Patrick M. Koch, Shoko Koyama, Michael Kramer, Carsten Kramer, Thomas P. Krichbaum, Cheng-Yu Kuo, Tod R. Lauer, Sang-Sung Lee, Yan-Rong Li, Zhiyuan Li, Michael Lindqvist, Kuo Liu, Elisabetta Liuzzo, Wen-Ping Lo, Andrei P. Lobanov, Laurent Loinard, Colin Lonsdale, Ru-Sen Lu, Nicholas R. MacDonald, Jirong Mao, Sera Markoff, Daniel P. Marrone, Alan P. Marscher, Iván Martí-Vidal, Satoki Matsushita, Lynn D. Matthews, Lia Medeiros, Karl M. Menten, Yosuke Mizuno, Izumi Mizuno, James M. Moran, Kotaro Moriyama, Monika Moscibrodzka, Cornelia Müller, Hiroshi Nagai, Neil M. Nagar, Masanori Nakamura, Ramesh Narayan, Gopal Narayanan, Iniyan Natarajan, Roberto Neri, Chunchong Ni, Aristeidis Noutsos, Hiroki Okino, Héctor Olivares, Tomoaki Oyama, Feryal Özel, Daniel C. M. Palumbo, Nimesh Patel, Ue-Li Pen, Dominic W. Pesce, Vincent Piétu, Richard Plambeck, Aleksandar PopStefanija, Oliver Porth, Ben Prather, Jorge A. Preciado-López, Dimitrios Psaltis, Hung-Yi Pu, Venkatessh Ramakrishnan, Ramprasad Rao, Mark G. Rawlings, Alexander W. Raymond, Luciano Rezzolla, Bart Ripperda, Freek Roelofs, Alan Rogers, Eduardo Ros, Mel Rose, Arash Roshanineshat, Helge Rottmann, Alan L. Roy, Chet Ruszczyk, Benjamin R. Ryan, Kazi L. J. Rygl, Salvador Sánchez, David Sánchez-Arguelles, Mahito Sasada, Tuomas Savolainen, F. Peter Schloerb, Karl-Friedrich Schuster, Lijing Shao, Zhiqiang Shen, Des Small, Bong Won Sohn, Jason SooHoo, Fumie Tazaki, Paul Tiede, Remo P. J. Tilanus, Michael Titus, Kenji Toma, Pablo Torne, Tyler Trent, Sascha Trippe, Shuichiro Tsuda, Ilse van Bemmel, Huib Jan van Langevelde, Daniel R. van Rossum, Jan Wagner, John Wardle, Jonathan Weintroub, Norbert Wex, Robert Wharton, Maciek Wielgus, George N. Wong, Qingwen Wu, André Young, Ken Young, Ziri Younsi, Feng Yuan, Ye-Fei Yuan, J. Anton Zensus, Guangyao Zhao, Shan-Shan Zhao,

Ziyan Zhu, Joseph R. Farah, Zheng Meyer-Zhao, Daniel Michalik, Andrew Nadolski, Hiroaki Nishioka, Nicolas Pradel, Rurik A. Primiani, Kamal Souccar, Laura Vertatschitsch, and Paul Yamaguchi. First M87 Event Horizon Telescope Results. VI. The Shadow and Mass of the Central Black Hole. *The Astrophysical Journal*, 875(1):L6, 2019.

[AAB+18] M. Armano, H. Audley, J. Baird, P. Binetruy, M. Born, D. Bortoluzzi, E. Castelli, A. Cavalleri, A. Cesarini, A. M. Cruise, K. Danzmann, M. De Deus Silva, I. Diepholz, G. Dixon, R. Dolesi, L. Ferraioli, V. Ferroni, E. D. Fitzsimons, M. Freschi, L. Gesa, F. Gibert, D. Giardini, R. Giusteri, C. Grimani, J. Grzymisch, I. Harrison, G. Heinzel, M. Hewitson, D. Hollington, D. Hoyland, M. Hueller, H. Inchauspé, O. Jennrich, P. Jetzer, N. Karnesis, B. Kaune, N. Korsakova, C. J. Killow, J. A. Lobo, I. Lloro, L. Liu, J. P. López-Zaragoza, R. Maarschalkerweerd, D. Mance, N. Meshksar, V. Martín, L. Martin-Polo, J. Martino, F. Martin-Porqueras, I. Mateos, P. W. McNamara, J. Mendes, L. Mendes, M. Nofrarias, S. Paczkowski, M. Perreur-Lloyd, A. Petiteau, P. Pivato, E. Plagnol, J. Ramos-Castro, J. Reiche, D. I. Robertson, F. Rivas, G. Russano, J. Slutsky, C. F. Sopuerta, T. Sumner, D. Texier, J. I. Thorpe, D. Vetrugno, S. Vitale, G. Wanner, H. Ward, P. J. Wass, W. J. Weber, L. Wissel, A. Wittchen, and P. Zweifel. Beyond the Required LISA Free-Fall Performance: New LISA Pathfinder Results down to 20 $\mu$hz. *Physical Review Letters*, 120(6):061101, feb 2018.

[AET02] J. W. Armstrong, F. B. Estabrook, and Massimo Tinto. Time-Delay Interferometry for Space-Based Gravitational Wave Searches. *The Astrophysical Journal*, 527(2):814–826, 2002.

[ASGF+07] Pau Amaro-Seoane, Jonathan R. Gair, Marc Freitag, M. Coleman Miller, Ilya Mandel, Curt J. Cutler, and Stanislav Babak. Intermediate and extreme mass-ratio inspirals - Astrophysics, science applications and detection using LISA. Technical Report 17, 2007.

[ATL02] J. W. Armstrong, Massimo Tinto, and Shane L. Larson. LISA optimal sensitivity. *Physical Review D - Particles, Fields, Gravitation and Cosmology*, 66(12):1–15, 2002.

[Bar15] Simon Barke. *Inter-Spacecraft Frequency Distribution for Future Gravitational Wave Observatories, From Newton to Einstein and Beyond, Limitations of Spaceborne Observatories, Constellation-wide Reference Frequency.* PhD thesis, 2015.

[BG13] C. P.L. Berry and J. R. Gair. Expectations for extreme-mass-ratio bursts from the galactic centre. Technical Report 4, 2013.

[BGS+17] Stanislav Babak, Jonathan Gair, Alberto Sesana, Enrico Barausse, Carlos F. Sopuerta, Christopher P.L. Berry, Emanuele Berti, Pau Amaro-Seoane, Antoine Petiteau, and Antoine Klein. Science with the space-based interferometer LISA. V. Extreme mass-ratio inspirals. *Physical Review D*, 2017.

[BLPH19] Jean-Baptiste Bayle, Marc Lilley, Antoine Petiteau, and Hubert Halloin. Effect of filters on the time-delay interferometry residual laser noise for LISA. *Physical Review D*, 99(8):084023, apr 2019.

[BRL+16] Katelyn Breivik, Carl L. Rodriguez, Shane L. Larson, Vassiliki Kalogera, and Frederic A. Rasio. Distinguishing Between Formation Channels for Binary Black Holes with LISA. *The Astrophysical Journal*, 830(1):L18, oct 2016.

[Buo03] Alessandra Buonanno. TASI Lectures on Gravitational Waves from the Early Universe. 2003.

[CF18] Chiara Caprini and Daniel G. Figueroa. Cosmological backgrounds of gravitational waves. Technical Report 16, 2018.

[CH03] Neil J. Cornish and Ronald W. Hellings. The effects of orbital motion on LISA time delay interferometry. *Classical and Quantum Gravity*, 2003.

[COSM18] Marco Celoria, Roberto Oliveri, Alberto Sesana, and Michela Mapelli. Lecture notes on black hole binary astrophysics, jul 2018.

[CRVP05] Bertrand Chauvineau, Tania Regimbau, Jean Yves Vinet, and Sophie Pireaux. Relativistic analysis of the LISA long range optical links. *Physical Review D - Particles, Fields, Gravitation and Cosmology*, 72(12), 2005.

[CTHM06] Rachel J. Cruz, James I. Thorpe, Michael Hartman, and Guido Mueller. Time delay interferometry using the UF LISA benchtop simulator. *AIP Conference Proceedings*, 873(December):319–325, 2006.

[DASpAh+17] Karsten Danzmann, Pau Amaro-Seoane pau, Heather Audley heatheraudley, Stanislav Babak stba, John Baker johngbaker, Enrico Barausse barausse, Peter Bender, Gerhard Heinzel gerhardheinzel, Thomas Hertog ThomasHertog, Martin Hewitson martinhewitson, Kelly Holley-Bockelmann, Philippe

Jetzer jetzer, Nikos Karnesis karnesis, Christian Killow christiankillow, Antoine Klein klein, Bill Klipstein WilliamKlipstein, Natalia Korsakova nataliakorsakova, Shane L Larson slarson, Jeffrey Livas JeffreyLivas-, Ivan Lloro lloro, Nary Man naryman, Davor Mance davormance, Joseph Martino, Kirk McKenzie kirkmckenzie, Sean T McWilliams, Guido Mueller, David Robertson DavidRobertson, Norna Robertson, Elena Rossi emr, Giuliana Russano, Bernard Schutz schutz, Alberto Sesana asesana, David Shoemaker, Jacob Slutsky jacobpslutsky, Carlos F Sopuerta sopuerta, Tim Sumner, Ira Thorpe jamesithorpe, Michael Troebs michaeltroebs, Michele Vallisneri michelevallisneri, Alberto Vecchio, Gudrun Wanner gudrunwanner, Harry Ward henryward, Peter Wass pwass, William Weber williamjosephweber, John Ziemer johnkziemer, and Peter Zweifel. Laser Interferometer Space Antenna, A proposal in response to the ESA call for L3 mission concepts. Technical report, 2017.

[DNKV05] S. V. Dhurandhar, K. Rajesh Nayak, S. Koshti, and J. Y. Vinet. Fundamentals of the LISA stable flight formation. *Classical and Quantum Gravity*, 22(3):481–487, 2005.

[DWM+10] Glenn De Vine, Brent Ware, Kirk McKenzie, Robert E. Spero, William M. Klipstein, and Daniel A. Shaddock. Experimental demonstration of time-delay interferometry for the laser interferometer space antenna. *Physical Review Letters*, 104(21):1–5, 2010.

[Ein93] Albert Einstein. A Letter of Critique to Lord Richard Bentley, 1693.

[Ein15] Albert Einstein. Grundgedanken der allgemeinen Relativitätstheorie und Anwendung dieser Theorie in der Astronomie. *Preussische Akademie der Wissenschaften, Sitzungsberichte*, 1915.

[Ein06] A. Einstein. Erklärung der Perihelbewegung des Merkur aus der allgemeinen Relativitätstheorie. In *Albert Einstein: Akademie-Vorträge*, pages 78–87. Wiley-VCH Verlag GmbH & Co. KGaA, Weinheim, FRG, sep 2006.

[FFW+19] Hassan Ismail Fawaz, Germain Forestier, Jonathan Weber, Lhassane Idoumghar, and Pierre-Alain Muller. Deep Neural Network Ensembles for Time Series Classification. 2019.

[Fra65] Joel N. Franklin. Numerical Simulation of Stationary and Non-Stationary Gaussian Random Processes. *SIAM Review*, 7(1):68–80, jan 1965.

[GAA+18] GRAVITY Collaboration, R. Abuter, A. Amorim, N. Anugu, M. Bauböck, M. Benisty, J. P. Berger, N. Blind, H. Bonnet, W. Brandner, A. Buron, C. Collin, F. Chapron, Y. Clénet, V. Coudé du Foresto, P. T. de Zeeuw, C. Deen, F. Delplancke-Ströbele, R. Dembet, J. Dexter, G. Duvert, A. Eckart, F. Eisenhauer, G. Finger, N. M. Förster Schreiber, P. Fédou, P. Garcia, R. Garcia Lopez, F. Gao, E. Gendron, R. Genzel, S. Gillessen, P. Gordo, M. Habibi, X. Haubois, M. Haug, F. Haußmann, Th. Henning, S. Hippler, M. Horrobin, Z. Hubert, N. Hubin, A. Jimenez Rosales, L. Jochum, L. Jocou, A. Kaufer, S. Kellner, S. Kendrew, P. Kervella, Y. Kok, M. Kulas, S. Lacour, V. Lapeyrère, B. Lazareff, J. B. Le Bouquin, P. Léna, M. Lippa, R. Lenzen, A. Mérand, E. Müller, U. Neumann, T. Ott, L. Palanca, T. Paumard, L. Pasquini, K. Perraut, G. Perrin, O. Pfuhl, P. M. Plewa, S. Rabien, A. Ramírez, J. Ramos, C. Rau, G. Rodríguez-Coira, R. R. Rohloff, G. Rousset, J. Sanchez-Bermudez, S. Scheithauer, M. Schöller, N. Schuler, J. Spyromilio, O. Straub, C. Straubmeier, E. Sturm, L. J. Tacconi, K. R. W. Tristram, F. Vincent, S. von Fellenberg, I. Wank, I. Waisberg, F. Widmann, E. Wieprecht, M. Wiest, E. Wiezorrek, J. Woillez, S. Yazici, D. Ziegler, and G. Zins. Detection of the gravitational redshift in the orbit of the star S2 near the Galactic centre massive black hole. *A&A*, 615:15, 2018.

[GET+09] S. Gillessen, F. Eisenhauer, S. Trippe, T. Alexander, R. Genzel, F. Martins, and T. Ott. Monitoring stellar orbits around the massive black hole in the Galactic center. *Astrophysical Journal*, 692(2):1075–1109, 2009.

[GHP+15] Pierre Grüning, Hubert Halloin, Pierre Prat, Sylvain Baron, Julien Brossard, Christelle Buy, Antoine Petiteau, Gerhard Heinzel, and Iouri Bykov. Status of the eLISA on table (LOT) electro-optical simulator for space based, long arms interferometers. *Experimental Astronomy*, 39(2):281–302, 2015.

[HAA+10] G Hobbs, A Archibald, Z Arzoumanian, D Backer, M Bailes, N D R Bhat, M Burgay, S Burke-Spolaor, D Champion, I Cognard, W Coles, J Cordes, P Demorest, G Desvignes, R D Ferdman, L Finn, P Freire, M Gonzalez, J Hessels, A Hotan, G Janssen, F Jenet, A Jessner, C Jordan, V Kaspi, M Kramer, V Kondratiev, J Lazio, K Lazaridis, K J Lee, Y Levin, A Lommen, D Lorimer, R Lynch, A Lyne, R Manchester, M McLaughlin, D Nice, S Oslowski, M Pilia, A Possenti, M Purver, S Ransom, J Reynolds, S Sanidas, J Sarkissian, A Sesana, R Shannon, X Siemens, I Stairs, B Stappers, D Stinebring, G Theureau, R van Haasteren, W van Straten, J P W

Verbiest, D R B Yardley, and X P You. The International Pulsar Timing Array project: using pulsars as a gravitational wave detector. *Classical and Quantum Gravity*, 27(8):084013, apr 2010.

[Hal18] Hubert Halloin. Note on Decimation and Interpolation Filters for LISA Simulation. Technical report, 2018.

[Hei18] Gerhard Heinzel. LISA Frequency Planning. Technical report, 2018.

[Hel01] Ronald W. Hellings. Elimination of clock jitter noise in spaceborne laser interferometers. *Physical Review D - Particles, Fields, Gravitation and Cosmology*, 2001.

[Hen07] Martin Hendry. An Introduction to General Relativity, Gravitational Waves and Detection Principles, 2007.

[HT98] Scott A. Hughes and Kip S. Thorne. Seismic gravity-gradient noise in interferometric gravitational-wave detectors. *Physical Review D*, 58(12):122002, nov 1998.

[KBS+16] Antoine Klein, Enrico Barausse, Alberto Sesana, Antoine Petiteau, Emanuele Berti, Stanislav Babak, Jonathan Gair, Sofiane Aoudia, Ian Hinder, Frank Ohme, and Barry Wardell. Science with the space-based interferometer eLISA: Supermassive black hole binaries. *Physical Review D*, 93(2), 2016.

[Le 59] Urbain Le Verrier. Lettre de M. Le Verrier à M. Faye sur la théorie de Mercure et sur le mouvement du périhélie de cette planète, 1859.

[LHB+17] M. Laporte, H. Halloin, E. Bréelle, C. Buy, P. Grüning, and P. Prat. Status of the LISA on Table experiment: A electro-optical simulator for LISA. *Journal of Physics: Conference Series*, 840(1), 2017.

[LIS18a] LISA Instrument Group. LISA Payload Definition Document. Technical Report 2.1, 2018.

[LIS18b] LISA Instrument Group. LISA Performance Model and Error Budget. Technical report, 2018.

[LIS19a] LISA Data Challenge Working Group. LISA Data Challenge Manual. Technical report, 2019.

[LIS19b] LISA Simulation Working Group. LISA End-to-End Performance Simulator Requirements. Technical report, 2019.

[LL18] LISA Simulation Working Group and LISA Science Study Team. LISA Science Requirements Document. Technical Report May 2018, 2018.

[MHA+16] D. V. Martynov, E. D. Hall, B. P. Abbott, R. Abbott, T. D. Abbott, C. Adams, R. X. Adhikari, R. A. Anderson, S. B. Anderson, K. Arai, M. A. Arain, S. M. Aston, L. Austin, S. W. Ballmer, M. Barbet, D. Barker, B. Barr, L. Barsotti, J. Bartlett, M. A. Barton, I. Bartos, J. C. Batch, A. S. Bell, I. Belopolski, J. Bergman, J. Betzwieser, G. Billingsley, J. Birch, S. Biscans, C. Biwer, E. Black, C. D. Blair, C. Bogan, C. Bond, R. Bork, D. O. Bridges, A. F. Brooks, D. D. Brown, L. Carbone, C. Celerier, G. Ciani, F. Clara, D. Cook, S. T. Countryman, M. J. Cowart, D. C. Coyne, A. Cumming, L. Cunningham, M. Damjanic, R. Dannenberg, K. Danzmann, C. F. Da Silva Costa, E. J. Daw, D. DeBra, R. T. DeRosa, R. DeSalvo, K. L. Dooley, S. Doravari, J. C. Driggers, S. E. Dwyer, A. Effler, T. Etzel, M. Evans, T. M. Evans, M. Factourovich, H. Fair, D. Feldbaum, R. P. Fisher, S. Foley, M. Frede, A. Freise, P. Fritschel, V. V. Frolov, P. Fulda, M. Fyffe, V. Galdi, J. A. Giaime, K. D. Giardina, J. R. Gleason, R. Goetz, S. Gras, C. Gray, R. J. S. Greenhalgh, H. Grote, C. J. Guido, K. E. Gushwa, E. K. Gustafson, R. Gustafson, G. Hammond, J. Hanks, J. Hanson, T. Hardwick, G. M. Harry, K. Haughian, J. Heefner, M. C. Heintze, A. W. Heptonstall, D. Hoak, J. Hough, A. Ivanov, K. Izumi, M. Jacobson, E. James, R. Jones, S. Kandhasamy, S. Karki, M. Kasprzack, S. Kaufer, K. Kawabe, W. Kells, N. Kijbunchoo, E. J. King, P. J. King, D. L. Kinzel, J. S. Kissel, K. Kokeyama, W. Z. Korth, G. Kuehn, P. Kwee, M. Landry, B. Lantz, A. Le Roux, B. M. Levine, J. B. Lewis, V. Lhuillier, N. A. Lockerbie, M. Lormand, M. J. Lubinski, A. P. Lundgren, T. MacDonald, M. MacInnis, D. M. Macleod, M. Mageswaran, K. Mailand, S. Márka, Z. Márka, A. S. Markosyan, E. Maros, I. W. Martin, R. M. Martin, J. N. Marx, K. Mason, T. J. Massinger, F. Matichard, N. Mavalvala, R. McCarthy, D. E. McClelland, S. McCormick, G. McIntyre, J. McIver, E. L. Merilh, M. S. Meyer, P. M. Meyers, J. Miller, R. Mittleman, G. Moreno, C. L. Mueller, G. Mueller, A. Mullavey, J. Munch, P. G. Murray, L. K. Nuttall, J. Oberling, J. O'Dell, P. Oppermann, Richard J. Oram, B. O'Reilly, C. Osthelder, D. J. Ottaway, H. Overmier, J. R. Palamos, H. R. Paris, W. Parker, Z. Patrick, A. Pele, S. Penn, M. Phelps, M. Pickenpack, V. Pierro, I. Pinto, J. Poeld, M. Principe, L. Prokhorov, O. Puncken,

V. Quetschke, E. A. Quintero, F. J. Raab, H. Radkins, P. Raffai, C. R. Ramet, C. M. Reed, S. Reid, D. H. Reitze, N. A. Robertson, J. G. Rollins, V. J. Roma, J. H. Romie, S. Rowan, K. Ryan, T. Sadecki, E. J. Sanchez, V. Sandberg, V. Sannibale, R. L. Savage, R. M. S. Schofield, B. Schultz, P. Schwinberg, D. Sellers, A. Sevigny, D. A. Shaddock, Z. Shao, B. Shapiro, P. Shawhan, D. H. Shoemaker, D. Sigg, B. J. J. Slagmolen, J. R. Smith, M. R. Smith, N. D. Smith-Lefebvre, B. Sorazu, A. Staley, A. J. Stein, A. Stochino, K. A. Strain, R. Taylor, M. Thomas, P. Thomas, K. A. Thorne, E. Thrane, K. V. Tokmakov, C. I. Torrie, G. Traylor, G. Vajente, G. Valdes, A. A. van Veggel, M. Vargas, A. Vecchio, P. J. Veitch, K. Venkateswara, T. Vo, C. Vorvick, S. J. Waldman, M. Walker, R. L. Ward, J. Warner, B. Weaver, R. Weiss, T. Welborn, P. Weßels, C. Wilkinson, P. A. Willems, L. Williams, B. Willke, I. Wilmut, L. Winkelmann, C. C. Wipf, J. Worden, G. Wu, H. Yamamoto, C. C. Yancey, H. Yu, L. Zhang, M. E. Zucker, and J. Zweizig. Sensitivity of the Advanced LIGO detectors at the beginning of gravitational wave astronomy. *Physical Review D*, 93(11):112004, jun 2016.

[NKDV06] K. Rajesh Nayak, S. Koshti, S. V. Dhurandhar, and J. Y. Vinet. On the minimum flexing of LISA's arms. *Classical and Quantum Gravity*, 23(5):1763–1778, 2006.

[NYZ01] G. Nelemans, L. R. Yungelson, and S. F. Portegies Zwart. The gravitational wave signal from the Galactic disk population of binaries containing two compact objects. *A&A*, 375:890–898, 2001.

[OHD12] Markus Otto, Gerhard Heinzel, and Karsten Danzmann. TDI and clock noise removal for the split interferometry configuration of LISA. *Classical and Quantum Gravity*, 29(20):205003, oct 2012.

[Ott15] Markus Otto. *Time-Delay Interferometry Simulations for the Laser Interferometer Space Antenna*. PhD thesis, Gottfried Wilhelm Leibniz Universität Hannover, 2015.

[PAH+08] Antoine Petiteau, Gérard Auger, Hubert Halloin, Olivier Jeannin, Eric Plagnol, Sophie Pireaux, Tania Regimbau, and Jean Yves Vinet. LISACode: A scientific simulator of LISA. *Physical Review D - Particles, Fields, Gravitation and Cosmology*, 77(2):1–11, 2008.

[Pet08] Antoine Petiteau. *De la simulation de LISA à l'analyse des données*. PhD thesis, jun 2008.

[RCP04] Louis J. Rubbo, Neil J. Cornish, and Olivier Poujade. Forward modeling of space-borne gravitational wave detectors. *Physical Review D - Particles, Fields, Gravitation and Cosmology*, 69(8):14, 2004.

[SBK+19] B. S. Sathyaprakash, Matthew Bailes, Mansi M. Kasliwal, Samaya Nissanke, Shreya Anand, Igor Andreoni, Monica Colpi, Michael Coughlin, Evan Hall, Vicky Kalogera, Dan Kasen, and Alberto Sesana. Multimessenger Universe with Gravitational Waves from Binaries. Technical report, mar 2019.

[SBP+19] Thomas S. Schwarze, Germán Fernández Barranco, Daniel Penkert, Marina Kaufer, Oliver Gerberding, and Gerhard Heinzel. Picometer-Stable Hexagonal Optical Bench to Verify LISA Phase Extraction Linearity and Precision. *Physical Review Letters*, 122(8), 2019.

[Sch12] Bernard Schutz. *A First Course in General Relativity*. 2012.

[Ses16] Alberto Sesana. Prospects for Multiband Gravitational-Wave Astronomy after GW150914. *Physical Review Letters*, 116(23), 2016.

[SOG+02] R. Schödel, T. Ott, R. Genzel, R. Hofmann, M. Lehnert, A. Eckart, N. Mouawad, T. Alexander, M. J. Reid, R. Lenzen, M. Hartung, F. Lacombe, D. Rouan, E. Gendron, G. Rousset, A. M. Lagrange, W. Brandner, N. Ageorges, C. Lidman, A. F M Moorwood, J. Spyromilio, N. Hubin, and K. M. Menten. A star in a 15.2-year orbit around the supermassive black hole at the centre of the Milky Way. *Nature*, 419(6908):694–696, 2002.

[Spe17] Spectratime. iSpace+® Space-Qualified MO Short Spec. Technical report, 2017.

[STEA03] Daniel A. Shaddock, Massimo Tinto, Frank B. Estabrook, and J. W. Armstrong. Data combinations accounting for LISA spacecraft motion. *Physical Review D*, 68(6):1–4, 2003.

[SWSV04] D. A. Shaddock, B. Ware, R. E. Spero, and M. Vallisneri. Postprocessed time-delay interferometry for LISA. *Physical Review D - Particles, Fields, Gravitation and Cosmology*, 2004.

[TA99] Massimo Tinto and J. W. Armstrong. Cancellation of laser noise in an unequal-arm interferometer detector of gravitational radiation. *Physical Review D - Particles, Fields, Gravitation and Cosmology*, 1999.

[TEA02] Massimo Tinto, F. B. Estabrook, and J. W. Armstrong. Time-delay interferometry for LISA. *Physical Review D - Particles, Fields, Gravitation and Cosmology*, 2002.

[TEA04] Massimo Tinto, F. B. Estabrook, and J. W. Armstrong. Time delay interferometry with moving spacecraft arrays. *Physical Review D - Particles, Fields, Gravitation and Cosmology*, 2004.

[TFD+11] R. Thompson, W. M. Folkner, G. De Vine, W. M. Klipstein, K. McKenzie, R. Spero, N. Yu, M. Stephens, J. Leitch, R. Pierce, T. T.Y. Lam, and D. A. Shaddock. A flight-like optical reference cavity for GRACE follow-on laser frequency stabilization. In *Proceedings of the IEEE International Frequency Control Symposium and Exposition*, 2011.

[TH18] Massimo Tinto and Olaf Hartwig. Time-delay interferometry and clock-noise calibration. *Physical Review D*, 2018.

[TVA05] Massimo Tinto, Michele Vallisneri, and J. W. Armstrong. Time-delay interferometric ranging for space-borne gravitational-wave detectors. *Physical Review D - Particles, Fields, Gravitation and Cosmology*, 2005.

[Val05a] Michele Vallisneri. Geometric time delay interferometry. *Physical Review D - Particles, Fields, Gravitation and Cosmology*, 2005.

[Val05b] Michele Vallisneri. Synthetic LISA: Simulating time delay interferometry in a model LISA. *Physical Review D - Particles, Fields, Gravitation and Cosmology*, 71(2):022001, jan 2005.

[VN02] J. Y. Vinet and K Rajesh Nayak. Algebraic approach to time-delay data analysis for LISA. *Physical Review D - Particles, Fields, Gravitation and Cosmology*, 65(10):16, 2002.

[Vol10] Marta Volonteri. Formation of supermassive black holes, jul 2010.

[Wan17] Yan Wang. *On inter-satellite laser ranging, clock synchronization and gravitational wave data analysis*. PhD thesis, 2017.

[WGR10] Gregory Weaver, Jeffrey Garstecki, and Samuel Reynolds. The performance of ultra-stable oscillators for the gravity recovery and interior laboratory (GRAIL). In *42nd Annual Precise Time and Time Interval (PTTI) Systems and Applications Meeting 2010*, pages 369–379, 2010.

[WHD14] Yan Wang, Gerhard Heinzel, and Karsten Danzmann. First stage of LISA data processing: Clock synchronization and arm-length determination via a hybrid-extended Kalman filter. *Physical Review D - Particles, Fields, Gravitation and Cosmology*, 90(6), 2014.